

---

Doctoral Dissertations

Student Theses and Dissertations

---

Summer 2019

## Designing novel multinary transition metal selenides as high-efficiency oxygen evolution reaction electrocatalysts and investigating surface properties

Xi Cao

Follow this and additional works at: [https://scholarsmine.mst.edu/doctoral\\_dissertations](https://scholarsmine.mst.edu/doctoral_dissertations)

 Part of the [Inorganic Chemistry Commons](#)

Department: Chemistry

---

### Recommended Citation

Cao, Xi, "Designing novel multinary transition metal selenides as high-efficiency oxygen evolution reaction electrocatalysts and investigating surface properties" (2019). *Doctoral Dissertations*. 3089.  
[https://scholarsmine.mst.edu/doctoral\\_dissertations/3089](https://scholarsmine.mst.edu/doctoral_dissertations/3089)

This thesis is brought to you by Scholars' Mine, a service of the Missouri S&T Library and Learning Resources. This work is protected by U. S. Copyright Law. Unauthorized use including reproduction for redistribution requires the permission of the copyright holder. For more information, please contact [scholarsmine@mst.edu](mailto:scholarsmine@mst.edu).

DESIGNING NOVEL MULTINARY TRANSITION METAL SELENIDES AS HIGH-  
EFFICIENCY OXYGEN EVOLUTION REACTION ELECTROCATALYSTS AND  
INVESTIGATING SURFACE PROPERTIES

by

XI CAO

A DISSERTATION

Presented to the Faculty of the Graduate School of the

MISSOURI UNIVERSITY OF SCIENCE AND TECHNOLOGY

In Partial Fulfillment of the Requirements for the Degree

DOCTOR OF PHILOSOPHY

in

CHEMISTRY

2019

Approved by

Manashi Nath, Advisor  
Klaus Woelk  
Jeffrey G. Winiarz  
Amitava Choudhury  
Julia E. Medvedeva  
Xinhua Liang

© 2019

Xi Cao

All Rights Reserved

## PUBLICATION DISSERTATION OPTION

This dissertation consists of the following six articles, which have been published or submitted for publication as follows:

Paper I: Pages 27 – 79 has been published in *ACS Catal.*, 2018, 8, pp 8273–8289.

Paper II: Pages 80 – 125 has been published in *J. Mater. Chem. A*, 2019, 7, pp 9877–9889.

Paper III: Pages 126 – 169 has been published in *ACS Sustainable Chem. Eng.*, 2019, 7, pp 9588–9600.

Paper IV: Pages 170 – 217 has been submitted to *ACS Appl. Mater. Interfaces*, 2019.

Paper V: Pages 218 – 252 has been submitted to *ACS Appl. Energy Mater.*, 2019.

Paper VI: Pages 253 – 272 has been invited as a contribution to *AIMS Materials Science*, 2019.

## ABSTRACT

Water splitting has been widely considered to be an efficient way to generate sustainable and renewable energy resources in fuel cells, metal-air batteries and other energy conversion devices. Exploring efficient electrocatalysts to expedite the anodic oxygen evolution reaction (OER) is a crucial task that needs to be addressed to boost the practical application of water splitting. This research focuses on the identification of OER electrocatalysts by systematically designing non-stoichiometric mixed transition metal-based selenide OER electrocatalysts through combinatorial electrodeposition and investigation of selenide-based naturally occurring minerals as effective OER electrocatalyst. Paper I describes the study of Ni-Fe-Co selenides as OER catalysts by combinatorial electrodeposition and the best composition  $(\text{Ni}_{0.25}\text{Fe}_{0.68}\text{Co}_{0.07})_3\text{Se}_4$  with the lowest overpotential. Paper II presents the exploration of Co-Ni-Cu selenide system through combinatorial electrodeposition of 66 different compositions as highly efficient OER electrocatalysts and the best quaternary  $(\text{Co}_{0.21}\text{Ni}_{0.25}\text{Cu}_{0.54})_3\text{Se}_2$  showing a similar crystal structure as its parent compound  $\text{Cu}_3\text{Se}_2$ . Paper III introduces the Fe-Co-Cu selenide system investigated through combinatorial electrodeposition, and the optimal quaternary is identified as  $(\text{Fe}_{0.48}\text{Co}_{0.38}\text{Cu}_{0.14})\text{Se}$ . Paper IV presents  $\text{CuCo}_2\text{Se}_4$  as high-efficiency bifunctional electrocatalyst for full water splitting and conducted DFT calculation of surface dependent OER activity on (100) and (111) facets. Paper V introduces the hydrothermal synthesis of naturally-occurring mineral Tyrrellite  $\text{Cu}(\text{Co}_{0.68}\text{Ni}_{0.32})_2\text{Se}_4$  as highly-efficient OER electrocatalyst. Paper VI describes three naturally occurring copper selenides ( $\text{Cu}_2\text{Se}$ ,  $\text{Cu}_3\text{Se}_2$  and  $\text{CuSe}_2$ ) as OER electrocatalyst and performed DFT calculation to understand their catalytic activity trend.

## ACKNOWLEDGMENTS

I would like to thank my advisor Dr. Manashi Nath for the opportunity to work closely with her as well as her insightful guidance and continuous encouragement throughout my PhD research. I continue to admire her energy and wealth of knowledge and I will never forget all her supports of my years in Missouri S&T. I will always be grateful to Dr. Julia Medvedeva for her computational calculations and her patience in helping me understand the DFT fundamentals. I have been so fortunate to work with Dr. Klaus Woelk and Dr. Jefferey Winiarz in coordinating the general chemistry lab. Their teaching and working philosophies had a significant influence on me and are invaluable to me for my future life. I would also like to express my gratitude to the advice from Dr. Amitava Choudhury and Dr. Xinhua Liang. Without valuable comments and guidance from them, I would have not been able to complete my dissertation, and I thank all my committee members.

I would like to thank my fellow research labmates: Dr. Jahangir Masud, Emily Johnson, Dr. Abdurazag T. Swesi, Dr. Wipula P.R. Liyange, Maalavan Arivu, Bahareh Golrokhamin, Umanga de Silva, Siddesh Umaphathi, Apurv Saxena and Rajarshi Kar for their support in the lab. I would like to thank Dr. Eric W. Bohannan for his exceptional assistance in XRD measurements, and Dr. Brian Porter for his superb technical support in XPS analysis.

Last but not the least, I would like to express my deepest gratitude to my families for their unconditional love throughout my life and for supporting me to pursue my goals.

## TABLE OF CONTENTS

|                                                                                                                                                                                             | Page |
|---------------------------------------------------------------------------------------------------------------------------------------------------------------------------------------------|------|
| PUBLICATION DISSERTATION OPTION .....                                                                                                                                                       | iii  |
| ABSTRACT .....                                                                                                                                                                              | iv   |
| ACKNOWLEDGMENTS .....                                                                                                                                                                       | v    |
| LIST OF ILLUSTRATIONS .....                                                                                                                                                                 | x    |
| LIST OF TABLES .....                                                                                                                                                                        | xvii |
| <br>SECTION                                                                                                                                                                                 |      |
| 1. INTRODUCTION .....                                                                                                                                                                       | 1    |
| 1.1. WATER SPLITTING.....                                                                                                                                                                   | 5    |
| 1.1.1. Water Splitting – A Brief History. ....                                                                                                                                              | 5    |
| 1.1.2. Mechanism of Water Splitting. ....                                                                                                                                                   | 5    |
| 1.1.3. Hydrogen Evolution Reaction (HER). ....                                                                                                                                              | 8    |
| 1.1.4. Oxygen Evolution Reaction (OER).....                                                                                                                                                 | 9    |
| 1.2. OXYGEN EVOLUTION REACTION ELECTROCATALYSTS .....                                                                                                                                       | 10   |
| 1.2.1. Merits and Criteria of OER Electrocatalysts. ....                                                                                                                                    | 10   |
| 1.2.2. Current Status of OER Electrocatalysts.....                                                                                                                                          | 12   |
| 1.2.3. Pure Transition Metal Selenides. ....                                                                                                                                                | 15   |
| 1.2.4. Mixed Transition Metal Selenides. ....                                                                                                                                               | 16   |
| 1.3. COMBINATORIAL METHOD .....                                                                                                                                                             | 21   |
| <br>PAPER                                                                                                                                                                                   |      |
| I. PHASE EXPLORATION AND IDENTIFICATION OF MULTINARY<br>TRANSITION METAL SELENIDES AS HIGH-EFFICIENCY OXYGEN<br>EVOLUTION ELECTROCATALYSTS THROUGH COMBINATORIAL<br>ELECTRODEPOSITION ..... | 27   |

|                                                                                                                                                                                      |     |
|--------------------------------------------------------------------------------------------------------------------------------------------------------------------------------------|-----|
| ABSTRACT.....                                                                                                                                                                        | 27  |
| 1. INTRODUCTION .....                                                                                                                                                                | 29  |
| 2. EXPERIMENTAL SECTION .....                                                                                                                                                        | 33  |
| 3. RESULTS AND DISCUSSION.....                                                                                                                                                       | 37  |
| 4. CONCLUSIONS.....                                                                                                                                                                  | 65  |
| AUTHOR INFORMATION.....                                                                                                                                                              | 65  |
| ACKNOWLEDGEMENTS .....                                                                                                                                                               | 66  |
| SUPPORTING INFORMATION.....                                                                                                                                                          | 66  |
| REFERENCES .....                                                                                                                                                                     | 71  |
| <br>                                                                                                                                                                                 |     |
| II. IDENTIFYING HIGH-EFFICIENCY OXYGEN EVOLUTION<br>ELECTROCATALYSTS FROM Co-Ni-Cu BASED SELENIDES THROUGH<br>COMBINATORIAL ELECTRODEPOSITION .....                                  | 80  |
| ABSTRACT.....                                                                                                                                                                        | 80  |
| 1. INTRODUCTION .....                                                                                                                                                                | 81  |
| 2. EXPERIMENTAL.....                                                                                                                                                                 | 85  |
| 3. RESULTS AND DISCUSSION.....                                                                                                                                                       | 89  |
| 4. CONCLUSIONS.....                                                                                                                                                                  | 108 |
| CONFLICT OF INTEREST .....                                                                                                                                                           | 109 |
| ACKNOWLEDGEMENTS .....                                                                                                                                                               | 109 |
| SUPPORTING INFORMATION.....                                                                                                                                                          | 110 |
| REFERENCES .....                                                                                                                                                                     | 121 |
| <br>                                                                                                                                                                                 |     |
| III. EXPANDING MULTINARY SELENIDE BASED HIGH-EFFICIENCY<br>OXYGEN EVOLUTION ELECTROCATALYSTS THROUGH<br>COMBINATORIAL ELECTRODEPOSITION: CASE STUDY WITH<br>Fe-Cu-Co SELENIDES ..... | 126 |
| ABSTRACT.....                                                                                                                                                                        | 126 |
| 1. INTRODUCTION .....                                                                                                                                                                | 127 |



|                                                                                                                                                                            |            |
|----------------------------------------------------------------------------------------------------------------------------------------------------------------------------|------------|
| 2. EXPERIMENTAL SECTION .....                                                                                                                                              | 132        |
| 3. RESULTS AND DISCUSSION .....                                                                                                                                            | 135        |
| 4. CONCLUSIONS.....                                                                                                                                                        | 153        |
| ASSOCIATED CONTENT .....                                                                                                                                                   | 154        |
| SUPPORTING INFORMATION.....                                                                                                                                                | 155        |
| REFERENCES .....                                                                                                                                                           | 162        |
| <b>IV. COPPER COBALT SELENIDE AS A HIGH-EFFICIENCY BIFUNCTIONAL<br/>ELECTROCATALYST FOR OVERALL WATER SPLITTING: COMBINED<br/>EXPERIMENTAL AND THEORETICAL STUDY .....</b> | <b>170</b> |
| ABSTRACT.....                                                                                                                                                              | 170        |
| 1. INTRODUCTION .....                                                                                                                                                      | 171        |
| 2. EXPERIMENTAL AND COMPUTATIONAL METHODS .....                                                                                                                            | 176        |
| 3. RESULTS AND DISCUSSION .....                                                                                                                                            | 179        |
| 4. CONCLUSIONS.....                                                                                                                                                        | 198        |
| ASSOCIATED CONTENT .....                                                                                                                                                   | 200        |
| SUPPORTING INFORMATION.....                                                                                                                                                | 201        |
| REFERENCES .....                                                                                                                                                           | 209        |
| <b>V. TYRRELLITE AS A NOVEL AND SUSTAINABLE EFFICIENT<br/>ELECTROCATALYSTS FOR OXYGEN EVOLUTION GENERATION.....</b>                                                        | <b>218</b> |
| ABSTRACT.....                                                                                                                                                              | 218        |
| 1. INTRODUCTION .....                                                                                                                                                      | 219        |
| 2. EXPERIMENTAL AND COMPUTATIONAL METHODS .....                                                                                                                            | 222        |
| 3. RESULTS AND DISCUSSION .....                                                                                                                                            | 225        |
| 4. CONCLUSIONS.....                                                                                                                                                        | 239        |
| ASSOCIATED CONTENT .....                                                                                                                                                   | 239        |
| SUPPORTING INFORMATION.....                                                                                                                                                | 241        |

|                                                                                                                                                                                                                              |     |
|------------------------------------------------------------------------------------------------------------------------------------------------------------------------------------------------------------------------------|-----|
| REFERENCES .....                                                                                                                                                                                                             | 246 |
| VI. NATURALLY OCCURRING MINERALS AS NOVEL OXYGEN<br>EVOLUTION REACTION ELECTROCATALYSTS: BERZELIANITE,<br>UMANGITE AND KRUT'AITE (Cu <sub>2</sub> Se, Cu <sub>3</sub> Se <sub>2</sub> AND CuSe <sub>2</sub> ) GENERATION ... | 253 |
| ABSTRACT .....                                                                                                                                                                                                               | 253 |
| 1. TEXT .....                                                                                                                                                                                                                | 253 |
| ACKNOWLEDGEMENT .....                                                                                                                                                                                                        | 263 |
| SUPPORTING INFORMATION .....                                                                                                                                                                                                 | 264 |
| REFERENCES .....                                                                                                                                                                                                             | 269 |
| SECTION                                                                                                                                                                                                                      |     |
| 2. CONCLUSIONS .....                                                                                                                                                                                                         | 273 |
| REFERENCES .....                                                                                                                                                                                                             | 277 |
| VITA .....                                                                                                                                                                                                                   | 294 |

## LIST OF ILLUSTRATIONS

| SECTION                                                                                                                                                                                                                                                                                                                                                                                                                                                                                                                                                  | Page |
|----------------------------------------------------------------------------------------------------------------------------------------------------------------------------------------------------------------------------------------------------------------------------------------------------------------------------------------------------------------------------------------------------------------------------------------------------------------------------------------------------------------------------------------------------------|------|
| Figure 1.1. Schematic of sustainable energy future. <sup>3</sup> .....                                                                                                                                                                                                                                                                                                                                                                                                                                                                                   | 2    |
| Figure 1.2. Diagram of a proton conducting solid oxide fuel cell. Designed by R. Dervisoglu.(Source: Wekipedia) .....                                                                                                                                                                                                                                                                                                                                                                                                                                    | 3    |
| Figure 1.3. Schematic representation of the water splitting via electrolysis, utilizing electricity derived from renewable sources such as wind and solar, and photoelectrolysis, where the electrodes directly harvest the solar energy.....                                                                                                                                                                                                                                                                                                            | 4    |
| Figure 1.4. Polarization curves of oxygen and hydrogen reactant for the electrolysis of water. ....                                                                                                                                                                                                                                                                                                                                                                                                                                                      | 6    |
| Figure 1.5. Two-cell conventional alkaline electrolyzer configuration. <sup>46</sup> .....                                                                                                                                                                                                                                                                                                                                                                                                                                                               | 8    |
| Figure 1.6. The volcano relation for pure metals in acidic solution. <sup>63</sup> .....                                                                                                                                                                                                                                                                                                                                                                                                                                                                 | 9    |
| Figure 1.7. Volcano plot showing activity for O <sub>2</sub> production metal oxide surfaces versus the enthalpy of transition of the oxide in acidic and basic solution. ....                                                                                                                                                                                                                                                                                                                                                                           | 13   |
| Figure 1.8. Benchmarking OER electrocatalysts at overpotential of 10 mA cm <sup>-2</sup> in alkaline medium. <sup>82</sup> .....                                                                                                                                                                                                                                                                                                                                                                                                                         | 14   |
| Figure 1.9. Trend in overpotential for OER is shown as a function of the 3d transition elements. ....                                                                                                                                                                                                                                                                                                                                                                                                                                                    | 17   |
| Figure 1.10. (c) CV scans of Ni <sub>1-x</sub> Fe <sub>x</sub> (OH) <sub>2</sub> /Ni <sub>1-x</sub> Fe <sub>x</sub> OOH films doped with different amount of Fe on IDA electrodes. (d) Conductivity data (points with solid connecting lines) for the same films. The potential onset of conductivity correlates with the position of the hydroxide/ oxyhydroxide oxidation wave shown as dotted lines for each film. The inset shows an enlarged region to make the conductivity turn-on for the rigorously Fe-free film apparent. <sup>124</sup> ..... | 18   |
| Figure 1.11. Experimental and theoretical study of catalytic activity of NiCo <sub>2</sub> Se <sub>4</sub> .....                                                                                                                                                                                                                                                                                                                                                                                                                                         | 20   |
| Figure 1.12. The amino acids used in couplings are represented by yellow, blue and red circles. <sup>183</sup> .....                                                                                                                                                                                                                                                                                                                                                                                                                                     | 22   |
| Figure 1.13. Contour plots of kinetic parameters extracted from Tafel plots recorded on 21 independent amorphous (mixed-) metal oxide films .....                                                                                                                                                                                                                                                                                                                                                                                                        | 23   |

|              |                                                                                                                                                                                                                                                                                                                                                                                                                                                                                                                                                                                                                                                            |    |
|--------------|------------------------------------------------------------------------------------------------------------------------------------------------------------------------------------------------------------------------------------------------------------------------------------------------------------------------------------------------------------------------------------------------------------------------------------------------------------------------------------------------------------------------------------------------------------------------------------------------------------------------------------------------------------|----|
| Figure 1.14. | Performance map of (Ni–Fe–Co–Ce)O <sub>x</sub> oxygen evolution catalysts.....                                                                                                                                                                                                                                                                                                                                                                                                                                                                                                                                                                             | 24 |
| Figure 1.15. | Overpotential at 10 mA cm <sup>-2</sup> of all OER electrocatalysts described in this dissertation.....                                                                                                                                                                                                                                                                                                                                                                                                                                                                                                                                                    | 25 |
| PAPER I      |                                                                                                                                                                                                                                                                                                                                                                                                                                                                                                                                                                                                                                                            |    |
| Figure 1.    | Schematic of combinatorial electrodeposition..                                                                                                                                                                                                                                                                                                                                                                                                                                                                                                                                                                                                             | 34 |
| Figure 2.    | SEM images and elemental compositions by EDS of most active electrocatalyst from different groups comprising three binaries compositions.....                                                                                                                                                                                                                                                                                                                                                                                                                                                                                                              | 38 |
| Figure 3.    | Linear Sweep voltammetries (LSVs) of ternary metal selenides along the edges of the trigonal phase diagram..                                                                                                                                                                                                                                                                                                                                                                                                                                                                                                                                               | 40 |
| Figure 4.    | Contour plots of overpotential $\eta$ (in units of V) at (a) onset of OER activity, and (b) current density of 10 mA cm <sup>-2</sup> for the entire Ni-Fe-Co trigonal phase space.....                                                                                                                                                                                                                                                                                                                                                                                                                                                                    | 42 |
| Figure 5.    | (a) LSVs of 7 best quaternary compositions measured in N <sub>2</sub> saturated 0.3 M KOH solution at a scan rate of 10 mV s <sup>-1</sup> , (b) Tafel plots of the catalysts. ....                                                                                                                                                                                                                                                                                                                                                                                                                                                                        | 43 |
| Figure 6.    | (a) Polarization curves of (Ni <sub>0.25</sub> Fe <sub>0.68</sub> Co <sub>0.07</sub> ) <sub>3</sub> Se <sub>4</sub> compared to the three binary catalyst films. (b)SEM image of (Ni <sub>0.25</sub> Fe <sub>0.68</sub> Co <sub>0.07</sub> ) <sub>3</sub> Se <sub>4</sub> film deposited for 300 s. XPS spectra of as deposited film (Ni <sub>0.25</sub> Fe <sub>0.68</sub> Co <sub>0.07</sub> ) <sub>3</sub> Se <sub>4</sub> . (c) Fe 2p <sub>3/2</sub> and 2p <sub>1/2</sub> peaks; (d) Co 2p <sub>3/2</sub> and 2p <sub>1/2</sub> peaks; (e) Ni 2p <sub>1/2</sub> and 2p <sub>3/2</sub> peaks; (f)Se 3d <sub>5/2</sub> and 3d <sub>3/2</sub> peaks..... | 50 |
| Figure 7.    | Cyclic voltammograms measured for the (Ni <sub>0.25</sub> Fe <sub>0.68</sub> Co <sub>0.07</sub> ) <sub>3</sub> Se <sub>4</sub> thin film in N <sub>2</sub> saturated 0.3 M KOH solution at different scan rates from 25 to 150 mV s <sup>-1</sup> ..                                                                                                                                                                                                                                                                                                                                                                                                       | 51 |
| Figure 8.    | Faradaic efficiency of the (Ni <sub>0.25</sub> Fe <sub>0.68</sub> Co <sub>0.07</sub> ) <sub>3</sub> Se <sub>4</sub> catalyst..                                                                                                                                                                                                                                                                                                                                                                                                                                                                                                                             | 53 |
| Figure 9.    | (a) Chronoamperometry plot of (Ni <sub>0.25</sub> Fe <sub>0.68</sub> Co <sub>0.07</sub> ) <sub>3</sub> Se <sub>4</sub> for 8 h at 0.50 V vs. Ag AgCl (sat.) applied potential. (b) Comparison of LSVs before and after 8 h stability in N <sub>2</sub> saturated 0.3 M KOH solution. (c) SEM image of (Ni <sub>0.25</sub> Fe <sub>0.68</sub> Co <sub>0.07</sub> ) <sub>3</sub> Se <sub>4</sub> after chronoamperometry. (d-g) XPS spectrum of (Ni <sub>0.25</sub> Fe <sub>0.68</sub> Co <sub>0.07</sub> ) <sub>3</sub> Se <sub>4</sub> after chronoamperometry.....                                                                                        | 57 |
| Figure 10.   | Crystal structures of 2×2×2 supercells of (a) Ni <sub>3</sub> Se <sub>2</sub> , (b) Fe <sub>3</sub> Se <sub>4</sub> , (c) (Ni <sub>0.37</sub> Fe <sub>0.36</sub> Co <sub>0.27</sub> ) <sub>3</sub> Se <sub>4</sub> and (d) (Ni <sub>0.25</sub> Fe <sub>0.68</sub> Co <sub>0.07</sub> ) <sub>3</sub> Se <sub>4</sub> .....                                                                                                                                                                                                                                                                                                                                  | 58 |
| Figure 11.   | A slab model of Ni <sub>3</sub> Se <sub>2</sub> supercell with 2×2×2 lattices.....                                                                                                                                                                                                                                                                                                                                                                                                                                                                                                                                                                         | 59 |

|            |                                                                                                                                                                                                                                                                                                                                                                                                                           |    |
|------------|---------------------------------------------------------------------------------------------------------------------------------------------------------------------------------------------------------------------------------------------------------------------------------------------------------------------------------------------------------------------------------------------------------------------------|----|
| Figure 12. | (a) Original crystal structure of Ni <sub>3</sub> Se <sub>2</sub> supercell with an OH <sup>-</sup> ion placed on the top of the active Ni-1 site, which is located on (001) free surface. The original bond distances of Ni-O and O-H are set as 1.86 Å and 0.96 Å, respectively; (b) the relaxed structure of Ni <sub>3</sub> Se <sub>2</sub> supercell with OH <sup>-</sup> ion adsorbed on the active Ni-1 site. .... | 60 |
| Figure 13. | (a) Original and (b) relaxed crystal structures of Fe <sub>3</sub> Se <sub>4</sub> supercells with an OH <sup>-</sup> ions adsorbed on the active Fe site on the (001) free surface. ....                                                                                                                                                                                                                                 | 61 |
| Figure 14. | Representatives of the original (a-c) and the corresponding relaxed (a'-c') crystal structure of (Ni <sub>0.37</sub> Fe <sub>0.36</sub> Co <sub>0.27</sub> ) <sub>3</sub> Se <sub>4</sub> supercells with OH <sup>-</sup> ions placed above the active Ni, Fe and Co sites on the (001) free surfaces. ....                                                                                                               | 63 |
| Figure 15. | Representatives of the original (a-c) and the corresponding relaxed (a'-c') crystal structure of (Ni <sub>0.25</sub> Fe <sub>0.68</sub> Co <sub>0.07</sub> ) <sub>3</sub> Se <sub>4</sub> supercells with OH <sup>-</sup> ions placed above the active Ni, Fe and Co sites on the (001) free surfaces. ....                                                                                                               | 64 |
| Figure 16. | (a) Average adsorption energy of OH <sup>-</sup> ion on the surface on different catalyst compositions as explained in the text, and (b) adsorption energy of OH <sup>-</sup> ions to different active sites: Ni, Fe, and Co as a function of the composition of Fe. ....                                                                                                                                                 | 64 |

## PAPER II

|           |                                                                                                                                                                                                                                                                                                                                                                                                                                                                                                                                                                                                                                                                                                         |    |
|-----------|---------------------------------------------------------------------------------------------------------------------------------------------------------------------------------------------------------------------------------------------------------------------------------------------------------------------------------------------------------------------------------------------------------------------------------------------------------------------------------------------------------------------------------------------------------------------------------------------------------------------------------------------------------------------------------------------------------|----|
| Figure 1. | Linear sweep voltammeteries (LSVs) of ternary metal selenides along the edges of the trigonal phase diagram. ....                                                                                                                                                                                                                                                                                                                                                                                                                                                                                                                                                                                       | 91 |
| Figure 2. | Contour plots of onset overpotential $\eta$ (in units of V) (a) and (b) overpotential $\eta$ (in units of V) at the current density of 10 mA cm <sup>-2</sup> for the entire Co-Ni-Cu trigonal phase space. The color gradient corresponds to the overpotential measured in volts. ....                                                                                                                                                                                                                                                                                                                                                                                                                 | 92 |
| Figure 3. | (a) LSVs of the seven best quaternary compositions measured in N <sub>2</sub> -saturated 1.0 M KOH solution at a scan rate of 10 mV s <sup>-1</sup> . (b) Tafel plots of the catalysts. ....                                                                                                                                                                                                                                                                                                                                                                                                                                                                                                            | 94 |
| Figure 4. | XRD patterns of as-deposited (Co <sub>0.21</sub> Ni <sub>0.25</sub> Cu <sub>0.54</sub> ) <sub>3</sub> Se <sub>2</sub> (black line) and Cu <sub>3</sub> Se <sub>2</sub> (blue line) thin films on Au coated glass along with reference Cu <sub>3</sub> Se <sub>2</sub> (PDF # 00-047-1745).. ....                                                                                                                                                                                                                                                                                                                                                                                                        | 96 |
| Figure 5. | (a) Polarization curves of (Co <sub>0.21</sub> Ni <sub>0.25</sub> Cu <sub>0.54</sub> ) <sub>3</sub> Se <sub>2</sub> in comparison to the binary selenide films. (b) SEM image of (Co <sub>0.21</sub> Ni <sub>0.25</sub> Cu <sub>0.54</sub> ) <sub>3</sub> Se <sub>2</sub> film and the inset is a higher magnification image. Deconvoluted XPS spectra of the as-deposited film (Co <sub>0.21</sub> Ni <sub>0.25</sub> Cu <sub>0.54</sub> ) <sub>3</sub> Se <sub>2</sub> : (c) Cu 2p <sub>1/2</sub> and 2p <sub>3/2</sub> peaks; (d) Co 2p <sub>3/2</sub> and 2p <sub>1/2</sub> peaks; (e) Ni 2p <sub>3/2</sub> and 2p <sub>1/2</sub> peaks; (f) Se 3d <sub>5/2</sub> and 3d <sub>3/2</sub> peaks. .... | 98 |

|           |                                                                                                                                                                                                                                                                                                                                                                                                                                                                                                        |     |
|-----------|--------------------------------------------------------------------------------------------------------------------------------------------------------------------------------------------------------------------------------------------------------------------------------------------------------------------------------------------------------------------------------------------------------------------------------------------------------------------------------------------------------|-----|
| Figure 6. | Cyclic voltammograms measured for the $(\text{Co}_{0.21}\text{Ni}_{0.25}\text{Cu}_{0.54})_3\text{Se}_2$ thin film in $\text{N}_2$ -saturated 1.0 M KOH solution at different scan rates from 2.5 to 20 $\text{mV s}^{-1}$ .....                                                                                                                                                                                                                                                                        | 99  |
| Figure 7. | The amount of theoretically calculated (black dots) oxygen and experimentally measured (red dots) oxygen of $(\text{Co}_{0.21}\text{Ni}_{0.25}\text{Cu}_{0.54})_3\text{Se}_2$ versus time at 0.7 V vs Ag AgCl (KCl saturated). .....                                                                                                                                                                                                                                                                   | 101 |
| Figure 8. | Nyquist plots obtained from EIS measurements of CoSe, $\text{Cu}_3\text{Se}_2$ , NiSe and $(\text{Co}_{0.21}\text{Ni}_{0.25}\text{Cu}_{0.54})_3\text{Se}_2$ catalysts at an applied potential of 0.5 V vs Ag AgCl (KCl saturated) in $\text{N}_2$ -saturated 1.0 M KOH solution.....                                                                                                                                                                                                                   | 102 |
| Figure 9. | (a) Comparison of LSVs before and after 12 h in $\text{N}_2$ -saturated 1.0 M KOH solution. The inset is the chronoamperometry plot of $(\text{Co}_{0.21}\text{Ni}_{0.25}\text{Cu}_{0.54})_3\text{Se}_2$ for 12 h at an applied potential of 1.505 V vs RHE. (b) SEM image of $(\text{Co}_{0.21}\text{Ni}_{0.25}\text{Cu}_{0.54})_3\text{Se}_2$ after chronoamperometry. (c–f) XPS spectra of $(\text{Co}_{0.21}\text{Ni}_{0.25}\text{Cu}_{0.54})_3\text{Se}_2$ after electrochemical measurement..... | 107 |

### PAPER III

|           |                                                                                                                                                                                                                                                                                                                                                                                                                     |     |
|-----------|---------------------------------------------------------------------------------------------------------------------------------------------------------------------------------------------------------------------------------------------------------------------------------------------------------------------------------------------------------------------------------------------------------------------|-----|
| Figure 1. | OER electrocatalytic performances of the various ternary metal selenides obtained along the edges of the trigonal phase diagram measured through linear sweep voltammetries (LSVs).....                                                                                                                                                                                                                             | 140 |
| Figure 2. | Trend of OER catalytic activity within the entire Fe–Co–Cu trigonal phase space.. .....                                                                                                                                                                                                                                                                                                                             | 141 |
| Figure 3. | (a) OER activity of the six best quaternary compositions measured by conducting LSVs in $\text{N}_2$ -saturated 1.0 M KOH solution at a scan rate of 10 $\text{mV s}^{-1}$ . (b) Tafel plots of these catalysts.....                                                                                                                                                                                                | 143 |
| Figure 4. | ECSA for the $(\text{Fe}_{0.48}\text{Co}_{0.38}\text{Cu}_{0.14})\text{Se}$ thin film was measured by performing cyclic voltammograms in $\text{N}_2$ -saturated 1.0 M KOH solution at different scan rates from 2.5 to 20 $\text{mV s}^{-1}$ .....                                                                                                                                                                  | 145 |
| Figure 5. | (a) Polarization curves of $(\text{Fe}_{0.48}\text{Co}_{0.38}\text{Cu}_{0.14})\text{Se}$ compared with the three binary catalyst films. (b) SEM image of $(\text{Fe}_{0.48}\text{Co}_{0.38}\text{Cu}_{0.14})\text{Se}$ film deposited for 300 s. (c) – (f) XPS spectra of the as-deposited $(\text{Fe}_{0.48}\text{Co}_{0.38}\text{Cu}_{0.14})\text{Se}$ showing, (c) Fe 2p (d) Cu 2p (e) Co 2p and (f) Se 3d. .... | 148 |
| Figure 6. | The amount of theoretically calculated oxygen (black dots) and experimentally measured oxygen (red dots) obtained for $(\text{Fe}_{0.48}\text{Co}_{0.38}\text{Cu}_{0.14})\text{Se}$ versus time at 0.7 V vs Ag AgCl (KCl saturated)...                                                                                                                                                                              | 149 |

|                  |                                                                                                                                                                                                                                                                                                                                                                                                                                                                                             |     |
|------------------|---------------------------------------------------------------------------------------------------------------------------------------------------------------------------------------------------------------------------------------------------------------------------------------------------------------------------------------------------------------------------------------------------------------------------------------------------------------------------------------------|-----|
| Figure 7.        | EIS measurements and the corresponding Nyquist plots for $(\text{Fe}_{0.48}\text{Co}_{0.38}\text{Cu}_{0.14})\text{Se}$ , $\text{CoSe}$ , $\text{Cu}_3\text{Se}_2$ and $\text{FeSe}$ catalysts obtained at an applied potential of 0.5 V vs $\text{Ag} \text{AgCl}$ (KCl saturated) in $\text{N}_2$ -saturated 1.0 M KOH solution. ....                                                                                                                                                      | 149 |
| Figure 8.        | (a) Comparison of LSVs before and after 18 h in $\text{N}_2$ -saturated 1.0 M KOH solution. The inset is the chronoamperometry plot of $(\text{Fe}_{0.48}\text{Co}_{0.38}\text{Cu}_{0.14})\text{Se}$ for 18 h at an applied potential of 1.50 V vs RHE. (b) SEM image of $(\text{Fe}_{0.48}\text{Co}_{0.38}\text{Cu}_{0.14})\text{Se}$ after electrochemical measurements. (c–f) XPS spectra of $(\text{Fe}_{0.48}\text{Co}_{0.38}\text{Cu}_{0.14})\text{Se}$ after chronoamperometry. .... | 152 |
| <br>PAPER IV<br> |                                                                                                                                                                                                                                                                                                                                                                                                                                                                                             |     |
| Figure 1.        | (a) PXRD pattern of the as-synthesized $\text{CuCo}_2\text{Se}_4$ nanoparticles. The inset of (a) shows the crystal structure of $\text{CuCo}_2\text{Se}_4$ created from the cif file corresponding to PDF # 04-019-0997. (b) SEM image of the as-synthesized $\text{CuCo}_2\text{Se}_4$ . Deconvoluted XPS spectra of (c) Co 2p, (d) Cu 2p and (e) Se 3d collected from the as-synthesized catalyst. ....                                                                                  | 181 |
| Figure 2.        | Polarization curves of $\text{CuCo}_2\text{Se}_4@\text{Au}$ , $\text{RuO}_2@\text{Au}$ and bare Au substrate in $\text{N}_2$ -saturated 1.0 M KOH at a scan rate of $10 \text{ mV s}^{-1}$ .....                                                                                                                                                                                                                                                                                            | 182 |
| Figure 3.        | The amount of theoretically calculated yield for oxygen (black dots) and experimentally measured oxygen (red dots) on $\text{CuCo}_2\text{Se}_4$ electrocatalytic surface versus time at 0.7 V vs $\text{Ag} \text{AgCl}$ (KCl saturated). ....                                                                                                                                                                                                                                             | 185 |
| Figure 4.        | (a) Comparison of LSV curves of $\text{CuCo}_2\text{Se}_4$ catalyst measured in $\text{N}_2$ -saturated 1.0 M KOH before and after 8 h chronoamperometry. The inset shows chronoamperometric measurement of $\text{CuCo}_2\text{Se}_4$ under continuous $\text{O}_2$ evolution. (b) Comparison of pxrd before and after 8 h chronoamperometry. XPS spectra of (c) Co 2p, (d) Cu 2p and (e) Se 3d after chronoamperometric measurement for 8 h.....                                          | 187 |
| Figure 5.        | HER activity of $\text{CuCo}_2\text{Se}_4@\text{Au}$ measured in $\text{N}_2$ -saturated 1.0 M KOH at a scan rate of $10 \text{ mV s}^{-1}$ compared with that of Pt mesh.. ....                                                                                                                                                                                                                                                                                                            | 188 |
| Figure 6.        | Slab supercells for (100) surface (a), (111) surface with Cu/Co termination (b) and (111) surface with Co-only termination (c). Color coded: navy – Co, yellow – Cu, green – Se.....                                                                                                                                                                                                                                                                                                        | 189 |
| Figure 7.        | (a) The total density of states (DOS) of bulk $\text{CuCo}_2\text{Se}_4$ and (b-d) partial density of states (PDOS) of Cu 3d, Co 3d and Se 4p calculated using GGA (dashed line) and GGA+U with $U = 6 \text{ eV}$ for Co d-states and $U = 4 \text{ eV}$ for Cu d-states (solid line).....                                                                                                                                                                                                 | 190 |

|            |                                                                                                                                                                                                                                                                                                                                                                              |     |
|------------|------------------------------------------------------------------------------------------------------------------------------------------------------------------------------------------------------------------------------------------------------------------------------------------------------------------------------------------------------------------------------|-----|
| Figure 8.  | Total density of states (TDOS) of bulk $\text{CuCo}_2\text{Se}_4$ (a), (100) surface (b), (111) surface with Co/Cu (c) and Co (d) termination. ....                                                                                                                                                                                                                          | 192 |
| Figure 9.  | Comparison of partial electronic density of states (PDOS) of Co atoms in the surface top layer with the one in the center layer. ....                                                                                                                                                                                                                                        | 193 |
| Figure 10. | Combined partial density of states (PDOS) of all Co atoms in each layer for (100) slab (a) and (111) Co/Cu terminated slab (b). ....                                                                                                                                                                                                                                         | 195 |
| Figure 11. | Partial density of states (PDOS) of Co atom in (100) surface before $\text{OH}^-$ attachment (a), Co atom after $\text{OH}^-$ attachment (b), $\text{OH}^-$ ions after attachment on Co atom (c). PDOS of Co atom in (111) surface before $\text{OH}^-$ attachment (d), Co atom after $\text{OH}^-$ attachment (e), $\text{OH}^-$ ions after attachment on Co atom (f). .... | 198 |

## PAPER V

|           |                                                                                                                                                                                                                                                                                                                                                                                                                                                                                                                                                                                                                  |     |
|-----------|------------------------------------------------------------------------------------------------------------------------------------------------------------------------------------------------------------------------------------------------------------------------------------------------------------------------------------------------------------------------------------------------------------------------------------------------------------------------------------------------------------------------------------------------------------------------------------------------------------------|-----|
| Figure 1. | (a) Pxd pattern of hydrothermally synthesized $\text{Cu}(\text{Co}_{0.68}\text{Ni}_{0.32})_2\text{Se}_4$ nanoparticles along with reference $\text{Cu}(\text{Co}_{0.68}\text{Ni}_{0.32})_2\text{Se}_4$ (PDF # 00-008-0001), the inset shows the crystal structure of $\text{Cu}(\text{Co}_{0.68}\text{Ni}_{0.32})_2\text{Se}_4$ . (b) SEM image of $\text{Cu}(\text{Co}_{0.68}\text{Ni}_{0.32})_2\text{Se}_4$ . (c) TEM image of $\text{Cu}(\text{Co}_{0.68}\text{Ni}_{0.32})_2\text{Se}_4$ . (d) HRTEM image and SAED pattern of $\text{Cu}(\text{Co}_{0.68}\text{Ni}_{0.32})_2\text{Se}_4$ nanoparticles. .... | 227 |
| Figure 2. | Deconvoluted XPS spectra of (a) Cu 2p, (b) Co 2p, (c) Ni 2p and (d) Se 3d of $\text{Cu}(\text{Co}_{0.68}\text{Ni}_{0.32})_2\text{Se}_4$ nanoparticles. ....                                                                                                                                                                                                                                                                                                                                                                                                                                                      | 228 |
| Figure 3. | (a) Polarization curves of $\text{Cu}(\text{Co}_{0.68}\text{Ni}_{0.32})_2\text{Se}_4@\text{CFP}$ and $\text{RuO}_2$ in $\text{N}_2$ -saturated 1.0 M KOH at a scan rate of $10 \text{ mV s}^{-1}$ . (b) Tafel plots of $\text{Cu}(\text{Co}_{0.68}\text{Ni}_{0.32})_2\text{Se}_4@\text{CFP}$ and $\text{RuO}_2$ . ....                                                                                                                                                                                                                                                                                           | 230 |
| Figure 4. | Cyclic voltammograms measured for $\text{Cu}(\text{Co}_{0.68}\text{Ni}_{0.32})_2\text{Se}_4$ in $\text{N}_2$ saturated 1.0 M KOH solution at different scan rates from 5 to $80 \text{ mV s}^{-1}$ . ....                                                                                                                                                                                                                                                                                                                                                                                                        | 232 |
| Figure 5. | The amount of theoretically calculated (black dots) oxygen and experimentally measured (orange dots) oxygen of $\text{Cu}(\text{Co}_{0.68}\text{Ni}_{0.32})_2\text{Se}_4$ versus time at 0.7 V vs Ag AgCl (KCl Saturated). ....                                                                                                                                                                                                                                                                                                                                                                                  | 232 |
| Figure 6. | (a) The comparison of LSVs of the catalyst before and after chronoamperometry for 22 h. (b) Pxd pattern of $\text{Cu}(\text{Co}_{0.68}\text{Ni}_{0.32})_2\text{Se}_4$ before and after 22 h chronoamperometry. XPS spectra of Cu 2p (c), Co 2p (d), Ni 2p (e) and Se 3d (f) of $\text{Cu}(\text{Co}_{0.68}\text{Ni}_{0.32})_2\text{Se}_4$ after electrochemical measurement. ....                                                                                                                                                                                                                                | 233 |



- Figure 7. Comparison of total density of states (TDOS) of (100) surface of  $\text{Cu}(\text{Co}_{0.68}\text{Ni}_{0.32})_2\text{Se}_4$  case 6 (red) and  $\text{CuCo}_2\text{Se}_4$  (blue) calculated with GGA+U with  $U = 6 \text{ eV}$  ..... 238
- Figure 8. Supercell slabs of relaxed  $\text{Cu}(\text{Co}_{0.68}\text{Ni}_{0.32})_2\text{Se}_4$  (100) surface,  $\text{Cu}(\text{Co}_{0.68}\text{Ni}_{0.32})_2\text{Se}_4$  (100) surface with  $\text{OH}^-$  attached on Ni atom, and  $\text{Cu}(\text{Co}_{0.68}\text{Ni}_{0.32})_2\text{Se}_4$  (100) surface with  $\text{OH}^-$  attached on Co atom. .... 238
- Figure 9. Partial density of states (PDOS) of Co atom before  $\text{OH}^-$  attachment (a), Co atom after  $\text{OH}^-$  attachment (b),  $\text{OH}^-$  attached to Co atom (c). PDOS of Ni atom before  $\text{OH}^-$  attachment (d), Ni atom after  $\text{OH}^-$  attachment (e),  $\text{OH}^-$  after attached on Ni atom (f). The calculations of the (100) slab of  $\text{Cu}(\text{Co}_{0.68}\text{Ni}_{0.32})_2\text{Se}_4$  are performed within GGA+U. .... 239

## PAPER VI

- Figure 1. XRD pattern of  $\text{Cu}_2\text{Se}$  (a),  $\text{Cu}_3\text{Se}_2$  (b) and  $\text{CuSe}_2$  (c). Scanning electron microscopy (SEM) images of  $\text{Cu}_2\text{Se}$  (d),  $\text{Cu}_3\text{Se}_2$  (e) and  $\text{CuSe}_2$  (f). .... 257
- Figure 2. XPS spectra of Cu 2p and Se 3d of  $\text{Cu}_2\text{Se}$  (a),  $\text{Cu}_3\text{Se}_2$  (b) and  $\text{CuSe}_2$  (c) respectively. .... 258
- Figure 3. Cyclic voltammograms measured for  $\text{Cu}_2\text{Se}$  (a),  $\text{Cu}_3\text{Se}_2$  (b) and  $\text{CuSe}_2$  (c) catalysts in  $\text{N}_2$ -saturated 1.0 M KOH solution at different scan rates from 5 to 40  $\text{mV s}^{-1}$ . .... 261
- Figure 4. Nyquist plots obtained from EIS measurements of  $\text{Cu}_2\text{Se}$ ,  $\text{Cu}_3\text{Se}_2$  and  $\text{CuSe}_2$  catalysts at an applied potential of 1.49, 1.51 and 1.54 V vs RHE in  $\text{N}_2$ -saturated 1.0 M KOH solution. .... 262

## LIST OF TABLES

|                                                                                                                                                               | Page |
|---------------------------------------------------------------------------------------------------------------------------------------------------------------|------|
| <b>PAPER I</b>                                                                                                                                                |      |
| Table 1. Summary of elemental analysis of metal selenide films determined by EDS and corresponding kinetic parameters extracted from polarization curves..... | 46   |
| Table 2. Equivalent Circuit Parameters Obtained from Fitting of EIS Experimental Data.....                                                                    | 53   |
| <b>PAPER II</b>                                                                                                                                               |      |
| Table 1. Equivalent Circuit Parameters Obtained from Fitting of EIS Experimental Data.....                                                                    | 102  |
| <b>PAPER III</b>                                                                                                                                              |      |
| Table 1. Equivalent circuit parameters obtained from fitting of EIS experimental data.....                                                                    | 150  |
| <b>PAPER IV</b>                                                                                                                                               |      |
| Table 1. Comparison of catalytic activity for different Co and/or Cu based OER / HER electrocatalysts in alkaline medium.....                                 | 199  |
| <b>PAPER VI</b>                                                                                                                                               |      |
| Table 1. Equivalent circuit parameters obtained from fitting of EIS experimental data.....                                                                    | 263  |

## 1. INTRODUCTION

The growing world is facing an energy crisis since the current energy resources are mainly from non-sustainable fossil fuels such as oil, coal and natural gas.<sup>1,2</sup> However, the over-dependence on fossil fuels leads to several problems that human beings have to face. On the one hand, fossil fuels are non-sustainable energy resources, its replenishing rate is not as fast as the increasing consumption rate of year by year, suffering from its insufficient availability. According to a report from the International Energy Agency, the global energy consumption will increase around 45 % from 2013 to 2040, where the fossil fuels might be depleted in few centuries.<sup>3</sup> On the other hand, combusting vast amount of fossil fuels releases lots of polluted by-products into the atmosphere, such as, carbon dioxide/monoxide (CO<sub>2</sub>/CO), sulfur oxides (SO<sub>x</sub>), nitrogen oxides (NO<sub>x</sub>) and particulate matter (PM<sub>10</sub>, PM<sub>2.5</sub>) etc.<sup>4,5</sup> The majority of particulate matter and toxic pollutant can harm the health of human beings, especially the human immune system.<sup>6,7,8</sup> Among these pollutants, carbon dioxide, CO<sub>2</sub>, has the smallest health risk, however, the emission of large amount of CO<sub>2</sub> and other greenhouse gases from combustion fossil fuels most likely result in global warming, with consequences such as polar ice cap melting, ocean level raising and land area reducing.<sup>9,10,11</sup> Furthermore, transportation has consumed over two thirds of petroleum resources in 2017 based on a report by U.S. Energy Information Administration.<sup>12</sup> Therefore, to offset these circumstances, it's crucial to develop renewable and effective sustainable energy alternatives with minimum environmental and health impacts.

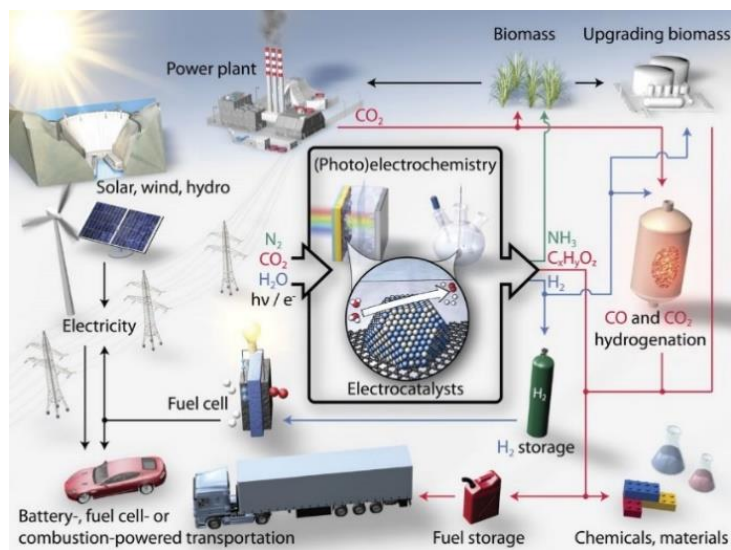


Figure 1.1. Schematic of sustainable energy future.<sup>3</sup>

Fuel cells are an appealing devices that can convert chemical energy into electrical energy through low-temperature combustion of fuels, which can be potentially utilized to assist combustion engines in the next-generation commercial vehicles as shown in Figure 1.2 or any other industrial machines.<sup>24,25,26</sup> A fuel cell can generate exceptional energy conversion with an efficiency around 40 – 80 %, which is far better than that of the traditional internal combustion engines.<sup>27,28</sup> Fuel materials consumed in the fuels cells are expected to release large amounts of energy through chemical reactions. The fuels mostly used nowadays are still dependent on fossil fuels ranging from petroleum, natural gas and coal, and still suffer from producing carbon-based by-products. This is unable to satisfy the non-polluting energy demand.

Hydrogen (H<sub>2</sub>), with its high energy density (143 MJ/kg)<sup>29</sup> and producing a clean reaction product (namely, water), has been considered as the most promising fuels of the 21<sup>st</sup> centry.<sup>30,31</sup> Nevertheless, the problem is that H<sub>2</sub> does not occur free in nature. The traditional way to produce H<sub>2</sub> industrially is by natural gas reforming, which is actually not

an ideal approach for H<sub>2</sub> production due to its low-purity, high-cost and emission of large amount of CO<sub>2</sub> as by-product.<sup>32,33</sup> To meet the demand of clean energy economy, it is necessary to develop novel approaches to generate high-purity hydrogen to make H<sub>2</sub> fuel into commercial bulk utilization. In that regard, water electrolysis into H<sub>2</sub> and O<sub>2</sub> gas assisting by sunlight or any other inexhaustible natural sources has been suggested as a potential way to generate clean H<sub>2</sub>.<sup>34,35,36,37</sup> This ideal process is shown in Figure 1.3. However, the efficiency and industrial competition of water electrolysis is greatly hindered by a complex anodic reaction – oxygen evolution reaction (OER) – requiring a high overpotential input to initial the reaction.<sup>38,39</sup> Thereby, the development and fabrication of high-efficiency and low-cost electrocatalyst for OER is current a major challenge in energy conversion.

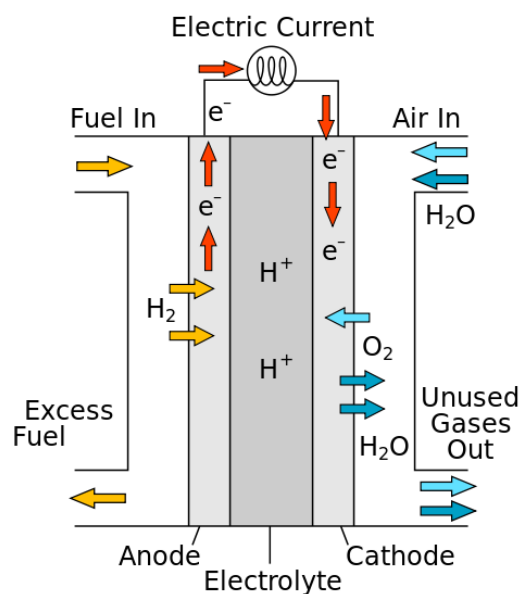


Figure 1.2. Diagram of a proton conducting solid oxide fuel cell. Designed by R. Dervisoglu.(Source: Wikipedia)

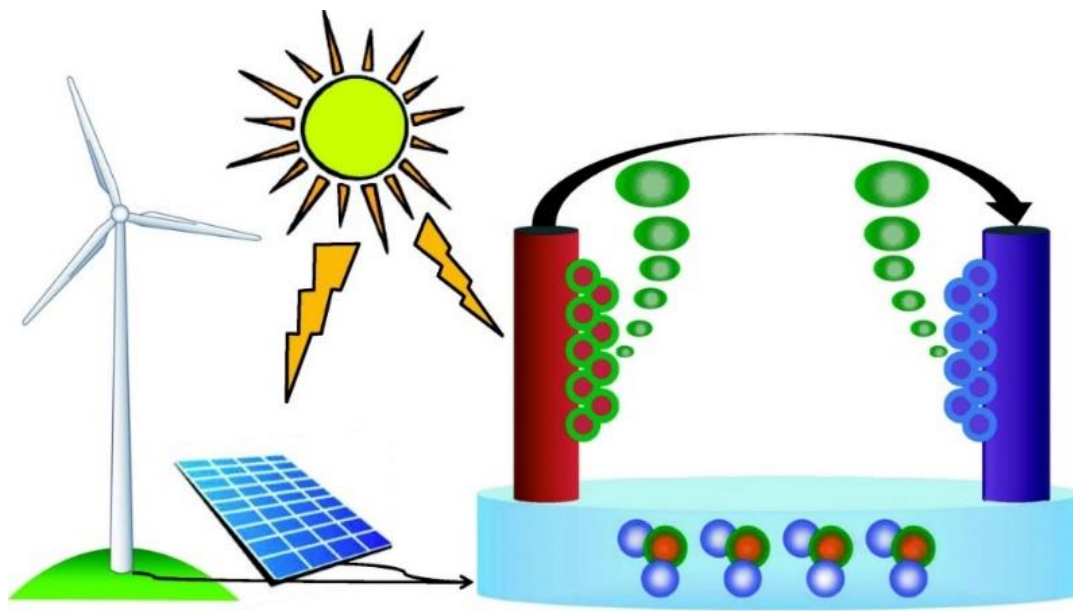


Figure 1.3. Schematic representation of the water splitting via electrolysis, utilizing electricity derived from renewable sources such as wind and solar, and photoelectrolysis, where the electrodes directly harvest the solar energy. Oxygen evolution catalysts (OEC) are located on the anode and hydrogen evolution catalysts (HEC) are located on the cathode.<sup>40</sup>

Clean energies, such as wind and solar power, have been viewed as two promising candidates for renewable and CO<sub>2</sub>-free emission energy sources as well as a great feasibility to be utilized worldwide.<sup>13,14</sup> However, both suffer from the spatial, diurnal and temporary availability which greatly limits their large-scale bulk applications. Therefore, it is required to efficiently capture and store them for potentially utilization. Over the past several decades, both academia and industries contributed with extensive efforts in developing high-performance sustainable energy conversion and storage devices to meet the urgent demand of alternative energy sources.<sup>15,16</sup> Several energy conversion and storage techniques have been designed to convert sunlight or electricity into renewable fuels, for instance, in fuel cells,<sup>17,18,19</sup> metal-air battery<sup>20,21,22,23</sup> and other electrochemical storage devices. Figure 1.1 shows the future of sustainable energy supply, indicating several

possible and applicable pathways to create important supplies for fuels and useful chemicals, and replace conventional energy resources with the advantage of avoiding environmental pollutions.<sup>3</sup>

## 1.1. WATER SPLITTING

**1.1.1. Water Splitting – A Brief History.** Water splitting, or water electrolysis was the first time reported by two Dutch scientists, Jan Rudolph Deiman and Adriaan Paets van Troostwijk, in 1798. Two gold wires in water were observed to explosively generate bubbles when they were connected to an electrostatic generator.<sup>41</sup> In 1800, William Nicholson and Anthony Carlisle repeated and confirmed the results through providing direct voltage to their device by a voltaic pile invented by Alessandro Volta.<sup>42</sup> The technique of water electrolysis in alkaline medium into industrial application was firstly developed by Dmitry Lachinov, in 1888, to generate hydrogen and oxygen and more than 400 industrial water electrolyzers were in operation in the next 16 years.<sup>42,43</sup> Water electrolysis has the great potential of producing high-purity hydrogen, however, its applications are often limited to the small scale, low efficiency and short durability.

**1.1.2. Mechanism of Water Splitting.** In general, the overall water splitting (or water electrolysis) reaction can be represented as following Equation (1).



This electrochemical process includes two half reactions as shown in Figure 1.4: the oxidation of water into molecular oxygen taken place at the anode, namely the oxygen evolution reaction (OER); while the reduction of water into molecular hydrogen occurs at cathode, namely the hydrogen evolution reaction (HER).<sup>44,45,46</sup> Water splitting is a

thermodynamically non-spontaneous reaction. At standard ambient temperature and pressure (25°C and 1 bar), the change in Gibbs energy ( $\Delta G$ ) to produce one mole of  $H_2$  is 237.178 kJ / mol.<sup>40</sup> Correspondingly, a voltage of at least 1.23 V should be applied to overcome the thermodynamic barrier in order to initiate the water electrolysis process.<sup>40</sup>

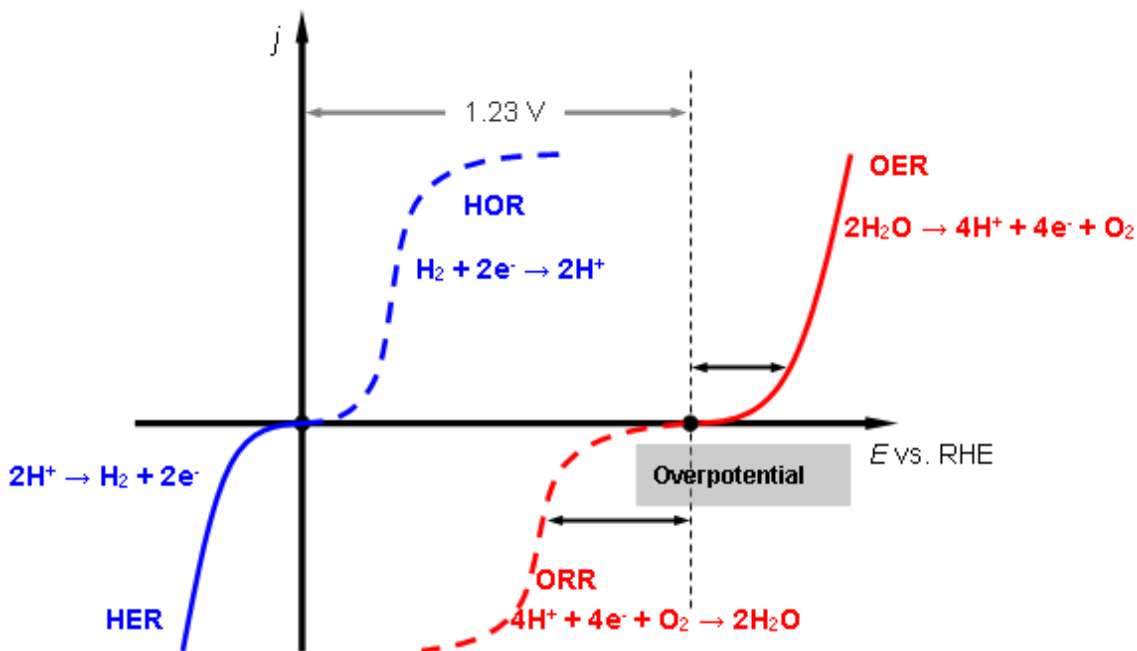


Figure 1.4. Polarization curves of oxygen and hydrogen reactant for the electrolysis of water. The plot is not to accurate scale.<sup>47</sup>

In alkaline condition, the HER and OER half reactions can be expressed by Equations (2) and (3), respectively.<sup>47,48</sup>



In acidic solution, the HER and OER half reactions can be described by following Equations (4) and (5).<sup>47</sup>





The efficiency of water splitting can be greatly affected by the electrolyte.<sup>49</sup> Pure water is barely used as an economic electrolyte for its low concentrations of hydronium ions ( $\text{H}^+$ ) and hydroxide ions ( $\text{OH}^-$ ) limit the ionic conductivity, leading to a high potential loss and a large potential input required to initialize the reaction.<sup>50</sup>

To meet the feasibility of large-scale industry applications, it is necessary to add water soluble substances into water to increase its ionic conductivity, reduce the uncompensated resistance of the electrolyte, and increase the efficiency of the water splitting.<sup>51</sup> Therefore, aqueous strong acid ( $\text{H}_2\text{SO}_4$ ) and strong bases (NaOH or KOH) are preferably used to increase the conductivity of water due to their high ionic mobility and strong conducting ability.<sup>52</sup> An acidic electrolyte has been generally used in the proton-exchange-membrane (PEM) based water electrolyzers attributed to the availability of proton exchanging through organic membranes, such as Nafion<sup>®</sup> and Felmion<sup>®</sup> etc.<sup>53,54</sup> However, the PEM-based electrolyzers suffer from the stability of electrode material under acidic medium limiting it to expensive precious metals such as Pt, Ir and Ru.<sup>54,52</sup> Commercialized water electrolysis devices require high efficiency, cost-effective and long-term capability. Accordingly, an alkaline water electrolyzer is more attractive for hydrogen production because available low-cost and earth-abundant transition metal based materials are more stable in the alkaline medium and can be utilized as electrocatalysts.<sup>46,47,55</sup> A schematic illustration of alkaline water electrolyzer is shown in Figure 1.5. Intensive efforts have been put forth to develop robust transition-metal-based electrolysis for alkaline water electrolysis.

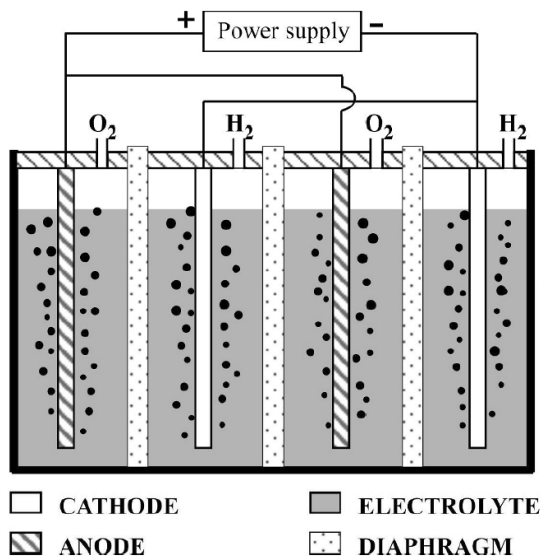


Figure 1.5. Two-cell conventional alkaline electrolyzer configuration.<sup>46</sup>

**1.1.3. Hydrogen Evolution Reaction (HER).** The hydrogen evolution reaction (HER) is a simple two-electron process. HER is conventionally regarded as comprising three steps known as the electrochemical adsorption of hydrogen (Volmer reaction), electrochemical desorption of hydrogen (Heyrovsky reaction) followed by the chemical desorption (Tafel).<sup>56,57,58,59</sup> In the following steps,  $H^*$  denotes an adsorbed hydrogen atom. In alkaline medium:



In acidic medium:



The electrocatalysts most used towards HER are typically noble metals, such as Pt, Au and

Pd, etc. with almost no overpotential and excellent durability for extended period use.<sup>60,61,62</sup> Figure 1.6 shows the correlation of pure metals as HER electrocatalysts in acidic solution with respect to the bond strength of M-H, suggesting the highest reaction rate of HER will occur on metals with intermediates M-H bond strength, neither too strong or too weak.<sup>63</sup> Besides pure metals, binary or ternary mixed metal alloys, such as Ni-Mo,<sup>64,65,66</sup> Ni-Co,<sup>67,68</sup> Ni-Mo-Fe<sup>69,70</sup> also showed promising HER catalytic activity. Considering the cathodic half reaction – HER is kinetically fast which is not the limiting step for water splitting, therefore the main subjects will focus on the designing electrocatalysts for anodic half-reaction of OER.

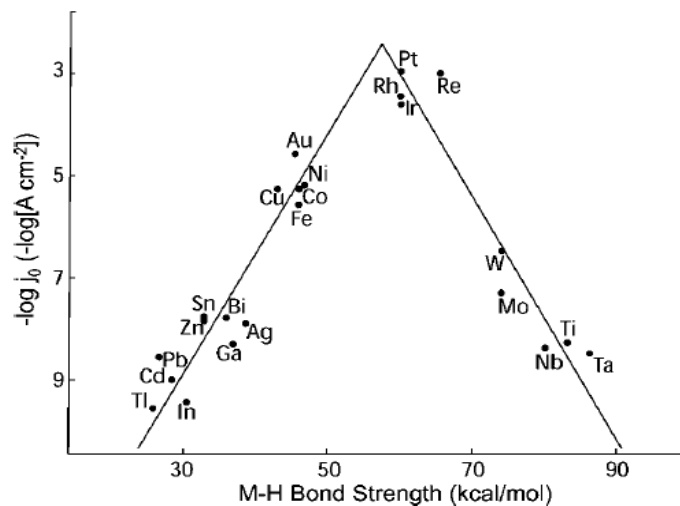
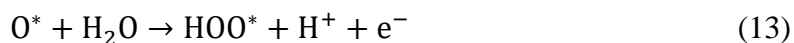
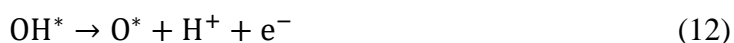


Figure 1.6. The volcano relation for pure metals in acidic solution.<sup>63</sup>

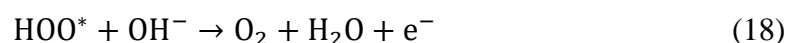
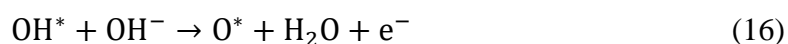
**1.1.4. Oxygen Evolution Reaction (OER).** Oxygen evolution reaction (OER) is a center reaction for fuel cells, solar water-splitting device and metal-air batteries.<sup>71,72</sup> OER is a complex four-electron process for which a mechanism has been proposed comprising of a series of intermediate steps including adsorption of hydroxyl species, two steps of

charge transfer and desorption of O<sub>2</sub>. The OER process in acidic and alkaline solutions is assumed as following. The asterisk indicates a surface site.<sup>38,73,74</sup>

In acidic medium:



In alkaline medium:



The OER, a kinetically sluggish reaction with 4 electrons involved and several intermediate states formed is relatively more complex compared to HER, which is the limiting half reaction for water splitting.<sup>75,76</sup> Both OER and HER half-reactions have to meet a maximum efficiency in order to reach the maximum efficiency of water splitting. Hence, it's a crucial task to develop robust and cost-effective OER electrocatalysts to optimize the efficiency of the overall water splitting and generate a sustainable hydrogen production.

## 1.2. OXYGEN EVOLUTION REACTION ELECTROCATALYSTS

**1.2.1. Merits and Criteria of OER Electrocatalysts.** Oxygen Evolution reaction (OER) is fundamentally important for the development of energy conversion and storage

devices, while the OER is suffering from the multi-step mechanism and low efficiency.<sup>74,77</sup> Therefore, an effective electrocatalyst is needed to lower the activation barrier and facilitate kinetics of the OER process and therefore increase the practical feasibility of large-scale water splitting reaction. In most cases, OER electrocatalysts are heterogeneous, meaning the reaction occurs at the interface of catalyst-electrolyte.

There are several factors influencing the behavior of an electrocatalyst towards OER, such as, activity, selectivity, stability. A perfect OER electrocatalyst should include all of the above three merits, meaning the catalyst should show excellent ability to increase the OER reaction rate, only facilitate oxygen evolution reaction over a certain range of applied electric potential as well as last for an extended period under practical conditions.<sup>76,78,79</sup> Typically, the strategies to improve the OER activity of an electrocatalyst are by increasing not only the electronic structure and phase composition, namely the intrinsic properties but also the extrinsic parameters such as the number and accessibility of catalytic active sites, electrocatalytically active surface area (ECSA) and the interface impedance at catalyst-electrolyte surface.<sup>3,80,81</sup>

Objective comparisons of electrocatalyst performance are necessary and play an important role in the development of novel catalysts and in the evaluation of their bulk application. To benchmark the catalytic performance, several kinetic parameters are generally measured to evaluate the catalytic activity of OER, such as the onset potential, overpotential ( $\eta$ ) at  $10 \text{ mA cm}^{-2}$ , Tafel slope and Faradaic efficiency.<sup>55,81,82</sup> The onset potential is the minimum potential required to start the reaction, while the potential required in excess of the thermodynamic voltage of OER process, (1.23 V vs RHE), is generically referred to as overpotential.<sup>82</sup> The overpotential is generally reported at a

current density per geometric area of  $10 \text{ mA cm}^{-2}$  which is equivalent to 10 % efficiency of solar water splitting device, and it can be obtained by following equation 1.<sup>49,56,83</sup> Moreover, Tafel slope is highly related to the kinetics of OER reaction, where the rate-determining steps can be obtained based on the value of Tafel slope.<sup>84,85</sup> Equation 2 represents the calculation of Tafel slope. In addition, Faradaic efficiency of pure  $\text{O}_2$  production is another important parameter to commonly characterize the performance of an electrocatalyst, which can be measured through rotating ring disk electrode (RRDE) setup or water-displacement method.<sup>82,86</sup>

$$\eta = E_{Applied} - 1.23 \quad (1)$$

Where,  $\eta$  is the overpotential,  $E_{Applied}$  is the potential applied at certain current density.

$$\eta = a + \frac{2.3RT}{\alpha nF} \log(j) \quad (2)$$

where  $\eta$  is the overpotential,  $j$  is the current density and the other symbols have their usual meanings. The Tafel slope is given by  $2.3RT/\alpha nF$ .

**1.2.2.Current Status of OER Electrocatalysts.** Numerous heterogeneous electrocatalysts towards oxygen evolution reaction has been reported in the last decade.<sup>79,88,89,90,91,92</sup> A volcano plot shown in Figure 1.7 for OER catalysts was reported by Trasatti in 1984 demonstrating the overpotential required for OER process directly correlated with enthalpy of the transition metal oxide in acidic and alkaline conditions.<sup>87</sup> As can be seen in Figure 1.7, the most efficient OER electrocatalysts tend to be precious metal based materials, namely platinum, ruthenium, iridium and their corresponding oxides or alloys.<sup>93,94,95,96</sup> In particular,  $\text{IrO}_2$  and rutile-type  $\text{RuO}_2$  has been widely accepted as state-of-the-art electrocatalysts.<sup>97,98</sup>

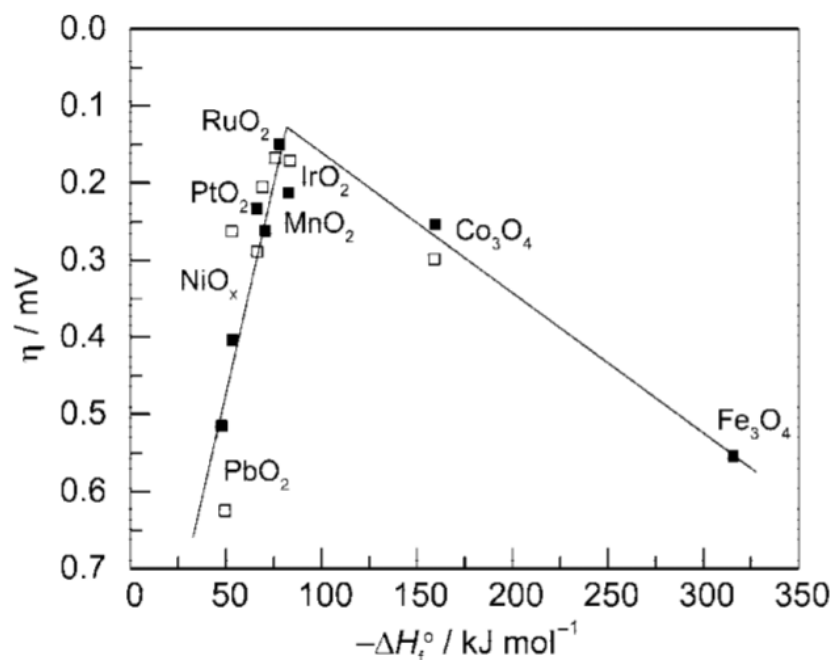


Figure 1.7. Volcano plot showing activity for O<sub>2</sub> production metal oxide surfaces versus the enthalpy of transition of the oxide in acidic and basic solution. Overpotential measured relative to 0.1 mA cm<sup>-2</sup> current density.<sup>87</sup>

In 2013, McCrory *et al.* have conducted a comprehensive comparison of several well-known metal oxide based OER catalysts indicating IrO<sub>2</sub> and RuO<sub>2</sub> show the best OER activity with the overpotential less than 300 mV as shown in Figure 1.8.<sup>82</sup> However, the scarcity on Earth and high price of their raw materials have highly limited their economically feasibility for any large-scale utilizations. Therefore, it is a crucial task for researchers to develop robust and cost-effective OER electrocatalysts.

Recently, transition metal based materials as OER electrocatalysts have attracted most of the attentions due to their large-abundance, low-cost and environmentally-benign.<sup>99,100,101,102,103,104</sup> Considerable efforts have been poured to develop OER electrocatalysts based on earth-abundant elements such as Fe, Co, Ni, Mn and transition

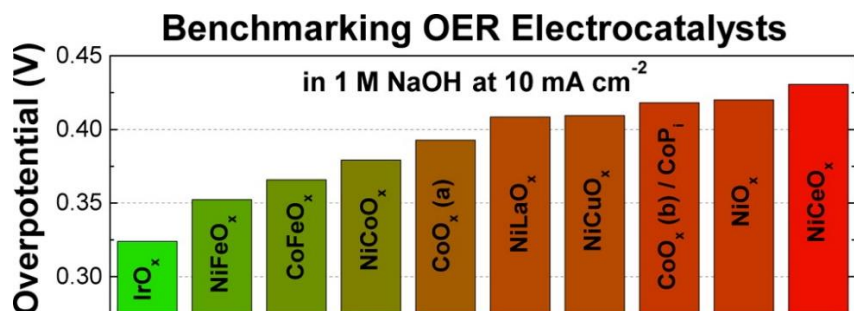


Figure 1.8. Benchmarking OER electrocatalysts at overpotential of  $10 \text{ mA cm}^{-2}$  in alkaline medium.<sup>82</sup>

metal sites to easily switch between different oxidation states (such as  $\text{Ni}^{2+/3+}$  and  $\text{Co}^{2+/3+}$  etc.) without hindrance under application of small electric bias,<sup>112,113</sup> (ii) the number of electrons occupying in the  $e_g$  orbitals of the transition metal ions on the surface which will likely affect the bond strength between catalytic sites and hydroxyl species and even influencing the surface oxygen binding energy,<sup>114,115,116</sup> therefore reducing the thermodynamic overpotential of the OER process.

To date, the transition metal based materials have been identified as promising OER electrocatalysts ranging from pure/mixed metal oxides,<sup>117,118,119,120,121,122,123</sup> (oxy)hydroxides,<sup>78,102,124,125</sup> and chalcogenides (sulfides,<sup>126,127,128</sup> selenides<sup>129,130,131,132</sup> and tellurides<sup>133,134,135</sup>) with advanced OER electroactivity and even comparable to state-of-the-art electrocatalysts. Chalcogenides has been widely reported showing better OER activity in comparison to oxides.<sup>133,136</sup> This can be expected that smaller electronegativity of chalcogen elements (S, Se and Te) lead to an increased covalency in the metal-chalcogen bond which facilitates the catalyst activation and onset of OER reaction by lowering the redox potential of the catalytic site.<sup>137,138</sup> Among the chalcogenides, selenides as a new series of OER electrocatalysts have attracted most of the attentions with outstanding catalytic activity as well as remarkable stability for extended period in alkaline medium. In



the following sections, the synthetic strategies of selenides and their applications in oxygen evolution reaction are discussed in detail.

**1.2.3.Pure Transition Metal Selenides.** Among the monometallic selenides, nickel and cobalt selenides are the most studied ones as OER electrocatalysts in alkaline solution and significant processes have been achieved over the last couple of years.

In 2013, nickel selenide ( $\text{NiSe}_2$ ) was reported to exhibit electrocatalytic activity towards the reduction of  $\text{I}^{3-}$  in dye-sensitized solar cells (DSSCs).<sup>139</sup> Nickel monoselenide ( $\text{NiSe}$ ) was discovered to display remarkable OER electrocatalytic activity for the first time by Sun's group in 2015, where  $\text{NiSe}$  nanowire/NF (nickel foam) required an overpotential of 270 mV to reach  $20 \text{ mA cm}^{-2}$  in 1.0 mM KOH.<sup>140</sup> Later, Shi et al reported  $\text{Ni}_3\text{Se}_2$  film on Cu foam ( $\text{Ni}_3\text{Se}_2/\text{CF}$ ) as a bifunctional catalyst required an overpotential of 340 mV and 100 mV to achieve  $50 \text{ mA cm}^{-2}$  in alkaline medium for OER and HER, respectively.<sup>141</sup> However, the  $\text{Ni}_3\text{Se}_2/\text{CF}$  as a 3D electrode showed high surface area which have significant influence on the catalytic activity. To avoid the effect of 3D substrate, Swesi et al electrochemically deposited  $\text{Ni}_3\text{Se}_2$  thin film on a flat substrate (Au/glass), which yielded a low overpotential of 290 mV at  $10 \text{ mA cm}^{-2}$  in alkaline solution.<sup>131</sup> Interestingly, A directional growth of  $\text{NiSe}_2$  thin film to intentionally expose Ni-rich plane was done by Swesi et al, which resulted in better OER catalytic activity than any other report.<sup>142</sup>

Apart from nickel selenides, cobalt selenides have been widely studied as excellent HER electrocatalysts.<sup>143,144,145,146</sup> Recently, there are several interesting studies about amorphous and crystalline cobalt selenides reported as highly efficient electrocatalysts towards OER. Yuan and his coworkers fabricated 3D core-shell structured  $\text{CoSe}_2@\text{C-CNT}$  nanohybrid and it yielded an overpotential of 306 mV at  $10 \text{ mA cm}^{-2}$  in 1.0 M KOH

medium.<sup>147</sup> Moreover, Coral-like CoSe nanostructures prepared by solvothermal method exhibited low overpotential of 295 mV at a current density of  $10 \text{ mA cm}^{-2}$ .<sup>148</sup> Interestingly, enhanced OER catalytic activity was observed by hydrothermally synthesized monoclinic  $\text{Co}_3\text{Se}_4$  thin nanowires on cobalt foam (CF) requiring an overpotential of 320 mV to reach  $397 \text{ mA cm}^{-2}$ .<sup>149</sup> Masud et al reported an electrochemically patterned growth of  $\text{Co}_7\text{Se}_8$  thin films as nanotubes or nanorods to improve the current density for OER process, interestingly, the nanotubular  $\text{Co}_7\text{Se}_8$  thin film exhibited the best OER activity yielding an overpotential of 260 mV at  $10 \text{ mA cm}^{-2}$ .<sup>150</sup>

**1.2.4. Mixed Transition Metal Selenides.** Transition metal doping, especially two or more metals in an electrocatalyst, has been widely considered as an efficient way to improve the catalytic performance towards OER.<sup>151,152,153</sup> Several hypotheses have been proposed to understand the boosted OER activity in addition of foreign metal dopants to the monometallic electrocatalysts: (i) the electron distribution of an electrocatalyst could be altered by introducing foreign atoms into its lattice structure to increase its electrical conductivity thereby increasing electron transfer efficiency within the catalyst itself.<sup>154</sup> (ii) through mixed transition metal *d-d* orbital delocalization, the metallic state near Fermi level of an electrocatalyst is expected to be markedly increased,<sup>137,155,156</sup> and (iii) the binding energy of metal active sites with intermediates could be optimized by doping transition metal atoms into lattice vacancies or distorting lattice structures on surface,<sup>114,116,157,158,159</sup> therefore reducing the thermodynamic overpotential of the OER process.

Regarding the 3d metal-based materials towards OER, the most accepted electrocatalytic activity trend is reported as  $\text{Ni} > \text{Co} > \text{Fe} > \text{Mn}$  reported by Markovic's group as shown in Figure 1.9.<sup>105</sup> Nickel based materials have been considered as a

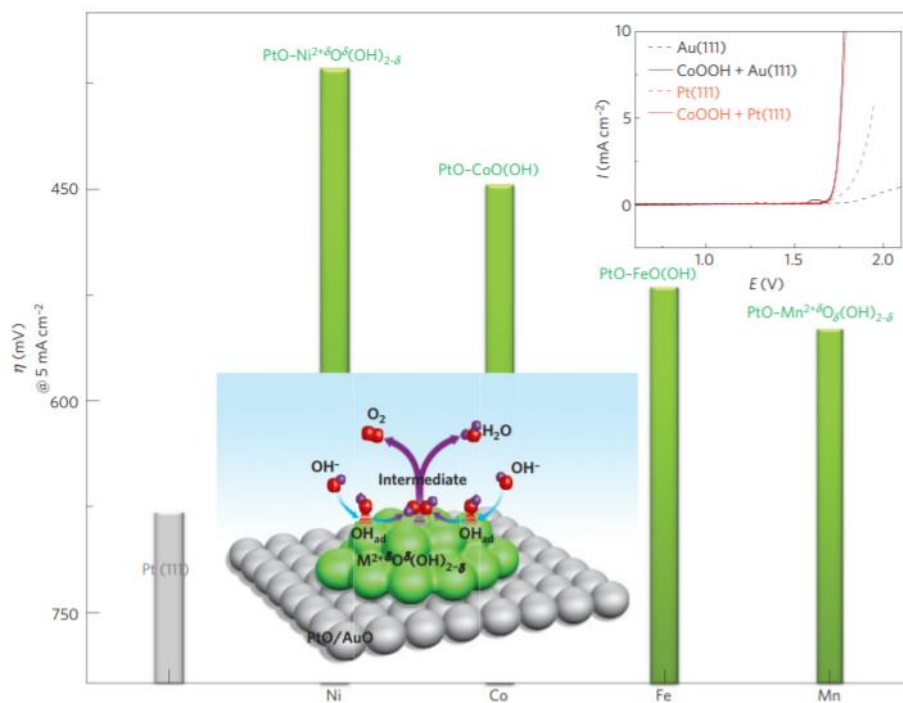


Figure 1.9. Trend in overpotential for OER is shown as a function of the 3d transition elements. The elements are arranged in the order of their oxophilicity from Mn to Ni on Pt surfaces. Pt is shown in the figure as a reference. Top inset: a comparison of polarization curves for Pt (111) and Au (111) with 40 % CoOOH for the OER.<sup>105</sup>

promising substitute of precious metal based OER electrocatalysts. Besides its low cost and earth abundance, nickel based compounds tend to show higher resistant to corrosion in the alkaline medium resulting a longer stability in comparison to other 3d metals.<sup>160</sup> Cobalt based catalysts are more likely to exhibit bifunctional behavior (OER and HER/ORR) towards water splitting, which can be attributed from the presence of mixed valence  $\text{Co}^{2+}$  and  $\text{Co}^{3+}$  in the Co based materials.<sup>161,162</sup> It has been widely accepted that  $\text{Co}^{3+}$  is mainly contributed to the OER process while  $\text{Co}^{2+}$  is associated to the reduction reactions such as HER or ORR.<sup>113,163</sup> Among these 3d metals, single iron based materials show the least conductivity leading to low catalytic activity.<sup>164</sup> Interestingly, the OER catalytic activity of other 3d metal based electrocatalysts can be dramatically increased

with introducing of Fe due to changes in electronic properties.<sup>124,165</sup> A study reported by Shannon's group in Figure 1.10 demonstrated the effect of OER catalytic activity and electrical conductivity in terms of the amount of iron dopants in thin films.<sup>124</sup>

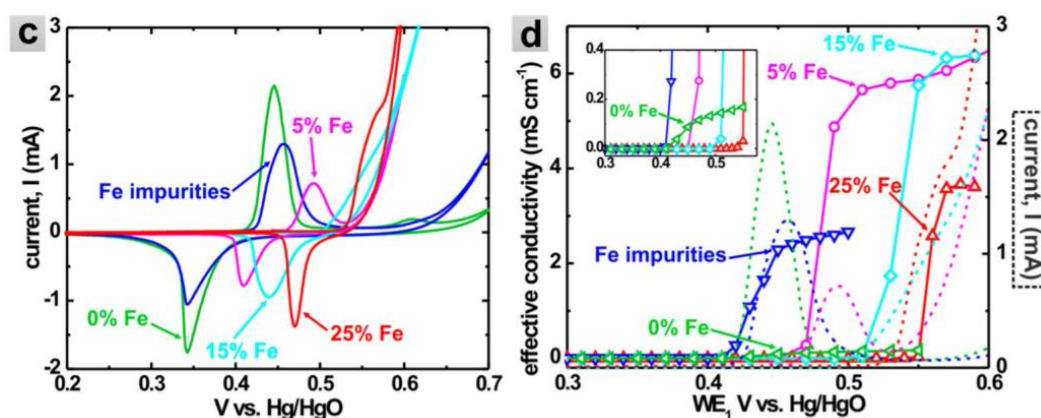


Figure 1.10. (c) CV scans of Ni<sub>1-x</sub>Fe<sub>x</sub>(OH)<sub>2</sub>/Ni<sub>1-x</sub>Fe<sub>x</sub>OOH films doped with different amount of Fe on IDA electrodes. (d) Conductivity data (points with solid connecting lines) for the same films. The potential onset of conductivity correlates with the position of the hydroxide/ oxyhydroxide oxidation wave shown as dotted lines for each film. The inset shows an enlarged region to make the conductivity turn-on for the rigorously Fe-free film apparent.<sup>124</sup>

By transition metal doping, a mixed metal selenide is expected to have diverse advantageous properties of two or more individual selenides within one material.<sup>166</sup> Currently, most of these binary or ternary metal selenides combined either of iron, cobalt or nickel, have attracted the most of attentions as remarkably outperformed its individual counterparts in OER process.

The combination of nickel-iron has been a popular choice for binary metal selenides as OER electrocatalysts. Porous (Ni<sub>0.75</sub>Fe<sub>0.25</sub>)Se<sub>2</sub> nanosheets with high surface area were synthesized on carbon fiber cloth (CFC) by selenization of NiFe nanosheet precursor resulting in a low overpotential of 255 mV at 35 mA cm<sup>-2</sup> and excellent durability for 28

h in alkaline solution.<sup>167</sup> Furthermore, Hu's group improved catalytic activity of ultrathin  $\text{Ni}_x\text{Fe}_{1-x}\text{Se}_2$  nanosheets which required only 195 mV for  $10 \text{ mA cm}^{-2}$  in alkaline solution.<sup>129</sup> Interestingly, Ni-Fe mixed diselenide nanocages were synthesized through the selenization of the Ni-Fe Prussian-blue analog nanocages in Se vapor leading to a superior catalytic performance.<sup>168</sup> Ni-Fe mixed diselenide yielded a current density of  $10 \text{ mA cm}^{-2}$  at a small overpotential of 240 mV and low Tafel slope of  $24 \text{ mV dec}^{-1}$  indicating the catalyst is kinetically favorable.<sup>168</sup> As spinel type structure  $\text{FeNi}_2\text{Se}_4$  nanoparticles, containing a hexagonal close packing of  $\text{Se}^{2-}$  with  $\text{Fe}^{3+}$  occupying the octahedral sites and  $\text{Ni}^{2+}$  occupying the tetrahedral sites, were investigated by Umaphathi et al as OER electrocatalyst.<sup>169</sup> It is a great interest that  $\text{FeNi}_2\text{Se}_4$ -NrGO nanocomposite affords a current density of  $10 \text{ mA cm}^{-2}$  with low overpotential of 170 mV due to the synergistic effect of  $\text{FeNi}_2\text{Se}_4$  and carbon matrix.<sup>169</sup>

Cobalt-nickel selenide is another combination of electrocatalysts to enhance the OER catalytic activity and numerous efforts have been contributed to design novel bimetallic Co-Ni selenide electrocatalysts. Co-Ni selenides can assume multiple molecular formula and structures such as: spinel, monoclinic, amorphous, etc., therefore, it requires researchers to develop various stoichiometric compounds and determine the one facilitating OER performance the most. Shinde. and his coworkers have synthesized  $\text{Ni}_{0.88}\text{Co}_{1.22}\text{Se}_4$  hollow microparticles through a two-step low temperature route and the resulting catalyst exhibiting a low overpotential of 320 mV at  $10 \text{ mA cm}^{-2}$  which is attributed to the numerous exposed catalytic active sites.<sup>170</sup> Moreover, Penroseite  $(\text{Ni},\text{Co})\text{Se}_2$  nanocages on 3D graphene aerogel (GA) were fabricated from NiCo PBA precursor by Wang's group.<sup>171</sup> Consequently, the resulting  $(\text{Ni},\text{Co})\text{Se}_2$ -GA exhibits an

overpotential of 250 mV at  $10 \text{ mA cm}^{-2}$  towards OER as well as excellent stability in alkaline medium.<sup>171</sup> Furthermore, NiCoSe<sub>2</sub> nanosheets were electrodeposited on 3D nickel foam (NF) in Akbar's study which only requires 183 mV to reach a current density of  $10 \text{ mA cm}^{-2}$ .<sup>172</sup> Interestingly, a monoclinic type NiCo<sub>2</sub>Se<sub>4</sub> holey nanosheets were investigated by Yu's group showing outstanding catalytic activity for OER with 295 mV at  $10 \text{ mA cm}^{-2}$ .<sup>173</sup> To further elucidate the great catalytic activity of NiCo<sub>2</sub>Se<sub>4</sub>, the authors compared NiCo<sub>2</sub>Se<sub>4</sub> with other related compounds in Figure 1.11 (a-b), remarkably, DFT calculation

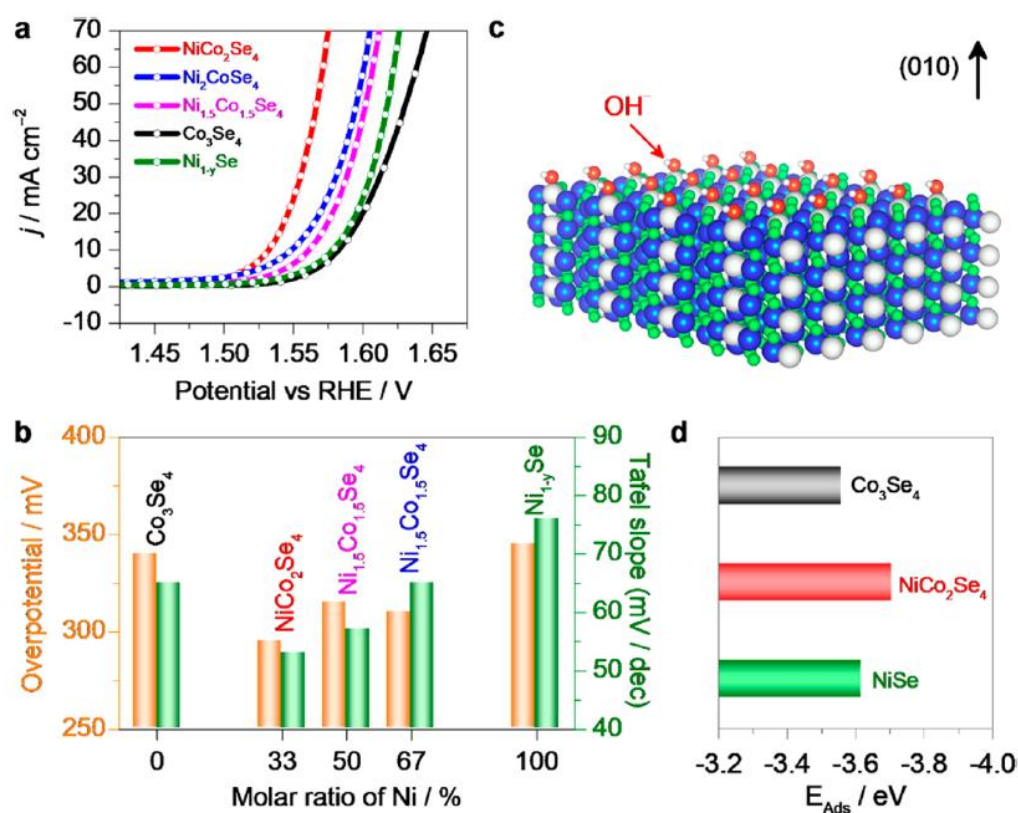


Figure 1.11. Experimental and theoretical study of catalytic activity of NiCo<sub>2</sub>Se<sub>4</sub>. (a) 95 % IR-corrected polarization curves of a series of Ni<sub>x</sub>Co<sub>3-x</sub>Se<sub>4</sub> ( $x = 0-3.0$ ). (b) Comparison of overpotentials and Tafel plots of Ni<sub>x</sub>Co<sub>3-x</sub>Se<sub>4</sub> in 1.0 M KOH solution. (c) Model of OH<sup>-</sup> on the (010) facet of NiCo<sub>2</sub>Se<sub>4</sub>. (d) OH<sup>-</sup> adsorption energy of Co<sub>3</sub>Se<sub>4</sub>, NiCo<sub>2</sub>Se<sub>4</sub>, and NiSe.<sup>173</sup>

shown in Figure 1.11 (c-d) was performed by calculating the hydroxyl species on (010) facet indicating ternary selenide is more kinetically favorable towards OER.<sup>173</sup>

As mentioned above, the performance of transition metal based electrocatalysts can be significantly enhanced with appropriate foreign metal doping. Besides binary metal selenides, trimetallic selenides are also a promising group of OER electrocatalysts, however, they are greatly less studied in comparison to bimetallic selenides. In general, either oxides or chalcogenides comprising three or more than three metals lead to amorphous structure.<sup>174,175,176,177</sup> For instance, amorphous NiFeCoSe<sub>x</sub> on CFC were fabricated by solvothermal selenization process and consequently the catalyst only requires a low overpotential of 150 mV at 10 mA cm<sup>-2</sup> in alkaline solution.<sup>178</sup> The superior OER catalytic activity of NiFeCoSe<sub>x</sub> can be attributed the synergistic effect of mixed transition metals.<sup>178</sup>

### 1.3. COMBINATORIAL METHOD

Combinatorial chemistry uses chemical synthetic methods to make a library of large number of materials with incremental variations of composition in vast regions for further exploration of desired properties.<sup>179</sup> The concept of combinatorial materials synthesis and high-throughput was introduced in the 1980s, and after that it has been widely used in both industries and academia. The main reason of combinatorial method being preferred is that it is more systematical and faster than traditional serial experiments. Therefore, at the very beginning, combinatorial methods were largely exploited in organic synthesis such as drug design and searching for new pharmaceuticals because they are more efficiently than traditional synthetic methods.<sup>180,181,182</sup> For instance, using combinatorial synthesis of

peptide library, a set of different amino acids (or other chemicals) is divided into an equal portions, and followed by mixing a different amino acid to each portion. Repeat the same rounds, finally  $n^2$  peptide sequences with mixing of all portions will be formed.<sup>183</sup> Figure 1.12 shows a schematic of split-mix synthesis.

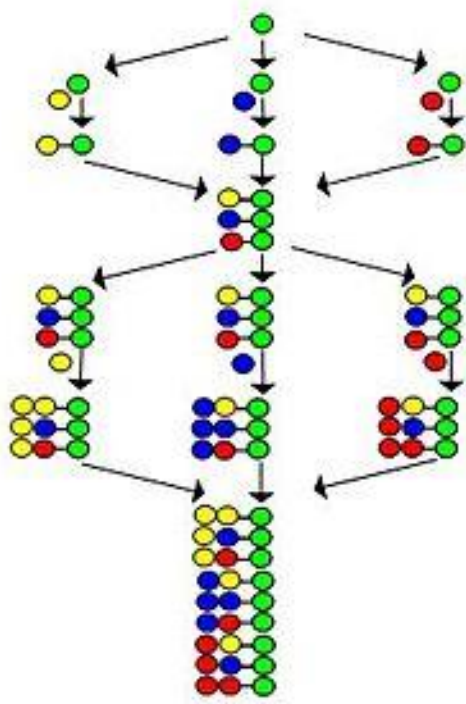


Figure 1.12. The amino acids used in couplings are represented by yellow, blue and red circles.<sup>183</sup>

Recently, combinatorial methods have been widely carried out by researchers in synthesizing a library of solid state materials for various applications ranging from photoluminescence, dielectrics, phosphor, superconductors to homo/heterogenous catalysts.<sup>184,185,186,187,188,189,190</sup> To make the combinatorial approaches applicable, it is important to create spatially varying material libraries. Many researchers have dedicated in developing new methods to create construction of gradients, including physical vapor



deposition (PVD),<sup>191,192</sup> pulsed laser deposition,<sup>193</sup> hydrothermal synthesis,<sup>194</sup> ink-jet printing,<sup>195,196</sup> and electrodeposition<sup>197,198</sup> and so on. Danielson et. al. have used electron beam PVD method on combinations of  $\text{La}_2\text{O}_3$ ,  $\text{Y}_2\text{O}_3$ ,  $\text{MgO}$ ,  $\text{SrCO}_3$ ,  $\text{SnO}_2$ ,  $\text{V}$ ,  $\text{Al}_2\text{O}_3$ ,  $\text{Eu}_2\text{O}_3$ ,  $\text{Tb}_4\text{O}_7$ ,  $\text{Tm}_2\text{O}_3$  and  $\text{CeO}_2$  to find out the optimal luminescent materials.<sup>199</sup> Wessler et. al. have demonstrated chemical solution deposition (CSD) to investigate through libraries based on targets of Ba, Ti, W, and S to generate promising materials for microwave dielectrics.<sup>185</sup>

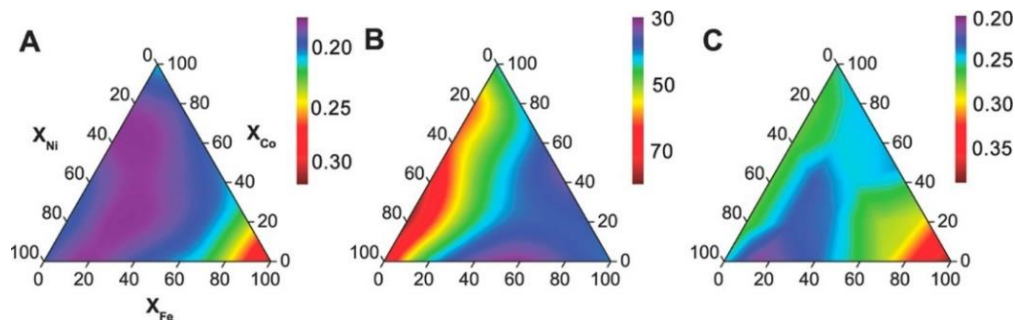


Figure 1.13. Contour plots of kinetic parameters extracted from Tafel plots recorded on 21 independent amorphous (mixed-) metal oxide films: (A) onset  $\eta$  in units of V; (B) Tafel slopes in units of  $\text{mV dec}^{-1}$ ; and (C)  $\eta$  (in units of V) required to reach  $j = 0.5 \text{ mA cm}^{-2}$ .<sup>200</sup>

Combinatorial methods have also been performed in developing high-efficiency catalysts for electrocatalytic and photo-electrocatalytic energy conversions such as fuel cells and batteries.<sup>201,202,203,204</sup> Guerin et. al. have reported that a series of Pt/C catalysts were used to search the trends of catalytic activities towards to CO electro-oxidation, oxygen reduction, and methanol oxidation.<sup>205</sup> Combinatorial method has also proven to be useful in systematical investigations of catalysts for water oxidation.<sup>206,207</sup> In 2012, Parkinson's group have demonstrated a library of mixed metal oxides containing Ir, Ru, Pt

and Rh by inkjet printing as OER catalysts, and they successfully identified that mixed metal oxides showed better activity than the state-of-the-art catalyst  $\text{IrO}_x$ .<sup>207</sup> Smith et. al. used photochemical metal–organic deposition (PMOD) to form amorphous metal oxide thin films with different compositions of Ni, Fe and Co to investigate the OER catalytic activity with respect to varying the metal compositions.<sup>200</sup> Trends of three essential kinetic parameters were plotted as a function of metal compositions as shown in Figure 1.13, where the best composition was discovered as  $\alpha\text{-Fe}_{20}\text{Ni}_{80}$ .<sup>200</sup> Similarly, Haber’s group generated a series of pseudo-quaternary  $(\text{Ni-Fe-Co-Ce})\text{O}_x$  to investigate the OER catalytic activity and the contour map is shown in Figure 1.14, eventually, a Ce-rich pseudo-ternary composition  $\text{Ni}_{0.2}\text{Co}_{0.3}\text{Ce}_{0.5}\text{O}_x$  yielded the lowest overpotential towards OER.<sup>208</sup> Following this work, in 2016, Haber’s group reported a series of photo-electrocatalysts  $(\text{Ni-Fe-Co-Ce})\text{O}_x$  coated on  $\text{BiVO}_4$  substrates as photoelectrocatalyst in photoanodes, surprisingly, the combination of Fe-Ce in the range of  $\text{Fe}_{(0.4-0.6)}\text{Ce}_{(0.6-0.4)}\text{O}_x$  exhibited the best interface to improve the photocatalytic efficiency.<sup>209</sup>

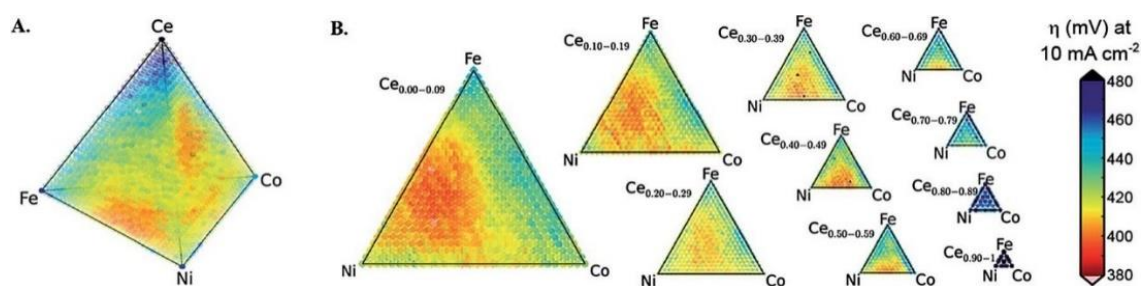


Figure 1.14. Performance map of  $(\text{Ni-Fe-Co-Ce})\text{O}_x$  oxygen evolution catalysts. The composition map of the overpotential required for performing oxygen evolution at  $10 \text{ mA cm}^{-2}$  from CP measurements is shown (A) in the quaternary composition tetrahedron and (B) as a series of pseudoternary slices through the quaternary space.<sup>208</sup>

As noted above, combinatorial method is promising for large-scale systematically study electrocatalysts for oxygen evolution reaction. Frequently these combinatorial methods lead to identification of composition regime that can show optimal performance, which otherwise would have been missed in targeted materials synthesis. In our lab, we performed a more efficient and economical method – combinatorial electrodeposition – to systematically investigate several trigonal phase diagrams and identified the optimal non-stoichiometric composition. The advantage of this modified combinatorial method is that direct electrodeposition on the functional electrodes produces binder and other additives-free catalyst composite, thereby reducing dead-weight and utilizes full potential of the catalyst.

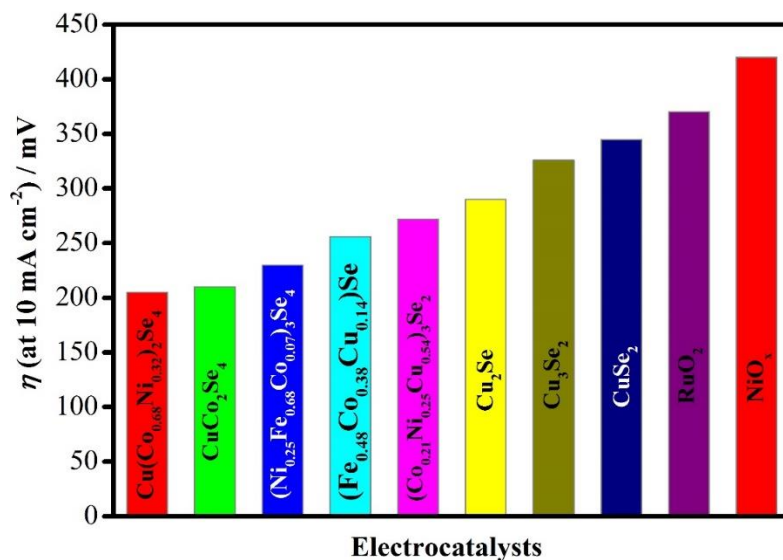


Figure 1.15. Overpotential at 10 mA cm<sup>-2</sup> of all OER electrocatalysts described in this dissertation.

In summary, this dissertation is mainly focused on developing mixed transition metal selenides as OER electrocatalysts in alkaline medium by combinatorial

electrodeposition and identifying the optimal compositions in three different systems, and more details will be presented in Chapter I to Chapter III. Based on the contour plot of catalytic activity with respect to the composition exhibited in Chapter II, several interesting naturally-occurring minerals with similar compositions were expected to show great performance as OER electrocatalysts which they were successfully fabricated through one-step hydrothermal route in our lab. Significant process towards designing novel high efficiency OER electrocatalyst has been made and the comparison plot of all OER catalysts described in this dissertation outperform the OER activity of  $\text{RuO}_2$  as shown in Figure 1.15.

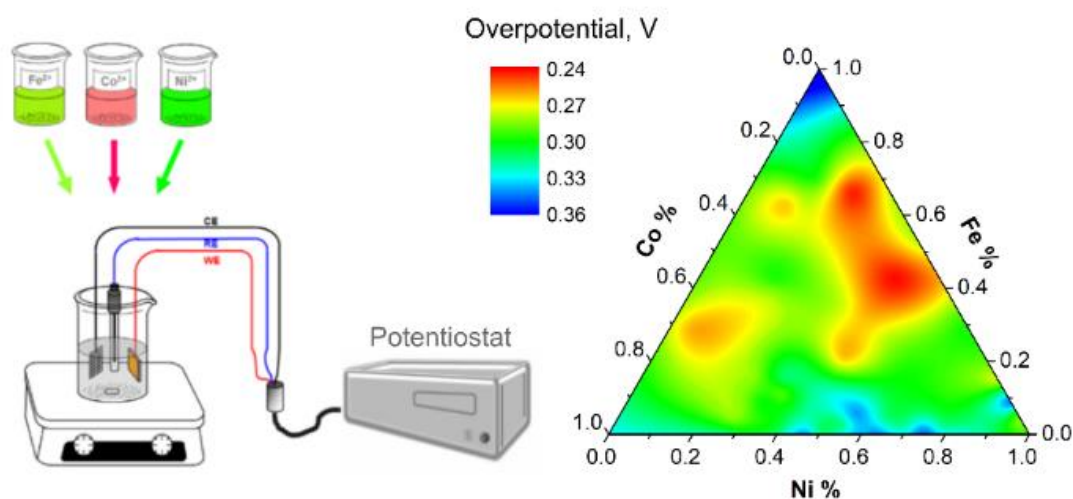
## PAPER

**I. PHASE EXPLORATION AND IDENTIFICATION OF MULTINARY TRANSITION METAL SELENIDES AS HIGH-EFFICIENCY OXYGEN EVOLUTION ELECTROCATALYSTS THROUGH COMBINATORIAL ELECTRODEPOSITION**

*Xi Cao,<sup>a</sup> Yu Hong,<sup>b</sup> Ning Zhang,<sup>b</sup> Qingzhi Chen,<sup>a</sup> Jahangir Masud,<sup>a</sup> Mohsen Asle Zaeem,<sup>b</sup> and Manashi Nath<sup>a\*</sup>*

<sup>a</sup>Department of Chemistry, Missouri University of Science & Technology, Rolla, Missouri 65409, United States.

<sup>b</sup>Department of Materials Science & Engineering, Missouri University of Science and Technology, Rolla, Missouri 65409, United States.

**ABSTRACT**

Designing high-efficiency electrocatalysts for water oxidation has become an increasingly important concept in the catalysis community due to its implications in clean energy generation and storage. In this respect transition metal-doped mixed-metal

selenides incorporating earth abundant elements such as Ni and Fe have attracted attention due to their unexpectedly high electrocatalytic activity toward the oxygen evolution reaction (OER) with low overpotential in alkaline medium. In this article, quaternary mixed-metal selenide compositions incorporating Ni-Fe-Co were investigated through combinatorial electrodeposition by exploring the ternary phase diagram of Ni-Fe-Co systems. The OER electrocatalytic activity of the resultant quaternary and ternary mixed metal selenide compositions was measured in order to systematically investigate the trend of catalytic activity as a function of catalyst composition. Accordingly, the composition(s) exhibiting the best catalytic efficiency for the quaternary Fe-Co-Ni mixed-metal selenide was identified. It was observed that the quaternary selenide outperformed the binary as well as the ternary metal selenides in this Ni-Fe-Co phase space. The elemental composition and relative abundance of the elements in the catalyst film was ascertained from energy dispersive spectroscopy (EDS) and X-ray photoelectron spectroscopy (XPS). Mapping of the OER catalytic activity as a function of catalyst composition indicated that catalytic efficiency was more pronounced in the Fe rich region with moderate amounts of Ni and trace amounts of Co doping, and the best performance was exhibited by  $(\text{Ni}_{0.25}\text{Fe}_{0.68}\text{Co}_{0.07})_3\text{Se}_4$ , which showed an overpotential of 230 mV (vs RHE) at  $10 \text{ mA cm}^{-2}$  with stability exceeding 8 h for continuous oxygen generation. It was also observed that typically the quaternary metal selenide composition was close to  $\text{AB}_2\text{Se}_4$ , which shows a spinel structure type. Electrochemical measurements along with density functional theory (DFT) calculations were performed to correlate the enhancement of catalytic activity toward the Fe-rich region with composition. First principles DFT calculations were used to estimate the hydroxyl adsorption energy ( $E_{ads}$ ) on the surface of the mixed-metal

selenides with varying compositions. This adsorption energy could be directly correlated to the onset of OER activity, and the results matched very well with the experimentally observed trend with respect to onset overpotential. The knowledge of the trend of catalytic activity as a function of composition will be very important for catalyst design through targeted material synthesis. This work represents an example of a systematic phase exploration for quaternary metal selenides and provides a strong foundation which can be expanded to study other mixed-metal selenide combinations.

**Keywords:** combinatorial electrodeposition, oxygen evolution reaction, water splitting, electrocatalyst, mixed-metal selenide

## 1. INTRODUCTION

The promise of hydrogen as being one of the most potent sources of clean energy has intensified research into cost effective production of pure hydrogen in copious quantities from fossil-fuel-free sources. In that regard, electrolysis of water into H<sub>2</sub> and O<sub>2</sub> gas by applying sunlight or any other inexhaustible natural resources has been an attractive method to generate the clean fuels.<sup>1,2</sup> However, the efficiency of the water-splitting reaction is limited by the challenging anodic oxygen evolution reaction (OER), which is an energy-exhaustive four-electron process, leading to a kinetically slow step and significant efficiency loss.<sup>3,4</sup> Typically for an electrocatalyst, the applied potential required in excess of the thermodynamic water splitting voltage (1.23 V vs RHE) is generically referred to as overpotential. An efficient electrocatalyst which can reduce the overpotential and enhance the energy efficiency plays a crucial role in increasing the feasibility of large-

scale water-splitting reactions. Therefore, significant efforts have been directed toward designing more efficient and stable catalysts for OER capable of reducing the overpotential.<sup>1,5-10</sup> Though precious metal oxides such as IrO<sub>2</sub> and RuO<sub>2</sub> show excellent OER electrocatalytic activities, their high price and scarcity of raw materials limit their applications.<sup>11-13</sup> Recently, considerable efforts have been made to develop robust OER electrocatalysts based on earth-abundant elements such as Co, Ni, and Fe.<sup>14-17</sup> In this quest for transition-metal-based highly efficient OER electrocatalysts, two important observations have been made: (i) increasing covalency around the transition-metal center increases catalytic activity<sup>18,19</sup> and (ii) transition-metal doping enhances catalytic activity by reducing the overpotential.<sup>20-27</sup> In keeping with the concept of increasing covalency enhancing OER catalytic activity it was observed that transition-metal chalcogenides show improved catalytic activity in comparison to the corresponding oxides in alkaline medium.<sup>18,19,28-34</sup> The effect of metal doping is also visible in several reports of ternary mixed metal oxides, hydroxides, and selenides, which have exhibited enhancement of catalytic activity in comparison to the corresponding binary phases.<sup>22,23,26,35-42</sup> It can be expected that transition-metal doping rearranges the electron density around the catalytically active metal center, thereby altering the potential required for catalyst activation which is necessary for initiating the oxygen evolution reaction.<sup>7,43-45</sup> Doping also affects the electron transfer rate within the catalyst, which influences the current density as well as reaction kinetics. Another aspect of doping is the ability to design quaternary compositions, such that the catalytic efficiency can be improved even further by providing multiple catalytically active transition metal centers with varying composition, facilitating electron transfer in the multi metal network, as well as providing



stability to the catalytic system. However, most of the reports of mixed metal-based OER electrocatalysts has been with limited compositional and/or stoichiometric variations. A systematic investigation of the trend of catalytic activity as a function of transition-metal doping is still very rare. Such a study will be even more effective in the transition-metal selenides, which show inherently better OER catalytic activity in comparison to the oxides.<sup>20,21,46-48</sup> Hence, a phase diagram exploration to systematically investigate the trend of catalytic activity as a function of ternary and quaternary transition-metal doping in the selenide lattice has become necessary. Combinatorial synthesis is an extremely effective method to screen compositions in the multinary phase space and study the evolution of properties as a function of systematic change in composition. Combinatorial phase exploration is widely used in organic synthesis, antioxidants, and drug designs.<sup>49-53</sup> Frequently these combinatorial methods lead to identification of a composition regime that can show optimal performance, which otherwise would have been missed in targeted materials synthesis. Such combinatorial methods have been reported recently to provide an efficient way to screen and discover promising OER electrocatalysts.<sup>54-57</sup> For example, the metal oxides have been recently explored through combinatorial methods, whereby Chen, Stahl, et al. identified the inverse spinel  $\text{NiFeAlO}_4$  as a highly efficient OER electrocatalyst,<sup>58</sup> while the Berlinguette group investigated the electrocatalytic response of amorphous metal oxide films by combinatorial methods.<sup>59</sup> As mentioned above, the transition-metal selenides have exhibited better catalytic efficiency in comparison to the oxides, which is attributed to the lower anion electronegativity and increased degree of covalency in the lattice. Our group has also recently reported nickel and cobalt selenides ( $\text{Ni}_3\text{Se}_2$ ,  $\text{NiSe}_2$ , and  $\text{Co}_7\text{Se}_8$ ) which exhibit high efficiency as OER electrocatalysts in

alkaline solution and have an excellent operational stability.<sup>18,28,46,47</sup> We have also observed that the mixed-metal selenides  $\text{CoNi}_2\text{Se}_4$  and  $\text{FeNi}_2\text{Se}_4$  show better catalytic activity than the corresponding oxide phases.<sup>20,21</sup> From these reports it is indicative that both Co and Fe doping in the Ni selenides can lead to enhancement of the OER catalytic activity in alkaline medium. However, a systematic study of the extent of enhancement of catalytic efficiencies as a function of composition variation through simultaneous Fe and Co doping in the selenides has not yet been reported. In this article we report the systematic investigation of OER electrocatalytic activity of mixed-metal selenides comprising Ni-Fe-Co through combinatorial electrodeposition exploring the trigonal phase diagram. Direct electrodeposition on the functional electrodes produces a catalyst composite free of binder and other additives, thereby reducing dead weight and utilizing the full potential of the catalyst. A systematic investigation of OER catalytic activity in the Ni-Fe-Co phase space revealed that the gradient of catalytic performance increased toward increasing Fe concentration and the best performance was exhibited by  $(\text{Ni}_{0.25}\text{Fe}_{0.68}\text{Co}_{0.07})_3\text{Se}_4$ , which showed an overpotential of 230 mV (vs RHE) at  $10 \text{ mA cm}^{-2}$ . Chronoamperometric measurements revealed that this catalyst was stable for an extended period of time under continuous oxygen evolution, while postactivity XPS and EDS characterization revealed that the compositional integrity of the catalyst remained unchanged. We also calculated the hydroxyl adsorption energy ( $E_{\text{ads}}$ ) on the surface of the mixed-metal selenide since the OER is initiated by the attachment of an OH group on the surface following catalyst activation. Comparison of  $E_{\text{ads}}$  across the compositional range showed that the  $E_{\text{ads}}$  shows a trend similar to that of the decreasing overpotential, confirming the trend of increasing catalytic activity (earlier catalyst activation and onset of OER) toward the Fe-rich region. This study

thus provides very useful information on the effect of systematic doping in transition metal selenide based electrocatalysts containing Ni, Fe, and Co, which can be used to design highly efficient OER electrocatalysts through targeted synthesis. Such a concept of combinatorial electrodeposition can also be extended to design high performance catalytic systems in various other ternary phase spaces.

## 2. EXPERIMENTAL SECTION

**Materials.** Nickel(II) sulfate ( $\text{NiSO}_4 \cdot 6\text{H}_2\text{O}$ , 99.0%), cobalt(II) sulfate ( $\text{CoSO}_4 \cdot 7\text{H}_2\text{O}$ , 99.0%), iron(II) sulfate ( $\text{FeSO}_4 \cdot 7\text{H}_2\text{O}$ , 99.0%), selenium dioxide ( $\text{SeO}_2$ ), ammonium sulfate ( $(\text{NH}_4)_2\text{SO}_4$ , 99%), and potassium hydroxide (KOH, 85%), were purchased from Fisher Scientific. All of the chemicals were used as received without further purification. Deionized (DI) water ( $18 \text{ M}\Omega/\text{cm}$ ) was used to prepare all the electrolytic solutions. Au-coated glass slides used as substrates in electrodeposition were purchased from Deposition Research Lab Incorporated (DRLI), Lebanon, MO.

**Combinatorial Electrodeposition of Catalyst Films.** All electrodeposition experiments were carried out in a beaker with an electrolyte volume of 50 mL in a three-electrode setup consisting of an Ag|AgCl (saturated KCl) reference electrode, glassy carbon (GC) as the counter electrode, and Au-coated glass with an area of  $0.283 \text{ cm}^2$  as the working electrode. Prior to electrodeposition, the substrates were sonicated in Micro-90 followed by an isopropyl alcohol rinse and eventually rinsed with deionized water (15 min each step) to ensure a clean surface. All solutions were freshly prepared and purged with  $\text{N}_2$  for 30 min before electrodeposition. The electrolytes used for deposition contained an

equimolar (10 mM) mixture of the metal sulfate precursors ( $\text{NiSO}_4 \cdot 6\text{H}_2\text{O}$ ,  $\text{CoSO}_4 \cdot 7\text{H}_2\text{O}$ ,  $\text{FeSO}_4 \cdot 7\text{H}_2\text{O}$ ), 10 mM  $\text{SeO}_2$ , and 25 mM  $(\text{NH}_4)_2\text{SO}_4$  dissolved in water.

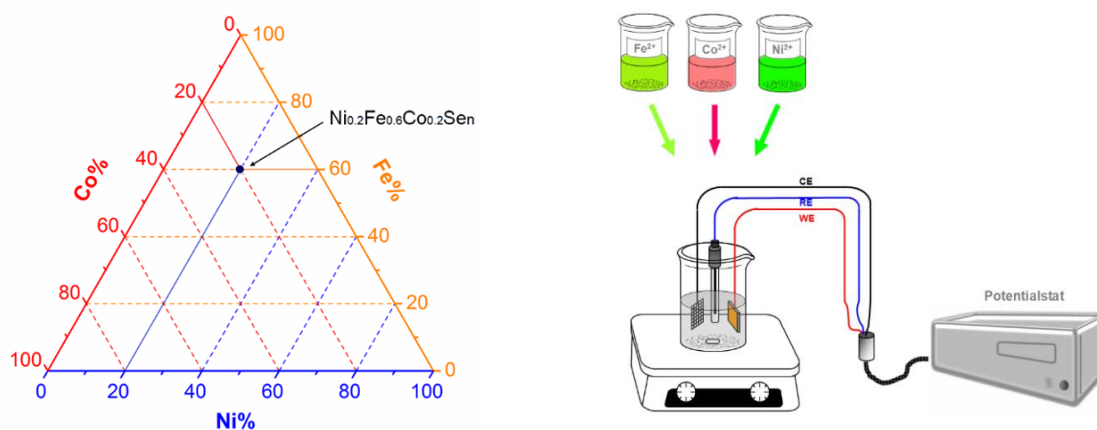


Figure 1. Schematic of combinatorial electrodeposition. (a) Ternary phase diagram for exploring compositions of the mixed metal selenide films examined in this work. Crossing vertices represent compositions of the precursor electrolyte with respect to the relative ratio of the corresponding metals. Black circle shows a typical example. (b) Electrodeposition.

Combinatorial synthesis of a series of binary and multinary mixed-metal selenide films were carried out by exploring the ternary phase diagram as shown in Figure 1a. In this trigonal phase diagram, the vertices represent binary selenides ( $\text{Ni}_3\text{Se}_2$ ,  $\text{FeSe}$ , and  $\text{CoSe}$ ), while along the three edges, ternary mixed metal selenides ( $\text{Ni}_x\text{Fe}_y\text{Se}_n$ ,  $\text{Ni}_x\text{Co}_y\text{Se}_n$ ,  $\text{Fe}_x\text{Co}_y\text{Se}_n$ ) can be obtained. The interior of this trigonal phase diagram represents the quaternary mixed-metal selenide. The amount of Se precursor ( $\text{SeO}_2$ ) added in solution was kept constant, and the relative molar ratio of the metal sulfate precursors ( $\text{NiSO}_4$ ,  $\text{FeSO}_4$ ,  $\text{CoSO}_4$ ) were varied as  $x:y:z$  for Ni:Fe:Co in the electrolytic bath, to explore various points within the trigonal phase diagram as shown in Figure 1. This relative molar ratio has been referred to as the precursor ratio, while the actual relative atomic ratio in the

electrodeposited film has been determined through energy dispersive spectral analysis (EDS). The precursor concentration for each metal (Ni, Fe, and Co) was varied from 0 to 100% along the respective axis in steps of 10% increments. Once a region of high catalytic activity was identified in the trigonal phase space, then that region of interest was reinvestigated by exploring a smaller trigonal region with 5% increments of the precursor for each element. The smaller triangle is shown in Figure S1 in the Supporting Information. All electrodeposition was carried out at room temperature in acidic solution (pH 2.8) on Au-coated glass substrates at an applied potential of  $-0.8$  V vs Ag|AgCl for 300 s. Electrodeposition was carried out in confined regions of the Au coated glass substrates. An IviumStat potentiostat was used for electrodeposition and all electrochemical studies. All resulting films were carefully washed several times with DI water to remove surface ions and then dried in air.

Characterization. X-ray photoelectron spectroscopy (XPS) measurements of catalysts were performed using a KRATOS AXIS 165 X-ray photoelectron spectrometer using a monochromatic Al X-ray source. Scanning electron microscopy (SEM) was carried out to examine the morphologies of the films by the FEI Helios NanoLab 600 FIB/FESEM at an accelerating voltage of 15 kV. Energy dispersive spectroscopy (EDS) along with elemental mapping analysis was also obtained from the SEM microscope. The elemental compositions of all compounds detected by EDS are shown in Table 1. In this article, the molecular formula of compounds (shown in Table S1 in the Supporting Information) will be defined by experimentally obtained EDS atomic ratios and will be written as  $(\text{Ni}_x\text{Fe}_y\text{Co}_z)_m\text{Se}_n$ , where  $x'$ ,  $y'$ , and  $z'$  are determined from EDS atomic ratios ( $x' + y' + z'$

= 1) and m and n are the experimentally obtained relative EDS atomic ratios between total metal ions and selenium.

**Electrochemical Measurements.** The catalytic properties of the thin films were investigated in 0.3 M KOH solution at room temperature in a three-electrode system using an IviumStat potentiostat. The OER catalytic performances were studied from linear scan voltammetry (LSV) plots, while the stabilities of the catalysts were studied by constant-potential chronoamperometry. The deposited thin films served as the working electrodes, a GC was the counter electrode, and an Ag|AgCl (saturated KCl) was the reference electrode. All measured potentials vs the Ag|AgCl (saturated KCl) were converted to the reversible hydrogen electrode (RHE) using the Nernst equation (eq 1) and corrected for the iR drop in the solution.

$$E_{RHE} = E_{Ag/AgCl} + 0.059pH + E_{Ag/AgCl}^{\circ} \quad (1)$$

Here, the converted potential vs RHE is the experimentally measured potential against the Ag|AgCl reference electrode, and the standard potential of Ag|AgCl at 25.1 °C was 0.197 V.

**Faradaic Efficiency.** The Faradaic efficiency of O<sub>2</sub> production by (Ni<sub>0.25</sub>Fe<sub>0.68</sub>Co<sub>0.07</sub>)<sub>3</sub>Se<sub>4</sub> electrocatalyst was measured using a rotating ring–disk electrode (RRDE) apparatus with the bipotentiostat mode of the IviumStat. Specifically, a combined ORR–OER experiment was designed to confirm and quantify O<sub>2</sub> production, as has been described previously.<sup>47,60</sup> In this process, (Ni<sub>0.25</sub>Fe<sub>0.68</sub>Co<sub>0.07</sub>)<sub>3</sub>Se<sub>4</sub> deposited on a glassy-carbon-disk electrode was used as the anode, while a Pt ring was used as the ring electrode in a RRDE setup. The Pt ring was carefully polished with an alumina slurry (0.05 μm) and then washed with DI water, sonicated for 5 min, and cleaned by an electrochemical method

in N<sub>2</sub>-saturated 0.5 M H<sub>2</sub>SO<sub>4</sub> at 1600 rpm. The disk with the catalyst was held at open circuit for few minutes, while the ring electrode was held at constant 0.16 V vs RHE in 0.3 M KOH solution. The current of the ring electrode was lower than 20 mA, which was in an acceptable region. The disk electrode was then held at sequentially different potentials for 20 s each, in the OER kinetic region, while the ring electrode was held at -0.16 V vs RHE, appropriate for O<sub>2</sub> reduction.

Calculation of Tafel Slope. The electrochemical kinetics of the (Ni<sub>0.25</sub>Fe<sub>0.68</sub>Co<sub>0.07</sub>)<sub>3</sub>Se<sub>4</sub> catalysts toward OER relating the overpotential  $\eta$  with the current density  $j$  has been carried out by

constructing the Tafel plots using eq 2:

$$\eta = a + \frac{2.3RT}{\alpha nF} \log(j) \quad (2)$$

where  $\eta$  is the overpotential,  $j$  is the current density, and the other symbols have their usual meanings. The Tafel slope is given by  $2.3RT/\alpha nF$ . The Tafel slopes were obtained from LSV plots with a scan rate ( $2 \text{ mV s}^{-1}$ ) in a unstirred solution.

### 3. RESULTS AND DISCUSSION

Morphologies and Elemental Compositions of Electrodeposited Films. Figure 2a–c shows morphologies of the three as-deposited binary films Ni<sub>3</sub>Se<sub>2</sub>, CoSe, and FeSe, representing the three vertices of the trigonal phase diagram (Figure 1a), respectively. A detailed SEM study of these as deposited films showed that films were mainly granular and composed of nanometer-sized grains with a broad size distribution (typically, 50 nm

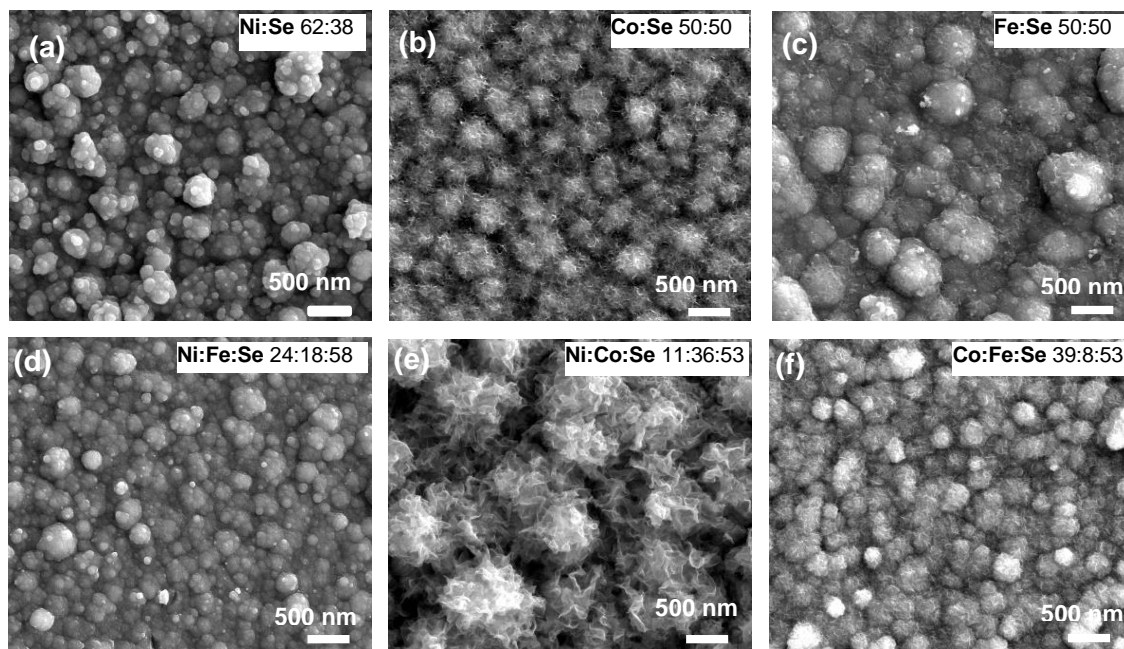


Figure 2. SEM images and elemental compositions by EDS of most active electrocatalyst from different groups comprising three binaries compositions (a)  $\text{Ni}_3\text{Se}_2$ , (b)  $\text{CoSe}$ , (c)  $\text{FeSe}$ , and ternary compositions (d)  $(\text{Ni}_{0.85}\text{Fe}_{0.15})_3\text{Se}_4$ , (e)  $(\text{Ni}_{0.24}\text{Co}_{0.76})\text{Se}$ , (f)  $(\text{Co}_{0.1}\text{Fe}_{0.9})_3\text{Se}_4$ .

to several hundred nanometers). Among these,  $\text{Ni}_3\text{Se}_2$  and  $\text{FeSe}$  grains were composed of aggregated clusters, while the morphology of  $\text{CoSe}$  showed a nanoflake-like geometry. As mentioned previously, the axes of the trigonal plot represent the ternary metal selenides  $\text{Ni}_x\text{Fe}_y\text{Se}_n$ ,  $\text{Fe}_x\text{Co}_y\text{Se}_n$ , and  $\text{Co}_x\text{Ni}_y\text{Se}_n$ , respectively. Figure 2d–f presents morphologies of the three ternary films  $(\text{Ni}_{0.85}\text{Fe}_{0.15})_3\text{Se}_4$ ,  $(\text{Ni}_{0.24}\text{Co}_{0.76})\text{Se}$ , and  $(\text{Co}_{0.9}\text{Fe}_{0.1})_3\text{Se}_4$ , respectively, which showed the best OER catalytic activity. Some changes in morphology and particle size can be observed in the ternary metal selenides in comparison to the binary selenides. For example, with 40% Fe doping into  $\text{Ni}_3\text{Se}_2$ ,  $(\text{Ni}_{0.85}\text{Fe}_{0.15})_3\text{Se}_4$ , it showed smaller sized grains in comparison to  $\text{Ni}_3\text{Se}_2$ . On the other hand, 90% Co doping into  $\text{FeSe}$ , yielded  $(\text{Co}_{0.9}\text{Fe}_{0.1})_3\text{Se}_4$  (shown in Table S1 in the Supporting Information), which exhibited grains covered with thin nanoflakes and closely resembled the morphology of  $\text{CoSe}$ . Interestingly,



(Ni<sub>0.24</sub>Co<sub>0.76</sub>)Se with 20% doping of Ni into CoSe showed a more rough surface and fluffy flowerlike morphology with a bigger particle size (~1 μm). The elemental compositions of these films were analyzed using EDS. The three binary phases were indeed composed of Ni, Co, or Fe and Se in approximate atomic ratios of 3:2 (Ni:Se), 1:1 (Co:Se), and 1:1 (Fe:Se), respectively. Thus, the three binaries can be written as Ni<sub>3</sub>Se<sub>2</sub>, CoSe, and FeSe, respectively. Similarly, molecular formulas of the three best ternaries can be written as (Ni<sub>0.85</sub>Fe<sub>0.15</sub>)<sub>2</sub>Se<sub>3</sub>, (Ni<sub>0.24</sub>Co<sub>0.76</sub>)Se, and (Co<sub>0.9</sub>Fe<sub>0.1</sub>)<sub>3</sub>Se<sub>4</sub>, respectively. All of the ternary phases identified in this study can be found in Table S1, giving the relative precursor ratio as well as the EDS ratio. It should be noted that the relative atomic percentage of an element increased (or decreased) with increasing (or decreasing) amounts of the corresponding metal precursor in the electrolytic bath, indicating the feasibility of compositional control obtainable through such combinatorial electrodeposition. It should be noted here that most of these electrodeposited films were amorphous in nature and did not yield a clean PXRD pattern, which is very typical of electrodeposited films at low temperature. Hence, compositional analysis was done on the basis of EDS and XPS studies.

**Electrochemical Characterization.** Linear sweep voltammetry (LSV) measurements were performed in N<sub>2</sub>-saturated 0.3 M KOH at a scan rate of 10 mV s<sup>-1</sup> to study the electrocatalytic properties of the deposited films. The onset overpotential (onset  $\eta$ ) and overpotential required to reach the current density 10 mA cm<sup>-2</sup> ( $\eta$  at 10 mA cm<sup>-2</sup>) were selected as two kinetic parameters to benchmark the electrocatalytic performance.<sup>60</sup> These two kinetic parameters for all binary, ternary, and quaternary metal selenide phases along with their corresponding EDS atomic ratios are summarized and shown Table 1. The

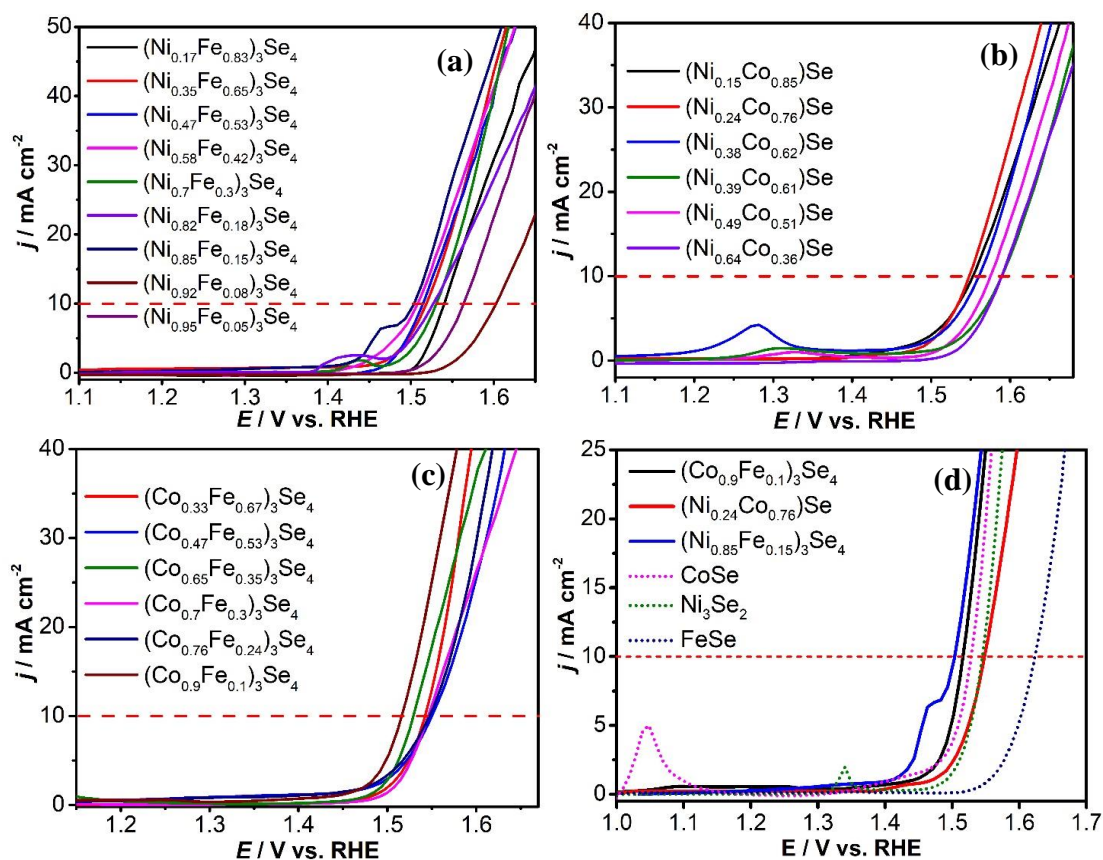


Figure 3. Linear Sweep voltammtries (LSVs) of ternary metal selenides along the edges of the trigonal phase diagram. (a) Ni-Fe group (b) Ni-Co group (c) Co-Fe group. (d) Comparison of most active ternary composition (solid line) from each group along with the three binary compositions (dotted line). The dotted red line in each panel marks the current density at  $10 \text{ mA cm}^{-2}$ .

OER polarization curves of three binary metal selenide films measured in  $0.3 \text{ M KOH}$  is shown in Figure S2 in the Supporting Information. Figure 3 shows the LSV plots of all ternary metal selenide films. As can be seen from the LSV plot of the Ni-Fe selenides group in Figure 3a, these nine Ni-Fe selenides were highly active for the OER. In this group it was observed that the catalytic activity improved with increasing Fe content and that  $(\text{Ni}_{0.85}\text{Fe}_{0.15})_3\text{Se}_4$  showed the best catalytic activity with the lowest applied potential of  $1.468 \text{ V vs RHE}$ , corresponding to an onset overpotential of  $0.238 \text{ V}$  and overpotential at

10 mA cm<sup>-2</sup> (0.27 V vs RHE). For the Ni-Co selenides group shown in Figure 3b, it was observed that (Ni<sub>0.24</sub>Co<sub>0.76</sub>)Se exhibited the best activity among this group with an onset overpotential of 0.25 V vs RHE and overpotential of 0.33 V vs RHE required to achieve 10 mA cm<sup>-2</sup>. The OER performance of the Co-Fe selenide group is shown in Figure 3c, wherein (Co<sub>0.9</sub>Fe<sub>0.1</sub>)<sub>3</sub>Se<sub>4</sub> showed the lowest onset overpotential of 0.25 V vs RHE and overpotential of 0.29 V vs RHE at 10 mA cm<sup>-2</sup>. It must be noted here that there are some preoxidation peaks observed in the LSV plots prior to onset of the OER, as can be seen in Figure 3a,b,d. These peaks are due to the changes in the oxidation states of the transition-metal cations in the catalyst during the anodic scan, as has been previously observed for Ni- and Co-based catalysts.<sup>24,26,61,62</sup> Specifically, the peak around 1.05 V vs RHE is due to Co<sup>2+</sup> to Co<sup>3+</sup> conversion, while those around 1.28 V (Figure 3b) and 1.34 V (Figure 3d) correspond to Ni<sup>2+</sup> to Ni<sup>3+</sup> conversion.<sup>20,21,24,26</sup> It has been commonly reported that transition-metal doping in the cationic site affects the position of the preoxidation peak.<sup>24,62</sup> Such a shift in the Ni<sup>2+</sup> oxidation peak is also visible in Figure 3a,b possibly due to various amounts of Fe and Co doping, respectively, in the nickel selenide system, which can directly affect the chemical potential of the Ni<sup>2+</sup> ion.<sup>24,62</sup> To understand the trend of catalytic activity as a function of transition-metal doping, the best-performing ternary phases have been compared with the binary selenides, as shown in Figure 3d. It can be seen from these comparative plots that 40% Fe doping into Ni<sub>3</sub>Se<sub>2</sub> improved the OER catalytic activity with a 40 mV drop in overpotential at 10 mA cm<sup>-2</sup> in comparison to Ni<sub>3</sub>Se<sub>2</sub>. Similarly, 10% Fe doping into CoSe decreased the overpotential at 10 mA cm<sup>-2</sup> by 10 mV in comparison to CoSe. However, Ni doping into CoSe did not show any significant improvement in the OER catalytic activity. It must be noted here that the positive effect of

transition-metal doping in enhancing OER catalytic activity has also been reported previously by other researchers. For example, it has been reported by various groups that Fe doping into Ni oxyhydroxide based OER electrocatalysts significantly improves the OER catalytic activity.<sup>7,17,23,44,61,62</sup>

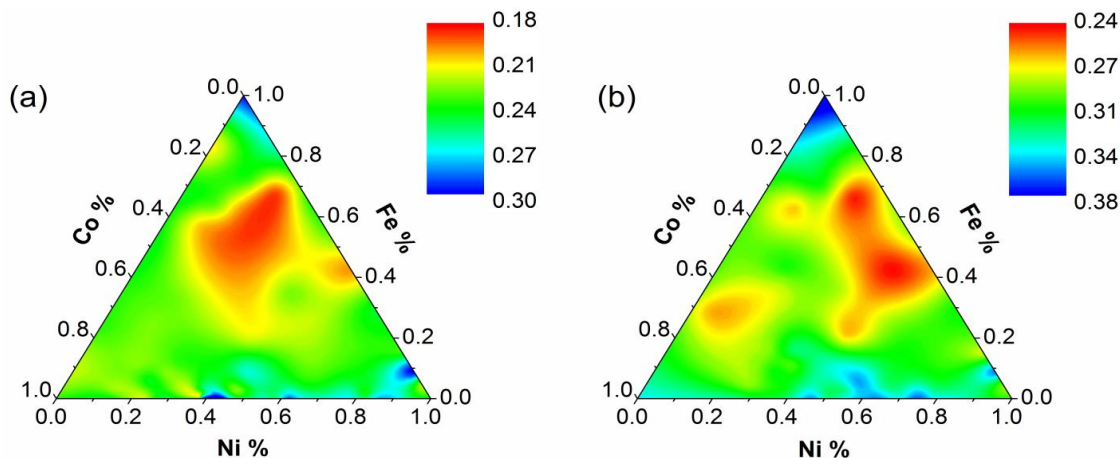


Figure 4. Contour plots of overpotential  $\eta$  (in units of V) at (a) onset of OER activity, and (b) current density of  $10 \text{ mA cm}^{-2}$  for the entire Ni-Fe-Co trigonal phase space. The actual relative atomic ratio of the elements as obtained by EDS was used to construct this plot. The color gradient corresponds to the overpotential measured in volts.

Table 1 gives the results of the trigonal phase diagram exploration with respect to relative precursor ratio in the electrolyte, experimentally observed EDS elemental ratio in the deposited film, onset overpotential, and overpotential at  $10 \text{ mA cm}^{-2}$ . In order to understand the trend of catalytic activity with respect to transition-metal doping better, contour plots were constructed from the data given in Table 1. Figure 4a shows the contour plots for onset  $\eta$ , while Figure 4b shows the contour plot for  $\eta$  at  $10 \text{ mA cm}^{-2}$ . The edges in each of these plots represent increasing amounts of the respective elements (as labeled in the figure), where the actual elemental ratio as determined from EDS was used. The

color gradient key on the upper right corner of these plots indicates decreasing catalytic activity from top (lowest overpotential) to bottom (highest overpotential). As can be seen in Figure 4a, an area deep inside the trigonal plot (quaternary phase space) shows the best catalytic activity. The region adjacent to the Ni and Fe axes as well as the vertices shows higher overpotential indicating less efficient catalytic activity. This observation further confirms that transition-metal doping increases OER catalytic activity in these metal selenides. From the contour plots it is apparent that quaternary phases show the lowest onset overpotential when the relative content of iron is kept at 60–80%, cobalt is maintained at 5–30%, and nickel is about 20–60% for binary and ternary selenides. As the amount of Fe increases while Ni and Co decrease in thin films, mixed-metal selenides are more likely to have lower onset  $\eta$  and  $\eta$  at  $10\text{mAcm}^{-2}$ , suggesting that Fe has a significant influence on the catalyst performance. A similar trend in overpotential also has been observed to achieve  $10\text{ mA cm}^{-2}$ , as shown in Figure 4b.

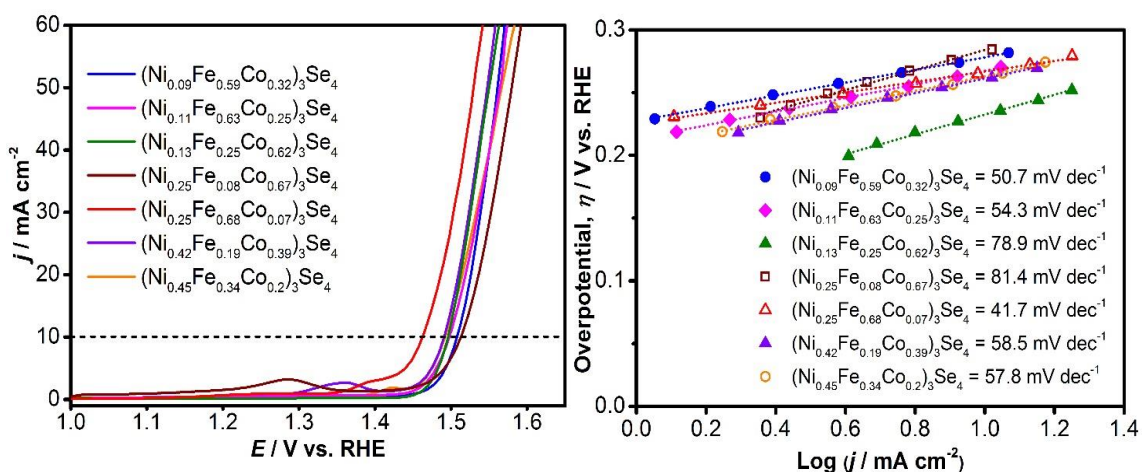


Figure 5. (a) LSVs of 7 best quaternary compositions measured in  $\text{N}_2$  saturated  $0.3\text{ M}$   $\text{KOH}$  solution at a scan rate of  $10\text{ mV s}^{-1}$ , (b) Tafel plots of the catalysts.

Figure 5a shows the polarization curves of the seven best performing quaternary phases, specifically  $(\text{Ni}_{0.45}\text{Fe}_{0.34}\text{Co}_{0.2})_3\text{Se}_4$ ,  $(\text{Ni}_{0.42}\text{Fe}_{0.19}\text{Co}_{0.39})_3\text{Se}_4$ ,  $(\text{Ni}_{0.09}\text{Fe}_{0.59}\text{Co}_{0.32})_3\text{Se}_4$ ,  $(\text{Ni}_{0.11}\text{Fe}_{0.63}\text{Co}_{0.25})_3\text{Se}_4$ ,  $(\text{Ni}_{0.13}\text{Fe}_{0.25}\text{Co}_{0.62})_3\text{Se}_4$ ,  $(\text{Ni}_{0.25}\text{Fe}_{0.68}\text{Co}_{0.07})_3\text{Se}_4$ , and  $(\text{Ni}_{0.25}\text{Fe}_{0.08}\text{Co}_{0.67})_3\text{Se}_4$ , in  $\text{N}_2$ -saturated 0.3 M KOH at a scan rate of  $10 \text{ mV s}^{-1}$ . As expected, these catalysts showed very efficient oxygen evolution activity. The onset overpotentials of  $(\text{Ni}_{0.45}\text{Fe}_{0.34}\text{Co}_{0.2})_3\text{Se}_4$  and  $(\text{Ni}_{0.42}\text{Fe}_{0.19}\text{Co}_{0.39})_3\text{Se}_4$  were 0.22 and 0.21 V (vs RHE), respectively, and they both yielded a current density of  $10 \text{ mA cm}^{-2}$  at an overpotential of 0.26 V (vs RHE). The onset overpotential of  $(\text{Ni}_{0.25}\text{Fe}_{0.08}\text{Co}_{0.67})_3\text{Se}_4$  was 0.22 V (vs RHE), and it needs 0.28 V (vs RHE) to achieve a current density of  $10 \text{ mA cm}^{-2}$ . The onset overpotential of  $(\text{Ni}_{0.09}\text{Fe}_{0.59}\text{Co}_{0.32})_3\text{Se}_4$  was 0.20 V, and 0.26 V (vs RHE) was required to reach  $10 \text{ mA cm}^{-2}$ . The onset overpotentials of  $(\text{Ni}_{0.13}\text{Fe}_{0.25}\text{Co}_{0.62})_3\text{Se}_4$  and  $(\text{Ni}_{0.11}\text{Fe}_{0.63}\text{Co}_{0.25})_3\text{Se}_4$  were 0.22 and 0.22 V (vs RHE), respectively, and they need 0.27 V (vs RHE) to achieve  $10 \text{ mA cm}^{-2}$ .  $(\text{Ni}_{0.25}\text{Fe}_{0.68}\text{Co}_{0.07})_3\text{Se}_4$  showed even better OER catalytic activity: the onset overpotential was 0.18 V (vs RHE), and it needed 0.23 V (vs RHE) to achieve a current density of  $10 \text{ mA cm}^{-2}$ . This is one of the first reports of quaternary transition-metal selenides, and the overpotential obtained is comparable to the low values that have been reported recently in mixed-metal selenides. Figure 5b shows the Tafel plot,  $\eta$  vs  $\log j$ , for these eight quaternary compositions. The Tafel slopes were obtained to be 57.8, 58.5, 50.7, 54.3, 78.9, 41.7, and 81.4  $\text{mV dec}^{-1}$  for  $(\text{Ni}_{0.45}\text{Fe}_{0.34}\text{Co}_{0.2})_3\text{Se}_4$ ,  $(\text{Ni}_{0.42}\text{Fe}_{0.19}\text{Co}_{0.39})_3\text{Se}_4$ ,  $(\text{Ni}_{0.09}\text{Fe}_{0.59}\text{Co}_{0.32})_3\text{Se}_4$ ,  $(\text{Ni}_{0.11}\text{Fe}_{0.63}\text{Co}_{0.25})_3\text{Se}_4$ ,  $(\text{Ni}_{0.13}\text{Fe}_{0.25}\text{Co}_{0.62})_3\text{Se}_4$ ,  $(\text{Ni}_{0.25}\text{Fe}_{0.68}\text{Co}_{0.07})_3\text{Se}_4$ , and  $(\text{Ni}_{0.25}\text{Fe}_{0.08}\text{Co}_{0.67})_3\text{Se}_4$ , respectively. On the basis of the above observations, it can be concluded that although transition-metal-doped mixed-metal selenides yield significant enhancement in OER catalytic activity in

terms of both overpotential at  $10 \text{ mA cm}^{-2}$  and low Tafel slope, the relative doping amount for each element still needs to be optimized to observe the best catalytic performance. From the contour plot (Figure 4b), Table 1, and LSV plot as shown in Figure 5a,  $(\text{Ni}_{0.25}\text{Fe}_{0.68}\text{Co}_{0.07})_3\text{Se}_4$  was identified as the best performing catalyst under the specific experimental conditions. Figure 6a shows the polarization curves of  $(\text{Ni}_{0.25}\text{Fe}_{0.68}\text{Co}_{0.07})_3\text{Se}_4$  in comparison with the binary selenides  $\text{Ni}_3\text{Se}_2$ ,  $\text{CoSe}$ , and  $\text{FeSe}$  in  $\text{N}_2$ -saturated  $0.3 \text{ M KOH}$  at a scan rate of  $10 \text{ mV s}^{-1}$ . As can be seen, the onset overpotentials of  $\text{Ni}_3\text{Se}_2$ ,  $\text{CoSe}$ , and  $\text{FeSe}$  were  $0.24$ ,  $0.22$ , and  $0.30 \text{ V vs RHE}$ , respectively. To achieve an OER current density at  $10 \text{ mA cm}^{-2}$ ,  $\text{Ni}_3\text{Se}_2$  requires  $0.32 \text{ V}$ ,  $\text{CoSe}$  requires  $0.30 \text{ V}$ , and  $\text{FeSe}$  requires  $0.40 \text{ V vs RHE}$ . With transition-metal doping, the onset overpotential of  $(\text{Ni}_{0.25}\text{Fe}_{0.68}\text{Co}_{0.07})_3\text{Se}_4$  decreased significantly to  $0.18 \text{ V (vs RHE)}$  and it yielded a current density of  $10 \text{ mA cm}^{-2}$  at an overpotential of only  $0.23 \text{ V (vs RHE)}$ . A comparison of OER activity for this quaternary composition with the three ternary selenides is shown in Figure S3 in the Supporting Information. A detailed SEM study in Figure 6b of the best electrocatalyst  $(\text{Ni}_{0.25}\text{Fe}_{0.68}\text{Co}_{0.07})_3\text{Se}_4$  thin film showed that the film was mainly composed of rhombus-like nanostructures with an average size distribution of  $100\text{--}800 \text{ nm}$ .

The composition of the  $(\text{Ni}_{0.25}\text{Fe}_{0.68}\text{Co}_{0.07})_3\text{Se}_4$  thin film was also investigated by X-ray photoelectron spectroscopy (XPS). The XPS spectrum of C 1s has been detected, and all binding energies for Ni, Fe, Co, and Se were calibrated with C 1s ( $284.5 \text{ eV}$ ) as a reference binding energy. The chemical composition and the oxidation state of the catalyst were investigated from the deconvoluted XPS spectra, and the corresponding results are presented in Figure 6c–f. The deconvoluted Ni 2p and Fe 2p exhibited the presence of mixed-valence metal ions. As shown in Figure 6c, the binding energies of around  $854.26$

Table 1. Summary of elemental analysis of metal selenide films determined by EDS and corresponding kinetic parameters extracted from polarization curves.

| Precursor Molar Ratio (mM) |     |     |    | Average atomic % (EDS) |      |      |      | Onset $\eta$ | $\eta$ 10mA cm <sup>-2</sup> | Tafel        |
|----------------------------|-----|-----|----|------------------------|------|------|------|--------------|------------------------------|--------------|
| Ni                         | Fe  | Co  | Se | Ni                     | Fe   | Co   | Se   | (V)          | (V)                          | Slope        |
| 10                         | -   | -   | 10 | 62.1                   | -    | -    | 37.9 | <b>0.24*</b> | <b>0.32</b>                  | <b>84.6</b>  |
| -                          | 10  | -   | 10 | -                      | 49.7 | -    | 50.3 | <b>0.30*</b> | <b>0.40</b>                  | <b>104.1</b> |
| -                          | -   | 10  | 10 | -                      | -    | 49.6 | 50.4 | <b>0.22*</b> | <b>0.30</b>                  | <b>125.2</b> |
| 9                          | -   | 1   | 10 | 47.8                   | -    | 8.9  | 43.3 | <b>0.29</b>  | <b>0.35</b>                  | <b>87.0</b>  |
| 8                          | -   | 2   | 10 | 42.2                   | -    | 13.1 | 44.7 | <b>0.28</b>  | <b>0.35</b>                  | <b>85.4</b>  |
| 7                          | -   | 3   | 10 | 33.8                   | -    | 19.4 | 46.8 | <b>0.29</b>  | <b>0.36</b>                  | <b>84.4</b>  |
| 6                          | -   | 4   | 10 | 34.4                   | -    | 20.8 | 44.8 | <b>0.28</b>  | <b>0.35</b>                  | <b>54.4</b>  |
| 5                          | -   | 5   | 10 | 19.8                   | -    | 30.8 | 49.4 | <b>0.30</b>  | <b>0.36</b>                  | <b>62.2</b>  |
| 4                          | -   | 6   | 10 | 26.1                   | -    | 27.4 | 46.5 | <b>0.27</b>  | <b>0.34</b>                  | <b>69.7</b>  |
| 3                          | -   | 7   | 10 | 19.7                   | -    | 32.0 | 48.3 | <b>0.26</b>  | <b>0.33</b>                  | <b>72.7</b>  |
| 2                          | -   | 8   | 10 | 11.4                   | -    | 36.1 | 52.5 | <b>0.25</b>  | <b>0.31</b>                  | <b>90.4</b>  |
| 1                          | -   | 9   | 10 | 7.0                    | -    | 41.0 | 52.0 | <b>0.27</b>  | <b>0.32</b>                  | <b>147.6</b> |
| -                          | 1   | 9   | 10 | -                      | 4.4  | 40.3 | 55.3 | <b>0.25</b>  | <b>0.29</b>                  | <b>57.6</b>  |
| -                          | 2   | 8   | 10 | -                      | 8.4  | 38.8 | 52.8 | <b>0.25</b>  | <b>0.33</b>                  | <b>79.7</b>  |
| -                          | 3   | 7   | 10 | -                      | 12.6 | 34.6 | 52.9 | <b>0.25</b>  | <b>0.33</b>                  | <b>91.7</b>  |
| -                          | 4   | 6   | 10 | -                      | 9.0  | 29.1 | 61.8 | <b>0.24</b>  | <b>0.31</b>                  | <b>63.2</b>  |
| -                          | 5   | 5   | 10 | -                      | 14.7 | 27.4 | 57.9 | <b>0.24</b>  | <b>0.30</b>                  | <b>58.6</b>  |
| -                          | 6   | 4   | 10 | -                      | 13.1 | 31.4 | 55.5 | <b>0.25</b>  | <b>0.31</b>                  | <b>79.3</b>  |
| -                          | 7   | 3   | 10 | -                      | 22.2 | 20.0 | 57.8 | <b>0.24</b>  | <b>0.32</b>                  | <b>69.9</b>  |
| -                          | 8   | 2   | 10 | -                      | 29.5 | 14.7 | 55.8 | <b>0.24</b>  | <b>0.31</b>                  | <b>91.6</b>  |
| -                          | 9   | 1   | 10 | -                      | 55.5 | 11.2 | 33.3 | <b>0.27</b>  | <b>0.32</b>                  | <b>56.6</b>  |
| 9                          | 1   | -   | 10 | 41.4                   | 3.8  | -    | 54.8 | <b>0.30</b>  | <b>0.37</b>                  | <b>99.2</b>  |
| 8                          | 2   | -   | 10 | 42.2                   | 2.3  | -    | 55.4 | <b>0.24</b>  | <b>0.33</b>                  | <b>56.6</b>  |
| 7                          | 3   | -   | 10 | 37.2                   | 8.0  | -    | 54.8 | <b>0.24</b>  | <b>0.29</b>                  | <b>106.2</b> |
| 6                          | 4   | -   | 10 | 34.1                   | 6.1  | -    | 59.8 | <b>0.238</b> | <b>0.27</b>                  | <b>78.9</b>  |
| 5                          | 5   | -   | 10 | 29.8                   | 12.8 | -    | 57.4 | <b>0.25</b>  | <b>0.30</b>                  | <b>52.4</b>  |
| 4                          | 6   | -   | 10 | 24.1                   | 17.7 | -    | 58.2 | <b>0.24</b>  | <b>0.28</b>                  | <b>57.6</b>  |
| 3                          | 7   | -   | 10 | 19.8                   | 22.2 | -    | 58.0 | <b>0.25</b>  | <b>0.28</b>                  | <b>51.3</b>  |
| 2                          | 8   | -   | 10 | 13.8                   | 26.0 | -    | 60.3 | <b>0.25</b>  | <b>0.29</b>                  | <b>55.6</b>  |
| 1                          | 9   | -   | 10 | 7.6                    | 37.3 | -    | 55.1 | <b>0.26</b>  | <b>0.31</b>                  | <b>52.5</b>  |
| 0.5                        | 8   | 1.5 | 10 | 4.0                    | 26.7 | 14.9 | 54.4 | <b>0.20*</b> | <b>0.26</b>                  | <b>56.0</b>  |
| 0.5                        | 8.5 | 1   | 10 | 4.9                    | 27.4 | 10.9 | 56.8 | <b>0.22*</b> | <b>0.27</b>                  | <b>41.3</b>  |
| 1                          | 8   | 1   | 10 | 6.8                    | 28.1 | 9.1  | 55.9 | <b>0.20</b>  | <b>0.28</b>                  | <b>162.1</b> |
| 1                          | 8.5 | 0.5 | 10 | 7.3                    | 34.5 | 5.9  | 52.3 | <b>0.23</b>  | <b>0.30</b>                  | <b>55.7</b>  |
| 1                          | 7   | 2   | 10 | 6.9                    | 15.8 | 18.6 | 58.7 | <b>0.21</b>  | <b>0.30</b>                  | <b>66.5</b>  |
| 1                          | 6   | 3   | 10 | 7.1                    | 14.2 | 21.2 | 57.6 | <b>0.22</b>  | <b>0.28</b>                  | <b>49.2</b>  |
| 1                          | 5   | 4   | 10 | 5.8                    | 11.4 | 28.0 | 54.9 | <b>0.22*</b> | <b>0.27</b>                  | <b>59.4</b>  |
| 1                          | 4   | 5   | 10 | 5.9                    | 5.3  | 34.7 | 54.1 | <b>0.22</b>  | <b>0.28</b>                  | <b>50.9</b>  |
| 1                          | 3   | 6   | 10 | 6.3                    | 4.3  | 42.8 | 46.5 | <b>0.22</b>  | <b>0.28</b>                  | <b>83.0</b>  |
| 1                          | 2   | 7   | 10 | 7.5                    | 4.7  | 32.5 | 55.3 | <b>0.22</b>  | <b>0.28</b>                  | <b>67.0</b>  |
| 1                          | 1   | 8   | 10 | 5.4                    | 0.8  | 32.8 | 61.0 | <b>0.22</b>  | <b>0.28</b>                  | <b>95.2</b>  |
| 1.5                        | 8   | 0.5 | 10 | 11.4                   | 31.7 | 3.3  | 53.5 | <b>0.18</b>  | <b>0.23</b>                  | <b>54.3</b>  |
| 2                          | 7   | 1   | 10 | 14.1                   | 13.7 | 10.1 | 62.0 | <b>0.20</b>  | <b>0.28</b>                  | <b>64.9</b>  |



Table 1. Summary of elemental analysis of metal selenide films determined by EDS and corresponding kinetic parameters extracted from polarization curves. (cont.)

|   |   |   |    |      |      |      |      |              |             |              |
|---|---|---|----|------|------|------|------|--------------|-------------|--------------|
| 2 | 6 | 2 | 10 | 12.8 | 6.4  | 15.4 | 65.4 | <b>0.22</b>  | <b>0.29</b> | <b>50.1</b>  |
| 2 | 5 | 3 | 10 | 11.2 | 5.0  | 25.8 | 58.0 | <b>0.23</b>  | <b>0.32</b> | <b>57.9</b>  |
| 2 | 4 | 4 | 10 | 9.6  | 2.6  | 31.4 | 56.4 | <b>0.24</b>  | <b>0.31</b> | <b>77.2</b>  |
| 2 | 3 | 5 | 10 | 11.9 | 3.9  | 32.3 | 51.9 | <b>0.22*</b> | <b>0.28</b> | <b>75.5</b>  |
| 2 | 2 | 6 | 10 | 11.5 | 0.8  | 36.3 | 51.3 | <b>0.22</b>  | <b>0.30</b> | <b>48.2</b>  |
| 2 | 1 | 7 | 10 | 12.2 | 0.4  | 32.3 | 55.1 | <b>0.24</b>  | <b>0.31</b> | <b>79.0</b>  |
| 3 | 6 | 1 | 10 | 20.9 | 16.1 | 9.5  | 53.5 | <b>0.22*</b> | <b>0.26</b> | <b>73.9</b>  |
| 3 | 5 | 2 | 10 | 18.8 | 8.5  | 17.3 | 55.4 | <b>0.21*</b> | <b>0.26</b> | <b>88.8</b>  |
| 3 | 4 | 3 | 10 | 19.5 | 5.6  | 23.8 | 51.2 | <b>0.24</b>  | <b>0.32</b> | <b>64.0</b>  |
| 3 | 3 | 4 | 10 | 18.1 | 2.6  | 29.6 | 49.6 | <b>0.24</b>  | <b>0.32</b> | <b>102.7</b> |
| 3 | 2 | 5 | 10 | 18.5 | 0.2  | 29.0 | 52.3 | <b>0.22</b>  | <b>0.30</b> | <b>148.7</b> |
| 3 | 1 | 6 | 10 | 17.2 | 1.0  | 27.7 | 54.2 | <b>0.23</b>  | <b>0.32</b> | <b>76.2</b>  |
| 4 | 5 | 1 | 10 | 26.8 | 13.3 | 9.1  | 50.8 | <b>0.21</b>  | <b>0.28</b> | <b>65.5</b>  |
| 4 | 4 | 2 | 10 | 21.2 | 4.3  | 21.3 | 53.2 | <b>0.26</b>  | <b>0.33</b> | <b>84.6</b>  |
| 4 | 3 | 3 | 10 | 23.9 | 2.6  | 22.9 | 50.5 | <b>0.25</b>  | <b>0.33</b> | <b>55.8</b>  |
| 4 | 2 | 4 | 10 | 17.1 | 0.8  | 26.4 | 55.7 | <b>0.24</b>  | <b>0.32</b> | <b>82.2</b>  |
| 4 | 1 | 5 | 10 | 22.7 | 0.9  | 24.8 | 51.5 | <b>0.22</b>  | <b>0.30</b> | <b>123.2</b> |
| 5 | 4 | 1 | 10 | 35.3 | 9.7  | 9.8  | 45.2 | <b>0.22</b>  | <b>0.30</b> | <b>56.6</b>  |
| 5 | 3 | 2 | 10 | 35.8 | 2.2  | 18.0 | 44.0 | <b>0.24</b>  | <b>0.31</b> | <b>58.6</b>  |
| 5 | 2 | 3 | 10 | 28.3 | 0.3  | 23.6 | 47.8 | <b>0.26</b>  | <b>0.34</b> | <b>53.0</b>  |
| 5 | 1 | 4 | 10 | 29.4 | 0.2  | 26.3 | 44.0 | <b>0.25</b>  | <b>0.33</b> | <b>98.4</b>  |
| 6 | 3 | 1 | 10 | 43.5 | 2.7  | 8.8  | 45.0 | <b>0.24</b>  | <b>0.31</b> | <b>52.1</b>  |
| 6 | 2 | 2 | 10 | 23.9 | 2.2  | 17.8 | 56.1 | <b>0.25</b>  | <b>0.35</b> | <b>79.5</b>  |
| 6 | 1 | 3 | 10 | 28.2 | 0.1  | 20.1 | 47.9 | <b>0.25</b>  | <b>0.33</b> | <b>52.7</b>  |
| 7 | 2 | 1 | 10 | 47.5 | 0.6  | 9.7  | 42.3 | <b>0.24</b>  | <b>0.31</b> | <b>57.0</b>  |
| 7 | 1 | 2 | 10 | 43.1 | 0.2  | 16.5 | 40.2 | <b>0.26</b>  | <b>0.32</b> | <b>53.7</b>  |
| 8 | 1 | 1 | 10 | 36.6 | 0.7  | 9.4  | 53.3 | <b>0.26</b>  | <b>0.35</b> | <b>76.8</b>  |

\*The highlighted cell represents catalyst composition corresponding to the best electrocatalytic performance. \* represents catalyst compositions for which the LSV plots have been shown in Figure 3 and Figure 5.

and 871.46 eV of Ni 2p are assigned to Ni<sup>2+</sup> and those of 855.60 and 873.61 eV are attributed to Ni<sup>3+</sup> with its shakeup satellite peaks at 876.83 and 860.43 eV.<sup>47,63,64</sup> Similarly, in the Fe 2p spectra (shown in Figure 6d), the peaks at 708.38 and 721.59 eV correspond to Fe<sup>2+</sup>, while those at 710.10 and 723.28 eV corroborate Fe<sup>3+</sup> with its shakeup satellite peaks at 713.56 and 730.9 eV.<sup>65-67</sup> In the Co 2p spectrum (shown in Figure 6e), two peaks at 779.81 and 794.71 eV correspond to Co 2p<sub>3/2</sub> and Co 2p<sub>1/2</sub>, respectively, indicating the presence of Co<sup>2+</sup>, as has been reported previously.<sup>68-70</sup> In the Se 3d spectrum (shown in

Figure 6f), the binding energies of Se 3d<sub>5/2</sub> and Se 3d<sub>3/2</sub> peaks were obtained at 54.15 and 54.85 eV, respectively, which were similar to those of reported metal selenides.<sup>71–75</sup> It must be mentioned here that all of these binding energies observed for the respective metal ions were characteristic of the selenide phases and did not show similarities with those obtained from the oxide phases. Even Se XPS did not show the presence of peaks corresponding to SeO<sub>x</sub>. From the semiquantitative XPS studies, it was further confirmed that the quaternary metal selenide belonged to the M<sub>3</sub>Se<sub>4</sub> family containing mixed-valence Ni and Fe ions. M<sub>3</sub>Se<sub>4</sub> compositions generally form spinel-type structures containing alternating layers of edge-shared *M<sub>III</sub>Se<sub>6</sub>* octahedra and *M<sub>II</sub>Se<sub>4</sub>* tetrahedra. Such compositions have been frequently encountered in transition-metal chalcogenide family as ferrites, NiFe<sub>2</sub>Se<sub>4</sub>, CoNi<sub>2</sub>Se<sub>4</sub>, and so on.<sup>20,21,76,77</sup> The transition-metal cations can occupy one or both of the divalent and trivalent cationic sites, and the presence of mixed valence for Fe and Ni has been reported.<sup>78–80</sup> The presence of Ni<sup>3+</sup> in these chalcogenides is very interesting, since in Ni-based OER electrocatalysts it has been widely known that Ni<sup>3+</sup> is the actual catalytically active site. The electrochemically active surface area (ECSA) for (Ni<sub>0.25</sub>Fe<sub>0.68</sub>Co<sub>0.07</sub>)<sub>3</sub>Se<sub>4</sub> thin film on Au-coated glass was estimated by measuring the electrochemical double-layer capacitance of the electrocatalyst. Cyclic voltammograms (CVs) with various scan rates were used to measure double-layer charging current in the non-Faradaic region. The working electrode with electrodeposited (Ni<sub>0.25</sub>Fe<sub>0.68</sub>Co<sub>0.07</sub>)<sub>3</sub>Se<sub>4</sub> catalyst was held in N<sub>2</sub>-saturated 0.3 M KOH, and then CVs were measured from –0.26 to –0.36 V vs Ag|AgCl (KCl saturated) at the following scan rates: 25, 50, 75, 100, and 150 mV/s (shown Figure 7). Since the double-layer current (*i<sub>DL</sub>*) was measured in the non-Faradaic region, it is assumed that the current response is due to double-layer charging instead of chemical

reactions or charge transfer. Therefore, a linear equation can be used to estimate the specific electrochemical double-layer capacitance ( $C_{DL}$ ) by double-layer current  $i_{DL}$  and the scan rate ( $v$ ) of CV, which is shown in eq 3.

$$i_{DL} = C_{DL} \times v \quad (3)$$

where, double-layer capacitance ( $C_{DL}$ ) is in unit of mF.

The inset plot in Figure 7 is the cathodic and anodic charging currents measured at  $-0.30$  V vs Ag|AgCl (KCl saturated) and plotted as a function of scan rate. The  $C_{DL}$  value was determined from the average of the cathodic and anodic slopes. Here, the electrochemical double-layer capacitance of  $(\text{Ni}_{0.25}\text{Fe}_{0.68}\text{Co}_{0.07})_3\text{Se}_4$  thin film on Au-coated glass was estimated to be 0.069 mF. The ECSA of the electrocatalyst was calculated using eq 4.

$$ECSA = C_{DL}/C_s \quad (4)$$

where  $C_s$  is the specific capacitance of the electrocatalyst per unit area under identical electrolyte conditions. Its value has been reported between 0.022 to 0.130  $\text{mF cm}^{-2}$  in alkaline solution.<sup>60</sup> In this study, the value of  $C_s$  was taken to be 0.040  $\text{mF cm}^{-2}$  on the basis of reported values.<sup>60</sup> The roughness factor (RF) was calculated by taking the ratio of ECSA with the geometric area of the electrode, 0.283  $\text{cm}^2$ . ECSA was estimated to be around 1.725, while RF was around 6.095. The high value of RF indicates that the as-deposited films were highly rough. This observation was also confirmed from SEM images, which showed a highly granular surface. It should be noted here that the catalytic activity is expected to improve with surface roughness since it leads to better and more extensive exposure of the catalytically active sites to the electrolyte.

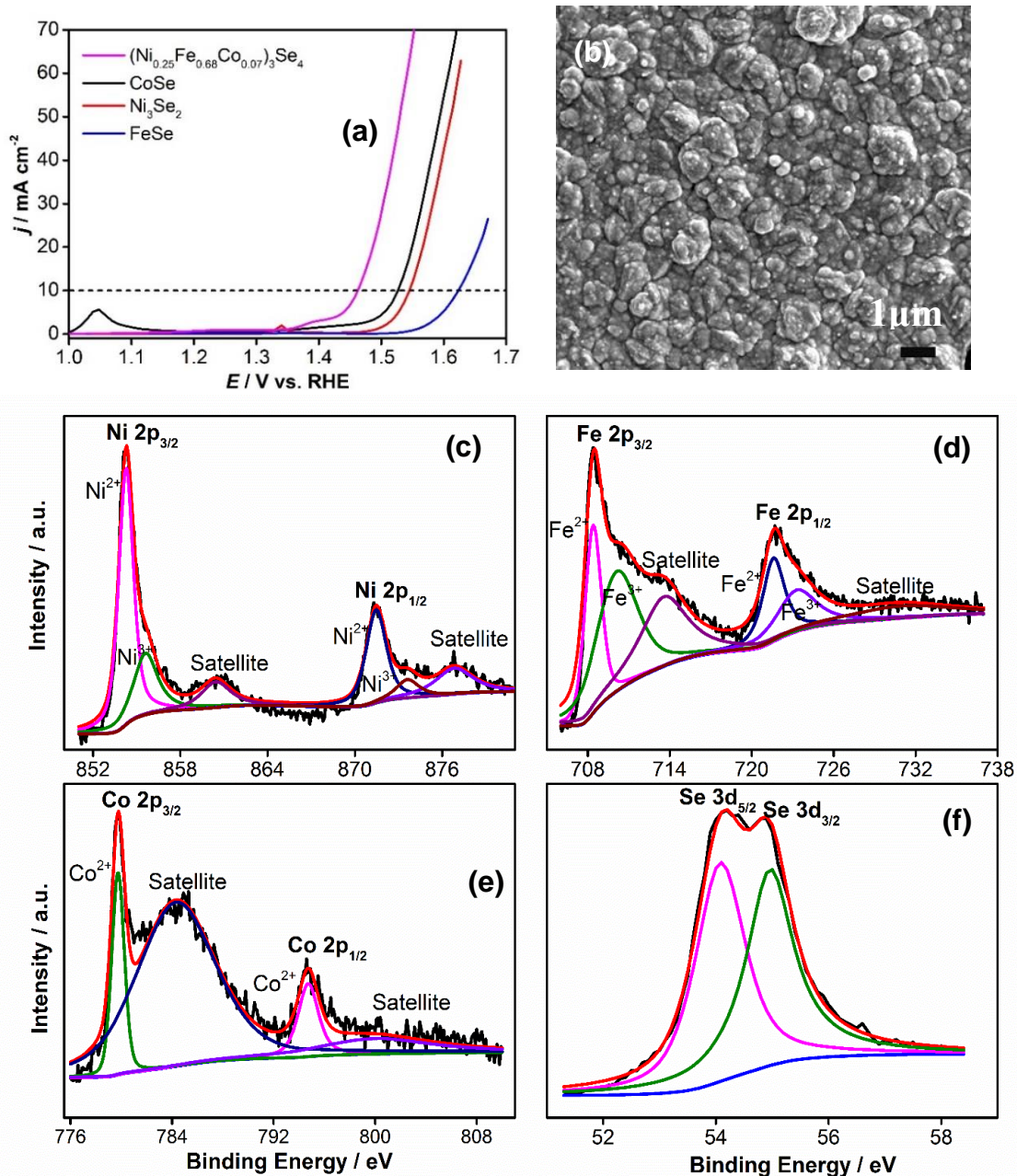


Figure 6. (a) Polarization curves of  $(\text{Ni}_{0.25}\text{Fe}_{0.68}\text{Co}_{0.07})_3\text{Se}_4$  compared to the three binary catalyst films. (b) SEM image of  $(\text{Ni}_{0.25}\text{Fe}_{0.68}\text{Co}_{0.07})_3\text{Se}_4$  film deposited for 300 s. XPS spectra of as deposited film  $(\text{Ni}_{0.25}\text{Fe}_{0.68}\text{Co}_{0.07})_3\text{Se}_4$ . (c) Fe 2p<sub>3/2</sub> and 2p<sub>1/2</sub> peaks; (d) Co 2p<sub>3/2</sub> and 2p<sub>1/2</sub> peaks; (e) Ni 2p<sub>1/2</sub> and 2p<sub>3/2</sub> peaks; (f) Se 3d<sub>5/2</sub> and 3d<sub>3/2</sub> peaks.

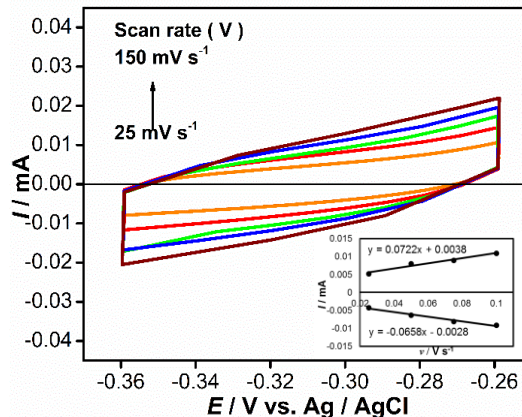


Figure 7. Cyclic voltammograms measured for the  $(\text{Ni}_{0.25}\text{Fe}_{0.68}\text{Co}_{0.07})_3\text{Se}_4$  thin film in  $\text{N}_2$  saturated 0.3 M KOH solution at different scan rates from 25 to  $150 \text{ mV s}^{-1}$ . The inset is a plot of both anodic and cathodic current measured at 0.3 V vs. Ag|AgCl (sat.) as a function of scan rate.

An RRDE setup was used to estimate the Faradaic efficiency of electrocatalysts during the OER process. Namely, in RRDE experiments, the central GC disk containing catalyst produced oxygen, while the Pt ring electrode, maintained at a fixed potential, collected the generated oxygen and reduced it. Prior to the RRDE experiment, the Pt ring was cleaned by CVs from  $-0.24$  to  $1.00$  V (vs Ag|AgCl) in  $\text{N}_2$ -saturated 0.5 M  $\text{H}_2\text{SO}_4$  at 1600 rpm. The 0.3 M KOH solution was purged with  $\text{N}_2$  for more than 20 min to get rid of any dissolved atmospheric  $\text{O}_2$ . While a constant rotation rate of 1600 rpm was maintained, the disk electrode was kept at several different potential steps from 1.50 to 1.60 V vs RHE for 20 s in each step, and meanwhile, the Pt ring electrode was held at a constant potential 0.164 V vs RHE to ensure that collected oxygen was reduced rapidly. Equation 5 is the relation between Faradaic efficiency and the ratio of the ring current ( $i_r$ ) and disk current ( $i_d$ ).

$$\varepsilon = \frac{2i_r}{i_d N} \quad (5)$$

Where  $N$  is the collection efficiency of RRDE, which was estimated by reported procedure: namely, through the ratio of the ring and disk current in in 0.001 M  $K_3Fe(CN)_6$  with 0.3 M of KOH.<sup>60,81</sup> In this work,  $N$  is 0.24. The Faradaic efficiency of the  $(Ni_{0.25}Fe_{0.68}Co_{0.07})_3Se_4$  catalyst and plots of the disk and ring currents along with applied disk potential are shown in Figure 8. At the applied disk potential  $E = 1.50$  V vs RHE, the highest Faradaic efficiency is around 99%, while with the potential increased to 1.60 V vs RHE, the efficiency went down to about 70%. This decrease is caused by the decreasing ratio of ring current and disk current, which means that the ring electrode might not efficiently collect the large amounts of oxygen produced from the disk electrode at higher applied disk potentials, and a large number of undissolved oxygen bubbles could be observed on the surface of the disk electrode. Therefore, at the applied disk potential  $E = 1.50$  V vs RHE, the Faradaic efficiency of 99% was treated as the OER efficiency of the electrocatalyst. The decreased Faradaic efficiencies at relatively high disk potential can be ignored here, because it is adequate for this applied disk potential ( $E = 1.5$  V vs RHE) to produce oxygen.

Electrochemical impedance spectroscopy (EIS) was also measured to investigate the internal resistance of the catalytic film as well as the charge-transfer resistance at the catalyst (electrode)–electrolyte interface as a function of composition. These factors will both have a large influence on the onset and propagation of OER catalytic activity. Hence, the best performing quaternary film,  $(Ni_{0.25}Fe_{0.68}Co_{0.07})_3Se_4$ , was compared with another quaternary film containing almost equal amounts of Ni, Fe, and Co,  $(Ni_{0.37}Fe_{0.36}Co_{0.27})_3Se_4$ , exhibiting moderate catalytic activity. EIS spectra were collected in  $N_2$ -saturated 0.3M KOH solution at 0.3, 0.4, and 0.5 V vs Ag|AgCl, respectively, and the Nyquist plots are

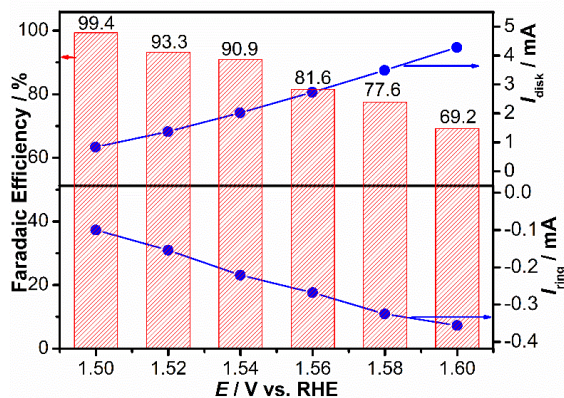


Figure 8. Faradaic efficiency of the  $(\text{Ni}_{0.25}\text{Fe}_{0.68}\text{Co}_{0.07})_3\text{Se}_4$  catalyst in  $\text{N}_2$  saturated 0.3 M KOH measured at 1600 rpm from a combined ORR-OER experiment using a RRDE setup where OER takes place at the disk electrode while ORR takes place at ring electrode. The corresponding disk and ring currents for the RRDE experiment were plotted as a function of the applied disk potentials.

Table 2. Equivalent Circuit Parameters Obtained from Fitting of EIS Experimental Data.

| $E_{\text{Applied}}$ | Catalysts                                                         | $R_s/\Omega$ | $R_{ct}/\Omega$ | $CPE_{dl}/F$ | $R_f/\Omega$ | $CPE_f/F$ |
|----------------------|-------------------------------------------------------------------|--------------|-----------------|--------------|--------------|-----------|
| 0.3V                 | $(\text{Ni}_{0.25}\text{Fe}_{0.68}\text{Co}_{0.07})_3\text{Se}_4$ | 4.9          | 15.90           | 0.36         | 1923         | 0.81      |
|                      |                                                                   | 5            | 15.17           | 0.35         | 913          | 0.88      |
|                      |                                                                   | 5            | 14.90           | 0.34         | 738          | 0.89      |
| 0.4V                 | $(\text{Ni}_{0.37}\text{Fe}_{0.36}\text{Co}_{0.27})_3\text{Se}_4$ | 5            | 25.32           | 0.4          | 6105         | 0.89      |
|                      |                                                                   | 5            | 23.80           | 0.39         | 5546         | 0.89      |
|                      |                                                                   | 5            | 22.75           | 0.38         | 4247         | 0.85      |

$R_s$  is the resistance of the electrolyte;  $R_{ct}$  is the electron transfer resistance;  $CPE_{dl}$  is the constant phase element of double-layer nonideal capacitance;  $R_f$  is resistance of the catalyst layer; and  $CPE_f$  is the capacitance.

shown in Figure S4 in the Supporting Information. The spectra were fitted to an equivalent circuit from which electrolyte resistance ( $R_s$ ), the electron charge transfer resistance ( $R_{ct}$ ), and film resistance ( $R_f$ ) could be obtained, and the values are given in Table 2. In all cases,

the electrolyte resistance was obtained as ca. 5  $\Omega$ , similar to values that have been reported before.<sup>46</sup> From the fitting of the equivalent circuit, it was clearly observed that the values of the electron transfer resistance ( $R_{ct}$ ) of  $(\text{Ni}_{0.25}\text{Fe}_{0.68}\text{Co}_{0.07})_3\text{Se}_4$  at various applied potentials were smaller than those for  $(\text{Ni}_{0.37}\text{Fe}_{0.36}\text{Co}_{0.27})_3\text{Se}_4$ , which indicated that interfacial charge transfer on the catalyst–electrolyte interface was kinetically faster on the surface of  $(\text{Ni}_{0.25}\text{Fe}_{0.68}\text{Co}_{0.07})_3\text{Se}_4$  in comparison to  $(\text{Ni}_{0.37}\text{Fe}_{0.36}\text{Co}_{0.27})_3\text{Se}_4$ . Such faster charge transfer across the interface can expedite the onset of OER activity as well as its further propagation, leading to the high efficiency of  $(\text{Ni}_{0.25}\text{Fe}_{0.68}\text{Co}_{0.07})_3\text{Se}_4$ .<sup>46,82</sup> On the other hand, the catalyst resistance ( $R_f$ ) will also affect the electron transfer within the catalyst film, thereby influencing the overall catalytic activity.<sup>83</sup> From the equivalent circuit (Figure S4 and Table 2), it was observed that  $(\text{Ni}_{0.25}\text{Fe}_{0.68}\text{Co}_{0.07})_3\text{Se}_4$  showed a lower  $R_f$  value in comparison to  $(\text{Ni}_{0.37}\text{Fe}_{0.36}\text{Co}_{0.27})_3\text{Se}_4$ . A lower charge-transfer resistance will facilitate the transfer of charge from the electrolyte to the catalyst surface through  $\text{OH}^-$  attachment, resulting in lower overpotential, while lower film resistance will lead to better transport of the generated charge carriers leading to faster kinetics. Transition-metal doping can change the conductivity of the film due to possible d electron reorganization and possible overlap of the d bands. Hence the enhancement of the OER catalytic activity in  $(\text{Ni}_{0.25}\text{Fe}_{0.68}\text{Co}_{0.07})_3\text{Se}_4$  can also be attributed to the superior conductivity of the film as well as lower charge-transfer resistance.

The stability of the catalyst for continuous oxygen evolution under operational conditions is a crucial factor to evaluate the practical usability of the catalyst. To establish the stability and durability of the quaternary selenide based OER electrocatalyst, chronoamperometric measurements ( $j$  vs time) were carried out for 8 h, as shown in Figure



9a, where a constant potential (0.5 V vs Ag|AgCl) was applied to achieve a current density of around  $10 \text{ mA cm}^{-2}$  in 0.3M KOH. The catalyst  $(\text{Ni}_{0.25}\text{Fe}_{0.68}\text{Co}_{0.07})_3\text{Se}_4$  showed excellent durability without any decrease in the current density even after 8 h. The stability of the catalyst was further confirmed through LSV remeasurement after 8 h of chronoamperometry. As can be seen from Figure 9b, the catalyst showed the same onset potential while the overpotential at  $10 \text{ mA cm}^{-2}$  became even better by about 20 mV even after 8 h. Such enhancement can be possibly explained by a changing morphology of the catalyst surface. Figure 9c shows the SEM image of the catalyst surface after 8 h of chronoamperometry, and it was observed that the surface roughness of the film increased significantly after catalytic activity. The increased surface roughness can be attributed to the escape of the evolved  $\text{O}_2$  gas, which tends to create a porous layer on the catalyst surface. Compositional stability of the catalyst after 8 h of chronoamperometry was confirmed by the XPS spectrum shown in Figure 9d–g and EDS analysis (Table S2), which showed that the catalyst was still primarily composed of Ni, Co, Fe, and Se with no trace of O. Such studies confirmed that this OER electrocatalyst was both functionally durable and compositionally stable even after a long period of continuous  $\text{O}_2$  evolution in alkaline medium.

DFT Calculations of Adsorption Energy. OER in alkaline medium is a multistep process which is initiated by the adsorption of a hydroxyl group ( $\text{OH}^-$ ) at the active site (mostly transition metal) on the catalyst surface.<sup>84</sup> The kinetics of the OER reaction is determined by the rate-determining step, which can be either the first or second hydroxyl attachment on the surface or the step of  $\text{O}_2$  release. In either case, optimal coverage of the surface through initial hydroxyl attachment becomes very influential in initiating the OER

process (i.e., low onset potential), and it has been observed that a less than optimal coverage of hydroxyl groups on the surface gives rise to higher Tafel slope.<sup>85</sup> Hence, we have tried to study the energetics of the first hydroxyl attachment on the surface of the mixed-metal selenides as a function of composition within the Ni-Co-Fe ternary phase space through density functional theory (DFT) calculations. It must be mentioned here that only the adsorption energy of the first hydroxyl attachment on the catalyst surface has been monitored here, while a more detailed computational study is required to follow all the elementary steps of the OER across the composition range in the ternary phase space to obtain a Sabatier plot relating the catalytic efficiency (Tafel slopes and overpotential) as a function of composition.<sup>1,86</sup>

To investigate the catalytic activities of the studied transition metal selenide films, first-principles calculations were used to determine the adsorption energy of OH<sup>-</sup> ion on different Ni<sub>x</sub>Fe<sub>y</sub>Co<sub>z</sub>Se<sub>n</sub> catalytic surfaces. Four specific compositions were studied. The end compositions on the Ni-Fe binary phase line were determined to be Ni<sub>3</sub>Se<sub>2</sub> and Fe<sub>3</sub>Se<sub>4</sub> on the basis of experimental verification (EDS analysis and PXRD). Hence, the quaternary compositions (Ni<sub>0.25</sub>Fe<sub>0.68</sub>Co<sub>0.07</sub>)<sub>3</sub>Se<sub>4</sub> and (Ni<sub>0.37</sub>Fe<sub>0.36</sub>Co<sub>0.27</sub>)<sub>3</sub>Se<sub>4</sub> were compared with the two terminal compositions. First-principles calculations were executed on the basis of density functional theory (DFT) and performed using the Vienna ab initio simulation package (VASP).<sup>87,88</sup> The core electrons were treated using projected augmented wave (PAW) pseudopotentials, while the exchange correlation energies were evaluated by the formulations of Perdew–Burke–Ernzerhof (PBE) and ultrasoft potentials within the generalized gradient approximation (GGA).<sup>89–91</sup> The rotationally invariant version of the

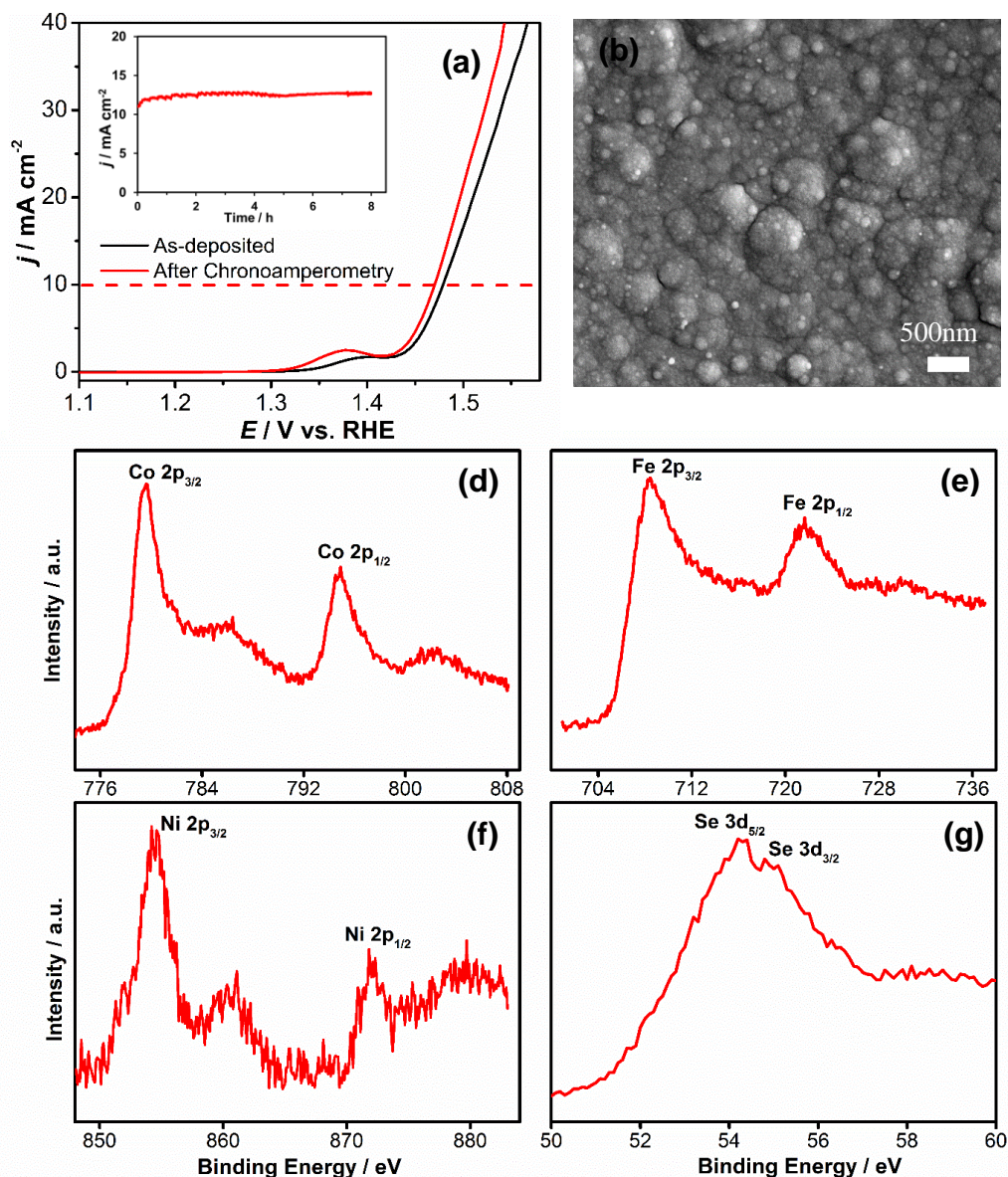


Figure 9. (a) Chronoamperometry plot of  $(\text{Ni}_{0.25}\text{Fe}_{0.68}\text{Co}_{0.07})_3\text{Se}_4$  for 8 h at 0.50 V vs. Ag|AgCl (sat.) applied potential. (b) Comparison of LSVs before and after 8 h stability in  $\text{N}_2$  saturated 0.3 M KOH solution. (c) SEM image of  $(\text{Ni}_{0.25}\text{Fe}_{0.68}\text{Co}_{0.07})_3\text{Se}_4$  after chronoamperometry. (d-g) XPS spectrum of  $(\text{Ni}_{0.25}\text{Fe}_{0.68}\text{Co}_{0.07})_3\text{Se}_4$  after chronoamperometry.

GGA+U method has been shown to successfully describe the cohesive energy, electronic structure, and mechanical and magnetic properties of the bulk and surfaces of materials.<sup>92</sup>

Therefore, in the current work, the GGA+U method was used to study the adsorption energy of  $\text{OH}^-$  ion on various Ni, Fe, and Co active sites of  $\text{Ni}_x\text{Fe}_y\text{Co}_z\text{Se}_n$  electrocatalysts. The cutoff energy for the plane wave was set to be 400 eV, which was found to be sufficient for convergence of the adsorption energies. It must be mentioned here that these studies were conducted solely to obtain a rough idea of the propensity of  $\text{OH}^-$  attachment on the various catalytic surfaces. More detailed calculations are required to directly correlate the kinetics of the OER as a function of varying composition and construct a volcano plot. We are currently working with our collaborators to execute these computational-time-demanding calculations, the results of which will be communicated separately.

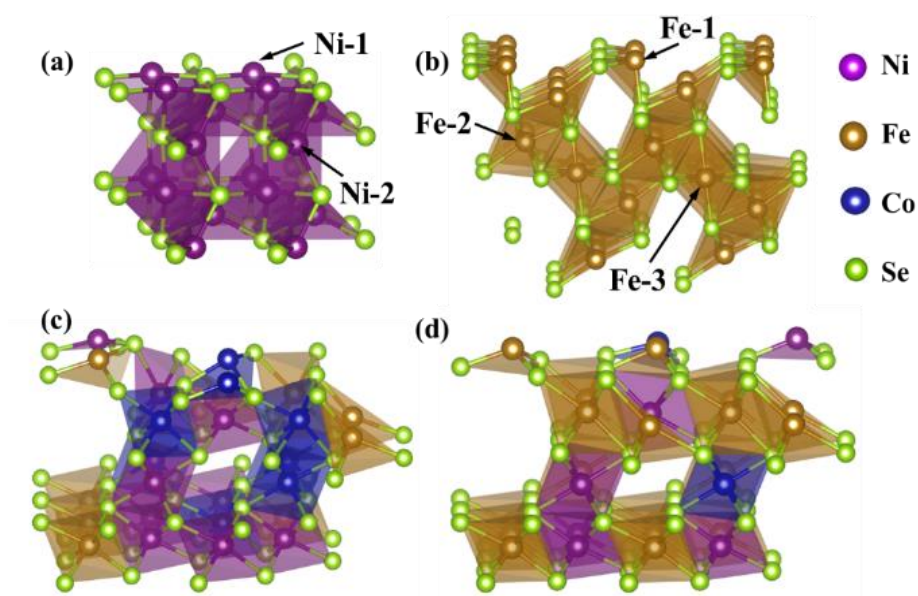


Figure 10. Crystal structures of  $2 \times 2 \times 2$  supercells of (a)  $\text{Ni}_3\text{Se}_2$ , (b)  $\text{Fe}_3\text{Se}_4$ , (c)  $(\text{Ni}_{0.37}\text{Fe}_{0.36}\text{Co}_{0.27})_3\text{Se}_4$  and (d)  $(\text{Ni}_{0.25}\text{Fe}_{0.68}\text{Co}_{0.07})_3\text{Se}_4$ . Different types of active Ni and Fe sites have been indicated as Ni-1, Ni-2, Fe-1, Fe-2 and Fe-3 in  $\text{Ni}_3\text{Se}_2$  and  $\text{Fe}_3\text{Se}_4$ .

The  $2 \times 2 \times 2$  supercells of  $\text{Ni}_3\text{Se}_2$ ,  $\text{Fe}_3\text{Se}_4$ ,  $(\text{Ni}_{0.25}\text{Fe}_{0.68}\text{Co}_{0.07})_3\text{Se}_4$ , and  $(\text{Ni}_{0.37}\text{Fe}_{0.36}\text{Co}_{0.27})_3\text{Se}_4$  were generated, as shown in Figure 10. One can note that  $\text{Ni}_3\text{Se}_2$

exhibits a rhombohedral R32 crystal structure with 3-fold symmetry, while the other three compounds have monoclinic structures. It is worth mentioning that the crystal structures of  $(\text{Ni}_{0.25}\text{Fe}_{0.68}\text{Co}_{0.07})_3\text{Se}_4$  and  $(\text{Ni}_{0.37}\text{Fe}_{0.36}\text{Co}_{0.27})_3\text{Se}_4$  were generated by randomly replacing Fe in  $\text{Fe}_3\text{Se}_4$  with Ni and Co. Two Ni sites (Ni-1 and Ni-2) located on the (001) plane, respectively (Figure 10a), were monitored in  $\text{Ni}_3\text{Se}_2$ . To maintain similarity the (001) plane was chosen as the active surface for all catalyst compositions, as mentioned above, and the  $\text{OH}^-$  adsorptions on the available metal sites (Fe, Co, and/or Ni) (Figure 10b–d) were calculated. k-point meshes of  $4 \times 4 \times 1$  and  $3 \times 2 \times 1$  were found to be sufficient to give a self-consistent field (SCF) convergence criterion of  $1 \times 10^{-4}$  eV for the rhombohedral  $\text{Ni}_3\text{Se}_2$  and monoclinic  $\text{Fe}_3\text{Se}_4$ ,  $(\text{Ni}_{0.37}\text{Fe}_{0.36}\text{Co}_{0.27})_3\text{Se}_4$ , and  $(\text{Ni}_{0.25}\text{Fe}_{0.68}\text{Co}_{0.07})_3\text{Se}_4$ , respectively.

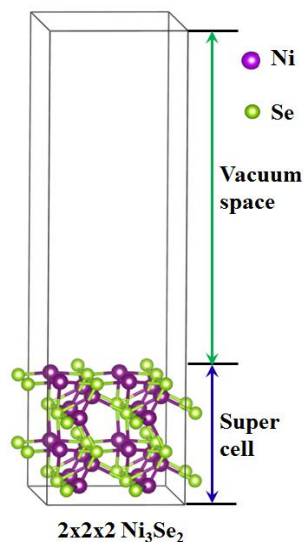


Figure 11. A slab model of  $\text{Ni}_3\text{Se}_2$  supercell with  $2 \times 2 \times 2$  lattices.

To simulate the free surface, a slab model with  $2 \times 2 \times 2$  supercells of the four compounds was employed, as illustrated in Figure 11. A relatively large vacuum gap of 20

$\text{\AA}$  was set in the slab model to prevent its interaction with the periodic image of the lower layer. The bottom lattice of the model was fixed at the ground-state bulk distances, while the top lattice was set to be free to move in all directions. For each selected structure, atomic positions were relaxed first to reach their equilibrium positions before interacting with  $\text{OH}^-$

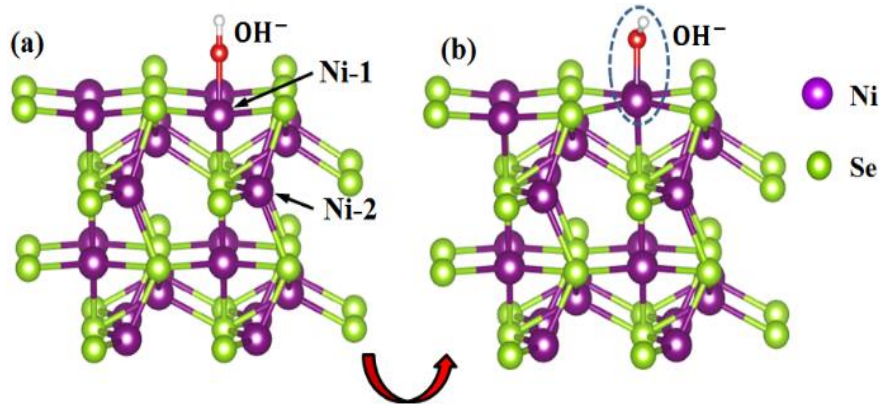


Figure 12. (a) Original crystal structure of Ni<sub>3</sub>Se<sub>2</sub> supercell with an OH<sup>-</sup> ion placed on the top of the active Ni-1 site, which is located on (001) free surface. The original bond distances of Ni-O and O-H are set as 1.86  $\text{\AA}$  and 0.96  $\text{\AA}$ , respectively; (b) the relaxed structure of Ni<sub>3</sub>Se<sub>2</sub> supercell with OH<sup>-</sup> ion adsorbed on the active Ni-1 site.

ion. The internal energy of this structure was denoted  $E_{\text{Ni}_x\text{Fe}_y\text{Co}_z\text{Se}_n}$ . Thereafter, the OH<sup>-</sup> ion was placed on the top of the active Ni/Fe/Co sites (on the relaxed free surface) at a distance of 1.86  $\text{\AA}$  to calculate the total formation energy,  $E_{\text{Ni}_x\text{Fe}_y\text{Co}_z\text{Se}_n+\text{OH}^-}$ .<sup>93</sup> The internal energy of the isolated OH<sup>-</sup> ion,  $E_{\text{OH}^-}$ , was also calculated. The adsorption energy was then calculated using eq 7.

$$E_{ad} = E_{\text{Ni}_x\text{Fe}_y\text{Co}_z\text{Se}_n+\text{OH}^-} - (E_{\text{Ni}_x\text{Fe}_y\text{Co}_z\text{Se}_n} + E_{\text{OH}^-}) \quad (7)$$

In Figure 12a, one OH<sup>-</sup> ion was placed right above the active Ni-1 site of Ni<sub>3</sub>Se<sub>2</sub>. After relaxation, attributed to the interaction between the Ni-1 site and the OH<sup>-</sup> ion, a distinct out-of-plane movement of the Ni-1 site was observed, and the Ni-1–O–H angle

changed from the original  $180^\circ$  to  $108.6^\circ$  (Figure 12b). The calculated adsorption energies on Ni-1 and Ni-2 sites were  $-2.23$  and  $-1.88$  eV, respectively. In contrast, there were three types of active Fe sites in  $\text{Fe}_3\text{Se}_4$ , which are shown in Figure 10b and Figure 13a as Fe-1, Fe-2, and Fe-3. Analogously, as can be seen in Figure 13b, an out-of-plane displacement of the Fe-1 site and a change in Fe-1–O–H angle were observed after adsorption interaction. The obtained adsorption energies on the active sites of Fe-1, Fe-2, and Fe-3 were  $-2.104$ ,  $-2.17$ , and  $-2.137$  eV, respectively.

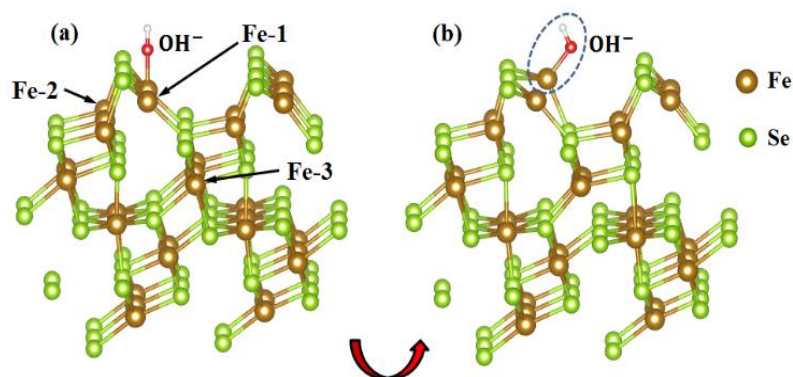


Figure 13. (a) Original and (b) relaxed crystal structures of  $\text{Fe}_3\text{Se}_4$  supercells with an  $\text{OH}^-$  ions adsorbed on the active Fe site on the (001) free surface.

In the compounds  $(\text{Ni}_{0.37}\text{Fe}_{0.36}\text{Co}_{0.27})_3\text{Se}_4$  and  $(\text{Ni}_{0.25}\text{Fe}_{0.68}\text{Co}_{0.07})_3\text{Se}_4$ , all three active Ni, Fe, and Co sites have three different types. We carried out 32 random DFT calculations in total in order to cover all the possible situations. Figure 14a–c and Figure 15a–c show the representatives of  $\text{OH}^-$  ions adhering to Ni, Fe, and Co sites. After relaxation, the out-of-plane displacement of Ni, Fe, and Co sites and the change in Ni/Fe/Co–O–H angles can be observed in Figure 14a–c and Figure 15 a–c. The obtained weighted average of adsorption energies in  $(\text{Ni}_{0.37}\text{Fe}_{0.36}\text{Co}_{0.27})_3\text{Se}_4$  and

$(\text{Ni}_{0.25}\text{Fe}_{0.68}\text{Co}_{0.07})_3\text{Se}_4$  were  $-2.06$  and  $-2.69$  eV, respectively. It has been observed previously that  $\text{OH}^-$  adsorption on the catalyst surface is facilitated by an increasing value of the adsorption energy since the process becomes energetically favorable. The weighted average of adsorption energy of the  $\text{OH}^-$  ion on the four catalyst compositions has been plotted in Figure 16a. It can be seen that as the composition of Fe in the active sites of Ni/Fe/Co increased to 66%, i.e.  $(\text{Ni}_{0.25}\text{Fe}_{0.68}\text{Co}_{0.07})_3\text{Se}_4$ , the average adsorption energy of the  $\text{OH}^-$  ion on the catalyst surface (cumulative of Ni, Fe, and Co sites) reached its minimum value of  $-2.69$  eV, which indicates the most active status of the catalyst surface with respect to obtaining optimal coverage. Separately, in the composition  $(\text{Ni}_{0.25}\text{Fe}_{0.68}\text{Co}_{0.07})_3\text{Se}_4$ , the adsorption energies of  $\text{OH}^-$  ions on different active sites of Ni, Fe, and Co all reached their minimum values, as shown in Figure 16b. This indicates that, on the basis of the  $\text{OH}^-$  adsorption kinetics, the composition  $(\text{Ni}_{0.25}\text{Fe}_{0.68}\text{Co}_{0.07})_3\text{Se}_4$  attains optimal coverage much more preferentially in comparison to the terminal compositions as well as ternary nonoptimal compositions such as  $(\text{Ni}_{0.37}\text{Fe}_{0.36}\text{Co}_{0.27})_3\text{Se}_4$ . This observation further underlines the importance of such a phase exploration study to properly understand the structure–function–property correlation and thereby develop proper design principles for optimal performance. An optimal coverage with  $\text{OH}^-$  will lead to a faster onset of the OER, and hence the contour plot of  $\text{OH}^-$  ion adsorption energy as a function of composition in Figure S5 in the Supporting Information was compared with the contour plot of OER onset potential (Figure 4). It is interesting to note that Figure S5 shows very good similarity in identifying the region of the most active catalysts, which is in good agreement with the experimental contour plot in Figure 4. The presence of mixed-metal doping in the ternary and quaternary selenide compositions thus plays multiple roles in enhancing the catalytic



activity of these electrocatalysts. It has been shown that multimetal doping in the Ni–Fe system can lead to a cathodic shift of the Ni(II) oxidation peak, leading to faster onset of OER catalytic activity.<sup>79,80,94</sup> This along with the energetically favorable OH<sup>-</sup> adsorption on the multiple metal sites on the surface may lead to a faster onset of OER catalytic activity on the surface with optimal doping of Fe which shows the best OH<sup>-</sup> adsorption energy.

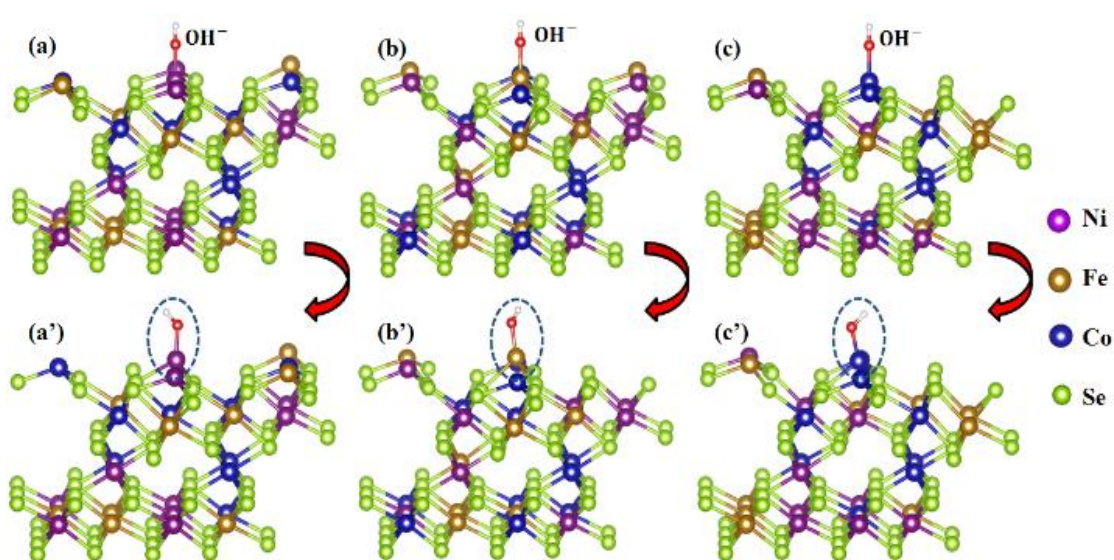


Figure 14. Representatives of the original (a-c) and the corresponding relaxed (a'-c') crystal structure of  $(\text{Ni}_{0.37}\text{Fe}_{0.36}\text{Co}_{0.27})_3\text{Se}_4$  supercells with  $\text{OH}^-$  ions placed above the active Ni, Fe and Co sites on the (001) free surfaces.

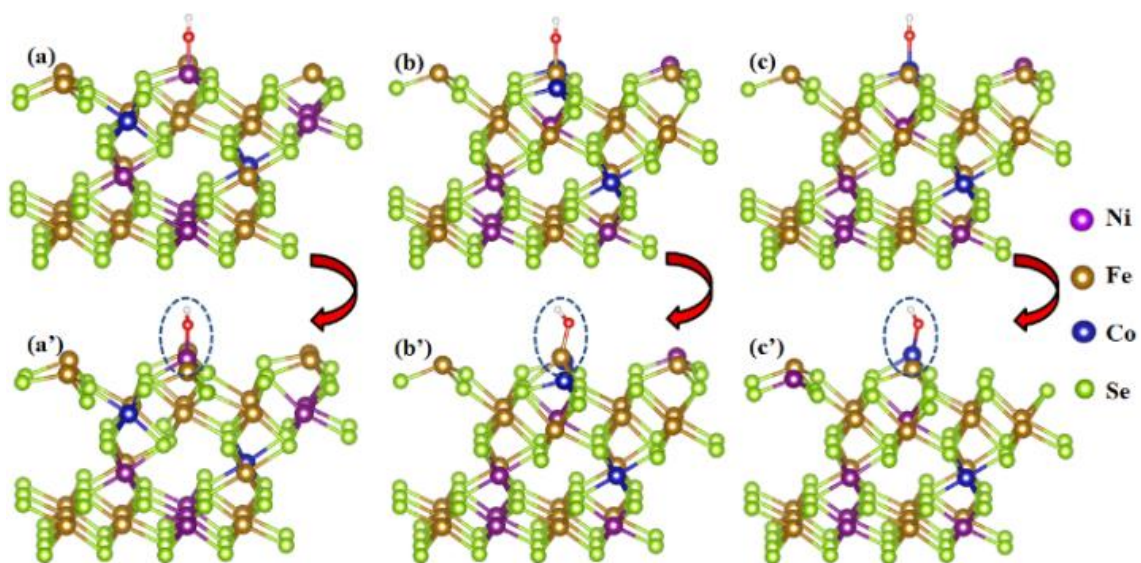


Figure 15. Representatives of the original (a-c) and the corresponding relaxed (a'-c') crystal structure of  $(\text{Ni}_{0.25}\text{Fe}_{0.68}\text{Co}_{0.07})_3\text{Se}_4$  supercells with  $\text{OH}^-$  ions placed above the active Ni, Fe and Co sites on the (001) free surfaces.

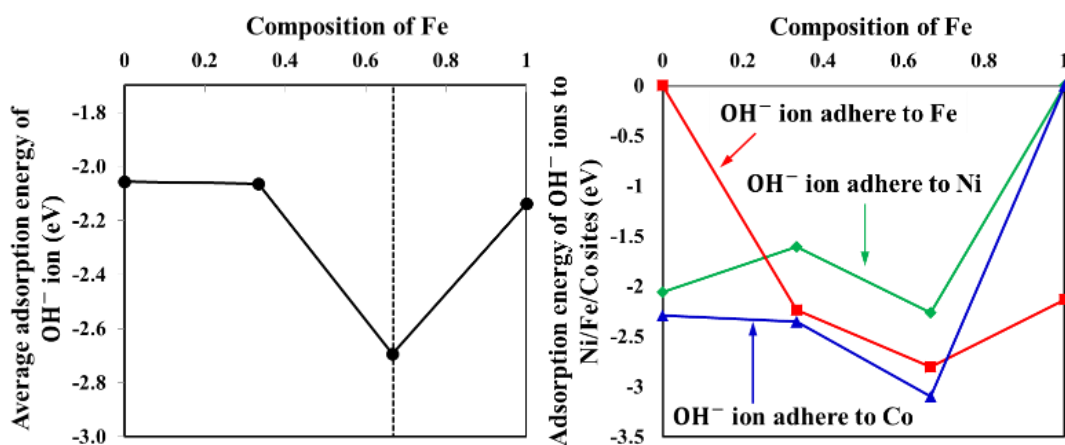


Figure 16. (a) Average adsorption energy of  $\text{OH}^-$  ion on the surface on different catalyst compositions as explained in the text, and (b) adsorption energy of  $\text{OH}^-$  ions to different active sites: Ni, Fe, and Co as a function of the composition of Fe.

## 4. CONCLUSIONS

In summary, we have demonstrated that a combinatorial electrodeposition approach for making mixed-metal selenides has been successful in finding mixed-metal selenide compositions in the Fe-Ni-Co phase space that show exceptional electrocatalytic performance for the oxygen evolution reaction in alkaline medium. Specifically, we have observed that increasing Co and Fe concentrations in the Ni selenide matrix progressively improves the catalytic efficiency. Through this phase-space exploration, we have successfully found a very promising composition as an OER electrocatalyst,  $(\text{Ni}_{0.25}\text{Fe}_{0.68}\text{Co}_{0.07})_3\text{Se}_4$ , which shows a low onset overpotential of 0.18 V and overpotential of 0.23 V to reach a current density of  $10 \text{ mA cm}^{-2}$  in  $\text{N}_2$ -saturated 0.3 M KOH. Electrochemical studies along with estimation of the hydroxyl adsorption energy of the surface indicated that that enhancement in catalytic activity can be partially due to the facilitated charge transfer at the electrode–electrolyte interface as well as charge transfer within the catalyst film. This study opens up a new avenue to investigate other mixed-metal selenide combinations, as well as provide opportunities to understand the effect of each transition-metal ion (along with the d electron occupancy) on the catalyst’s performance.

## AUTHOR INFORMATION

Corresponding Author \* Email: [nathm@mst.edu](mailto:nathm@mst.edu)

Author Contributions: All authors have given approval to the final version of the manuscript.

Notes: The authors declare no competing financial interest.

Supporting Information. The Supporting Information includes trigonal phase diagram, LSV plots, Nyquist plots, ternary contour plot of adsorption energy, EDS table before and after chronoamperometry and atomic percentage table. The Supporting Information is available free of charge on the ACS Publications website.

## ACKNOWLEDGMENTS

The authors would like to acknowledge financial support from National Science Foundation (DMR 1710313), American Chemical Society Petroleum Research Fund (54793-ND10), and Energy Research and Development Center (ERDC) Missouri S&T. The authors would also like to acknowledge Materials Research Center for equipment usage.

## SUPPORTING INFORMATION

### PHASE EXPLORATION AND IDENTIFICATION OF MULTINARY TRANSITION METAL SELENIDES AS HIGH-EFFICIENCY OXYGEN EVOLUTION ELECTROCATALYSTS THROUGH COMBINATORIAL ELECTRODEPOSITION

*Xi Cao,<sup>a</sup> Yu Hong,<sup>b</sup> Ning Zhang,<sup>b</sup> Qingzhi Chen,<sup>a</sup> Jahangir Masud,<sup>a</sup> Mohsen Asle Zaeem,<sup>b</sup>  
and Manashi Nath<sup>a\*</sup>*

<sup>a</sup>Department of Chemistry, Missouri University of Science & Technology, Rolla, Missouri 65409, United States.

<sup>b</sup>Department of Materials Science & Engineering, Missouri University of Science and Technology, Rolla, Missouri 65409, United States.

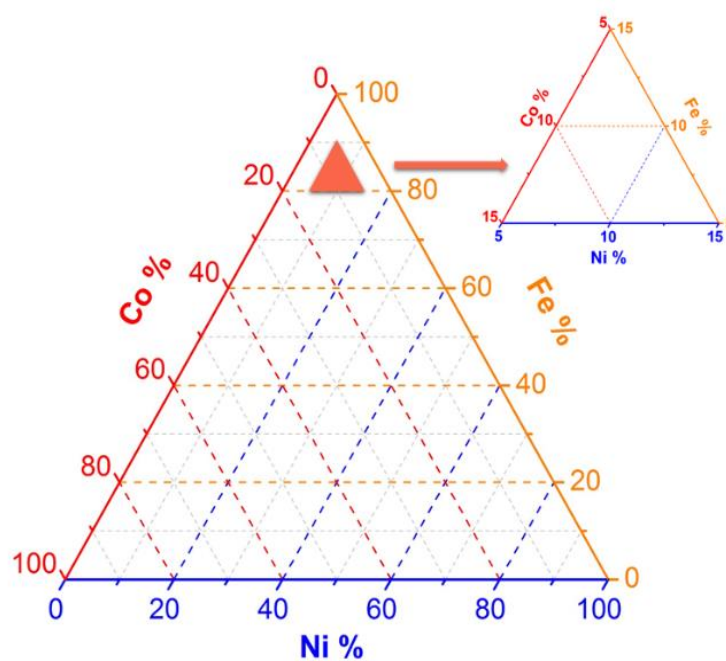


Figure S1. Triangle diagram used to further investigate the best composition region.

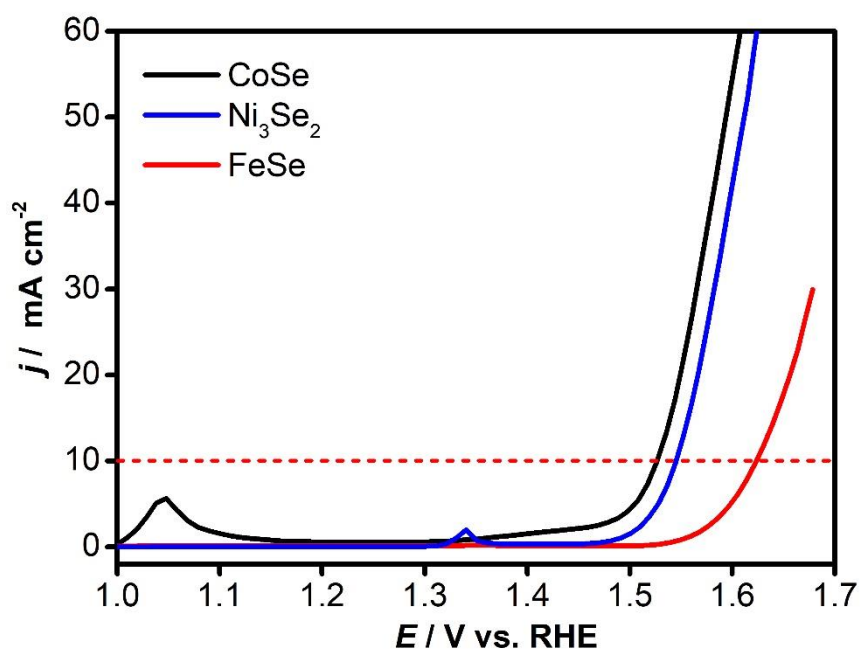


Figure S2. Polarization curves of three pure metal selenides.

Table S1. The precursor ratio of compounds shown in the plots and their corresponding formulas by EDS atomic ratio.

| Precursor ratio |           |                                                                       | Molecular formula from EDS atomic ratio                                                  |
|-----------------|-----------|-----------------------------------------------------------------------|------------------------------------------------------------------------------------------|
| Ni              | Fe        | Co                                                                    |                                                                                          |
| 10              |           |                                                                       | Ni <sub>3</sub> Se <sub>2</sub>                                                          |
|                 | 10        |                                                                       | FeSe                                                                                     |
|                 |           | 10                                                                    | CoSe                                                                                     |
| Ni-Co Group     | <b>Ni</b> | <b>Co</b>                                                             |                                                                                          |
|                 | 7         | 3                                                                     | (Ni <sub>0.64</sub> Co <sub>0.36</sub> )Se                                               |
|                 | 5         | 5                                                                     | (Ni <sub>0.39</sub> Co <sub>0.61</sub> )Se                                               |
|                 | 4         | 6                                                                     | (Ni <sub>0.49</sub> Co <sub>0.51</sub> )Se                                               |
|                 | 3         | 7                                                                     | (Ni <sub>0.38</sub> Co <sub>0.62</sub> )Se                                               |
|                 | 2         | 8                                                                     | (Ni <sub>0.24</sub> Co <sub>0.76</sub> )Se                                               |
|                 | 1         | 9                                                                     | (Ni <sub>0.15</sub> Co <sub>0.85</sub> )Se                                               |
| Co-Fe Group     | <b>Fe</b> | <b>Co</b>                                                             |                                                                                          |
|                 | 8         | 2                                                                     | (Co <sub>0.33</sub> Fe <sub>0.67</sub> ) <sub>3</sub> Se <sub>4</sub>                    |
|                 | 7         | 3                                                                     | (Co <sub>0.47</sub> Fe <sub>0.53</sub> ) <sub>3</sub> Se <sub>4</sub>                    |
|                 | 6         | 4                                                                     | (Co <sub>0.7</sub> Fe <sub>0.3</sub> ) <sub>3</sub> Se <sub>4</sub>                      |
|                 | 5         | 5                                                                     | (Co <sub>0.65</sub> Fe <sub>0.35</sub> ) <sub>3</sub> Se <sub>4</sub>                    |
|                 | 4         | 6                                                                     | (Co <sub>0.76</sub> Fe <sub>0.24</sub> ) <sub>3</sub> Se <sub>4</sub>                    |
|                 | 1         | 9                                                                     | (Co <sub>0.9</sub> Fe <sub>0.1</sub> ) <sub>3</sub> Se <sub>4</sub>                      |
| Ni-Fe Group     | <b>Ni</b> | <b>Fe</b>                                                             |                                                                                          |
|                 | 9         | 1                                                                     | (Ni <sub>0.92</sub> Fe <sub>0.08</sub> ) <sub>3</sub> Se <sub>4</sub>                    |
|                 | 8         | 2                                                                     | (Ni <sub>0.95</sub> Fe <sub>0.05</sub> ) <sub>3</sub> Se <sub>4</sub>                    |
|                 | 7         | 3                                                                     | (Ni <sub>0.82</sub> Fe <sub>0.18</sub> ) <sub>3</sub> Se <sub>4</sub>                    |
|                 | 6         | 4                                                                     | (Ni <sub>0.85</sub> Fe <sub>0.15</sub> ) <sub>3</sub> Se <sub>4</sub>                    |
|                 | 5         | 5                                                                     | (Ni <sub>0.7</sub> Fe <sub>0.3</sub> ) <sub>3</sub> Se <sub>4</sub>                      |
|                 | 4         | 6                                                                     | (Ni <sub>0.58</sub> Fe <sub>0.42</sub> ) <sub>3</sub> Se <sub>4</sub>                    |
|                 | 3         | 7                                                                     | (Ni <sub>0.47</sub> Fe <sub>0.53</sub> ) <sub>3</sub> Se <sub>4</sub>                    |
|                 | 2         | 8                                                                     | (Ni <sub>0.35</sub> Fe <sub>0.65</sub> ) <sub>3</sub> Se <sub>4</sub>                    |
| 1               | 9         | (Ni <sub>0.17</sub> Fe <sub>0.83</sub> ) <sub>3</sub> Se <sub>4</sub> |                                                                                          |
| <b>Ni</b>       | <b>Fe</b> | <b>Co</b>                                                             |                                                                                          |
| 0.5             | 8         | 1.5                                                                   | (Ni <sub>0.09</sub> Fe <sub>0.59</sub> Co <sub>0.32</sub> ) <sub>3</sub> Se <sub>4</sub> |
| 0.5             | 8.5       | 1                                                                     | (Ni <sub>0.11</sub> Fe <sub>0.63</sub> Co <sub>0.25</sub> ) <sub>3</sub> Se <sub>4</sub> |
| 1               | 5         | 4                                                                     | (Ni <sub>0.13</sub> Fe <sub>0.25</sub> Co <sub>0.62</sub> ) <sub>3</sub> Se <sub>4</sub> |
| 1.5             | 8         | 0.5                                                                   | (Ni <sub>0.25</sub> Fe <sub>0.68</sub> Co <sub>0.07</sub> ) <sub>3</sub> Se <sub>4</sub> |
| 2               | 3         | 5                                                                     | (Ni <sub>0.25</sub> Fe <sub>0.08</sub> Co <sub>0.67</sub> ) <sub>3</sub> Se <sub>4</sub> |
| 3               | 5         | 2                                                                     | (Ni <sub>0.42</sub> Fe <sub>0.19</sub> Co <sub>0.39</sub> ) <sub>3</sub> Se <sub>4</sub> |
| 3               | 6         | 1                                                                     | (Ni <sub>0.45</sub> Fe <sub>0.34</sub> Co <sub>0.2</sub> ) <sub>3</sub> Se <sub>4</sub>  |

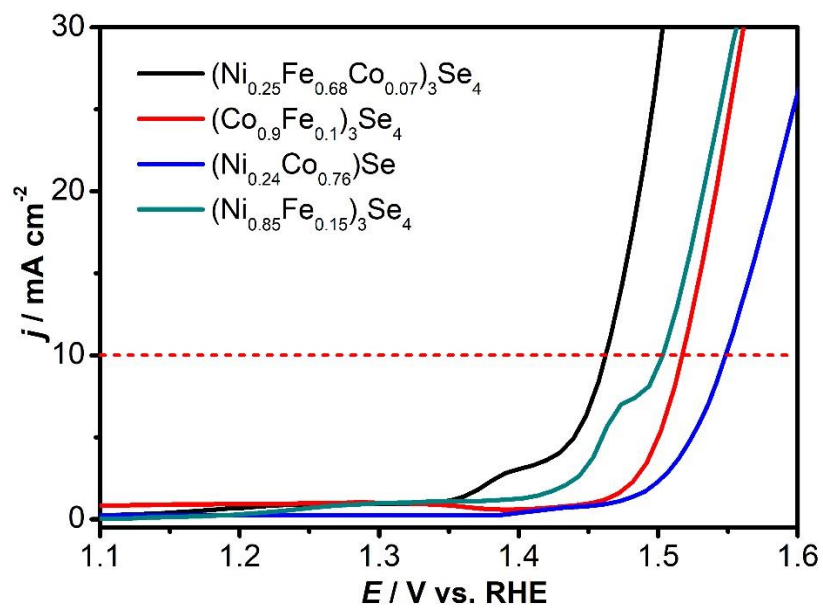


Figure S3. Linear sweep voltammeteries (LSVs) measured for selected catalysts in  $\text{N}_2$  saturated 0.3 M KOH solution at a scan rate of  $0.01 \text{ V s}^{-1}$ . The red dotted line shows the current density of  $10 \text{ mA cm}^{-2}$ .

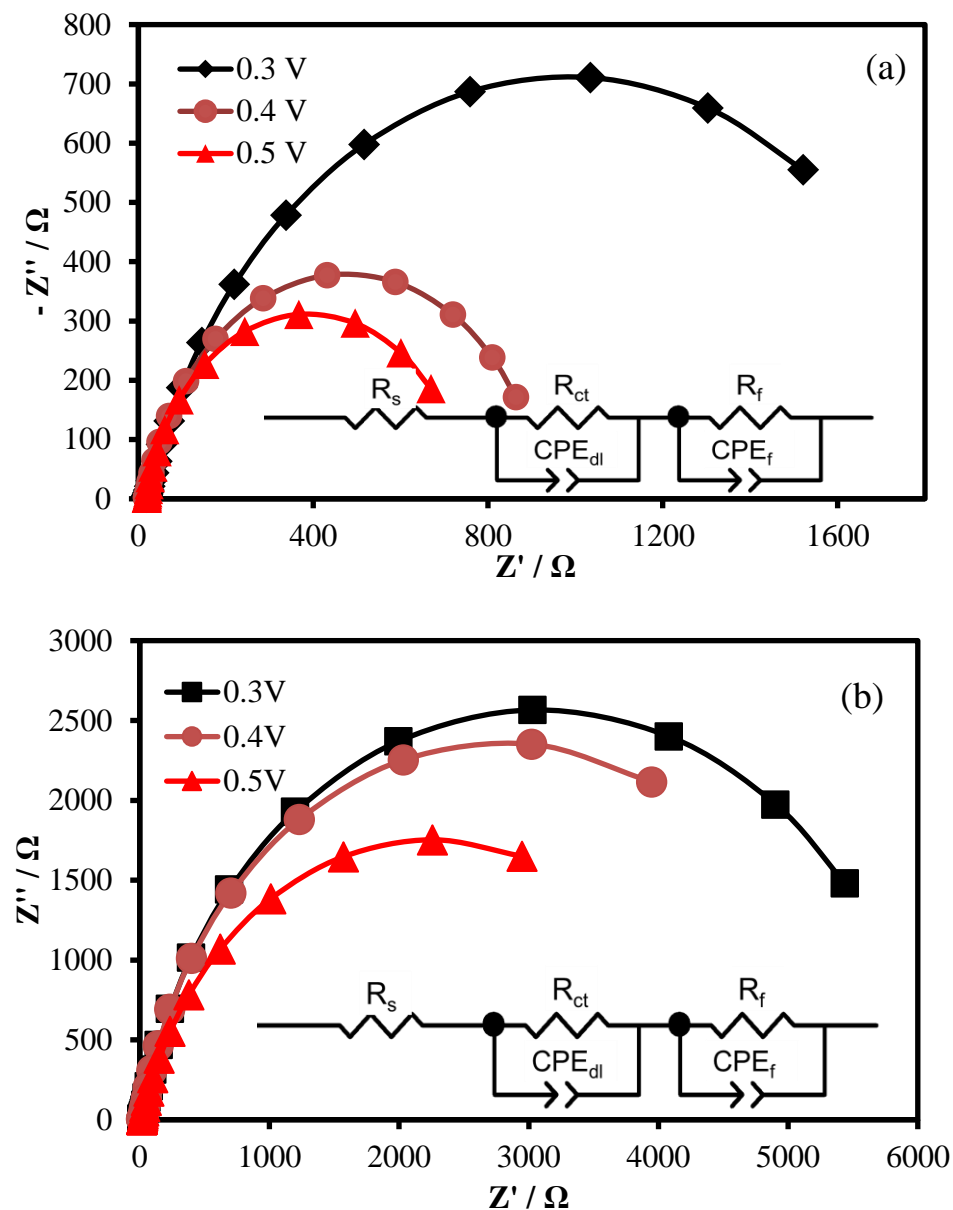


Figure S4. Nyquist plots obtained from EIS measurements of  $(\text{Ni}_{0.25}\text{Fe}_{0.68}\text{Co}_{0.07})_3\text{Se}_4$  and  $(\text{Ni}_{0.37}\text{Fe}_{0.36}\text{Co}_{0.27})_2\text{Se}_3$  catalysts at various applied potentials of 0.3, 0.4 and 0.5 V vs  $\text{Ag}^+/\text{AgCl}$  in  $\text{N}_2$ -saturated 0.3 M KOH solution. Symbols indicate the raw data, while solid lines represent the corresponding fit to equivalent circuit model. Inset shows the equivalent circuit of catalysts.



Table S2. Comparison of EDS atomic ratio of the catalyst before and after 8 h chronoamperometry.

|                             | EDS (Atomic %) |      |     |      |
|-----------------------------|----------------|------|-----|------|
|                             | Ni             | Fe   | Co  | Se   |
| As-deposited                | 11.4           | 31.7 | 3.3 | 53.5 |
| After 8 h Chronoamperometry | 14.1           | 35.9 | 5.4 | 44.6 |

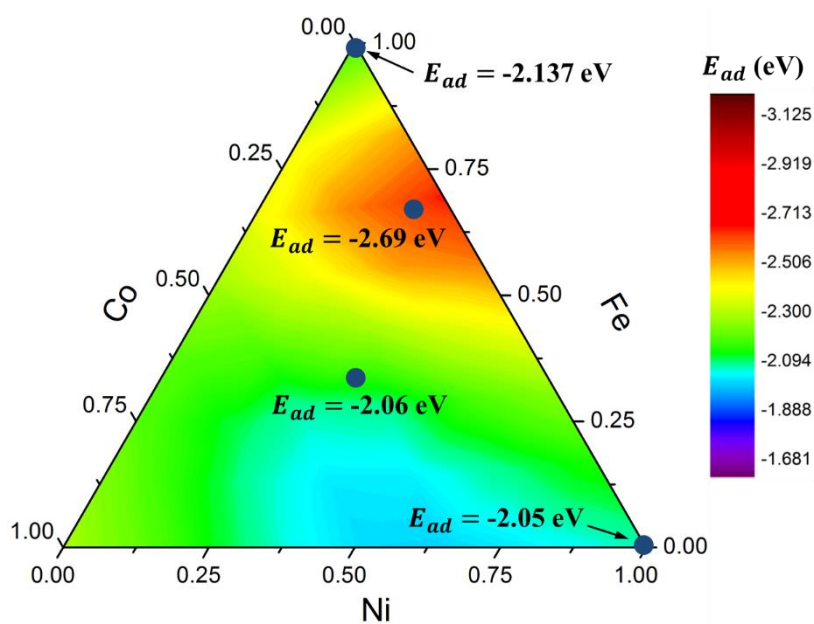


Figure S5. Ternary contour plot of  $\text{OH}^-$  ions adsorption energy as a function of composition.

## REFERENCES

- (1) Walter, M. G.; Warren, E. L.; Mckone, J. R.; Boettcher, S. W.; Mi, Q.; Santori, E. A.; Lewis, N. S. Solar Water Splitting Cells. *Chem. Rev.* **2010**, *110*, 6446–6473.
- (2) Cook, T. R.; Dogutan, D. K.; Reece, S. Y.; Surendranath, Y.; Teets, T. S.; Nocera, D. G. Solar Energy Supply and Storage for the Legacy and Nonlegacy Worlds. *Chem. Rev.* **2010**, *110*, 6474–6502.

- (3) Carrette, L.; Friedrich, K. A.; Stimming, U. Fuel Cells-Fundamentals and Applications. *Fuel Cells* **2001**, *1*, 5–39.
- (4) Suen, N. T.; Hung, S. F.; Quan, Q.; Zhang, N.; Xu, Y. J.; Chen, H. M. Electrocatalysis for the Oxygen Evolution Reaction: Recent Development and Future Perspectives. *Chem. Soc. Rev.* **2017**, *46*, 337–365.
- (5) Suntivich, J.; May, K. J.; Gasteiger, H. a; Goodenough, J. B.; Shao-horn, Y. A Perovskite Oxide Optimized for Molecular Orbital Principles. *Science*. **2011**, *334*, 1383–1385.
- (6) Lee, S. W.; Carlton, C.; Risch, M.; Surendranath, Y.; Chen, S.; Furutsuki, S.; Yamada, A.; Nocera, D. G.; Shao-Horn, Y. The Nature of Lithium Battery Materials under Oxygen Evolution Reaction Conditions. *J. Am. Chem. Soc.* **2012**, *134*, 16959–16962.
- (7) Burke, M. S.; Enman, L. J.; Batchellor, A. S.; Zou, S.; Boettcher, S. W. Oxygen Evolution Reaction Electrocatalysis on Transition Metal Oxides and (Oxy)hydroxides: Activity Trends and Design Principles. *Chem. Mater.* **2015**, *27*, 7549–7558.
- (8) Man, I. C.; Su, H. Y.; Calle-Vallejo, F.; Hansen, H. A.; Martínez, J. I.; Inoglu, N. G.; Kitchin, J.; Jaramillo, T. F.; Nørskov, J. K.; Rossmeisl, J. Universality in Oxygen Evolution Electrocatalysis on Oxide Surfaces. *ChemCatChem* **2011**, *3*, 1159–1165.
- (9) Hu, S.; Shaner, M. R.; Beardslee, J. A.; Lichterman, M.; Brunschwig, B. S.; Lewis, N. S. Amorphous TiO<sub>2</sub> Coatings Stabilize Si, GaAs, and GaP Photoanodes for Efficient Water Oxidation. *Science*. **2014**, *344*, 1005–1009.
- (10) Lewis, N. S. Toward Cost-Effective Solar Energy Use. *Science*. **2007**, *315*, 798–801.
- (11) Cherevko, S.; Geiger, S.; Kasian, O.; Kulyk, N.; Grote, J. P.; Savan, A.; Shrestha, B. R.; Merzlikin, S.; Breitbach, B.; Ludwig, A.; Mayrhofer, K. J. J. Oxygen and Hydrogen Evolution Reactions on Ru, RuO<sub>2</sub>, Ir, and IrO<sub>2</sub> Thin Film Electrodes in Acidic and Alkaline Electrolytes: A Comparative Study on Activity and Stability. *Catal. Today* **2016**, *262*, 170–180.
- (12) Stoerzinger, K. A.; Qiao, L.; Biegalski, M. D.; Shao-Horn, Y. Orientation-Dependent Oxygen Evolution Activities of Rutile IrO<sub>2</sub> and RuO<sub>2</sub>, *J. Phys. Chem. Lett.* **2014**, *5*, 1636–1641.
- (13) Lee, Y.; Suntivich, J.; May, K. J.; Perry, E. E.; Shao-Horn, Y. Synthesis and Activities of Rutile IrO<sub>2</sub> and RuO<sub>2</sub> Nanoparticles for Oxygen Evolution in Acid and Alkaline Solutions. *J. Phys. Chem. Lett.* **2012**, *3*, 399–404.
- (14) Singh, A.; Spiccia, L. Water Oxidation Catalysts Based on Abundant 1<sup>st</sup> Row Transition Metals. *Coord. Chem. Rev.* **2013**, *257*, 2607–2622.
- (15) Galán-Mascarós, J. R. Water Oxidation at Electrodes Modified with Earth-Abundant Transition-Metal Catalysts. *ChemElectroChem* **2015**, *2*, 37–50.

- (16) Du, P.; Eisenberg, R. Catalysts Made of Earth-Abundant Elements (Co, Ni, Fe) for Water Splitting: Recent Progress and Future Challenges. *Energy Environ. Sci.* **2012**, *5*, 6012–6021.
- (17) Gong, M.; Dai, H. A Mini Review on NiFe-Based Materials as Highly Active Oxygen Evolution Reaction Electrocatalysts. *Nano Res.* **2015**, *8*, 23–39.
- (18) Swesi, A. T.; Masud, J.; Liyanage, W. P. R.; Umapathi, S.; Bohannan, E.; Medvedeva, J.; Nath, M. Textured NiSe<sub>2</sub> Film: Bifunctional Electrocatalyst for Full Water Splitting at Remarkably Low Overpotential with High Energy Efficiency. *Sci. Rep.* **2017**, *7*, 2401.
- (19) Masud, J.; Ioannou, P. C.; Levesanos, N.; Kyritsis, P.; Nath, M. A Molecular Ni-Complex Containing Tetrahedral Nickel Selenide Core as Highly Efficient Electrocatalyst for Water Oxidation. *ChemSusChem.* **2016**, 3128–3132.
- (20) Umapathi, S.; Masud, J.; Swesi, A. T.; Nath, M. FeNi<sub>2</sub>Se<sub>4</sub>-Reduced Graphene Oxide Nanocomposite: Enhancing Bifunctional Electrocatalytic Activity for Oxygen Evolution and Reduction through Synergistic Effects. *Adv. Sustain. Syst.* **2017**, *1*, 1700086.
- (21) Amin, B. G.; Swesi, A. T.; Masud, J.; Nath, M. CoNi<sub>2</sub>Se<sub>4</sub> as an Efficient Bifunctional Electrocatalyst for Overall Water Splitting. *Chem. Commun.* **2017**, *53*, 5412–5415.
- (22) Xu, X.; Song, F.; Hu, X. A Nickel Iron Diselenide-Derived Efficient Oxygen-Evolution Catalyst. *Nat. Commun.* **2016**, *7*, 12324.
- (23) Gong, M.; Li, Y.; Wang, H.; Liang, Y.; Wu, J. Z.; Zhou, J.; Wang, J.; Regier, T.; Wei, F.; Dai, H. An Advanced Ni-Fe Layered Double Hydroxide Electrocatalyst for Water Oxidation. *J. Am. Chem. Soc.* **2013**, *135*, 8452–8455.
- (24) Trotochaud, L.; Young, S. L.; Ranney, J. K.; Boettcher, S. W. Nickel-Iron Oxyhydroxide Oxygen-Evolution Electrocatalysts: The Role of Intentional and Incidental Iron Incorporation. *J. Am. Chem. Soc.* **2014**, *136*, 6744–6753.
- (25) Louie, M. W.; Bell, A. T. An Investigation of Thin-Film Ni-Fe Oxide Catalysts for the Electrochemical Evolution of Oxygen. *J. Am. Chem. Soc.* **2013**, *135*, 12329–12337.
- (26) Burke, M. S.; Kast, M. G.; Trotochaud, L.; Smith, A. M.; Boettcher, S. W. Cobalt-Iron (Oxy)hydroxide Oxygen Evolution Electrocatalysts: The Role of Structure and Composition on Activity, Stability, and Mechanism. *J. Am. Chem. Soc.* **2015**, *137*, 3638–3648.
- (27) Klaus, S.; Cai, Y.; Louie, M. W.; Trotochaud, L.; Bell, A. T. Effects of Fe Electrolyte Impurities on Ni(OH)<sub>2</sub>/NiOOH Structure and Oxygen Evolution Activity. *J. Phys. Chem. C* **2015**, *119*, 7243–7254.
- (28) Masud, J.; Nath, M. Co<sub>7</sub>Se<sub>8</sub> Nanostructures as Catalysts for Oxygen Reduction Reaction with High Methanol Tolerance. *ACS Energy Lett.* **2016**, *1*, 27–31.

- (29) Liao, M.; Zeng, G.; Luo, T.; Jin, Z.; Wang, Y.; Kou, X.; Xiao, D. Three-Dimensional Coral-like Cobalt Selenide as an Advanced Electrocatalyst for Highly Efficient Oxygen Evolution Reaction. *Electrochim. Acta* **2016**, *194*, 59–66.
- (30) Liang, Y.; Moon, J. S.; Mu, R.; Winiarz, J. G. Functionalization of CdSe Semiconductor Nanocrystals with Organic Charge-Transporting Ligands. *J. Mater. Chem. C* **2015**, *3*, 4134–4140.
- (31) Zhou, W.; Wu, X. J.; Cao, X.; Huang, X.; Tan, C.; Tian, J.; Liu, H.; Wang, J.; Zhang, H. Ni<sub>3</sub>S<sub>2</sub> nanorods/Ni Foam Composite Electrode with Low Overpotential for Electrocatalytic Oxygen Evolution. *Energy Environ. Sci.* **2013**, *6*, 2921–2924.
- (32) Ganesan, P.; Prabu, M.; Sanetuntikul, J.; Shanmugam, S. Cobalt Sulfide Nanoparticles Grown on Nitrogen and Sulfur Codoped Graphene Oxide: An Efficient Electrocatalyst for Oxygen Reduction and Evolution Reactions. *ACS Catal.* **2015**, *5*, 3625–3637.
- (33) Stern, L. A.; Feng, L.; Song, F.; Hu, X. Ni<sub>2</sub>P as a Janus Catalyst for Water Splitting: The Oxygen Evolution Activity of Ni<sub>2</sub>P Nanoparticles. *Energy Environ. Sci.* **2015**, *8*, 2347–2351.
- (34) Masud, J.; Umaphathi, S.; Ashokaan, N.; Nath, M. Iron Phosphide Nanoparticles as an Efficient Electrocatalyst for the OER in Alkaline Solution. *J. Mater. Chem. A* **2016**, *4*, 9750–9754.
- (35) Shinde, D. V.; De Trizio, L.; Dang, Z.; Prato, M.; Gaspari, R.; Manna, L. Hollow and Porous Nickel Cobalt Perselenide Nanostructured Microparticles for Enhanced Electrocatalytic Oxygen Evolution. *Chem. Mater.* **2017**, *29*, 7032–7041.
- (36) Wang, Z.; Li, J.; Tian, X.; Wang, X.; Yu, Y.; Owusu, K. A.; He, L.; Mai, L. Porous Nickel-Iron Selenide Nanosheets as Highly Efficient Electrocatalysts for Oxygen Evolution Reaction. *ACS Appl. Mater. Interfaces* **2016**, *8*, 19386–19392.
- (37) Liu, B.; Zhao, Y. F.; Peng, H. Q.; Zhang, Z. Y.; Sit, C. K.; Yuen, M. F.; Zhang, T. R.; Lee, C. S.; Zhang, W. J. Nickel–Cobalt Diselenide 3D Mesoporous Nanosheet Networks Supported on Ni Foam: An All-pH Highly Efficient Integrated Electrocatalyst for Hydrogen Evolution. *Adv. Mater.* **2017**, *29*, 1606521.
- (38) Gardner, G. P.; Go, Y. B.; Robinson, D. M.; Smith, P. F.; Hadermann, J.; Abakumov, A.; Greenblatt, M.; Dismukes, G. C. Structural Requirements in Lithium Cobalt Oxides for the Catalytic Oxidation of Water. *Angew. Chem. Int. Ed.* **2012**, *51*, 1616–1619.
- (39) Gardner, G. P.; Go, Y. B.; Robinson, D. M.; Smith, P. F.; Hadermann, J.; Abakumov, A.; Greenblatt, M.; Dismukes, G. C. Structural Requirements in Lithium Cobalt Oxides for the Catalytic Oxidation of Water. *Angew. Chem. Int. Ed.* **2012**, *51*, 1616–1619.
- (40) Wachs, I. E.; Routray, K. Catalysis Science of Bulk Mixed Oxides. *ACS Catal.* **2012**, *2*, 1235–1246.

- (41) Landon, J.; Demeter, E.; Inoğlu, N.; Keturakis, C.; Wachs, I. E.; Vasić, R.; Frenkel, A. I.; Kitchin, J. R. Spectroscopic Characterization of Mixed Fe-Ni Oxide Electrocatalysts for the Oxygen Evolution Reaction in Alkaline Electrolytes. *ACS Catal.* **2012**, *2*, 1793–1801.
- (42) Chen, S.; Qiao, S. Z. Hierarchically Porous Nitrogen-Doped Graphene-NiCo<sub>2</sub>O<sub>4</sub> Hybrid Paper as an Advanced Electrocatalytic Water-Splitting Material. *ACS Nano* **2013**, *7*, 10190–10196.
- (43) Zhou, T.; Cao, Z.; Zhang, P.; Ma, H.; Gao, Z.; Wang, H.; Lu, Y.; He, J.; Zhao, Y. Transition Metal Ions Regulated Oxygen Evolution Reaction Performance of Ni-Based Hydroxides Hierarchical Nanoarrays. *Sci. Rep.* **2017**, *7*, 46154.
- (44) Enman, L. J.; Burke, M. S.; Batchellor, A. S.; Boettcher, S. W. Effects of Intentionally Incorporated Metal Cations on the Oxygen Evolution Electrocatalytic Activity of Nickel (Oxy)hydroxide in Alkaline Media. *ACS Catal.* **2016**, *6*, 2416–2423.
- (45) Xu, X.; Su, C.; Zhou, W.; Zhu, Y.; Chen, Y.; Shao, Z. Co-Doping Strategy for Developing Perovskite Oxides as Highly Efficient Electrocatalysts for Oxygen Evolution Reaction. *Adv. Sci.* **2016**, *3*, 1500187.
- (46) Masud, J.; Swesi, A. T.; Liyanage, W. P. R.; Nath, M. Cobalt Selenide Nanostructures: An Efficient Bifunctional Catalyst with High Current Density at Low Coverage. *ACS Appl. Mater. Interfaces* **2016**, *8*, 17292–17302.
- (47) Swesi, A. T.; Masud, J.; Nath, M. Nickel Selenide as a High-Efficiency Catalyst for Oxygen Evolution Reaction. *Energy Environ. Sci.* **2016**, *9*, 1771–1782.
- (48) Wu, X.; He, D.; Zhang, H.; Li, H.; Li, Z.; Yang, B.; Lin, Z.; Lei, L.; Zhang, X. Ni<sub>0.85</sub>Se as an Efficient Non-Noble Bifunctional Electrocatalyst for Full Water Splitting. *Int. J. Hydrog. Energy* **2016**, *41*, 10688–10694.
- (49) Lew, A.; Krutzik, P. O.; Hart, M. E.; Chamberlin, A. R. Increasing Rates of Reaction: Microwave-Assisted Organic Synthesis for Combinatorial Chemistry. *J. Comb. Chem.* **2002**, *4*, 95–105.
- (50) Jandeleit, B.; J. Schaefer, D.; Powers, T. S.; Turner, H. W.; Weinberg, W. H. Combinatorial Materials Science and Catalysis. *Angew. Chem. Int. Ed.* **1999**, *38*, 2494–2532.
- (51) Osborne, S. E.; Ellington, A. D. Nucleic Acid Selection and the Challenge of Combinatorial Chemistry. *Chem. Rev.* **1997**, *97*, 349–370.
- (52) Senkan, S. M.; Ozturk, S. Discovery and Optimization of Heterogeneous Catalysts by Using Combinatorial Chemistry. *Angew. Chem. Int. Ed.* **1999**, *38*, 791–795.

- (53) Saito, K.; Jin, D. H.; Ogawa, T.; Muramoto, K.; Hatakeyama, E.; Yasuhara, T.; Nokihara, K. Antioxidative Properties of Tripeptide Libraries Prepared by the Combinatorial Chemistry. *J. Agric. Food Chem.* **2003**, *51*, 3668–3674.
- (54) Seley, D.; Ayers, K.; Parkinson, B. A. Combinatorial Search for Improved Metal Oxide Oxygen Evolution Electrocatalysts in Acidic Electrolytes. *ACS Comb. Sci.* **2013**, *15*, 82–89.
- (55) Shinde, A.; Guevarra, D.; Liu, G.; Sharp, I. D.; Toma, F. M.; Gregoire, J. M.; Haber, J. A. Discovery of Fe-Ce Oxide/BiVO<sub>4</sub> Photoanodes through Combinatorial Exploration of Ni-Fe-Co-Ce Oxide Coatings. *ACS Appl. Mater. Interfaces* **2016**, *8*, 23696–23705.
- (56) Guevarra, D.; Shinde, A.; Suram, S. K.; Sharp, I. D.; Toma, F. M.; Haber, J. A.; Gregoire, J. M. Development of Solar Fuels Photoanodes through Combinatorial Integration of Ni-La-Co-Ce Oxide Catalysts on BiVO<sub>4</sub>. *Energy Environ. Sci.* **2016**, *9*, 565–580.
- (57) Sliozberg, K.; Stein, H. S.; Khare, C.; Parkinson, B. A.; Ludwig, A.; Schuhmann, W. Fe-Cr-Al Containing Oxide Semiconductors as Potential Solar Water-Splitting Materials. *ACS Appl. Mater. Interfaces* **2015**, *7*, 4883–4889.
- (58) Chen, J. Y. C.; Miller, J. T.; Gerken, J. B.; Stahl, S. S. Inverse Spinel NiFeAlO<sub>4</sub> as a Highly Active Oxygen Evolution Electrocatalyst: Promotion of Activity by a Redox-Inert Metal Ion. *Energy Environ. Sci.* **2014**, *7*, 1382–1386.
- (59) Smith, R. D. L.; Prévot, M. S.; Fagan, R. D.; Trudel, S.; Berlinguette, C. P. Water Oxidation Catalysis: Electrocatalytic Response to Metal Stoichiometry in Amorphous Metal Oxide Films Containing Iron, Cobalt, and Nickel. *J. Am. Chem. Soc.* **2013**, *135*, 11580–11586.
- (60) McCrory, C. C. L.; Jung, S.; Peters, J. C.; Jaramillo, T. F. Benchmarking Heterogeneous Electrocatalysts for the Oxygen Evolution Reaction. *J. Am. Chem. Soc.* **2013**, *135*, 16977–16987.
- (61) Stevens, M. B.; Trang, C. D. M.; Enman, L. J.; Deng, J.; Boettcher, S. W. Reactive Fe-Sites in Ni/Fe (Oxy)hydroxide Are Responsible for Exceptional Oxygen Electrocatalysis Activity. *J. Am. Chem. Soc.* **2017**, *139*, 11361–11364.
- (62) Zaffran, J.; Stevens, M. B.; Trang, C. D. M.; Nagli, M.; Shehadeh, M.; Boettcher, S. W.; Caspary Toroker, M. Influence of Electrolyte Cations on Ni(Fe)OOH Catalyzed Oxygen Evolution Reaction. *Chem. Mater.* **2017**, *29*, 4761–4767.
- (63) Jiang, N.; Bogoev, L.; Popova, M.; Gul, S.; Yano, J.; Sun, Y. Electrodeposited Nickel-Sulfide Films as Competent Hydrogen Evolution Catalysts in Neutral Water. *J. Mater. Chem. A* **2014**, *2*, 19407–19414.
- (64) van der Heide, H.; Hemmel, R.; van Bruggen, C. F.; Haas, C. X-Ray Photoelectron Spectra of 3d Transition Metal Pyrites. *J. Solid State Chem.* **1980**, *33*, 17–25.

- (65) Han, D. S.; Batchelor, B.; Abdel-Wahab, A. Sorption of selenium(IV) and selenium(VI) onto Synthetic Pyrite ( $\text{FeS}_2$ ): Spectroscopic and Microscopic Analyses. *J. Colloid Interface Sci.* **2012**, *368*, 496-504.
- (66) Du, H.; Gu, S.; Liu, R.; Li, C. M. Highly Active and Inexpensive Iron Phosphide Nanorods Electrocatalyst towards Hydrogen Evolution Reaction. *Int. J. Hydrog. Energy* **2015**, *40*, 14272–14278.
- (67) Qian, C.; Kim, F.; Ma, L.; Tsui, F.; Yang, P.; Liu, J. Solution-Phase Synthesis of Single-Crystalline Iron Phosphide Nanorods/Nanowires. *J. Am. Chem. Soc.* **2004**, *126*, 1195–1198.
- (68) Song, J. M.; Zhang, S. S.; Yu, S. H. Multifunctional  $\text{Co}_{0.85}\text{Se-Fe}_3\text{O}_4$  Nanocomposites: Controlled Synthesis and Their Enhanced Performances for Efficient Hydrogenation of P-Nitrophenol and Adsorbents. *Small* **2014**, *10*, 717–724.
- (69) Gao, J.; Zhang, B.; Zhang, X.; Xu, B. Magnetic-Dipolar-Interaction-Induced Self-Assembly Affords Wires of Hollow Nanocrystals of Cobalt Selenide. *Angew. Chem. Int. Ed.* **2006**, *45*, 1220–1223.
- (70) Tao, F.; Zhao, Y. Q.; Zhang, G. Q.; Li, H. L. Electrochemical Characterization on Cobalt Sulfide for Electrochemical Supercapacitors. *Electrochem. Commun.* **2007**, *9*, 1282–1287.
- (71) Chen, H.; Chen, S.; Fan, M.; Li, C.; Chen, D.; Tian, G.; Shu, K. Bimetallic Nickel Cobalt Selenides: A New Kind of Electroactive Material for High-Power Energy Storage. *J. Mater. Chem. A* **2015**, *3*, 23653–23659.
- (72) Yang, J.; Cheng, G. H.; Zeng, J. H.; Yu, S. H.; Liu, X. M.; Qian, Y. T. Shape Control and Characterization of Transition Metal Diselenides  $\text{MSe}_2$  ( $\text{M} = \text{Ni, Co, Fe}$ ) Prepared by a Solvothermal-Reduction Process. *Chem. Mater.* **2001**, *13*, 848–853.
- (73) Panneerselvam, A.; Malik, M. A.; Afzaal, M.; O'Brien, P.; Helliwell, M. The Chemical Vapor Deposition of Nickel Phosphide or Selenide Thin Films from a Single Precursor. *J. Am. Chem. Soc.* **2008**, *130*, 2420–2421.
- (74) Wang, W.; Geng, Y.; Yan, P.; Liu, F.; Xie, Y.; Qian, Y. A Novel Mild Route to Nanocrystalline Selenides at Room Temperature. *J. Am. Chem. Soc.* **1999**, *121*, 4062–4063.
- (75) Solorza-Feria, O.; Ellmer, K.; Giersig, M.; Alonso-Vante, N. Novel Low-temperature Synthesis of Transition Metal for Multielectron Charge Transfer: Molecular Oxygen Reduction. *Electrochim. Acta* **1994**, *39*, 1647–1653.
- (76) Hayashi, A.; Imada, K.; Inoue, K.; Ueda, Y.; Kosuge, K. Phase Diagram of  $(\text{M}'_x\text{M}_{1-x})_3\text{Se}_4$  ( $0 \leq x \leq 1$ ) ( $\text{M, M}' = 3d\text{-Transition Metal}$ ). *Bull. Inst. Chem. Res.* **1986**, *64*, 186–206.

- (77) Snyder, G. J.; Caillat, T.; Fleurial, J. P. Thermoelectric Properties of Cr<sub>3</sub>S<sub>4</sub>-Type Selenides. *MRS Proceedings*. **1998**, 545, 333.
- (78) Friebel, D.; Louie, M. W.; Bajdich, M.; Sanwald, K. E.; Cai, Y.; Wise, A. M.; Cheng, M. J.; Sokaras, D.; Weng, T. C.; Alonso-Mori, R.; Davis, R. C.; Bargar, J. R.; Nørskov, J. K.; Nilsson, A.; Bell, A. T. Identification of Highly Active Fe Sites in (Ni,Fe)OOH for Electrocatalytic Water Splitting. *J. Am. Chem. Soc.* **2015**, *137*, 1305-1313.
- (79) Görlin, M.; Chernev, P.; De Araújo, J. F.; Reier, T.; Dresp, S.; Paul, B.; Krähnert, R.; Dau, H.; Strasser, P. Oxygen Evolution Reaction Dynamics, Faradaic Charge Efficiency, and the Active Metal Redox States of Ni-Fe Oxide Water Splitting Electrocatalysts. *J. Am. Chem. Soc.* **2016**, *138*, 5603-5614.
- (80) Görlin, [M.](#); Ferreira de Araújo, [J.](#); Schmies, [H.](#); Bernsmeier, [D.](#); [Dresp](#), S; [Gliech](#), M.; Jusys, [Z.](#); Chernev, [P.](#); Kraehnert, R.; Dau [H.](#); Strasser, [P.](#) Tracking Catalyst Redox States and Reaction Dynamics in Ni-Fe Oxyhydroxide Oxygen Evolution Reaction Electrocatalysts: The Role of Catalyst Support and Electrolyte pH. [J. Am. Chem. Soc.](#) **2017**, [139](#), 2070-2082.
- (81) Qiu, Y.; Xin, L.; Li, W. Electrocatalytic Oxygen Evolution over Supported Small Amorphous Ni-Fe Nanoparticles in Alkaline Electrolyte. *Langmuir* **2014**, *30*, 7893–7901.
- (82) Meng, Y.; Song, W.; Huang, H.; Ren, Z.; Chen, S. Y.; Suib, S. L. Structure-Property Relationship of Bifunctional MnO<sub>2</sub> Nanostructures: Highly Efficient, Ultra-Stable Electrochemical Water Oxidation and Oxygen Reduction Reaction Catalysts Identified in Alkaline Media. *J. Am. Chem. Soc.* **2014**, *136*, 11452–11464.
- (83) Gao, Y.; Li, H.; Yang, G. Amorphous Nickel Hydroxide Nanosheets with Ultrahigh Activity and Super-Long-Term Cycle Stability as Advanced Water Oxidation Catalysts. *Crypt. Growth Des.* **2015**, *15*, 4475–4483.
- (84) Suen, N. T.; Hung, S. F.; Quan, Q.; Zhang, N.; Xu, Y. J.; Chen, H. M. Electrocatalysis for the Oxygen Evolution Reaction: Recent Development and Future Perspectives. *Chem. Soc. Rev.* **2017**, *46*, 337-365.
- (85) Shinagawa, T.; Garcia-Esparza, A. T.; Takanabe, K. Insight on Tafel Slopes from a Microkinetic Analysis of Aqueous Electrocatalysis for Energy Conversion. *Sci. Rep.* **2015**, *5*, 13801.
- (86) Jiao, Y.; Zheng, Y.; Jaroniec, M.; Qiao, S. Z. Design of Electrocatalysts for Oxygen- and Hydrogen-Involving Energy Conversion Reactions. *Chem. Soc. Rev.* **2015**, *44*, 2060–2086.
- (87) Kresse, G.; Furthmüller, J. Efficient Iterative Schemes for Ab Initio Total-Energy Calculations Using a Plane-Wave Basis Set. *Phys. Rev. B* **1996**, *54*, 11169–11186.
- (88) Kresse, G.; Joubert, D. From Ultrasoft Pseudopotentials to the Projector Augmented-Wave Method. *Phys. Rev. B* **1999**, *59*, 1758–1775.



- (89) Blöchl, P. E. Projector Augmented-Wave Method. *Phys. Rev. B* **1994**, *50*, 17953–17979.
- (90) Perdew, J. P.; Chevary, J. A.; Vosko, S. H.; Jackson, K. A.; Pederson, M. R.; Singh, D. J.; Fiolhais, C. Atoms, Molecules, Solids, and Surfaces: Applications of the Generalized Gradient Approximation for Exchange and Correlation. *Phys. Rev. B* **1992**, *46*, 6671–6687.
- (91) Vanderbilt, D. Soft Self-Consistent Pseudopotentials in a Generalized Eigenvalue Formalism. *Phys. Rev. B* **1990**, *41*, 7892–7895.
- (92) Lee, Y. L.; Gadre, M. J.; Shao-Horn, Y.; Morgan, D. Ab Initio GGA+U Study of Oxygen Evolution and Oxygen Reduction Electrocatalysis on the (001) Surfaces of Lanthanum Transition Metal Perovskites  $\text{LaBO}_3$  (B = Cr, Mn, Fe, Co and Ni). *Phys. Chem. Chem. Phys.* **2015**, *17*, 21643–21663.
- (93) Huang, D.; Holm, R. H. Reactions of the Terminal  $\text{Ni}^{\text{II}}\text{-OH}$  Group in Substitution and Electrophilic Reactions with Carbon Dioxide and Other Substrates: Structural Definition of Binding Modes in an Intramolecular  $\text{Ni}^{\text{II}}\cdots\text{Fe}^{\text{II}}$  Bridged Site. *J. Am. Chem. Soc.* **2010**, *132*, 4693–4701.
- (94) Dionigi, F.; Strasser, P. NiFe-Based (Oxy)hydroxide Catalysts for Oxygen Evolution Reaction in Non-Acidic Electrolytes. *Adv. Energy Mater.* **2016**, *6*, 1600621.

## II. IDENTIFYING HIGH-EFFICIENCY OXYGEN EVOLUTION ELECTROCATALYSTS FROM Co-Ni-Cu BASED SELENIDES THROUGH COMBINATORIAL ELECTRODEPOSITION

*Xi Cao,<sup>a</sup> Emily Johnson<sup>b</sup> and Manashi Nath<sup>\*a</sup>*

<sup>a</sup>.Department of Chemistry, Missouri University of Science & Technology, Rolla, Missouri 65409, United States.

<sup>b</sup>.Department of Chemical and Biochemical Engineering, Missouri University of Science & Technology, Rolla, Missouri 65409, United States.

### ABSTRACT

Water splitting has been widely considered to be an efficient way to generate sustainable and renewable energy resources in fuel cells, metal–air batteries and other energy conversion devices. Exploring efficient electrocatalysts to expedite the anodic oxygen evolution reaction (OER) is a crucial task that needs to be addressed in order to boost the practical application of water splitting. Intensive efforts have been devoted to develop mixed transition metal based chalcogenides as effective OER electrocatalysts. Herein, we have reported synthesis of a series of mixed metal selenides containing Co, Ni and Cu employing combinatorial electrodeposition, and systematically investigated how the transition metal doping affects the OER catalytic activity in alkaline medium. Energy dispersive spectroscopy (EDS) was performed to detect the elemental compositions and confirm the feasibility of compositional control of 66 metal selenide thin films. It was observed that the OER catalytic activity is sensitive to the concentration of Cu in the catalysts, and the catalyst activity tended to increase with increasing Cu concentration.

However, increasing the Cu concentration beyond a certain limit led to decrease in catalytic efficiency, and copper selenide by itself, although catalytically active, showed higher onset potential and overpotential for OER compared to the ternary and quaternary mixed metal selenides. Interestingly, the best quaternary composition  $(\text{Co}_{0.21}\text{Ni}_{0.25}\text{Cu}_{0.54})_3\text{Se}_2$  showed similar crystal structure as its parent compound of  $\text{Cu}_3\text{Se}_2$  with slight decrease in lattice spacings of (101) and (210) lattice planes (0.0222 Å and 0.0148 Å, respectively) evident from the powder X-ray diffraction pattern.  $(\text{Co}_{0.21}\text{Ni}_{0.25}\text{Cu}_{0.54})_3\text{Se}_2$  thin film exhibited excellent OER catalytic activity and required an overpotential of 272 mV to reach a current density of  $10 \text{ mA cm}^{-2}$ , which is 54 mV lower than  $\text{Cu}_3\text{Se}_2$ , indicating a synergistic effect of transition metal doping in enhancing catalytic activity.

**Keywords:** oxygen evolution reaction, cobalt hydroxide, cobalt oxyhydroxide, cobalt oxide, surface area measurement

## 1. INTRODUCTION

The growing demand for energy and increasing concerns about the environmental pollution from burning fossil fuels have led to an intense interest in discovering alternative sources of energy from sustainable resources.<sup>1,2</sup> In that regard, hydrogen ( $\text{H}_2$ ) has been widely considered as a promising alternative energy substitute for fossil fuels resulting from its high energy density and reduced environmental impacts.<sup>3-5</sup> The traditional way to produce  $\text{H}_2$  is through natural gas reforming in industry which results in low purity and high cost.<sup>6</sup> Water electrolysis assisted by electricity or sunlight is an emerging and efficient technology to generate high purity  $\text{H}_2$  on demand, where  $\text{H}_2$  evolution reaction (HER)

happens at the cathode and O<sub>2</sub> evolution reaction (OER) takes place at the anode.<sup>3,7,8</sup> However, water electrolysis to produce H<sub>2</sub> for large-scale application, unfortunately, has been highly hindered due to the kinetically sluggish OER resulting from the four-electron transfer process involved in the reaction.<sup>9,10</sup> An effective electrocatalyst is needed to lower the activation barrier and facilitate kinetics of the OER process and therefore increase the practical feasibility of largescale water splitting reaction. During the past several decades, large number of research efforts have led to the discovery of robust, stable, and effective OER electrocatalysts that can reduce the overpotential for water oxidation and hence increase the energy efficiency.<sup>2,11-14</sup> Among these, precious metal based OER catalysts, such as IrO<sub>2</sub> and RuO<sub>2</sub>, show excellent catalytic activity and high durability in the alkaline medium, nevertheless, these catalysts suffer from scarcity on earth's surface, and are consequently too expensive for bulk utilization in industry.<sup>15,16</sup> Recently, intensive research efforts have been concentrated on the investigation of earth abundant transition metal-based materials as high efficiency OER catalysts, comprising elements such as Ni, Fe, Co, and Mn.<sup>17-23</sup> Several factors were proposed to relate the high OER catalytic activity to the transition-metal-based compositions: (i) the ability of catalytically active 3d metal sites to easily switch between different oxidation states (Ni<sup>2+/3+</sup>, Co<sup>2+/3+</sup> etc.) without hindrance under application of small electric bias,<sup>7,24</sup> (ii) the number of electrons occupying the e<sub>g</sub> orbitals of the 3d metal ions on the surface which will likely affect the bond strength between catalytic sites and hydroxyl species and even influencing the surface oxygen binding energy,<sup>25-27</sup> therefore reducing the thermodynamic overpotential of the OER process. Besides transition metal cations, anions can also influence the OER catalytic activity as well by changing covalency of the metal–ligand bond which leads to tuning of

the redox potential of the catalytically active transition metal center.<sup>28</sup> Recently, transition-metal-based chalcogenides such as sulfides,<sup>29–31</sup> phosphides<sup>32–34</sup> and selenides<sup>35–38</sup> exhibited improved efficiency in comparison to the corresponding oxides and (oxy)hydroxides<sup>13,39–43</sup> in alkaline medium. Among the chalcogenides, selenides and tellurides have been reported to have a better catalytic activity since the smaller electronegativity of selenium/tellurium leads to an increased covalency in the metal–chalcogen bond which facilitates the catalyst activation and onset of OER reaction by lowering the redox potential of the catalytic site.<sup>44,45</sup> Interestingly, incorporation of dopant elements into pure transition metal-based catalysts has been observed to dramatically enhance the OER catalytic activity in both oxides and chalcogenides.<sup>13,27,30,46–48</sup> This observation is most likely attributed to several factors including increasing the amount of active sites among the catalytic systems; tuning of the electron density over the catalytic centers through inductive effect of the neighboring dopant atoms, as well as tuning the hydroxyl ( $\text{OH}^-$ ) adsorption energy at the catalytic center to an optimal energy level, which leads to lowering of the potential to initiate the multistep OER process.<sup>49–51</sup> Researchers have thus devoted considerable efforts to investigate efficient mixed-transition-metal-based OER catalysts. However, such work exhibiting systematic compositional and/or stoichiometric variation of multinary catalyst compositions are limited.<sup>52–54</sup> It is necessary to develop an efficient and systematic screening method to explore the compositional space for multinary catalytic systems and discover nonstoichiometric compositions which might be missed in the targeted synthesis technique without prior knowledge. Smith et al. for example, has carried out a systematic study of the OER activity trend of amorphous oxides containing Ni, Fe and Co and identified the best composition as  $\alpha\text{-Fe}_{20}\text{Ni}_{80}$  oxide, while A.

Shinde et al. showed the improved photocatalytic activity of  $\text{Fe}_{(0.4-0.6)}\text{Ce}_{(0.6-0.4)}\text{O}_x$  modified  $\text{BiVO}_4$  photoanode created through high-throughput inkjet printing.<sup>55,56</sup> Our group has recently reported a more efficient and economical method – combinatorial electrodeposition – to systematically investigate the Ni–Fe–Co trigonal phase diagram and identified the quaternary selenide  $(\text{Ni}_{0.25}\text{Fe}_{0.68}\text{Co}_{0.07})_3\text{Se}_4$  as an efficient OER electrocatalyst with low overpotential of 230 mV at  $10 \text{ mA cm}^{-2}$  as well as an excellent durability in alkaline medium.<sup>57</sup> Given the fact that Ni, Fe, Co and Mn based compounds have been intensively explored as active OER catalysts in recent years, researchers have started expanding their investigation of other transition metals with high d-electron count, such as copper. While, copper is one of the most earth-abundant and low-cost elements with high electrical conductivity, however, Cu-based compounds have been less explored as water oxidation electrocatalysts. Thomas J. Meyer's group has studied simple Cu(II) ions and homogeneous Cu(II) polypeptide complex as OER catalysts in buffer solution.<sup>58,59</sup> Apart from such homogeneous catalysts, Cu-based electrocatalysts (such as  $\text{CuO}$ ,  $\text{CuFe}_2\text{O}_4$ ,  $\text{CuCO}_2\text{O}_4$  and  $\text{CuCO}_2\text{S}_4$  etc.) have been studied and exhibited moderate OER catalytic activities.<sup>60–64</sup> Cu with its high *d*-electron density can modulate the electron density around the other transition metal centers through *d–d* band formation, which consequently will affect the OH adsorption on the catalytically active site and the reaction kinetics. Cu also imparts better conductivity to the catalyst composite which will lead to better charge transport through the catalytic film and hence better OER catalytic activity. Recently, we have also showed that  $\text{Cu}_2\text{Se}$  nanoparticles and electrodeposited films exhibited an improved catalytic activity in comparison of Cu-based oxides and complexes in alkaline medium.<sup>65</sup> However, the effect of Cu doping in OER active catalyst

composition has been hitherto unknown. In this article, we have reported for the first time, a systematic study of Co–Ni–Cu selenides through combinatorial electrodeposition to investigate the effect of transition metal doping and have identified the optimal OER catalyst in this group. Most of the quaternary metal selenides crystallized in the  $\text{Cu}_3\text{Se}_2$  (umangite) structure type, which also shows excellent OER catalytic activity by itself, with a low overpotential of 326 mV at  $10 \text{ mA cm}^{-2}$ , and has been reported for the first time in this article. Through detailed electrochemical measurements it was observed that in this mixed metal group, the catalytic activity in quaternary composition is better than ternary as well as binary selenides. Moreover, it was also observed that the catalytic activity was sensitive to the concentration of Cu in the catalyst. The best performing quaternary composition was identified as  $(\text{Co}_{0.21}\text{Ni}_{0.25}\text{Cu}_{0.54})_3\text{Se}_2$ , requiring an overpotential of 272 mV to reach  $10 \text{ mA cm}^{-2}$ . Powder X-ray diffraction (pxrd) pattern confirmed that  $(\text{Co}_{0.21}\text{Ni}_{0.25}\text{Cu}_{0.54})_3\text{Se}_2$  showed the same crystal structure of  $\text{Cu}_3\text{Se}_2$  with slight decrease in lattice spacing ( $0.0222 \text{ \AA}$  and  $0.0148 \text{ \AA}$  for (101) and (210) plane, respectively), indicating that small amount Ni and Co dopants led to only small change of the lattice parameters of  $\text{Cu}_3\text{Se}_2$ .

## 2. EXPERIMENTAL

Materials. Nickel (II) sulfate [ $\text{NiSO}_4 \cdot 6\text{H}_2\text{O}$ , 99 %], cobalt (II) sulfate [ $\text{CoSO}_4 \cdot 7\text{H}_2\text{O}$ , 99 %], copper (II) sulfate [ $\text{CuSO}_4 \cdot 5\text{H}_2\text{O}$ , 99 %], selenium dioxide [ $\text{SeO}_2$ ], lithium chloride [ $\text{LiCl}$ , 99 %], potassium hydroxide [ $\text{KOH}$ , 85 %], were purchased from Fisher Scientific. All the chemicals were used as received without further purification. Deionized (DI) water ( $18 \text{ M}\Omega/\text{cm}$ ) was used to prepare all the electrolytes. Au-coated glass

substrates were purchased from Deposition Research Lab Incorporated (DRLI), Lebanon, Missouri.

combinatorial electrodeposition of thin films. Electrodeposition of a series of ternary (or quaternary) thin films by exploring the trigonal phase diagram, shown in Figure S1, was carried out following method similar to the one reported previously from our group.<sup>57</sup> The electrolytes containing 10 mM NiSO<sub>4</sub>·6H<sub>2</sub>O (or CoSO<sub>4</sub>·7H<sub>2</sub>O, CuSO<sub>4</sub>·5H<sub>2</sub>O), 10 mM SeO<sub>2</sub> and 25 mM LiCl were freshly prepared and purged with N<sub>2</sub> for 30 min before electrodeposition. Prior to electrodeposition, the Au-coated glass substrates were carefully cleaned in micro-90, followed by isopropanol and rinsed with deionized water. Then all the cleaned substrates were confined with Teflon tape containing a hole of fixed dimensions, to make sure all the thin films had the same geometric area. All the electrodeposition experiments were carried out using an IviumStat potentiostat, with an electrolyte volume of 50 mL in a three-electrode setup consisting of an Ag|AgCl (KCl saturated) reference electrode, glassy carbon (GC) counter electrode, and Au-coated glass as working electrode. Thin films were formed by applying a potential of  $-0.85\text{ V vs Ag|AgCl (KCl saturated)}$  for 300 s at room temperature. The deposition potential was selected by analyzing the film composition over a range of deposition potentials as listed in Table S1 which revealed that  $-0.85\text{ V vs Ag|AgCl}$  was the optimal potential to achieve compositional control and stability of the deposited film.

Characterization. The as-electrodeposited thin films were characterized through powder X-ray diffraction (XRD) using Philips X-Pert and Cu K $\alpha$  (1.5418 Å) radiation. Because the product was a very thin layer formed on the substrate, the ppxrd was collected at grazing angle incidence in thin film geometry (GI mode with Göbel mirrors). X-ray



photoelectron spectroscopy (XPS) measurements of the catalysts were performed using a KRATOS AXIS 165 X-ray Photoelectron Spectrometer with the monochromatic Al X-ray source. All XPS analyses were performed on the pristine films without any sputtering. Scanning electron microscopy (SEM) was carried out to examine the morphology of film by the FEI Helios NanoLab 600 FIB / FESEM at an accelerating voltage of 15 kV. Energy dispersive spectroscopy (EDS) analysis was also obtained from the same SEM microscope. In this work, EDS analysis was performed on three to five different regions on each sample surface to calculate the average elemental ratio. The molecular formula of each compound is written as  $(\text{Co}_x\text{Ni}_y\text{Cu}_z)\text{Se}_n$ , where  $x, y, z$  are the relative atomic ratios obtained from EDS analysis ( $x + y + z = 1$ ) while  $n$  is the amount of Se relative to the total metal.

Electrochemical Measurements. The electrocatalytic efficiencies were measured in a three-electrode electrochemical cell with an IviumStat potentiostat. The OER catalytic activity was measured by linear scan voltammetry (LSV) while the stability was studied by constant potential chronoamperometry in  $\text{N}_2$ -saturated 1.0 M KOH solution at room temperature. All LSV plots shown in this work were all  $iR$  corrected. The deposited thin films served as the working electrode, GC as the counter electrode and Ag|AgCl (KCl saturated) as the reference electrode. All experimentally measured potentials vs Ag|AgCl (KCl saturated) were converted to the reversible hydrogen electrode (RHE) using the Nernst equation shown as Equation (1).

$$E_{RHE} = E_{Ag|AgCl} + 0.059pH + E_{Ag|AgCl}^o \quad (1)$$

Here, the standard potential of Ag|AgCl (KCl saturated) at 25.1 °C is 0.197 V vs RHE.

Calculation of Tafel Slope The electrochemical kinetics of the  $(\text{Co}_x\text{Ni}_y\text{Cu}_z)\text{Se}_n$  catalysts towards OER relating the overpotential  $\eta$  with the current density  $j$  has been carried out by calculating the Tafel slopes using the Equation. 2.

$$\eta = a + \frac{2.3RT}{\alpha nF} \log(j) \quad (2)$$

Where  $\eta$  is the overpotential,  $j$  is the current density and the other symbols have their usual meaning. The Tafel slope is given by  $2.3RT/\alpha nF$ . The Tafel slopes were calculated from LSV with a scan rate ( $2 \text{ mV s}^{-1}$ ) in non-stirred  $\text{N}_2$ -saturated 1.0 M KOH solution.

Electrochemically Active Surface Area (ECSA) The electrochemically active surface area (ECSA) of the catalyst was measured from the electrochemical double layer capacitance as described in previous reports.<sup>57</sup> Cyclic voltammograms (CVs) with various scan rates were used to measure the double layer charging current in a non-faradaic region. The double-layer current ( $i_{DL}$ ) occurring in non-Faradaic region can be assumed to be from the response of double-layer charging instead of chemical reaction or charge transfer. The electrochemical double-layer capacitance ( $C_{DL}$ ) can be estimated from the plot of cathodic and anodic double-layer current  $i_{DL}$  versus scan rates ( $\nu$ ) as shown in Equation (3). The  $C_{DL}$  was simply determined from the average of the cathodic and anodic slopes. ECSA can be calculated by eqn (4), by dividing the double-layer capacitance ( $C_{DL}$ ) by the specific capacitance ( $C_s$ ), where double-layer capacitance ( $C_{DL}$ ) is in unit of mF.

$$i_{DL} = C_{DL} \times \nu \quad (3)$$

$$ECSA = C_{DL}/C_s \quad (4)$$

In our study of surface area, the specific capacitance ( $C_s$ ) was assumed to be 0.040  $\text{mF cm}^{-2}$  based on reported value.<sup>35,66</sup> Roughness factor (RF) is calculated by the ECSA, and divided by the geometric area  $0.07 \text{ cm}^2$ .

### 3. RESULTS AND DISCUSSION

Structural and Elemental Compositions of Electrodeposited Thin Films The binary, ternary and quaternary mixed metal selenide films were deposited through combinatorial electrodeposition exploring a trigonal phase space of Ni – Cu – Co with a fixed amount of Se, as shown in Figure S1. In this trigonal phase diagram, the vertices represent binary selenides ( $\text{CoSe}$ ,  $\text{NiSe}$  and  $\text{Cu}_3\text{Se}_2$ ), while the axes of the triangle refer to the ternary selenides  $\text{Co}_x\text{Cu}_y\text{Se}_n$ ,  $\text{Ni}_x\text{Co}_y\text{Se}_n$  and  $\text{Ni}_x\text{Cu}_y\text{Se}_n$ , respectively. The interior of this triangle represents the quaternary mixed-metal selenide ( $\text{Co}_x\text{Ni}_y\text{Cu}_z\text{Se}_n$ ). The compositions of three binary selenides were confirmed using powder X-ray diffraction (pxrd) as shown in Figure S2, which revealed that electrodeposited copper selenide, ( $\text{Cu}_3\text{Se}_2$ , shown in Figure S2a) and nickel selenide ( $\text{NiSe}$ , shown in Figure S2b) were crystalline and the diffraction peaks matched perfectly with the standard diffraction pattern of  $\text{Cu}_3\text{Se}_2$  (PDF # 00-047-1745) and  $\text{NiSe}$  (PDF # 01- 075-0610), respectively. However, no clear diffraction peaks corresponding to cobalt selenide could be observed in the pxrd pattern as shown in Figure S2c (the observed diffraction peaks correspond to Au from the Au-glass substrate), indicating that the electrodeposited cobalt selenide is predominantly amorphous. The elemental compositions of three binary catalysts were further analyzed using energy dispersive spectroscopy (EDS) as shown in Table S2. Since the pxrd patterns were generally not very well-defined in electrodeposited films,<sup>37</sup> the composition of the binary selenides were ascertained by using both EDS and PXRD analyses as applicable. It can be seen that the three as-prepared binary catalysts were composed of Cu, Ni or Co and Se with approximate atomic ratio of 3 : 2 (Cu : Se), 1 : 1 (Ni : Se) and 1 : 1 (Co : Se) respectively, which is consistent with the pxrd characterizations, and three binaries has been denoted as

Cu<sub>3</sub>Se<sub>2</sub>, CoSe and NiSe, respectively. Similarly, molecular formulae of all ternaries and quaternaries identified in this study were ascertained in the same way by using the EDS elemental ratio and have been listed in Table S3. It can be also observed in Table S2 that the relative atomic percentage of an element increased (or decreased) with increasing (or decreasing) amounts of the corresponding metal precursor in the electrolytic bath, indicating the feasibility of compositional control through such a combinatorial electrodeposition.

**Electrochemical Characterization** The linear sweep voltammetry (LSV) was performed in N<sub>2</sub>-saturated 1.0 M KOH solution at a scan rate of 10 mV s<sup>-1</sup> to study the OER catalytic activity. Two kinetic parameters were selected to benchmark the electrocatalytic performance: (i) onset overpotential (onset  $\eta$ ) and (ii) overpotential required to reach a current density 10 mA cm<sup>-2</sup> ( $\eta$  at 10 mA cm<sup>-2</sup>).<sup>66,67</sup> These two kinetic parameters for all electrodeposited selenides along with their corresponding EDS atomic ratios have been summarized and shown in Table S2. Figure S3 shows the OER polarization curves measured in N<sub>2</sub>-saturated 1.0 M KOH for three binary selenides. The catalytic activity trend for three binaries was CoSe > Cu<sub>3</sub>Se<sub>2</sub> > NiSe. The LSV plots of the Co–Cu selenides group, presented in Figure 1a, indicate they are indeed highly active towards OER. It can be observed that (Co<sub>0.40</sub>Cu<sub>0.60</sub>)<sub>3</sub>Se<sub>2</sub> showed the best catalytic activity in this group with the lowest onset overpotential of 257 mV and overpotential of 278 mV to reach a current density of 10 mA cm<sup>-2</sup>. For the Ni–Co selenides group shown in Figure 1b, it was observed that the catalytic activity improved with increasing the amount of Co and (Ni<sub>0.51</sub>Co<sub>0.49</sub>)Se exhibited the best activity with an onset overpotential of 259 mV and overpotential of 289 mV at 10 mA cm<sup>-2</sup>. The OER performance of Ni–Cu selenides group

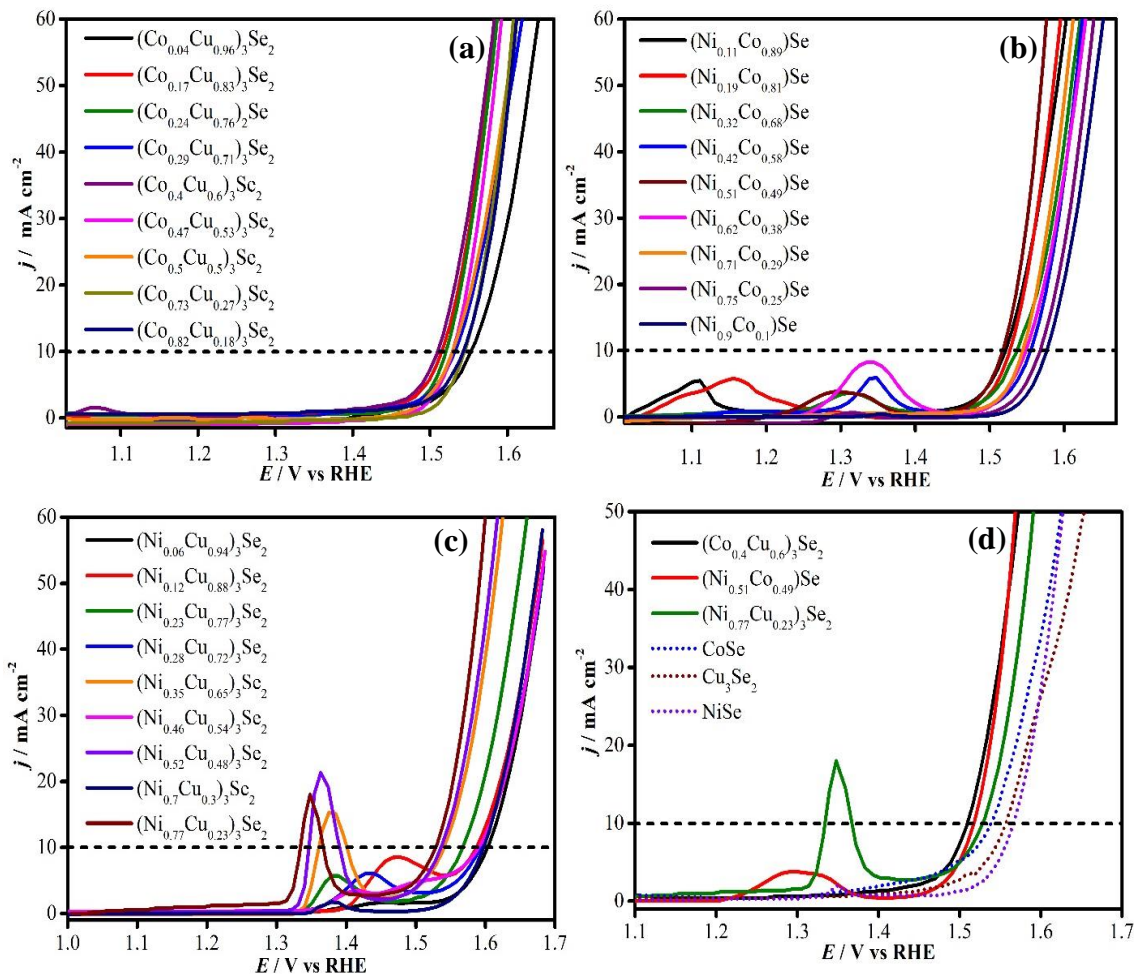


Figure 1. Linear sweep voltammies (LSVs) of ternary metal selenides along the edges of the trigonal phase diagram. (a) Co-Cu group (b) Ni-Co group (c) Ni-Cu group. (d) Comparison of the best performing ternary composition (solid line) from each group along with the binary compositions (dotted line). The dotted black line in each panel marks the current density at  $10 \text{ mA cm}^{-2}$ .

in Figure. 1c showed that decreasing the amount of Cu boosted the OER activity, wherein the best composition  $(\text{Ni}_{0.77}\text{Cu}_{0.23})_3\text{Se}_2$  in this group required an onset overpotential of 268 mV and overpotential of 299 mV to achieve  $10 \text{ mA cm}^{-2}$ . It should be noted here that some pre-oxidation peaks were observed in the OER LSV curves as shown in Figure 1a–d. These peaks have been widely observed in Ni- and Co based electrocatalysts, resulting from the

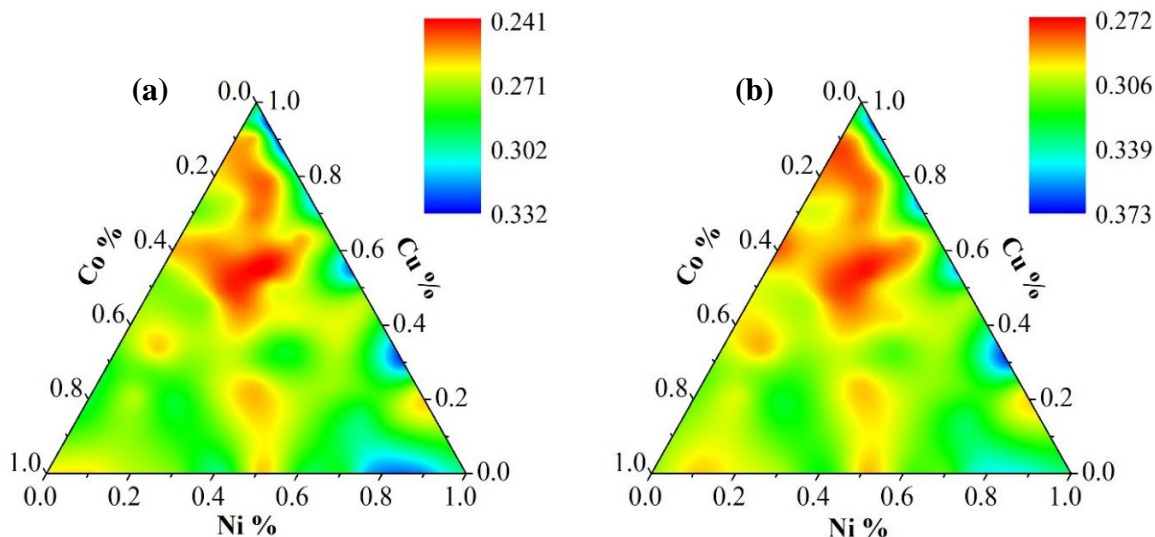


Figure 2. Contour plots of onset overpotential  $\eta$  (in units of V) (a) and (b) overpotential  $\eta$  (in units of V) at the current density of  $10 \text{ mA cm}^{-2}$  for the entire Co-Ni-Cu trigonal phase space. The color gradient corresponds to the overpotential measured in volts.

transition metal's oxidation state changing in the catalyst during application of a high anodic potential.<sup>13,68–70</sup> In Figure 1, peaks around 1.15 V vs. RHE correspond to  $\text{Co}^{2+}$  to  $\text{Co}^{3+}$  conversion, while those around 1.35 V vs. RHE are due to  $\text{Ni}^{2+}$  to  $\text{Ni}^{3+}$  oxidation.<sup>68,69</sup> These pre-oxidation peaks are also considered to be catalyst activation steps, especially for Ni-based catalysts, where  $\text{Ni}^{3+}$  is the actual catalytically active center. Interestingly, more predominant peaks of  $\text{Co}^{2+}$  to  $\text{Co}^{3+}$  conversion can be found in Figure 1b when the Co content is higher in the catalysts, while there's no specific relationship of the intensity of Ni pre-oxidation peak with respect to the Ni amount in catalyst, presumably due to the fact that Ni can coexist in the +2 and +3 oxidation states in as-synthesized catalysts depending on the crystal structure and stoichiometry.<sup>71</sup> Figure 1d shows the comparative plots of the best performing ternary selenide compositions in each group compared with the three binary selenides. It can be seen that 40% of Co doped into  $\text{Cu}_3\text{Se}_2$  enhanced the OER catalytic activity with a decrease of onset overpotential and overpotential at  $10 \text{ mA cm}^{-2}$

by 25 mV and 48 mV, respectively. The onset overpotential drop indicated an improvement in the intrinsic property of  $(\text{Co}_{0.40}\text{Cu}_{0.60})_3\text{Se}_2$  compared to  $\text{Cu}_3\text{Se}_2$ . Similarly, 49% Co doped into NiSe decreased the onset overpotential and overpotential at  $10 \text{ mA cm}^{-2}$  by 41 mV and 46 mV, respectively. However, there was no significant improvement of OER activity with 23% of Cu doped into NiSe. It should be mentioned that the enhancement in catalytic activity by introducing transition metal dopants into the lattice may be attributed to the extensive electron delocalization occurring through d–d orbital interactions between the catalytic centers, leading to modulation of electron density near the catalytic center, thereby, facilitating catalyst activation and charge transfer within the catalyst. For instance, the catalytic activity of Ni- and Co-based electrocatalysts can be dramatically improved with the introduction of Fe.<sup>13,72–74</sup> To compare the electrocatalytic properties of the quaternary selenides as a function of compositional variation, contour plots as shown in Figure 2 were constructed based on the relative atomic ratio obtained through EDS and the two kinetic parameters (onset  $\eta$  and  $\eta$  at  $10 \text{ mA cm}^{-2}$ ) as given in Table S2. The contour plot provided in Figure 2a shows the trend of OER onset overpotential, while the trend of overpotential at the current density of  $10 \text{ mA cm}^{-2}$  as a function of film composition has been shown in Figure 2b. As can be seen in Figure 2a, an area inside of the trigonal plot (quaternary phases) and adjacent to the Co axis (Co–Cu selenides) showed lower overpotential indicating the best catalytic activity within the Ni–Co–Cu ternary phase space, while axis produced a lower onset  $\eta$ , specially, when copper amount was larger than 40%. Similar trends were also observed in Figure 2b. The trends indicated the mixed metal selenides were more likely to have optimal catalytic performance in the presence of 40–90% Cu, indicating copper doping had a remarkable positive effect on the OER catalytic

activity. This observation further confirmed that transition-metal doping can optimize the intrinsic property of electrocatalysts and improve the catalytic activity by dramatically reducing the onset  $\eta$  and  $\eta$  at  $10 \text{ mA cm}^{-2}$ .

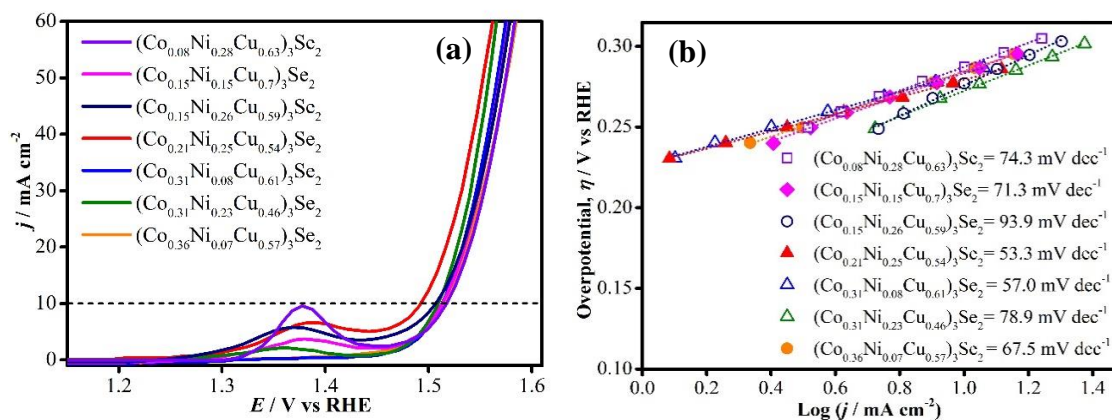


Figure 3. (a) LSVs of the seven best quaternary compositions measured in  $\text{N}_2$ -saturated  $1.0 \text{ M KOH}$  solution at a scan rate of  $10 \text{ mV s}^{-1}$ . (b) Tafel plots of the catalysts.

The OER LSV plots of seven quaternary compounds with best catalytic performance in  $\text{N}_2$ -saturated  $1.0 \text{ M KOH}$  at a scan rate of  $10 \text{ mV s}^{-1}$  has been presented in Figure 3a. These compositions can be represented as,  $(\text{Co}_{0.08}\text{Ni}_{0.28}\text{Cu}_{0.63})_3\text{Se}_2$ ,  $(\text{Co}_{0.15}\text{Ni}_{0.15}\text{Cu}_{0.7})_3\text{Se}_2$ ,  $(\text{Co}_{0.15}\text{Ni}_{0.26}\text{Cu}_{0.59})_3\text{Se}_2$ ,  $(\text{Co}_{0.21}\text{Ni}_{0.25}\text{Cu}_{0.54})_3\text{Se}_2$ ,  $(\text{Co}_{0.31}\text{Ni}_{0.08}\text{Cu}_{0.61})_3\text{Se}_2$ ,  $(\text{Co}_{0.31}\text{Ni}_{0.23}\text{Cu}_{0.46})_3\text{Se}_2$  and  $(\text{Co}_{0.36}\text{Ni}_{0.07}\text{Cu}_{0.57})_3\text{Se}_2$ . It was interesting to note that for the quaternary selenides, the metal to selenium ratio was obtained as 3 : 2 and that all these phases could be formulated as  $M_3\text{Se}_2$  ( $M$  = total metal concentration). As can be seen, the onset  $\eta$  of  $(\text{Co}_{0.08}\text{Ni}_{0.28}\text{Cu}_{0.63})_3\text{Se}_2$  was 256 mV and it required  $\eta$  of 287 mV to reach a current density of at  $10 \text{ mA cm}^{-2}$ . The onset  $\eta$  of  $(\text{Co}_{0.15}\text{Ni}_{0.15}\text{Cu}_{0.7})_3\text{Se}_2$  was 251 mV and it yielded a current density of  $10 \text{ mA cm}^{-2}$  at a  $\eta$  of 283 mV. The onset  $\eta$  of  $(\text{Co}_{0.15}\text{Ni}_{0.26}\text{Cu}_{0.59})_3\text{Se}_2$  was 246 mV and  $\eta$  at  $10 \text{ mA cm}^{-2}$  was 278



mV. The onset  $\eta$  and  $\eta$  at  $10 \text{ mA cm}^{-2}$  of  $(\text{Co}_{0.31}\text{Ni}_{0.08}\text{Cu}_{0.61})_3\text{Se}_2$  were 254 mV and 282 mV, respectively. The onset  $\eta$  of  $(\text{Co}_{0.31}\text{Ni}_{0.23}\text{Cu}_{0.46})_3\text{Se}_2$  was 248 mV and it needed a  $\eta$  of 280 mV to achieve a current density of  $10 \text{ mA cm}^{-2}$ . The onset  $\eta$  of  $(\text{Co}_{0.36}\text{Ni}_{0.07}\text{Cu}_{0.57})_3\text{Se}_2$  was 257 mV and 284 mV at  $10 \text{ mA cm}^{-2}$ .  $(\text{Co}_{0.21}\text{Ni}_{0.25}\text{Cu}_{0.54})_3\text{Se}_2$  exhibited the best catalytic activity within this group with an onset  $\eta$  of 241 mV and a  $\eta$  of 272 mV to reach  $10 \text{ mA cm}^{-2}$ . SEM images of several of these quaternary selenides  $(\text{Co}_{0.08}\text{Ni}_{0.28}\text{Cu}_{0.63})_3\text{Se}_2$ ,  $(\text{Co}_{0.31}\text{Ni}_{0.23}\text{Cu}_{0.46})_3\text{Se}_2$ ,  $(\text{Co}_{0.15}\text{Ni}_{0.26}\text{Cu}_{0.59})_3\text{Se}_2$  and  $(\text{Co}_{0.21}\text{Ni}_{0.25}\text{Cu}_{0.54})_3\text{Se}_2$  has been shown in Figure S4 exhibiting a nanoflake like geometry for most of these films. The SEM results further suggested that the morphology did not change drastically with respect to the elemental composition.

Tafel slope is an important parameter to evaluate the kinetics of an electrocatalyst. Therefore, the Tafel slopes of all catalysts reported in this work were calculated and shown in Table S2. The Tafel plots ( $\eta$  vs.  $\log j$ ) of the seven quaternary selenides were plotted and the Tafel slopes have been shown in Figure 3b. The Tafel slopes were 74.3, 71.3, 93.9, 53.3, 57.0, 78.9 and 67.5  $\text{mV dec}^{-1}$  for  $(\text{Co}_{0.08}\text{Ni}_{0.28}\text{Cu}_{0.63})_3\text{Se}_2$ ,  $(\text{Co}_{0.15}\text{Ni}_{0.15}\text{Cu}_{0.7})_3\text{Se}_2$ ,  $(\text{Co}_{0.15}\text{Ni}_{0.26}\text{Cu}_{0.59})_3\text{Se}_2$ ,  $(\text{Co}_{0.21}\text{Ni}_{0.25}\text{Cu}_{0.54})_3\text{Se}_2$ ,  $(\text{Co}_{0.31}\text{Ni}_{0.08}\text{Cu}_{0.61})_3\text{Se}_2$ ,  $(\text{Co}_{0.31}\text{Ni}_{0.23}\text{Cu}_{0.46})_3\text{Se}_2$  and  $(\text{Co}_{0.36}\text{Ni}_{0.07}\text{Cu}_{0.57})_3\text{Se}_2$ , respectively. As can be seen, they all showed small Tafel slopes suggesting that they were all kinetically favorable and the second and third step in OER were likely to be the rate-determining steps.<sup>66,75</sup> Based on these observations, it is obvious that the best catalytic activity was exhibited by the quaternary compound of composition  $(\text{Co}_{0.21}\text{Ni}_{0.25}\text{Cu}_{0.54})_3\text{Se}_2$  with the lowest overpotentials and Tafel slopes, which is significantly more efficient than other well-known precious metal based catalysts, such as  $\text{RuO}_x$ .<sup>15</sup>

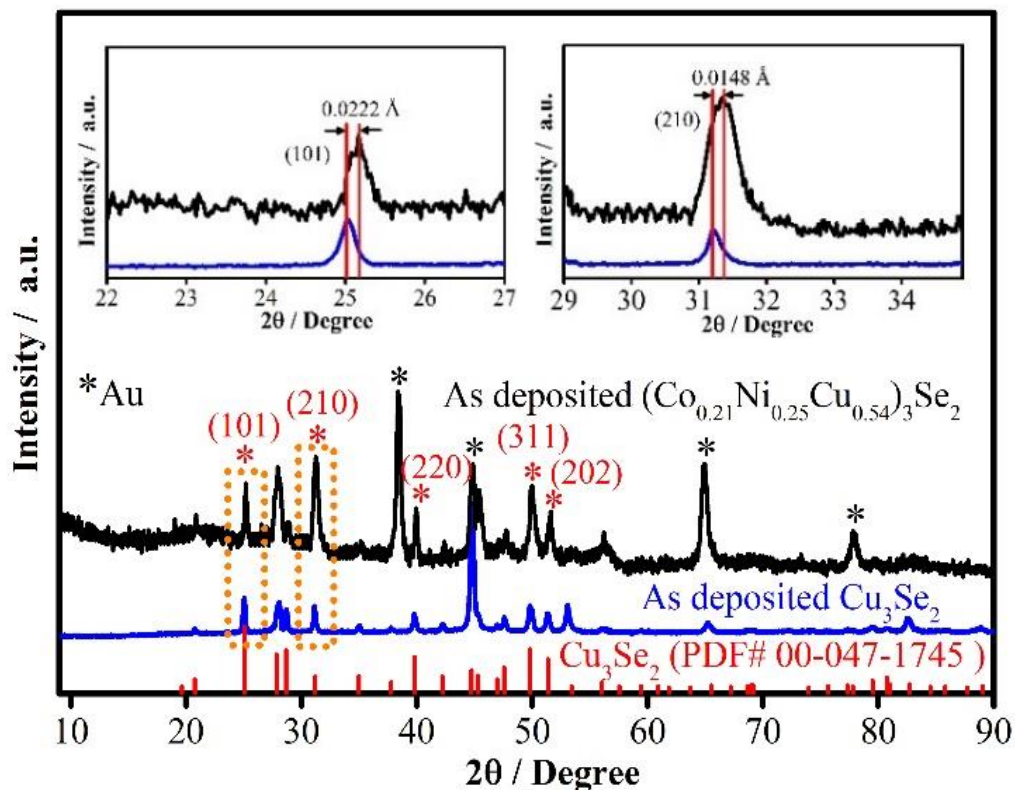


Figure 4. XRD patterns of as-deposited  $(\text{Co}_{0.21}\text{Ni}_{0.25}\text{Cu}_{0.54})_3\text{Se}_2$  (black line) and  $\text{Cu}_3\text{Se}_2$  (blue line) thin films on Au coated glass along with reference  $\text{Cu}_3\text{Se}_2$  (PDF # 00-047-1745). The insets are the comparisons of zoomed-in (101) and (210) peaks of  $(\text{Co}_{0.21}\text{Ni}_{0.25}\text{Cu}_{0.54})_3\text{Se}_2$  (black line) compared with those of  $\text{Cu}_3\text{Se}_2$  (blue line).

The quaternary composition,  $(\text{Co}_{0.21}\text{Ni}_{0.25}\text{Cu}_{0.54})_3\text{Se}_2$  thin film showing the best catalytic activity, was further characterized through pXRD and other analytical techniques to study its composition and morphology. The pXRD pattern of the as deposited thin film was compared with the as-deposited  $\text{Cu}_3\text{Se}_2$  film as shown in Figure 4. As can be seen, all the peaks of as-deposited  $\text{Cu}_3\text{Se}_2$  perfectly matched with the reference XRD pattern of  $\text{Cu}_3\text{Se}_2$  (PDF # 00-047-1745), suggesting the high crystallinity and purity of the thin film. Interestingly,  $(\text{Co}_{0.21}\text{Ni}_{0.25}\text{Cu}_{0.54})_3\text{Se}_2$  thin film showed similar pXRD pattern as that of standard  $\text{Cu}_3\text{Se}_2$  (PDF # 00-047-1745) with some shift of the diffraction peaks which

indicated that 21% of Co and 25% Ni were actually doped inside the parent compound  $\text{Cu}_3\text{Se}_2$  lattice leading to similar crystal structure with slight volume change of the crystal lattice. For example, the peaks around a two-theta of  $25^\circ$  showed a shift of 0.16 degree towards higher-angle side, indicating slight change in the lattice parameters on heteroatom doping in the parent  $\text{Cu}_3\text{Se}_2$  lattice. Peaks observed at  $25.0^\circ$ ,  $31.2^\circ$ ,  $39.8^\circ$ ,  $49.8^\circ$ , and  $51.3^\circ$  were indexed to the (101), (210), (220), (311) and (202) lattice planes, respectively. The d-spacing of two dominant planes of (101) and (210) in  $(\text{Co}_{0.21}\text{Ni}_{0.25}\text{Cu}_{0.54})_3\text{Se}_2$  were compared with that of  $\text{Cu}_3\text{Se}_2$  which showed decreases of 0.0222 Å (0.62 %) and 0.0148 Å (0.52%) for (101) and (210) lattice spacings respectively relative to the parent compound  $\text{Cu}_3\text{Se}_2$  as inserted in Figure 4.<sup>76</sup> The size of crystalline domains of  $(\text{Co}_{0.21}\text{Ni}_{0.25}\text{Cu}_{0.54})_3\text{Se}_2$  was estimated to be 3–4 nm from the pxd pattern using the Scherrer equation,<sup>77</sup> indicating the electrodeposited film was actually polycrystalline.

To understand the trend of catalytic activity with respect to transition metal doping, the LSV curve of the best performing quaternary  $(\text{Co}_{0.21}\text{Ni}_{0.25}\text{Cu}_{0.54})_3\text{Se}_2$  was compared with those of  $\text{Cu}_3\text{Se}_2$ , NiSe and CoSe in  $\text{N}_2$ -saturated 1.0 M KOH collected at a scan rate of  $10 \text{ mV s}^{-1}$  as shown in Figure 5a. As can be seen, to reach a current density of  $10 \text{ mA cm}^{-2}$ , the overpotentials required for CoSe,  $\text{Cu}_3\text{Se}_2$  and NiSe were 308, 326 and 335 mV, respectively. The onset overpotentials of CoSe,  $\text{Cu}_3\text{Se}_2$  and NiSe were 262, 282 and 300 mV, respectively. CoSe showed the best catalytic activity among binary selenides. With Ni and Co doped into  $\text{Cu}_3\text{Se}_2$ , the onset overpotential of  $(\text{Co}_{0.21}\text{Ni}_{0.25}\text{Cu}_{0.54})_3\text{Se}_2$  significantly dropped to 241 mV and it yielded an overpotential of only 272 mV to achieve a current density of  $10 \text{ mA cm}^{-2}$ . The Tafel slope for  $(\text{Co}_{0.21}\text{Ni}_{0.25}\text{Cu}_{0.54})_3\text{Se}_2$  ( $53.3 \text{ mV dec}^{-1}$ ) was lower than that of NiSe ( $66.2 \text{ mV dec}^{-1}$ ),  $\text{Cu}_3\text{Se}_2$  ( $82.9 \text{ mV dec}^{-1}$ ) and CoSe ( $177.4$

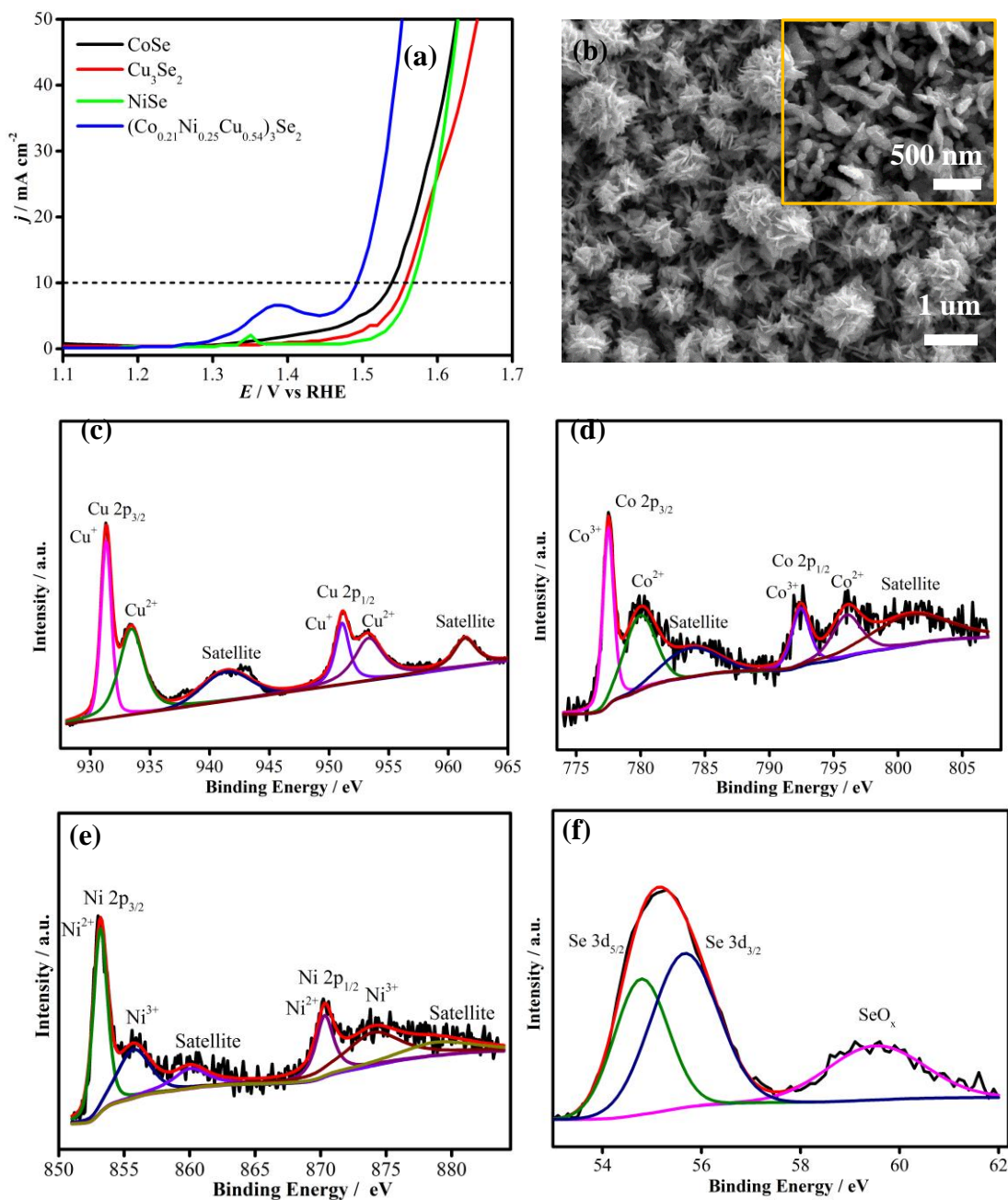


Figure 5. (a) Polarization curves of  $(\text{Co}_{0.21}\text{Ni}_{0.25}\text{Cu}_{0.54})_3\text{Se}_2$  in comparison to the binary selenide films. (b) SEM image of  $(\text{Co}_{0.21}\text{Ni}_{0.25}\text{Cu}_{0.54})_3\text{Se}_2$  film and the inset is a higher magnification image. Deconvoluted XPS spectra of the as-deposited film  $(\text{Co}_{0.21}\text{Ni}_{0.25}\text{Cu}_{0.54})_3\text{Se}_2$ : (c) Cu 2p<sub>1/2</sub> and 2p<sub>3/2</sub> peaks; (d) Co 2p<sub>3/2</sub> and 2p<sub>1/2</sub> peaks; (e) Ni 2p<sub>3/2</sub> and 2p<sub>1/2</sub> peaks; (f) Se 3d<sub>5/2</sub> and 3d<sub>3/2</sub> peaks.

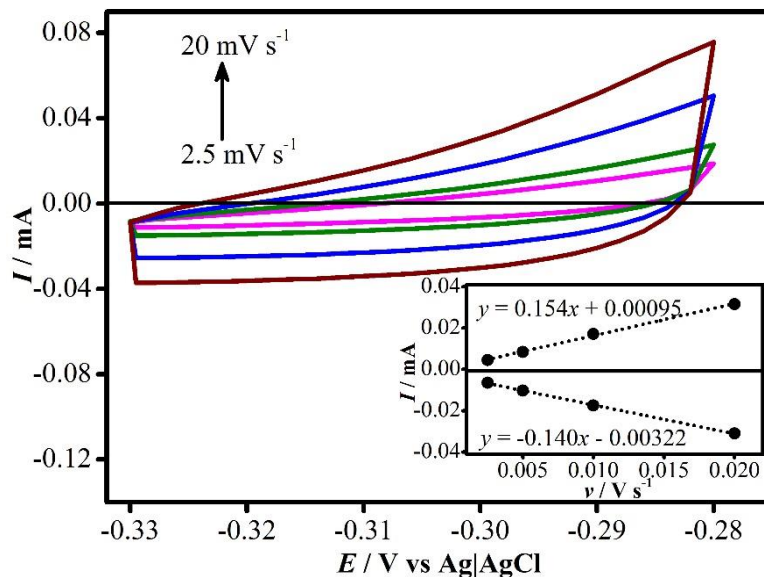


Figure 6. Cyclic voltammograms measured for the  $(\text{Co}_{0.21}\text{Ni}_{0.25}\text{Cu}_{0.54})_3\text{Se}_2$  thin film in  $\text{N}_2$ -saturated 1.0 M KOH solution at different scan rates from 2.5 to  $20 \text{ mV s}^{-1}$ . The inset is a plot of both anodic and cathodic currents measured at  $-0.30 \text{ V vs Ag|AgCl}$  (KCl saturated) as a function of scan rate.

$\text{mV dec}^{-1}$ ) as shown in Table S2, indicating the quaternary selenide is kinetically more favorable than the binaries. A comparison of LSV curves of  $(\text{Co}_{0.21}\text{Ni}_{0.25}\text{Cu}_{0.54})_3\text{Se}_2$  with three best performance ternary selenides  $(\text{Co}_{0.40}\text{Cu}_{0.60})_3\text{Se}_2$ ,  $(\text{Ni}_{0.51}\text{Co}_{0.49})\text{Se}$  and  $(\text{Ni}_{0.77}\text{Cu}_{0.23})_3\text{Se}_2$  has been shown in Figure S5 and their kinetic values has been listed in Table S4. As can be seen in Table S4,  $(\text{Co}_{0.21}\text{Ni}_{0.25}\text{Cu}_{0.54})_3\text{Se}_2$  catalyst showed a more efficient OER activity than the best ternary selenide  $(\text{Co}_{0.40}\text{Cu}_{0.60})_3\text{Se}_2$  by shifting the onset  $\eta$  and  $\eta$  (at  $10 \text{ mA cm}^{-2}$ ) by 16 and 6 mV in cathodic direction. It can be concluded that the quaternary mixed-metal selenides yielded a significant enhancement in OER catalytic activity in terms of both overpotential at  $10 \text{ mA cm}^{-2}$  and low Tafel slope. A detailed SEM image of the  $(\text{Co}_{0.21}\text{Ni}_{0.25}\text{Cu}_{0.54})_3\text{Se}_2$  thin film has been shown in Figure 5b which indicates that the surface morphology of the thin film was mainly composed of rice-like and even

hydrangea-like nanostructures with a broad size distribution of 100–500 nm. Such nanostructured grains are highly advantageous for electrocatalytic activity since they provide large active surface area. X-ray photoelectron spectroscopy (XPS) was carried out to study the elemental composition of the  $(\text{Co}_{0.21}\text{Ni}_{0.25}\text{Cu}_{0.54})_3\text{Se}_2$  thin film and the corresponding oxidation states as shown in Figure 5c–f. Binding energies for all elements (Cu, Co, Ni and Se) were calibrated with respect to the reference XPS spectrum of C 1s (284.5 eV). In the spectrum of Cu 2p shown in Figure 5c, the peaks at 931.3 and 951.1 eV of Cu 2p were assigned to  $\text{Cu}^+$   $2p_{3/2}$  and  $\text{Cu}^+$   $2p_{1/2}$  respectively, while those at 933.4 and 953.3 eV were attributed to  $\text{Cu}^{2+}$   $2p_{3/2}$  and  $\text{Cu}^{2+}$   $2p_{1/2}$  with its shakeup satellite peaks at 941.4 and 961.4 eV.<sup>78</sup> As can be seen in the Co 2p spectrum (shown in Figure 5d), the peaks at 777.5 and 792.4 eV corresponded to  $\text{Co}^{3+}$   $2p_{3/2}$  and  $\text{Co}^{3+}$   $2p_{1/2}$ , while those at 780.1 and 795.7 eV were referred to  $\text{Co}^{2+}$   $2p_{3/2}$  and  $\text{Co}^{2+}$   $2p_{1/2}$  with its shakeup satellite peaks at 784.3 and 801.3 eV.<sup>31,37</sup> Similarly, the Ni 2p XPS spectrum in Figure 5e showed peaks at 853.1 and 873.2 eV assigning to  $\text{Ni}^{2+}$   $2p_{3/2}$  and  $\text{Ni}^{2+}$   $2p_{1/2}$  and peaks at 855.7 and 874.1 eV assigning to  $\text{Ni}^{3+}$   $2p_{3/2}$  and  $\text{Ni}^{3+}$   $2p_{1/2}$ , respectively, while the satellite peaks can be observed at 856.0 and 874.1 eV.<sup>53,57</sup> Figure 5f showed the Se 3d spectrum where the peaks of  $3d_{5/2}$  and  $3d_{3/2}$  at the binding energies of 54.6 and 55.4 eV confirmed the presence of  $\text{Se}^{2-}$  and the peak around 59 eV indicated the existence of  $\text{SeO}_x$  which might be from the surface oxidation of selenide as reported by previous work.<sup>79–81</sup> It can be observed that the presence of mixed-valence metal ions in the deconvoluted spectra of Cu 2p, Co 2p and Ni 2p were all characterized as the selenide phases.

The electrochemically active surface area (ECSA) of the electrodeposited  $(\text{Co}_{0.21}\text{Ni}_{0.25}\text{Cu}_{0.54})_3\text{Se}_2$  thin film was calculated from the double layer capacitance (CDL)

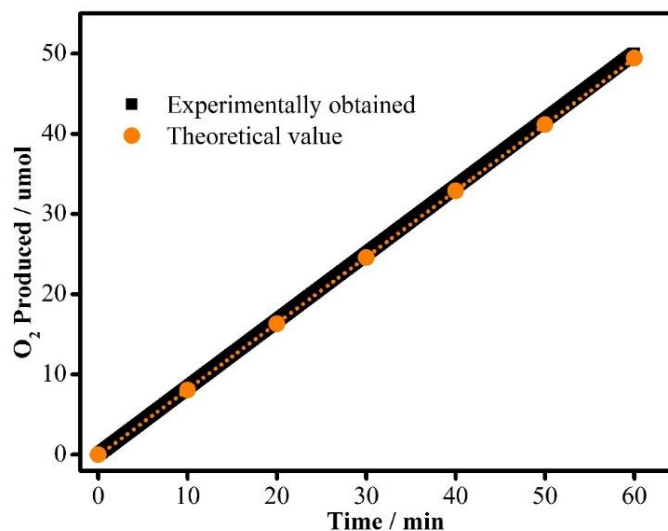


Figure 7. The amount of theoretically calculated (black dots) oxygen and experimentally measured (red dots) oxygen of  $(\text{Co}_{0.21}\text{Ni}_{0.25}\text{Cu}_{0.54})_3\text{Se}_2$  versus time at 0.7 V vs Ag|AgCl (KCl saturated).

measurement. Specifically, cyclic voltammograms (CVs) of  $(\text{Co}_{0.21}\text{Ni}_{0.25}\text{Cu}_{0.54})_3\text{Se}_2$  were measured in the  $\text{N}_2$ -saturated 1.0 M KOH from  $-0.28$  to  $-0.33$  V vs. Ag|AgCl (KCl saturated) at various scan rates between 2.5 and 20  $\text{mV s}^{-1}$  as shown in Figure 6. The cathodic and anodic current was measured at  $-0.30$  V vs Ag|AgCl (KCl saturated) (Figure 6) and plotted as a function of scan rates as shown the inset of Figure 6.  $C_{DL}$  can be obtained by averaging the cathodic and anodic slopes. The value of ECSA for  $(\text{Co}_{0.21}\text{Ni}_{0.25}\text{Cu}_{0.54})_3\text{Se}_2$  catalyst was calculated by eqn (4).  $(\text{Co}_{0.21}\text{Ni}_{0.25}\text{Cu}_{0.54})_3\text{Se}_2$  showed a relatively high ECSA of  $3.68 \text{ cm}^2$  and high roughness factor of 52.57 confirming the highly textured granular surface of the catalysts as shown in the SEM images in Figure 5b. It should be mentioned that the catalytic activity is expected to be improved by increasing roughness of the catalyst surface due to a more extensive exposure of the catalytically active sites to the electrolyte. The faradaic efficiency of electrodeposited  $(\text{Co}_{0.21}\text{Ni}_{0.25}\text{Cu}_{0.54})_3\text{Se}_2$  thin film for OER was evaluated by the water displacement method,

and the theoretical amount of evolved  $O_2$  was compared with the experimentally measured  $O_2$  as shown in Figure 7. Nearly 100% Faradaic efficiency was observed, demonstrating superior catalytic efficiency of the  $(Co_{0.21}Ni_{0.25}Cu_{0.54})_3Se_2$  catalyst for OER.

Table 1. Equivalent Circuit Parameters Obtained from Fitting of EIS Experimental Data

| Catalysts                             | $R_s/\Omega$ | $R_{ct}/\Omega$ | $CPE_{dl}/F$ | $R_f/\Omega$ | $CPE_f/F$ |
|---------------------------------------|--------------|-----------------|--------------|--------------|-----------|
| $(Co_{0.21}Ni_{0.25}Cu_{0.54})_3Se_2$ | 4.9          | 11.2            | 0.26         | 147.3        | 0.81      |
| CoSe                                  | 5.0          | 14.2            | 0.35         | 312.6        | 0.83      |
| $Cu_3Se_2$                            | 5.0          | 18.4            | 0.48         | 1021.8       | 0.87      |
| NiSe                                  | 5.0          | 279.1           | 0.66         | 1297.0       | 0.91      |

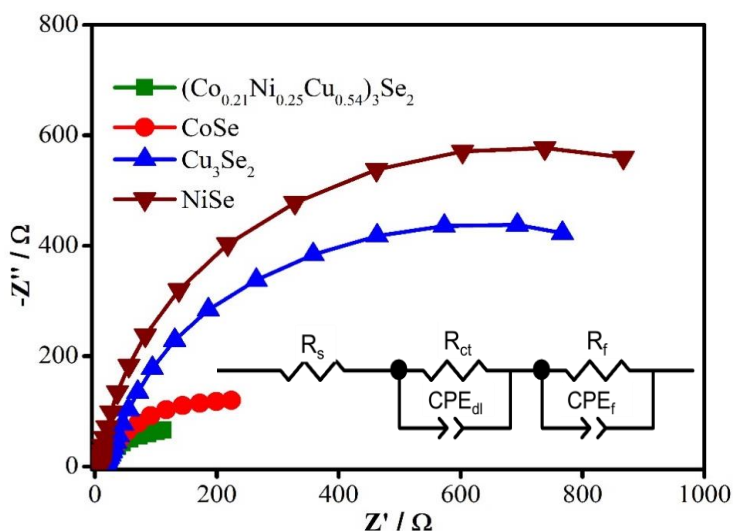


Figure 8. Nyquist plots obtained from EIS measurements of CoSe,  $Cu_3Se_2$ , NiSe and  $(Co_{0.21}Ni_{0.25}Cu_{0.54})_3Se_2$  catalysts at an applied potential of 0.5 V vs Ag|AgCl (KCl saturated) in  $N_2$ -saturated 1.0 M KOH solution. Symbols indicate the raw data, while solid lines represent the corresponding fit to equivalent circuit model. Inset shows the equivalent circuit of catalysts.



To further study the effect of mixed metal composition on the intrinsic property of the materials such as charge transport and conductivity which influences OER catalytic activity, electrochemical impedance spectroscopy (EIS) was performed. From the EIS data, the internal resistance of thin films and charge-transfer resistance at the electrode and electrolyte interface was estimated which are the two parameters that influence the kinetic efficiency of an OER electrocatalyst. Therefore, the Nyquist plot of the best quaternary  $(\text{Co}_{0.21}\text{Ni}_{0.25}\text{Cu}_{0.54})_3\text{Se}_2$  composition was compared with those of three binary compounds  $\text{Cu}_3\text{Se}_2$ ,  $\text{CoSe}$  and  $\text{NiSe}$  as shown in Figure 8. The Nyquist plots were collected in  $\text{N}_2$ -saturated 1.0 M KOH at an applied potential of 0.5 V vs.  $\text{Ag}|\text{AgCl}$  (KCl saturated). The Nyquist plots were fitted to an equivalent circuit as inserted in Figure 8, comprising electrolyte resistance ( $R_s$ ), electron charge transfer resistance at the electrode (catalyst)-electrolyte interface ( $R_{ct}$ ), and film resistance ( $R_f$ ), and these values has been given in Table 1. The high frequency region of the Nyquist plots has been magnified and shown in Figure S6. As can be seen in Table 1, the resistance of 1.0 M KOH was estimated to be 5.0  $\Omega$ , which is similar to the previous reports and was used for  $iR$  correction of all the LSV plots reported in this work.<sup>37,57</sup> From the fitting of the equivalent circuit, it can be observed that  $(\text{Co}_{0.21}\text{Ni}_{0.25}\text{Cu}_{0.54})_3\text{Se}_2$  showed the smallest charge transfer resistance ( $R_{ct}$ ) in comparison to  $\text{Cu}_3\text{Se}_2$ ,  $\text{CoSe}$  and  $\text{NiSe}$ , suggesting that the charge transfer rate at the thin film – electrolyte interface of  $(\text{Co}_{0.21}\text{Ni}_{0.25}\text{Cu}_{0.54})_3\text{Se}_2$  was kinetically faster than binary selenides. Such faster interfacial charge transfer at the electrocatalyst surface can facilitate the rate of the formation of intermediates on the surface and therefore decrease the OER onset potential resulting in a high catalytic efficiency of  $(\text{Co}_{0.21}\text{Ni}_{0.25}\text{Cu}_{0.54})_3\text{Se}_2$ .<sup>69,82,83</sup> Similarly, the film resistance ( $R_f$ ) can also influence the overpotential at 10  $\text{mA cm}^{-2}$  by facilitating

charge transfer within the catalytic film, hence affecting the catalytic activity. It can be seen that  $(\text{Co}_{0.21}\text{Ni}_{0.25}\text{Cu}_{0.54})_3\text{Se}_2$  exhibited a lower  $R_f$  value compared to that of three binaries shown in Table 1, suggesting the thin film showed a superior conductivity. The reduction in film resistance can be correlated with the increase in intrinsic conductivity with the incorporation of Cu atoms in the lattice. Overall, the enhancement of the OER activity of  $(\text{Co}_{0.21}\text{Ni}_{0.25}\text{Cu}_{0.54})_3\text{Se}_2$  can be attributed to the improved charge transfer resistance at the electrode–electrolyte interface, and thin film resistance with transition metal doping within the catalyst composite. Ni and Co dopants into  $\text{Cu}_3\text{Se}_2$  can lead to redistribution of the electron density around the catalytically active center in  $(\text{Co}_{0.21}\text{Ni}_{0.25}\text{Cu}_{0.54})_3\text{Se}_2$ , which can improve surface structure and optimize the bond strengths between the catalyst surface and intermediate adsorbates. The stability and durability of the  $(\text{Co}_{0.21}\text{Ni}_{0.25}\text{Cu}_{0.54})_3\text{Se}_2$  catalyst is an important parameter to evaluate its practical application and hence the catalytic film was studied under constant oxygen evolution for an extended period of time.

Chronoamperometric measurement was performed for 12 h in  $\text{N}_2$ -saturated 1.0 M KOH solution at a constant applied potential of 1.505 V vs. RHE to reach a current density of  $10 \text{ mA cm}^{-2}$  as shown in the inset of Figure 9a. It was observed that large amount of  $\text{O}_2$  bubbles were continuously produced at the electrode surface during the chronoamperometric study. As can be seen, the  $(\text{Co}_{0.21}\text{Ni}_{0.25}\text{Cu}_{0.54})_3\text{Se}_2$  catalyst exhibited an exceptional stability of the OER catalytic activity for over 12 h in 1.0 M KOH and the current density was even slightly improved. The LSV curves before and after the catalytic activity were also compared to further confirm the catalyst stability and are shown in Figure 9a.

As expected, the overpotential at  $10 \text{ mA cm}^{-2}$  was increased by about 5 mV after chronoamperometry while the onset potential was almost the same. The activity enhancement can be attributed to the increased surface roughness of catalyst after 12 h of chronoamperometry shown in Figure 9b. As can be seen from the SEM image, the surface morphology showed some changes mainly by creating lots of porous cracks on the surface which is believed to be due to the  $\text{O}_2$  gas being evolved from the catalyst surface. These cracks can further facilitate electrolyte access to the catalytic site and facilitate catalyst activation through hydroxyl attachment on the catalytic site. The increase of surface roughness after prolonged catalytic activity has been further confirmed by measuring the ECSA of  $(\text{Co}_{0.21}\text{Ni}_{0.25}\text{Cu}_{0.54})_3\text{Se}_2$  after chronoamperometry for 12 h as shown in Figure S7. On comparing the ECSA and roughness factor of the film before and after chronoamperometry, it was observed that both ECSA and RF showed a significant increase after catalytic activity, as shown in Table S5. Such increase in surface roughness can be attributed to the evolution of large quantities of  $\text{O}_2$  from the surface which makes it porous. The crystalline structure of the film after 12 h of chronoamperometry was also studied through pXRD. Figure S8 shows the comparison of the pXRD patterns of  $(\text{Co}_{0.21}\text{Ni}_{0.25}\text{Cu}_{0.54})_3\text{Se}_2$  before and after chronoamperometry. As can be seen from Figure S8, the diffraction pattern looks similar with slightly reduced peak intensities, confirming the structural stability of the catalyst during the prolonged period of catalytic activity. Compositional stability of the  $(\text{Co}_{0.21}\text{Ni}_{0.25}\text{Cu}_{0.54})_3\text{Se}_2$  catalyst after prolonged OER activity was also confirmed by the XPS spectra shown in Figure 9c – f which showed that the catalyst was still primarily composed of Cu, Ni, Co and Se with no trace of oxygen. The comparison of XPS spectra for, Cu 2p, Ni 2p, Co 2p and Se 3d in before and after

chronoamperometry has been shown in Figure S9. The O 1s XPS spectra was also measured before and after chronoamperometry as shown in Figure S10. Analysis of the deconvoluted O 1s spectra revealed that there was chemisorbed oxygen species on the surface. However, there was no evidence of metal-bound oxygen (i.e. metal oxides), even after 12 h of chronoamperometry although some  $\text{SeO}_x$  was detected on the catalyst surface, corroborating well with the Se XPS spectra before and after activity. The XPS spectra along with EDS (shown in Table S6) of  $(\text{Co}_{0.21}\text{Ni}_{0.25}\text{Cu}_{0.54})_3\text{Se}_2$  before and after chronoamperometry further demonstrated the compositional stability of the catalyst. These studies confirmed that this OER electrocatalyst was both functionally durable and compositionally stable even after a long period of continuous  $\text{O}_2$  evolution in alkaline medium.

It is interesting to note that while Ni and Co-selenide deposited as the monoselenide phases, copper selenide crystallized as  $\text{Cu}_3\text{Se}_2$ , and the quaternary phases showed composition similar to  $M_3\text{Se}_2$ , indicating that  $\text{Cu}_3\text{Se}_2$  structure type probably had a better stability under the reaction conditions and the quaternary phases were formed by substituting Cu with Ni and Co. It was also interesting to note that while Ni substitution in  $\text{Cu}_3\text{Se}_2$  improved the catalytic activity, Cu substitution in NiSe did not exhibit similar improving trend. A comparison of the crystal structures of NiSe and  $\text{Cu}_3\text{Se}_2$  (Figure S11) revealed that while NiSe contains octahedrally coordinated Ni atoms,  $\text{Cu}_3\text{Se}_2$  was built by edge-shared and corner-shared  $\text{CuSe}_4$  tetrahedral units. When Cu atoms are substituted with Ni and Co in the quaternary compositions,  $[(\text{Co}_x\text{Ni}_y\text{Cu}_z)_3\text{Se}_2]$ , it is expected that Ni and Co will also have tetrahedral coordination. Having lower coordination number at the catalytic site might be

beneficial for initiation of catalytic activity which typically occurs via surface hydroxyl attachment. Low coordination of the catalytic site may facilitate the initiation step which

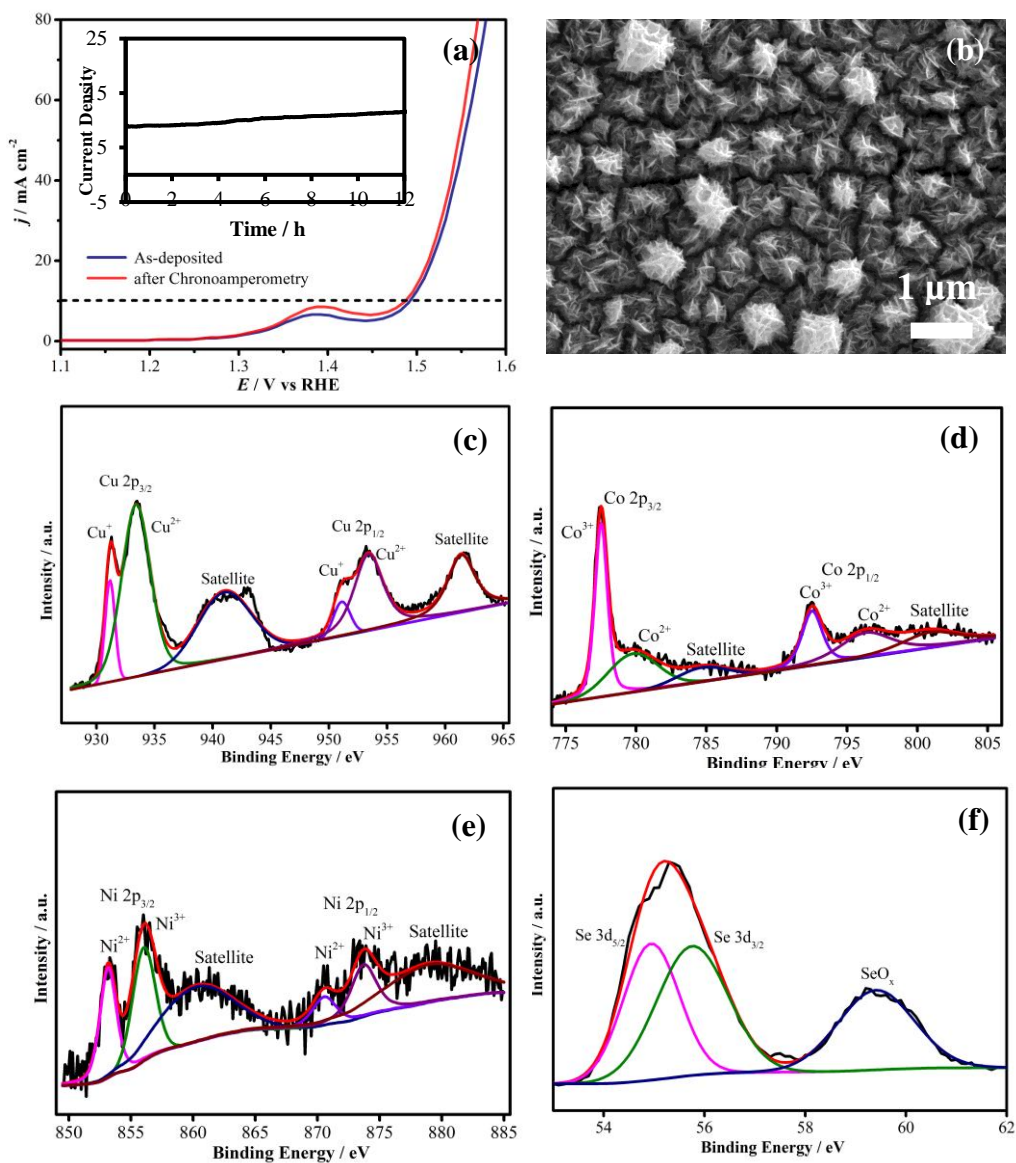


Figure 9. (a) Comparison of LSVs before and after 12 h in  $\text{N}_2$ -saturated 1.0 M KOH solution. The inset is the chronoamperometry plot of  $(\text{Co}_{0.21}\text{Ni}_{0.25}\text{Cu}_{0.54})_3\text{Se}_2$  for 12 h at an applied potential of 1.505 V vs RHE. (b) SEM image of  $(\text{Co}_{0.21}\text{Ni}_{0.25}\text{Cu}_{0.54})_3\text{Se}_2$  after chronoamperometry. (c–f) XPS spectra of  $(\text{Co}_{0.21}\text{Ni}_{0.25}\text{Cu}_{0.54})_3\text{Se}_2$  after electrochemical measurement.

can occur by coordination expansion without the need for anion displacement. In NiSe on the other hand, all the catalytically active transition metal sites are in octahedral coordination. Having an octahedral coordination of the catalytic site, makes the initiation step more challenging since the hydroxyl attachment in the surface necessitates anion displacement and is more energy intensive as a result. Hence Ni in a tetrahedral site may exhibit better onset of catalytic activity compared to Ni in the octahedral site. This may be one of the reasons (Ni,Co)-doped  $\text{Cu}_3\text{Se}_2$  show significantly better catalytic activity than NiSe and Cu/Co-doped NiSe. The effect of structure type was also visible in the ternary selenides in the Ni–Co–Cu phase space. For the Co – Cu selenides, all the ternary films form the  $M_3\text{Se}_2$  composition, and they can be described as Co-doped  $\text{Cu}_3\text{Se}_2$ . The Ni–Cu selenide group on the other hand, forms the  $M\text{Se}$  structure type and are closer to Cu doped NiSe systems. As explained above these stoichiometries are distinctly different from each other and contains different coordinations of the transition metal ions and such differences in coordination geometry may lead to different OER catalytic activity.

#### 4. CONCLUSIONS

In summary, we have successfully screened the Co–Ni–Cu ternary phase space and shown that Co and Ni-doped copper selenide shows high efficiency for OER in alkaline medium surpassing that of the binary and ternary selenides within the same phase space. The series of mixed metal selenides were synthesized through combinatorial electrodeposition exploring the ternary Co–Ni–Cu phase diagram. Systematic investigation of the OER activity with respect to the composition showed that the quaternary selenides showed higher activity in comparison to ternaries and binaries. A slightly higher amount

of Cu doping increased the catalytic activity, however, a very high concentration of Cu can produce negative effect for the activity. Higher activities were observed for quaternary selenides showing a  $\text{Cu}_3\text{Se}_2$  crystal structure with slight change in lattice spacings due to Ni and Co doping. The optimal quaternary composition  $(\text{Co}_{0.21}\text{Ni}_{0.25}\text{Cu}_{0.54})_3\text{Se}_2$  exhibited a superior catalytic activity with low onset overpotential of 241 mV and overpotential of 272 mV to achieve a current density of  $10 \text{ mA cm}^{-2}$  in  $\text{N}_2$ -saturated 1.0 M KOH. Specifically, with proper amount of Co and Ni introduced,  $(\text{Co}_{0.21}\text{Ni}_{0.25}\text{Cu}_{0.54})_3\text{Se}_2$  showed enhanced catalytic activity with 54 mV lower overpotential than its parent  $\text{Cu}_3\text{Se}_2$  (umangite) at  $10 \text{ mA cm}^{-2}$ . The concept that introduction of Cu can significantly improve the catalytic efficiencies of the transition metal selenides will be immensely useful for other catalyst systems with different crystal structures and stoichiometries.

### CONFLICTS OF INTEREST

The authors declare no conflict of interest.

### ACKNOWLEDGMENTS

The authors would like to acknowledge financial support from National Science Foundation (DMR 1710313), American Chemical Society Petroleum Research Fund (54793-ND10), and Energy Research and Development Center (ERDC) Missouri S&T. The authors would also like to acknowledge Materials Research Center for equipment usage.

## SUPPORTING INFORMATION

**IDENTIFYING HIGH-EFFICIENCY OXYGEN EVOLUTION  
ELECTROCATALYSTS FROM CO-NI-CU BASED SELENIDES THROUGH  
COMBINATORIAL ELECTRODEPOSITION**

*Xi Cao<sup>a</sup>, Emily Johnson<sup>b</sup> and Manashi Nath<sup>\*a</sup>*

<sup>a</sup>Department of Chemistry, Missouri University of Science & Technology, Rolla, Missouri 65409, United States.

<sup>b</sup>Department of Chemical and Biochemical Engineering, Missouri University of Science & Technology, Rolla, Missouri 65409, United States.

\*Email: [nathm@mst.edu](mailto:nathm@mst.edu)

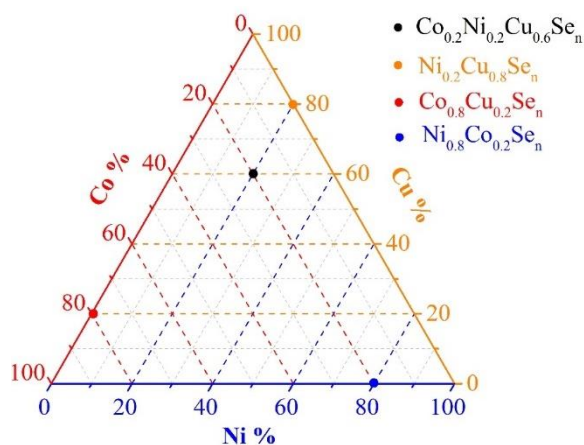


Figure S1. Trigonal phase diagram for exploring compositions of the mixed-metal (Co, Ni, Cu) selenide films examined in this work. Crossing vertices represent compositions of the precursor electrolyte with respect to the relative ratio of the corresponding metals. Color spots indicate typical examples.



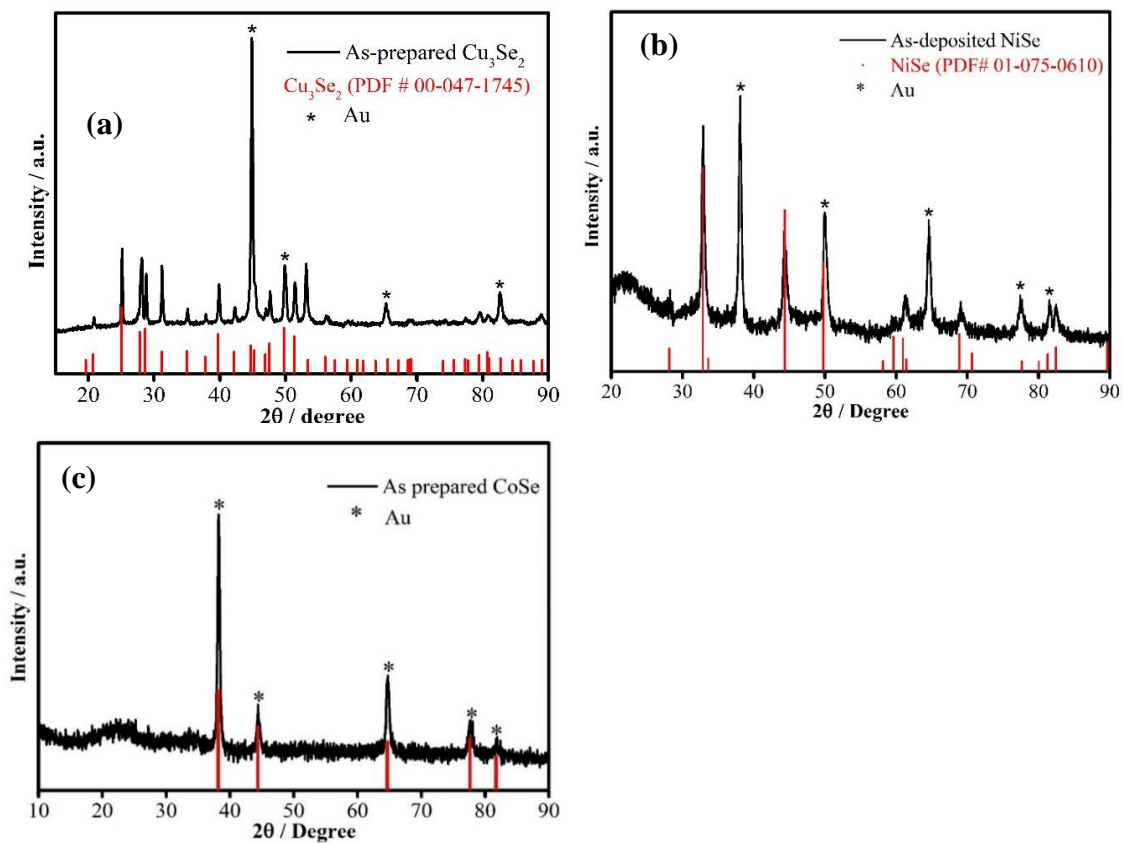


Figure S2. XRD pattern of  $\text{Cu}_3\text{Se}_2$  (a), NiSe (b) and CoSe (c).

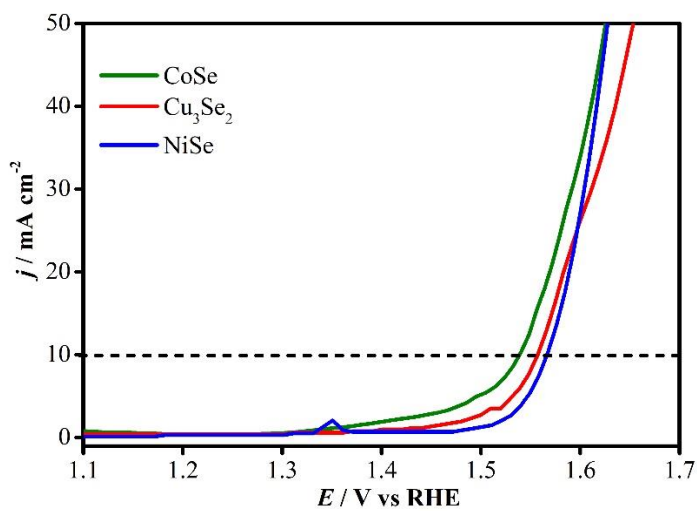


Figure S3. Polarization curves of three binary selenides.

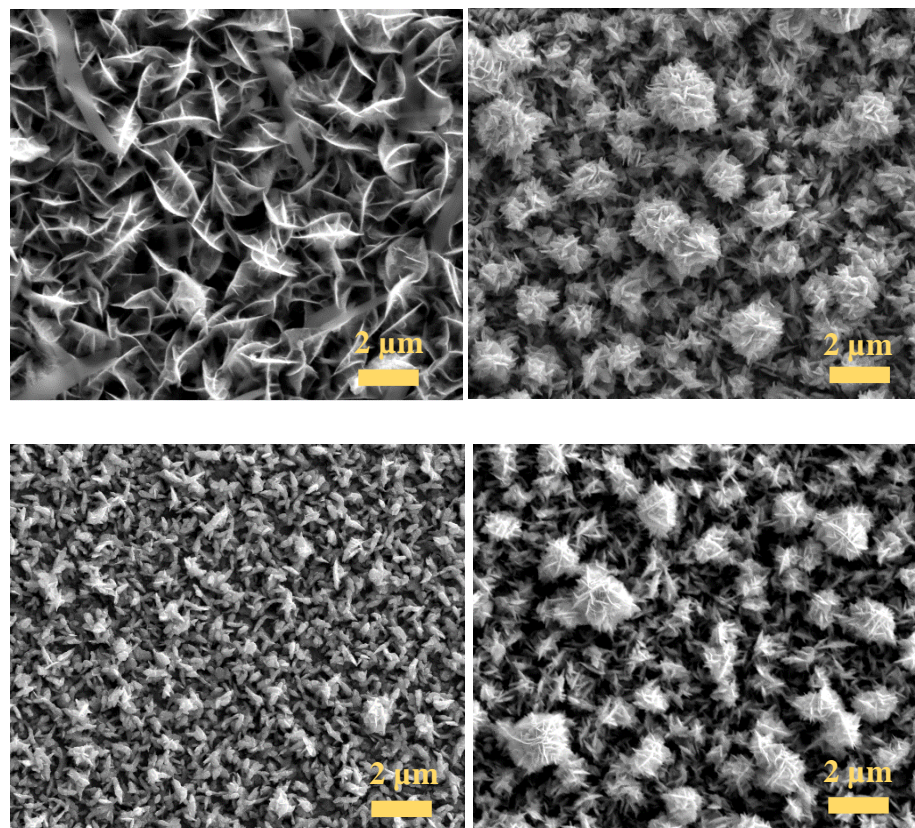


Figure S4. SEM images of selected best performing quaternary  $(\text{Co}_{0.08}\text{Ni}_{0.28}\text{Cu}_{0.63})_3\text{Se}_2$  (a),  $(\text{Co}_{0.31}\text{Ni}_{0.23}\text{Cu}_{0.46})_3\text{Se}_2$  (b),  $(\text{Co}_{0.15}\text{Ni}_{0.26}\text{Cu}_{0.59})_3\text{Se}_2$  (c) and  $(\text{Co}_{0.21}\text{Ni}_{0.25}\text{Cu}_{0.54})_3\text{Se}_2$  (d).

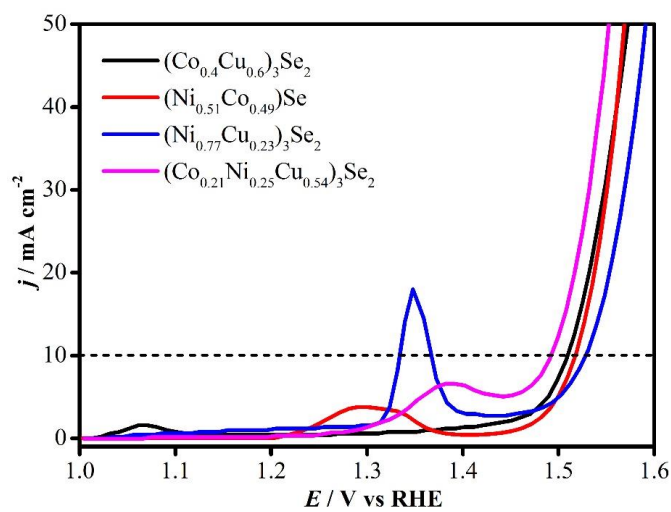


Figure S5. Polarization curves of best quaternary and best ternary selenides.

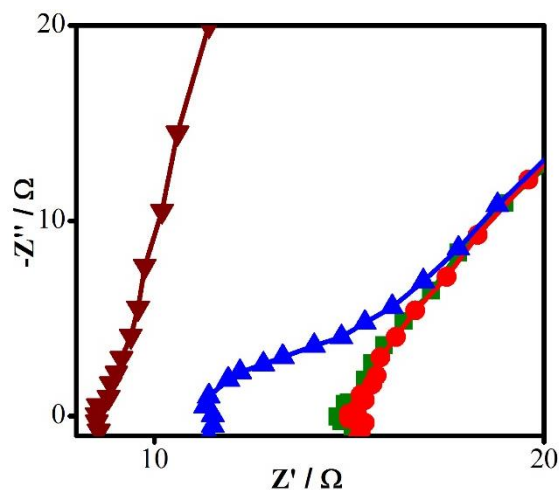


Figure S6. Zoomed-in Nyquist Plots of  $(\text{Co}_{0.21}\text{Cu}_{0.25}\text{Ni}_{0.54})_3\text{Se}_2$  (green), CoSe (red), NiSe (wine) and  $\text{Cu}_3\text{Se}_2$  (blue).

Table S1. The EDS atomic ratio of ternaries with respect to their precursor's ratio at applied potential of -0.7 V or -1.0 V vs Ag/AgCl.

| $E_{\text{applied}} / \text{V}$<br>vs<br>Ag/AgCl | Precursor Molar Ratio (mM) |    |    |    | Averaged atomic % (EDS) |      |      |      |
|--------------------------------------------------|----------------------------|----|----|----|-------------------------|------|------|------|
|                                                  | Ni                         | Cu | Co | Se | Ni                      | Cu   | Co   | Se   |
| -0.7 V                                           | 2                          | 8  | -  | 10 | 0                       | 57.2 | -    | 42.8 |
|                                                  | 4                          | 6  | -  | 10 | 0                       | 52.5 | -    | 47.5 |
|                                                  | 6                          | 4  | -  | 10 | 0.2                     | 43.4 | -    | 56.4 |
|                                                  | 8                          | 2  | -  | 10 | 0.3                     | 30.4 | -    | 69.3 |
|                                                  | -                          | 8  | 2  | 10 | -                       | 55.7 | 0    | 44.3 |
|                                                  | -                          | 6  | 4  | 10 | -                       | 49.2 | 1.8  | 48.9 |
|                                                  | -                          | 4  | 6  | 10 | -                       | 42.2 | 2.2  | 55.1 |
|                                                  | -                          | 2  | 8  | 10 | -                       | 33.2 | 2.6  | 64.2 |
|                                                  | -1.0 V                     | 6  | 4  | -  | 10                      | 28.6 | 37.1 | -    |
| -                                                |                            | 4  | 6  | 10 | -                       | 32   | 35   | 33   |

Table S2. Summary of Elemental Analysis of Metal Selenide Films Determined by EDS and Corresponding Kinetic Parameters Extracted from Polarization Curves.

| Precursor Molar Ratio (mM) |    |    |    | Averaged atomic % (EDS) |      |      |      | Onset $\eta$ | $\eta$ 10mA cm <sup>-2</sup> | Tafel |
|----------------------------|----|----|----|-------------------------|------|------|------|--------------|------------------------------|-------|
| Ni                         | Cu | Co | Se | Ni                      | Cu   | Co   | Se   | (V)          | (V)                          | Slope |
| 10                         | 0  | 0  | 10 | 50.5                    | 0.0  | 0.0  | 49.5 | 0.300        | 0.335                        | 66.2  |
| 0                          | 10 | 0  | 10 | 0.0                     | 63.8 | 0.0  | 36.2 | 0.282        | 0.326                        | 82.9  |
| 0                          | 0  | 10 | 10 | 0.0                     | 0.0  | 47.0 | 53.0 | 0.262        | 0.308                        | 177.4 |
| 1                          | 9  | 0  | 10 | 3.6                     | 56.1 | 0.0  | 40.3 | 0.332        | 0.373                        | 85.5  |
| 2                          | 8  | 0  | 10 | 7.4                     | 53.2 | 0.0  | 39.4 | 0.326        | 0.356                        | 115.6 |
| 3                          | 7  | 0  | 10 | 14.4                    | 49.1 | 0.0  | 36.4 | 0.304        | 0.337                        | 96.4  |
| 4                          | 6  | 0  | 10 | 18.2                    | 46.8 | 0.0  | 35.0 | 0.315        | 0.363                        | 111.2 |
| 5                          | 5  | 0  | 10 | 23.7                    | 43.2 | 0.0  | 33.0 | 0.278        | 0.311                        | 98.0  |
| 6                          | 4  | 0  | 10 | 28.5                    | 33.4 | 0.0  | 38.1 | 0.322        | 0.359                        | 141.7 |
| 7                          | 3  | 0  | 10 | 32.7                    | 30.8 | 0.0  | 36.5 | 0.275        | 0.306                        | 89.4  |
| 8                          | 2  | 0  | 10 | 35.4                    | 15.1 | 0.0  | 49.5 | 0.326        | 0.369                        | 67.1  |
| 9                          | 1  | 0  | 10 | 47.6                    | 14.1 | 0.0  | 38.3 | 0.268        | 0.299                        | 90.4  |
| 0                          | 9  | 1  | 10 | 0.0                     | 57.6 | 2.6  | 39.8 | 0.297        | 0.323                        | 88.4  |
| 0                          | 8  | 2  | 10 | 0.0                     | 48.9 | 10.1 | 41.0 | 0.260        | 0.284                        | 77.0  |
| 0                          | 7  | 3  | 10 | 0.0                     | 50.0 | 15.6 | 34.4 | 0.268        | 0.290                        | 60.2  |
| 0                          | 6  | 4  | 10 | 0.0                     | 45.2 | 18.3 | 36.5 | 0.279        | 0.302                        | 91.2  |
| 0                          | 5  | 5  | 10 | 0.0                     | 38.3 | 24.9 | 36.8 | 0.257        | 0.278                        | 72.5  |
| 0                          | 4  | 6  | 10 | 0.0                     | 31.2 | 27.7 | 41.1 | 0.277        | 0.299                        | 68.7  |
| 0                          | 3  | 7  | 10 | 0.0                     | 31.0 | 31.6 | 37.3 | 0.275        | 0.299                        | 78.2  |
| 0                          | 2  | 8  | 10 | 0.0                     | 16.2 | 44.6 | 39.2 | 0.291        | 0.315                        | 66.6  |
| 0                          | 1  | 9  | 10 | 0.0                     | 9.6  | 44.7 | 45.7 | 0.291        | 0.312                        | 87.0  |
| 1                          | 0  | 9  | 10 | 6.2                     | 0.0  | 49.2 | 44.7 | 0.262        | 0.292                        | 71.5  |
| 2                          | 0  | 8  | 10 | 9.8                     | 0.0  | 41.1 | 49.1 | 0.269        | 0.298                        | 58.1  |
| 3                          | 0  | 7  | 10 | 16.3                    | 0.0  | 34.6 | 49.2 | 0.278        | 0.306                        | 74.3  |
| 4                          | 0  | 6  | 10 | 22.3                    | 0.0  | 31.2 | 46.5 | 0.298        | 0.325                        | 72.9  |
| 5                          | 0  | 5  | 10 | 26.9                    | 0.0  | 25.7 | 47.3 | 0.259        | 0.289                        | 60.7  |
| 6                          | 0  | 4  | 10 | 28.4                    | 0.0  | 17.4 | 54.2 | 0.294        | 0.318                        | 60.3  |
| 7                          | 0  | 3  | 10 | 38.1                    | 0.0  | 15.2 | 46.7 | 0.291        | 0.315                        | 60.4  |
| 8                          | 0  | 2  | 10 | 47.1                    | 0.0  | 15.8 | 37.1 | 0.311        | 0.339                        | 59.9  |
| 9                          | 0  | 1  | 10 | 53.2                    | 0.0  | 6.2  | 40.6 | 0.320        | 0.346                        | 51.2  |
| 1                          | 1  | 8  | 10 | 5.7                     | 11.5 | 36.9 | 45.8 | 0.270        | 0.299                        | 59.8  |
| 1                          | 2  | 7  | 10 | 5.9                     | 15.5 | 35.4 | 43.2 | 0.280        | 0.310                        | 63.4  |

Table S2. Summary of Elemental Analysis of Metal Selenide Films Determined by EDS and Corresponding Kinetic Parameters Extracted from Polarization Curves. (cont.)

|   |   |   |    |      |      |      |      |       |       |       |
|---|---|---|----|------|------|------|------|-------|-------|-------|
| 1 | 3 | 6 | 10 | 6.1  | 19.6 | 33.8 | 40.5 | 0.260 | 0.289 | 58.3  |
| 1 | 4 | 5 | 10 | 4.5  | 36.9 | 22.9 | 35.7 | 0.257 | 0.284 | 67.5  |
| 1 | 5 | 4 | 10 | 4.9  | 38.6 | 19.7 | 36.8 | 0.254 | 0.282 | 57.0  |
| 1 | 6 | 3 | 10 | 5.5  | 44.4 | 10.7 | 39.4 | 0.266 | 0.298 | 56.3  |
| 1 | 7 | 2 | 10 | 3.0  | 53.5 | 4.4  | 39.2 | 0.259 | 0.287 | 65.5  |
| 1 | 8 | 1 | 10 | 3.0  | 56.7 | 2.8  | 37.6 | 0.261 | 0.296 | 102.9 |
| 2 | 1 | 7 | 10 | 11.5 | 11.1 | 34.9 | 42.5 | 0.291 | 0.327 | 74.1  |
| 2 | 2 | 6 | 10 | 11.8 | 19.8 | 32.2 | 36.2 | 0.274 | 0.311 | 60.0  |
| 2 | 3 | 5 | 10 | 9.7  | 29.0 | 24.0 | 37.3 | 0.272 | 0.304 | 61.3  |
| 2 | 4 | 4 | 10 | 9.7  | 28.8 | 20.2 | 41.3 | 0.251 | 0.283 | 69.6  |
| 2 | 5 | 3 | 10 | 11.1 | 40.1 | 15.3 | 33.5 | 0.256 | 0.288 | 83.6  |
| 2 | 6 | 2 | 10 | 9.9  | 45.4 | 9.8  | 35.0 | 0.251 | 0.283 | 71.3  |
| 2 | 7 | 1 | 10 | 9.5  | 52.2 | 3.9  | 34.4 | 0.256 | 0.288 | 67.6  |
| 3 | 1 | 6 | 10 | 15.9 | 12.8 | 28.3 | 43.1 | 0.272 | 0.313 | 67.2  |
| 3 | 2 | 5 | 10 | 15.4 | 21.3 | 19.4 | 43.9 | 0.261 | 0.293 | 57.9  |
| 3 | 3 | 4 | 10 | 14.4 | 28.9 | 19.2 | 37.5 | 0.248 | 0.280 | 78.9  |
| 3 | 4 | 3 | 10 | 16.0 | 33.9 | 13.1 | 37.0 | 0.241 | 0.272 | 53.3  |
| 3 | 5 | 2 | 10 | 14.9 | 43.8 | 8.9  | 32.4 | 0.264 | 0.298 | 56.2  |
| 3 | 6 | 1 | 10 | 16.9 | 40.1 | 6.3  | 36.7 | 0.264 | 0.298 | 74.2  |
| 4 | 1 | 5 | 10 | 22.2 | 14.4 | 22.2 | 41.2 | 0.256 | 0.287 | 55.3  |
| 4 | 2 | 4 | 10 | 20.4 | 17.4 | 19.5 | 42.8 | 0.280 | 0.308 | 51.9  |
| 4 | 3 | 3 | 10 | 17.6 | 32.0 | 13.3 | 37.1 | 0.263 | 0.293 | 53.6  |
| 4 | 4 | 2 | 10 | 17.1 | 38.5 | 10.1 | 34.3 | 0.246 | 0.278 | 93.9  |
| 4 | 5 | 1 | 10 | 19.7 | 43.8 | 5.6  | 30.9 | 0.256 | 0.287 | 74.3  |
| 5 | 1 | 4 | 10 | 26.3 | 21.5 | 16.3 | 35.9 | 0.290 | 0.317 | 73.7  |
| 5 | 2 | 3 | 10 | 21.5 | 23.6 | 12.0 | 42.9 | 0.265 | 0.294 | 114.2 |
| 5 | 3 | 2 | 10 | 18.2 | 30.6 | 10.0 | 41.2 | 0.259 | 0.291 | 87.2  |
| 5 | 4 | 1 | 10 | 22.1 | 38.4 | 4.8  | 34.7 | 0.270 | 0.299 | 82.2  |
| 6 | 1 | 3 | 10 | 34.8 | 14.4 | 12.6 | 38.2 | 0.273 | 0.309 | 69.0  |
| 6 | 2 | 2 | 10 | 32.4 | 21.7 | 7.3  | 38.6 | 0.268 | 0.305 | 78.3  |
| 6 | 3 | 1 | 10 | 29.0 | 27.3 | 4.5  | 39.2 | 0.270 | 0.307 | 64.9  |
| 7 | 1 | 2 | 10 | 43.1 | 9.7  | 10.8 | 36.4 | 0.296 | 0.332 | 71.7  |
| 7 | 2 | 1 | 10 | 39.2 | 14.8 | 7.9  | 38.2 | 0.280 | 0.315 | 78.0  |
| 8 | 1 | 1 | 10 | 46.8 | 9.5  | 7.0  | 36.7 | 0.279 | 0.315 | 91.1  |

Table S3. The precursor ratio of compounds shown in the plots and their corresponding formulas by EDS atomic ratio.

| Precursor ratio |           |           | Molecular formula<br>from EDS atomic ratio                            |
|-----------------|-----------|-----------|-----------------------------------------------------------------------|
| Ni              | Cu        | Co        |                                                                       |
| 10              |           |           | NiSe                                                                  |
|                 | 10        |           | Cu <sub>3</sub> Se <sub>2</sub>                                       |
|                 |           | 10        | CoSe                                                                  |
| Co-Cu<br>Group  | <b>Co</b> | <b>Cu</b> |                                                                       |
|                 | 1         | 9         | (Co <sub>0.04</sub> Cu <sub>0.96</sub> ) <sub>3</sub> Se <sub>2</sub> |
|                 | 2         | 8         | (Co <sub>0.17</sub> Cu <sub>0.83</sub> ) <sub>3</sub> Se <sub>2</sub> |
|                 | 3         | 7         | (Co <sub>0.24</sub> Cu <sub>0.76</sub> ) <sub>3</sub> Se <sub>2</sub> |
|                 | 4         | 6         | (Co <sub>0.29</sub> Cu <sub>0.71</sub> ) <sub>3</sub> Se <sub>2</sub> |
|                 | 5         | 5         | (Co <sub>0.40</sub> Cu <sub>0.60</sub> ) <sub>3</sub> Se <sub>2</sub> |
|                 | 6         | 4         | (Co <sub>0.47</sub> Cu <sub>0.53</sub> ) <sub>3</sub> Se <sub>2</sub> |
|                 | 7         | 3         | (Co <sub>0.5</sub> Cu <sub>0.5</sub> ) <sub>3</sub> Se <sub>2</sub>   |
|                 | 8         | 2         | (Co <sub>0.73</sub> Cu <sub>0.27</sub> ) <sub>3</sub> Se <sub>2</sub> |
|                 | 9         | 1         | (Co <sub>0.82</sub> Cu <sub>0.18</sub> ) <sub>3</sub> Se <sub>2</sub> |
| Ni-Co<br>Group  | <b>Ni</b> | <b>Co</b> |                                                                       |
|                 | 1         | 9         | (Ni <sub>0.11</sub> Co <sub>0.89</sub> )Se                            |
|                 | 2         | 8         | (Ni <sub>0.19</sub> Co <sub>0.81</sub> )Se                            |
|                 | 3         | 7         | (Ni <sub>0.32</sub> Co <sub>0.68</sub> )Se                            |
|                 | 4         | 6         | (Ni <sub>0.42</sub> Co <sub>0.58</sub> )Se                            |
|                 | 5         | 5         | (Ni <sub>0.51</sub> Co <sub>0.49</sub> )Se                            |
|                 | 6         | 4         | (Ni <sub>0.62</sub> Co <sub>0.38</sub> )Se                            |
|                 | 7         | 3         | (Ni <sub>0.71</sub> Co <sub>0.29</sub> )Se                            |
|                 | 8         | 2         | (Ni <sub>0.75</sub> Co <sub>0.28</sub> )Se                            |
|                 | 9         | 1         | (Ni <sub>0.9</sub> Co <sub>0.1</sub> )Se                              |
| Ni-Cu<br>Group  | <b>Ni</b> | <b>Cu</b> |                                                                       |
|                 | 1         | 9         | (Ni <sub>0.06</sub> Cu <sub>0.94</sub> ) <sub>3</sub> Se <sub>2</sub> |
|                 | 2         | 8         | (Ni <sub>0.12</sub> Cu <sub>0.88</sub> ) <sub>3</sub> Se <sub>2</sub> |
|                 | 3         | 7         | (Ni <sub>0.23</sub> Cu <sub>0.77</sub> ) <sub>3</sub> Se <sub>2</sub> |
|                 | 4         | 6         | (Ni <sub>0.28</sub> Cu <sub>0.72</sub> ) <sub>3</sub> Se <sub>2</sub> |
|                 | 5         | 5         | (Ni <sub>0.35</sub> Cu <sub>0.65</sub> ) <sub>3</sub> Se <sub>2</sub> |

Table S3. The precursor ratio of compounds shown in the plots and their corresponding formulas by EDS atomic ratio. (cont.)

|                |           |           |                                                                   |
|----------------|-----------|-----------|-------------------------------------------------------------------|
| Ni-Cu<br>Group | 6         | 4         | $(\text{Ni}_{0.46}\text{Cu}_{0.54})_3\text{Se}_2$                 |
|                | 7         | 3         | $(\text{Ni}_{0.52}\text{Cu}_{0.48})_3\text{Se}_2$                 |
|                | 8         | 2         | $(\text{Ni}_{0.7}\text{Cu}_{0.3})_3\text{Se}_2$                   |
|                | 9         | 1         | $(\text{Ni}_{0.77}\text{Cu}_{0.23})_3\text{Se}_2$                 |
| <b>Co</b>      | <b>Ni</b> | <b>Cu</b> |                                                                   |
| 1              | 4         | 5         | $(\text{Co}_{0.08}\text{Ni}_{0.28}\text{Cu}_{0.63})_3\text{Se}_2$ |
| 2              | 2         | 6         | $(\text{Co}_{0.15}\text{Ni}_{0.15}\text{Cu}_{0.7})_3\text{Se}_2$  |
| 2              | 4         | 4         | $(\text{Co}_{0.15}\text{Ni}_{0.26}\text{Cu}_{0.59})_3\text{Se}_2$ |
| 3              | 3         | 4         | $(\text{Co}_{0.21}\text{Ni}_{0.25}\text{Cu}_{0.54})_3\text{Se}_2$ |
| 4              | 1         | 5         | $(\text{Co}_{0.31}\text{Ni}_{0.08}\text{Cu}_{0.61})_3\text{Se}_2$ |
| 4              | 3         | 3         | $(\text{Co}_{0.31}\text{Ni}_{0.23}\text{Cu}_{0.46})_3\text{Se}_2$ |
| 5              | 1         | 4         | $(\text{Co}_{0.36}\text{Ni}_{0.07}\text{Cu}_{0.57})_3\text{Se}_2$ |

Table S4. Comparison of three binary selenides, best performing ternary selenides and best quaternary selenide.

| Catalysts                                                         | Onset $\eta$ /<br>V | $\eta$ at 10 mA<br>$\text{cm}^{-2}/\text{V}$ | Tafel slope /<br>$\text{mV dec}^{-1}$ |
|-------------------------------------------------------------------|---------------------|----------------------------------------------|---------------------------------------|
| NiSe                                                              | 0.300               | 0.335                                        | 66.2                                  |
| $\text{Cu}_3\text{Se}_2$                                          | 0.282               | 0.326                                        | 82.9                                  |
| CoSe                                                              | 0.262               | 0.308                                        | 177.4                                 |
| $(\text{Co}_{0.4}\text{Cu}_{0.6})_3\text{Se}_2$                   | 0.257               | 0.278                                        | 72.5                                  |
| $(\text{Ni}_{0.51}\text{Co}_{0.49})\text{Se}$                     | 0.259               | 0.289                                        | 60.7                                  |
| $(\text{Ni}_{0.77}\text{Cu}_{0.23})_3\text{Se}_2$                 | 0.268               | 0.299                                        | 90.4                                  |
| $(\text{Co}_{0.21}\text{Ni}_{0.25}\text{Cu}_{0.54})_3\text{Se}_2$ | 0.241               | 0.272                                        | 53.3                                  |

Table S5. Comparison of ECSA and roughness factor (RF) of  $(\text{Co}_{0.21}\text{Ni}_{0.25}\text{Cu}_{0.54})_3\text{Se}_2$  before and after chronoamperometry.

|        | ECSA / $\text{cm}^2$ | RF    |
|--------|----------------------|-------|
| Before | 3.68                 | 52.57 |
| After  | 5.63                 | 80.36 |

Table S6. Comparison of EDS atomic ratio of  $(\text{Co}_{0.21}\text{Ni}_{0.25}\text{Cu}_{0.54})_3\text{Se}_2$  before and after electrochemical measurement.

|                       | EDS (Atomic %) |      |      |      |
|-----------------------|----------------|------|------|------|
|                       | Ni             | Cu   | Co   | Se   |
| <b>As-deposited</b>   | 16.1           | 33.9 | 13.1 | 37.0 |
| <b>After activity</b> | 15.3           | 35.6 | 12.4 | 36.7 |

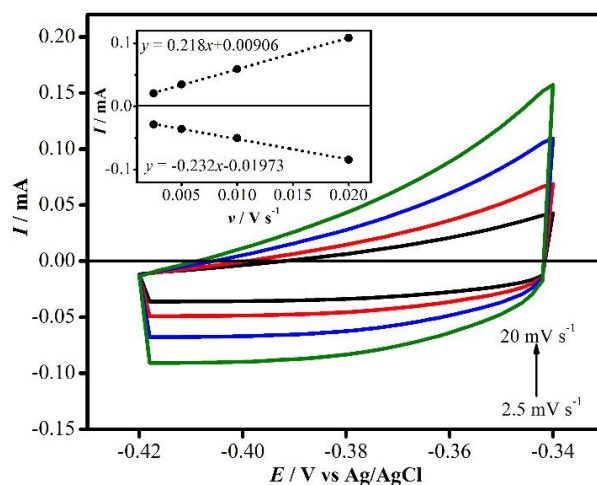


Figure S7. Cyclic voltammograms measured for the  $(\text{Co}_{0.21}\text{Ni}_{0.25}\text{Cu}_{0.54})_3\text{Se}_2$  after 12 h chronoamperometry in  $\text{N}_2$  saturated 1.0 M KOH solution at different scan rates from 2.5 to 20  $\text{mV s}^{-1}$ . The inset is a plot of both anodic and cathodic currents measured at -0.36 V vs Ag|AgCl (KCl saturated) as a function of scan rate.

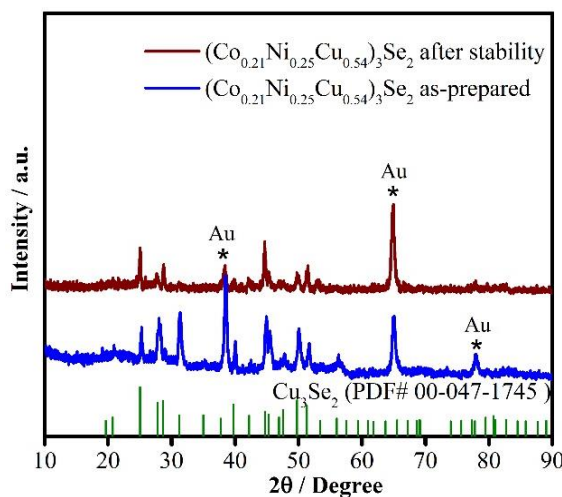


Figure S8. XRD patterns of as-prepared  $(\text{Co}_{0.21}\text{Ni}_{0.25}\text{Cu}_{0.54})_3\text{Se}_2$  and  $(\text{Co}_{0.21}\text{Ni}_{0.25}\text{Cu}_{0.54})_3\text{Se}_2$  after 12 h chronoamperometry along with reference  $\text{Cu}_3\text{Se}_2$  (PDF # 00-047-1745).



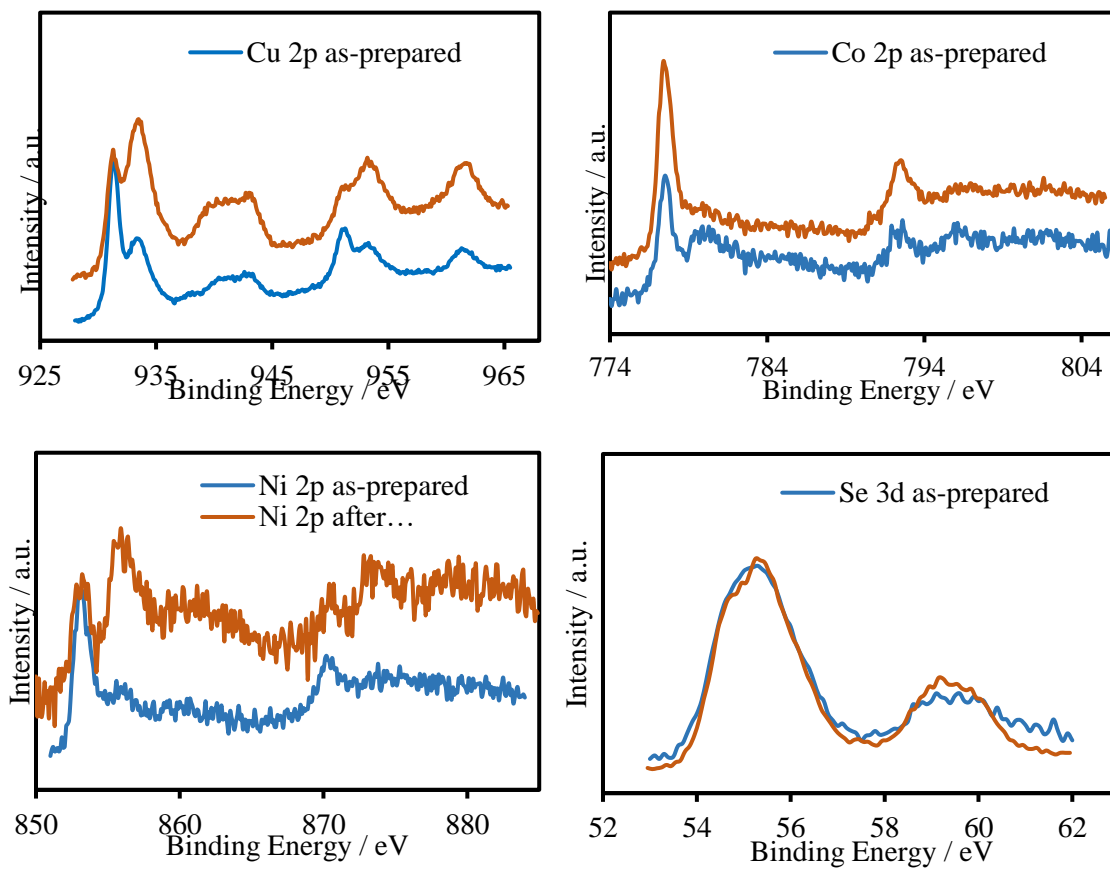


Figure S9. Comparison of XPS spectra of  $(\text{Co}_{0.21}\text{Ni}_{0.25}\text{Cu}_{0.54})_3\text{Se}_2$  catalyst before and after chronoamperometry.

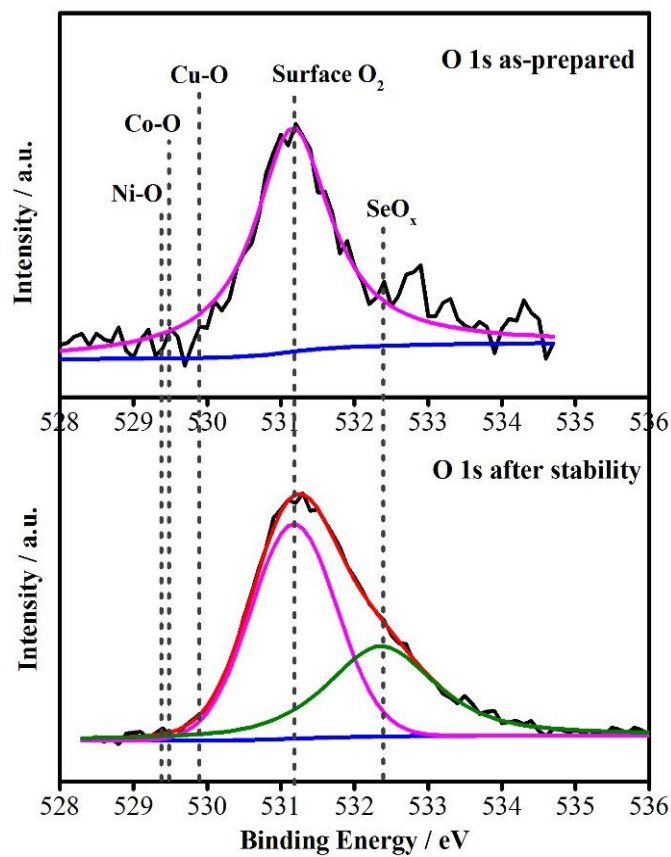


Figure S10. Comparison of XPS spectra of  $(\text{Co}_{0.21}\text{Ni}_{0.25}\text{Cu}_{0.54})_3\text{Se}_2$  catalyst before and after chronoamperometry.

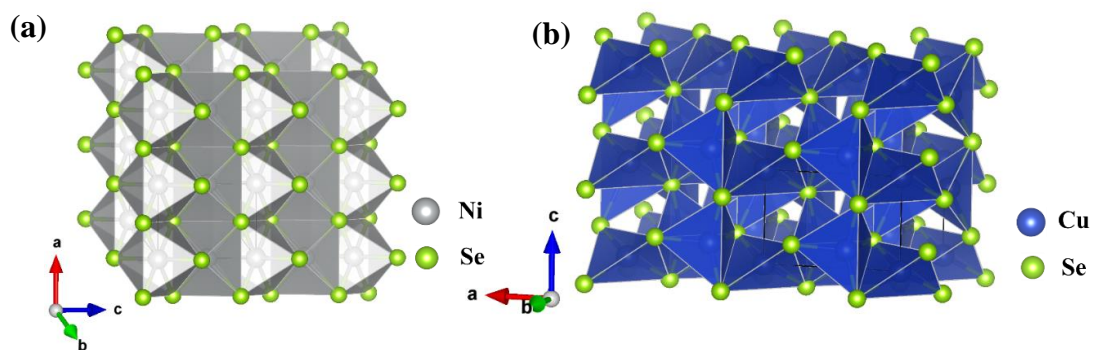


Figure S11. Crystal structure of (a) NiSe and (b)  $\text{Cu}_3\text{Se}_2$ .

## REFERENCES

- (1) J. Chow, R. J. Kopp and P. R. Portney, *Science*, 2009, **302**, 1528–1531.
- (2) N. S. Lewis, *Science*, 2007, **315**, 798–801.
- (3) M. G. Walter, E. L. Warren, J. R. Mckone, S. W. Boettcher, Q. Mi, E. A. Santori and N. S. Lewis, *Chem. Rev.*, 2010, **110**, 6446–6473.
- (4) J. A. Turner, *Science*, 2004, **305**, 972–974.
- (5) M. S. Dresselhaus and I. L. Thomas, *Nature*, 2001, **414**, 332–337.
- (6) G. W. Crabtree, M. S. Dresselhaus and M. V. Buchanan, *Phys. Today*, 2004, **57**, 39–44.
- (7) N. T. Suen, S. F. Hung, Q. Quan, N. Zhang, Y. J. Xu and H. M. Chen, *Chem. Soc. Rev.*, 2017, **46**, 337–365.
- (8) H. Dau, C. Limberg, T. Reier, M. Risch, S. Roggan and P. Strasser, *ChemCatChem*, 2010, **2**, 724–761.
- (9) M. T. M. Koper, *J. Electroanal. Chem.*, 2011, **660**, 254–260.
- (10) J. Rossmeisl, A. Logadottir and J. K. Nørskov, *Chem. Phys.*, 2005, **319**, 178–184.
- (11) T. Reier, M. Oezaslan and P. Strasser, *ACS Catal.*, 2012, **2**, 1765–1772.
- (12) W. T. Hong, M. Risch, K. A. Stoerzinger, A. Grimaud, J. Suntivich and Y. Shao-Horn, *Energy Environ. Sci.*, 2015, **8**, 1404–1427.
- (13) M. Gong and H. Dai, *Nano Res.*, 2015, **8**, 23–39.
- (14) L. Yang, S. Jiang, Y. Zhao, L. Zhu, S. Chen, X. Wang, Q. Wu, J. Ma, Y. Ma and Z. Hu, *Angew. Chem. Int. Ed.*, 2011, **50**, 7132–7135.
- (15) Y. Lee, J. Suntivich, K. J. May, E. E. Perry and Y. Shao-Horn, *J. Phys. Chem. Lett.*, 2012, **3**, 399–404.
- (16) H. Over, *Chem. Rev.*, 2012, **112**, 3356–3426.
- (17) Y. Li, P. Hasin and Y. Wu, *Adv. Mater.*, 2010, **22**, 1926–1929.
- (18) F. Dionigi and P. Strasser, *Adv. Energy Mater.*, 2016, **6**, 1600621.

- (19) R. Subbaraman, D. Tripkovic, K. C. Chang, D. Strmcnik, A. P. Paulikas, P. Hirunsit, M. Chan, J. Greeley, V. Stamenkovic and N. M. Markovic, *Nat. Mater.*, 2012, **11**, 550–557.
- (20) H. Osgood, S. V. Devaguptapu, H. Xu, J. Cho and G. Wu, *Nano Today*, 2016, **11**, 601–625.
- (21) M. Gong, Y. Li, H. Wang, Y. Liang, J. Z. Wu, J. Zhou, J. Wang, T. Regier, F. Wei and H. Dai, *J. Am. Chem. Soc.*, 2013, **135**, 8452–8455.
- (22) A. Kargar, S. Yavuz, T. K. Kim, C. H. Liu, C. Kuru, C. S. Rustomji, S. Jin and P. R. Bandaru, *ACS Appl. Mater. Interfaces*, 2015, **7**, 17851–17856.
- (23) Q. Chen and J. A. Switzer, *ACS Appl. Mater. Interfaces*, 2018, **10**, 21365–21371.
- (24) T. Maiyalagan, K. A. Jarvis, S. Therese, P. J. Ferreira and A. Manthiram, *Nat. Commun.*, 2014, **5**, 3949.
- (25) J. Suntivich, K. J. May, H. A. Gasteiger, J. B. Goodenough and Y. Shao-Horn., *Science*, 2011, **334**, 1383–1385.
- (26) A. Grimaud, K. J. May, C. E. Carlton, Y. L. Lee, M. Risch, W. T. Hong, J. Zhou and Y. Shao-Horn, *Nat. Commun.*, 2013, **4**, 2439.
- (27) X. Long, J. Li, S. Xiao, K. Yan, Z. Wang, H. Chen and S. Yang, *Angew. Chem. Int. Ed.*, 2014, **53**, 7584–7588.
- (28) U. De Silva, J. Masud, N. Zhang, Y. Hong, W. P. R. Liyanage, M. Asle Zaem and M. Nath, *J. Mater. Chem. A*, 2018, **6**, 7608–7622.
- (29) M. Shen, C. Ruan, Y. Chen, C. Jiang, K. Ai and L. Lu, *ACS Appl. Mater. Interfaces*, 2015, **7**, 1207–1218.
- (30) Q. Liu, J. Jin and J. Zhang, *ACS Appl. Mater. Interfaces*, 2013, **5**, 5002–5008.
- (31) P. Ganesan, M. Prabu, J. Sanetuntikul and S. Shanmugam, *ACS Catal.*, 2015, **5**, 3625–3637.
- (32) J. Chang, Y. Xiao, M. Xiao, J. Ge, C. Liu and W. Xing, *ACS Catal.*, 2015, **5**, 6874–6878.
- (33) L. A. Stern, L. Feng, F. Song and X. Hu, *Energy Environ. Sci.*, 2015, **8**, 2347–2351.
- (34) P. He, X. Y. Yu and X. W. Lou, *Angew. Chem. Int. Ed.*, 2017, **56**, 3897–3900.
- (35) A. T. Swesi, J. Masud and M. Nath, *Energy Environ. Sci.*, 2016, **9**, 1771–1782.
- (36) X. Xu, F. Song and X. Hu, *Nat. Commun.*, 2016, **7**, 12324.

- (37) J. Masud, A. T. Swesi, W. P. R. Liyanage and M. Nath, *ACS Appl. Mater. Interfaces*, 2016, **8**, 17292–17302.
- (38) W. Li, X. Gao, D. Xiong, F. Wei, W. G. Song, J. Xu and L. Liu, *Adv. Energy Mater.*, 2017, **7**, 1602579.
- (39) S. C. Petitto, E. M. Marsh, G. A. Carson and M. A. Langell, *J. Mol. Catal. A: Chem.*, 2008, **281**, 49–58.
- (40) L. Zhuang, L. Ge, Y. Yang, M. Li, Y. Jia, X. Yao and Z. Zhu, *Adv. Mater.*, 2017, **29**, 1606793.
- (41) H. Y. Wang, Y. Y. Hsu, R. Chen, T. S. Chan, H. M. Chen and B. Liu, *Adv. Energy Mater.*, 2015, **5**, 1500091.
- (42) J. Landon, E. Demeter, N. Inoğlu, C. Keturakis, I. E. Wachs, R. Vasić, A. I. Frenkel and J. R. Kitchin, *ACS Catal.*, 2012, **2**, 1793–1801.
- (43) Y. C. Liu, J. A. Koza and J. A. Switzer, *Electrochim. Acta*, 2014, **140**, 359–365.
- (44) K. Xu, H. Ding, H. Lv, S. Tao, P. Chen, X. Wu, W. Chu, C. Wu and Y. Xie, *ACS Catal.*, 2017, **7**, 310–315.
- (45) G. Zhang, S. Zang, Z. A. Lan, C. Huang, G. Li and X. Wang, *J. Mater. Chem. A*, 2015, **3**, 17946–17950.
- (46) J. X. Feng, H. Xu, Y. T. Dong, S. H. Ye, Y. X. Tong and G. R. Li, *Angew. Chem. Int. Ed.*, 2016, **55**, 3694–3698.
- (47) S. Zou, M. S. Burke, M. G. Kast, J. Fan, N. Danilovic and S. W. Boettcher, *Chem. Mater.*, 2015, **27**, 8011–8020.
- (48) L. Han, X. Y. Yu and X. W. Lou, *Adv. Mater.*, 2016, **28**, 4601–4605.
- (49) M. Görlin, J. F. De Araujo, H. Schmies, D. Bernsmeier, S. Dresp, M. Gliech, Z. Jusys, P. Chernev, R. Kraehnert, H. Dau and P. Strasser, *J. Am. Chem. Soc.*, 2017, **139**, 2070–2082.
- (50) M. Görlin, P. Chernev, J. F. De Araújo, T. Reier, S. Dresp, B. Paul, R. Krähnert, H. Dau and P. Strasser, *J. Am. Chem. Soc.*, 2016, **138**, 5603–5614.
- (51) L. J. Enman, M. S. Burke, A. S. Batchellor and S. W. Boettcher, *ACS Catal.*, 2016, **6**, 2416–2423.
- (52) Y. Xu, W. Bian, J. Wu, J. H. Tian and R. Yang, *Electrochim. Acta*, 2015, **151**, 276–283.
- (53) Z. Wang, J. Li, X. Tian, X. Wang, Y. Yu, K. A. Owusu, L. He and L. Mai, *ACS Appl. Mater. Interfaces*, 2016, **8**, 19386–19392.

- (54) G. Liu, K. Wang, X. Gao, D. He and J. Li, *Electrochim. Acta*, 2016, **211**, 871–878.
- (55) R. D. L. Smith, M. S. Prévot, R. D. Fagan, S. Trudel and C. P. Berlinguette, *J. Am. Chem. Soc.*, 2013, **135**, 11580–11586.
- (56) A. Shinde, D. Guevarra, G. Liu, I. D. Sharp, F. M. Toma, J. M. Gregoire and J. A. Haber, *ACS Appl. Mater. Interfaces*, 2016, **8**, 23696–23705.
- (57) X. Cao, Y. Hong, N. Zhang, Q. Chen, J. Masud, M. A. Zaeem and M. Nath, *ACS Catal.*, 2018, **8**, 8273–8289.
- (58) Z. Chen and T. J. Meyer, *Angew. Chem. Int. Ed.*, 2013, **52**, 700–703.
- (59) M. T. Zhang, Z. Chen, P. Kang and T. J. Meyer, *J. Am. Chem. Soc.*, 2013, **135**, 2048–2051.
- (60) M. Qian, X. Liu, S. Cui, H. Jia and P. Du, *Electrochim. Acta*, 2018, **263**, 318–327.
- (61) Y. Liu, Z. Niu, Y. Lu, L. Zhang and K. Yan, *J. Alloys Compd.*, 2018, **735**, 654–659.
- (62) L. Yang, L. Xie, X. Ren, Z. Wang, Z. Liu, G. Du, A. M. Asiri, Y. Yao and X. Sun, *Chem. Commun.*, 2018, **54**, 78–81.
- (63) X. Du, X. Zhang, Z. Xu, Z. Yang and Y. Gong, *Int. J. Hydrogen Energy*, 2018, **43**, 5012–5018.
- (64) P. Zhang, L. Li, D. Nordlund, H. Chen, L. Fan, B. Zhang, X. Sheng, Q. Daniel and L. Sun, *Nat. Commun.*, 2018, **9**, 381.
- (65) J. Masud, W. P. R. Liyanage, X. Cao, A. Saxena and M. Nath, *ACS Appl. Energy Mater.*, 2018, **1**, 4075–4083.
- (66) C. C. L. Mccrory, S. Jung, J. C. Peters and T. F. Jaramillo, *J. Am. Chem. Soc.*, 2013, **135**, 16977–16987.
- (67) C. C. L. McCrory, S. Jung, I. M. Ferrer, S. M. Chatman, J. C. Peters and T. F. Jaramillo, *J. Am. Chem. Soc.*, 2015, **137**, 4347–4357.
- (68) L. Trotochaud, S. L. Young, J. K. Ranney and S. W. Boettcher, *J. Am. Chem. Soc.*, 2014, **136**, 6744–6753.
- (69) M. S. Burke, M. G. Kast, L. Trotochaud, A. M. Smith and S. W. Boettcher, *J. Am. Chem. Soc.*, 2015, **137**, 3638–3648.
- (70) M. K. Bates, Q. Jia, H. Doan, W. Liang and S. Mukerjee, *ACS Catal.*, 2016, **6**, 155–161.

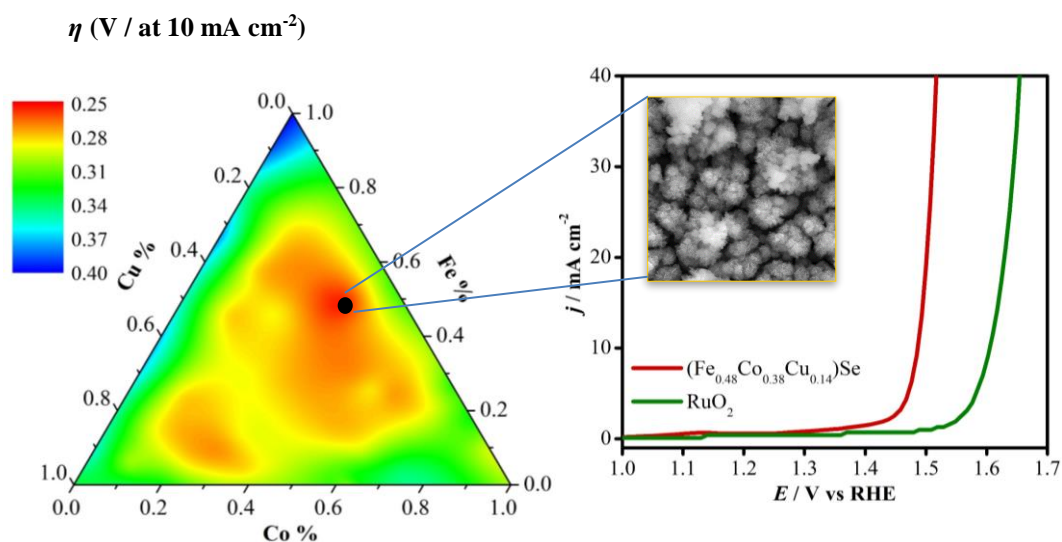
- (71) L. J. Enman, M. S. Burke, A. S. Batchellor and S. W. Boettcher, *ACS Catal.*, 2016, **6**, 2416–2423.
- (72) X. Xu, F. Song and X. Hu, *Nat. Commun.*, 2016, **7**, 12324.
- (73) J. Deng, M. R. Nellist, M. B. Stevens, C. Dette, Y. Wang and S. W. Boettcher, *Nano Lett.*, 2017, **17**, 6922–6926.
- (74) A. S. Batchellor, G. Kwon, F. A. L. Laskowski, D. M. Tiede and S. W. Boettcher, *J. Phys. Chem. C*, 2017, **121**, 25421–25429.
- (75) Y. Liang, Y. Li, H. Wang, J. Zhou, J. Wang, T. Regier and H. Dai, *Nat. Mater.*, 2011, **10**, 780–786.
- (76) L. R. B. Elton and D. F. Jackson, *Am. J. Phys.*, 1966, **34**, 1036–1038.
- (77) U. Holzwarth and N. Gibson, *Nat. Nanotechnol.*, 2011, **6**, 534.
- (78) M. Chauhan, K. P. Reddy, C. S. Gopinath and S. Deka, *ACS Catal.*, 2017, **7**, 5871–5879.
- (79) A. Panneerselvam, M. A. Malik, M. Afzaal, P. O'Brien and M. Helliwell, *J. Am. Chem. Soc.*, 2008, **130**, 2420–2421.
- (80) W. Wang, Y. Geng, P. Yan, F. Liu, Y. Xie and Y. Qian, *J. Am. Chem. Soc.*, 1999, **121**, 4062–4063.
- (81) J. Nai, Y. Lu, L. Yu, X. Wang and X. W. D. Lou, *Adv. Mater.*, 2017, **29**, 1703870.
- (82) P. Liao, J. A. Keith and E. A. Carter, *J. Am. Chem. Soc.*, 2012, **134**, 13296–13309.
- (83) N. B. Halck, V. Petrykin, P. Krtil and J. Rossmeisl, *Phys. Chem.*, 2014, **16**, 13682–13688.

### III. EXPANDING MULTINARY SELENIDE BASED HIGH-EFFICIENCY OXYGEN EVOLUTION ELECTROCATALYSTS THROUGH COMBINATORIAL ELECTRODEPOSITION: CASE STUDY WITH Fe-Cu-Co SELENIDES

*Xi Cao,<sup>a</sup> Emily Johnson<sup>b</sup> and Manashi Nath<sup>\*a</sup>*

a. Department of Chemistry, Missouri University of Science & Technology, Rolla, Missouri 65409, United States.

b. Department of Chemical and Biochemical Engineering, Missouri University of Science & Technology, Rolla, Missouri 65409, United States.



#### ABSTRACT

Developing low-cost electrocatalysts with high efficiency for water splitting is a critical task to make this technology viable for large-scale clean energy generation. Transition metal selenides, comprising earth abundant elements, such as Fe, Co and Cu, have gained attention as superior electrocatalysts for oxygen evolution reaction (OER) in



the alkaline medium. In this article, we have systematically investigated the evolution of OER catalytic activity as a function of composition for a series of Fe–Co–Cu quaternary selenides by exploring a trigonal phase diagram. The OER activity was dependent on the quantity of Cu and Fe in the Co–Fe–Cu–Se quaternary selenide electrocatalysts, while surprisingly, Fe–Cu ternary selenides exhibit reduced OER activity in comparison to their pure parent compounds FeSe and Cu<sub>3</sub>Se<sub>2</sub>. Quaternary selenides exhibited more efficient catalytic activity with increasing amount of Fe or Cu in the catalysts, and the quaternary mixed metal selenide thin film of composition (Fe<sub>0.48</sub>Co<sub>0.38</sub>Cu<sub>0.14</sub>)Se showed the best catalytic performance with a small overpotential of 256 mV at 10 mA cm<sup>-2</sup> and a low Tafel slope of 40.8 mV dec<sup>-1</sup> in N<sub>2</sub>-saturated 1.0 M KOH solution. The outstanding catalytic performance of quaternary selenides may be explained by the possible electron cloud delocalization among the transition metal sites in the catalytic system through *d*-bands, leading to lower charge transport resistance at the catalyst–electrolyte interface as well better film conductivity, as has also been observed through electrochemical impedance spectroscopy. Such enhanced charge transfers eventually facilitate the rate of O<sub>2</sub> release from the catalyst surface leading to enhanced activity.

**Keywords:** mixed metal selenides, oxygen evolution electrocatalyst, water splitting, electrocatalyst

## 1. INTRODUCTION

Hydrogen has been widely considered as an ideal alternative for sustainable energy to diminish the utilization of fossil fuels, especially in recent times when fossil fuel

depletion has reached an all-time high along with the environmental pollution caused by carbon dioxide, a byproduct of fossil fuel combustion.<sup>1-3</sup> While hydrogen fuel holds tremendous promise as a clean source of energy, the production of pure hydrogen is a challenge that must be met before hydrogen fuel can replace the mature conventional technologies. Alkaline water electrolysis is a well-established technology to produce high-purity hydrogen in copious quantities for use in fuel cells and other energy storage devices.<sup>4,5</sup> Water splitting includes two critical half-cell reactions: hydrogen evolution reaction (HER) at the cathode ( $2\text{H}_2\text{O} + 2\text{e}^- \rightarrow \text{H}_2 + 2\text{OH}^-$ ) and oxygen evolution reaction (OER) at the anode ( $4\text{OH}^- \rightarrow \text{O}_2 + 4\text{e}^- + 2\text{H}_2\text{O}$ ).<sup>6-9</sup> Among these, OER is the more challenging kinetically sluggish process with multistep four-electron transfers involved which has greatly reduced the efficiency of water splitting reaction thereby limiting the applicability of this technology to produce hydrogen on a large scale. An efficient electrocatalyst is required to speed up OER by lowering the activation barrier and reducing the overpotential required for water oxidation. In this context, a large number of research endeavors have been devoted to designing high-efficiency and low-cost OER electrocatalysts.<sup>10-14</sup> Although research over the last several decades has identified some state-of-the-art OER electrocatalysts based on noble-metal-based oxides, such as  $\text{IrO}_2$  and  $\text{RuO}_2$  exhibiting low overpotentials and excellent stability, the scarcity and high cost of these precious metals have hindered their large scale industrial applications.<sup>15,16</sup> Consequently, over the past several years, researchers have focused on exploring earth abundant transition metal based chemistry to identify and develop low-cost electrocatalysts comprising first row transition metals (primarily Fe, Ni, and Co). The quest for these transition metal electrocatalysts has led to oxides and (oxy)hydroxides, that could

potentially replace precious metals due to their comparable activity and durability.<sup>17–24</sup> Continued research conducted by our group as well as by other groups over the last couple of years has made it quite apparent that transition–metal based selenides are more likely to exhibit an improved OER catalytic activity and a reduced overpotential compared to oxides. Such enhancement of OER catalytic activity is attributed to the increased covalency of the metal–ligand bond as well as lowering the electrochemical redox potential of the catalytically active transition metal site.<sup>25–30</sup> It was also observed that the smaller electronegativity of selenium compared to oxygen led to the enhancement of preferential attachment of hydroxyl ions on the catalytically active metal sites and facilitated further steps of the OER process.<sup>31–33</sup> Accordingly, binary metal selenides (Ni<sub>3</sub>Se<sub>2</sub>, NiSe<sub>2</sub>, CoSe, and Co<sub>7</sub>Se<sub>8</sub>) have been widely investigated as excellent OER electrocatalysts with impressively low overpotentials.<sup>26,34–36</sup> Ternary mixed metal selenides such as Ni<sub>x</sub>Fe<sub>1–x</sub>Se<sub>2</sub>, Ni<sub>0.89</sub>Co<sub>0.11</sub>Se<sub>2</sub>, FeNi<sub>2</sub>Se<sub>4</sub> and NiCoSe<sub>2</sub> exhibit more efficient catalytic activity suggesting that introduction of transition metal dopants improves catalytic activity.<sup>37–40</sup> Further studies revealed that transition metal doping increased the number of actual catalytically active sites and accelerated the rate determining steps by modulating the OH<sup>–</sup> adsorption kinetics on the catalyst surface through tuning the local electron density around the catalytic site.<sup>41,42</sup> Similar effects can also be observed in the transition metal oxides/(oxy)hydroxides, such as Fe or Co doped NiO/NiOOH exhibiting a much higher catalytic activity than NiO/NiOOH itself.<sup>43–46</sup> More recently, we have systematically studied how transition metal doping in catalytically active selenide compositions affect OER activity through the exploration of a trigonal phase diagram of Ni–Fe–Co selenides and demonstrated that quaternary mixed metal selenides exhibited better OER activity than

binary or even ternary selenides.<sup>33</sup> In the Ni–Fe–Co selenide system, quaternary selenides with a progressively increasing amount of Fe showed higher catalytic activity and the optimal composition was identified as  $(\text{Ni}_{0.25}\text{Fe}_{0.68}\text{Co}_{0.07})_3\text{Se}_4$  which could achieve  $10 \text{ mA cm}^{-2}$  at a small overpotential of 230 mV and showed remarkable durability in alkaline medium.<sup>33</sup> While Ni and Co have traditionally shown excellent OER activity and have been given primary attention due to their relative abundance on the earth's crust compared to precious metals, another abundant element with high *d*-electron occupancy, namely copper, has been explored far less for electrocatalytic water splitting. Cu-based OER electrocatalysts will be even more impactful since copper is one of the most abundant elements on the earth's crust found in lots of minerals.<sup>47</sup> Very recently, there has been a couple of reports where  $\text{Cu}_2\text{O}$  has been reported as an OER active catalyst.<sup>48,49</sup> We have synthesized  $\text{Cu}_2\text{Se}$  via electrodeposition as well as hydrothermal and high temperature chemical vapor deposition methods and have shown that  $\text{Cu}_2\text{Se}$  exhibited better electrocatalytic activity compared to the oxide analogue.<sup>50</sup> Additionally, introduction of Cu with highly occupied *d*-levels imparts enhanced conductivity to the matrix which will improve charge transport on the catalyst surface. Hence, to understand the effect of transition metal doping in copper selenide on the OER catalytic activity, we have performed a systemic study of the phase diagram of Co–Ni–Cu selenides.<sup>51</sup> These studies reveal that OER catalytic activity is influenced by the amount of Cu introduced into the catalytic system, specifically for quaternary selenides, and the best-performing catalyst composition in this case was identified as  $(\text{Co}_{0.21}\text{Ni}_{0.25}\text{Cu}_{0.54})_3\text{Se}_2$  thin film which required an overpotential of 272 mV to reach  $10 \text{ mA cm}^{-2}$ .<sup>51</sup> Fe has been shown to act as an enhancer for OER catalytic activity in oxides and selenides,<sup>33,52,53</sup> and quaternary selenides

incorporating both Cu and Fe are expected to have better OER catalytic activity. Inspired by this idea, we have systematically investigated a series of mixed metal selenides comprising various amounts of Fe, Co and Cu by exploring a trigonal phase diagram through combinatorial electrodeposition as has been reported in this article. Surprisingly, Fe–Cu ternary selenides showed reduced OER activity in comparison to their pure parent compounds FeSe and Cu<sub>3</sub>Se<sub>2</sub>, indicating that neither Fe nor Cu doping can improve the activity of Cu<sub>3</sub>Se<sub>2</sub> or FeSe, respectively. On the other hand, with introduction of Co dopant into the composition, all Fe–Co–Cu quaternary selenides showed enhanced catalytic activity with low overpotential as well as lower Tafel slopes. The catalytic activity of the quaternary selenides improved as the relative amounts of either Fe or Cu increased in the catalysts. The optimal catalyst composition in this phase space was identified as (Fe<sub>0.48</sub>Co<sub>0.38</sub>Cu<sub>0.14</sub>)Se which required an overpotential of 256 mV to achieve 10 mA cm<sup>-2</sup> and a showed Tafel slope of 40.8 mV dec<sup>-1</sup>. The low value of Tafel slope indicates that the catalyst has favorable kinetics for OER in alkaline medium. It is interesting to note that even in the absence of Ni, which has been recognized as one of the most active catalytic sites, it is possible to have high-efficiency catalytic activity for OER through transition metal doping. The enhanced catalytic activity can be attributed to the possible electron cloud delocalization through formation of *d*-bands between the different transition metal centers within the catalytic system.<sup>7,54</sup> This systematic exploration of mixed-metal selenides comprised iron, cobalt and copper offers more opportunities to understand the evolution of the catalytic property as a function of covalency and *d*-electron occupancy of the transition metals and will have far-reaching implications in practical application of electrocatalytic water splitting.

## 2. EXPERIMENTAL SECTION

Materials. The metal precursors comprising iron (II) sulfate [ $\text{FeSO}_4 \cdot 7\text{H}_2\text{O}$ , 99.0 %], cobalt (II) sulfate [ $\text{CoSO}_4 \cdot 7\text{H}_2\text{O}$ , 99.0 %], copper (II) sulfate [ $\text{CuSO}_4 \cdot 5\text{H}_2\text{O}$ , 99.0 %], selenium dioxide [ $\text{SeO}_2$ ], ammonium sulfate [ $(\text{NH}_4)_2\text{SO}_4$ , 99 %] and potassium hydroxide [ $\text{KOH}$ , 85.0 %] were obtained from Fisher Scientific and used as received. All solutions were prepared in deionized (DI) water (18  $\text{M}\Omega$  / cm). The Au-coated glass substrates used in electrodeposition were purchased from Deposition Research Lab Incorporated (DRLI), Lebanon, Missouri.

Combinatorial electrodeposition of thin films. Systematic exploration of a trigonal phase diagram was carried out to synthesize a series of transition metal doped ternary and quaternary selenide films through combinatorial electrodeposition as shown in Figure S1. This method is very similar to our previously reported work featuring Co–Fe–Ni selenides, and the process has been described in detail in a previous publication.<sup>33</sup> Specifically, the electrolyte contained a combination of freshly prepared 10 mM  $\text{FeSO}_4 \cdot 7\text{H}_2\text{O}$ ,  $\text{CoSO}_4 \cdot 7\text{H}_2\text{O}$ , and  $\text{CuSO}_4 \cdot 5\text{H}_2\text{O}$  solutions along with 10 mM  $\text{SeO}_2$  and 25 mM  $(\text{NH}_4)_2\text{SO}_4$ . Before electrodeposition, all electrolytes were purged in  $\text{N}_2$  for 30 min to remove dissolved oxygen. Prior to electrodeposition, Au-coated glass substrates were sonicated in micro-90, isopropyl alcohol followed by rinsing with deionized water to obtain a clean surface.<sup>33,51</sup> To ensure the same geometric area for all electrodeposited thin films studied in this article, the cleaned substrates were confined with Teflon tape punched with a hole of known geometric area. An IviumStat potentiostat was used for all the electrodeposition experiments. The films were deposited on Au-coated glass working electrode using a three-electrode electrochemical cell consisting of a  $\text{Ag}|\text{AgCl}$  (KCl saturated) reference electrode

and a glassy carbon (GC) counter electrode. The electrodeposition potential was maintained at  $-0.8$  V *vs* Ag|AgCl (KCl saturated) for 300 s at room temperature.

**Characterization.** A KRATOS AXIS 165 X-ray photoelectron spectrometer along with the monochromatic Al X-ray source were used to conduct X-ray photoelectron spectroscopy (XPS) of the catalyst. All XPS analysis was collected on the as-prepared sample surface without any sputtering. The morphologies of the thin film before and after electrochemical activity were observed with scanning electron microscopy (SEM) using the FEI Helios NanoLab 600 FIB/FESEM at an accelerating voltage of 15 kV and a working distance of around 5.0 mm. Energy dispersive spectroscopy (EDS) from the same SEM microscope was used to evaluate the elemental compositions of all electrodeposited films. In this work, the elemental analysis was obtained at three to five different spots on the surface of each compound and the average EDS data was considered for obtaining the relative atomic ratio of the constituent elements. For all compounds, the molecular formula was written as  $(\text{Fe}_x\text{Co}_y\text{Cu}_z)\text{Se}_n$ , where  $x$ ,  $y$ ,  $z$ , and  $n$  were the EDS atomic ratios of the transition elements to total amount of selenium, respectively.

**Electrochemical Measurements.** A typical three-electrode electrochemical cell connected to an IviumStat potentiostat was used for measuring the electrocatalytic performances. Linear sweep voltammetry (LSV) was carried out to study the OER catalytic activity, while the catalyst stability was investigated by carrying out constant potential chronoamperometry for an extended period of time in  $\text{N}_2$ -saturated 1.0 M KOH at room temperature. In all the electrochemical experiments, the deposited thin films served as the working electrode, while GC was used as the counter electrode and Ag|AgCl (KCl saturated) as the reference electrode. The Nernst equation as shown in Equation 1 was used

to convert the experimentally measured potentials vs Ag|AgCl (KCl saturated) to the reversible hydrogen electrode (RHE).

$$E_{RHE} = E_{Ag|AgCl} + 0.059pH + E_{Ag|AgCl}^0 \quad (1)$$

The standard potential of Ag|AgCl (KCl saturated) at 25.1 °C was 0.197 V. All the potentials reported in this article have been iR corrected.

Calculation of Tafel plot. Tafel equation relating the overpotential  $\eta$  with the current density  $j$  as shown in Equation 2 was used to study the electrochemical kinetics of the  $(Fe_xCo_yCu_z)Se_n$  thin films for OER.

$$\eta = a + \frac{2.3RT}{\alpha nF} \log(j) \quad (2)$$

Here  $\eta$  refers to the overpotential and  $j$  represents the current density. The Tafel slope is given by  $2.3RT/\alpha nF$ . The Tafel plots in this work were calculated from the LSV collected at a scan rate of  $2 \text{ mV s}^{-1}$  in a nonstirred  $N_2$ -saturated 1.0 M KOH solution.

Electrochemically active surface area (ECSA) Electrochemical double layer capacitance was used to measure the ECSA of these catalysts following standard methods described in detail in previous reports.<sup>17,33</sup> In the measurement of ECSA through double layer capacitance it is assumed that the current obtained in the non-Faradaic region is caused by double-layer charging instead of electrochemical reactions or charge transfer. The double layer current ( $i_{DL}$ ) was obtained by performing cyclic voltammograms (CVs) with various scan rates in a nonstirred  $N_2$ -saturated 1.0 M KOH solution.

The ratio of double-layer current  $i_{DL}$  and the scan rate ( $v$ ) of CV yielded specific electrochemical double-layer capacitance ( $C_{DL}$ ) as shown in eq 3. The cathodic and anodic charging currents were a function of scan rates, and the  $C_{DL}$  can be calculated by averaging



the absolute values of cathodic and anodic slopes. Equation 4 can be used to calculate ECSA.

$$i_{DL} = C_{DL} \times v \quad (3)$$

$$ECSA = C_{DL}/C_s \quad (4)$$

Here, double-layer capacitance ( $C_{DL}$ ) is in units of mF. Based on other reported values, the specific capacitance ( $C_s$ ) was assumed to be 0.040 mF cm<sup>-2</sup> in the alkaline solution.<sup>17,26</sup> Roughness factor (RF) was estimated from the ratio of ECSA and the geometric area (0.07 cm<sup>2</sup>).

### 3. RESULTS AND DISCUSSION

Structural and Elemental Compositions of Electrodeposited Thin Films. The trigonal phase diagram as shown in Figure S1 was systematically explored to electrodeposit a series of mixed metal selenides. This method, referred to as combinatorial electrodeposition, is similar to our previous published reports where the process has been described in detail with different transition metals.<sup>33,51</sup> In the trigonal phase diagram, the vertices represented three binary selenides (CoSe, FeSe, and Cu<sub>3</sub>Se<sub>2</sub>), while the sides of the triangle referred to the ternary selenides Fe<sub>x</sub>Co<sub>y</sub>Se<sub>n</sub>, Fe<sub>x</sub>Cu<sub>y</sub>Se<sub>n</sub> and Co<sub>x</sub>Cu<sub>y</sub>Se<sub>n</sub>, respectively. The interior of this trigonal phase diagram represented the quaternary mixed-metal selenides (Fe<sub>x</sub>Co<sub>y</sub>Cu<sub>z</sub>Se<sub>n</sub>). It should be noted here that all the electrodeposited thin films of ternary and quaternary compositions were amorphous in nature and did not yield clear X-ray powder diffraction (PXRD) patterns, making proper phase determination from PXRD alone less probable. The elemental composition of the electrodeposited films on the other hand, were determined from the average relative atomic ratio obtained from

EDS analysis as listed in Table S1, juxtaposed with the precursor ratio in the electrolyte that produced the respective film. Typically, EDS was collected at several regions on the sample surface and interestingly, it showed similar quantification results for the elemental ratios, indicating that while the films were not crystalline, they were indeed of uniform composition throughout each catalytic surface. As can be seen in Table S1, three as-prepared binary thin films were composed of Fe, Co or Cu and Se with approximate atomic ratios of 1 : 1 (Fe : Se), 1 : 1 (Co : Se), and 3 : 2 (Cu : Se) respectively, hence the molecular formulas of three binaries were written as FeSe, CoSe, and Cu<sub>3</sub>Se<sub>2</sub> as shown in Table S2, respectively. The molecular formulas identified in the various current voltage plots of the ternary and quaternary selenides can be found in Table S2. Careful observation of Table S1 revealed that increasing (or decreasing) amounts of the metal precursor in the electrolytic bath led to an increase (or decrease) of the relative atomic percentage of the corresponding element in the electrodeposited film. This demonstrates the ability to control thin film composition through combinatorial electrodeposition.

**Electrochemical Characterization.** Linear sweep voltammetry (LSV) was carried out in N<sub>2</sub>-saturated 1.0 M KOH at a scan rate of 10 mV s<sup>-1</sup> to measure OER catalytic activity of the deposited films. The electrocatalytic performance was benchmarked in comparison with other highly active catalysts by comparing the onset overpotential (onset  $\eta$ ) and the overpotential required to reach a current density of 10 mA cm<sup>-2</sup> ( $\eta$  at 10 mA cm<sup>-2</sup>) obtained from the LSV data.<sup>17</sup> Table S1 lists the onset overpotential, overpotential at 10 mA cm<sup>-2</sup> and the corresponding EDS atomic ratios of all the electrodeposited selenides reported in this work. The OER polarization curves of the three binary selenide films can be found in Figure S2, demonstrating the OER catalytic activity trend of binary

films was  $\text{CoSe} > \text{Cu}_3\text{Se}_2 > \text{FeSe}$ . The LSV plots for all the ternary selenide films as shown in Figure 1. In Figure 1a, Co–Cu selenides were obviously the best group in comparison to the other two, and the optimal composition in this group was identified as  $(\text{Co}_{0.93}\text{Cu}_{0.07})_3\text{Se}_2$  which onset overpotential was 235 mV and overpotential was 272 mV at  $10 \text{ mA cm}^{-2}$ . Interestingly, the LSV plots of Fe–Cu selenide group in Figure 1b displayed the worst catalytic activity among the three ternary groups. The ternary composition in this group exhibiting the best catalytic activity with an onset overpotential of 307 mV and an overpotential of 347 mV to reach a current density of  $10 \text{ mA cm}^{-2}$  was identified as  $(\text{Fe}_{0.78}\text{Cu}_{0.22})_3\text{Se}_4$ . Some of the LSV plots from the Co–Fe selenide group shown in Figure 1c were also included in our previous work on combinatorial electrodeposition of Ni–Co–Fe multinary selenides.<sup>33</sup> In this group,  $(\text{Co}_{0.90}\text{Fe}_{0.10})_3\text{Se}_4$  that exhibited the lowest onset overpotential of 257 mV and overpotential of 295 mV at  $10 \text{ mA cm}^{-2}$ .<sup>33</sup> It is worth mentioning that several preoxidation peaks were observed in these LSVs prior to the OER process corresponding to oxidation of transition metal ions within the catalyst composite as shown in Figures 1a,d. Preoxidation peaks are commonly noted in the Ni- and Co based electrocatalysts, which result from the change in oxidation state of transition metal during the anodic scan.<sup>55–58</sup> As can be seen in Figures 1a,d, the peaks observed around 1.10 V vs RHE were attributed to the conversion of  $\text{Co}^{2+}$  to  $\text{Co}^{3+}$ .<sup>33,57,59</sup> Interestingly, the intensity of Co preoxidation peaks increased with increasing the amount of Co in the electrocatalysts, which further confirmed combinatorial electrodeposition as a feasible method for compositional control. The polarization curves of the most efficient ternary selenide composition from each group has been compared with those of the binaries in Figure 1d to illustrate the effect of transition metal doping on OER catalytic activity. It was observed

that doping CoSe with 7 % Cu improved the OER catalytic activity by decreasing  $\eta$  at 10 mA cm<sup>-2</sup> by about 26 mV. Similarly, 22 % Cu dopant in FeSe lowered the overpotential by 46 mV to reach a current density of 10 mA cm<sup>-2</sup>. However, it should be noted that the catalytic activity of (Fe<sub>0.78</sub>Cu<sub>0.22</sub>)<sub>3</sub>Se<sub>4</sub> was still observed to be worse than the binary copper selenide, Cu<sub>3</sub>Se<sub>2</sub>. Doping of 10 % Fe into CoSe did not lead to any observable change in the OER catalytic activity. It has been widely reported that incorporation of transition-metal dopants improved the OER catalytic activity: for example, a small amount of Fe doped into Ni- or Co based electrocatalysts can radically ameliorate the OER activity.<sup>43,60-66</sup> It is interesting to note that in these ternary metal selenides, transition metal doping forces the formation of a different stoichiometry and structure type compared to the binary selenide. The ternary films of Co-Cu selenides formed the  $M_3Se_2$  composition, and accordingly they could be described as Co-doped Cu<sub>3</sub>Se<sub>2</sub>. On the other hand, the Co-Fe selenide group formed the structure type  $M_3Se_4$ . Interestingly, the Fe-Cu group exhibits different stoichiometries at different relative ratios of Fe and Cu. At a high Cu concentration with minimal Fe doping, the deposition adopts  $M_3Se_2$  composition and can be described as doped Fe-doped Cu<sub>3</sub>Se<sub>2</sub>. At high relative ratio of Fe with minimal Cu doping, the structure can be described as  $M_3Se_4$  (Cu-doped Fe<sub>3</sub>Se<sub>4</sub>). At comparable relative ratios of Fe:Cu, the stoichiometries obtained were closer to monoselenides, and can be described as  $MSe$ . It should also be noted that each of these stoichiometries are distinctly different from each other with respect to crystal structure and may also contain different coordination geometry around the transition metal ions, as discussed later. Different stoichiometries of the metal selenides also give rise to different catalytic properties, as has been observed with the Ni-selenide, Ni<sub>3</sub>Se<sub>2</sub>, NiSe, NiSe<sub>2</sub>, and Ni<sub>3</sub>Se<sub>4</sub>.<sup>26,27,67,68</sup>

Additionally, for mixed metal catalysts, it has been shown that the OER activity depends not only on the quantity of transition metal dopants but is also strongly related to the location of metal dopants in the catalytic system. D. Friebel et al. have reported that Fe in  $\text{Ni}_{1-x}\text{Fe}_x\text{OOH}$  showed a 500-fold increase in OER activity when Fe was doped into the octahedral sites where the edge-sharing of  $[\text{NiO}_6]$  and  $[\text{FeO}_6]$  occurred affecting the local electronic structure of the catalyst.<sup>69</sup> We have also previously reported through density functional theory (DFT) calculations that introducing dopants into the surface layers altered the adsorption energy of hydroxyl species on the active metal sites, thereby lowering the potential to initiate OER and leading to enhancement of the catalytic activity.<sup>33</sup> Hence, it is not surprising to see Fe–Cu selenides showing less efficient OER catalytic activity, which can be a reflection of the inherent property of the structure type and composition.

The trend of OER catalytic activity in the family of Co–Fe–Cu–Se quaternary selenides comprising 66 individual compositions is shown in the contour plots of Figure 2, created from the two overpotential values (onset and  $\eta$  at  $10 \text{ mA cm}^{-2}$ ) in Table S1 and the EDS atomic ratios. Contour plots were constructed to investigate the trend of OER onset potential and overpotential at  $10 \text{ mA cm}^{-2}$  as a function of composition as shown in Figures 2a, 2b, respectively. The range of overpotentials obtained is represented with a color gradient with the catalytic activity becoming better from bottom to top of the gradient scale corresponding to the lower value of the overpotential. Typically, regions with red color showed better catalytic activity compared to the blue colored regions which showed the highest overpotentials. The very interior region in the trigonal phase diagram showed the lowest overpotential as shown in Figure 2a, demonstrating the best catalytic activity, while the areas adjacent to three axes exhibited less efficient catalytic activity. This demonstrated

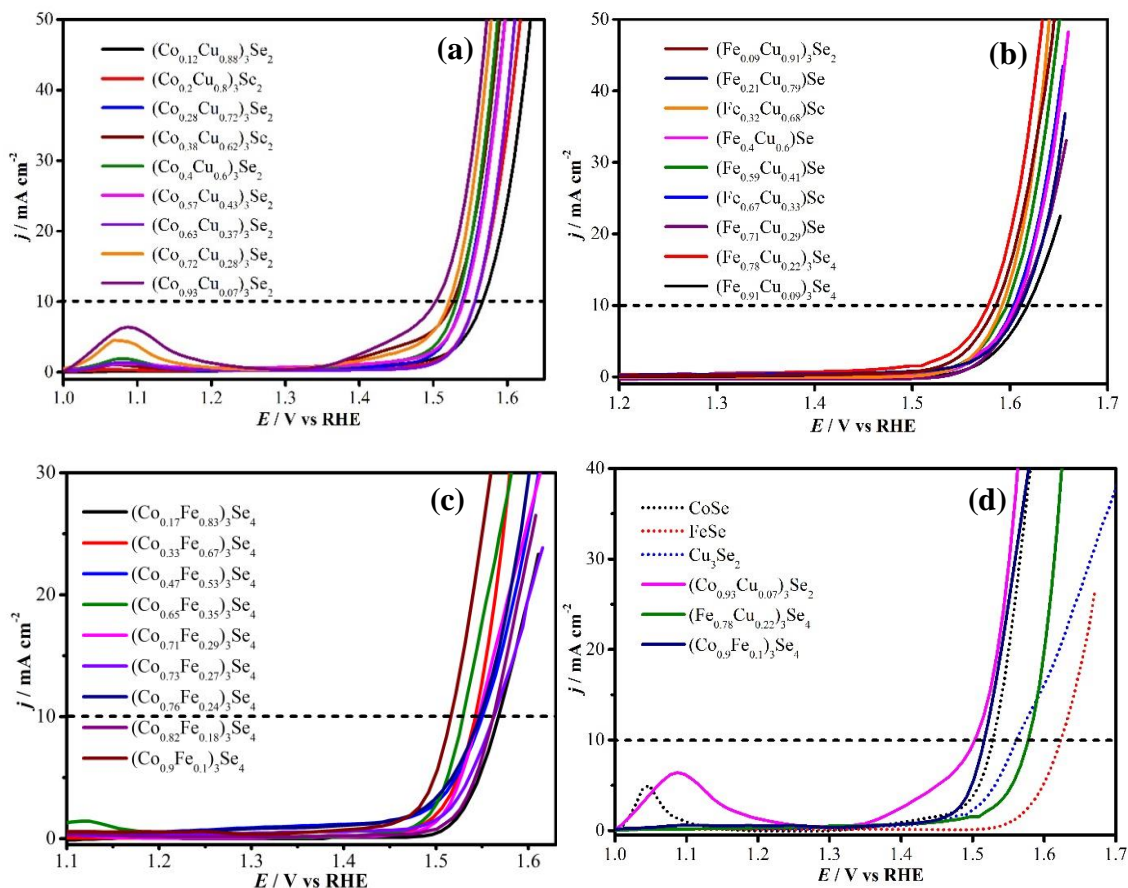


Figure 1. OER electrocatalytic performances of the various ternary metal selenides obtained along the edges of the trigonal phase diagram measured through linear sweep voltammeteries (LSVs). (a) Co–Cu group (b) Fe–Cu group, and (c) Co–Fe group. (d) OER activity of the most active ternary composition (solid line) from each group was compared with the three binary compositions (dotted line). The dashed black line in each panel indicates the current density at  $10 \text{ mA cm}^{-2}$ .

that heavily doped quaternary selenides were most likely to exhibit higher OER catalytic activity in comparison to binary or ternary selenides in this Cu–Co–Fe phase space. As can be seen, the best quaternary selenides were confined to the region where Cu was around 10 – 50 %, Co was about 15 – 50 %, and Fe was roughly 30 – 70 %. The trends indicated that the quaternary selenides showed the best catalytic performance when the level of Fe was higher, suggesting that while Fe played an important role in improving the catalytic

activity, it probably was not the main catalytic site, since Fe-rich ternary phases showed poor catalytic activity as can be observed in the Co–Fe group (Figure 1c). Meanwhile, the amount of Cu affected the catalytic activity as well with the OER activity being enhanced by a modest amount of Cu. It should be noted that a relatively higher amount of Fe or Cu compared to that of Co in the catalyst is more likely to produce better activity with lower overpotentials. However, as explained above, Fe–Cu–Se ternary selenide still showed poor performance, indicating that Fe and Cu sites by themselves do not have higher catalytic activity. However, the inductive effect of these ions on the neighboring Co sites increased the catalytic activity of Co, thereby lowering the overpotentials. These observations further confirmed the benefits of such systematic studies in discovering untargeted mixed–metal based electrocatalysts.

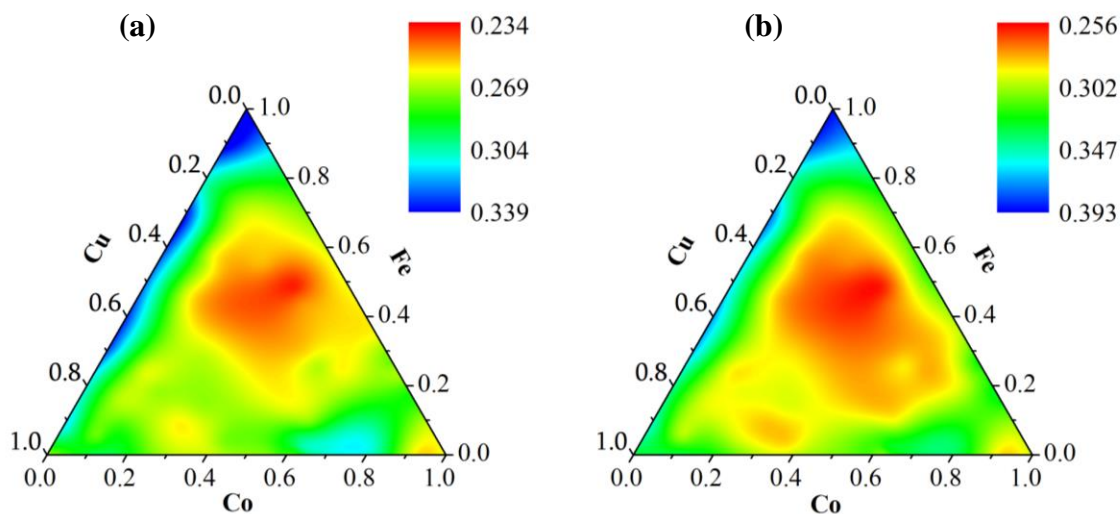


Figure 2. Trend of OER catalytic activity within the entire Fe–Co–Cu trigonal phase space. Mapping of overpotential  $\eta$  (in units of V) (a) at the onset of OER activity and (b) at a current density of 10 mA cm<sup>-2</sup>. These contour plots were created by using the actual relative atomic ratio of the elements as obtained from EDS. The color gradient represents the overpotential measured in volts.

Figure 3 indicates the LSV polarization curves of the six best performing quaternary mixed metal selenides measured in N<sub>2</sub>-saturated 1.0 M KOH at scan rate of 10 mV s<sup>-1</sup>. These six compounds showed excellent catalytic activity for the OER process. The onset  $\eta$  of (Fe<sub>0.09</sub>Co<sub>0.29</sub>Cu<sub>0.62</sub>)<sub>3</sub>Se<sub>2</sub> was 248 mV and it needed a  $\eta$  of 272 mV to reach a current density of 10 mA cm<sup>-2</sup>. The onset  $\eta$  and the  $\eta$  at 10 mA cm<sup>-2</sup> of (Fe<sub>0.25</sub>Co<sub>0.61</sub>Cu<sub>0.14</sub>)Se were 258 and 278 mV, respectively. The onset  $\eta$  of (Fe<sub>0.29</sub>Co<sub>0.51</sub>Cu<sub>0.2</sub>)Se was 256 mV and it generated a current density of 10 mA cm<sup>-2</sup> and a  $\eta$  of 278 mV. The onset  $\eta$  of (Fe<sub>0.44</sub>Co<sub>0.41</sub>Cu<sub>0.15</sub>)Se was 250 mV and required 271 mV to achieve a current density of 10 mA cm<sup>-2</sup>. The onset  $\eta$  and the  $\eta$  at 10 mA cm<sup>-2</sup> of (Fe<sub>0.55</sub>Co<sub>0.26</sub>Cu<sub>0.19</sub>)Se were 255 and 276 mV respectively. The thin film (Fe<sub>0.48</sub>Co<sub>0.38</sub>Cu<sub>0.14</sub>)Se displayed the best catalytic activity in this work, with an onset  $\eta$  of 235 mV and  $\eta$  of 256 mV at 10 mA cm<sup>-2</sup>. It is important to note that most of the quaternary compounds adopted the monoselenide *MSe* structure type except for the ones with high Cu concentration, which adopted the *M*<sub>3</sub>Se<sub>2</sub> structure type.

The Tafel slopes of all electrocatalysts were obtained, and the results are listed in Table S1. The Tafel plots ( $\eta$  vs log *j*) and slopes of the six best performing quaternary selenides are graphed in Figure 3b. The Tafel slopes of (Fe<sub>0.55</sub>Co<sub>0.26</sub>Cu<sub>0.19</sub>)Se, (Fe<sub>0.09</sub>Co<sub>0.29</sub>Cu<sub>0.62</sub>)<sub>3</sub>Se<sub>2</sub>, (Fe<sub>0.44</sub>Co<sub>0.41</sub>Cu<sub>0.15</sub>)Se, (Fe<sub>0.48</sub>Co<sub>0.38</sub>Cu<sub>0.14</sub>)Se, (Fe<sub>0.29</sub>Co<sub>0.51</sub>Cu<sub>0.2</sub>)Se, and (Fe<sub>0.25</sub>Co<sub>0.61</sub>Cu<sub>0.14</sub>)Se were 45.2, 59.5, 41.1, 40.8, 41.8, and 41.3 mV dec<sup>-1</sup>, respectively. Tafel slopes are closely related to the number of electrons involved in the rate determining step of the OER process. For the six quaternaries with small Tafel slopes, it is likely that the second electron transfer step of OER is the rate-determining step, suggesting that they have faster kinetics for oxygen evolution.<sup>7,70</sup> (Fe<sub>0.48</sub>Co<sub>0.38</sub>Cu<sub>0.14</sub>)Se showed the



lowest overpotential as well as the lowest Tafel slope, which further confirmed that it is indeed the best catalyst composition in this quaternary phase space.

Electrochemical double-layer capacitance of the  $(\text{Fe}_{0.48}\text{Co}_{0.38}\text{Cu}_{0.14})\text{Se}$  thin film was measured to estimate its ECSA. Double-layer charging current was measured in the non-Faradaic region at various scan rates using CVs. In this study,  $(\text{Fe}_{0.48}\text{Co}_{0.38}\text{Cu}_{0.14})\text{Se}$  thin film as the working electrode was suspended in  $\text{N}_2$ -saturated 1.0 M KOH and the CVs, found in Figure 4, were measured from  $-0.16$  to  $-0.05$  V vs Ag|AgCl (KCl saturated) at scan rates of 2.5 to 20  $\text{mV s}^{-1}$ . The ECSA was calculated using eq 4, and the value was estimated to be  $1.38 \text{ cm}^2$  with a roughness factor (RF) of 19.7. The high value of RF confirmed the highly granular surface of the film as seen in the SEM image of Figure 5b. Since rough surfaces allow for amplified contact of the electrolyte with the catalytically active sites, catalytic activity tends to increase with increasing surface roughness.

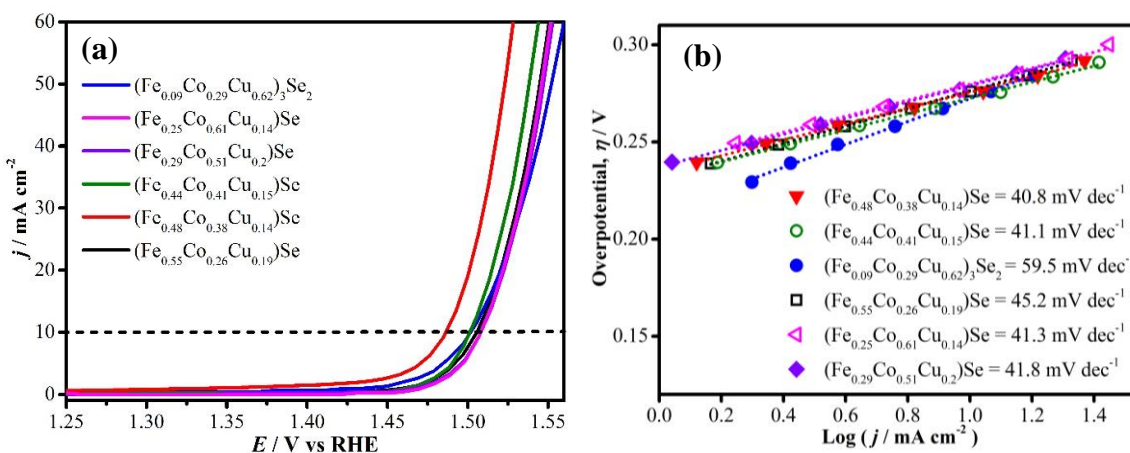


Figure 3. (a) OER activity of the six best quaternary compositions measured by conducting LSVs in  $\text{N}_2$ -saturated 1.0 M KOH solution at a scan rate of  $10 \text{ mV s}^{-1}$ . (b) Tafel plots of these catalysts.

The catalytic activity of the best performing quaternary ( $\text{Fe}_{0.48}\text{Co}_{0.38}\text{Cu}_{0.14}$ )Se was compared with those of CoSe, FeSe, and  $\text{Cu}_3\text{Se}_2$  in  $\text{N}_2$ -saturated 1.0 M KOH at a scan rate of  $10 \text{ mV s}^{-1}$  to understand the effect of transition metal doping on catalytic activity as shown in Figure 5a. The onset overpotentials of the binary selenides were 263, 346, and 270 mV for CoSe, FeSe, and  $\text{Cu}_3\text{Se}_2$ , respectively. To achieve an OER current density of  $10 \text{ mA cm}^{-2}$ , the overpotentials were 298, 393, and 330 mV for CoSe, FeSe and  $\text{Cu}_3\text{Se}_2$ , respectively. As a result of transition metal doping, the onset  $\eta$  and  $\eta$  at  $10 \text{ mA cm}^{-2}$  of ( $\text{Fe}_{0.48}\text{Co}_{0.38}\text{Cu}_{0.14}$ )Se were decreased to 235 and 256 mV respectively, which were lower than those of any of the binary selenides. The Tafel slope of ( $\text{Fe}_{0.48}\text{Co}_{0.38}\text{Cu}_{0.14}$ )Se ( $40.8 \text{ mV dec}^{-1}$ ) was also lower than those of CoSe ( $62.9 \text{ mV dec}^{-1}$ ), FeSe ( $103.5 \text{ mV dec}^{-1}$ ), and  $\text{Cu}_3\text{Se}_2$  ( $93.4 \text{ mV dec}^{-1}$ ) as shown in Table S1, suggesting the OER activity on the quaternary selenide surface is increased kinetic factors compared to that on the binaries. This can be attributed to transition metal doping, which increases the amount of actual catalytically active sites as well as influence the energetics of hydroxyl attachment, thereby facilitating the OER reaction rate.<sup>7,14,71-73</sup> The LSV curve of ( $\text{Fe}_{0.48}\text{Co}_{0.38}\text{Cu}_{0.14}$ )Se was also compared with the catalytic performance of the best ternary phases from each group, viz. ( $\text{Fe}_{0.78}\text{Cu}_{0.22}$ ) $_3\text{Se}_4$ , ( $\text{Co}_{0.93}\text{Cu}_{0.07}$ ) $_3\text{Se}_2$ , ( $\text{Co}_{0.9}\text{Fe}_{0.1}$ ) $_3\text{Se}_4$  shown in Figure S3. As can be seen, ( $\text{Fe}_{0.48}\text{Co}_{0.38}\text{Cu}_{0.14}$ )Se exhibited ameliorated OER activity compared to the best ternary composition ( $\text{Co}_{0.93}\text{Cu}_{0.07}$ ) $_3\text{Se}_2$  with a decrease in  $\eta$  at  $10 \text{ mA cm}^{-2}$  by 16 mV. Overall, the OER catalytic activity was decidedly enhanced in mixed metal selenides in terms of both overpotential and Tafel slope.

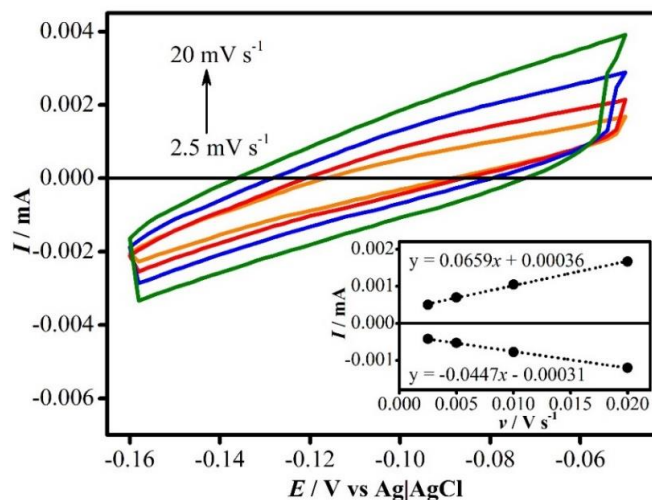


Figure 4. ECSA for the  $(\text{Fe}_{0.48}\text{Co}_{0.38}\text{Cu}_{0.14})\text{Se}$  thin film was measured by performing cyclic voltammograms in  $\text{N}_2$ -saturated 1.0 M KOH solution at different scan rates from 2.5 to  $20 \text{ mV s}^{-1}$ . The inset shows the plot of both anodic and cathodic currents measured at  $-0.10 \text{ V vs Ag|AgCl}$  (KCl saturated) as a function of scan rate.

The morphology and composition of the best performing quaternary selenide was further studied through surface analytical techniques. Detailed SEM imaging of the  $(\text{Fe}_{0.48}\text{Co}_{0.38}\text{Cu}_{0.14})\text{Se}$  film as shown in Figure 5b suggested that the morphology of the thin film surface was composed primarily of cauliflower-like microstructures with a wide size distribution of 0.5 to  $2.5 \mu\text{m}$ . XPS was carried out to further study the elemental composition and identify oxidation states of the constituent elements in  $(\text{Fe}_{0.48}\text{Co}_{0.38}\text{Cu}_{0.14})\text{Se}$  thin film. The XPS spectra of Fe 2p, Cu 2p, Co 2p, and Se 3d are shown in the Figure 5c-f. It should be noted that the binding energy in all XPS spectra have been calibrated with respect to the standard C 1s ( $284.5 \text{ eV}$ ) reference spectra. The spectrum of Fe 2p in Figure 5c showed peaks at  $708.45$  and  $722.27 \text{ eV}$  corresponding to  $\text{Fe}^{2+}$ , while peaks at  $710.26$  and  $724.75 \text{ eV}$  were assigned to  $\text{Fe}^{3+}$  with satellite peaks at  $716.08$  and  $730.57 \text{ eV}$ .<sup>74–76</sup> In the Cu 2p spectrum as shown in Figure 5d, peaks at  $930.32$

and 950.12 eV were attributed to  $\text{Cu}^+$ , and those at 932.16 and 952.23 eV corresponded to  $\text{Cu}^{2+}$  respectively. Peaks at 939.75 and 960.15 eV were assigned to the satellite peaks.<sup>77,78</sup> In the Co 2p spectrum shown in Figure 5e, peaks at 779.14 and 794.48 eV referred to  $\text{Co}^{2+}$ , and those at 783.80 and 800.61 eV corresponded to its satellite peaks, respectively.<sup>79,80</sup> In the Se 3d spectrum shown in Figure 5f, peaks at 55.24 and 56.22 eV were assigned to Se  $3d_{5/2}$  and Se  $3d_{3/2}$  respectively, while the big sharp peak around 59.0 eV was attributed to  $\text{SeO}_x$  which might be a result of the surface oxidation of selenide.<sup>81,82</sup> The deconvoluted spectra revealed that both Fe 2p and Cu 2p were mixed valence metal cations while Co 2p was present as only divalent ions. The XPS spectra also confirmed that the film composition was exclusively selenide with no indication of presence of other metal oxide/oxyhydroxide impurity.

The Faradaic efficiency of the electrodeposited  $(\text{Fe}_{0.48}\text{Co}_{0.38}\text{Cu}_{0.14})\text{Se}$  thin film for OER was assessed with the water displacement method,<sup>83</sup> and the measured quantity of  $\text{O}_2$  evolved was compared to the theoretical yield as shown in Figure 6. A Faradaic efficiency of nearly 100% was measured for this electrocatalyst. As mentioned above, transition metal doping is expected to influence electron density through an inductive effect around the catalytic centers, and hence will influence charge transport at the catalyst–electrolyte interface as well as through the catalyst composite. Electrochemical impedance spectroscopy (EIS) was executed on the best performing quaternary composition along with the three binary selenide films to examine the result of transition metal doping on the various charge transfer pathways. Figure 7 shows the Nyquist plots of the best-performance quaternary selenide,  $(\text{Fe}_{0.48}\text{Co}_{0.38}\text{Cu}_{0.14})\text{Se}$ , compared with those of three binary selenides ( $\text{FeSe}$ ,  $\text{CoSe}$  and  $\text{Cu}_3\text{Se}_2$ ), which were collected at an applied potential of 0.5 V vs  $\text{Ag|AgCl}$

(KCl saturated) in N<sub>2</sub>-saturated 1.0 M KOH solution. The Nyquist plots were fitted to an equivalent circuit as shown in inset of Figure 7, which included the electrolyte resistance ( $R_s$ ), interfacial electron charge transfer resistance ( $R_{ct}$ ), and the constant phase element of double layer ( $CPE_{dl}$ ). The values of these parameters are listed in Table 1. In the higher frequency region, the low value of  $R_s$  of *ca.* 5.0  $\Omega$  was attributed to the uncompensated solution resistance of 1.0 M KOH (Figure S4). Derived from the equivalent circuit, the charge transfer resistance ( $R_{ct}$ ) and constant phase element of double layer ( $CPE_{dl}$ ) were obtained in the lower-frequency region. The charge transfer resistance  $R_{ct}$  is related to the electron transfer across the electrode-electrolyte interface and hence represents the kinetics of the electrocatalysis and its value is inversely proportional to the reaction rate.<sup>84–86</sup> From Table 1, it can be seen that (Fe<sub>0.48</sub>Co<sub>0.38</sub>Cu<sub>0.14</sub>)Se showed the smallest  $R_{ct}$  value, indicating that, at the film–electrolyte interface, the charge transfer rate was kinetically faster for (Fe<sub>0.48</sub>Co<sub>0.38</sub>Cu<sub>0.14</sub>)Se than those of binaries (CoSe, Cu<sub>3</sub>Se<sub>2</sub>, and FeSe). Fast interfacial charge transfer leads to high catalytic efficiency of (Fe<sub>0.48</sub>Co<sub>0.38</sub>Cu<sub>0.14</sub>)Se by facilitating the rate of intermediate formation on the catalyst surface and decreasing the OER onset overpotential as a result.<sup>87,88</sup> Likewise, the catalytic activity can be influenced by the thin film resistance ( $R_f$ ) by enhancing electron transfer within the bulk of the catalyst composite, leading to an increased current density. It can be observed that (Fe<sub>0.48</sub>Co<sub>0.38</sub>Cu<sub>0.14</sub>)Se showed the smallest  $R_f$  value in comparison to those of three binaries in Table 1, indicating the quaternary selenide had an enhanced conductivity and helped the local electron transfer in the catalytic system. From these studies it is very apparent that transition metal doping improves surface electronic structure and thereby enhancing various charge transport pathways for OER catalytic activity.

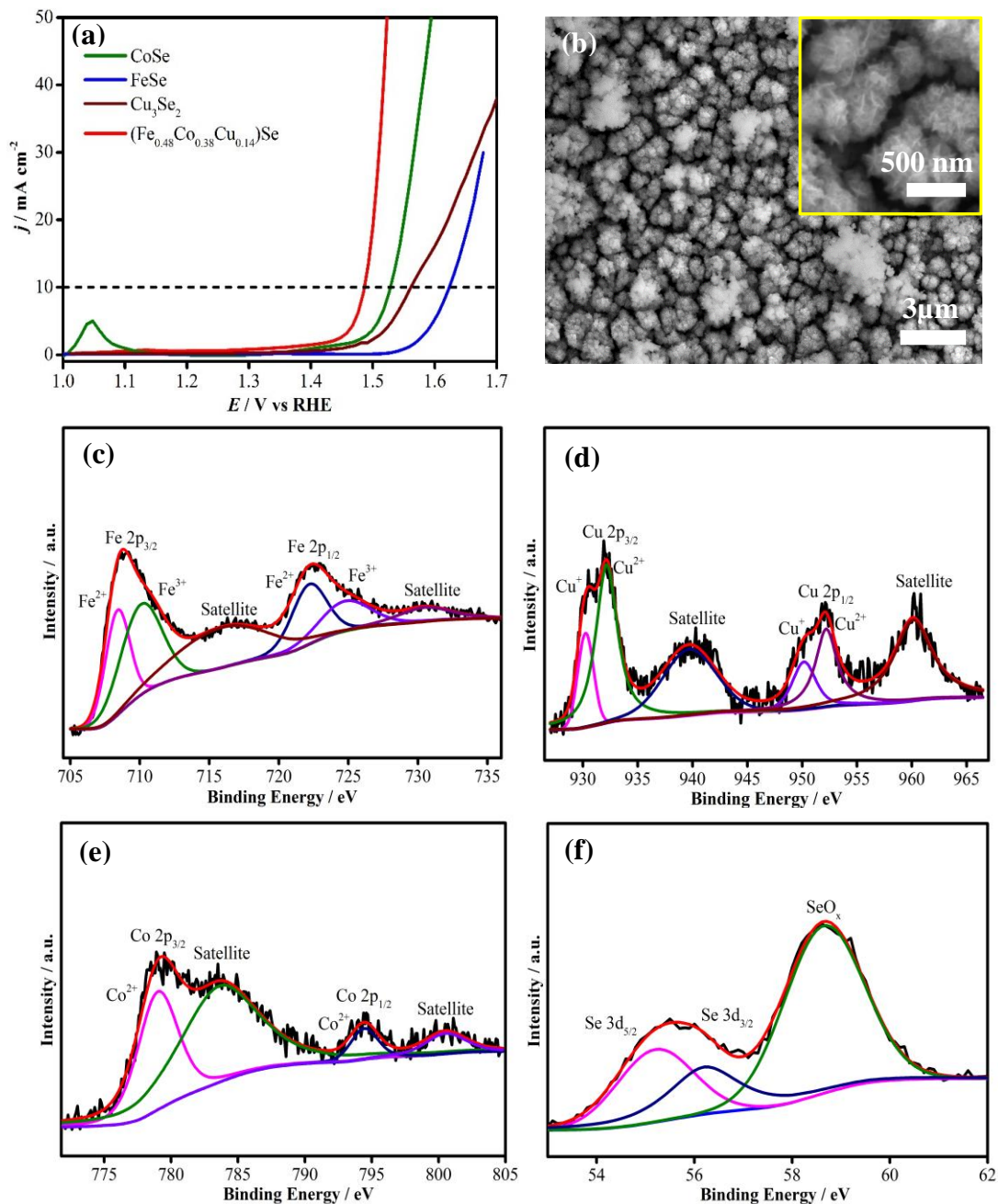


Figure 5. (a) Polarization curves of (Fe<sub>0.48</sub>Co<sub>0.38</sub>Cu<sub>0.14</sub>)Se compared with the three binary catalyst films. (b) SEM image of (Fe<sub>0.48</sub>Co<sub>0.38</sub>Cu<sub>0.14</sub>)Se film deposited for 300 s. (c) – (f) XPS spectra of the as-deposited (Fe<sub>0.48</sub>Co<sub>0.38</sub>Cu<sub>0.14</sub>)Se showing, (c) Fe 2p (d) Cu 2p (e) Co 2p and (f) Se 3d.

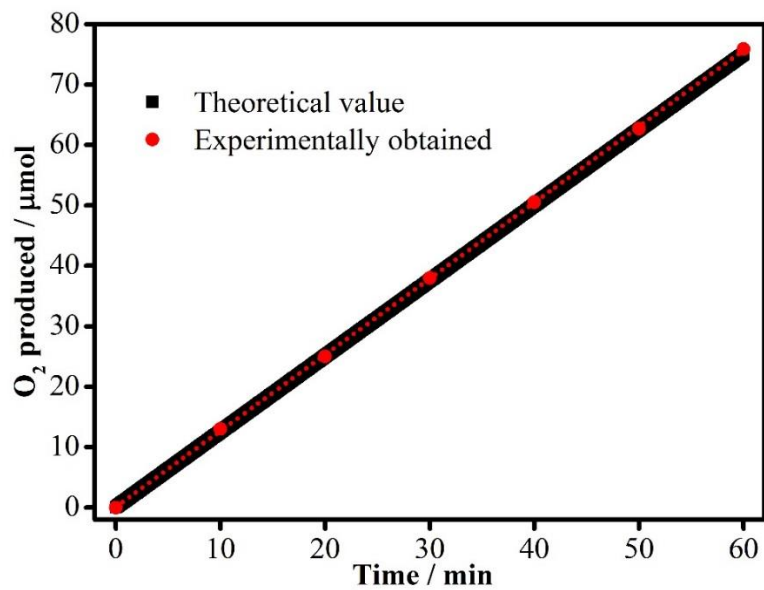


Figure 6. The amount of theoretically calculated oxygen (black dots) and experimentally measured oxygen (red dots) obtained for  $(\text{Fe}_{0.48}\text{Co}_{0.38}\text{Cu}_{0.14})\text{Se}$  versus time at 0.7 V vs Ag|AgCl (KCl saturated).

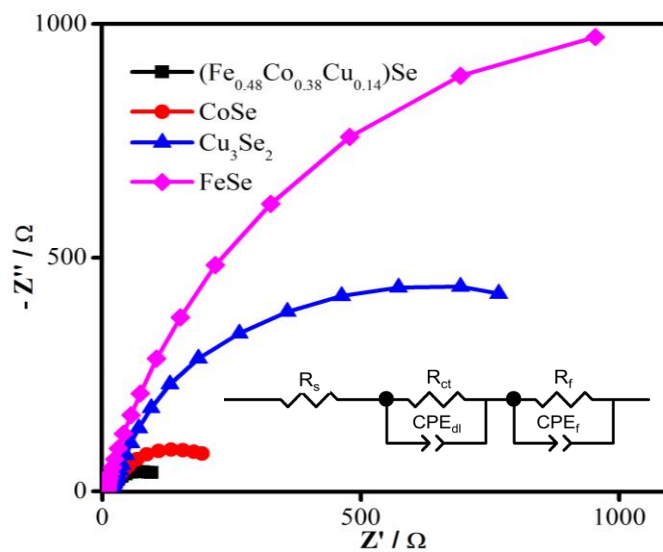


Figure 7. EIS measurements and the corresponding Nyquist plots for  $(\text{Fe}_{0.48}\text{Co}_{0.38}\text{Cu}_{0.14})\text{Se}$ , CoSe,  $\text{Cu}_3\text{Se}_2$  and FeSe catalysts obtained at an applied potential of 0.5 V vs Ag|AgCl (KCl saturated) in  $\text{N}_2$ -saturated 1.0 M KOH solution. Symbols indicate the raw data, while solid lines represent the corresponding fit to equivalent circuit model (inset).

Table 1. Equivalent circuit parameters obtained from fitting of EIS experimental data.

| Catalysts                         | $R_s/\Omega$ | $R_{ct}/\Omega$ | $CPE_{dl}/F$ | $R_f/\Omega$ | $CPE_f/F$ |
|-----------------------------------|--------------|-----------------|--------------|--------------|-----------|
| $(Fe_{0.48}Co_{0.38}Cu_{0.14})Se$ | 5.0          | 10.9            | 0.24         | 113.1        | 0.80      |
| CoSe                              | 5.0          | 13.2            | 0.30         | 248.9        | 0.83      |
| $Cu_3Se_2$                        | 5.0          | 18.4            | 0.48         | 1022.3       | 0.87      |
| FeSe                              | 5.0          | 291.9           | 0.75         | 2040.0       | 0.93      |

$R_s$  is the resistance of the electrolyte;  $R_{ct}$  is the electron transfer resistance;  $CPE_{dl}$  is the constant phase element of double-layer nonideal capacitance;  $R_f$  is resistance of the catalyst layer; and  $CPE_f$  is the capacitance.

The stability of any OER electrocatalyst is a critical factor to evaluate its potential in large-scale industrial application. Hence, the stability of  $(Fe_{0.48}Co_{0.38}Cu_{0.14})Se$  thin film under continuous oxygen evolution for extended period of time (18 h) was estimated through chronoamperometric study, as shown in the inset of Figure 8a. The chronoamperometric study was performed at a constant potential of 1.50 V vs RHE, where the thin film reached a current density of  $10 \text{ mA cm}^{-2}$  in 1.0 M KOH solution. It can be observed that  $(Fe_{0.48}Co_{0.38}Cu_{0.14})Se$  catalyst showed outstanding stability without any current density loss even after 18 h in the harsh alkaline medium. To confirm further the stability, the LSV of  $(Fe_{0.48}Co_{0.38}Cu_{0.14})Se$  was remeasured with chronoamperometry after 18 h and was compared with that of the as-deposited catalyst shown in Figure 8a, which revealed the quaternary selenide showed almost the same catalytic activity before and after stability study with similar onset potential and overpotential at  $10 \text{ mA cm}^{-2}$ . The SEM shown in Figure 8b exhibited that the surface morphology of  $(Fe_{0.48}Co_{0.38}Cu_{0.14})Se$  had been slightly modified by making the surface rougher possibly due to the evolution of large



amounts of O<sub>2</sub> on catalyst surface, resulting in the production of pores. The compositional stability of the catalyst after electrochemical measurement was corroborated using XPS spectra, shown in Figure 8c-f, which revealed that the catalyst was predominantly comprised of Fe, Co, Cu, and Se which were still in the mixed oxidation states. The XPS peak positions for Fe, Co, and Cu did not show any changes, indicating that the composition of the film was still selenide based. The comparison of EDS before and after chronoamperometry in Table S3 further demonstrated that the relative elemental ratio was preserved even after prolonged catalytic activity, signifying compositional stability of the catalyst.

Interestingly, while the ternary selenides adopt various nonstoichiometric compositions including  $M_3Se_4$ ,  $MSe$ , and  $M_3Se_2$  depending on the transition metal doping, the quaternary selenides are mostly forced to adopt the monoselenide,  $MSe$  type phase. The primary difference between the  $M_3Se_2$  and  $MSe$  structure type can be illustrated with  $Cu_3Se_2$  and  $CoSe$  as shown in Figure S5 in the Supporting Information. In  $Cu_3Se_2$ , the transition metal is tetrahedrally coordinated to 4 Se atoms, and the  $CuSe_4$  tetrahedra are linked further through edge sharing of the polyhedra.  $CoSe$  on the other hand represents the fully filled NiAs structure type containing octahedrally coordinated Co atoms, while the Se atoms show tetrahedral coordination. On doping in  $CoSe$  lattice, it can be expected that the transition metal dopant atoms will occupy the octahedral sites, while similar dopants in  $Cu_3Se_2$  will occupy the tetrahedral sites. From the trend in catalytic activity observed here, it is apparent that for Co and Fe, the transition metal in octahedral coordination shows better catalytic activity than that in tetrahedral coordination. It has been reported previously also that Fe in the octahedral site shows better enhancement of catalytic

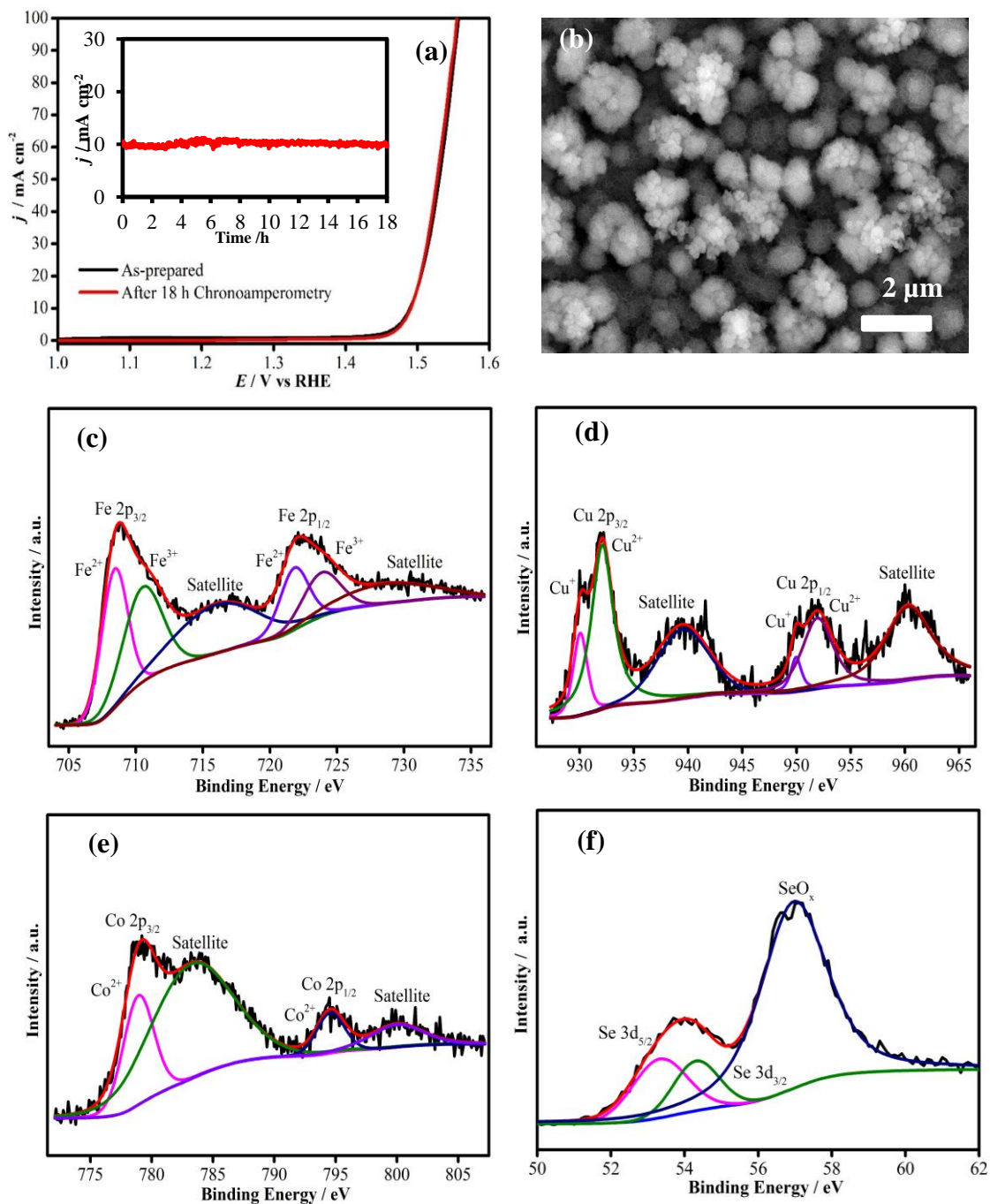


Figure 8. (a) Comparison of LSVs before and after 18 h in N<sub>2</sub>-saturated 1.0 M KOH solution. The inset is the chronoamperometry plot of  $(\text{Fe}_{0.48}\text{Co}_{0.38}\text{Cu}_{0.14})\text{Se}$  for 18 h at an applied potential of 1.50 V vs RHE. (b) SEM image of  $(\text{Fe}_{0.48}\text{Co}_{0.38}\text{Cu}_{0.14})\text{Se}$  after electrochemical measurements. (c–f) XPS spectra of  $(\text{Fe}_{0.48}\text{Co}_{0.38}\text{Cu}_{0.14})\text{Se}$  after chronoamperometry.

property.<sup>60,64,89</sup> Cu on the other hand shows better activity in tetrahedral coordination. Apart from influence of structure type and coordination geometry, other factors can also play a crucial role in determining the OER catalytic property. For example, it was reported by previous researchers that a catalyst surface containing anion vacancies and defects was favorable for the adsorption and desorption of hydroxyl species during the OER process, leading to small charge transfer resistance at the electrode–electrolyte interface and which further enhances the OER activity.<sup>90–92</sup> Hence, the structural defects might also play a crucial role in affecting the catalytic activity of these amorphous electrocatalysts reported in this article. However, to analyze comprehensively the role of structural defects on the OER catalytic activity, one needs to perform detailed DFT studies for each stoichiometry and related structure type. We have initiated such DFT studies and have recently observed that for one particular stoichiometry based on Cu–Co–Se, identified from this phase diagram, the structural defects on different lattice planes indeed has a significant influence on the OER catalytic activity. The results of these DFT studies will be published separately.

#### 4. CONCLUSIONS

The ternary phase space of Co–Fe–Cu has been successfully explored through combinatorial electrodeposition, which has identified the optimal doping compositions that yield maximum catalytic efficiency in this family of compounds. EDS characterization of all selenide films revealed the ability of compositional control through combinatorial electrodeposition as the relative elemental composition of the thin films were proportional to the corresponding precursor ratios in the electrolytes. A full investigation of OER kinetic parameters from sixty-six compounds revealed the trend of catalytic activity as follows: (i)

the catalytic activity is sensitive to the amount of transition metal dopants, and the presence of a relatively higher amount of Fe or Cu and a lower amount of Co leads to small overpotentials, while overpotentials tend to decrease at Fe concentration 30–70 %; (ii) quaternary selenides are more likely to show lower overpotentials as well as Tafel slopes than ternary and binary selenides indicating the inductive effect of heteroatoms plays a crucial role in influencing the catalytic activity; (iii) Co might still be better catalytic site, although Fe and Cu have a more positive influence on increasing its activity; (iv) the enhancement in catalytic activity is supported by improved charge transfer at the catalyst–electrolyte interface and within the catalyst composite. Specifically, the best composition in this work demonstrating promising catalytic activity has been identified as  $(\text{Fe}_{0.48}\text{Co}_{0.38}\text{Cu}_{0.14})\text{Se}$  thin film with a low onset overpotential and overpotential to attain a current density of  $10 \text{ mA cm}^{-2}$  of 235 and 256 mV respectively, in  $\text{N}_2$ -saturated 1.0 M KOH. This study proposes a new avenue for systematic study of mixed transition metal selenides as OER electrocatalysts employing combinatorial electrodeposition.

## ASSOCIATED CONTENT

### Author Information

### Corresponding Author

\* Email: nathm@mst.edu

### Author Contributions

All authors have given approval to the final version of the manuscript.

### Notes

The authors declare no competing financial interest.

Supporting Information. The Supporting Information includes trigonal phase diagram, LSV plots, summary table, EDS table before and after chronoamperometry, atomic percentage table and crystal structures. The Supporting Information is available free of charge on the ACS Publications website.

Acknowledgments. The authors would like to acknowledge financial support from National Science Foundation (DMR 1710313), American Chemical Society Petroleum Research Fund (54793-ND10), and Energy Research and Development Center (ERDC) Missouri S&T. The authors would also like to acknowledge Dr. Wenyan Liu for help with the ICP-AES measurements and Materials Research Center (MRC) for equipment usage.

## SUPPORTING INFORMATION

### **EXPANDING MULTINARY SELENIDE BASED HIGH-EFFICIENCY OXYGEN EVOLUTION ELECTROCATALYSTS THROUGH COMBINATORIAL ELECTRODEPOSITION: CASE STUDY WITH Fe-Cu-Co SELENIDES**

Xi Cao<sup>a</sup>, Emily Johnson<sup>b</sup> and Manashi Nath<sup>a\*</sup>

<sup>a</sup>Department of Chemistry, Missouri University of Science & Technology, Rolla, Missouri 65409, United States.

<sup>b</sup>Department of Chemical and Biochemical Engineering, Missouri University of Science & Technology, Rolla, Missouri 65409, United States.

\*Email: [nathm@mst.edu](mailto:nathm@mst.edu)

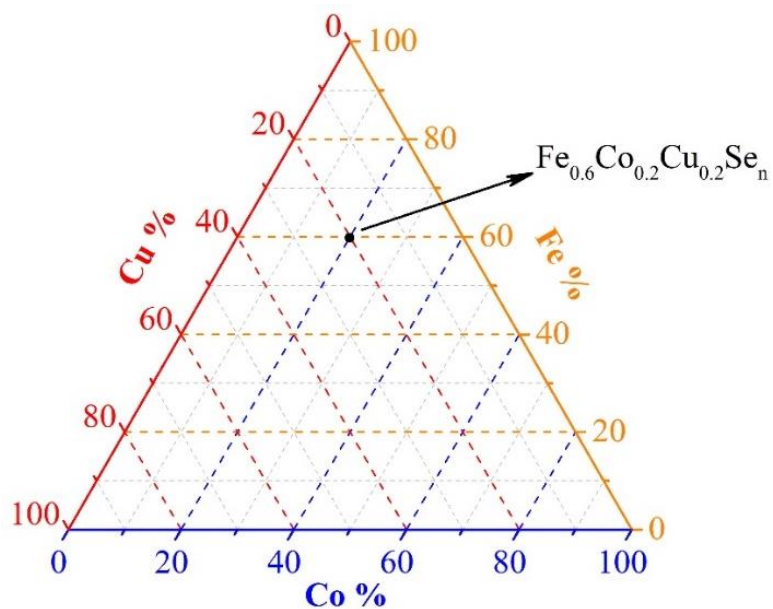


Figure S1. Trigonal phase diagram for exploring compositions of the mixed-metal (Fe, Co, Cu) selenide films examined in this work. Crossing vertices represent compositions of the precursor electrolyte with respect to the relative ratio of the corresponding metals. The black circle shows a typical example.

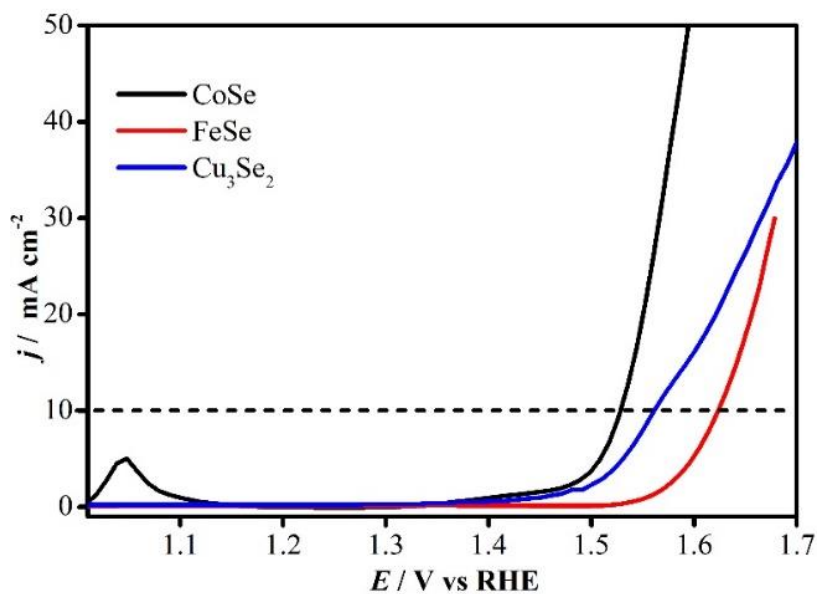


Figure S2. Polarization curves of three binary selenides.

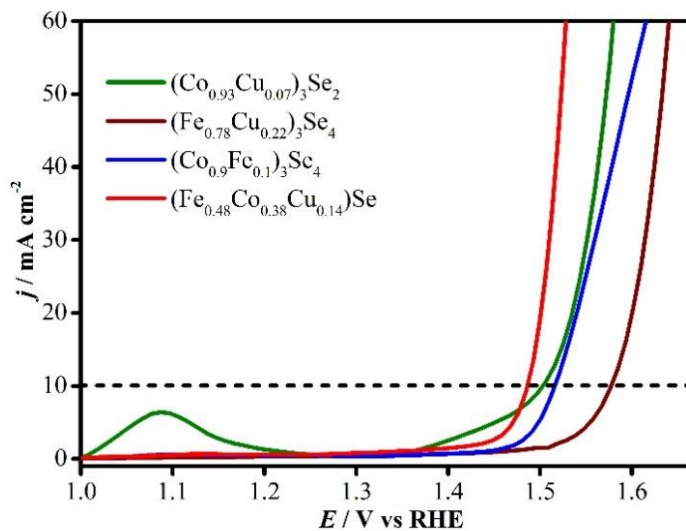


Figure S3. Linear sweep voltammies (LSVs) measured for selected catalysts in  $N_2$ -saturated 1.0 M KOH solution at a scan rate of  $10 \text{ mV s}^{-1}$ . The black dashed line shows the current density of  $10 \text{ mA cm}^{-2}$ .

Table S1. Summary of elemental analysis of metal selenide films determined by EDS and corresponding kinetic parameters extracted from polarization curves.

| Precursor Molar Ratio (mM) |    |    |    | Average atomic % (EDS) |      |      |      | Onset $\eta$ | $\eta_{10\text{mA}}$ | Tafel |
|----------------------------|----|----|----|------------------------|------|------|------|--------------|----------------------|-------|
| Co                         | Fe | Cu | Se | Co                     | Fe   | Cu   | Se   | (V)          | $\text{cm}^{-2}$ (V) | Slope |
| 10                         | -  | -  | 10 | 49.6                   | -    | -    | 50.4 | 0.263        | 0.298                | 62.9  |
| -                          | 10 | -  | 10 | -                      | 49.7 | -    | 50.3 | 0.346        | 0.393                | 103.5 |
| -                          | -  | 10 | 10 | -                      | -    | 63.8 | 36.2 | 0.270        | 0.330                | 93.4  |
| 1                          | 9  | -  | 10 | 11.2                   | 55.5 | -    | 33.3 | 0.293        | 0.338                | 56.6  |
| 2                          | 8  | -  | 10 | 14.7                   | 29.5 | -    | 55.8 | 0.271        | 0.313                | 91.6  |
| 3                          | 7  | -  | 10 | 20.0                   | 22.2 | -    | 57.8 | 0.263        | 0.32                 | 69.9  |
| 4                          | 6  | -  | 10 | 31.4                   | 13.1 | -    | 55.5 | 0.275        | 0.315                | 79.3  |
| 5                          | 5  | -  | 10 | 27.4                   | 14.7 | -    | 57.9 | 0.260        | 0.3                  | 58.6  |
| 6                          | 4  | -  | 10 | 29.1                   | 9.0  | -    | 61.8 | 0.264        | 0.316                | 63.2  |
| 7                          | 3  | -  | 10 | 34.6                   | 12.6 | -    | 52.9 | 0.279        | 0.333                | 91.7  |
| 8                          | 2  | -  | 10 | 38.8                   | 8.4  | -    | 52.8 | 0.288        | 0.332                | 79.7  |
| 9                          | 1  | -  | 10 | 40.3                   | 4.4  | -    | 55.3 | 0.257        | 0.295                | 57.6  |
| -                          | 9  | 1  | 10 | -                      | 39.9 | 4.0  | 56.1 | 0.349        | 0.388                | 67.9  |
| -                          | 8  | 2  | 10 | -                      | 35.5 | 10.0 | 54.6 | 0.307        | 0.347                | 86.4  |
| -                          | 7  | 3  | 10 | -                      | 33.3 | 16.4 | 50.3 | 0.341        | 0.379                | 64.0  |

Table S1. Summary of elemental analysis of metal selenide films determined by EDS and corresponding kinetic parameters extracted from polarization curves. (cont.)

|   |   |   |    |      |      |      |      |       |       |       |
|---|---|---|----|------|------|------|------|-------|-------|-------|
| - | 6 | 4 | 10 | -    | 35.5 | 14.6 | 49.9 | 0.337 | 0.374 | 65.7  |
| - | 5 | 5 | 10 | -    | 29.0 | 20.4 | 50.7 | 0.331 | 0.367 | 63.8  |
| - | 4 | 6 | 10 | -    | 20.8 | 30.7 | 48.5 | 0.338 | 0.376 | 73.5  |
| - | 3 | 7 | 10 | -    | 16.6 | 35.1 | 48.3 | 0.327 | 0.361 | 58.9  |
| - | 2 | 8 | 10 | -    | 10.9 | 42.0 | 48.2 | 0.342 | 0.381 | 77.6  |
| - | 1 | 9 | 10 | -    | 5.3  | 55.8 | 38.9 | 0.320 | 0.356 | 68.5  |
| 1 | - | 9 | 10 | 7.2  | -    | 53.8 | 39.1 | 0.297 | 0.337 | 84.4  |
| 2 | - | 8 | 10 | 13.1 | -    | 50.9 | 36.1 | 0.288 | 0.325 | 71.0  |
| 3 | - | 7 | 10 | 17.9 | -    | 46.0 | 36.1 | 0.272 | 0.308 | 81.1  |
| 4 | - | 6 | 10 | 24.8 | -    | 39.9 | 35.3 | 0.258 | 0.296 | 92.0  |
| 5 | - | 5 | 10 | 26.6 | -    | 39.3 | 34.1 | 0.263 | 0.301 | 73.3  |
| 6 | - | 4 | 10 | 40.0 | -    | 30.4 | 29.5 | 0.272 | 0.311 | 74.9  |
| 7 | - | 3 | 10 | 36.3 | -    | 25.9 | 37.8 | 0.288 | 0.325 | 60.5  |
| 8 | - | 2 | 10 | 37.0 | -    | 21.9 | 41.0 | 0.257 | 0.291 | 84.7  |
| 9 | - | 1 | 10 | 51.3 | -    | 3.8  | 45.0 | 0.235 | 0.272 | 106.9 |
| 1 | 1 | 8 | 10 | 6.2  | 3.4  | 51.9 | 38.5 | 0.265 | 0.288 | 60.6  |
| 1 | 2 | 7 | 10 | 4.5  | 6.3  | 45.2 | 43.9 | 0.275 | 0.3   | 57.6  |
| 1 | 3 | 6 | 10 | 5.3  | 8.9  | 40.4 | 45.4 | 0.267 | 0.295 | 57.4  |
| 1 | 4 | 5 | 10 | 6.7  | 12.3 | 32.1 | 48.9 | 0.261 | 0.286 | 43.8  |
| 1 | 5 | 4 | 10 | 5.9  | 22.0 | 20.0 | 52.2 | 0.261 | 0.286 | 43.2  |
| 1 | 6 | 3 | 10 | 6.0  | 25.7 | 15.7 | 52.6 | 0.269 | 0.29  | 44.1  |
| 1 | 7 | 2 | 10 | 6.3  | 28.8 | 14.7 | 50.3 | 0.261 | 0.285 | 48.3  |
| 1 | 8 | 1 | 10 | 6.0  | 31.3 | 7.1  | 55.7 | 0.267 | 0.295 | 45.1  |
| 2 | 1 | 7 | 10 | 6.9  | 3.2  | 49.1 | 41.0 | 0.289 | 0.313 | 60.7  |
| 2 | 2 | 6 | 10 | 8.1  | 4.4  | 44.5 | 43.0 | 0.285 | 0.306 | 56.7  |
| 2 | 3 | 5 | 10 | 10.0 | 10.2 | 34.7 | 45.1 | 0.273 | 0.295 | 77.9  |
| 2 | 4 | 4 | 10 | 13.7 | 15.6 | 25.0 | 45.7 | 0.268 | 0.289 | 43.3  |
| 2 | 5 | 3 | 10 | 12.8 | 25.7 | 17.3 | 44.2 | 0.245 | 0.267 | 51.0  |
| 2 | 6 | 2 | 10 | 13.4 | 27.8 | 9.3  | 49.6 | 0.255 | 0.276 | 45.2  |
| 2 | 7 | 1 | 10 | 17.0 | 31.3 | 9.1  | 42.6 | 0.269 | 0.291 | 54.1  |
| 3 | 1 | 6 | 10 | 14.5 | 2.5  | 43.8 | 39.2 | 0.272 | 0.297 | 50.2  |
| 3 | 2 | 5 | 10 | 17.1 | 5.4  | 36.3 | 41.3 | 0.248 | 0.272 | 59.5  |
| 3 | 3 | 4 | 10 | 16.0 | 6.8  | 27.3 | 49.9 | 0.272 | 0.296 | 41.7  |
| 3 | 4 | 3 | 10 | 17.3 | 15.3 | 21.4 | 46.0 | 0.26  | 0.281 | 42.6  |
| 3 | 5 | 2 | 10 | 22.4 | 23.8 | 7.7  | 46.2 | 0.25  | 0.271 | 41.1  |



Table S1. Summary of elemental analysis of metal selenide films determined by EDS and corresponding kinetic parameters extracted from polarization curves. (cont.)

|   |   |   |    |      |      |      |      |       |       |      |
|---|---|---|----|------|------|------|------|-------|-------|------|
| 3 | 6 | 1 | 10 | 18.5 | 23.7 | 6.6  | 51.2 | 0.235 | 0.256 | 40.8 |
| 4 | 1 | 5 | 10 | 22.9 | 2.1  | 36.2 | 38.8 | 0.263 | 0.283 | 57.8 |
| 4 | 2 | 4 | 10 | 20.6 | 4.9  | 29.0 | 45.5 | 0.268 | 0.289 | 49.2 |
| 4 | 3 | 3 | 10 | 24.1 | 9.5  | 20.1 | 46.3 | 0.262 | 0.282 | 44.0 |
| 4 | 4 | 2 | 10 | 25.4 | 14.8 | 10.2 | 49.6 | 0.256 | 0.278 | 41.8 |
| 4 | 5 | 1 | 10 | 25.6 | 15.2 | 4.6  | 54.6 | 0.259 | 0.28  | 41.4 |
| 5 | 1 | 4 | 10 | 26.0 | 2.6  | 32.6 | 38.9 | 0.277 | 0.296 | 53.0 |
| 5 | 2 | 3 | 10 | 31.1 | 7.7  | 19.5 | 41.8 | 0.263 | 0.283 | 40.6 |
| 5 | 3 | 2 | 10 | 31.5 | 14.7 | 10.8 | 43.0 | 0.272 | 0.292 | 41.4 |
| 5 | 4 | 1 | 10 | 32.3 | 13.1 | 7.7  | 46.9 | 0.258 | 0.278 | 41.3 |
| 6 | 1 | 3 | 10 | 31.8 | 3.4  | 18.6 | 46.2 | 0.292 | 0.313 | 46.1 |
| 6 | 2 | 2 | 10 | 33.1 | 4.8  | 16.3 | 45.8 | 0.272 | 0.292 | 43.7 |
| 6 | 3 | 1 | 10 | 37.4 | 10.8 | 3.7  | 48.2 | 0.273 | 0.294 | 45.0 |
| 7 | 1 | 2 | 10 | 40.3 | 1.0  | 22.3 | 36.4 | 0.316 | 0.34  | 64.8 |
| 7 | 2 | 1 | 10 | 42.2 | 2.4  | 13.9 | 41.5 | 0.312 | 0.337 | 61.7 |
| 8 | 1 | 1 | 10 | 53.1 | 1.5  | 11.1 | 34.3 | 0.31  | 0.337 | 57.6 |

Table S2. The precursor ratio of compounds shown in the plots and their corresponding formulae by EDS atomic ratio.

| Precursor ratio |           |                                                                       | Molecular formula from EDS atomic ratio                               |
|-----------------|-----------|-----------------------------------------------------------------------|-----------------------------------------------------------------------|
| Co              | Fe        | Cu                                                                    |                                                                       |
| 10              |           |                                                                       | CoSe                                                                  |
|                 | 10        |                                                                       | FeSe                                                                  |
|                 |           | 10                                                                    | Cu <sub>3</sub> Se <sub>2</sub>                                       |
| Co-Cu Group     | <b>Co</b> | <b>Cu</b>                                                             |                                                                       |
|                 | 1         | 9                                                                     | (Co <sub>0.12</sub> Cu <sub>0.88</sub> ) <sub>3</sub> Se <sub>2</sub> |
|                 | 2         | 8                                                                     | (Co <sub>0.2</sub> Cu <sub>0.8</sub> ) <sub>3</sub> Se <sub>2</sub>   |
|                 | 3         | 7                                                                     | (Co <sub>0.28</sub> Cu <sub>0.72</sub> ) <sub>3</sub> Se <sub>2</sub> |
|                 | 4         | 6                                                                     | (Co <sub>0.38</sub> Cu <sub>0.62</sub> ) <sub>3</sub> Se <sub>2</sub> |
|                 | 5         | 5                                                                     | (Co <sub>0.4</sub> Cu <sub>0.6</sub> ) <sub>3</sub> Se <sub>2</sub>   |
|                 | 6         | 4                                                                     | (Co <sub>0.57</sub> Cu <sub>0.43</sub> ) <sub>3</sub> Se <sub>2</sub> |
|                 | 7         | 3                                                                     | (Co <sub>0.58</sub> Cu <sub>0.42</sub> ) <sub>3</sub> Se <sub>2</sub> |
|                 | 8         | 2                                                                     | (Co <sub>0.63</sub> Cu <sub>0.37</sub> ) <sub>3</sub> Se <sub>2</sub> |
| 9               | 1         | (Co <sub>0.93</sub> Cu <sub>0.07</sub> ) <sub>3</sub> Se <sub>2</sub> |                                                                       |

Table S2. The precursor ratio of compounds shown in the plots and their corresponding formulae by EDS atomic ratio. (cont.)

|                |           |           |                                                                   |
|----------------|-----------|-----------|-------------------------------------------------------------------|
| Co-Fe<br>Group | <b>Fe</b> | <b>Co</b> |                                                                   |
|                | 8         | 2         | $(\text{Co}_{0.33}\text{Fe}_{0.67})_3\text{Se}_4$                 |
|                | 7         | 3         | $(\text{Co}_{0.47}\text{Fe}_{0.53})_3\text{Se}_4$                 |
|                | 6         | 4         | $(\text{Co}_{0.7}\text{Fe}_{0.3})_3\text{Se}_4$                   |
|                | 5         | 5         | $(\text{Co}_{0.65}\text{Fe}_{0.35})_3\text{Se}_4$                 |
|                | 4         | 6         | $(\text{Co}_{0.76}\text{Fe}_{0.24})_3\text{Se}_4$                 |
|                | 1         | 9         | $(\text{Co}_{0.90}\text{Fe}_{0.10})_3\text{Se}_4$                 |
| Fe-Cu<br>Group | <b>Fe</b> | <b>Cu</b> |                                                                   |
|                | 9         | 1         | $(\text{Fe}_{0.91}\text{Cu}_{0.09})_3\text{Se}_4$                 |
|                | 8         | 2         | $(\text{Fe}_{0.78}\text{Cu}_{0.22})_3\text{Se}_4$                 |
|                | 7         | 3         | $(\text{Fe}_{0.67}\text{Cu}_{0.33})\text{Se}$                     |
|                | 6         | 4         | $(\text{Fe}_{0.71}\text{Cu}_{0.29})\text{Se}$                     |
|                | 5         | 5         | $(\text{Fe}_{0.59}\text{Cu}_{0.41})\text{Se}$                     |
|                | 4         | 6         | $(\text{Fe}_{0.4}\text{Cu}_{0.6})\text{Se}$                       |
|                | 3         | 7         | $(\text{Fe}_{0.32}\text{Cu}_{0.68})\text{Se}$                     |
|                | 2         | 8         | $(\text{Fe}_{0.21}\text{Cu}_{0.79})\text{Se}$                     |
|                | 1         | 9         | $(\text{Fe}_{0.09}\text{Cu}_{0.91})_3\text{Se}_2$                 |
| <b>Co</b>      | <b>Fe</b> | <b>Cu</b> |                                                                   |
| 2              | 6         | 2         | $(\text{Fe}_{0.55}\text{Co}_{0.26}\text{Cu}_{0.18})\text{Se}$     |
| 3              | 2         | 5         | $(\text{Fe}_{0.09}\text{Co}_{0.29}\text{Cu}_{0.62})_3\text{Se}_2$ |
| 3              | 5         | 2         | $(\text{Fe}_{0.44}\text{Co}_{0.41}\text{Cu}_{0.15})\text{Se}$     |
| 3              | 6         | 1         | $(\text{Fe}_{0.48}\text{Co}_{0.38}\text{Cu}_{0.14})\text{Se}$     |
| 4              | 4         | 2         | $(\text{Fe}_{0.29}\text{Co}_{0.58}\text{Cu}_{0.13})\text{Se}$     |
| 5              | 4         | 1         | $(\text{Fe}_{0.25}\text{Co}_{0.61}\text{Cu}_{0.14})\text{Se}$     |

Table S3. Comparison of EDS atomic ratio of  $(\text{Fe}_{0.48}\text{Co}_{0.38}\text{Cu}_{0.14})\text{Se}$  before and after electrochemical measurement.

|                       | EDS (Atomic %) |      |     |      |
|-----------------------|----------------|------|-----|------|
|                       | Co             | Fe   | Cu  | Se   |
| <b>As-deposited</b>   | 18.5           | 23.7 | 6.6 | 51.2 |
| <b>After activity</b> | 17.3           | 24.5 | 9.5 | 48.7 |

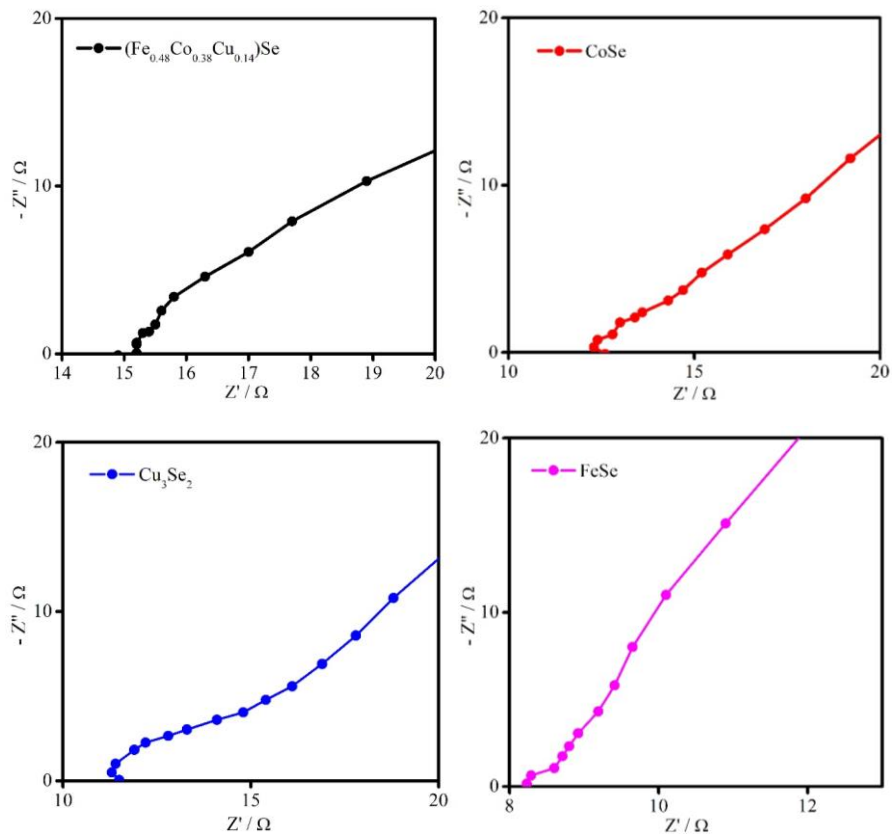


Figure S4. Zoomed-in Nyquist Plots of  $(\text{Fe}_{0.48}\text{Co}_{0.38}\text{Cu}_{0.14})\text{Se}$  (a),  $\text{CoSe}$  (b),  $\text{Cu}_3\text{Se}_2$  (c) and  $\text{FeSe}$  (d).

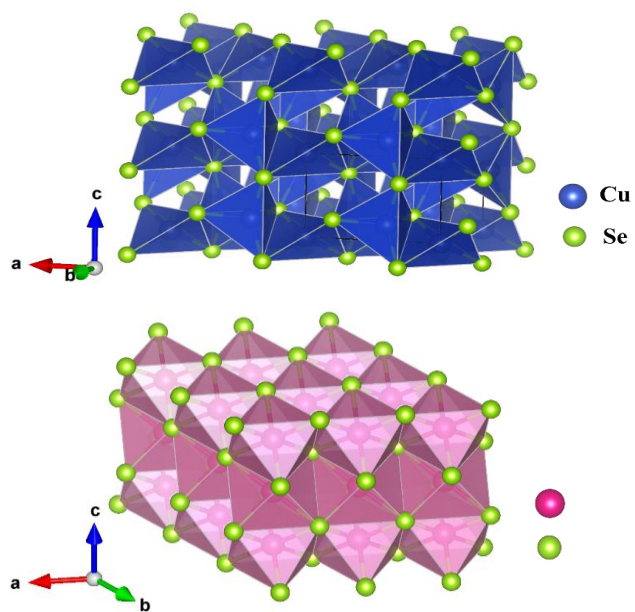


Figure S5. Crystal structure of  $\text{Cu}_3\text{Se}_2$  (a) and  $\text{CoSe}$  (b).

## REFERENCES

- (1) Chow, J.; Kopp, R. J.; Portney, P. R. Energy Resources and Global Development. *Science* **2003**, *302*, 1528–1531.
- (2) Turner, J. A. Sustainable Hydrogen Production. *Science* **2004**, *305*, 972–974.
- (3) Dresselhaus, M. S.; Thomas, I. L. Alternative Energy Technologies. *Nature* **2001**, *414*, 332–337.
- (4) Lewis, N. S. Toward Cost-Effective Solar Energy Use. *Science* **2007**, *315*, 798–801.
- (5) Walter, M. G.; Warren, E. L.; Mckone, J. R.; Boettcher, S. W.; Mi, Q.; Santori, E. A.; Lewis, N. S. Solar Water Splitting Cells. *Chem. Rev.* **2010**, *110*, 6446–6473.
- (6) Rossmeisl, J.; Logadottir, A.; Nørskov, J. K. Electrolysis of Water on (Oxidized) Metal Surfaces. *Chem. Phys.* **2005**, *319*, 178–184.
- (7) Suen, N.-T.; Hung, S.-F.; Quan, Q.; Zhang, N.; Xu, Y.-J.; Chen, H. M. Electrocatalysis for the Oxygen Evolution Reaction: Recent Development and Future Perspectives. *Chem. Soc. Rev.* **2017**, *46*, 337–365
- (8) Dau, H.; Limberg, C.; Reier, T.; Risch, M.; Roggan, S.; Strasser, P. The Mechanism of Water Oxidation: From Electrolysis via Homogeneous to Biological Catalysis. *ChemCatChem* **2010**, *2*, 724–761.
- (9) Yan, Y.; Xia, B. Y.; Zhao B.; Wang, X. A Review on Noble-Metal-Free Bifunctional Heterogeneous Catalysts for Overall Electrochemical Water Splitting. *J. Mater. Chem. A* **2016**, *4*, 17587–17603.
- (10) Görlin, Y.; Jaramillo, T. F. A Bifunctional Nonprecious Metal Catalyst for Oxygen Reduction and Water Oxidation. *J. Am. Chem. Soc.* **2010**, *132*, 13612–13614.
- (11) Chen, Q.; Switzer, J. A. Photoelectrochemistry of Ultrathin, Semitransparent, and Catalytic Gold Films Electrodeposited Epitaxially onto n-Silicon (111). *ACS Appl. Mater. Interfaces* **2018**, *10*, 21365–21371.
- (12) Mahenderkar, N. K.; Chen, Q.; Liu, Y. C.; Duchild, A. R.; Hofheins, S.; Chason, E.; Switzer, J. A. Epitaxial Lift-off of Electrodeposited Single-Crystal Gold Foils for Flexible Electronics. *Science* **2017**, *355*, 1203–1206.
- (13) Wang, H.; Lee, H.; Deng, Y.; Lu, Z.; Hsu, P.; Liu, Y.; Lin, D.; Cui, Y. Bifunctional Non-Noble Metal Oxide Nanoparticle Electrocatalysts through Lithium-Induced Conversion for Overall Water Splitting. *Nat. Commun.* **2015**, *6*, 7261.

- (14) Suntivich, J.; May, K. J.; Gasteiger, H. A.; Goodenough, J. B.; Shao-Horn, Y. A Perovskite Oxide Optimized for Oxygen Evolution Catalysis from Molecular Orbital Principles. *Science* **2011**, *334*, 1383–1385.
- (15) Over, H. Surface Chemistry of Ruthenium Dioxide in Heterogeneous Catalysis and Electrocatalysis: From Fundamental to Applied Research. *Chem. Rev.* **2012**, *112*, 3356–3426.
- (16) Reier, T.; Teschner, D.; Lunkenbein, T.; Bergmann, A.; Selve, S.; Kraehnert, R.; Schlogl, R.; Strasser, P. Electrocatalytic Oxygen Evolution on Iridium Oxide: Uncovering Catalyst-Substrate Interactions and Active Iridium Oxide Species. *J. Electrochem. Soc.* **2014**, *161*, 876–882.
- (17) McCrory, C. C. L.; Jung, S.; Peters, J. C.; Jaramillo, T. F. Benchmarking Heterogeneous Electrocatalysts for the Oxygen Evolution Reaction. *J. Am. Chem. Soc.* **2013**, *135*, 16977–16987.
- (18) Gao, X.; Zhang, H.; Li, Q.; Yu, X.; Hong, Z.; Zhang, X.; Liang, C.; Lin, Z. Hierarchical NiCo<sub>2</sub>O<sub>4</sub> Hollow Microcuboids as Bifunctional Electrocatalysts for Overall Water-Splitting. *Angew. Chem. Int. Ed.* **2016**, *55*, 6290–6294.
- (19) Görlin, M.; Chernev, P.; De Araújo, J. F.; Reier, T.; Dresch, S.; Paul, B.; Krähnert, R.; Dau, H.; Strasser, P. Oxygen Evolution Reaction Dynamics, Faradaic Charge Efficiency, and the Active Metal Redox States of Ni-Fe Oxide Water Splitting Electrocatalysts. *J. Am. Chem. Soc.* **2016**, *138*, 5603–5614.
- (20) Chen, Q.; Switzer, J. A. Electrodeposition of Nanometer-Thick Epitaxial Films of Silver onto Single-Crystal Silicon Wafers. *J. Mater. Chem. C* **2019**, *7*, 1720–1725
- (21) Gong, M.; Li, Y.; Wang, H.; Liang, Y.; Wu, J. Z.; Zhou, J.; Wang, J.; Regier, T.; Wei, F.; Dai, H. An Advanced Ni-Fe Layered Double Hydroxide Electrocatalyst for Water Oxidation. *J. Am. Chem. Soc.* **2013**, *135*, 8452–8455.
- (22) Kuang, M.; Han, P.; Wang, Q.; Li, J.; Zheng, G. CuCo Hybrid Oxides as Bifunctional Electrocatalyst for Efficient Water Splitting. *Adv. Funct. Mater.* **2016**, *26*, 8555–8561.
- (23) Chemelewski, W. D.; Lee, H. C.; Lin, J. F.; Bard, A. J.; Mullins, C. B. Amorphous FeOOH Oxygen Evolution Reaction Catalyst for Photoelectrochemical Water Splitting. *J. Am. Chem. Soc.*, **2014**, *136*, 2843–2850.
- (24) Deng, X.; Tüysüz, H. Cobalt-Oxide-Based Materials as Water Oxidation Catalyst: Recent Progress and Challenges. *ACS Catal.* **2014**, *4*, 3701–3714.
- (25) Anantharaj, S.; Ede, S. R.; Sakthikumar, K.; Karthick, K.; Mishra, S.; Kundu, S. Recent Trends and Perspectives in Electrochemical Water Splitting with an Emphasis on Sulfide, Selenide, and Phosphide Catalysts of Fe, Co, and Ni: A Review. *ACS Catal.* **2016**, *6*, 8069–8097.

- (26) Swesi, A. T.; Masud, J.; Nath, M. Nickel Selenide as a High-Efficiency Catalyst for Oxygen Evolution Reaction. *Energy Environ. Sci.* **2016**, *9*, 1771–1782.
- (27) Tang, C.; Cheng, N.; Pu, Z.; Xing, W.; Sun, X. NiSe Nanowire Film Supported on Nickel Foam: An Efficient and Stable 3D Bifunctional Electrode for Full Water Splitting. *Angew. Chem. Int. Ed.* **2015**, *54*, 9351–9355.
- (28) Kwak, I. H.; Im, H. S.; Jang, D. M.; Kim, Y. W.; Park, K.; Lim, Y. R.; Cha, E. H.; Park, J. CoSe<sub>2</sub> and NiSe<sub>2</sub> Nanocrystals as Superior Bifunctional Catalysts for Electrochemical and Photoelectrochemical Water Splitting. *ACS Appl. Mater. Interfaces* **2016**, *8*, 5327–5334.
- (29) Li, W.; Gao, X.; Xiong, D.; Wei, F.; Song, W. G.; Xu, J.; Liu, L. Hydrothermal Synthesis of Monolithic Co<sub>3</sub>Se<sub>4</sub> Nanowire Electrodes for Oxygen Evolution and Overall Water Splitting with High Efficiency and Extraordinary Catalytic Stability. *Adv. Energy Mater.* **2017**, *7*, 1602579.
- (30) De Silva, U.; Masud, J.; Zhang, N.; Hong, Y.; Liyanage, W. P. R.; Asle Zaeem, M.; Nath, M. Nickel Telluride as a Bifunctional Electrocatalyst for Efficient Water Splitting in Alkaline Medium. *J. Mater. Chem. A* **2018**, *6*, 7608–7622.
- (31) Xu, K.; Ding, H.; Lv, H.; Tao, S.; Chen, P.; Wu, X.; Chu, W.; Wu, C.; Xie, Y. Understanding Structure-Dependent Catalytic Performance of Nickel Selenides for Electrochemical Water Oxidation. *ACS Catal.* **2017**, *7*, 310–315.
- (32) Carlson, R. R.; Meek, D. W. Dipole Moments of Several Tertiary Phosphine Oxides, Sulfides, and Selenides and of Some Tertiary Arsine Oxides and Sulfides. *Inorg. Chem.* **1974**, *13*, 1741–1747.
- (33) Cao, X.; Hong, Y.; Zhang, N.; Chen, Q.; Masud, J.; Asle Zaeem, M.; Nath, M. Phase Exploration and Identification of Multinary Transition-Metal Selenides as High-Efficiency Oxygen Evolution Electrocatalysts through Combinatorial Electrodeposition. *ACS Catal.* **2018**, *8*, 8273–8289.
- (34) Swesi, A. T.; Masud, J.; Liyanage, W. P. R.; Umaphathi, S.; Bohannan, E.; Medvedeva, J.; Nath, M. Textured NiSe<sub>2</sub> Film: Bifunctional Electrocatalyst for Full Water Splitting at Remarkably Low Overpotential with High Energy Efficiency. *Sci. Rep.* **2017**, *7*, 2401.
- (35) Gao, M. R.; Cao, X.; Gao, Q.; Xu, Y. F.; Zheng, Y. R.; Jiang, J.; Yu, S. H. Nitrogen-Doped Graphene Supported CoSe<sub>2</sub> Nanobelt Composite Catalyst for Efficient Water Oxidation. *ACS Nano* **2014**, *8*, 3970–3978.
- (36) Masud, J.; Swesi, A. T.; Liyanage, W. P. R.; Nath, M. Cobalt Selenide Nanostructures: An Efficient Bifunctional Catalyst with High Current Density at Low Coverage. *ACS Appl. Mater. Interfaces* **2016**, *8*, 17292–17302.

- (37) Liu, B.; Zhao, Y. F.; Peng, H. Q.; Zhang, Z. Y.; Sit, C. K.; Yuen, M. F.; Zhang, T. R.; Lee, C. S.; Zhang, W. J. Nickel–Cobalt Diselenide 3D Mesoporous Nanosheet Networks Supported on Ni Foam: An All-pH Highly Efficient Integrated Electrocatalyst for Hydrogen Evolution. *Adv. Mater.* **2017**, *29*, 1606521.
- (38) Xu, X.; Song, F.; Hu, X. A Nickel Iron Diselenide-Derived Efficient Oxygen-Evolution Catalyst. *Nat. Commun.* **2016**, *7*, 12324.
- (39) Umapathi, S.; Masud, J.; Swesi, A. T.; Nath, M. FeNi<sub>2</sub>Se<sub>4</sub>–Reduced Graphene Oxide Nanocomposite: Enhancing Bifunctional Electrocatalytic Activity for Oxygen Evolution and Reduction through Synergistic Effects. *Adv. Sustainable Syst.* **2017**, *1*, 1700086.
- (40) Akbar, K.; Jeon, J. H.; Kim, M.; Jeong, J.; Yi, Y.; Chun, S.-H. Bifunctional Electrodeposited 3D NiCoSe<sub>2</sub>/Nickel Foam Electrocatalysts for Its Applications in Enhanced Oxygen Evolution Reaction and for Hydrazine Oxidation. *ACS Sustainable Chem. Eng.* **2018**, *6*, 7735–7742.
- (41) Suen, N. T.; Hung, S. F.; Quan, Q.; Zhang, N.; Xu, Y. J.; Chen, H. M. Electrocatalysis for the Oxygen Evolution Reaction: Recent Development and Future Perspectives. *Chem. Soc. Rev.* **2017**, *46*, 337–365.
- (42) Maiyalagan, T.; Jarvis, K. A.; Therese, S.; Ferreira, P. J.; Manthiram, A. Spinel-Type Lithium Cobalt Oxide as a Bifunctional Electrocatalyst for the Oxygen Evolution and Oxygen Reduction Reactions. *Nat. Commun.* **2014**, *5*, 3949.
- (43) Gong, M.; Dai, H. A Mini Review on NiFe-Based Materials as Highly Active Oxygen Evolution Reaction Electrocatalysts. *Nano Res.* **2015**, *8*, 23–39.
- (44) Enman, L. J.; Burke, M. S.; Batchellor, A. S.; Boettcher, S. W. Effects of Intentionally Incorporated Metal Cations on the Oxygen Evolution Electrocatalytic Activity of Nickel (Oxy) Hydroxide in Alkaline Media. *ACS Catal.* **2016**, *6*, 2416–2423.
- (45) Görlin, M.; Ferreira de Araujo, J.; Schmies, H.; Bernsmeier, D.; Dresp, S.; Gliech, M.; Jusys, Z.; Chernev, P.; Kraehnert, R.; Dau, H.; Strasser, P. Tracking Catalyst Redox States and Reaction Dynamics in Ni-Fe Oxyhydroxide Oxygen Evolution Reaction Electrocatalysts: The Role of Catalyst Support and Electrolyte pH. *J. Am. Chem. Soc.* **2017**, *139*, 2070–2082.
- (46) Yang, Y.; Fei, H.; Ruan, G.; Xiang, C.; Tour, J. M. Efficient Electrocatalytic Oxygen Evolution on Amorphous Nickel-Cobalt Binary Oxide Nanoporous Layers. *ACS Nano* **2014**, *8*, 9518–9523.
- (47) Simon, G.; Kresler, S. E.; Essene, E. J. Phase Relations among Selenides, Sulfides, Tellurides, and Oxides: II. Applications to Selenide-Bearing Ore Deposits. *Econ. Geol.* **1997**, *92*, 468–484.

- (48) Xu, H.; Feng, J. X.; Tong, Y. X.; Li, G. R. Cu<sub>2</sub>O-Cu Hybrid Foams as High-Performance Electrocatalysts for Oxygen Evolution Reaction in Alkaline Media. *ACS Catal.* **2017**, *7*, 986–991.
- (49) Zhang, H.; Zhang, Z.; Li, N.; Yan, W.; Zhu, Z. Cu<sub>2</sub>O@C Core/Shell Nanoparticle as an Electrocatalyst for Oxygen Evolution Reaction. *J. Catal.* **2017**, *352*, 239–245.
- (50) Masud, J.; Liyanage, W. P. R.; Cao, X.; Saxena, A.; Nath, M. Copper Selenides as High-Efficiency Electrocatalysts for Oxygen Evolution Reaction. *ACS Appl. Energy Mater.* **2018**, *1*, 4075–4083.
- (51) Cao, X.; Johnson, E.; Nath, M. Identifying High-efficiency Oxygen Evolution Electrocatalysts from Co-Ni-Cu Based Selenides through Combinatorial Electrodeposition. Submitted to *J. Mater. Chem. A* **2019**, doi: 10.1039/c9ta00863b.
- (52) Batchellor, A. S.; Kwon, G.; Laskowski, F. A. L.; Tiede, D. M.; Boettcher, S. W. Domain Structures of Ni and NiFe (Oxy)Hydroxide Oxygen-Evolution Catalysts from X-Ray Pair Distribution Function Analysis. *J. Phys. Chem. C* **2017**, *121*, 25421–25429.
- (53) Zhuang, L.; Ge, L.; Yang, Y.; Li, M.; Jia, Y.; Yao, X.; Zhu, Z. Ultrathin Iron-Cobalt Oxide Nanosheets with Abundant Oxygen Vacancies for the Oxygen Evolution Reaction. *Adv. Mater.* **2017**, *29*, 1606793.
- (54) Santos, E.; Schmickler, W. d-Band Catalysis in Electrochemistry. *ChemPhysChem* **2006**, *7*, 2282–2285.
- (55) Stevens, M. B.; Trang, C. D. M.; Enman, L. J.; Deng, J.; Boettcher, S. W. Reactive Fe-Sites in Ni/Fe (Oxy)Hydroxide Are Responsible for Exceptional Oxygen Electrocatalysis Activity. *J. Am. Chem. Soc.* **2017**, *139*, 11361–11364.
- (56) Xu, D.; Stevens, M. B.; Rui, Y.; DeLuca, G.; Boettcher, S. W.; Reichmanis, E.; Li, Y.; Zhang, Q.; Wang, H. The Role of Cr Doping in Ni–Fe Oxide/(Oxy)Hydroxide Electrocatalysts for Oxygen Evolution. *Electrochim. Acta* **2018**, *265*, 10–18.
- (57) Burke, M. S.; Kast, M. G.; Trotochaud, L.; Smith, A. M.; Boettcher, S. W. Cobalt-Iron (Oxy)Hydroxide Oxygen Evolution Electrocatalysts: The Role of Structure and Composition on Activity, Stability, and Mechanism. *J. Am. Chem. Soc.* **2015**, *137*, 3638–3648.
- (58) Xu, X.; Liang, H.; Ming, F.; Qi, Z.; Xie, Y.; Wang, Z. Prussian Blue Analogues Derived Penroseite (Ni,Co)Se<sub>2</sub> Nanocages Anchored on 3D Graphene Aerogel for Efficient Water Splitting. *ACS Catal.* **2017**, *7*, 6394–6399.
- (59) Zhao, X.; Zhang, H.; Yan, Y.; Cao, J.; Li, X.; Zhou, S.; Peng, Z.; Zeng, J. Engineering the Electrical Conductivity of Lamellar Silver-Doped Cobalt (II) Selenide Nanobelts for Enhanced Oxygen Evolution. *Angew. Chem. Int. Ed.* **2017**, *56*, 328–332.



- (60) Trotochaud, L.; Young, S. L.; Ranney, J. K.; Boettcher, S. W. Nickel-Iron Oxyhydroxide Oxygen-Evolution Electrocatalysts: The Role of Intentional and Incidental Iron Incorporation. *J. Am. Chem. Soc.* **2014**, *136*, 6744–6753.
- (61) Qi, J.; Zhang, W.; Xiang, R.; Liu, K.; Wang, H. Y.; Chen, M.; Han, Y.; Cao, R. Porous Nickel–Iron Oxide as a Highly Efficient Electrocatalyst for Oxygen Evolution Reaction. *Adv. Sci.* **2015**, *2*, 1500199.
- (62) Wang, Z.; Li, J.; Tian, X.; Wang, X.; Yu, Y.; Owusu, K. A.; He, L.; Mai, L. Porous Nickel-Iron Selenide Nanosheets as Highly Efficient Electrocatalysts for Oxygen Evolution Reaction. *ACS Appl. Mater. Interfaces* **2016**, *8*, 19386–19392.
- (63) Li, Y. F.; Selloni, A. Mechanism and Activity of Water Oxidation on Selected Surfaces of Pure and Fe-Doped NiO<sub>x</sub>. *ACS Catal.* **2014**, *4*, 1148–1153.
- (64) Landon, J.; Demeter, E.; Inoğlu, N.; Keturakis, C.; Wachs, I. E.; Vasić, R.; Frenkel, A. I.; Kitchin, J. R. Spectroscopic Characterization of Mixed Fe-Ni Oxide Electrocatalysts for the Oxygen Evolution Reaction in Alkaline Electrolytes. *ACS Catal.* **2012**, *2*, 1793–1801.
- (65) Enman, L. J.; Stevens, M. B.; Dahan, M. H.; Nellist, M. R.; Toroker, M. C.; Boettcher, S. W. Operando X-Ray Absorption Spectroscopy Shows Iron Oxidation Is Concurrent with Oxygen Evolution in Cobalt–Iron (Oxy)Hydroxide Electrocatalysts. *Angew. Chem. Int. Ed.* **2018**, *57*, 12840–12844.
- (66) Zhang, X.; Zhang, X.; Xu, H.; Wu, Z.; Wang, H.; Liang, Y. Iron-Doped Cobalt Monophosphide Nanosheet/Carbon Nanotube Hybrids as Active and Stable Electrocatalysts for Water Splitting. *Adv. Funct. Mater.* **2017**, *27*, 1606635.
- (67) Zhang, J.; Wang, Y.; Zhang, C.; Gao, H.; Lv, L.; Han, L.; Zhang, Z. Self-Supported Porous NiSe<sub>2</sub> Nanowrinkles as Efficient Bifunctional Electrocatalysts for Overall Water Splitting. *ACS Sustain. Chem. Eng.* **2018**, *6*, 2231–2239.
- (68) Anantharaj, S.; Kennedy, J.; Kundu, S. Microwave-Initiated Facile Formation of Ni<sub>3</sub>Se<sub>4</sub> Nanoassemblies for Enhanced and Stable Water Splitting in Neutral and Alkaline Media. *ACS Appl. Mater. Interfaces* **2017**, *9*, 8714–8728.
- (69) Friebel, D.; Louie, M. W.; Bajdich, M.; Sanwald, K. E.; Cai, Y.; Wise, A. M.; Cheng, M. J.; Sokaras, D.; Weng, T. C.; Alonso-Mori, R.; Davis, R. C.; Bargar, J. R.; Nørskov, J.K.; Nilsson, A.; Bell, A. T. Identification of Highly Active Fe Sites in (Ni,Fe)OOH for Electrocatalytic Water Splitting. *J. Am. Chem. Soc.* **2015**, *137*, 1305–1313.
- (70) Shinagawa, T.; Garcia-Esparza, A. T.; Takanebe, K. Insight on Tafel Slopes from a Microkinetic Analysis of Aqueous Electrocatalysis for Energy Conversion. *Sci. Rep.* **2015**, *5*, 13801.

- (71) Chi, J. Q.; Yan, K. L.; Xiao, Z.; Dong, B.; Shang, X.; Gao, W. K.; Li, X.; Chai, Y. M.; Liu, C. G. Trimetallic Ni-Fe-Co Selenides Nanoparticles Supported on Carbon Fiber Cloth as Efficient Electrocatalyst for Oxygen Evolution Reaction. *Int. J. Hydrogen Energy* **2017**, *42*, 20599–20607.
- (72) Smith, R. D. L.; Prévot, M. S.; Fagan, R. D.; Trudel, S.; Berlinguette, C. P. Water Oxidation Catalysis: Electrocatalytic Response to Metal Stoichiometry in Amorphous Metal Oxide Films Containing Iron, Cobalt, and Nickel. *J. Am. Chem. Soc.* **2013**, *135*, 11580–11586.
- (73) Grimaud, A.; May, K. J.; Carlton, C. E.; Lee, Y. L.; Risch, M.; Hong, W. T.; Zhou, J.; Shao-Horn, Y. Double Perovskites as a Family of Highly Active Catalysts for Oxygen Evolution in Alkaline Solution. *Nat. Commun.* **2013**, *4*, 2439.
- (74) Shen, M.; Ruan, C.; Chen, Y.; Jiang, C.; Ai, K.; Lu, L. Covalent Entrapment of Cobalt-Iron Sulfides in N-Doped Mesoporous Carbon: Extraordinary Bifunctional Electrocatalysts for Oxygen Reduction and Evolution Reactions. *ACS Appl. Mater. Interfaces* **2015**, *7*, 1207–1218.
- (75) Zhang, P.; Li, L.; Nordlund, D.; Chen, H.; Fan, L.; Zhang, B.; Sheng, X.; Daniel, Q.; Sun, L. Dendritic Core-Shell Nickel-Iron-Copper Metal/Metal Oxide Electrode for Efficient Electrocatalytic Water Oxidation. *Nat. Commun.* **2018**, *9*, 381.
- (76) Liu, Y.; Niu, Z.; Lu, Y.; Zhang, L.; Yan, K. Facile Synthesis of  $\text{CuFe}_2\text{O}_4$  crystals Efficient for Water Oxidation and  $\text{H}_2\text{O}_2$  reduction. *J. Alloys Compd.* **2018**, *735*, 654–659.
- (77) Chen, H.; Gao, Y.; Ye, L.; Yao, Y.; Chen, X.; Wei, Y.; Sun, L. A  $\text{Cu}_2\text{Se-Cu}_2\text{O}$  Film Electrodeposited on Titanium Foil as a Highly Active and Stable Electrocatalyst for the Oxygen Evolution Reaction. *Chem. Commun.* **2018**, *54*, 4979–4982.
- (78) Niu, Y.; Qian, X.; Xu, C.; Liu, H.; Wu, W.; Hou, L. Cu-Ni- $\text{CoSe}_x$  Quaternary Porous Nanocubes as Enhanced Pt-Free Electrocatalysts for Highly Efficient Dye-Sensitized Solar Cells and Hydrogen Evolution in Alkaline Medium. *Chem. Eng. J.* **2019**, *357*, 11–20.
- (79) Ali, Z.; Asif, M.; Huang, X.; Tang, T.; Hou, Y. Hierarchically Porous  $\text{Fe}_2\text{CoSe}_4$  Binary-Metal Selenide for Extraordinary Rate Performance and Durable Anode of Sodium-Ion Batteries. *Adv. Mater.* **2018**, *30*, 1802745.
- (80) Zhao, Y.; Jin, B.; Zheng, Y.; Jin, H.; Jiao, Y.; Qiao, S. Z. Charge State Manipulation of Cobalt Selenide Catalyst for Overall Seawater Electrolysis. *Adv. Energy Mater.* **2018**, *8*, 1801926.
- (81) Yu, J.; Cheng, G.; Luo, W. 3D Mesoporous Rose-like Nickel-Iron Selenide Microspheres as Advanced Electrocatalysts for the Oxygen Evolution Reaction. *Nano Res.* **2018**, *11*, 2149–2158.

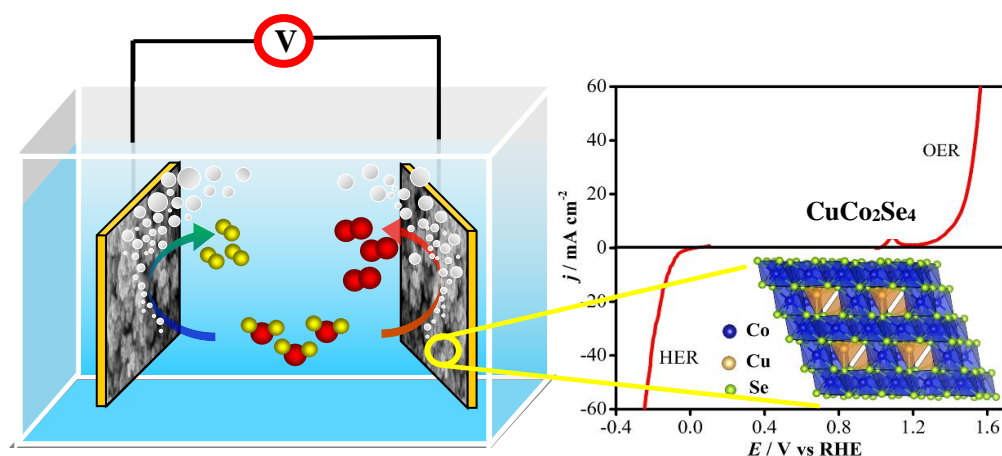
- (82) Quan, L.; Liu, T.; Yi, M.; Chen, Q.; Cai, D.; Zhan, H. Construction of Hierarchical Nickel Cobalt Selenide Complex Hollow Spheres for Pseudocapacitors with Enhanced Performance. *Electrochim. Acta* **2018**, *281*, 109–116.
- (83) Jia, J.; Seitz, L. C.; Benck, J. D.; Huo, Y.; Chen, Y.; Ng, J. W. D.; Bilir, T.; Harris, J. S.; Jaramillo, T. F. Solar Water Splitting by Photovoltaic-Electrolysis with a Solar-to-Hydrogen Efficiency over 30 %. *Nat. Commun.* **2016**, *7*, 13237.
- (84) Xiao, P.; Sk, M. A.; Thia, L.; Ge, X.; Lim, R. J.; Wang, J. Y.; Lim, K. H.; Wang, X. Molybdenum Phosphide as an Efficient Electrocatalyst for the Hydrogen Evolution Reaction. *Energy Environ. Sci.* **2014**, *7*, 2624–2629.
- (85) Merki, D.; Vrubel, H.; Rovelli, L.; Fierro, S.; Hu, X. Fe, Co, and Ni Ions Promote the Catalytic Activity of Amorphous Molybdenum Sulfide Films for Hydrogen Evolution. *Chem. Sci.* **2012**, *3*, 2515–2525.
- (86) Sivanantham, A.; Ganesan, P.; Shanmugam, S. Hierarchical NiCo<sub>2</sub>S<sub>4</sub> Nanowire Arrays Supported on Ni Foam: An Efficient and Durable Bifunctional Electrocatalyst for Oxygen and Hydrogen Evolution Reactions. *Adv. Funct. Mater.* **2016**, *26*, 4661–4672.
- (87) Chen, P.; Xu, K.; Zhou, T.; Tong, Y.; Wu, J.; Cheng, H.; Lu, X.; Ding, H.; Wu, C.; Xie, Y. Strong-Coupled Cobalt Borate Nanosheets/Graphene Hybrid as Electrocatalyst for Water Oxidation under Both Alkaline and Neutral Conditions. *Angew. Chem. Int. Ed.* **2016**, *55*, 2488–2492.
- (88) Jia, X.; Zhao, Y.; Chen, G.; Shang, L.; Shi, R.; Kang, X.; Waterhouse, G. I. N.; Wu, L. Z.; Tung, C. H.; Zhang, T. Ni<sub>3</sub>FeN Nanoparticles Derived from Ultrathin NiFe-Layered Double Hydroxide Nanosheets: An Efficient Overall Water Splitting Electrocatalyst. *Adv. Energy Mater.* **2016**, *6*, 1502585.
- (89) Schwanke, C.; Stein, H. S.; Xi, L.; Sliozberg, K.; Schuhmann, W.; Ludwig, A.; Lange, K. M. Correlating Oxygen Evolution Catalysts Activity and Electronic Structure by a High-Throughput Investigation of Ni<sub>1-y-z</sub>Fe<sub>y</sub>Cr<sub>z</sub>O<sub>x</sub>. *Sci. Rep.* **2017**, *7*, 44192.
- (90) Yan, X.; Tian, L.; Li, K.; Atkins, S.; Zhao, H.; Murowchick, J.; Liu, L.; Chen, X. FeNi<sub>3</sub>/NiFeO<sub>x</sub> Nanohybrids as Highly Efficient Bifunctional Electrocatalysts for Overall Water Splitting. *Adv. Mater. Interfaces* **2016**, *3*, 1600368.
- (91) Yan, X.; Tian, L.; Atkins, S.; Liu, Y.; Murowchick, J.; Chen, X. Converting CoMoO<sub>4</sub> into CoO/MoO<sub>x</sub> for Overall Water Splitting by Hydrogenation. *ACS Sustain. Chem. Eng.* **2016**, *4*, 3743–3749.
- (92) Liu, L.; Niu, D.; Song, F.; Lyu, L.; He, J.; Yan, X.; Li, K.; Hu, X.; Chen, X. From Water Oxidation to Reduction: Transformation from Ni<sub>x</sub>Co<sub>3-x</sub>O<sub>4</sub> Nanowires to NiCo/NiCoO<sub>x</sub> Heterostructures. *ACS Appl. Mater. Interfaces* **2016**, *8*, 3208–3214.

#### IV. COPPER COBALT SELENIDE AS A HIGH-EFFICIENCY BIFUNCTIONAL ELECTROCATALYST FOR OVERALL WATER SPLITTING: COMBINED EXPERIMENTAL AND THEORETICAL STUDY

*Xi Cao<sup>a</sup>, Julia E. Medvedeva<sup>b\*</sup> and Manashi Nath<sup>a\*</sup>*

<sup>a</sup>Department of Chemistry, Missouri University of Science and Technology, Rolla, Missouri 65409, United States.

<sup>b</sup>Department of Physics, Missouri University of Science and Technology, Rolla, Missouri 65409, United States.



#### ABSTRACT

Non-precious metal-based catalysts for full water splitting is still being sought after by several groups of researchers owing to their promising practical application in energy conversion devices. In this article, nanostructured CuCo<sub>2</sub>Se<sub>4</sub> comprising earth-abundant elements has been reported to exhibit superior bifunctional electrocatalytic activity for both oxygen evolution reaction (OER) and hydrogen evolution reaction (HER) under alkaline conditions. The CuCo<sub>2</sub>Se<sub>4</sub> electrocatalyst with a spinel structure type requires a low

overpotential of 320 mV to reach a current density of 50 mA cm<sup>-2</sup> for OER and 125 mV to achieve 10 mA cm<sup>-2</sup> for HER, respectively, which is lower than other reported transition metal chalcogenide electrocatalysts based on Co/Cu, and significantly lower than the well-known precious metal oxide catalysts (IrO<sub>x</sub> and RuO<sub>x</sub>). To understand the origin of high catalytic performance in CuCo<sub>2</sub>Se<sub>4</sub>, density functional theory (DFT) has been utilized to study the structural, electronic, and magnetic properties of bulk CuCo<sub>2</sub>Se<sub>4</sub> as well as slabs with (100) and (111) surface orientations with and without OH<sup>-</sup> adsorption. The theoretical results show that CuCo<sub>2</sub>Se<sub>4</sub> is in the metallic state with a high electrical conductivity which plays a crucial role in the catalytic activity. Among Co and Cu, it was observed that Co showed better OER catalytic activity. Importantly, a surface enhancement of the local magnetic moment on the Co atoms is found to be limited to the top layer in the (100) slab, whereas it affects all layers of the (111) slab, strongly favoring the OH<sup>-</sup> adsorption on the Co atom at the (111) surface and making the (111) surface more catalytically active. The different surface energies of the (111) and (100) surfaces was also observed from DFT studies which will have a pronounced influence on the observed catalytic activity of these surfaces.

**Keywords:** water splitting, oxygen evolution reaction, electrocatalyst, metal selenide, DFT calculation

## 1. INTRODUCTION

In recent years, generation of alternative renewable energy from sustainable resources has been a topic of growing concern due to faster depletion of fossil fuels and

related environmental concerns.<sup>1</sup> Among all the available options, hydrogen appears to be the most promising choice as a clean fuel, which can be widely utilized in fuel cells and other energy storage and conversion devices.<sup>2,3</sup> Among all the possible ways to produce hydrogen, water electrolysis ( $2\text{H}_2\text{O} \rightarrow 2\text{H}_2 + \text{O}_2$ ) can be one of the most useful and clean method to generate hydrogen *on-demand* in copious quantities if the efficiency of the process can be improved significantly.<sup>2,3</sup> Water splitting is composed of two half reactions, oxygen evolution reaction (OER,  $4\text{OH}^- \rightarrow \text{O}_2 + 2\text{H}_2\text{O} + 4\text{e}^-$ ) occurring at the anode and hydrogen evolution reaction (HER,  $2\text{H}_2\text{O} + 2\text{e}^- \rightarrow \text{H}_2 + 2\text{OH}^-$ ) happening at the cathode.<sup>4,5,6</sup> The efficiency of water electrolysis is significantly influenced by the efficiency of OER which is a kinetically sluggish process comprising multistep proton-coupled electron transfers and the formation of O=O bond which requires high overpotential to initiate the process.<sup>7,8,9,10</sup> Hence, practical applications of producing hydrogen through water splitting has been greatly hindered by the slow OER rate. Thus, it's a crucial task to develop highly efficient OER electrocatalysts to reduce the applied overpotential, facilitate the overall process, and hence improve the energy conversion efficiency.<sup>11,12</sup> Most of the conventionally used state-of-the-art OER electrocatalysts are precious metal-based oxides, such as  $\text{IrO}_x$  and  $\text{RuO}_x$ ,<sup>13,14,15</sup> however, the scarcity and high cost of precious metals have significantly limited their large-scale industrial applications. Consequently, there has been extensive efforts devoted to develop high efficiency and low-cost transition metal based OER electrocatalysts.<sup>16,17,18,19,20,21,22</sup> Such effort has led to the discovery of several first-row transition metal (Mn, Fe, Co, Ni and Cu etc.) oxides and (oxy)hydroxides as efficient OER electrocatalysts.<sup>23,24,25,26,27,28,29</sup> Besides oxides and hydroxides, selenides have emerged recently as a new class of highly active OER

electrocatalysts showing impressive improvements of catalytic activity compared to oxides.<sup>30,31,32,33,34,35,36</sup> In our group, we have extensively investigated the OER electrocatalytic activity of transition metal chalcogenides, especially selenides (such as Ni<sub>3</sub>Se<sub>2</sub>, NiSe<sub>2</sub>, Co<sub>7</sub>Se<sub>8</sub>, Cu<sub>2</sub>Se etc.)<sup>37,38,39,40</sup> and tellurides (Ni<sub>3</sub>Te<sub>2</sub>)<sup>41</sup> and have observed that the catalytic activity increases with decreasing electronegativity of the lattice anion. Hence, the electronegativity of oxygen (3.44) being larger than that of elemental selenium (2.55), leads to selenides being better OER catalysts, and the reason behind such a trend is believed to be due to an increased covalency of the metal-chalcogen bond, which alters the electronic band structure, reduces the redox potential of the catalytically active transition metal site, reduces bandgap and improves the electrical conductivity resulting in high current density.<sup>42,43</sup> A study reported by K. Xu et.al comparing oxides (e.g. NiO) and selenides (e.g. Ni<sub>3</sub>Se<sub>2</sub>) also confirmed that selenides have a more intrinsic metallic state than oxide phase,<sup>44</sup> which might have a positive effect on the OER by facilitating charge transfer on the catalyst surface, and formation of the intermediates. We have also observed that the catalyst activation step occurs at a lower potential as the covalency increases in the metal-chalcogen bond, leading to Ni<sub>3</sub>Te<sub>2</sub> showing lower onset potential and overpotential for OER than Ni<sub>3</sub>Se<sub>2</sub>.<sup>41</sup> All these considerations can possibly explain the improved OER catalytic activity of the selenides and tellurides compared to analogous oxide phases. Apart from changing covalency of the anion lattice, doping in the transition metal site also leads to redistribution of charge density around the catalytically active site, and accordingly, mixed metal selenides have showed a much more efficient catalytic performance towards OER. Recently, our group and others have reported mixed metal selenides such as Ni<sub>x</sub>Fe<sub>1-x</sub>Se<sub>2</sub>, (Fe<sub>0.48</sub>Co<sub>0.38</sub>Cu<sub>0.14</sub>)Se, (Co<sub>0.21</sub>Ni<sub>0.25</sub>Cu<sub>0.54</sub>)<sub>3</sub>Se<sub>2</sub> and (Ni<sub>0.25</sub>Fe<sub>0.68</sub>Co<sub>0.07</sub>)<sub>3</sub>Se<sub>4</sub> as excellent

OER electrocatalysts with low onset potential and increased energy conversion efficiency.<sup>45,46,47,48</sup> From some of these previous studies it was observed that the oxidized redox couples of the transition metal (e.g.  $\text{Co}^{3+/4+}$ ) plays a very crucial role in influencing the catalytic activity.<sup>49,50,51</sup> Specifically it was noted that higher *d*-electron occupancy preferably with one electron in the doubly degenerate  $e_g$  orbital significantly improves the catalytic activity.<sup>50</sup> Although catalyst compositions containing Co, Ni, and Fe has been extensively researched for OER activity, Cu which satisfies the *d*-electron occupancy criteria above, has not been investigated extensively for OER catalytic activity until recently.<sup>52,53</sup> Bikkarolla et al. synthesized  $\text{CuCo}_2\text{O}_4$  nanoparticles on nitrogenated graphene and showed an overpotential of 360 mV to reach  $10 \text{ mA cm}^{-2}$  and high stability in alkaline media.<sup>54</sup> In another report, two-dimensional  $\text{CuCo}_2\text{S}_4$  nanosheets were synthesized by a simple hydrothermal method and showed high OER activity at low mass loading.<sup>55</sup> Addition of Cu to the composition is expected to increase the metallicity in the catalyst composite thereby facilitating the charge transfer rate. Hence, introduction of Cu in the catalyst composition deserves more attention especially since Cu is one of the most earth-abundant non-precious elements. Apart from the chemical composition of the catalyst site, crystal structure and coordination geometry also play a subtle role in influencing the catalytic activity. Accordingly, spinel type compounds containing mixed valence metal ions in variable coordination geometries have attracted a lot of attention in that respect since they are believed to have high OER activity at the trivalent metal sites thereby facilitating the charge transfer rates between the reactant species or intermediates and the catalyst surface.<sup>12,56</sup>



In this article, we have reported for the first time high-efficiency bifunctional catalytic activity of  $\text{CuCo}_2\text{Se}_4$  nanoparticles for OER and HER in harsh alkaline medium. The catalyst composite exhibits a low onset potential of 1.43 V vs RHE and an overpotential of 320 mV to achieve  $50 \text{ mA cm}^{-2}$  for OER in alkaline solution, which is one of the lowest overpotentials that has been reported to date. Moreover, the catalyst also shows excellent HER activity with a low overpotential of 125 mV (at  $10 \text{ mA cm}^{-2}$ ) in alkaline medium. A water electrolysis cell comprising  $\text{CuCo}_2\text{Se}_4$  nanoparticles modified electrode as both OER and HER catalysts only required a cell voltage of 1.782 V to drive a current density of  $50 \text{ mA cm}^{-2}$  for the overall water splitting. We have also employed density functional theory (DFT) to study the electronic band structure of  $\text{CuCo}_2\text{Se}_4$  and to correlate the results with the observed high OER catalytic activity. The calculated electronic and magnetic properties of bulk  $\text{CuCo}_2\text{Se}_4$  were compared with those for slabs with (100) and (111) lattice orientations, to investigate surface dependent catalytic activity. The calculations suggest that  $\text{CuCo}_2\text{Se}_4$  is in the metallic state with a high electrical conductivity. The (100) slab has a low surface energy ( $E_{\text{surface}}$ ) of 136 meV/f.u., suggesting it is likely to be the most thermodynamically stable surface orientation, while the (111) slab with a higher  $E_{\text{surface}}$ , 243 meV/f.u., and intense metallic nature near the Fermi level is expected to be the most active surface for OER.<sup>57,58</sup> We have also estimated and compared the  $\text{OH}^-$  adsorption energy on the Co and Cu sites in the (100) and (111) lattice planes, and observed that while both Cu and Co atoms play a crucial role as the catalytically active sites, Co atom is a more favourable active site since the adsorption energy of  $\text{OH}^-$  on Co is 531 meV higher than that on Cu atom (100 surface), suggesting  $\text{OH}^-$  prefers to stick to Co atom instead of Cu on the surface.

## 2. EXPERIMENTAL AND COMPUTATIONAL METHODS

Chemicals and Materials. All chemicals were analytical grade and used without further purification. Distilled water (18 M $\Omega$ /cm) was used to prepare all the solutions. Cobalt chloride hexahydrate [CoCl<sub>2</sub>·6H<sub>2</sub>O] was purchased from J T Baker Chemical Co., copper chloride dihydrate [CuCl<sub>2</sub>·2H<sub>2</sub>O] and potassium hydroxide [KOH] from Fisher Scientific, selenium dioxide [SeO<sub>2</sub>] and hydrazine monohydrate [N<sub>2</sub>H<sub>4</sub>·H<sub>2</sub>O] from Acros chemicals. Carbon fiber paper (CFP) and Au-coated glass used as conductive substrates were purchased from FuelCellsEtc, Texas and Deposition Research Lab Incorporated (DRLI), Lebanon Missouri, respectively. All Au coated glass substrates were carefully cleaned by treatments in Micro-90, isopropanol and deionized (DI) water while CFP were cleaned by simply soaking into isopropanol.

Synthesis of CuCo<sub>2</sub>Se<sub>4</sub>. In a typical synthesis of CuCo<sub>2</sub>Se<sub>4</sub> by hydrothermal method, 10 mM of CuCl<sub>2</sub>·2H<sub>2</sub>O, 20 mM of CoCl<sub>2</sub>·6H<sub>2</sub>O and 40 mM of SeO<sub>2</sub> were mixed in 10 mL of deionized water, then the mixture was stirred on a magnetic stirrer to form a homogenous solution. After 10 min of stirring, 0.5 mL of hydrazine (N<sub>2</sub>H<sub>4</sub>·H<sub>2</sub>O) was added carefully and then a brown colloidal solution was formed. The resulting solution was stirred for another 10 min and then transferred into a 23 mL Teflon-lined stainless-steel autoclave. The autoclave was tightly sealed and maintained at 145 °C for 24 h and then naturally cooled down to room temperature. The final blackish product was collected by means of centrifugation, followed by washing several times with distilled water and absolute ethanol. The product was dried in the vacuum oven at room temperature overnight.

Electrode Preparation. To prepare the catalyst ink, 2.0 mg CuCo<sub>2</sub>Se<sub>4</sub> nanoparticles were dispersed into 1.0 mL 0.8 % Nafion<sup>®</sup> ethanol solution, followed by 30 min

ultrasonication. Both Au coated glass and CFP substrates were covered with a Teflon tape, leaving an exposed geometric area of  $0.070 \text{ cm}^2$  on which  $20 \mu\text{L}$  of the homogeneous catalyst ink was drop-casted. The electrodes with a loading of  $\sim 0.57 \text{ mg cm}^{-2}$  were dried at room temperature. After being heated at a constant temperature of  $130 \text{ }^\circ\text{C}$  for 30 min in a vacuum oven, the electrodes were ready for the electrocatalytic measurements.

**Characterization.** The catalyst composite was characterized through powder X-ray diffraction (PXRD) using Philips X-Pert X-ray diffractometer (PANalytical, Almelo, The Netherlands) with a  $\text{Cu K}\alpha$  ( $1.5418 \text{ \AA}$ ) radiation. The morphology of the product was observed with a scanning electron microscope (SEM, Hitachi S4700) using an acceleration voltage of 15 kV and a working distance of 12 mm. Energy dispersive spectroscopy (EDS) was also obtained from the same SEM to identify the relative atomic ratio of the constituent elements in the catalyst composite. X-ray photoelectron spectroscopy (XPS) of the catalyst before and after catalytic activity was carried out using a KRATOS AXIS 165 X-ray Photoelectron Spectrometer with the monochromatic Al X-ray source. All XPS analysis was performed on the pristine catalyst surface without any sputtering.

**Electrochemical measurements.** The electrocatalytic performances of  $\text{CuCo}_2\text{Se}_4$  were investigated in 1.0 M KOH solution at room temperature in a three-electrode system by an IviumStat potentiostat. The OER and HER catalytic activities were studied from linear scan voltammetry (LSV) while the stability of the catalyst was estimated by chronoamperometry at a constant applied potential. A three-electrode cell comprising  $\text{CuCo}_2\text{Se}_4$  drop-casted on various substrates (Au coated glass or CFP) serving as the working electrode, a glassy carbon (GC) as the counter electrode and an  $\text{Ag|AgCl}$  (KCl saturated) reference as the reference electrode was used for all electrochemical

measurements. All measured potentials vs Ag|AgCl (KCl saturated) were converted to the reversible hydrogen electrode (RHE) according to the Nernst equation (eq. 1).

$$E_{RHE} = E_{Ag|AgCl} + 0.059pH + E_{Ag|AgCl}^{\circ} \quad (1)$$

Where  $E_{RHE}$  is the calculated potential vs RHE, and  $E_{Ag|AgCl}^{\circ}$  is the standard thermodynamic potential of Ag|AgCl (KCl saturated) at 25.1 °C (0.197 V), and  $E_{Ag|AgCl}$  is the experimentally measured potential vs Ag|AgCl (KCl saturated) reference electrode.

Calculation of Tafel Slope. The Tafel slope is an important parameter to explain the kinetics of electrocatalytic performance of CuCo<sub>2</sub>Se<sub>4</sub> and the equation is shown below.

$$\eta = a + \frac{2.3RT}{anF} \log(j) \quad (2)$$

Where  $\eta$  is the overpotential,  $\alpha$  is transfer coefficient and the other symbols have their usual meaning. The Tafel slope is given by  $2.3RT/anF$ .

Density Functional Theory Calculations. The electronic properties of CuCo<sub>2</sub>Se<sub>4</sub> in bulk and slab geometries were studied using first-principles density functional calculations as implemented in the Vienna ab initio simulation package (VASP).<sup>59,60,61,62</sup> The generalized gradient approximation in the Perdew-Burke-Ernzerhof (PBE) form,<sup>63,64</sup> within the projector augmented-wave method was used.<sup>65,66</sup> The generalized gradient approximation with an on-site Coulomb U term (GGA+U) method has been shown to successfully describe the cohesive energy, electronic structure, and mechanical and magnetic properties of bulk and surfaces of 3d-metal based materials.<sup>67,68,69,70</sup> In this work, GGA+U method<sup>71</sup> with U = 0 and 6 eV for Co-d states and U = 0 and 4 eV for Cu-d states was used to study the electronic structure and magnetic properties of bulk and slabs of CuCo<sub>2</sub>Se<sub>4</sub> as well as the adsorption energy of OH<sup>-</sup> at the surfaces. Moreover, it allowed for straightforward comparisons with previous reports. The internal atomic positions for all

structures were optimized using force and total energy minimization until the Hellmann-Feynman force on each atom was below 0.01 eV/Å. Brillouin-zone sampling was done with  $\Gamma$ -centered Monkhorst-pack with k-mesh of at least 4x4x4; the cut-off energy of 500 eV was used for bulk and slab geometries.

### 3. RESULTS AND DISCUSSION

Figure 1a shows the powder pxd pattern of the as-synthesized  $\text{CuCo}_2\text{Se}_4$  which exhibits a close similarity with the standard  $\text{CuCo}_2\text{Se}_4$  pattern (PDF # 04-019-0997). A trace amount of  $\text{Cu}_2\text{Se}$  (PDF # 00-006-0680) could also be detected in the pxd pattern. Approximate size of the crystalline domains was calculated from the line broadening of the diffraction peaks to be approximately 2.67 nm using the Scherrer equation.<sup>72</sup> Interestingly,  $\text{CuCo}_2\text{Se}_4$  belongs to a spinel structure type,  $AB_2X_4$ , ( $X$  = chalcogen atom). Among the metals  $A$  and  $B$ ,  $A$  is a divalent cation occupying the partially occupied tetrahedral layer, while  $B$  is a trivalent cation occupying the fully occupied octahedral metal layer. From the crystal structure illustration (inset of Figure 1a), it was observed that there is only one type of Co/Cu atom, and the bond lengths of Co-Se and Cu-Se are  $\sim 2.385$  and  $2.378$  Å, respectively. Cu atoms predominantly occupied the tetrahedral sites, while Co atoms were in the octahedral coordination sites.

SEM images of as-synthesized  $\text{CuCo}_2\text{Se}_4$  catalyst showed small granular and nanocoral-like morphology with wide size distribution (20 – 200 nm) as shown in Figure 1b. Such nanostructured geometries are highly advantageous for catalytic applications since they provide high active surface area. The chemical composition and oxidation states of as-prepared  $\text{CuCo}_2\text{Se}_4$  catalyst were further determined by X-ray photoelectron

spectroscopy (XPS) shown in Figure 1c-e. It should be mentioned that all binding energies of Co, Cu and Se were calibrated with respect to a reference binding energy of C 1s (284.5 eV). Co 2p XPS peaks were observed at 777.8 and 793.3 eV confirming the presence of Co-selenide phases.<sup>73</sup> Similarly the Cu 2p XPS peaks observed at 933.8 and 954.1 eV confirmed the presence of copper-selenide linkages.<sup>74</sup> The oxidation states of Cu, Co and Se in as prepared catalyst were further evaluated from the deconvoluted XPS spectra presented in Figure 1c-e. The deconvoluted Co 2p and Cu 2p spectra confirmed the presence of mixed oxidation states of  $\text{Co}^{2+}/\text{Co}^{3+}$  and  $\text{Cu}^+/\text{Cu}^{2+}$ , respectively. The Co 2p XPS spectrum in Figure 1c could be deconvoluted to reveal peaks at 780.5 and 796.8 eV corresponding to  $\text{Co}^{2+} 2p_{3/2}$  and  $\text{Co}^{2+} 2p_{1/2}$ ; while peaks at 777.8 and 793.3 eV correspond to  $\text{Co}^{3+} 2p_{3/2}$  and  $\text{Co}^{3+} 2p_{1/2}$ , respectively.<sup>33,75</sup> The obvious satellite peaks of Co 2p can be found at 785.5 and 802.2 eV.<sup>33,75</sup> Similarly, in the Cu 2p deconvoluted spectra (Figure 1d), the peaks at 931.5 and 952.5 eV correspond to  $\text{Cu}^+ 2p_{3/2}$  and  $\text{Cu}^+ 2p_{1/2}$  while those at 933.8 and 954.1 eV assign to  $\text{Cu}^{2+} 2p_{3/2}$  and  $\text{Cu}^{2+} 2p_{1/2}$  with its shake-up satellite peaks at 941.8 and 961.7 eV.<sup>55,76</sup> In the Se 3d spectra (Figure 1e), the peaks at 54.0 and 54.9 eV correspond to Se  $3d_{5/2}$  and Se  $3d_{3/2}$ , respectively, which confirm the presence of  $\text{Se}^{2-}$ .<sup>38,77</sup> The peak at  $\approx 59$  eV indicates the existence of  $\text{SeO}_x$  species which might due to the surface oxidation of selenide. However, no metal oxides were detected on the catalyst surface from XPS analysis. It was found that the cations in the as-prepared catalyst contained 8 % of  $\text{Co}^{3+}$ , 45 % of  $\text{Co}^{2+}$ , 9 % of  $\text{Cu}^+$  and 38 % of  $\text{Cu}^{2+}$ .

To measure the electrocatalytic performances,  $\text{CuCo}_2\text{Se}_4$  nanoparticles were drop-casted on Au coated glass following standard procedures as described above. Linear sweep voltammetry (LSV) was performed to measure all the catalytic activities in alkaline

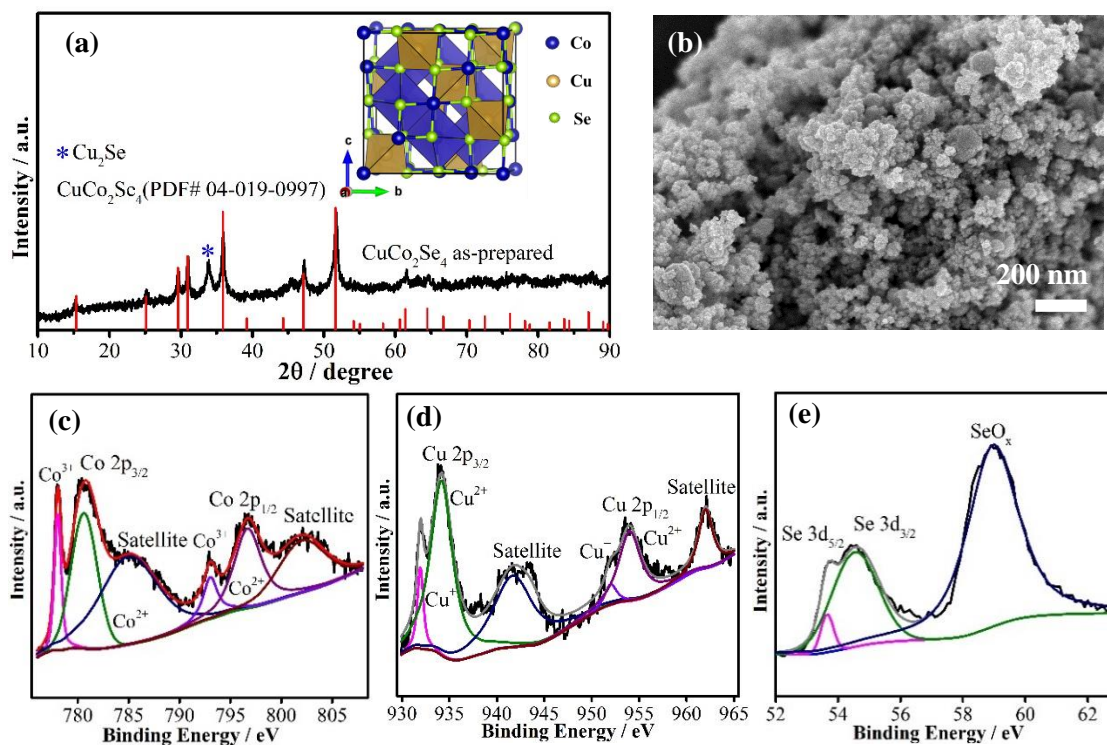


Figure 1. (a) PXRD pattern of the as-synthesized  $\text{CuCo}_2\text{Se}_4$  nanoparticles. The inset of (a) shows the crystal structure of  $\text{CuCo}_2\text{Se}_4$  created from the cif file corresponding to PDF # 04-019-0997. (b) SEM image of the as-synthesized  $\text{CuCo}_2\text{Se}_4$ . Deconvoluted XPS spectra of (c) Co 2p, (d) Cu 2p and (e) Se 3d collected from the as-synthesized catalyst.

solution (1.0 M KOH), while the catalyst durability was studied through chronoamperometry measurements by applying a constant voltage. The electrochemically active surface area (ECSA) as shown in Figure S1 was estimated by measuring the double layer charging current in non-Faradaic region at different scan rates following reported procedure.<sup>8</sup> The anodic and cathodic capacitive current ( $i_{DL}$ ) at 0.01 V vs Ag|AgCl (KCl saturated) was plotted as a function of scan rate ( $\nu$ ) as shown in Figure S1 (insert), and the value of  $C_{DL}$  can be obtained from the average of anodic and cathodic slopes according to eq. 2. The ECSA of  $\text{CuCo}_2\text{Se}_4$  catalyst is obtained through eq. 3 while the roughness factor (RF) is calculated from the ratio of ECSA and the geometric area ( $0.07 \text{ cm}^2$ ).

$$i_{DL} = C_{DL} \cdot \nu \quad (2)$$

$$ECSA = C_{DL}/C_S \quad (3)$$

$C_{DL}$  is the double layer capacitance and  $C_S$  is the specific capacitance of the electrocatalyst per unit area under identical electrolyte condition. In this study,  $C_S$  was taken as 0.040 mF cm<sup>-2</sup> based on reported values.<sup>8</sup> The ECSA of the catalyst was estimated to be 5.61 cm<sup>2</sup> and RF was calculated as 80.18, confirming that the active surface of these nanostructured catalysts was indeed highly rough. It is well known that the catalytic activity is expected to be improved by rough catalyst surface due to a more extensive exposure of the catalytically active sites to the electrolyte.

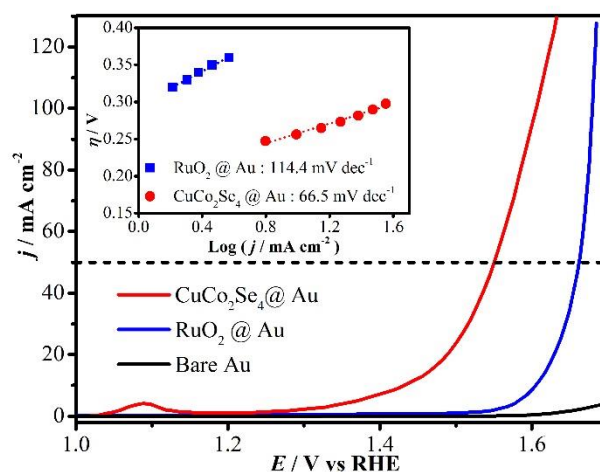


Figure 2. Polarization curves of CuCo<sub>2</sub>Se<sub>4</sub>@Au, RuO<sub>2</sub>@Au and bare Au substrate in N<sub>2</sub>-saturated 1.0 M KOH at a scan rate of 10 mV s<sup>-1</sup>. The inset shows Tafel plots of CuCo<sub>2</sub>Se<sub>4</sub>@Au and RuO<sub>2</sub>@Au.

For comparison of the electrocatalytic performance of CuCo<sub>2</sub>Se<sub>4</sub> with known standards, state-of-the-art OER catalyst RuO<sub>2</sub>@Au with a similar loading was also prepared in our laboratory by electrodeposition following a typical procedure described in



supplementary information<sup>78</sup> and its catalytic activity was measured under the exact same condition. Figure 2 shows the OER polarization curves of  $\text{CuCo}_2\text{Se}_4$ @Au-glass,  $\text{RuO}_2$ @Au-glass and bare Au coated glass measured in  $\text{N}_2$ -saturated 1.0 M KOH at a scan rate of  $10 \text{ mV s}^{-1}$ . As expected, negligible catalytic activity was obtained on bare Au-coated glass while  $\text{CuCo}_2\text{Se}_4$ @Au was highly active towards OER and exhibited efficient oxygen evolution activity with a very low onset potential of 1.43 V vs RHE as shown in Figure 2 and in the magnified plots shown in Figure S2. The current density of  $\text{CuCo}_2\text{Se}_4$  increased very rapidly after onset and it yielded a current density of  $50 \text{ mA cm}^{-2}$  at an overpotential of only 320 mV, which was much better compared to the state-of-the-art  $\text{RuO}_2$  ( $430 \text{ mV}$  at  $50 \text{ mA cm}^{-2}$ ). In order to investigate the effect of substrates, the OER activity of  $\text{CuCo}_2\text{Se}_4$  catalyst also studied on various substrates (Au coated glass and carbon fiber paper) as shown in Figure S3.  $\text{CuCo}_2\text{Se}_4$  exhibited almost same activities on both the substrates, which meant the catalyst itself was intrinsically very efficient for OER independent of 2D flat or 3D porous substrates. The catalytic activity of  $\text{CuCo}_2\text{Se}_4$  was also compared with the binary metal selenides,  $\text{Cu}_3\text{Se}_2$ ,  $\text{Cu}_2\text{Se}$ ,  $\text{Co}_7\text{Se}_8$  and  $\text{CoSe}$  (shown in Figure S4) to understand the influence of transition metal doping in the catalytic site as well as influence of crystal structure. As can be seen clearly, the mixed metal selenide was more active than any of the binary metal selenides. Tafel slope is an important kinetic parameter to explain the high catalytic performance of  $\text{CuCo}_2\text{Se}_4$ , which showed a modest slope of  $66.5 \text{ mV decade}^{-1}$  (inset of Figure 2), indicating OER on  $\text{CuCo}_2\text{Se}_4$  surface was kinetically favourable.

To further understand the high OER activity of  $\text{CuCo}_2\text{Se}_4$  catalyst, electrochemical impedance spectroscopy (EIS) was performed to evaluate the internal resistance of the

catalyst composite as well as the charge-transfer resistance at the catalyst (electrode)-electrolyte interface. The Nyquist plot of  $\text{CuCo}_2\text{Se}_4$  catalyst was obtained at an applied potential of 1.45 V vs RHE in  $\text{N}_2$ -saturated 1.0 M KOH solution as shown in Figure S5. The electrolyte resistance ( $R_s$ ), resistance of the catalytic composite ( $R_{\text{catalyst}}$ ), and the charge transfer resistance ( $R_{\text{ct}}$ ) can be obtained from the equivalent circuit as fitted from the Nyquist plot of  $\text{CuCo}_2\text{Se}_4$  catalyst (insert in Figure S5), and the values obtained from the fit have been listed in Table S1. As can be seen, the uncompensated electrolyte resistance  $R_s$  was obtained as 5.0  $\Omega$ , which was subsequently used for  $iR$  correction. From the fitting of the equivalent circuit it was estimated that the  $R_{\text{ct}}$  and  $R_{\text{catalyst}}$  of catalyst was 9.34 and 716.6  $\Omega$ , respectively. The charge transfer resistance derived from lower frequency region was closely related to the kinetics the OER process on the catalyst surfaces. Hence, the smaller the value of  $R_{\text{ct}}$  indicates a more efficient electron transfer at the catalyst-electrolyte interface leading to faster OER reaction rate and subsequently showing better catalytic activity consistent with the low overpotential obtained from electrocatalytic measurements as reported above. Lower catalyst resistance ( $R_{\text{catalyst}}$ ) on the other hand, leads to better charge transport within the catalyst composite resulting in faster kinetics and higher current density at low potentials.<sup>79,80</sup>

The OER Faradaic efficiency of  $\text{CuCo}_2\text{Se}_4$  catalyst was evaluated by water-displacement method, and the theoretical amount of evolved  $\text{O}_2$  was compared with the experimentally measured  $\text{O}_2$  as shown in Figure 3. A Faradaic efficiency of nearly 100% was obtained for  $\text{CuCo}_2\text{Se}_4$  catalyst toward OER reaction. achieve a current density of around 8.0  $\text{mA cm}^{-2}$ , was used to investigate the stability of the  $\text{CuCo}_2\text{Se}_4$  catalyst for 8 h (shown in Figure 4a insert). As can be seen, the current density was slightly increased after

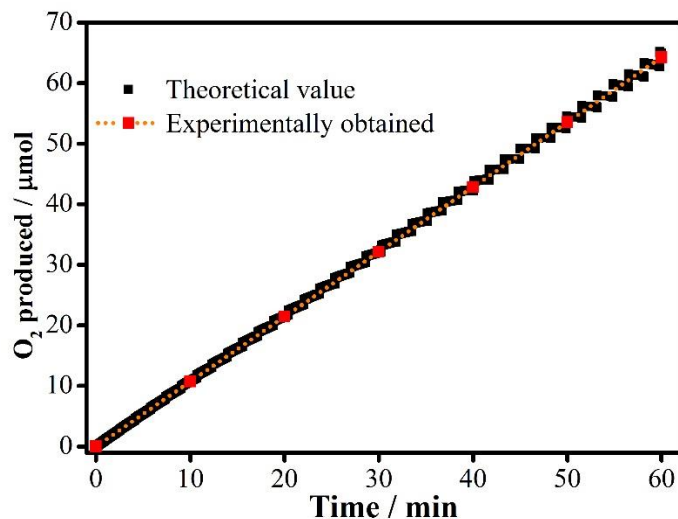


Figure 3. The amount of theoretically calculated yield for oxygen (black dots) and experimentally measured oxygen (red dots) on  $\text{CuCo}_2\text{Se}_4$  electrocatalytic surface versus time at 0.7 V vs  $\text{Ag|AgCl}$  (KCl saturated).

8 h aging in alkaline medium indicating an increase of catalytic activity. Such increase of catalytic activity has been previously observed in Nafion<sup>®</sup>-containing catalytic films and can be explained by increasing porosity of the Nafion<sup>®</sup> composite as  $\text{O}_2$  is evolved during continuous OER. Figure 4a shows the comparison of LSV polarization curves before and after 8 h of chronoamperometry in 1.0 M KOH indicating excellent stability of the catalyst under conditions of continuous  $\text{O}_2$  evolution with improved activity after 8 h. To confirm the compositional stability, the crystalline structure of  $\text{CuCo}_2\text{Se}_4$  after 8 h of chronoamperometry was studied by pXRD which indicated only the presence of  $\text{CuCo}_2\text{Se}_4$  as the major crystalline phase without any other metal oxides or hydroxides as shown in Figure 4b. The morphology of the catalyst after 8 h chronoamperometry was investigated by SEM as shown in Figure S6, which showed that the catalyst had similar morphologies before and after prolonged catalytic activity. XPS spectra collected after chronoamperometry demonstrated that the peaks of Co 2p, Cu 2p and Se 3d (shown in

Figure 4c-e) remain unchanged in terms of peak position. A comparison of the XPS peaks of pristine  $\text{CuCo}_2\text{Se}_4$  and the sample after 8 h chronoamperometry as shown in Figure S7 also revealed the close similarity of the peaks indicating no change in surface composition. In the XPS spectra as shown in Figure 4c-e was deconvoluted to analyze the different oxidation states of the elements and it was observed that the cations after 8 h aging catalyst included 14 % of  $\text{Co}^{3+}$ , 38 % of  $\text{Co}^{2+}$ , 9 %  $\text{Cu}^+$  and 39 % of  $\text{Cu}^{2+}$ . It is interesting to observe that the sample after chronoamperometry contained similar percentage of  $\text{Cu}^+$  and  $\text{Cu}^{2+}$ , while the amount of  $\text{Co}^{3+}$  increased by 6 % and  $\text{Co}^{2+}$  decreased by 7 % in comparison with the as-prepared  $\text{CuCo}_2\text{Se}_4$ . The  $\text{CuCo}_2\text{Se}_4$  catalyst after 8 h chronoamperometry was also studied by EDS which exhibited that the atomic ratio of Cu, Co and Se before and after chronoamperometry were almost same (relative atomic percentages has been listed in Table S2 in supporting information). All these post-OER activity and compositional analysis revealed that the catalyst was indeed stable under corrosive alkaline conditions.

$\text{CuCo}_2\text{Se}_4$  nanoparticles also exhibited remarkable electrocatalytic activity for hydrogen evolution reaction (HER) at the cathode in  $\text{N}_2$ -saturated 1.0 M KOH. Polarization curves of  $\text{CuCo}_2\text{Se}_4$ @Au-glass were measured with a scan rate of  $10 \text{ mV s}^{-1}$  and compared with Pt mesh under the same condition shown in Figure 5. It can be seen that an overpotential of 125 and 232 mV for  $\text{CuCo}_2\text{Se}_4$  was required to achieve a cathodic current density of 10 and  $50 \text{ mA cm}^{-2}$ , respectively, which was just slightly higher than that of Pt.<sup>81</sup> With a very low onset potential of -47 mV vs RHE obtained from the magnified LSV plot shown in Figure S8, the cathodic current density of  $\text{CuCo}_2\text{Se}_4$  catalyst increased rapidly indicating excellent conductivity of the catalyst. The stability of the catalyst for continuous  $\text{H}_2$  evolution was measured at -0.11 V vs RHE to achieve a cathodic current density

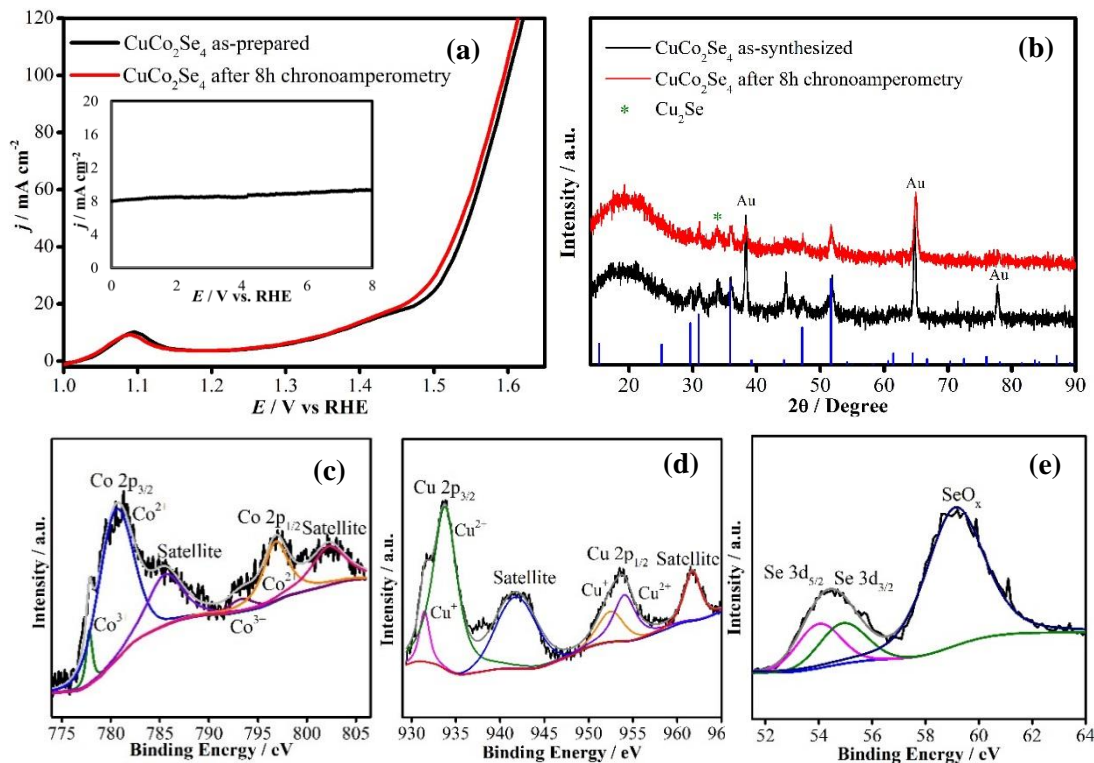


Figure 4. (a) Comparison of LSV curves of  $\text{CuCo}_2\text{Se}_4$  catalyst measured in  $\text{N}_2$ -saturated 1.0 M KOH before and after 8 h chronoamperometry. The inset shows chronoamperometric measurement of  $\text{CuCo}_2\text{Se}_4$  under continuous  $\text{O}_2$  evolution. (b) Comparison of pxrd before and after 8 h chronoamperometry. XPS spectra of (c) Co 2p, (d) Cu 2p and (e) Se 3d after chronoamperometric measurement for 8 h.

around  $-7 \text{ mA cm}^{-2}$  in 1.0 M KOH for 4.5 h shown in the inset of Figure 5. As can be seen, the current density was similar before and after 4.5 h aging. The LSVs before and after chronoamperometry has been compared in Figure 5 showed almost same behaviour towards HER further confirmed the stability as a HER catalyst in alkaline medium.

Since  $\text{CuCo}_2\text{Se}_4@Au$  exhibited highly efficient bifunctional electrocatalytic activity for both OER and HER in alkaline medium, so an electrolyzer was made using  $\text{CuCo}_2\text{Se}_4@Au$ -glass electrodes as both cathode and anode for water splitting at room temperature (Figure S9).  $\text{CuCo}_2\text{Se}_4@Au||Pt$  and  $\text{RuO}_2||Pt$  couples were also measured in  $\text{N}_2$ -saturated 1.0 M KOH solution in comparison of  $\text{CuCo}_2\text{Se}_4@Au||\text{CuCo}_2\text{Se}_4@Au$  as

shown in Figure S10. As expected, combining  $\text{CuCo}_2\text{Se}_4@Au$  anode and Pt cathode exhibited the highest efficiency while the  $\text{RuO}_2||\text{Pt}$  couple produced diminished catalytic activity.  $\text{CuCo}_2\text{Se}_4@Au||\text{CuCo}_2\text{Se}_4@Au$  electrolyzer required a cell voltage of 1.782 V to reach a current density of  $50 \text{ mA cm}^{-2}$  shown in Table S3.

To better understand the effects of the electronic properties of  $\text{CuCo}_2\text{Se}_4$  on its outstanding OER catalytic activities, DFT calculations were performed to evaluate the electronic band structure for bulk  $\text{CuCo}_2\text{Se}_4$ , slab with (100) terminated surface, and slab with (111) surfaces with Co/Cu termination and Co-only termination, as shown in Figure 6. All the crystal structures for bulk and the slabs of  $\text{CuCo}_2\text{Se}_4$  (Figure 6) were plotted using VESTA software.<sup>82</sup> The corresponding supercells are  $\text{Cu}_8\text{Co}_{16}\text{Se}_{32}$  (4 formula units, f.u.) as shown in Figure 6 (a),  $\text{Cu}_{14}\text{Co}_{28}\text{Se}_{56}$  (7 f.u.) in Figure 6 (b), and  $\text{Cu}_{24}\text{Co}_{48}\text{Se}_{96}$  (12 f.u.) in Figure 6 (c), respectively. To study the surface properties in the 2D structures under periodic boundary conditions, a relatively large vacuum layer of around  $10 \text{ \AA}$  was used to

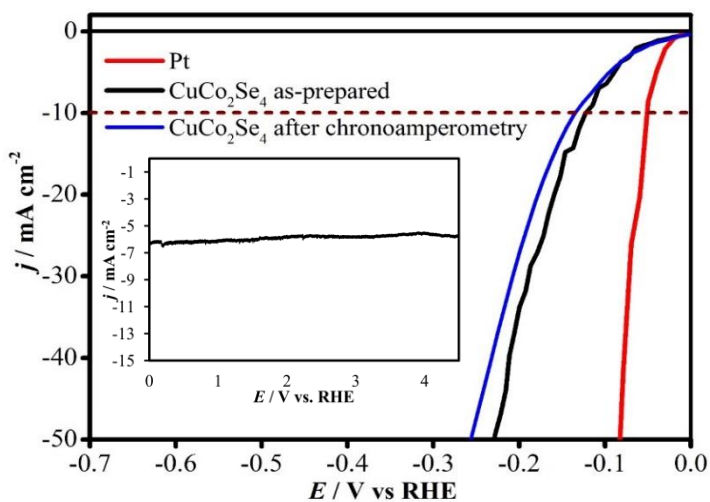


Figure 5. HER activity of  $\text{CuCo}_2\text{Se}_4@Au$  measured in  $\text{N}_2$ -saturated 1.0 M KOH at a scan rate of  $10 \text{ mV s}^{-1}$  compared with that of Pt mesh. The plot also shows the polarization curve after chronoamperometry. Inset shows the chronoamperometric study of  $\text{CuCo}_2\text{Se}_4@Au$  for 4.5 h of continuous  $\text{H}_2$  evolution.

separate the 2x2 slabs in order to avoid interaction between them. The slab thickness is about 17 Å for both the (100) and (111) surfaces that corresponds to seven Co-containing layers.

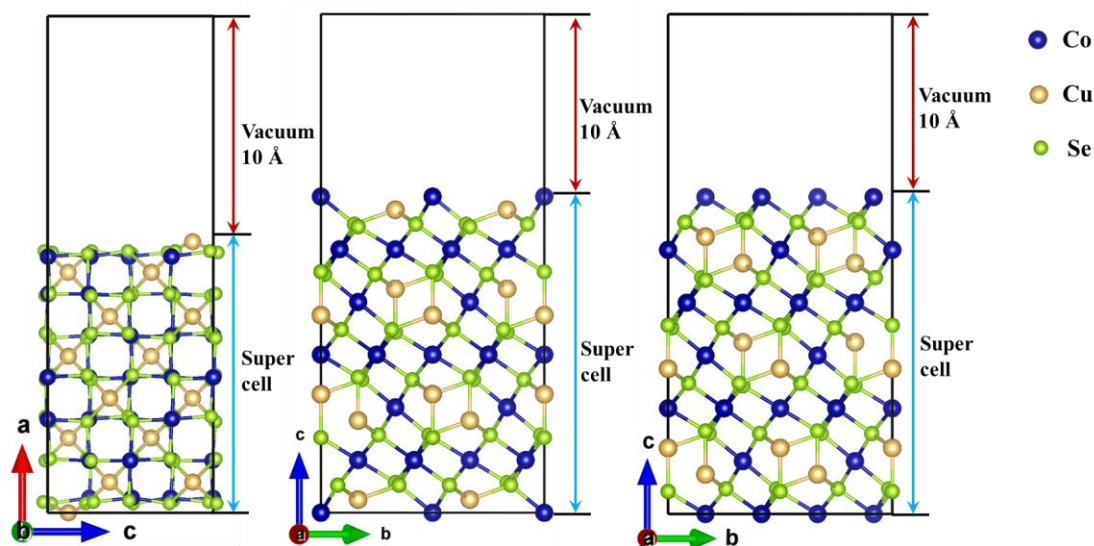


Figure 6. Slab supercells for (100) surface (a), (111) surface with Cu/Co termination (b) and (111) surface with Co-only termination (c). Color coded: navy – Co, yellow – Cu, green – Se.

The total density of states (DOS) and partial density of states (PDOS) of bulk CuCo<sub>2</sub>Se<sub>4</sub> calculated using GGA+U with  $U = 6$  eV for Co  $d$ -states and  $U = 4$  eV for Cu  $d$ -states are presented as solid lines in Figure 7. The valence band (VB) mainly consists of the  $d$ -orbitals from Co and Cu hybridized with the  $p$ -orbitals of Se, while the conduction band (CB) is mainly composed of both the empty  $d$ -orbitals in Co and the antibonding  $p$ -orbitals of Se. This result suggests the occurrence of  $d$ - $d$  transitions between Co and Cu, and the charge transfer between metal and Se.<sup>83</sup> Importantly, the continuous distribution of the DOS near the Fermi level indicates that CuCo<sub>2</sub>Se<sub>4</sub> is in the metallic state with a high electrical conductivity,<sup>44</sup> resulting from the PDOS contribution of Co and Se atoms as

shown in Figure 7 (c) and (d). This result is also consistent with the electrochemical impedance spectra (EIS) measurement shown in Figure S5 and Table S1 which revealed that  $\text{CuCo}_2\text{Se}_4$  catalyst has a relatively low catalyst resistance as well as charge transfer resistance, therefore facilitates fast electron transport during the electrocatalytic process.<sup>48</sup> The DOS and PDOS plots calculated using GGA method are also given as dashed lines in Figure 7 for comparison. Most importantly, GGA or GGA+U with  $U=5$  eV or smaller result in a non-magnetic solution, whereas the magnetic moment of  $0.79 \mu_B$  on Co atoms was obtained for  $U=6$  eV. For the latter case, there is a significant effect of  $U_{\text{eff}}$  on the occupied Co 3d states than on Cu 3d states in VB; the changes in CB are caused primarily by the magnetic interactions on Co atoms that push the spin-down empty 3d-states of Co to a higher energy.

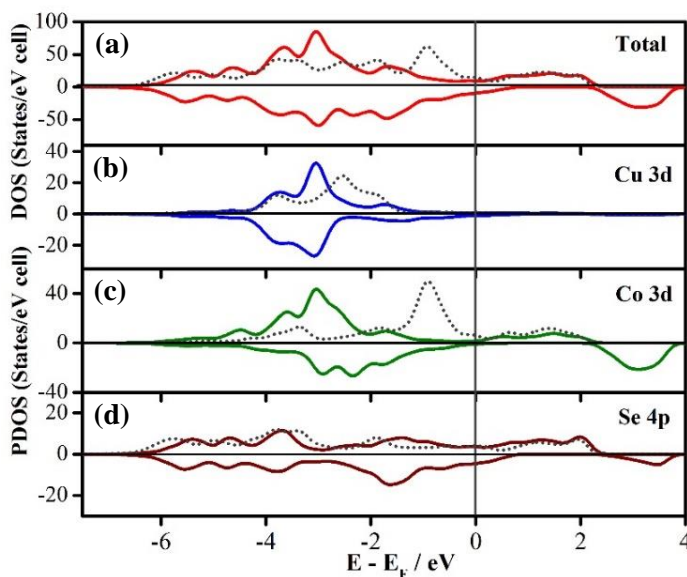


Figure 7. (a) The total density of states (DOS) of bulk  $\text{CuCo}_2\text{Se}_4$  and (b-d) partial density of states (PDOS) of Cu 3d, Co 3d and Se 4p calculated using GGA (dashed line) and GGA+U with  $U = 6$  eV for Co d-states and  $U = 4$  eV for Cu d-states (solid line).



In Figure 8, the total density of states (TDOS) of bulk  $\text{CuCo}_2\text{Se}_4$ , (100) slab, (111) slab with Co/Cu and (111) only-Co terminated planes, all calculated within GGA+U, are compared. It can be noticed that bulk and both (100) and (111) surfaces are in the metallic state. The (100) surface shown in Figure 8 (b) exhibits a similar TDOS in the vicinity of the Fermi level as that of the bulk  $\text{CuCo}_2\text{Se}_4$ , while (111) surfaces as shown in Figure 8 (c) and (d) show a more intense TDOS near the Fermi level; thus, suggesting a higher electronic conductivity. It's also interesting to observe the trend that the width of the CB narrows, effectively shifting the top of the CB around 2 eV toward the Fermi level from bulk to (100), (111) Co/Cu and (111) Co surfaces, indicating that the (111) surface has more metallic character and the *d-d* localization might take place among Cu and Co atoms. During the OER process, the active sites can be stabilized by the charge transfer and enhance the efficiency of absorbing intermediate species, which has been widely agreed upon as being one of the important factors to affect the OER catalytic activity.<sup>84,85,86</sup> Hence, it's reasonable to conclude that the (111) surface with Co-terminated lattice plane is more catalytic favorable than (111) Co/Cu and (100) plane or even bulk. Based on the calculated surface Gibbs free energy, the  $E_{\text{surface}}$  is 136 meV for (100), 280 meV for (111) Co/Cu, and 242 meV for (111) Co. Hence, the thermodynamic stability of surface orientations is then as follows: (100) > (111) Co > (111) Co/Cu, indicating that the (100) surface should be more thermodynamically favorable. For the (111) surface, termination with Co layer is more stable than that with Co/Cu, so it is easier to form (111) Co termination under directional growth. It is important to stress that the thermodynamically stable plane will not necessary have more metallic states to reduce the overpotential: In fact, Yagi group has reported that the surface with higher energy can lead to a higher adsorption energy of

hydroxide species to facilitate the catalytic activity.<sup>87</sup> In another report, Wang's group has also studied  $\text{Co}_3\text{O}_4$  nanocrystals exposed with different lattice planes and showed that (111) is the most catalytically active plane with the highest  $E_{\text{surface}}$ .<sup>88</sup> Indeed, a surface with higher energy is expected to have structural defects that attract hydroxide species as adsorbents to reduce the surface energy. Hence in this work, we focused on the comparison between the (100) and (111) Co/Cu terminated planes and investigated the  $\text{OH}^-$  absorption on Co and Cu sites for both surface orientations.

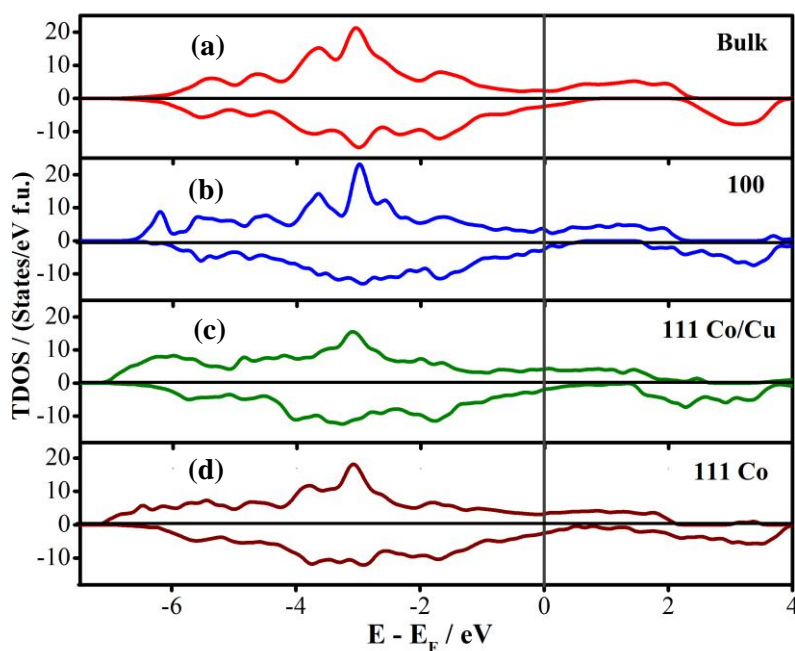


Figure 8. Total density of states (TDOS) of bulk  $\text{CuCo}_2\text{Se}_4$  (a), (100) surface (b), (111) surface with Co/Cu (c) and Co (d) termination.

To further analyze the electronic properties of the (100) and (111) surfaces, the DOS of top layer in (100) and (111) Co/Cu, the PDOS of a single Co atom located in the top surface layer (layer 0) and in the center layer (layer 3, close to the bulk property) have been plotted and compared in Figure 9. As can be seen in Figure 9 (a), the Co atom in the surface layer contributes at the bottom of VB in the (100) case, i.e., shifted by almost 3 eV

toward a more negative energy as compared to the Co atom in the center layer. In marked contrast, the energy position of the Co VB states remains almost same in the (111) Co/Cu case shown in Figure 9 (b). Hence, in the (100) case, the electronic properties of the surface top layer deviate significantly from those in bulk – in accord with the variation of the Co magnetic moments given in Table S4, whereas the changes occur even in the center layer for the (111) Co/Cu slab. For the Co atom located in the surface layer, the VB of both (100) and (111) Co/Cu are similar, while the CB in (111) is slightly closer to the Fermi level.

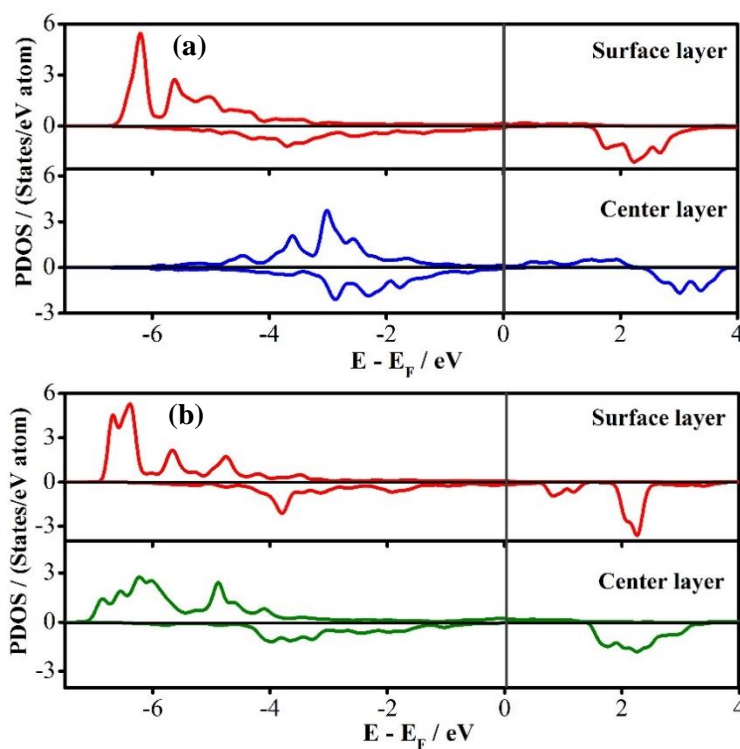


Figure 9. Comparison of partial electronic density of states (PDOS) of Co atoms in the surface top layer with the one in the center layer in the (100) slab (a) and (111) slab with Co/Cu termination (b).

To understand the differences in the electronic and magnetic properties of the top layer and the inside layers, the combined PDOS of all Co atoms from each layer of (100)

slab and (111) Co/Cu slab have been plotted and presented in Figure 10. In this case, the layer 0 refers to the surface layer, while the deeper layers are denoted as layer 1, layer 2 and layer 3 (center). Notably, in Figure 10 (a), the surface layer shows a much unique DOS compared with that of the inside layers in the (100) slab. The DOS of the top layer is less intense near the Fermi level while it is likely to be increased for the deeper layers. The origin of the energy shift of the surface states is in the stronger magnetic exchange interactions that split these Co *d*-states apart. The magnetic moment on Co, given in Table S4, decreases from layer 0 (2.10  $\mu_B$ ) to layer 3 (0.78  $\mu_B$ ) – in accord with shorter Co-Se bond distances and stronger bond distortion for the surface layer, also listed in Table S4. Thus, the central layer in the (100) slab resembles the electronic and magnetic properties of bulk  $\text{CuCo}_2\text{Se}_4$ . In contrast, there is no apparent correlation between the Co magnetic moment and the layer depth in the (111) slab: the top layer 0 has the highest magnetic moment (2.29  $\mu_B$ ), as it is in the (100) case, however, the following layer 1 has the lowest magnetic moment (1.47  $\mu_B$ ) and the magnetic moment is large in the layers 2 and 3 (~2.1  $\mu_B$ ), more than double of that in the bulk value (0.79  $\mu_B$ ). Therefore, the structural reconstruction and the surface enhancement of the magnetic properties of Co atoms is much deeper for the slab with (111) surface orientation than that for the (100) slab where only the top surface layer is affected. It should be noted here that in contrast to (100) slab with similar metal composition of the layers, in the (111) slab, the layer 1 and layer 3 consist of only Co atoms while both Co and Cu atoms are present in the layer 0 and layer 2. The Co atoms in layer 0 has Co-Se bond distance of 2.23 Å which is the shortest one in comparison to that in bulk (2.40 Å). As a result, both the spin up and spin down states are narrower for Co atom in the surface layer as compared to deeper layers, Figure 10 (b), however, the Co

atom in the top layer has spin down CB states closest to the Fermi level (at  $\sim 1$  eV). These states participate in  $\text{OH}^-$  adsorption, as shown below.

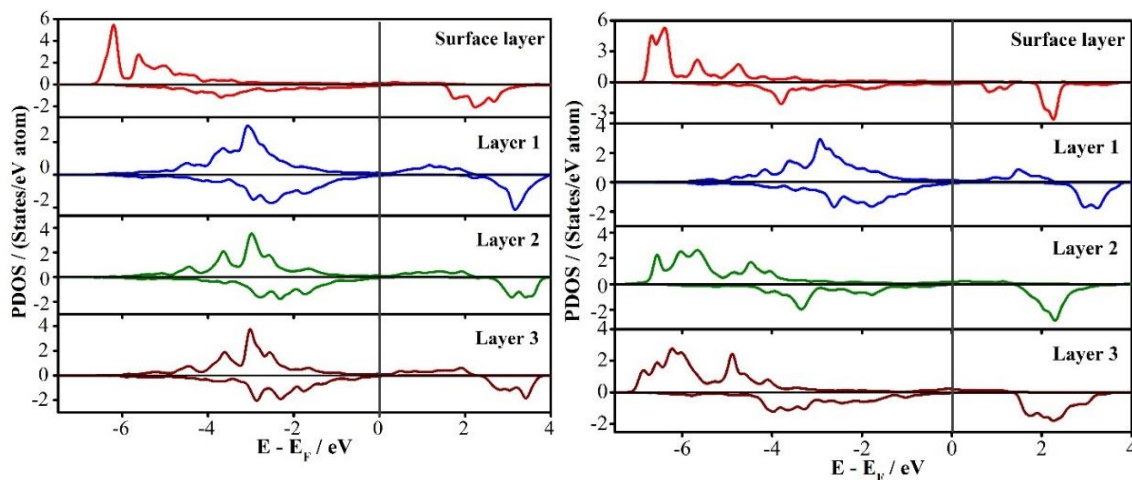


Figure 10. Combined partial density of states (PDOS) of all Co atoms in each layer for (100) slab (a) and (111) Co/Cu terminated slab (b).

To investigate which metal atom on the surface is more likely to be the catalytically active site for OER, the adsorption of  $\text{OH}^-$  on (100) and (111) Co/Cu terminated slabs was modeled by placing  $\text{OH}^-$  ion in the vicinity of the active metal site (Co or Cu) of the relaxed free surface at an initial distance of about 2.2 Å from the metal atom. The GGA+U total energy of the fully-optimized structure with  $\text{OH}^-$  bonded to the surface Co atom is 0.53 eV and 2.03 eV higher than that bonded to the Cu atom for the (100) and (111) surface, respectively. The large energy difference, especially in the (111) case, suggests that Co atom is the highly preferred catalytically active site. We should note here that the energy difference between the adsorption of  $\text{OH}^-$  on Co vs Cu is much smaller within GGA (U=0 eV), namely, 0.04 eV and 0.52 eV for the (100) and (111) case, respectively, suggesting that magnetism plays a crucial role in favoring the  $\text{OH}^-$  adsorption on Co. The comparison

of PDOS of Co and Cu atoms with and without OH<sup>-</sup> attachment is shown in Figure 11 and Figure S11, respectively. For both Co and Cu with OH<sup>-</sup> ion attached, there is a significant orbital splitting of the occupied metal states associated with rearranged electron cloud. In addition, in all cases except for Cu-OH at (111) surface, a strong hybridization of the metal states with the states of OH<sup>-</sup> ion leads to a more intense density of states in the VB near the Fermi level as compared to OH<sup>-</sup> free surfaces. Further, comparing the energetics of the OH<sup>-</sup> ion bonded to Co on (100) vs (111) surface, we find that the OH<sup>-</sup> adsorption on the (111) Co/Cu terminated surface is energetically more favorable by as much as 7 eV as shown in Table S5. While the Co-O distances or Co-O-H angles are relatively similar for the (100) and (111) slabs, namely, 1.81 Å and 1.76 Å or 110.4° and 123.1°, respectively, we believe that the huge energy difference for OH<sup>-</sup> ion adsorption on Co at two different surface orientations is due to the fact that the Co atom at the (111) surface is 3-coordinated with Se atoms, whereas it is 5-coordinated at the (100) surface. Upon bonding to the OH complex, the magnetic moment on the Co atom increases from 2.1 μ<sub>B</sub> to 2.6 μ<sub>B</sub> for (100) slab and from 2.3 μ<sub>B</sub> to 2.4 μ<sub>B</sub> for (111) slab with Co/Cu termination, whereas the Co-Se distances increase from 2.33 Å to 2.45 Å and from 2.23 Å to 2.30 Å, respectively. Accordingly, the calculated PDOS of Co, Figure 11, shows that the occupied spin-up Co states become more localized upon bonding with OH<sup>-</sup> due to the weaker Co-Se interactions and are shifted to the lower negative energy because of the stronger magnetic exchange splitting. On the other hand, the PDOS exhibit opposite trends in the empty spin-down states of Co for (100) and (111) slabs, namely, the shift to the lower and higher energy, respectively, as shown in Figure 11. Finally, we aligned the DOS of the (100) and (111) Co/Cu terminated slabs with OH<sup>-</sup> ion attached to Co atom on each surface with respect to

the semi-core O-2s states and observed that the Fermi level of the (111) surface is about 0.2-0.3 eV lower as compared to that of the (100) surface – in accord with the preferred OH<sup>-</sup> adsorption on the (111) surface orientation of CuCo<sub>2</sub>Se<sub>4</sub>.

From the DFT studies of the electronic properties and the OH<sup>-</sup> adsorption calculations on the different surfaces of CuCo<sub>2</sub>Se<sub>4</sub>, it can be concluded that Co atom is the active catalytic site for the CuCo<sub>2</sub>Se<sub>4</sub> system. However, the presence of Cu on the neighbouring sites influences the electronic density around the Co ions as well as its magnetic moment. Specifically, the alternate Co-only and Cu/Co layers in the slab with (111) surface orientation (Figure 6), results in significant variance of the layer-dependent magnetic moment of Co and, hence, its electronic properties, making surface enhancement of the magnetic interactions penetrate deeper into the (111) slab and OH<sup>-</sup> adsorption energetically favourable on the (111) surface. Furthermore, in cobalt based materials, Co<sup>3+</sup> has been widely accepted as the effective active site resulting in the Co<sup>2+</sup>→Co<sup>3+</sup> redox conversion during the OER process.<sup>85</sup> The Co<sup>2+</sup>→Co<sup>3+</sup> oxidation is visible as the peak at around 1.1 V (vs RHE) in the OER LSV, which is consistent with the data shown in Figure 2. Such catalyst activation will be enhanced as the presence of Cu redistributes the electron density around Co through *d-d* interactions as was also observed in the DFT studies. The increased amount of Co<sup>3+</sup> seen in XPS also confirms that Co sites are more likely to serve as the active catalytic site for OER. Specifically, with the spinel structure catalysts, the metal ions occupying the octahedral sites has been observed to be more active for OER.<sup>89,90</sup> The availability of additional sites for OH<sup>-</sup> adsorption on Cu will also possibly increase the hydrophilicity of the surface leading to better wettability and improved catalytic

performance. The inclusion of Cu also enhances the metallic states and electrical conductivity within the composite.

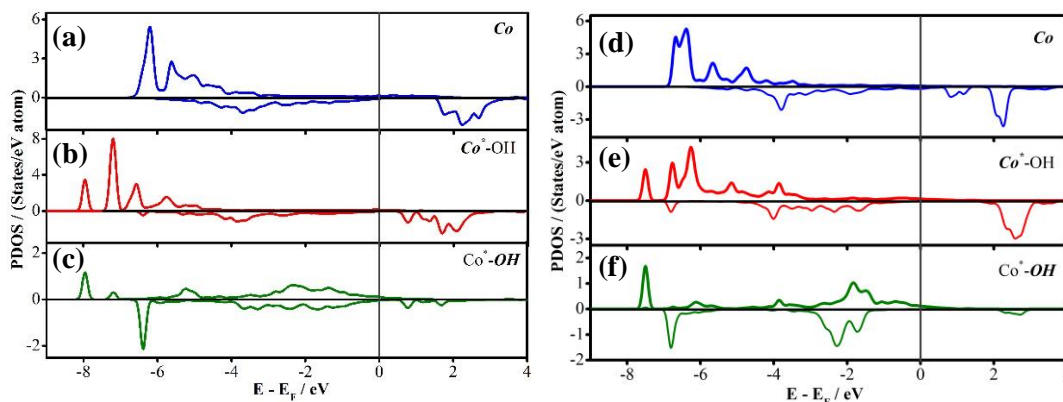


Figure 11. Partial density of states (PDOS) of Co atom in (100) surface before  $\text{OH}^-$  attachment (a), Co atom after  $\text{OH}^-$  attachment (b),  $\text{OH}^-$  ions after attachment on Co atom (c). PDOS of Co atom in (111) surface before  $\text{OH}^-$  attachment (d), Co atom after  $\text{OH}^-$  attachment (e),  $\text{OH}^-$  ions after attachment on Co atom (f).

#### 4. CONCLUSIONS

In summary, for the first time,  $\text{CuCo}_2\text{Se}_4$  nanoparticles are shown as an out-performing bifunctional electrocatalyst for overall water splitting. The OER and HER electrocatalytic property was studied through detailed electrochemical measurements which revealed that the catalyst required a low overpotential of 320 mV and 232 mV to achieve  $50 \text{ mA cm}^{-2}$  for OER and HER, respectively, and exhibited promising durability in alkaline solution. The overpotential for OER was significantly lower than that of  $\text{RuO}_2$  and was amongst the lowest for selenide based OER electrocatalysts. A comparison with the other reported Co and/or Cu-based OER/HER catalyst (Table 1) revealed that  $\text{CuCo}_2\text{Se}_4$  presented in this paper is even better than the best Cu and/or Co-based OER



catalyst. Importantly, the catalyst can be applied for full water splitting and can achieve a current density of  $50 \text{ mA}\cdot\text{cm}^{-2}$  at a cell voltage of 1.782 V with energy efficiency of 83.05 %. The  $\text{CuCo}_2\text{Se}_4$  nanostructure synthesized through one-step hydrothermal method provides a new composition of high-efficiency electrocatalysts comprising economical and earth abundant transition metals. First-principles electronic structure calculations of bulk and (100) and (111) lattice plane terminated slabs of  $\text{CoCu}_2\text{Se}_4$  as well as comparison of  $\text{OH}^-$  adsorption energies on the corresponding surfaces provided significant insight into the origin of observed catalytic performance and possible catalytically active sites in this material. Based on the extensive DFT calculations, it was concluded that Co is the actual catalytically active site in this material. However, the presence of neighboring Cu atoms enhances the catalytic activity on the Co site through electron redistribution, as well as enhancement of the local magnetic moment which effects the  $\text{OH}^-$  adsorption energy on the catalytic site, leading to faster onset of OER and reduction of overpotential. Such knowledge regarding the effect of transition metal doping on the OER catalytic activity as well the positive effect of the presence of Cu near the catalytic site, can be extended to design other OER catalytic system with predictively high efficiencies.

Table 1. Comparison of catalytic activity for different Co and/or Cu based OER / HER electrocatalysts in alkaline medium.

| Electrocatalyst            | Electrolyte | OER                        |                                                                | HER                        |                                                                | Reference |
|----------------------------|-------------|----------------------------|----------------------------------------------------------------|----------------------------|----------------------------------------------------------------|-----------|
|                            |             | Onset potential (V vs RHE) | Overpotential (mV vs RHE) @ $10 \text{ mA}\cdot\text{cm}^{-2}$ | Onset potential (V vs RHE) | Overpotential (mV vs RHE) @ $10 \text{ mA}\cdot\text{cm}^{-2}$ |           |
| $\text{CuCo}_2\text{Se}_4$ | 1 M KOH     | 1.43                       | 320 <sup>a</sup>                                               | 0.07                       | 120                                                            | This work |
| $\text{Co}_7\text{Se}_8$   | 1 M KOH     | 1.45                       | 290                                                            | 0.317                      | 472                                                            | 38        |

Table 1. Comparison of catalytic activity for different Co and/or Cu based OER / HER electrocatalysts in alkaline medium. (cont.)

|                                                                     |                              |      |                  |                  |     |    |
|---------------------------------------------------------------------|------------------------------|------|------------------|------------------|-----|----|
| Cu <sub>2</sub> Se                                                  | 1 M KOH                      | 1.50 | 320              | -                | -   | 39 |
| CuCo <sub>2</sub> O <sub>4</sub> /Nr<br>GO                          | 1 M KOH                      | 1.52 | 360              | -                | -   | 54 |
| CuCo <sub>2</sub> S <sub>4</sub>                                    | 1 M KOH                      | 1.43 | 310              | -                | -   | 55 |
| (Ni,<br>Co) <sub>0.85</sub> Se                                      | 1 M KOH                      | 1.47 | 255              | -                | -   | 91 |
| CoSe <sub>2</sub>                                                   | 1 M KOH                      | 1.55 | 430              | 0.1 <sup>b</sup> | 160 | 92 |
| CuO                                                                 | 1 M KOH                      | 1.59 | 470              | -                | -   | 93 |
| CuO                                                                 | 1 M KOH                      | 1.57 | 420              | -                | -   | 94 |
| CuCo <sub>2</sub> S <sub>4</sub> /CF                                | 1 M KOH                      | 1.43 | 295 <sup>c</sup> | -                | -   | 95 |
| Cu <sub>3</sub> P/NF                                                | 1 M KOH                      | 1.49 | 320              | 0.12             | 150 | 96 |
| CuO–<br>TCNQ/CF                                                     | 1 M KOH                      | 1.55 | 355 <sup>a</sup> | -                | -   | 97 |
| Co <sub>3</sub> O <sub>4</sub> /NiCo <sub>2</sub><br>O <sub>4</sub> | 1 M KOH                      | 1.53 | 340              | -                | -   | 98 |
| Cu <sub>2</sub> MoS <sub>4</sub>                                    | 0.1 M<br>phosphate<br>buffer | -    | -                | 0.55             | 750 | 99 |

<sup>a</sup> Overpotential at 50 mA cm<sup>-2</sup>. <sup>b</sup> HER was studied in 0.5 M H<sub>2</sub>SO<sub>4</sub>. <sup>c</sup> Overpotential at 100 mA cm<sup>-2</sup>

## ASSOCIATED CONTENT

Supporting Information. Procedure of electrodeposition of RuO<sub>2</sub>, ECSA, OER LSV comparison plots, zoomed-in HER and HER LSV plots, EIS plot and table, SEM comparison before and after stability, XPS comparison before and after stability, LSV plot and table of water electrolyzer, DFT result table, PDOS of Cu atoms and OER comparison table.

Author Information

Corresponding Author

\*Manashi Nath: nathm@mst.edu

#### Author Contributions

The manuscript was written through contributions of all authors. All authors have given approval to the final version of the manuscript.

#### Funding Sources

This work was supported by funding from National Science Foundation (DMR 1710313) and American Chemical Society Petroleum Research Fund (54793-ND10).

#### Notes

Any additional relevant notes should be placed here.

**Acknowledgments.** The authors would like to acknowledge the funding from National Science Foundation (DMR 1710313) and American Chemical Society Petroleum Research Funds (54793-ND10). The authors would also like to acknowledge Materials Research Center (MRC) for equipment usage. Computational resources were provided by DOE-supported NERSC (National Energy Research Scientific Computing) center for high-performance computing.

## **SUPPORTING INFORMATION**

### **COPPER COBALT SELENIDE AS A HIGH-EFFICIENCY BIFUNCTIONAL ELECTROCATALYST FOR OVERALL WATER SPLITTING: COMBINED EXPERIMENTAL AND THEORETICAL STUDY**

*Xi Cao<sup>a</sup>, Julia E. Medvedeva<sup>b\*</sup> and Manashi Nath<sup>a\*</sup>*

<sup>a</sup>Department of Chemistry, Missouri University of Science & Technology, Rolla, Missouri 65409, United States.

<sup>b</sup>Department of Chemical and Biochemical Engineering, Missouri University of Science & Technology, Rolla, Missouri 65409, United States.

Electrodeposition of RuO<sub>2</sub> on Au coated glass: In a previous reported procedure of electrodeposition of RuO<sub>2</sub>,<sup>s1</sup> RuCl<sub>3</sub> (0.452 g) and KCl (2.952 g) were mixed in 40 ml of 0.01M HCl, cyclic voltammetry from 0.015 to 0.915 V (vs Ag|AgCl) was applied for 100 cycles at a scan rate of 50 mV s<sup>-1</sup>. Finally, the products were heated at 200 °C for 3 h under air.

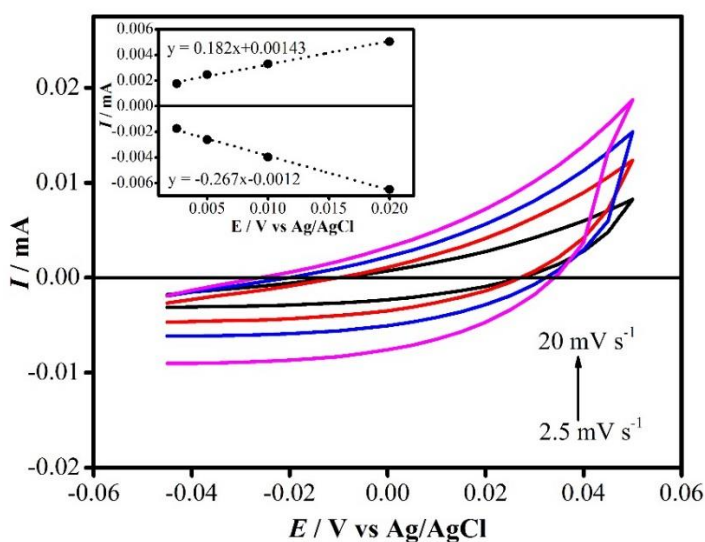


Figure S1. Cyclic voltammograms measured for CuCo<sub>2</sub>Se<sub>4</sub>@Au in N<sub>2</sub>-saturated 1.0 M KOH solution at different scan rates from 2.5 to 20 mV s<sup>-1</sup>. The inset is a plot of both anodic and cathodic current measured at 0.01 V vs Ag|AgCl (KCl saturated) as a function of scan rate.

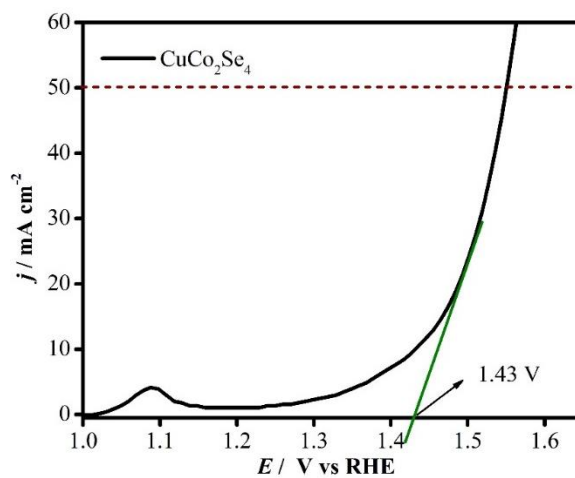


Figure S2. Zoom-in LSV curve of  $\text{CoCu}_2\text{Se}_4$ @Au in  $\text{N}_2$ -saturated 1.0 M KOH at a scan rate of  $10 \text{ mV s}^{-1}$  in order to obtain the onset potential.

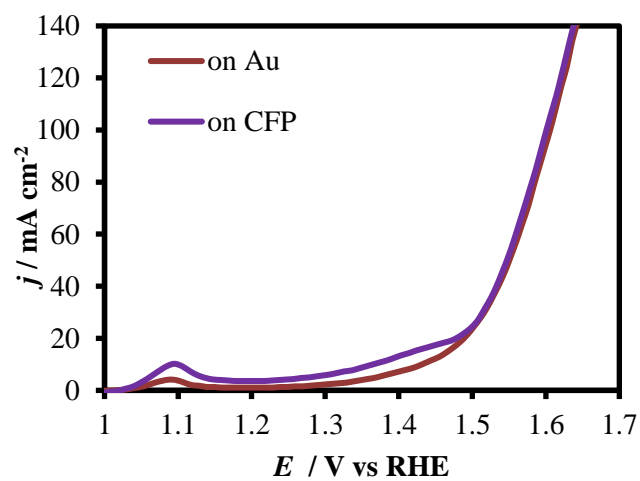


Figure S3. LSV curves of  $\text{CoCu}_2\text{Se}_4$  on Au and CFP in  $\text{N}_2$ -saturated 1.0 M KOH at a scan rate of  $10 \text{ mV s}^{-1}$ .

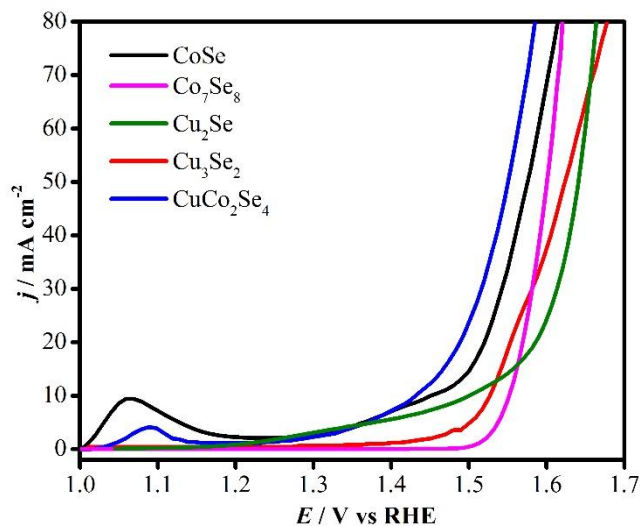


Figure S4. Comparison of OER LSVs of CoSe, Co<sub>7</sub>Se<sub>8</sub>, Cu<sub>3</sub>Se<sub>2</sub>, Cu<sub>2</sub>Se and CuCo<sub>2</sub>Se<sub>4</sub> measured in N<sub>2</sub>-saturated 1.0 M KOH at a scan rate of 10 mV s<sup>-1</sup>.

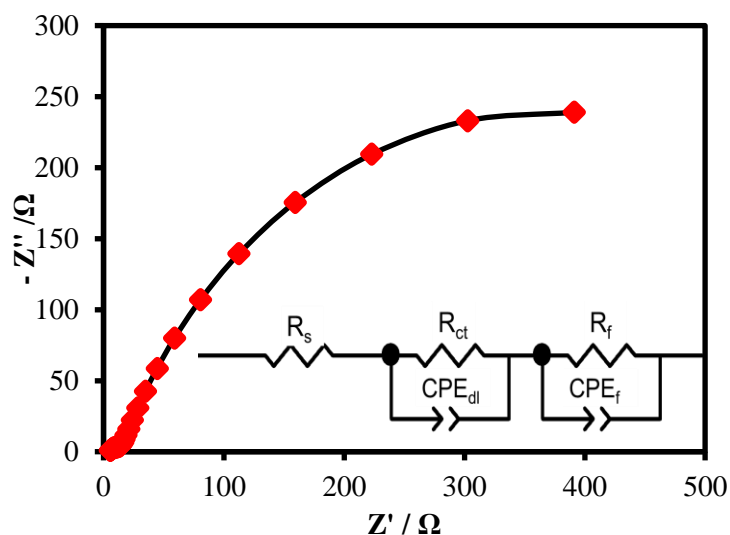


Figure S5. Nyquist plot obtained from EIS measurements of the catalyst and applied potential of 1.45 V vs RHE in N<sub>2</sub>-saturated 1.0 M KOH solution. Symbols indicate the raw data, while solid lines represent the corresponding fit to equivalent circuit model. Inset shows the equivalent circuit of catalysts.

Table S1. Equivalent Circuit Parameters Obtained from Fitting of EIS Experimental Data.

| Parameters            | Value |
|-----------------------|-------|
| $R_s/\Omega$          | 5.0   |
| $R_{ct}/\Omega$       | 9.34  |
| $CPE_{dl}/F$          | 0.63  |
| $R_{catalyst}/\Omega$ | 716.6 |
| $CPE_{catalyst}/F$    | 0.75  |

$R_s$  is the resistance of the electrolyte;  $R_{ct}$  is the electron transfer resistance;  $CPE_{dl}$  is the constant phase element of double-layer nonideal capacitance;  $R_{catalyst}$  is resistance of the catalyst layer; and  $CPE_{catalyst}$  is the capacitance.

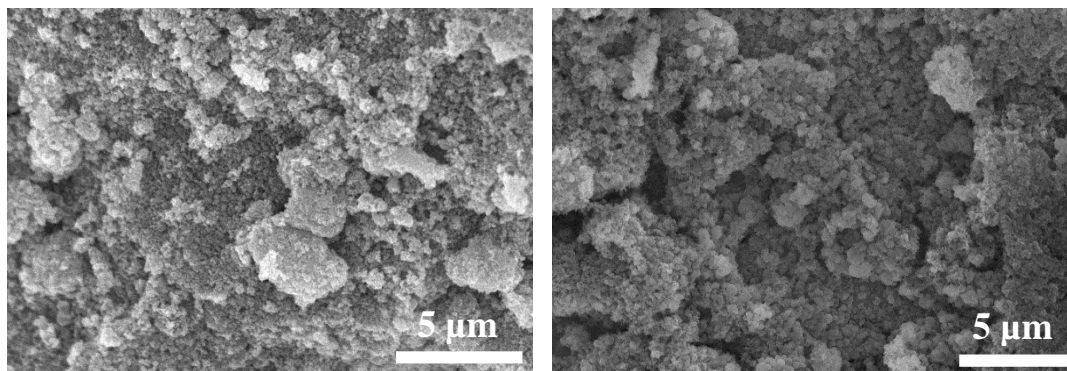


Figure S6. SEM images of as-synthesized  $CuCo_2Se_4$  (a) and  $CuCo_2Se_4$  after 8 h chronoamperometry in 1.0 M KOH.

Table S2. Comparison of EDS atomic ratio of the catalyst before and after 8 h chronoamperometry.

|                            | EDS ( Atomic % ) |      |      |
|----------------------------|------------------|------|------|
|                            | Co               | Cu   | Se   |
| As-deposited               | 30.9             | 17.0 | 52.1 |
| After 8h chronoamperometry | 30.9             | 17.5 | 51.6 |

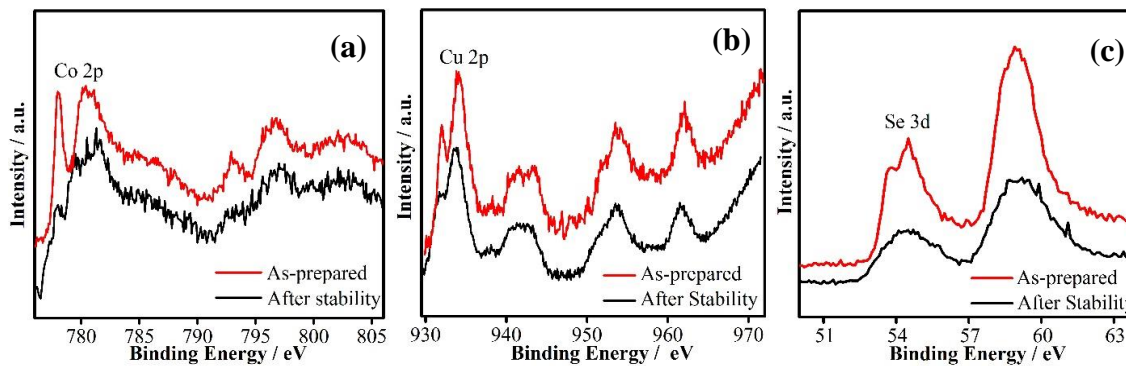


Figure S7. Comparison of XPS of  $\text{CuCo}_2\text{Se}_4$  before and after stability (a) Co 2p, (b) Cu 2p and (c) Se 3d.

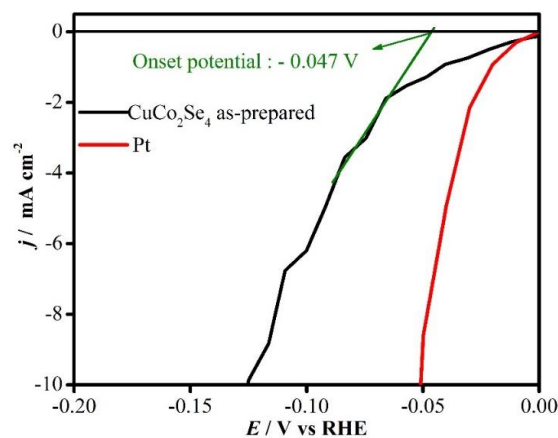


Figure S8. Zoom-in Figure of HER plots in order to measure the HER onset potential.

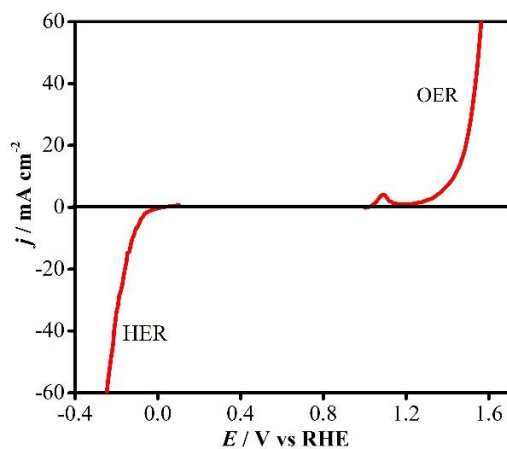


Figure S9. Overall water splitting of  $\text{CuCo}_2\text{Se}_4@Au$  in  $\text{N}_2$ -saturated 1.0 M KOH solution.



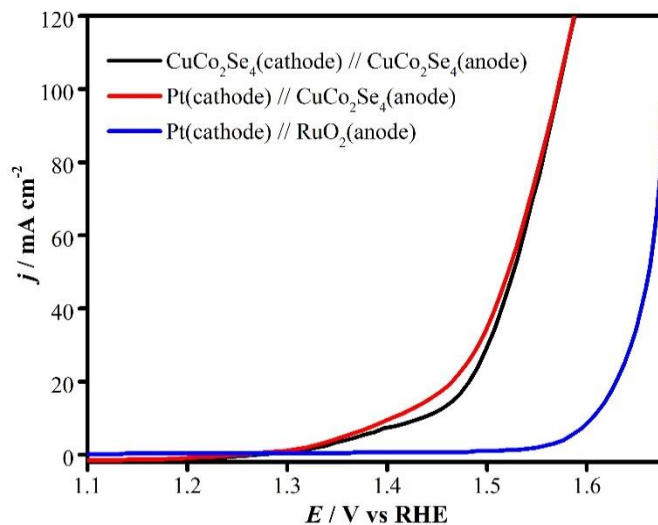


Figure S10. LSV curves of water electrolysis at a scan rate of  $10 \text{ mV s}^{-1}$  in  $\text{N}_2$ -saturated  $1.0 \text{ M KOH}$  solution. Black curve shows  $\text{CuCo}_2\text{Se}_4$  catalyst as both anode and cathode, red one represents  $\text{CuCo}_2\text{Se}_4$  catalyst as anode while Pt as cathode, and blue curve shows  $\text{RuO}_2$  as anode while Pt as cathode.

Energy Efficiency for overall water splitting:

Table S3. Calculation of energy efficiency of water electrolyzer (%)

| Catalyst                   | OER, V <sup>a</sup>        | HER, V <sup>a</sup>        | $E_{\text{cell}} / \text{V}$ | Energy efficiency <sup>b</sup> / % |
|----------------------------|----------------------------|----------------------------|------------------------------|------------------------------------|
|                            | at $50 \text{ mA cm}^{-2}$ | at $50 \text{ mA cm}^{-2}$ | at $50 \text{ mA cm}^{-2}$   | at $50 \text{ mA cm}^{-2}$         |
| $\text{CuCo}_2\text{Se}_4$ | 1.55                       | 0.232                      | 1.782                        | 83.05                              |
| Pt                         |                            | 0.08                       | 1.74                         | 85.06                              |
| $\text{RuO}_2$             | 1.66                       |                            |                              |                                    |

<sup>a</sup>All voltages are vs RHE. <sup>b</sup>Energy efficiency of water electrolysis  $\cong (1.48 \text{ V}/E_{\text{cell}}) \times 100$ .

Table S4. Comparison of total energy, magnetic moment, distance of Co-Se and bond length distortion at different layers among bulk  $\text{CoCu}_2\text{Se}_4$ , (100) surface and (111) with Co/Cu and Co termination as calculated from GGA+U.

|              | $E_{\text{surface}}$ /<br>eV | Magnetic Moment/<br>$\mu_B$ |         | Distance (Co-Se) /<br>Å                | Distortion (bond<br>length) |
|--------------|------------------------------|-----------------------------|---------|----------------------------------------|-----------------------------|
| Bulk         |                              | 0.79                        |         | 2.4                                    | 0                           |
| 100          | 136                          | 2.1                         | Layer 0 | 2.26<br>2.35 (2×)<br>2.3<br>2.4        | 0.018                       |
|              |                              | 0.9                         | Layer 1 | 2.35 (2×)<br>2.40 (2×)<br>2.39<br>2.42 | 0.0099                      |
|              |                              | 0.86                        | Layer 2 | 2.4<br>2.41<br>2.38 (4×)               | 0.0044                      |
|              |                              | 0.78                        | Layer 3 | 2.37 (2×)<br>2.39 (4×)                 | 0.0029                      |
| 111<br>Co/Cu | 280                          | 2.29                        | Layer 0 | 2.23 (3×)                              | 0.0002                      |
|              |                              | 1.47                        | Layer 1 | 2.36 (3×)<br>2.41<br>2.40 (2×)         | 0.0087                      |
|              |                              | 2.07                        | Layer 2 | 2.39 (4×)<br>2.38 (2×)                 | 0.0018                      |
|              |                              | 2.13                        | Layer 3 | 2.38 (2×)<br>2.39 (4×)                 | 0.0009                      |
| 111 Co       | 242                          | 2.23                        | Layer 0 | 2.22<br>2.25<br>2.27<br>2.35           | 0.0175                      |
|              |                              | 2.16                        | Layer 1 | 2.36<br>2.37 (2×)<br>2.39              | 0.00381                     |
|              |                              | 0.91                        | Layer 2 | 2.37 (2×)<br>2.38 (2×)<br>2.39         | 0.00307                     |
|              |                              | 0.84                        | Layer 3 | 3.38 (2×)<br>2.39 (4×)                 | 0.00193                     |

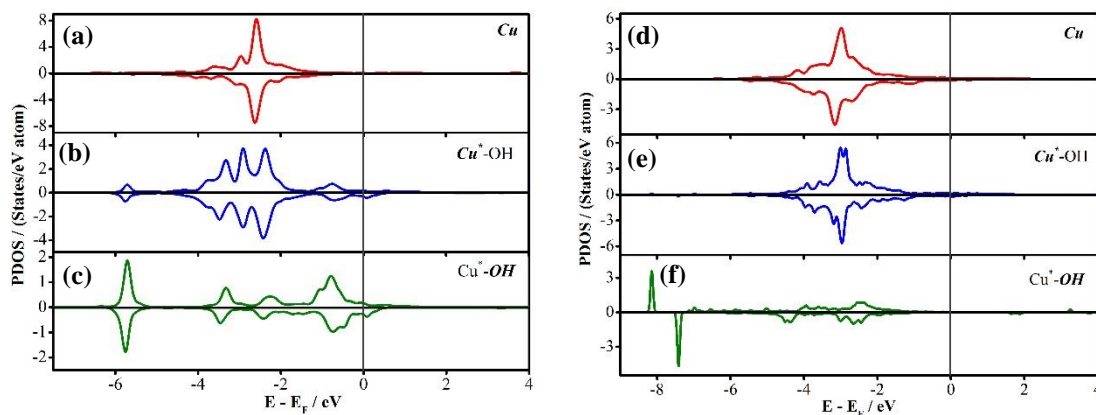


Figure S11. Partial density of states (PDOS) of Cu atom in (100) surface before  $\text{OH}^-$  attachment (a), Cu atom after  $\text{OH}^-$  attachment (b),  $\text{OH}^-$  after attached on Cu atom (c). PDOS of Cu atom in (111) surface before  $\text{OH}^-$  attachment (d), Cu atom after  $\text{OH}^-$  attachment (e),  $\text{OH}^-$  after attached on Cu atom (f).

Table S5.  $\text{OH}^-$  adsorption Energy on Co and Cu atoms in (100) and (111) Co/Cu surfaces.

| Surface        | Atom attached with $\text{OH}^-$ | Adsorption Energy / eV |
|----------------|----------------------------------|------------------------|
| (100)          | Co                               | -2.96                  |
|                | Cu                               | -2.43                  |
| (111)<br>Co/Cu | Co                               | -10.02                 |
|                | Cu                               | -7.99                  |

## SUPPORTING REFERENCE

- S1 K. M. Kim, J. H. Nam, Y. G. Lee, W. Il Cho and J. M. Ko, *Curr. Appl. Phys.*, 2013, 13, 1702–1706.

## REFERENCES

- (1) Lewis, N. S. Toward Cost-Effective Solar Energy Use. *Science* **2007**, 315, 798–801.
- (2) Walter, M. G.; Warren, E. L.; Mckone, J. R.; Boettcher, S. W.; Mi, Q.; Santori, E. A.; Lewis, N. S. Solar Water Splitting Cells. *Chem. Rev.*, **2010**, 110, 6446–6473.
- (3) Turner, J. A. Sustainable Hydrogen Production. *Science* **2004**, 305, 972–974.

- (4) Suen, N.-T.; Hung, S.-F.; Quan, Q.; Zhang, N.; Xu, Y.-J.; Chen, H. M. Electrocatalysis for the Oxygen Evolution Reaction: Recent Development and Future Perspectives. *Chem. Soc. Rev.* **2017**, *46*, 337–365.
- (5) Rossmeisl, J.; Logadottir, A.; Nørskov, J. K. Electrolysis of Water on (Oxidized) Metal Surfaces. *Chem. Phys.* **2005**, *319*, 178–184.
- (6) Jiao, Y.; Zheng, Y.; Jaroniec, M.; Qiao, S. Z. Design of Electrocatalysts for Oxygen- and Hydrogen-Involving Energy Conversion Reactions. *Chem. Soc. Rev.* **2015**, *44*, 2060–2086.
- (7) Matsumoto, Y.; Sato, E. Electrocatalytic Properties of Transition Metal Oxides for Oxygen Evolution Reaction. *Mater. Chem. Phys.* **1986**, *14*, 397–426.
- (8) Mccrory, C. C. L.; Jung, S.; Peters, J. C.; Jaramillo, T. F. Benchmarking Heterogeneous Electrocatalysts for the Oxygen Evolution Reaction. *J. Am. Chem. Soc.* **2013**, *135*, 16977–16987.
- (9) Hamann, T. W. Water Splitting: An Adaptive Junction. *Nat. Mater.* **2013**, *13*, 3–4.
- (10) Dau, H.; Limberg, C.; Reier, T.; Risch, M.; Roggan, S.; Strasser, P. The Mechanism of Water Oxidation: From Electrolysis via Homogeneous to Biological Catalysis. *ChemCatChem* **2010**, *2*, 724–761.
- (11) Roger, I.; Shipman, M. A.; Symes, M. D. Earth-Abundant Catalysts for Electrochemical and Photoelectrochemical Water Splitting. *Nat. Rev. Chem.* **2017**, *1*, 0003.
- (12) Gong, M.; Dai, H. A Mini Review of NiFe-Based Materials as Highly Active Oxygen Evolution Reaction Electrocatalysts. *Nano Res.* **2015**, *8*, 23–39.
- (13) Geiger, S.; Kasian, O.; Shrestha, B. R.; Mingers, A. M.; Mayrhofer, K. J. J.; Cherevko, S. Activity and Stability of Electrochemically and Thermally Treated Iridium for the Oxygen Evolution Reaction. *J. Electrochem. Soc.* **2016**, *163*, F3132–F3138.
- (14) Lee, Y.; Suntivich, J.; May, K. J.; Perry, E. E.; Shao-Horn, Y. Synthesis and Activities of Rutile IrO<sub>2</sub> and RuO<sub>2</sub> Nanoparticles for Oxygen Evolution in Acid and Alkaline Solutions. *J. Phys. Chem. Lett.* **2012**, *3*, 399–404.
- (15) Reier, T.; Oezaslan, M.; Strasser, P. Electrocatalytic Oxygen Evolution Reaction (OER) on Ru, Ir, and Pt Catalysts: A Comparative Study of Nanoparticles and Bulk Materials. *ACS Catal.* **2012**, *2*, 1765–1772.
- (16) Mahenderkar, N. K.; Chen, Q.; Liu, Y.-C.; Duchild, A. R.; Hofheins, S.; Chason, E.; Switzer, J. A. Epitaxial Lift-off of Electrodeposited Single-Crystal Gold Foils for Flexible Electronics. *Science* **2017**, *355*, 1203–1206.

- (17) Jiao, F.; Frei, H. Nanostructured Cobalt Oxide Clusters in Mesoporous Silica as Efficient Oxygen-Evolving Catalysts. *Angew. Chem. Int. Ed.* **2009**, *48*, 1841–1844.
- (18) Zhu, W.; Yue, X.; Zhang, W.; Yu, S.; Zhang, Y.; Wang, J.; Wang, J. Nickel Sulfide Microsphere Film on Ni Foam as an Efficient Bifunctional Electrocatalyst for Overall Water Splitting. *Chem. Commun.* **2016**, *52*, 1486–1489.
- (19) Wang, Y.; Xie, C.; Liu, D.; Huang, X.; Huo, J.; Wang, S. Nanoparticle-Stacked Porous Nickel-Iron Nitride Nanosheet: A Highly Efficient Bifunctional Electrocatalyst for Overall Water Splitting. *ACS Appl. Mater. Interfaces* **2016**, *8*, 18652–18657.
- (20) Hong, W. T.; Risch, M.; Stoerzinger, K. A.; Grimaud, A.; Suntivich, J.; Shao-Horn, Y. Toward the Rational Design of Non-Precious Transition Metal Oxides for Oxygen Electrocatalysis. *Energy Environ. Sci.* **2015**, *8*, 1404–1427.
- (21) Yu, X.-Y.; Feng, Y.; Guan, B.; Lou, X. W.; Paik, U. Carbon Coated Porous Nickel Phosphides Nanoplates for Highly Efficient Oxygen Evolution Reaction. *Energy Environ. Sci.* **2016**, *9*, 1246–1250.
- (22) Chen, Q.; Switzer, J. A. Electrodeposition of Nanometer-Thick Epitaxial Films of Silver onto Single-Crystal Silicon Wafers. *J. Mater. Chem. C* **2019**, *7*, 1720–1725.
- (23) Landon, J.; Demeter, E.; Inoğlu, N.; Keturakis, C.; Wachs, I. E.; Vasić, R.; Frenkel, A. I.; Kitchin, J. R. Spectroscopic Characterization of Mixed Fe-Ni Oxide Electrocatalysts for the Oxygen Evolution Reaction in Alkaline Electrolytes. *ACS Catal.* **2012**, *2*, 1793–1801.
- (24) Gao, M.; Sheng, W.; Zhuang, Z.; Fang, Q.; Gu, S.; Jiang, J.; Yan, Y. Efficient Water Oxidation Using Nanostructured  $\alpha$ -Nickel-Hydroxide as an Electrocatalyst. *J. Am. Chem. Soc.* **2014**, *136*, 7077–7084.
- (25) Liu, Y.-C.; Koza, J. A.; Switzer, J. A. Conversion of Electrodeposited  $\text{Co(OH)}_2$  to  $\text{CoOOH}$  and  $\text{Co}_3\text{O}_4$ , and Comparison of Their Catalytic Activity for the Oxygen Evolution Reaction. *Electrochim. Acta* **2014**, *140*, 359–365.
- (26) Burke, M. S.; Enman, L. J.; Batchellor, A. S.; Zou, S.; Boettcher, S. W. Oxygen Evolution Reaction Electrocatalysis on Transition Metal Oxides and (Oxy)Hydroxides: Activity Trends and Design Principles. *Chem. Mater.* **2015**, *27*, 7549–7558.
- (27) Chen, Q.; Switzer, J. A. Photoelectrochemistry of Ultrathin, Semitransparent, and Catalytic Gold Films Electrodeposited Epitaxially onto n-Silicon (111). *ACS Appl. Mater. Interfaces* **2018**, *10*, 21365–21371.
- (28) Yang, Y.; Fei, H.; Ruan, G.; Xiang, C.; Tour, J. M. Efficient Electrocatalytic Oxygen Evolution on Amorphous Nickel-Cobalt Binary Oxide Nanoporous Layers. *ACS Nano* **2014**, *8*, 9518–9523.

- (29) Luo, X. F.; Wang, J.; Liang, Z. S.; Chen, S. Z.; Liu, Z. L.; Xu, C. W. Manganese Oxide with Different Morphology as Efficient Electrocatalyst for Oxygen Evolution Reaction. *Int. J. Hydrogen Energy* **2017**, *42*, 7151–7157.
- (30) Liu, T.; Liu, Q.; Asiri, A. M.; Luo, Y.; Sun, X. An Amorphous CoSe Film Behaves as an Active and Stable Full Water-Splitting Electrocatalyst under Strongly Alkaline Conditions. *Chem. Commun.* **2015**, *51*, 16683–16686.
- (31) Anantharaj, S.; Kennedy, J.; Kundu, S. Microwave-Initiated Facile Formation of Ni<sub>3</sub>Se<sub>4</sub> Nanoassemblies for Enhanced and Stable Water Splitting in Neutral and Alkaline Media. *ACS Appl. Mater. Interfaces* **2017**, *9*, 8714–8728.
- (32) Wang, Z.; Li, J.; Tian, X.; Wang, X.; Yu, Y.; Owusu, K. A.; He, L.; Mai, L. Porous Nickel-Iron Selenide Nanosheets as Highly Efficient Electrocatalysts for Oxygen Evolution Reaction. *ACS Appl. Mater. Interfaces* **2016**, *8*, 19386–19392.
- (33) Shinde, D. V.; De Trizio, L.; Dang, Z.; Prato, M.; Gaspari, R.; Manna, L. Hollow and Porous Nickel Cobalt Perselenide Nanostructured Microparticles for Enhanced Electrocatalytic Oxygen Evolution. *Chem. Mater.* **2017**, *29*, 7032–7041.
- (34) Xu, X.; Liang, H.; Ming, F.; Qi, Z.; Xie, Y.; Wang, Z. Prussian Blue Analogues Derived Penroseite (Ni,Co)Se<sub>2</sub> Nanocages Anchored on 3D Graphene Aerogel for Efficient Water Splitting. *ACS Catal.* **2017**, *7*, 6394–6399.
- (35) Anantharaj, S.; Ede, S. R.; Sakthikumar, K.; Karthick, K.; Mishra, S.; Kundu, S. Recent Trends and Perspectives in Electrochemical Water Splitting with an Emphasis on Sulfide, Selenide, and Phosphide Catalysts of Fe, Co, and Ni: A Review. *ACS Catal.* **2016**, *6*, 8069–8097.
- (36) Kelso, M. V.; Tubbesing, J. Z.; Chen, Q.; Switzer, J. A. Epitaxial Electrodeposition of Chiral Metal Surfaces on Silicon (643). *J. Am. Chem. Soc.* **2018**, *140*, 15812–15819.
- (37) Swesi, A. T.; Masud, J.; Nath, M. Nickel Selenide as a High-Efficiency Catalyst for Oxygen Evolution Reaction. *Energy Environ. Sci.* **2016**, *9*, 1771–1782.
- (38) Masud, J.; Swesi, A. T.; Liyanage, W. P. R.; Nath, M. Cobalt Selenide Nanostructures: An Efficient Bifunctional Catalyst with High Current Density at Low Coverage. *ACS Appl. Mater. Interfaces* **2016**, *8*, 17292–17302.
- (39) Masud, J.; Liyanage, W. P. R.; Cao, X.; Saxena, A.; Nath, M. Copper Selenides as High-Efficiency Electrocatalysts for Oxygen Evolution Reaction. *ACS Appl. Energy Mater.* **2018**, *1*, 4075–4083.
- (40) Swesi, A. T.; Masud, J.; Liyanage, W. P. R.; Umaphathi, S.; Bohannan, E.; Medvedeva, J.; Nath, M. Textured NiSe<sub>2</sub> Film: Bifunctional Electrocatalyst for Full Water Splitting at Remarkably Low Overpotential with High Energy Efficiency. *Sci. Rep.* **2017**, *7*, 2401.

- (41) De Silva, U.; Masud, J.; Zhang, N.; Hong, Y.; Liyanage, W. P. R.; Asle Zaeem, M.; Nath, M. Nickel Telluride as a Bifunctional Electrocatalyst for Efficient Water Splitting in Alkaline Medium. *J. Mater. Chem. A* **2018**, *6*, 7608–7622.
- (42) Carlson, R. R.; Meek, D. W. Dipole Moments of Several Tertiary Phosphine Oxides, Sulfides, and Selenides and of Some Tertiary Arsenic Oxides and Sulfides. *Inorg. Chem.* **1974**, *13*, 1741–1747.
- (43) Zhang, G.; Zang, S.; Lan, Z. A.; Huang, C.; Li, G.; Wang, X. Cobalt Selenide: A Versatile Cocatalyst for Photocatalytic Water Oxidation with Visible Light. *J. Mater. Chem. A* **2015**, *3*, 17946–17950.
- (44) Xu, K.; Ding, H.; Lv, H.; Tao, S.; Chen, P.; Wu, X.; Chu, W.; Wu, C.; Xie, Y. Understanding Structure-Dependent Catalytic Performance of Nickel Selenides for Electrochemical Water Oxidation. *ACS Catal.* **2017**, *7*, 310–315.
- (45) Xu, X.; Song, F.; Hu, X. A Nickel Iron Diselenide-Derived Efficient Oxygen-Evolution Catalyst. *Nat. Commun.* **2016**, *7*, 12324.
- (46) Cao, X.; Johnson, E.; Nath, M. Expanding Multinary Selenide based High-Efficiency Oxygen Evolution Electrocatalysts through Combinatorial Electrodeposition: Case Study with Fe-Cu-Co Selenides. Submitted to *ACS Sustainable Chem. Eng.* **2019**.
- (47) Cao, X.; Johnson, E.; Nath, M. Identifying High-efficiency Oxygen Evolution Electrocatalysts from Co-Ni-Cu Based Selenides through Combinatorial Electrodeposition. accepted by *J. Mater. Chem. A*. **2019**, DOI: 10.1039/C9TA00863B.
- (48) Cao, X.; Hong, Y.; Zhang, N.; Chen, Q.; Masud, J.; Zaeem, M. A.; Nath, M. Phase Exploration and Identification of Multinary Transition-Metal Selenides as High-Efficiency Oxygen Evolution Electrocatalysts through Combinatorial Electrodeposition. *ACS Catal.* **2018**, *8*, 8273–8289.
- (49) Hong, W. T.; Welsch, R. E.; Shao-Horn, Y. Descriptors of Oxygen-Evolution Activity for Oxides: A Statistical Evaluation. *J. Phys. Chem. C* **2016**, *120*, 78–86.
- (50) Suntivich, J.; May, K. J.; Gasteiger, H. A.; Goodenough, J. B.; Shao-Horn, Y. A Perovskite Oxide Optimized for Oxygen Evolution Catalysis from Molecular Orbital Principles. *Science* **2011**, *334*, 1383–1385.
- (51) Maiyalagan, T.; Jarvis, K. A.; Therese, S.; Ferreira, P. J.; Manthiram, A. Spinel-Type Lithium Cobalt Oxide as a Bifunctional Electrocatalyst for the Oxygen Evolution and Oxygen Reduction Reactions. *Nat. Commun.* **2014**, *5*, 3949.
- (52) Liu, Y.; Niu, Z.; Lu, Y.; Zhang, L.; Yan, K. Facile Synthesis of CuFe<sub>2</sub>O<sub>4</sub> crystals Efficient for Water Oxidation and H<sub>2</sub>O<sub>2</sub> reduction. *J. Alloys Compd.* **2018**, *735*, 654–659.

- (53) Chen, Z.; Meyer, T. J. Copper(II) Catalysis of Water Oxidation. *Angew. Chem. Int. Ed.* **2013**, *52*, 700–703.
- (54) Bikkarolla, S. K.; Papakonstantinou, P. CuCo<sub>2</sub>O<sub>4</sub> Nanoparticles on Nitrogenated Graphene as Highly Efficient Oxygen Evolution Catalyst. *J. Power Sources* **2015**, *281*, 243–251.
- (55) Chauhan, M.; Reddy, K. P.; Gopinath, C. S.; Deka, S. Copper Cobalt Sulfide Nanosheets Realizing a Promising Electrocatalytic Oxygen Evolution Reaction. *ACS Catal.* **2017**, *7*, 5871–5879.
- (56) Zhao, Q.; Yan, Z.; Chen, C.; Chen, J. Spinels: Controlled Preparation, Oxygen Reduction/Evolution Reaction Application, and Beyond. *Chem. Rev.* **2017**, *117*, 10121–10211.
- (57) Han, X.; He, G.; He, Y.; Zhang, J.; Zheng, X.; Li, L.; Zhong, C.; Hu, W.; Deng, Y.; Ma, T. Y. Engineering Catalytic Active Sites on Cobalt Oxide Surface for Enhanced Oxygen Electrocatalysis. *Adv. Energy Mater.* **2018**, *8*, 1702222.
- (58) Liu, Y.; Kelly, T. G.; Chen, J. G.; Mustain, W. E. Metal Carbides as Alternative Electrocatalyst Supports. *ACS Catal.* **2013**, *3*, 1184–1194.
- (59) Kresse, G.; Hafner, J. Ab Initio Molecular Dynamics for Liquid Metals. *Phys. Rev. B* **1993**, *47*, 558–561.
- (60) Kresse, G.; Hafner, J. Ab Initio Molecular-Dynamics Simulation of the Liquid-Metal–amorphous-Semiconductor Transition in Germanium. *Phys. Rev. B* **1994**, *49*, 14251–14269.
- (61) Kresse, G.; Furthmüller, J. Efficient Iterative Schemes for Ab Initio Total-Energy Calculations Using a Plane-Wave Basis Set. *Phys. Rev. B* **1996**, *54*, 11169–11186.
- (62) Kresse, G.; Furthmüller, J. Efficiency of Ab-Initio Total Energy Calculations for Metals and Semiconductors Using a Plane-Wave Basis Set. *Comput. Mater. Sci.* **1996**, *6*, 15–50.
- (63) Perdew, J. P.; Burke, K.; Ernzerhof, M. Generalized Gradient Approximation Made Simple. *Phys. Rev. Lett.* **1996**, *77*, 3865–3868.
- (64) Perdew, J. P.; Burke, K.; Ernzerhof, M. Erratum: Generalized Gradient Approximation Made Simple. *Phys. Rev. Lett.* **1997**, *78*, 1396–1396.
- (65) Blöchl, P. E. Projector Augmented-Wave Method. *Phys. Rev. B* **1994**, *50*, 17953–17979.
- (66) Kresse, G.; Joubert, D. From Ultrasoft Pseudopotentials to the Projector Augmented-Wave Method. *Phys. Rev. B* **1999**, *59*, 1758–1775.



- (67) Philipsen, P. H. T.; Baerends, E. J. Cohesive Energy of 3d Transition Metals: Density Functional Theory Atomic and Bulk Calculations. *Phys. Rev. B* **1996**, *54*, 5326–5333.
- (68) Kohn, W.; Becke, A. D.; Parr, R. G. Density Functional Theory of Electronic Structure. *J. Phys. Chem.* **1996**, *100*, 12974–12980.
- (69) Chien, C. H.; Chiou, S. H.; Guo, G. Y.; Yao, Y. Der. Electronic Structure and Magnetic Moments of 3d Transition Metal-Doped ZnO. *J. Magn. Magn. Mater.* **2004**, *282*, 275–278.
- (70) Fonin, M.; Pentcheva, R.; Dedkov, Y. S.; Sperlich, M.; Vyalikh, D. V.; Scheffler, M.; Rüdiger, U.; Güntherodt, G. Surface Electronic Structure of the Fe<sub>3</sub>O<sub>4</sub> (100): Evidence of a Half-Metal to Metal Transition. *Phys. Rev. B* **2005**, *72*, 104436.
- (71) Dudarev, S.; Botton, G. Electron-Energy-Loss Spectra and the Structural Stability of Nickel Oxide: An LSDA+U Study. *Phys. Rev. B* **1998**, *57*, 1505–1509.
- (72) Holzwarth, U.; Gibson, N. The Scherrer Equation versus the 'Debye-Scherrer Equation'. *Nat. Nanotechnol.* **2011**, *6*, 534.
- (73) van der Heide, H.; Hemmel, R.; van Bruggen, C. F.; Haas, C. X-Ray Photoelectron Spectra of 3d Transition Metal Pyrites. *J. Solid State Chem.* **1980**, *33*, 17–25.
- (74) Cahen, D.; Ireland, P. J.; Kazmerski, L. L.; Thiel, F. A. X-Ray Photoelectron and Auger Electron Spectroscopic Analysis of Surface Treatments and Electrochemical Decomposition of CuInSe<sub>2</sub> Photoelectrodes. *J. Appl. Phys.* **1985**, *57*, 4761–4771.
- (75) Chen, H.; Chen, S.; Fan, M.; Li, C.; Chen, D.; Tian, G.; Shu, K.; Walsh, F. C.; Zhu, J.; Chen, M. Bimetallic Nickel Cobalt Selenides: A New Kind of Electroactive Material for High-Power Energy Storage. *J. Mater. Chem. A* **2015**, *3*, 23653–23659.
- (76) Mi, L.; Wei, W.; Zheng, Z.; Zhu, G.; Hou, H.; Chen, W.; Guan, X. Ag<sup>+</sup> Insertion into 3D Hierarchical Rose-like Cu<sub>1.8</sub>Se Nanocrystals with Tunable Band Gap and Morphology Genetic. *Nanoscale* **2014**, *6*, 1124–1133.
- (77) An, W.; Liu, L.; Gao, Y.; Liu, Y.; Liu, J. Ni<sub>0.9</sub>Co<sub>1.92</sub>Se<sub>4</sub> nanostructures: Binder-Free Electrode of Coral-like Bimetallic Selenide for Supercapacitors. *RSC Adv.* **2016**, *6*, 75251–75257.
- (78) Kim, K. M.; Nam, J. H.; Lee, Y. G.; Cho, W. Il; Ko, J. M. Supercapacitive Properties of Electrodeposited RuO<sub>2</sub> Electrode in Acrylic Gel Polymer Electrolytes. *Curr. Appl. Phys.* **2013**, *13*, 1702–1706.
- (79) Xiao, P.; Sk, M. A.; Thia, L.; Ge, X.; Lim, R. J.; Wang, J. Y.; Lim, K. H.; Wang, X. Molybdenum Phosphide as an Efficient Electrocatalyst for the Hydrogen Evolution Reaction. *Energy Environ. Sci.* **2014**, *7*, 2624–2629.

- (80) Sivanantham, A.; Ganesan, P.; Shanmugam, S. Hierarchical NiCo<sub>2</sub>S<sub>4</sub> Nanowire Arrays Supported on Ni Foam: An Efficient and Durable Bifunctional Electrocatalyst for Oxygen and Hydrogen Evolution Reactions. *Adv. Funct. Mater.* **2016**, *26*, 4661–4672.
- (81) Sheng, W.; Gasteiger, H. A.; Shao-Horn, Y. Hydrogen Oxidation and Evolution Reaction Kinetics on Platinum: Acid vs Alkaline Electrolytes. *J. Electrochem. Soc.* **2010**, *157*, B1529–B1536.
- (82) Momma, K.; Izumi, F. VESTA 3 for Three-Dimensional Visualization of Crystal, Volumetric and Morphology Data. *J. Appl. Crystallogr.* **2011**, *44*, 1272–1276.
- (83) Gao, R.; Zhang, H.; Yan, D. Nano Energy Iron Diselenide Nanoplatelets : Stable and efficient Water-Electrolysis Catalysts. *Nano Energy* **2017**, *31*, 90–95.
- (84) Friebel, D.; Louie, M. W.; Bajdich, M.; Sanwald, K. E.; Cai, Y.; Wise, A. M.; Cheng, M. J.; Sokaras, D.; Weng, T. C.; Alonso-Mori, R. Identification of Highly Active Fe Sites in (Ni,Fe)OOH for Electrocatalytic Water Splitting. *J. Am. Chem. Soc.* **2015**, *137*, 1305–1313.
- (85) Burke, M. S.; Kast, M. G.; Trotochaud, L.; Smith, A. M.; Boettcher, S. W. Cobalt-Iron (Oxy)Hydroxide Oxygen Evolution Electrocatalysts: The Role of Structure and Composition on Activity, Stability, and Mechanism. *J. Am. Chem. Soc.* **2015**, *137*, 3638–3648.
- (86) Trotochaud, L.; Young, S. L.; Ranney, J. K.; Boettcher, S. W. Nickel-Iron Oxyhydroxide Oxygen-Evolution Electrocatalysts: The Role of Intentional and Incidental Iron Incorporation. *J. Am. Chem. Soc.* **2014**, *136*, 6744–6753.
- (87) Ohzuku, H.; Ikeno, H.; Yamada, I.; Yagi, S. First-Principles Calculations of the OH<sup>-</sup> Adsorption Energy on Perovskite Oxide. *AIP Conference Proceedings* **2016**, *1763*, 040005.
- (88) Su, D.; Dou, S.; Wang, G. Single Crystalline Co<sub>3</sub>O<sub>4</sub> Nanocrystals Exposed with Different Crystal Planes for Li-O<sub>2</sub> Batteries. *Sci. Rep.* **2015**, *4*, 5767.
- (89) Liu, Q.; Chen, Z.; Yan, Z.; Wang, Y.; Wang, E.; Wang, S.; Wang, S.; Sun, G. Crystal-Plane-Dependent Activity of Spinel Co<sub>3</sub>O<sub>4</sub> Towards Water Splitting and the Oxygen Reduction Reaction. *ChemElectroChem* **2018**, *5*, 1080–1086.
- (90) Gao, R.; Zhu, J.; Xiao, X.; Hu, Z.; Liu, J.; Liu, X. Facet-Dependent Electrocatalytic Performance of Co<sub>3</sub>O<sub>4</sub> for Rechargeable Li-O<sub>2</sub> battery. *J. Phys. Chem. C* **2015**, *119*, 4516–4523.
- (91) Xia, C.; Jiang, Q.; Zhao, C.; Hedhili, M. N.; Alshareef, H. N. Selenide-Based Electrocatalysts and Scaffolds for Water Oxidation Applications. *Adv. Mater.* **2016**, *28*, 77–85.

- (92) Kwak, I. H.; Im, H. S.; Jang, D. M.; Kim, Y. W.; Park, K.; Lim, Y. R.; Cha, E. H.; Park, J. CoSe<sub>2</sub> and NiSe<sub>2</sub> Nanocrystals as Superior Bifunctional Catalysts for Electrochemical and Photoelectrochemical Water Splitting. *ACS Appl. Mater. Interfaces* **2016**, *8*, 5327–5334.
- (93) Liu, X.; Cui, S.; Qian, M.; Sun, Z.; Du, P. In Situ Generated Highly Active Copper Oxide Catalysts for the Oxygen Evolution Reaction at Low Overpotential in Alkaline Solutions. *Chem. Commun.* **2016**, *52*, 5546–5549.
- (94) Qian, M.; Liu, X.; Cui, S.; Jia, H.; Du, P. Copper Oxide Nanosheets Prepared by Molten Salt Method for Efficient Electrocatalytic Oxygen Evolution Reaction with Low Catalyst Loading. *Electrochim. Acta* **2018**, *263*, 318–327.
- (95) Yang, L.; Xie, L.; Ren, X.; Wang, Z.; Liu, Z.; Du, G.; Asiri, A. M.; Yao, Y.; Sun, X. Hierarchical CuCo<sub>2</sub>S<sub>4</sub> Nanoarray for High-efficient and Durable Water Oxidation Electrocatalysis. *Chem. Commun.* **2017**, *54*, 78–81.
- (96) Han, A.; Zhang, H.; Yuan, R.; Ji, H.; Du, P. Crystalline Copper Phosphide Nanosheets as an Efficient Janus Catalyst for Overall Water Splitting. *ACS Appl. Mater. Interfaces* **2017**, *9*, 2240–2248.
- (97) Ren, X.; Ji, X.; Wei, Y.; Wu, D.; Zhang, Y.; Ma, M.; Liu, Z.; Asiri, A. M.; Wei, Q.; Sun, X. In Situ Electrochemical Development of Copper Oxide Nanocatalysts within a TCNQ Nanowire Array: A Highly Conductive Electrocatalyst for the Oxygen Evolution Reaction. *Chem. Commun.* **2018**, *54*, 1425–1428.
- (98) Hu, H.; Guan, B.; Xia, B.; Lou, X. W. Designed Formation of Co<sub>3</sub>O<sub>4</sub>/NiCo<sub>2</sub>O<sub>4</sub> Double-Shelled Nanocages with Enhanced Pseudocapacitive and Electrocatalytic Properties. *J. Am. Chem. Soc.* **2015**, *137*, 5590–5595.
- (99) Tran, P. D.; Nguyen, M.; Pramana, S. S.; Bhattacharjee, A.; Chiam, S. Y.; Fize, J.; Field, M. J.; Artero, V.; Wong, L. H.; Loo, J.; Barber, J. Copper Molybdenum Sulfide: A New Efficient Electrocatalyst for Hydrogen Production from Water. *Energy Environ. Sci.* **2012**, *5*, 8912–8916.

## V. TYRRELLITE AS A NOVEL AND SUSTAINABLE EFFICIENT ELECTROCATALYSTS FOR OXYGEN EVOLUTION GENERATION

*Xi Cao<sup>a</sup>, Julia E. Medvedeva<sup>b\*</sup> and Manashi Nath<sup>a\*</sup>*

<sup>a</sup>Department of Chemistry, Missouri University of Science and Technology, Rolla, Missouri 65409, United States.

<sup>b</sup>Department of Physics, Missouri University of Science and Technology, Rolla, Missouri 65409, United States.

### ABSTRACT

Due to the increasing demand for sustainable and efficient catalysts for oxygen evolution (OER), examining the electrocatalytic performance of naturally-occurring minerals are of interest for energy conversion and hold promise given their unique structures and compositions. Here we present a nanostructured Tyrrellite– $\text{Cu}(\text{Co}_{0.68}\text{Ni}_{0.32})_2\text{Se}_4$  as highly efficient OER catalyst with an overpotential of 205 mV at  $10 \text{ mA cm}^{-2}$  and excellent stability for 22 h in harsh alkaline medium. Density functional theory (DFT) calculations were carried out to understand the origins of the observed high OER activity of  $\text{Cu}(\text{Co}_{0.68}\text{Ni}_{0.32})_2\text{Se}_4$  by studying the electronic and magnetic properties of bulk and (100) slab and by comparing the calculated adsorption energy of  $\text{OH}^-$  complex on Ni and Co sites at the (100)-orientated surface. The theoretical results reveal that presence of Ni enhances the magnetic moment on the nearby Co atoms in both bulk and (100) surface making the Co atom the preferable active center and leading to the superior OER activity.

**Keywords:** Tyrrellite, Oxygen evolution reaction, Water splitting, Electrocatalyst

## 1. INTRODUCTION

The increasing global demand for energy encourages the search for clean and sustainable alternative energy resources as part of a crucial enterprise.<sup>1,2</sup> Hydrogen (H<sub>2</sub>) with high energy density has been considered as an ideal substitute to fossil fuels.<sup>3,4</sup> Water electrolysis is divided into two half reactions: hydrogen evolution reaction (HER) at the cathode and oxygen evolution reaction (OER) at the anode, which provides a simple way to produce high-purity hydrogen.<sup>5,6</sup> However, OER is a kinetically slow four-electron involved process, which greatly restrains the large scale application of water electrocatalysis.<sup>7,8</sup> Therefore, it is urgent to seek for efficient electrocatalysts to reduce the overpotential required by OER and determine ways to enhance the energy conversion efficiency.<sup>9</sup> Ir and Ru-based compounds have been investigated as the most efficient OER electrocatalysts, however their scarcity and high cost prohibit the practical application.<sup>10,11</sup> Recently, lots of great efforts have been devoted to discover highly active, durable and non-noble-metal based electrocatalysts.<sup>12,13,14,15,16,17,18</sup> In this regards, transition metals (Fe, Co, Ni, Cu and Mn) based catalysts with promising catalytic capability have attracted most of attentions.<sup>19,20,21,22,23</sup> Apart from the well-studied metal oxides and (oxy)hydroxides,<sup>24,25,26,27,28,29,30</sup> metal selenides have been widely reported by our group and other researchers as a new type of promising OER electrocatalyst with high catalytic activity in terms of lowering overpotential and increasing current density, such as Ni<sub>3</sub>Se<sub>2</sub>, CoSe<sub>2</sub>, Cu<sub>2</sub>Se, CoCu<sub>2</sub>Se<sub>4</sub>, (NiFeCo)<sub>3</sub>Se<sub>4</sub>, (Co<sub>0.21</sub>Ni<sub>0.25</sub>Cu<sub>0.54</sub>)<sub>3</sub>Se<sub>2</sub> and (Fe<sub>0.48</sub>Co<sub>0.38</sub>Cu<sub>0.14</sub>)Se etc.<sup>31,32,33,34,35,36,37</sup> Excellent catalytic performance of these metal selenides is believed to

benefit from their intrinsic metallic properties compared to oxides.<sup>38,39</sup> Of these selenides, mixed metal selenides are expected to show a much better catalytic activity due to the possibility of charge delocalization between the metal cations through *d-d* orbital overlap under OER condition, thereby stabilizing the active sites and increasing the adsorption rate of hydroxyl species to further form the intermediates on the catalyst surface.<sup>35,36,40,41,42</sup> As emerging OER electrocatalysts, tons of methods have been developed to design high-efficiency nanostructured mixed metal selenides, unfortunately, the complexity of synthesis method generally limits its large-scale industrial application.<sup>43,44,45</sup> Accordingly, utilizing naturally-occurring minerals as electrocatalyst has been considered as an exciting way to split water attributed the advantages of their large amount and free in nature. The catalytic activity of naturally-occurring minerals has been demonstrated in both probiotic terrestrial chemistry and many modern industrial applications.<sup>46,47,48,49</sup> Sivula's group has recently presented that an iron-based naturally-occurring Gibeon meteorite for the oxygen evolution reaction with a low overpotential of 270 mV at 10 mA cm<sup>-2</sup> and Tafel slope of 37 mV decade<sup>-1</sup>.<sup>50</sup> However, most of the naturally-occurring minerals have been rarely considered as water oxidation electrocatalyst, typically, due to their poor electrical conductivity resulting from the impurity phases formed in naturally-occurring minerals, such as silica, which can dramatically affect the electron transport ability, and, therefore, hinder the catalytic activity.<sup>51,52</sup> Inspired by the above arguments, we targeted on synthesis of Tyrrellite Cu(Co<sub>0.68</sub>Ni<sub>0.32</sub>)<sub>2</sub>Se<sub>4</sub>, which is both mixed metal selenide and pure phase naturally-occurring mineral. Tyrrellite originates from northern Canada, especially the area between Lake Athabasca and Hudson Bay.<sup>53</sup> Mineralogically, it belongs to the class of Thiospinel AB<sub>2</sub>X<sub>4</sub> (X = S, Se, Te) containing alternating layers of edge-shared B<sub>III</sub>Se<sub>6</sub>

octahedra and  $A_{II}Se_4$  tetrahedra.<sup>54,55</sup> Such compositions have been frequently encountered in transition metal chalcogenide family as  $NiFe_2Se_4$ ,  $CoNi_2Se_4$ ,  $CuCo_2Se_4$ .<sup>54</sup> In Tyrrellite, Cu cation occupies divalent site while Ni and Co are in trivalent cationic site. The presence of Ni and Co in the octahedral site in Tyrrellite is very interesting, since it has been widely accepted that trivalent  $Ni^{3+}$  and  $Co^{3+}$  cations are actually responsible for the active sites, especially in the Ni or Co based electrocatalysts.<sup>26,56,57,58</sup> Hence,  $Cu(Co_{0.68}Ni_{0.32})_2Se_4$  is expected to be a superior OER electrocatalyst with richness of trivalent  $Co^{3+}$  and  $Ni^{3+}$  species in the system. In this article, for the first time, we have presented a simple one-step method to synthesize nanostructured Tyrrellite and have investigated its catalytic activity toward OER in alkaline medium. Nanostructured Tyrrellite is a highly efficient OER electrocatalyst, its onset potential is 1.42 V vs RHE and it only requires an overpotential of 205 mV to reach a current density of  $10 \text{ mA cm}^{-2}$ , which is one of the best electrocatalysts till date. To further understand the high OER activity of  $Cu(Co_{0.68}Ni_{0.32})_2Se_4$ , density functional theory (DFT) calculations were performed to determine the electronic properties of bulk and (100) slab of the mixed-metal selenide, as well as to calculate the adsorption energy of  $OH^-$  on the top of Ni and Co atoms at the (100) surface. It was found that the presence of both Ni and Co atoms in the octahedral site improved its metallic state near the Fermi level due to the *d-d* orbital delocalization. Moreover, Co served as a more favorable active site than Ni resulting from an optimal adsorption energy and bond strength. The synergistic effects between Ni and Co in the octahedral site plays an important role in enhancing the OER catalytic activity of  $Cu(Co_{0.68}Ni_{0.32})_2Se_4$ .

## 2. EXPERIMENTAL AND COMPUTATIONAL METHODS

Materials. Nickel chloride hexahydrate [ $\text{NiCl}_2 \cdot 6\text{H}_2\text{O}$ ] purchased from J T Baker Chemical Co, cobalt chloride hexahydrate [ $\text{CoCl}_2 \cdot 6\text{H}_2\text{O}$ ], copper chloride dihydrate [ $\text{CuCl}_2 \cdot 2\text{H}_2\text{O}$ ] and potassium hydroxide [KOH] from Fisher Scientific. Selenium dioxide [ $\text{SeO}_2$ ] and hydrazine monohydrate [ $\text{N}_2\text{H}_4 \cdot \text{H}_2\text{O}$ ] from Acros chemicals. All chemicals were analytical grade and used without further purification. Deionized (DI) water ( $18 \text{ M}\Omega / \text{cm}$ ) was used to prepare all the solutions.

Synthesis of  $\text{Cu}(\text{Co}_{0.68}\text{Ni}_{0.32})_2\text{Se}_4$ . To synthesize Tyrrellite  $\text{Cu}(\text{Co}_{0.68}\text{Ni}_{0.32})_2\text{Se}_4$ , 10 mM of  $\text{CuCl}_2 \cdot 2\text{H}_2\text{O}$ , 7 mM of  $\text{CoCl}_2 \cdot 6\text{H}_2\text{O}$  and 3 mM of  $\text{NiCl}_2 \cdot 6\text{H}_2\text{O}$  were dissolved in 10 mL distilled water under continuously stirring, then 40 mM of  $\text{SeO}_2$  was added into the solution. After 15 min stirring, 1 mL of  $\text{N}_2\text{H}_4 \cdot \text{H}_2\text{O}$  was carefully added into the mixture and then a dark brown blurred solution formed. The resulting solution was stirred for another 15 min and then transferred into a 23 mL Teflon-lined stainless-steel autoclave, which was tightly sealed and maintained at  $185 \text{ }^\circ\text{C}$  for 24 h. The resulting greyish powders were by means of centrifugation, washed with distilled water and absolute ethanol to remove ions possibly remaining in the product, and finally dried at room temperature in the vacuum oven for 12 h.

Electrode preparation. Carbon fiber paper (CFP) as substrate was purchased from FuelCellsEtc, Texas. All CFP substrates were cleaned with isopropanol and eventually rinsed with distilled water to ensure the clean surface. Catalyst ink was prepared by ultrasonically dispersing 2.0 mg  $\text{Cu}(\text{Co}_{0.68}\text{Ni}_{0.32})_2\text{Se}_4$  powder in 1.0 mL 0.8 % Nafion<sup>®</sup> ethanol solution followed with sonicating for 30 min. CFP substrates were covered with a Teflon tape, leaving an exposed geometric area of  $0.070 \text{ cm}^2$ . A quantity of 20  $\mu\text{L}$  of the



ink was drop casted onto CFP, leading to the catalyst loading  $\sim 0.040 \text{ mg cm}^{-2}$ . The as-prepared electrodes were dried at room temperature and then heated at constant  $130 \text{ }^\circ\text{C}$  for 30 min in a vacuum oven.

**Characterization.** The crystal structure of  $\text{Cu}(\text{Co}_{0.68}\text{Ni}_{0.32})_2\text{Se}_4$  powder was characterized through powder X-ray diffraction (PXRD) Philips X-Pert using CuK $\alpha$  ( $1.5418 \text{ \AA}$ ) radiation (PANalytical, Almelo, The Netherlands). The morphologies of  $\text{Cu}(\text{Co}_{0.68}\text{Ni}_{0.32})_2\text{Se}_4$  were observed with a scanning electron microscope (SEM, Hitachi S4700). Energy dispersive spectroscopy (EDS) in the same microscope was used to identify the element distribution and atomic ratios. High resolution transition electron microscopy (TEM) images and selected area electron diffraction (SAED) was obtained using FEI Tecnai F20. The probe current is 1.2 nA with a spot size of less than 2 nm. STEM mode in the TEM was also used for dark field imaging where the convergence angle was 13 mrad and the camera length was 30 mm.

**Electrochemical measurements.** The catalytic performances of  $\text{Cu}(\text{Co}_{0.68}\text{Ni}_{0.32})_2\text{Se}_4$  were investigated in  $\text{N}_2$ -saturated 1.0 M KOH solution at room temperature in a three-electrode system with an IviumStat potentiostat. The OER and HER catalytic activities were studied from linear scan voltammetry (LSV) while the stability of the catalyst were evaluated by chronoamperometry.  $\text{Cu}(\text{Co}_{0.68}\text{Ni}_{0.32})_2\text{Se}_4$  on CFP served as working electrode, glassy carbon (GC) as counter electrode and Ag|AgCl (KCl Saturated) electrode as reference electrode. All measured potentials vs Ag|AgCl (KCl Saturated) were converted to the reversible hydrogen electrode (RHE) according the Nernst equation below and corrected for the  $iR$  drop in the solution.

$$E_{RHE} = E_{Ag|AgCl} + 0.059pH + E_{Ag|AgCl}^\circ \quad (1)$$

Where  $E_{RHE}$  is the calculated potential vs RHE, and  $E_{Ag|AgCl}^{\circ}$  is the standard thermodynamic potential of Ag|AgCl (KCl Saturated) at 25.1 °C (0.197 V), and  $E_{Ag|AgCl}$  is the experimentally measured potential vs Ag|AgCl (KCl Saturated) reference electrode.

ECSA. Electrochemically active surface area (ECSA) for  $Cu(Co_{0.68}Ni_{0.32})_2Se_4$  was determined by measuring the electrochemical double layer capacitance in the non-faradaic region according to the equation

$$ECSA = C_{DL}/C_S \quad (2)$$

$$i_{DL} = C_{DL} \cdot \nu \quad (3)$$

Where  $C_{DL}$  is the double layer capacitance and  $C_S$  is the specific capacitance of the electrocatalyst per unit area under identical electrolyte conditions. The value of  $C_S$  has been reported between 0.022 to 0.130 mF cm<sup>2</sup> in alkaline solution.<sup>28,57</sup> In this study,  $C_S$  is 0.040 mF cm<sup>-2</sup> based on reported values.<sup>28</sup>

Tafel plots. The Tafel slope is an important parameter to evaluate the catalytic performance of  $Cu(Co_{0.68}Ni_{0.32})_2Se_4$  and the equation is shown below.

$$\eta = a + \frac{2.3RT}{anF} \log(j) \quad (4)$$

Where  $\eta$  is the overpotential,  $\alpha$  is transfer coefficient and the other symbols have their usual meanings. The Tafel slope is given by  $2.3RT/anF$ .

Density Functional Theory Calculations. The electronic properties of  $Cu(Co_{0.68}Ni_{0.32})_2Se_4$  in bulk and slab geometries were studied using first-principles density functional calculations as implemented in the Vienna ab initio simulation package (VASP).<sup>60,61,62,63</sup> The generalized gradient approximation in the Perdew-Burke-Ernzerhof (PBE) form,<sup>64,65</sup> within the projector augmented-wave method was used.<sup>66,67</sup> The generalized gradient approximation with an on-site Coulomb U term (GGA+U) method

has been shown to successfully describe the cohesive energy, electronic structure, and mechanical and magnetic properties of bulk and surfaces of 3d-metal based materials.<sup>68,69,70,71</sup> In this work, GGA+U method<sup>72</sup> with U=0 and 6 eV for Co-d and Ni-d states and with U=0eV and 4eV for Cu states was used to study the electronic structure and magnetic properties of bulk with a supercell of  $\text{Cu}_8\text{Co}_{11}\text{Ni}_5\text{Se}_{32}$  and (100) slab with a supercell of  $\text{Cu}_{14}\text{Co}_{19}\text{Ni}_9\text{Se}_{56}$  with different distribution of Ni atoms among the octahedral sites in both bulk and slab structures. Further, the adsorption energy of  $\text{OH}^-$  complex at the (100) surfaces was calculated to allow for straightforward comparison with previous reports. The internal atomic positions for all structures were optimized using force and total energy minimization until the Hellmann-Feynman force on each atom was below 0.01 eV/Å. Brillouin-zone sampling was done with  $\Gamma$ -centered Monkhorst-pack with k-mesh of at least 4x4x4; the cut-off energy of 500 eV was used for bulk and slab geometries. All the crystal structures of the slabs  $\text{Cu}(\text{Co}_{0.68}\text{Ni}_{0.32})_2\text{Se}_4$  (100) surface were plotted using VESTA software and shown in Figure S3.<sup>73</sup>

### 3. RESULTS AND DISCUSSION

Figure 1(a) shows the pXRD pattern of the obtained  $\text{Cu}(\text{Co}_{0.68}\text{Ni}_{0.32})_2\text{Se}_4$  nanoparticles in the diffraction angle range of 10 - 90°. All diffraction peaks of  $\text{Cu}(\text{Co}_{0.68}\text{Ni}_{0.32})_2\text{Se}_4$  are perfectly matched with the standard diffraction pattern of Tyrrellite (PDF # 00-008-0001). According to the Scherrer formula, the average crystal domains of  $\text{Cu}(\text{Co}_{0.68}\text{Ni}_{0.32})_2\text{Se}_4$  is about 4.89 nm, implying that  $\text{Cu}(\text{Co}_{0.68}\text{Ni}_{0.32})_2\text{Se}_4$  are very small. Tyrrellite belongs to a spinel structure type,  $AB_2X_4$ , containing chalcogenide anion X and metals (A and B), where A is a divalent cation occupying the partially occupied metal layer,

while  $B$  is a trivalent cation occupying the fully occupied metal layers. In Tyrrellite, Cu occupies the divalent site with +2 oxidation state while Ni and Co share the trivalent site with +3 oxidation state. Meanwhile, the atomic ratio from energy dispersive X-ray (EDS) spectrum (as shown in Table S1) further confirms the elemental composition. The high magnification SEM image demonstrates the morphology of  $\text{Cu}(\text{Co}_{0.68}\text{Ni}_{0.32})_2\text{Se}_4$  is mainly composed of spherical nanoparticles with various sizes. Detailed transmission TEM image shown in Figure 1(c) further reveals the nanostructure of  $\text{Cu}(\text{Co}_{0.68}\text{Ni}_{0.32})_2\text{Se}_4$ . High-resolution TEM (HRTEM) image in Figure 1(d) confirms the crystalline nature of the catalyst and clear lattice fringes with interplane distances of 0.578 nm and 0.354 nm correspond to the (111) and (220) plane of  $\text{Cu}(\text{Co}_{0.68}\text{Ni}_{0.32})_2\text{Se}_4$ , respectively. Selected area electron diffraction (SAED) pattern shown in the inset of Figure 1(d), further confirms the crystallinity of the as prepared Tyrrellite, and the diffraction spots were indexed to (111), (220), (311) and (400) lattice planes of Tyrrellite crystal structure.

The surface composition and oxidation states of as-prepared  $\text{Cu}(\text{Co}_{0.68}\text{Ni}_{0.32})_2\text{Se}_4$  was investigated through deconvoluted XPS spectra as presented in Figure 2 (a-d). The deconvoluted Cu 2p and Co 2p peaks reveal the presence of variable oxidation states of  $\text{Cu}^+/\text{Cu}^{2+}$  and  $\text{Co}^{2+}/\text{Co}^{3+}$ , respectively. The Cu 2p XPS spectrum in Figure 2a shows peaks at 931.3 and 951.1 eV corresponding to  $\text{Cu}^+ 2p_{3/2}$  and  $\text{Cu}^+ 2p_{1/2}$ ; while peaks at 933.5 and 953.3 eV correspond to  $\text{Cu}^{2+} 2p_{3/2}$  and  $\text{Cu}^{2+} 2p_{1/2}$ , respectively.<sup>33,74</sup> Two obvious satellite peaks of Cu 2p can be found at 941.2 and 961.4 eV. Similarly, the deconvoluted Co 2p spectrum is shown in Figure 2b, where the binding energies at 779.5 and 796.0 eV belong to  $\text{Co}^{2+} 2p_{3/2}$  and  $\text{Co}^{2+} 2p_{1/2}$  and peaks at 777.3 and 794.6 eV are for  $\text{Co}^{3+} 2p_{3/2}$  and  $\text{Co}^{3+}$

$2p_{1/2}$ , respectively, while the shakeup satellite peaks of Co 2p were observed at 783.1 and 802.2 eV.<sup>75,76</sup> The Ni 2p XPS spectrum in Figure 2c shows peaks at 853.1 and 870.2 eV

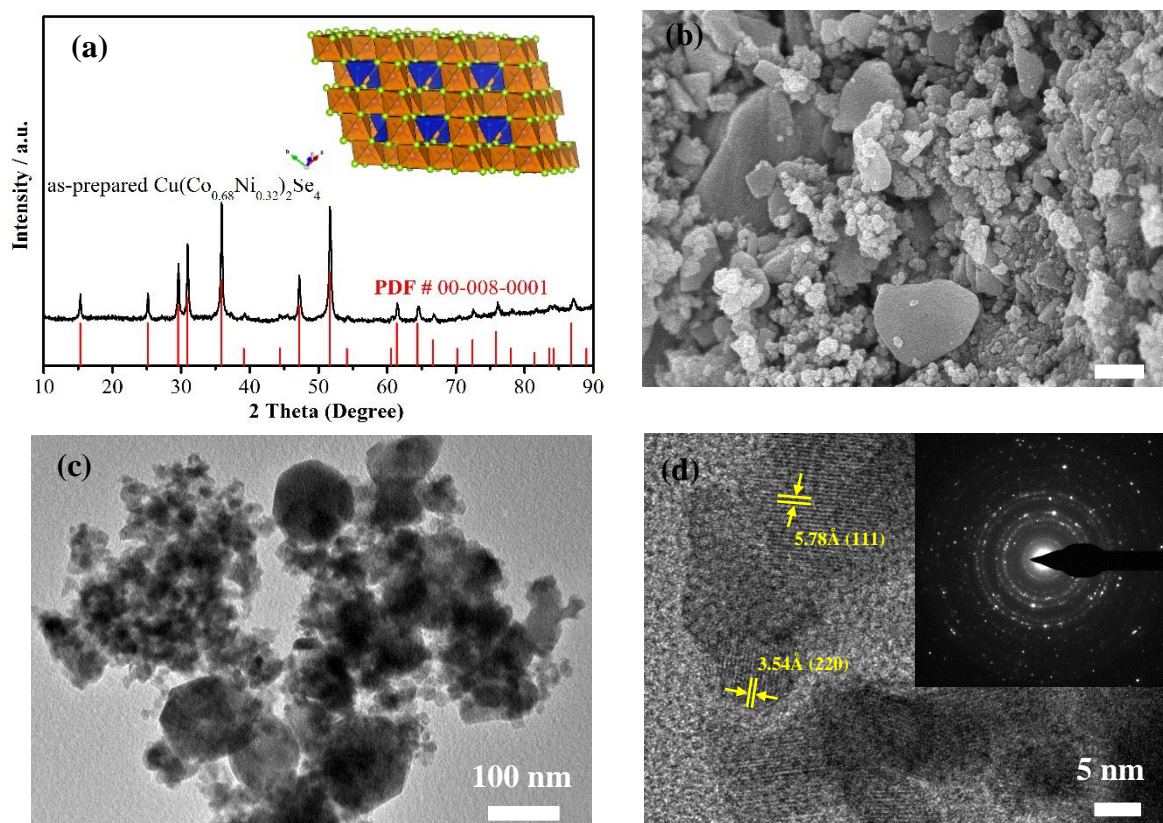


Figure 1. (a) Pxd pattern of hydrothermally synthesized  $\text{Cu}(\text{Co}_{0.68}\text{Ni}_{0.32})_2\text{Se}_4$  nanoparticles along with reference  $\text{Cu}(\text{Co}_{0.68}\text{Ni}_{0.32})_2\text{Se}_4$  (PDF # 00-008-0001), the inset shows the crystal structure of  $\text{Cu}(\text{Co}_{0.68}\text{Ni}_{0.32})_2\text{Se}_4$ . (b) SEM image of  $\text{Cu}(\text{Co}_{0.68}\text{Ni}_{0.32})_2\text{Se}_4$ . (c) TEM image of  $\text{Cu}(\text{Co}_{0.68}\text{Ni}_{0.32})_2\text{Se}_4$ . (d) HRTEM image and SAED pattern of  $\text{Cu}(\text{Co}_{0.68}\text{Ni}_{0.32})_2\text{Se}_4$  nanoparticles.

assigning to  $\text{Ni}^{2+} 2p_{3/2}$  and  $\text{Ni}^{2+} 2p_{1/2}$  and peaks at 854.9 and 872.5 eV assigning to  $\text{Ni}^{3+} 2p_{3/2}$  and  $\text{Ni}^{3+} 2p_{1/2}$ , respectively, while the satellite peaks can be observed at 860.5 and 879.0 eV.<sup>35,77</sup> Figure 2d shows the Se 3d spectrum where the peaks of  $3d_{5/2}$  and  $3d_{3/2}$  at the binding energies of 53.4 and 54.5 eV confirm the presence of  $\text{Se}^{2-}$  and the peak at  $\approx 59$  eV indicates the existence of  $\text{SeO}_x$  which might be from the surface oxidation of selenide.<sup>56</sup> Metal oxides were not detected on the surface from XPS analysis. The percentage of

variable oxidation states of metal ions of the catalyst have been calculated based on the area under the peaks in the deconvoluted XPS spectra. The as-synthesized catalyst contained 11 %  $\text{Cu}^+$ , 30 %  $\text{Cu}^{2+}$ , 30 %  $\text{Co}^{2+}$ , 10 %  $\text{Co}^{3+}$ , 5 %  $\text{Ni}^{2+}$  and 14 %  $\text{Ni}^{3+}$ . In the present case, there is a mixing valence of Co and Cu cations both in the A and the B sites with  $\text{Cu}^{2+}$  predominantly occupying the A sites and the B site is predominantly occupied by  $\text{Co}^{3+}$  and  $\text{Ni}^{3+}$ , while there's substitution of  $\text{Cu}^+$ ,  $\text{Co}^{2+}$  and  $\text{Ni}^{2+}$  in A site and B site, respectively.

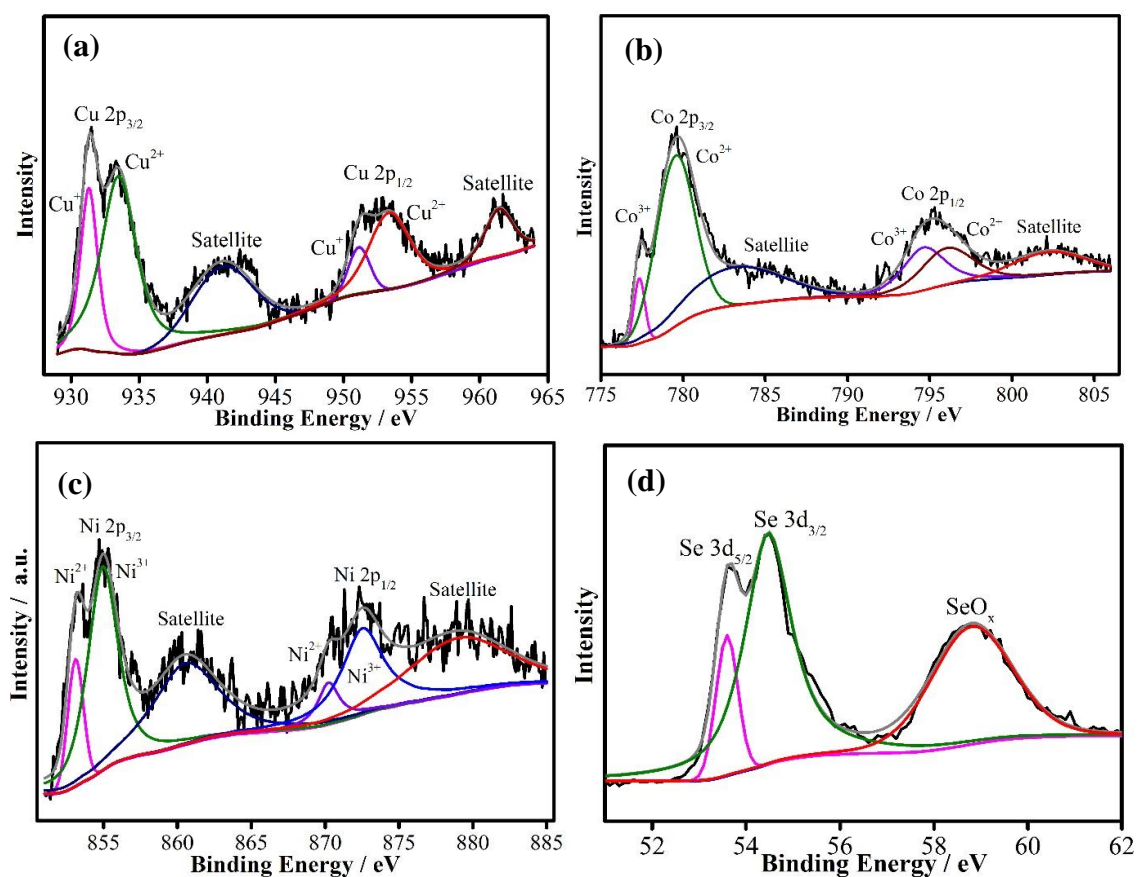


Figure 2. Deconvoluted XPS spectra of (a) Cu 2p, (b) Co 2p, (c) Ni 2p and (d) Se 3d of  $\text{Cu}(\text{Co}_{0.68}\text{Ni}_{0.32})_2\text{Se}_4$  nanoparticles.

The OER electrocatalytic activity of the  $\text{Cu}(\text{Co}_{0.68}\text{Ni}_{0.32})_2\text{Se}_4$ @CFP was evaluated in  $\text{N}_2$ -saturated 1.0 M KOH using a three-electrode electrochemical cell at a scan rate of  $10 \text{ mV s}^{-1}$ , along with GC as counter electrode and Ag|AgCl (KCl Saturated) as reference electrode. Bare CFP and the state-of-the-art OER catalyst  $\text{RuO}_2$  electrodeposited on CFP with the same amount of loading were also measured under the same condition for comparison. Due to the effect of ohmic resistance of solution, the collected anodic currents cannot directly reflect the real intrinsic behavior of the electrocatalysts, an  $iR$  correction was applied to all OER LSV polarization curves.<sup>28,78</sup> Figure 2(a) shows the polarization curves of the  $\text{Cu}(\text{Co}_{0.68}\text{Ni}_{0.32})_2\text{Se}_4$ @CFP, bare CFP and  $\text{RuO}_2$ . It's obvious that the bare CFP exhibits negligible catalytic activity towards to OER, while  $\text{Cu}(\text{Co}_{0.68}\text{Ni}_{0.32})_2\text{Se}_4$ @CFP shows efficient OER performance with a low onset potential of 1.42 V vs RHE. The OER catalytic current density of  $\text{Cu}(\text{Co}_{0.68}\text{Ni}_{0.32})_2\text{Se}_4$ @CFP increases dramatically and it only requires 205 mV and 250 mV to reach a current density of  $10 \text{ mA cm}^{-2}$  and  $50 \text{ mA cm}^{-2}$ , respectively, which is better than  $\text{RuO}_2$ @CFP (320 mV and 430 mV at  $10 \text{ mA cm}^{-2}$  and  $50 \text{ mA cm}^{-2}$  respectively). The Tafel slope is a crucial factor to evaluate the OER kinetics. As observed in Figure 1(b), the Tafel slope value of  $\text{Cu}(\text{Co}_{0.68}\text{Ni}_{0.32})_2\text{Se}_4$  ( $90.4 \text{ mV dec}^{-1}$ ) is lower than that of  $\text{RuO}_2$  ( $114.4 \text{ mV dec}^{-1}$ ), indicating a more favorable OER kinetics of  $\text{Cu}(\text{Co}_{0.68}\text{Ni}_{0.32})_2\text{Se}_4$ .

The electrochemically surface area (ECSA) is a very important parameter to understand the reason that  $\text{Cu}(\text{Co}_{0.68}\text{Ni}_{0.32})_2\text{Se}_4$  exhibits high OER performance, since a larger active surface area often leads to enhancement of the catalytic activity.<sup>79</sup> Figure 4 shows the typical cyclic voltammetry (CV) curves of  $\text{Cu}(\text{Co}_{0.68}\text{Ni}_{0.32})_2\text{Se}_4$  in  $\text{N}_2$  saturated 1.0 M KOH at different scan rates. By plotting the capacitive current ( $i_{DL}$ ) versus the scan

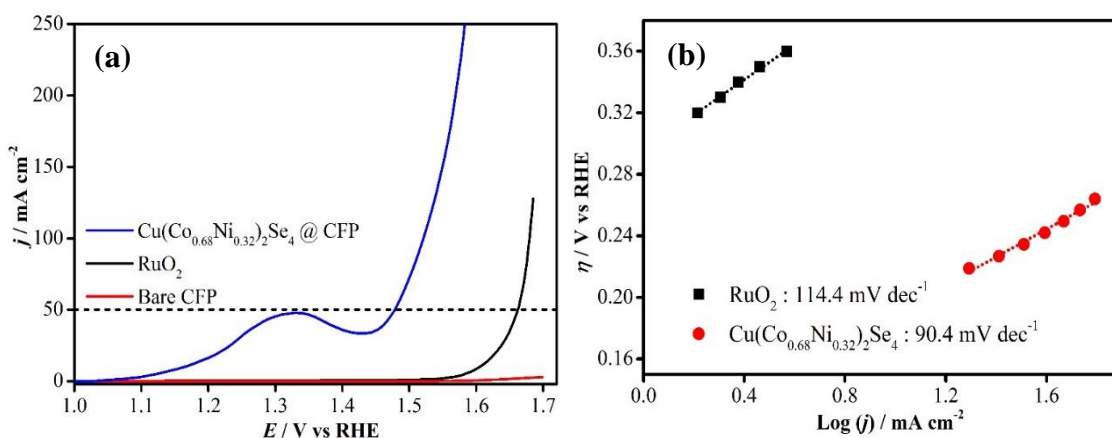


Figure 3. (a) Polarization curves of Cu(Co<sub>0.68</sub>Ni<sub>0.32</sub>)<sub>2</sub>Se<sub>4</sub>@CFP and RuO<sub>2</sub> in N<sub>2</sub>-saturated 1.0 M KOH at a scan rate of 10 mV s<sup>-1</sup>. (b) Tafel plots of Cu(Co<sub>0.68</sub>Ni<sub>0.32</sub>)<sub>2</sub>Se<sub>4</sub>@CFP and RuO<sub>2</sub>.

rate ( $\nu$ ) according to the eq. (3), a straight line was obtained where the slope of this line is the  $C_{DL}$  value. Roughness factor (RF) is calculated by ECSA dividing the geometric area 0.07 cm<sup>2</sup>. The ECSA is around 5.425 and the RF of the catalyst is around 77.5. The high RF indicates the catalyst has a high surface area which can be confirmed from the SEM image.

The OER Faradaic efficiency of Cu(Co<sub>0.68</sub>Ni<sub>0.32</sub>)<sub>2</sub>Se<sub>4</sub> catalyst was evaluated by water-displacement method, and the theoretical amount of evolved O<sub>2</sub> was compared with the experimentally measured O<sub>2</sub> as shown in Figure 5. Nearly 100 % of efficiency of Cu(Co<sub>0.68</sub>Ni<sub>0.32</sub>)<sub>2</sub>Se<sub>4</sub> catalyst was observed for OER reaction. The long-term stability of the Cu(Co<sub>0.68</sub>Ni<sub>0.32</sub>)<sub>2</sub>Se<sub>4</sub> was examined by chronoamperometry with applying a constant potential 1.45 vs RHE in N<sub>2</sub>-saturated 1.0 M KOH to achieve a current density around 13 mA cm<sup>-2</sup> shown in Figure 6. It can be noticed that Cu(Co<sub>0.68</sub>Ni<sub>0.32</sub>)<sub>2</sub>Se<sub>4</sub> was stable with a negligible loss of current density even after 22 h. The inset in Figure 6 exhibits the



comparison of polarization curves before and after 22 h chronoamperometry implying the excellent stability of the catalyst under the condition of continuous O<sub>2</sub> evolving. The compositional stability of Cu(Co<sub>0.68</sub>Ni<sub>0.32</sub>)<sub>2</sub>Se<sub>4</sub> catalyst after 22 h chronoamperometry was tested by EDS technique shown in Table S1, the atomic ratio of Cu, Co, Ni and Se before and after chronoamperometry were almost same suggesting the composition of Tyrrellite was stable. Figure 7 shows the comparison of pXRD pattern of Cu(Co<sub>0.68</sub>Ni<sub>0.32</sub>)<sub>2</sub>Se<sub>4</sub> before and after chronoamperometry indicating the same crystalline structure of Tyrrellite without the presence of any other metal oxides or hydroxides. The composition of Tyrrellite after chronoamperometry was also confirmed through XPS which showed no change in the Ni, Co, Cu and Se binding energies and even the oxidation states as shown in Figure 6 (c-f). The XPS comparison of Cu(Co<sub>0.68</sub>Ni<sub>0.32</sub>)<sub>2</sub>Se<sub>4</sub> before and after chronoamperometric measurement was shown in Figure S2, the XPS peaks of all elements were kept the same suggesting the stability of Tyrrellite during OER process.

To further explore the superior OER catalytic activity of Cu(Co<sub>0.68</sub>Ni<sub>0.32</sub>)<sub>2</sub>Se<sub>4</sub> and to shed light on the microscopic origin of the observed behavior, DFT calculations were carried out to study the electronic properties of bulk Cu(Co<sub>0.68</sub>Ni<sub>0.32</sub>)<sub>2</sub>Se<sub>4</sub> and a slab with (100) terminated surface, as well as to calculate the OH<sup>-</sup> adsorption energy on the (100) surface. In the bulk Tyrrellite Cu<sub>8</sub>Co<sub>11</sub>Ni<sub>5</sub>Se<sub>32</sub> supercell, five Ni atoms were randomly substituted for Co atoms in the octahedral sites. To determine the energetically-preferable distribution of the five Ni atoms in the supercell, five structures with different locations of the Ni substitutions were investigated. Among the five structures, the nearest neighbor Ni-Ni distances ranged from 3.54 to 6.12 Å, resulting in the magnetic moment on Ni atoms to vary from 0.61 μ<sub>B</sub> (for an “isolated” Ni atom, i.e., the one with a Ni nearest neighbor at

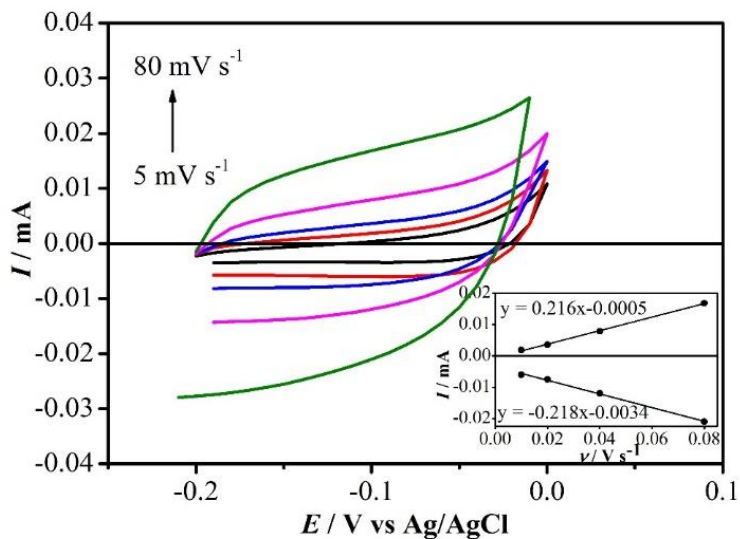


Figure 4. Cyclic voltammograms measured for  $\text{Cu}(\text{Co}_{0.68}\text{Ni}_{0.32})_2\text{Se}_4$  in  $\text{N}_2$  saturated 1.0 M KOH solution at different scan rates from 5 to  $80 \text{ mV s}^{-1}$ . The inset is a plot of both anodic and cathodic current measured at  $-0.1 \text{ V vs Ag|AgCl}$  (KCl Saturated) as a function of scan rate.

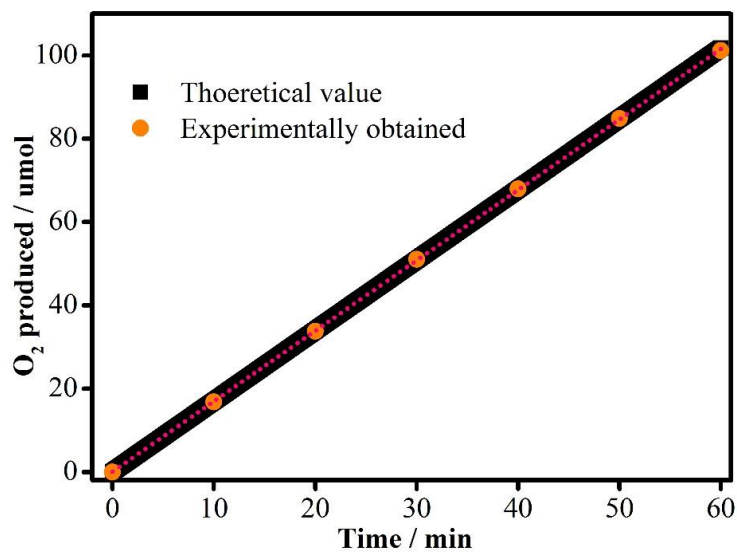


Figure 5. The amount of theoretically calculated (black dots) oxygen and experimentally measured (orange dots) oxygen of  $\text{Cu}(\text{Co}_{0.68}\text{Ni}_{0.32})_2\text{Se}_4$  versus time at  $0.7 \text{ V vs Ag|AgCl}$  (KCl Saturated).

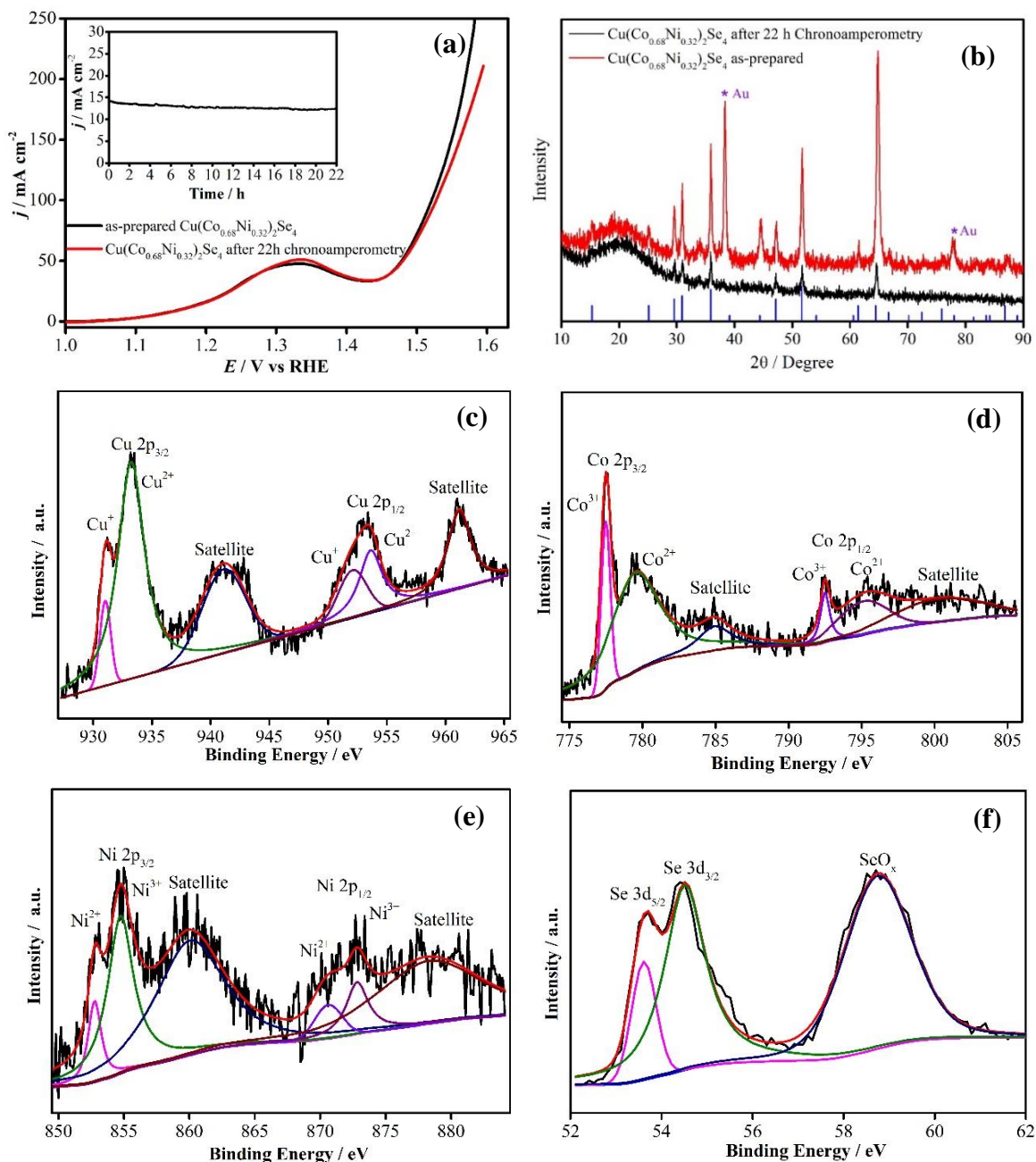


Figure 6. (a) The comparison of LSVs of the catalyst before and after chronoamperometry for 22 h. The inset is chronoamperometric measurement of  $\text{Cu}(\text{Co}_{0.68}\text{Ni}_{0.32})_2\text{Se}_4$  nanoparticles under continuous  $\text{O}_2$  evolution for 22 h held at constant potential to obtain  $\approx 13 \text{ mA cm}^{-2}$  current density. (b) Pxd pattern of  $\text{Cu}(\text{Co}_{0.68}\text{Ni}_{0.32})_2\text{Se}_4$  before and after 22 h chronoamperometry. XPS spectra of Cu 2p (c), Co 2p (d), Ni 2p (e) and Se 3d (f) of  $\text{Cu}(\text{Co}_{0.68}\text{Ni}_{0.32})_2\text{Se}_4$  after electrochemical measurement.

6.12 Å)  $0.95 \mu_B$  (for a Ni atom with two Ni neighbors at a short distance of 3.54 Å). Most importantly, we find that the magnetic moment on Co atoms is enhanced by the presence of Ni from  $0.85 \mu_B$  in the Ni-free case to as much as  $1.06 \mu_B$  for specific Co atoms in some of the structures. Further analysis reveal that the increased magnetic moment is associated with the longer Co-Se distances in the Ni-doped structures: due to the presence of Ni, the average Co-Se distance for the nearby Co increases from 2.39 Å (Ni-free case,  $\text{Cu}_8\text{Co}_{16}\text{Se}_{32}$ ) to 2.41 Å. Despite the differences in the distribution of Ni atoms in bulk  $\text{Cu}_8\text{Co}_{11}\text{Ni}_5\text{Se}_{32}$  and in the resulting magnetic moments on the Ni and Co atoms, we find that the total energies of the considered five structures are nearly identical as shown in Table S2, indicating that the distribution of Ni atoms does not affect the stability of bulk  $\text{Cu}(\text{Co}_{0.68}\text{Ni}_{0.32})_2\text{Se}_4$ .

The oxygen evolution reaction is a surface process, hence, it is necessary to evaluate the surface properties of  $\text{Cu}(\text{Co}_{0.68}\text{Ni}_{0.32})_2\text{Se}_4$  to further understand its excellent OER activity. Although our investigations suggested no preferred distribution of Ni atoms in bulk  $\text{Cu}_8\text{Co}_{11}\text{Ni}_5\text{Se}_{32}$ , it may not be the case for a slab and it is necessary to investigate how substitutional Ni atoms are distributed in the presence of a surface, specifically, the (100)-oriented plane. For this,  $\text{Cu}_{14}\text{Co}_{19}\text{Ni}_9\text{Se}_{56}$  supercell was created with a relatively large vacuum layer of 10 Å added to separate the periodic slabs in order to avoid interaction between them. The slab thickness is about 18 Å for the (100) surface that corresponds to seven Ni/Co-containing layers. After the Ni-free slab was optimized, six structures were created by placing substitutional Ni atoms at the surface layer, within the second or third layers closer to the center of the slab, or within top and second or second and third layers, as shown in Figure S3. To determine the preferred distribution of Ni atoms within the slab,

all structures were fully optimized; then the total energies were compared for non-magnetic GGA (U=0 eV) and magnetic GGA+U cases. As can be seen in Table S3, magnetism plays a critical role in determining the stable configuration. In the non-magnetic case (GGA, U=0 eV), Ni atoms prefer to substitute Co in the surface layer and the total energy gradually increases as some or all Ni atoms are placed in the second or third layers instead. However, the magnetic GGA+U calculations show a strong preference for Ni to substitute Co in the second layer. Placing the Ni atoms in the third layer increases the total energy by 1.02 eV, while distributing Ni atoms between the second and third layers raises the energy by 1.40 eV with respect to the lowest case, suggesting the Ni has a preference for a single layer. In this case, clustering of Ni atoms leads to an enhanced magnetic moment on Ni, e.g., 1.18  $\mu_B$  in case 2, Table S3. The highest energy configurations correspond to the Ni atoms located in the surface layers. Importantly, the magnetic moments of both Ni and Co are enhanced in the presence of the surface with more pronounced changes observed for Co atoms, c.f., Tables S2 and S3. The presence of Ni in the slab increases the magnetic moment of Co even further – in agreement with the results for bulk, as discussed above; for comparison, the magnetic moment on Co for Ni-free (100) interface ranges from 0.78  $\mu_B$  (for Co in the central layer) to 2.11  $\mu_B$  (for Co on the surface).

In Figure 7, the total density of states (TDOS) of  $\text{Cu}(\text{Co}_{0.68}\text{Ni}_{0.32})_2\text{Se}_4$  case 6 (100) surface was compared with that of  $\text{CuCo}_2\text{Se}_4$  (100) surface to elucidate how Ni dopants influence the electronic structure and OER catalytic activity of Tyrrellite. As can be observed,  $\text{Cu}(\text{Co}_{0.68}\text{Ni}_{0.32})_2\text{Se}_4$  (100) surface exhibited a similar DOS near the Fermi level in comparison of  $\text{CuCo}_2\text{Se}_4$  (100) surface, while the bottom of the CB has shifted toward the Fermi level, indicating  $\text{Cu}(\text{Co}_{0.68}\text{Ni}_{0.32})_2\text{Se}_4$  is in more metallic states and the *d-d* orbital

delocalization might take place among the metal atoms. It has been reported that the *d*-band rearrangement of mixed metals in the catalytic system optimizes the bond strength of metal center–OH species, thereby reduces the thermodynamic potentials and enhance the efficiency of OER process.<sup>35,80,81</sup> The TODS comparison of Cu(Co<sub>0.68</sub>Ni<sub>0.32</sub>)<sub>2</sub>Se<sub>4</sub> case 2 (100) surface with CuCo<sub>2</sub>Se<sub>4</sub> is shown in Figure S4. As can be seen, similar trend can be observed.

It has been widely reported that metals in the octahedral sites served as the catalytic active centers in a spinel-structured catalyst.<sup>82,83,84</sup> In our previous work, Co atoms have been proved as preferable active sites in CuCo<sub>2</sub>Se<sub>4</sub> catalyst due to a lower adsorption energy and a more stable attachment of OH<sup>-</sup> species on Co site.<sup>34</sup> As reported above, Cu(Co<sub>0.68</sub>Ni<sub>0.32</sub>)<sub>2</sub>Se<sub>4</sub> showed a better OER activity than CuCo<sub>2</sub>Se<sub>4</sub> with 32 % of Ni replacing Co in the octahedral site, suggesting that Ni plays a crucial role in boosting the OER activity. Therefore, the adsorption energy of OH<sup>-</sup> on (100) plane was calculated by placing OH<sup>-</sup> on the top of an active metal (Co / Ni) sites to further investigate the OER active sites. For this, two slab structures with different Ni distributions, namely, case 2 and case 6, c.f., Table S3 and Figure S3, were used in order to understand the role of Ni on the electronic and magnetic properties of Cu(Co<sub>0.68</sub>Ni<sub>0.32</sub>)<sub>2</sub>Se<sub>4</sub>. Figure 8 presents the supercell slabs of the relaxed (100) surface (case 6) with OH<sup>-</sup> attached on Co or Ni sites. Comparing the OH complex attached to Ni or Co surface atoms in this case, we find that Co is energetically more preferable for OH adsorption than Ni by 0.40 eV in GGA and by 0.85 eV in GGA+U. We note that the difference between the OH adsorption on Co vs Ni is significantly larger than that for Co vs Cu (0.04 eV in GGA and 0.53 eV in GGA+U) for the Ni-free CuCo<sub>2</sub>Se<sub>4</sub> (100) surface, as reported.<sup>34</sup> Most importantly, we find that the

presence of Ni at the surface layer improves the OH adsorption on Co: the calculated adsorption energy changes from  $-2.96$  eV for Ni-free (100) slab<sup>34</sup> to  $-3.21$  eV for (100) slab in case 6 (this work). The OH adsorption energy is  $-1.44$  eV when all Ni atoms are located in the second layer (case 2) of the slab. Thus, we believe that the as-grown  $\text{Cu}(\text{Co}_{0.68}\text{Ni}_{0.32})_2\text{Se}_4$  nanoparticles are expected to show an improved OH adsorption associated with random distribution of Ni across the slab layers, whereas annealing or a heat treatment of the nanoparticles may result in preferential Ni distribution and reduce the OH adsorption.

To understand the microscopic reason of the surface Ni enhancement of the OH adsorption on Co, we compare the structural, electronic, and magnetic properties of the (100) slabs before and after OH attachment. Upon bonding to the OH complex, the magnetic moment on the Co atom increases from  $2.11 \mu_B$  to  $2.46 \mu_B$  for case 2 and from  $2.12 \mu_B$  to  $2.57 \mu_B$  for case 6, whereas the magnetic moment of surface Ni atom with attached OH complex decreases from  $0.98 \mu_B$  to  $0.77 \mu_B$ , Table S4. The bond length of metal–OH, bond angle of metal–O–H and magnetic moment before and after attaching  $\text{OH}^-$  are listed in Table S4. It can be noted that the  $\text{OH}^-$  group bonded with Co atom more tightly than with Ni atom. The PDOS of OH-free Co atom, of Co atom with attached  $\text{OH}^-$  and of  $\text{OH}^-$  are shown in Figure 9 (a-c) while that of OH-free Ni atom, of Ni atom with attached  $\text{OH}^-$  and of  $\text{OH}^-$  are presented in Figure 9 (d-f). As it can be seen, the PDOS of Ni remains nearly the same before and after attaching  $\text{OH}^-$ , while that of Co has slightly shifted toward the negative energies and exhibit state splitting due to stronger magnetic interactions after attaching  $\text{OH}^-$ .

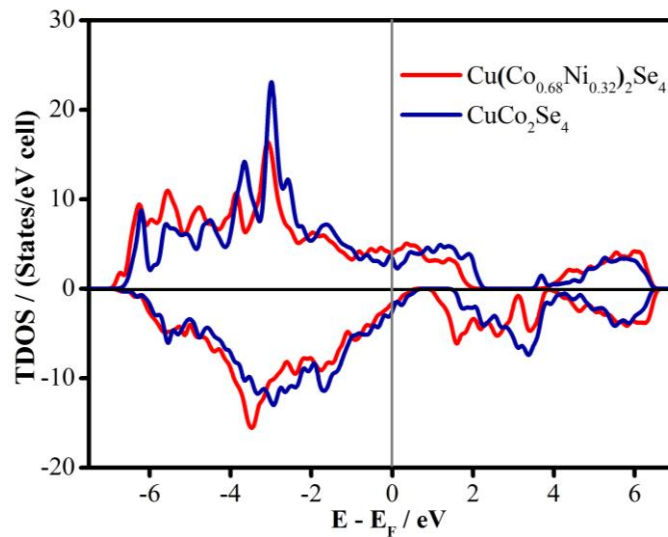


Figure 7. Comparison of total density of states (TDOS) of (100) surface of  $\text{Cu}(\text{Co}_{0.68}\text{Ni}_{0.32})_2\text{Se}_4$  case 6 (red) and  $\text{CuCo}_2\text{Se}_4$  (blue) calculated with GGA+U with  $U = 6$  eV.

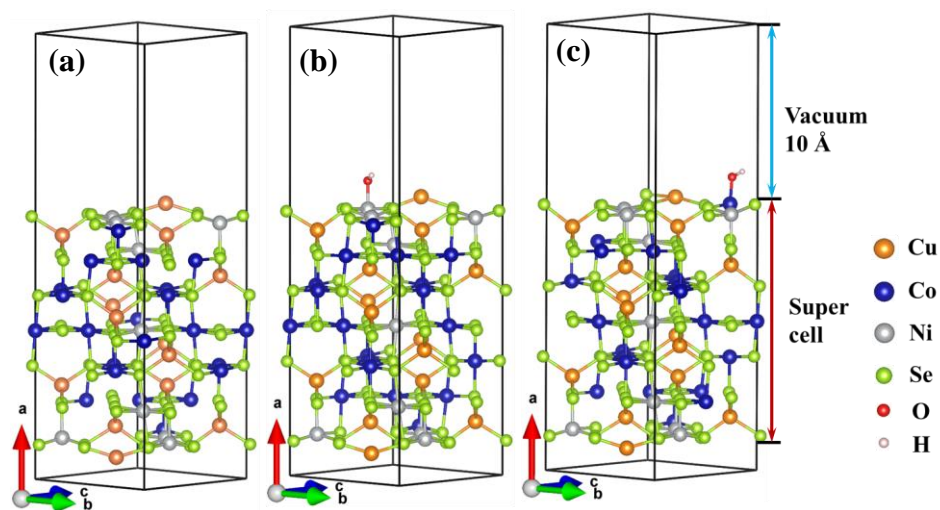


Figure 8. Supercell slabs of relaxed  $\text{Cu}(\text{Co}_{0.68}\text{Ni}_{0.32})_2\text{Se}_4$  (100) surface,  $\text{Cu}(\text{Co}_{0.68}\text{Ni}_{0.32})_2\text{Se}_4$  (100) surface with  $\text{OH}^-$  attached on Ni atom, and  $\text{Cu}(\text{Co}_{0.68}\text{Ni}_{0.32})_2\text{Se}_4$  (100) surface with  $\text{OH}^-$  attached on Co atom.



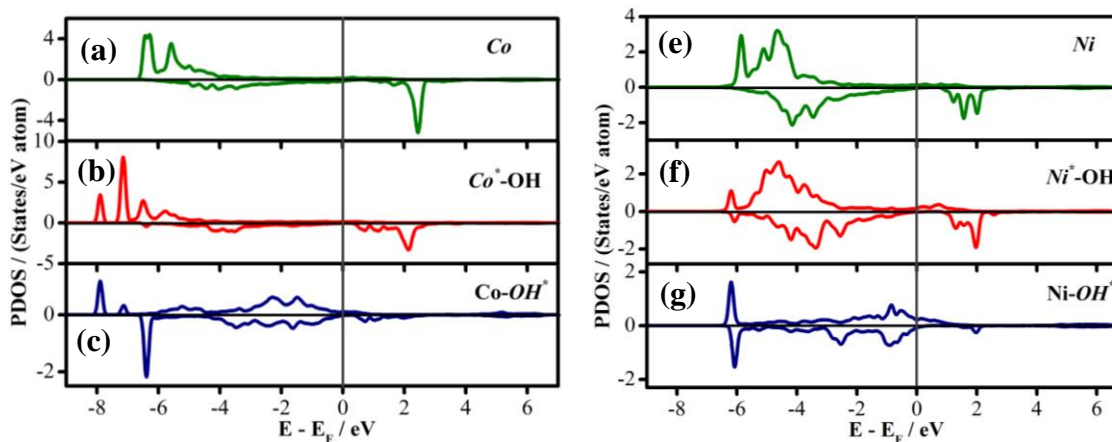


Figure 9. Partial density of states (PDOS) of Co atom before  $\text{OH}^-$  attachment (a), Co atom after  $\text{OH}^-$  attachment (b),  $\text{OH}^-$  attached to Co atom (c). PDOS of Ni atom before  $\text{OH}^-$  attachment (d), Ni atom after  $\text{OH}^-$  attachment (e),  $\text{OH}^-$  after attached on Ni atom (f). The calculations of the (100) slab of  $\text{Cu}(\text{Co}_{0.68}\text{Ni}_{0.32})_2\text{Se}_4$  are performed within GGA+U.

#### 4. CONCLUSIONS

In summary, we have the first time reported selenide based mineral–Tyrrellite  $\text{Cu}(\text{Co}_{0.68}\text{Ni}_{0.32})_2\text{Se}_4$  nanoparticles as an out-performing OER electrocatalyst. Through detailed electrochemical measurements, the catalyst required a low overpotential 205 mV to achieve  $10 \text{ mA cm}^{-2}$  for OER and exhibited a promising durability in alkaline solution. The overpotential for OER is significantly lower than  $\text{RuO}_2$  and it is one of the best reported OER electrocatalysts till date. One-step hydrothermal synthesis of nanostructured Tyrrellite provided a new method for the exploration of high-efficiency electrocatalysts by mixing economical and earth abundant transition metals.

#### ASSOCIATED CONTENT

Supporting Information. Synthesis method of  $\text{RuO}_2$ , EDS table before and after chronoamperometry, CV of Tyrrellite, XPS comparison figure before and after

chronoamperometry, Gibbs free energy table of bulk  $\text{Cu}(\text{Co}_{0.68}\text{Ni}_{0.32})_2\text{Se}_4$ , schematics of slab supercells of five cases of (100) surface, Gibbs free energy of six cases (100) surface, comparison table with and without attaching  $\text{OH}^-$ .

#### Author Information:

Corresponding Author

\*Manashi Nath: nathm@mst.edu

#### Author Contributions

The manuscript was written through contributions of all authors. All authors have given approval to the final version of the manuscript.

#### Funding Sources

This work was supported by funding from National Science Foundation (DMR 1710313) and American Chemical Society Petroleum Research Fund (54793-ND10).

#### Notes

Any additional relevant notes should be placed here.

Acknowledgments. The authors would like to acknowledge the funding from National Science Foundation (DMR 1710313) and American Chemical Society Petroleum Research Funds (54793-ND10). The authors would also like to acknowledge Materials Research Center (MRC) for equipment usage and computational resources provided by DOE-supported NERSC (*National Energy Research Scientific Computing*) center for high-performance computing.

## SUPPORTING INFORMATION

### TYRRELLITE AS A NOVEL AND SUSTAINABLE EFFICIENT ELECTROCATALYSTS FOR OXYGEN EVOLUTION GENERATION

*Xi Cao<sup>a</sup>, Julia E. Medvedeva<sup>b\*</sup> and Manashi Nath<sup>a\*</sup>*

<sup>a</sup>Department of Chemistry, Missouri University of Science & Technology, Rolla, Missouri 65409, United States.

<sup>b</sup>Department of Chemical and Biochemical Engineering, Missouri University of Science & Technology, Rolla, Missouri 65409, United States.

\*Email: [nathm@mst.edu](mailto:nathm@mst.edu)

## 1. EXPERIMENTAL

Electrodeposition of RuO<sub>2</sub> on CFP:<sup>s1</sup> In a typical procedure of electrodeposition of RuO<sub>2</sub>, RuCl<sub>3</sub> (0.452 g) and KCl (2.952 g) were mixed in 40 ml of 0.01M HCl, cyclic voltammetry from 0.015 to 0.915 V (vs. Ag/AgCl) was applied for 100 cycles at a scan rate of 50 mV s<sup>-1</sup>. Finally the products were heated at 200 °C for 3 h under air.

Table S1. EDS comparison of Cu(Co<sub>0.68</sub>Ni<sub>0.32</sub>)<sub>2</sub>Se<sub>4</sub> catalyst before and after electrochemical measurement.

|                         | EDS (Atomic %) |      |      |      |
|-------------------------|----------------|------|------|------|
|                         | Ni             | Co   | Cu   | Se   |
| As-synthesized          | 10.3           | 20.9 | 15.4 | 53.4 |
| After Chronoamperometry | 12.3           | 23.7 | 15.8 | 48.2 |

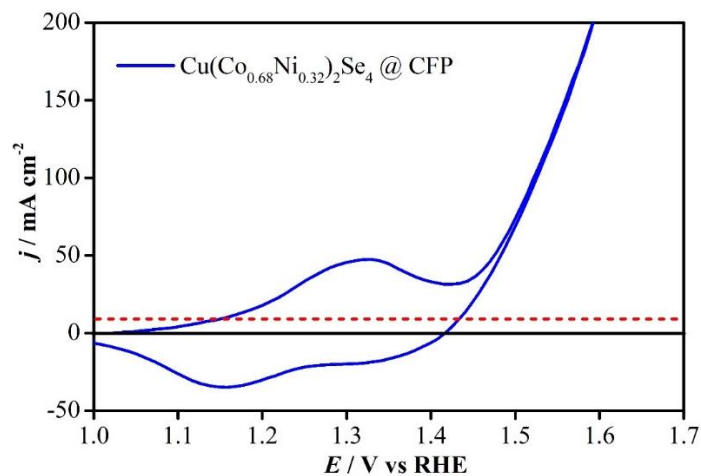


Figure S1. Cyclic voltammetry of  $\text{Cu}(\text{Co}_{0.68}\text{Ni}_{0.32})_2\text{Se}_4$  catalyst in  $\text{N}_2$  saturated 1.0 M KOH.

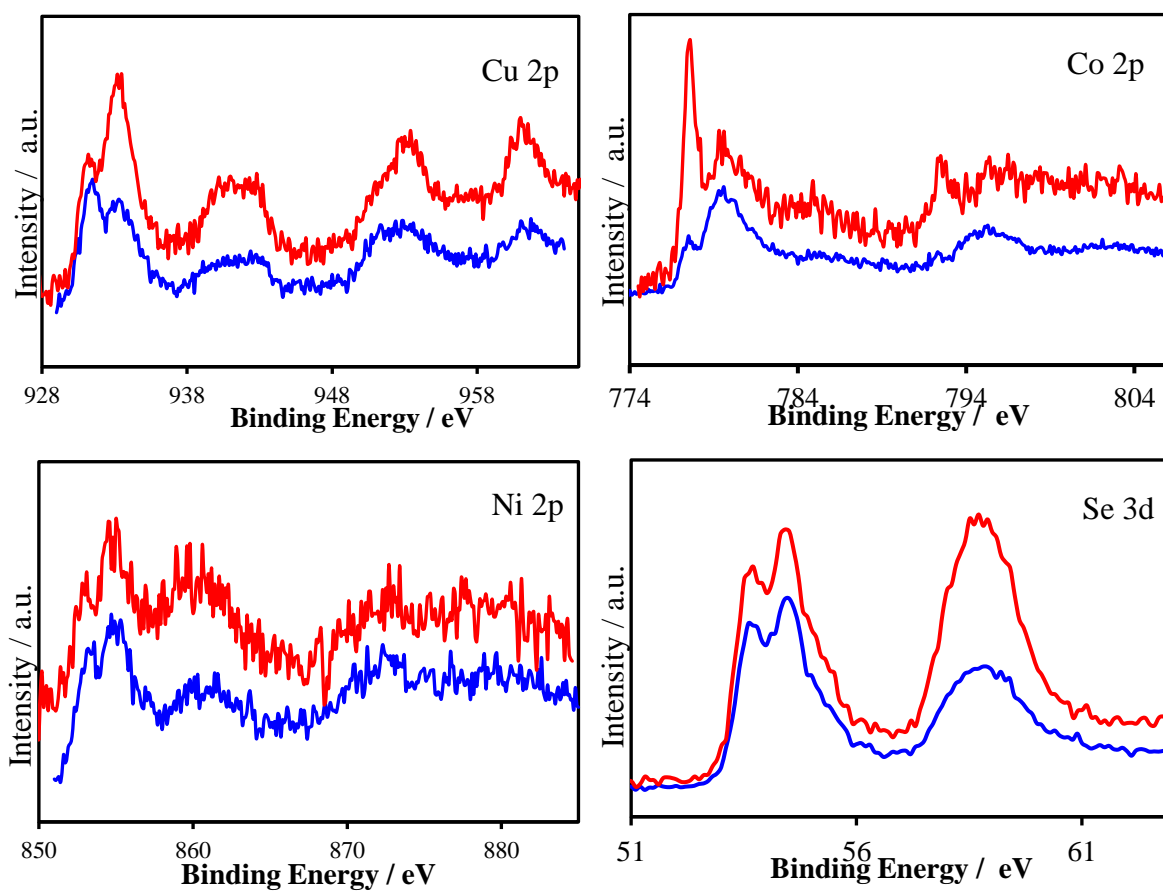


Figure S2. XPS spectra of  $\text{Cu}(\text{Co}_{0.68}\text{Ni}_{0.32})_2\text{Se}_4$  before (navy) and after (red) electrochemical measurement.

Table S2. DFT calculated Ni-Ni distances, Ni and Co magnetic moments, and the total energy difference of bulk  $\text{Cu}(\text{Co}_{0.68}\text{Ni}_{0.32})_2\text{Se}_4$  with Ni atoms substituting different Co atoms. The total energies are given with respect to the lowest energy case.

|        | Ni-Ni distribution and distances                                            | Ni magnetic moments, $\mu_B$ | Co magnetic moments, $\mu_B$ | $\Delta E$ , meV |
|--------|-----------------------------------------------------------------------------|------------------------------|------------------------------|------------------|
| Case 1 | 4 Ni dimers at 3.54 Å;<br>1 isolated Ni at 6.12 Å                           | 0.61-0.84                    | 0.82-1.03                    | 3                |
| Case 2 | 4 Ni dimers at 3.54 Å;<br>1 isolated Ni at 6.12 Å                           | 0.61-0.84                    | 0.82-1.03                    | 3                |
| Case 3 | 1 Ni trimer at 3.54 Å;<br>2 Ni dimers at 3.54 Å;<br>2 isolated Ni at 6.12 Å | 0.63-0.95                    | 0.93-1.02                    | 12               |
| Case 4 | 1 Ni trimer at 3.54 Å;<br>2 Ni dimers at 3.54 Å;<br>2 isolated Ni at 6.12 Å | 0.71-0.90                    | 0.82-1.06                    | 0                |
| Case 5 | 4 Ni dimers at 3.54 Å;<br>1 isolated Ni at 6.12 Å                           | 0.61-0.84                    | 0.82-1.03                    | 3                |

Table S3. DFT GGA and GGA+U calculated total energies of six  $\text{Cu}(\text{Co}_{0.68}\text{Ni}_{0.32})_2\text{Se}_4$  (100) slabs with Ni atoms substituting different Co atoms in the slab, given with respect to the lowest case in each method. For comparison, the magnetic moment on Co atoms in Ni-free  $\text{CuCo}_2\text{Se}_4$  (100) slab is 0.78-2.11  $\mu_B$ .

|        | Configuration for Ni atoms                 | GGA, non-magnetic $\Delta E$ / eV | GGA+U, magnetic $\Delta E$ / eV | GGA+U Ni magnetic moment, $\mu_B$ | GGA+U Co magnetic moment, $\mu_B$ |
|--------|--------------------------------------------|-----------------------------------|---------------------------------|-----------------------------------|-----------------------------------|
| Case 1 | Surface layer                              | 0                                 | 2.76                            | 0.82-0.97                         | 0.78-0.92                         |
| Case 2 | 2 <sup>nd</sup> layer                      | 1.12                              | 0                               | 0.95-1.18                         | 0.93-2.11                         |
| Case 3 | 3 <sup>rd</sup> layer                      | 1.89                              | 1.02                            | 0.98-0.99                         | 0.87-2.13                         |
| Case 4 | Surface and 2 <sup>nd</sup> layers         | 0.95                              | 2.30                            | 0.80-1.02                         | 0.85-2.12                         |
| Case 5 | 2 <sup>nd</sup> and 3 <sup>rd</sup> layers | 2.15                              | 1.40                            | 0.92-1.00                         | 0.92-2.18                         |
| Case 6 | Surface and 2 <sup>nd</sup> layers         | 0.50                              | 2.75                            | 0.95-1.02                         | 0.85-2.12                         |

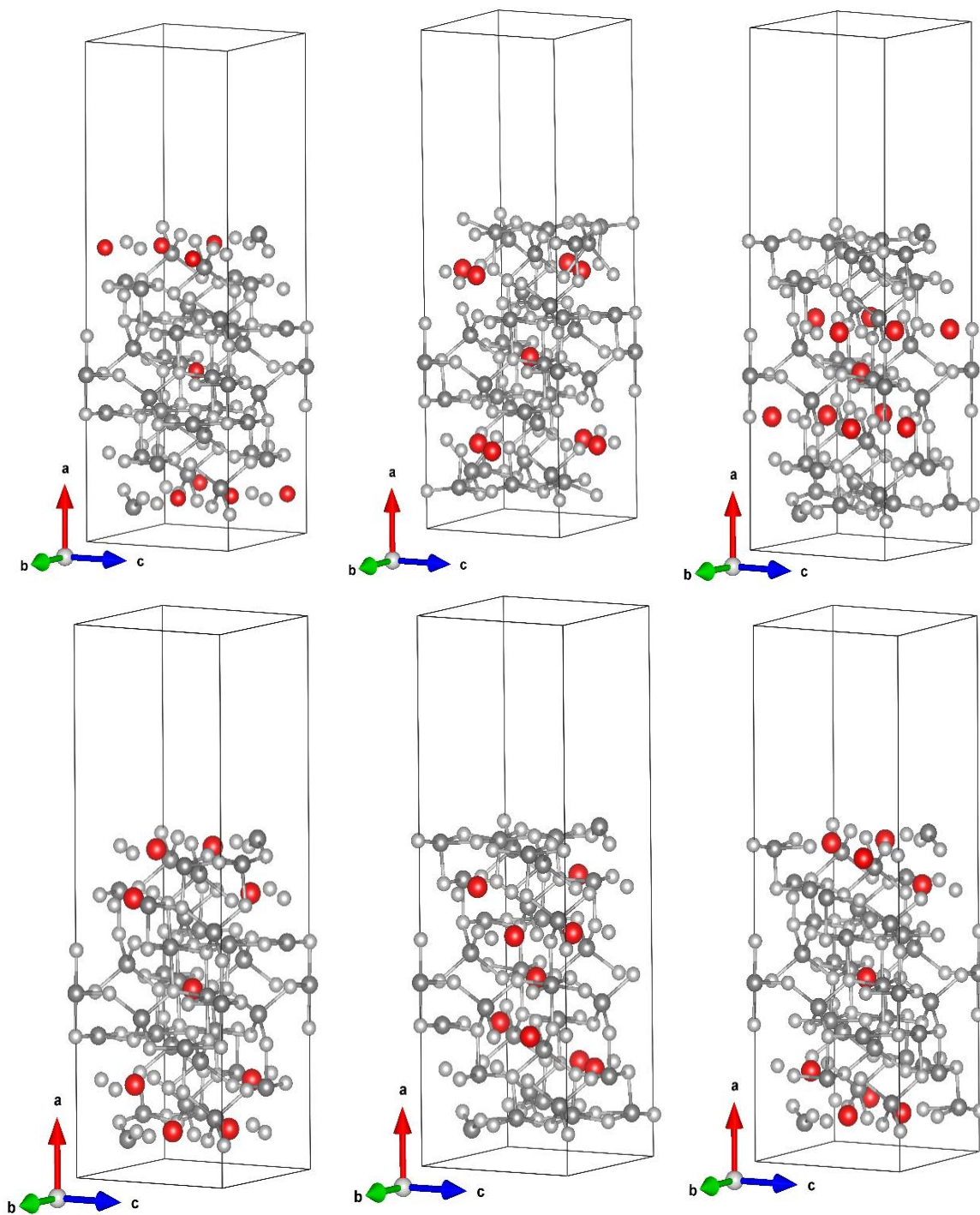


Figure S3. Simplified slab supercells of case 1 (a), case 2 (b), case 3 (c), case4 (d), case 5 (e) and case 6 (f). All atoms except Ni are set as grey in order to exhibit the different localizations of Ni atoms in each slab.

Table S4. Comparison of the calculated adsorption energy, magnetic moment, bond length and bond angle of  $\text{OH}^-$  attached on the surface Ni or Co atom with those with no  $\text{OH}^-$  attachment for case 2 and 6.

|                                      | Case 2           |                    | Case 6           |                    |                  |                    |
|--------------------------------------|------------------|--------------------|------------------|--------------------|------------------|--------------------|
|                                      | Co atom          |                    | Ni atom          |                    | Co atom          |                    |
|                                      | no $\text{OH}^-$ | with $\text{OH}^-$ | no $\text{OH}^-$ | with $\text{OH}^-$ | no $\text{OH}^-$ | with $\text{OH}^-$ |
| OH adsorption energy, eV             | -                | -1.44              | -                | -2.36              | -                | -3.21              |
| Magnetic moment / $\mu_B$            | 2.11             | 2.46               | 0.98             | 0.77               | 2.12             | 2.57               |
| Bond length (metal-O) / $\text{\AA}$ | -                | 1.83               | -                | 1.87               | -                | 1.81               |
| Bond angle (metal-O-H) / $^\circ$    | -                | 110.80             | -                | 109.98             | -                | 110.41             |

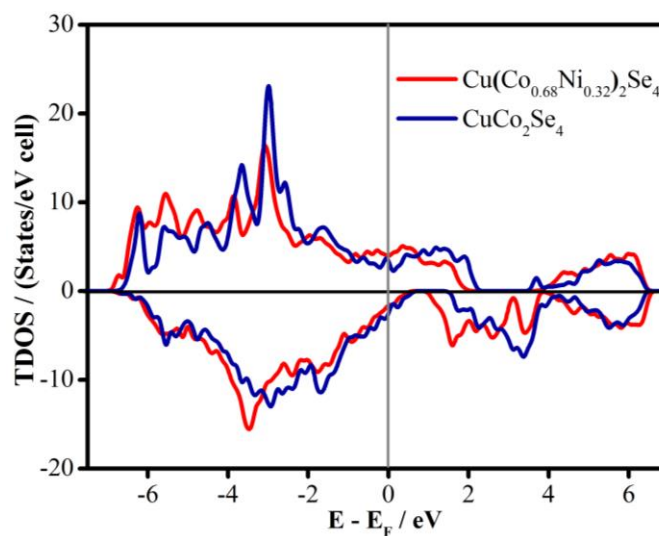


Figure S4. Comparison of total density of states (TDOS) of (100) surface of  $\text{Cu}(\text{Co}_{0.68}\text{Ni}_{0.32})_2\text{Se}_4$  case 2 (red) and  $\text{CuCo}_2\text{Se}_4$  (blue) calculated with GGA+U with  $U = 6$  eV.

## 2. REFERENCE

- s1 K. M. Kim, J. H. Nam, Y. G. Lee, W. Il Cho and J. M. Ko, *Curr. Appl. Phys.*, 2013, **13**, 1702–1706.

## REFERENCES

- (1) Lewis, N. S.; Nocera, D. G. Powering the Planet: Chemical Challenges in Solar Energy Utilization. *Proc. Natl. Acad. Sci.* **2006**, *103*, 15729–15735.
- (2) Chow, J.; Kopp, R. J.; Portney, P. R. Energy Resources and Global Development. *Science* **2003**, *302*, 1528–1532.
- (3) Dresselhaus, M.S.; Thomas, I. Alternative Energy Technologies. *Nature* **2001**, *414*, 332–337.
- (4) Turner, J. A. A Realizable Renewable Energy Future. *Science* **1999**, *285*, 687–689.
- (5) Singh, A.; Spiccia, L. Water Oxidation Catalysts Based on Abundant 1<sup>st</sup> Row Transition Metals. *Coord. Chem. Rev.* **2013**, *257*, 2607–2622.
- (6) Roger, I.; Shipman, M. A.; Symes, M. D. Earth-Abundant Catalysts for Electrochemical and Photoelectrochemical Water Splitting. *Nat. Rev. Chem.* **2017**, *1*, 0003.
- (7) Suntivich, J.; May, K. J.; Gasteiger, H. a; Goodenough, J. B.; Shao-horn, Y. A Perovskite Oxide Optimized for Molecular Orbital Principles. *Science* **2011**, *334*, 2010–2012.
- (8) Jiao, Y.; Zheng, Y.; Jaroniec, M.; Qiao, S. Z. Design of Electrocatalysts for Oxygen- and Hydrogen-Involving Energy Conversion Reactions. *Chem. Soc. Rev.* **2015**, *44*, 2060–2086.
- (9) Du, P.; Eisenberg, R. Catalysts Made of Earth-Abundant Elements (Co, Ni, Fe) for Water Splitting: Recent Progress and Future Challenges. *Energy Environ. Sci.* **2012**, *5*, 6012–6021.
- (10) Lee, Y.; Suntivich, J.; May, K. J.; Perry, E. E.; Shao-Horn, Y. Synthesis and Activities of Rutile IrO<sub>2</sub> and RuO<sub>2</sub> Nanoparticles for Oxygen Evolution in Acid and Alkaline Solutions. *J. Phys. Chem. Lett.* **2012**, *3*, 399–404.
- (11) Cherevko, S.; Geiger, S.; Kasian, O.; Kulyk, N.; Grote, J. P.; Savan, A.; Shrestha, B. R.; Merzlikin, S.; Breitbach, B.; Ludwig, A.; Mayrhofer, K. J. J. Oxygen and Hydrogen Evolution Reactions on Ru, RuO<sub>2</sub>, Ir, and IrO<sub>2</sub> Thin Film Electrodes in Acidic and Alkaline Electrolytes: A Comparative Study on Activity and Stability. *Catal. Today* **2016**, *262*, 170–180.
- (12) Lewis, N. S. Toward Cost-Effective Solar Energy Use. *Science* **2007**, *315*, 798–801.
- (13) Burke, M. S.; Enman, L. J.; Batchellor, A. S.; Zou, S.; Boettcher, S. W. Oxygen Evolution Reaction Electrocatalysis on Transition Metal Oxides and (Oxy)Hydroxides: Activity Trends and Design Principles. *Chem. Mater.* **2015**, *27*, 7549–7558.



- (14) He, Z.; Koza, J. A.; Liu, Y. C.; Chen, Q.; Switzer, J. A. Room-Temperature Electrochemical Reduction of Epitaxial Bi<sub>2</sub>O<sub>3</sub> Films to Epitaxial Bi Films. *RSC Adv.* **2016**, *6*, 96832–96836.
- (15) Tio, A.; Stabilize, C.; Photoanodes, G.; Hu, S.; Shaner, M. R.; Beardslee, J. A.; Lichterman, M.; Bruce, S.; Lewis, N. S. Amorphous TiO<sub>2</sub> Coatings Stabilize Si, GaAs, and GaP Photoanodes for Efficient Water Oxidation. **2014**, *1005*, 2547–2552.
- (16) Mahenderkar, N. K.; Chen, Q.; Liu, Y.-C.; Duchild, A. R.; Hofheins, S.; Chason, E.; Switzer, J. A. Epitaxial Lift-off of Electrodeposited Single-Crystal Gold Foils for Flexible Electronics. **2017**, *1206*, 1203–1206.
- (17) Xu, B.; Cao, X.; Wang, G.; Li, Y.; Wang, Y.; Su, J. Controlled Synthesis and Novel Luminescence Properties of String SrWO<sub>4</sub>:Eu<sup>3+</sup> Nanobeans. *Dalt. Trans.* **2014**, *43*, 11493–11501.
- (18) Li, Y.; Cao, X.; Wang, G.; Liu, S.; Feng, L.; Xu, B.; Wang, Y.; Su, J. Synthesis and Tunable Upconversion Luminescence of NaLuF<sub>4</sub>: Yb<sup>3+</sup>/Er<sup>3+</sup> Nanocrystals by Pb<sup>2+</sup> Tridoping. *Sci. Adv. Mater.* **2014**, *6*, 1037–1042.
- (19) Zhou, T.; Cao, Z.; Zhang, P.; Ma, H.; Gao, Z.; Wang, H.; Lu, Y.; He, J.; Zhao, Y. Transition Metal Ions Regulated Oxygen Evolution Reaction Performance of Ni-Based Hydroxides Hierarchical Nanoarrays. *Sci. Rep.* **2017**, *7*, 46154.
- (20) Gong, M.; Dai, H. A Mini Review of NiFe-Based Materials as Highly Active Oxygen Evolution Reaction Electrocatalysts. *Nano Res.* **2015**, *8*, 23–39.
- (21) Hu, C.; Zhang, L.; Zhao, Z.-J.; Luo, J.; Shi, J.; Huang, Z.; Gong, J. Edge Sites with Unsaturated Coordination on Core–Shell Mn<sub>3</sub>O<sub>4</sub>@Mn<sub>x</sub>Co<sub>3-x</sub>O<sub>4</sub> Nanostructures for Electrocatalytic Water Oxidation. *Adv. Mater.* **2017**, *29*, 1701820.
- (22) Chen, J. Y. C.; Miller, J. T.; Gerken, J. B.; Stahl, S. S. Inverse Spinel NiFeAlO<sub>4</sub> as a Highly Active Oxygen Evolution Electrocatalyst: Promotion of Activity by a Redox-Inert Metal Ion. *Energy Environ. Sci.* **2014**, *7*, 1382–1386.
- (23) Chen, Q.; Switzer, J. A. Photoelectrochemistry of Ultrathin, Semitransparent, and Catalytic Gold Films Electrodeposited Epitaxially onto n-Silicon (111). *ACS Appl. Mater. Interfaces* **2018**, *10*, 21365–21371.
- (24) Dionigi, F.; Strasser, P. NiFe-Based (Oxy)Hydroxide Catalysts for Oxygen Evolution Reaction in Non-Acidic Electrolytes. *Adv. Energy Mater.* **2016**, *6*, 1600621.
- (25) Gardner, G. P.; Go, Y. B.; Robinson, D. M.; Smith, P. F.; Hadermann, J.; Abakumov, A.; Greenblatt, M.; Dismukes, G. C. Structural Requirements in Lithium Cobalt Oxides for the Catalytic Oxidation of Water. *Angew. Chem. Int. Ed.* **2012**, *51*, 1616–1619.

- (26) Burke, M. S.; Kast, M. G.; Trotochaud, L.; Smith, A. M.; Boettcher, S. W. Cobalt-Iron (Oxy)Hydroxide Oxygen Evolution Electrocatalysts: The Role of Structure and Composition on Activity, Stability, and Mechanism. *J. Am. Chem. Soc.* **2015**, *137*, 3638–3648.
- (27) Smith, R. D. L.; Preot, M. S.; Fagan, R. D.; Trudel, S.; Berlinguette, C. P. Water Oxidation Catalysis: Electrocatalytic Response to Metal Stoichiometry in Amorphous Metal Oxide Films Containing Iron, Cobalt, and Nickel. *J. Am. Chem. Soc.* **2013**, *135*, 11580–11586.
- (28) Mccrory, C. C. L.; Jung, S.; Peters, J. C.; Jaramillo, T. F. Benchmarking Heterogeneous Electrocatalysts for the Oxygen Evolution Reaction. *J. Am. Chem. Soc.* **2013**, *135*, 16977–16987.
- (29) Chen, Q.; Switzer, J. A. Electrodeposition of Nanometer-Thick Epitaxial Films of Silver onto Single-Crystal Silicon Wafers. *J. Mater. Chem. C* **2019**, *7*, 1720–1725.
- (30) Meagan V. Kelso; Naveen K. Mahenderkar; Qingzhi Chen; John Z. Tubbesing; Jay A. Switzer. Spin Coating Epitaxial Films. *Science* **2019**, *364*, 166–169.
- (31) Swesi, A. T.; Masud, J.; Nath, M. Nickel Selenide as a High-Efficiency Catalyst for Oxygen Evolution Reaction. *Energy Environ. Sci.* **2016**, *9*, 1771–1782.
- (32) Liu, X.; Liu, Y.; Fan, L.-Z. MOF-Derived CoSe<sub>2</sub> Microspheres with Hollow Interiors as High-Performance Electrocatalysts for the Enhanced Oxygen Evolution Reaction. *J. Mater. Chem. A* **2017**, *5*, 15310–15314.
- (33) Masud, J.; Liyanage, W. P. R.; Cao, X.; Saxena, A.; Nath, M. Copper Selenides as High-Efficiency Electrocatalysts for Oxygen Evolution Reaction. *ACS Appl. Energy Mater.* **2018**, *8*, 4075–4083.
- (34) Cao, X.; Medvedeva, J. E.; Nath, M. Copper Cobalt Selenide as a High-Efficiency Bifunctional Electrocatalyst for Overall Water Splitting: Combined Experimental and Theoretical Study. **2019**, *ACS Appl. Mater. & Interfaces*, submitted.
- (35) Cao, X.; Hong, Y.; Zhang, N.; Chen, Q.; Masud, J.; Zaeem, M. A.; Nath, M. Phase Exploration and Identification of Multinary Transition-Metal Selenides as High-Efficiency Oxygen Evolution Electrocatalysts through Combinatorial Electrodeposition. *ACS Catal.* **2018**, *8*, 8273–8289.
- (36) Cao, X.; Johnson, E.; Nath, M. Identifying High-Efficiency Oxygen Evolution Electrocatalysts from Co–Ni–Cu Based Selenides through Combinatorial Electrodeposition. *J. Mater. Chem.* **2019**, *7*, 9877–9889.
- (37) Cao, X.; Johnson, E.; Nath, M. Expanding Multinary Selenide Based High-Efficiency Oxygen Evolution Electrocatalysts through Combinatorial Electrodeposition: Case Study with Fe-Cu-Co Selenides. *ACS Sustain. Chem. Eng.* **2019**, acssuschemeng.9b01095.

- (38) Xu, K.; Ding, H.; Lv, H.; Tao, S.; Chen, P.; Wu, X.; Chu, W.; Wu, C.; Xie, Y. Understanding Structure-Dependent Catalytic Performance of Nickel Selenides for Electrochemical Water Oxidation. *ACS Catal.* **2017**, *7*, 310–315.
- (39) Liu, T.; Liu, Q.; Asiri, A. M.; Luo, Y.; Sun, X. An Amorphous CoSe Film Behaves as an Active and Stable Full Water-Splitting Electrocatalyst under Strongly Alkaline Conditions. *Chem. Commun.* **2015**, *51*, 16683–16686.
- (40) Kim, J.-H.; Shin, K.; Kawashima, K.; Youn, D. H.; Lin, J.; Hong, T. E.; Liu, Y.; Wygant, B. R.; Wang, J.; Henkelman, G.; Mullins, B. C. Enhanced Activity Promoted by CeO<sub>x</sub> on a CoO<sub>x</sub> Electrocatalyst for the Oxygen Evolution Reaction. *ACS Catal.* **2018**, 4257–4265.
- (41) Zaffran, J.; Stevens, M. B.; Trang, C. D. M.; Nagli, M.; Shehadeh, M.; Boettcher, S. W.; Casparly Toroker, M. Influence of Electrolyte Cations on Ni(Fe)OOH Catalyzed Oxygen Evolution Reaction. *Chem. Mater.* **2017**, *29*, 4761–4767.
- (42) Chi, J. Q.; Yan, K. L.; Xiao, Z.; Dong, B.; Shang, X.; Gao, W. K.; Li, X.; Chai, Y. M.; Liu, C. G. Trimetallic Ni–Fe–Co Selenides Nanoparticles Supported on Carbon Fiber Cloth as Efficient Electrocatalyst for Oxygen Evolution Reaction. *Int. J. Hydrogen Energy* **2017**, *42*, 20599–20607.
- (43) Xia, C.; Jiang, Q.; Zhao, C.; Hedhili, M. N.; Alshareef, H. N. Selenide-Based Electrocatalysts and Scaffolds for Water Oxidation Applications. *Adv. Mater.* **2016**, *28*, 77–85.
- (44) Fang, Z.; Peng, L.; Lv, H.; Zhu, Y.; Yan, C.; Wang, S.; Kalyani, P.; Wu, X.; Yu, G. Metallic Transition Metal Selenide Holey Nanosheets for Efficient Oxygen Evolution Electrocatalysis. *ACS Nano* **2017**, *11*, 9550–9557.
- (45) Nai, J.; Lu, Y.; Yu, L.; Wang, X.; Lou, X. W. D. Formation of Ni–Fe Mixed Diselenide Nanocages as a Superior Oxygen Evolution Electrocatalyst. *Adv. Mater.* **2017**, *29*, 1703870.
- (46) Cleaves II, H. J.; Scott, A. M.; Hill, F. C.; Leszczynski, J.; Sahai, N.; Hazen, R. Prebiotic Chemistry Themed Issue. *Chem. Soc. Rev.* **2012**, *41*, 5502–5525.
- (47) Hochella, M. F.; Lower, S. K.; Maurice, P. A.; Penn, R. L.; Sahai, N.; Sparks, D. L.; Twining, B. S. Nanominerals, Mineral Nanoparticles, and Earth Systems. *Science* **2008**, *319*, 1631–1636.
- (48) Kondrat, S. A.; Smith, P. J.; Wells, P. P.; Chater, P. A.; Carter, J. H.; Morgan, D. J.; Fiordaliso, E. M.; Wagner, J. B.; Davies, T. E.; Lu, L.; et al. Stable Amorphous Georgerite as a Precursor to a High-Activity Catalyst. *Nature* **2016**, *531*, 83–87.
- (49) Kwan, W. P.; Voelker, B. M. Rates of Hydroxyl Radical Generation and Organic Compound Oxidation in Mineral-Catalyzed Fenton-like Systems. *Environ. Sci. Technol.* **2003**, *37*, 1150–1158.

- (50) Le Formal, F.; Guijarro, N.; Bourée, W. S.; Gopakumar, A.; Prévot, M. S.; Daubry, A.; Lombardo, L.; Sornay, C.; Voit, J.; Magrez, A.; et al. A Gibeon Meteorite Yields a High-Performance Water Oxidation Electrocatalyst. *Energy Environ. Sci.* **2016**, *9*, 3448–3455.
- (51) Yanina, S. V.; Rosso, K. M. Linked Reactivity at Mineral-Water Interfaces Through Bulk Crystal Conduction. *Science* **2008**, *613*, 218–222.
- (52) Konkana, B.; Puring, K. J.; Sinev, I.; Piontek, S.; Khavryuchenko, O.; Dürholt, J. P.; Schmid, R.; Tüysüz, H.; Muhler, M.; Schuhmann, W.; Apfel, U.-P. Pentlandite Rocks as Sustainable and Stable Efficient Electrocatalysts for Hydrogen Generation. *Nat. Commun.* **2016**, *7*, 12269.
- (53) Yang, H.; Hubler, D. K.; Lavina, B.; Downs, R. T.; Costin, G. Tyrrellite,  $\text{Cu}(\text{Co}_{0.68}\text{Ni}_{0.32})_2\text{Se}_4$ , Isostructural with Spinel. *Acta Crystallogr. Sect. C* **2007**, *63*, i73–i74.
- (54) Akihiko Hayashi, Katsuhiko Imada, Kazumichi Inoue, Y. U. and K. K. Phase Diagram of  $(\text{M}'_x\text{M}_{1-x})_3\text{Se}_4$  ( $0 \leq x \leq 1$ ) (M, M' = 3d-Transition Metal). *Bull. Inst. Chem. Res.* **1986**, *64*, 186–206.
- (55) Kjekshus, A.; Pearson, W. B. Phases with the Nickel Arsenide and Closely-Related Structures. *Prog. Solid State Chem.* **1964**, *1*, 83–174.
- (56) Umapathi, S.; Masud, J.; Swesi, A. T.; Nath, M.  $\text{FeNi}_2\text{Se}_4$ -Reduced Graphene Oxide Nanocomposite: Enhancing Bifunctional Electrocatalytic Activity for Oxygen Evolution and Reduction through Synergistic Effects. *Adv. Sustain. Syst.* **2017**, *1*, 1700086.
- (57) Enman, L. J.; Burke, M. S.; Batchellor, A. S.; Boettcher, S. W. Effects of Intentionally Incorporated Metal Cations on the Oxygen Evolution Electrocatalytic Activity of Nickel (Oxy)Hydroxide in Alkaline Media. *ACS Catal.* **2016**, *6*, 2416–2423.
- (58) Amin, B. G.; Swesi, A. T.; Masud, J.; Nath, M.  $\text{CoNi}_2\text{Se}_4$  as an Efficient Bifunctional Electrocatalyst for Overall Water Splitting. *Chem. Commun* **2017**, *5412*, 5412–5415.
- (59) Swesi, A. T.; Masud, J.; Liyanage, W. P. R.; Umapathi, S.; Bohannan, E.; Medvedeva, J.; Nath, M. Textured  $\text{NiSe}_2$  Film: Bifunctional Electrocatalyst for Full Water Splitting at Remarkably Low Overpotential with High Energy Efficiency. *Sci. Rep.* **2017**, *7*, 2401.
- (60) Kresse, G.; Hafner, J. Ab Initio Molecular Dynamics for Liquid Metals. *Phys. Rev. B* **1993**, *47*, 558–561.
- (61) Kresse, G.; Hafner, J. Ab Initio Molecular-Dynamics Simulation of the Liquid-Metal–Amorphous-Semiconductor Transition in Germanium. *Phys. Rev. B* **1994**, *49*, 14251–14269.
- (62) Kresse, G.; Furthmüller, J. Efficient Iterative Schemes for Ab Initio Total-Energy Calculations Using a Plane-Wave Basis Set. *Phys. Rev. B* **1996**, *54*, 11169–11186.

- (63) Kresse, G.; Furthmüller, J. Efficiency of Ab-Initio Total Energy Calculations for Metals and Semiconductors Using a Plane-Wave Basis Set. *Comput. Mater. Sci.* **1996**, *6*, 15–50.
- (64) Perdew, J. P.; Burke, K.; Ernzerhof, M. Generalized Gradient Approximation Made Simple. *Phys. Rev. Lett.* **1996**, *77*, 3865–3868.
- (65) Perdew, J. P.; Burke, K.; Ernzerhof, M. Erratum: Generalized Gradient Approximation Made Simple. *Phys. Rev. Lett.* **1997**, *78*, 1396–1396.
- (66) Blöchl, P. E. Projector Augmented-Wave Method. *Phys. Rev. B* **1994**, *50*, 17953–17979.
- (67) Joubert, D. From Ultrasoft Pseudopotentials to the Projector Augmented-Wave Method. *Phys. Rev. B* **1999**, *59*, 1758–1775.
- (68) Philipsen, P. H. T.; Baerends, E. J. Cohesive Energy of 3d Transition Metals: Density Functional Theory Atomic and Bulk Calculations. *Phys. Rev. B* **1996**, *54*, 5326–5333.
- (69) Kohn, W.; Becke, A. D.; Parr, R. G. Density Functional Theory of Electronic Structure. *J. Phys. Chem.* **1996**, *100*, 12974–12980.
- (70) Chien, C. H.; Chiou, S. H.; Guo, G. Y.; Yao, Y. Der. Electronic Structure and Magnetic Moments of 3d Transition Metal-Doped ZnO. *J. Magn. Magn. Mater.* **2004**, *282*, 275–278.
- (71) Fonin, M.; Pentcheva, R.; Dedkov, Y. S.; Sperlich, M.; Vyalikh, D. V.; Scheffler, M.; Rüdiger, U.; Güntherodt, G. Surface Electronic Structure of the Fe<sub>3</sub>O<sub>4</sub> (100): Evidence of a Half-Metal to Metal Transition. *Phys. Rev. B* **2005**, *72*, 104436.
- (72) Dudarev, S.; Botton, G. Electron-Energy-Loss Spectra and the Structural Stability of Nickel Oxide: An LSDA+U Study. *Phys. Rev. B* **1998**, *57*, 1505–1509.
- (73) Momma, K.; Izumi, F. VESTA3 for Three-Dimensional Visualization of Crystal, Volumetric and Morphology Data. *J. Appl. Crystallogr.* **2011**, *44*, 1272–1276.
- (74) Chauhan, M.; Reddy, K. P.; Gopinath, C. S.; Deka, S. Copper Cobalt Sulfide Nanosheets Realizing a Promising Electrocatalytic Oxygen Evolution Reaction. *ACS Catal.* **2017**, *7*, 5871–5879.
- (75) Masud, J.; Swesi, A. T.; Liyanage, W. P. R.; Nath, M. Cobalt Selenide Nanostructures: An Efficient Bifunctional Catalyst with High Current Density at Low Coverage. *ACS Appl. Mater. Interfaces* **2016**, *8*, 17292–17302.
- (76) Cheng, S.; Shi, T.; Chen, C.; Zhong, Y.; Huang, Y.; Tao, X.; Li, J.; Liao, G.; Tang, Z. Construction of Porous CuCo<sub>2</sub>S<sub>4</sub> nanorod Arrays via Anion Exchange for High-Performance Asymmetric Supercapacitor. *Sci. Rep.* **2017**, *7*, 6681.

- (77) Liu, B.; Zhao, Y. F.; Peng, H. Q.; Zhang, Z. Y.; Sit, C. K.; Yuen, M. F.; Zhang, T. R.; Lee, C. S.; Zhang, W. J. Nickel–Cobalt Diselenide 3D Mesoporous Nanosheet Networks Supported on Ni Foam: An All-pH Highly Efficient Integrated Electrocatalyst for Hydrogen Evolution. *Adv. Mater.* **2017**, *29*, 1606521.
- (78) Debe, M. K. Electrocatalyst Approaches and Challenges for Automotive Fuel Cells. *Nature* **2012**, *486*, 43–51.
- (79) McCrory, C. C. L.; Jung, S.; Ferrer, I. M.; Chatman, S. M.; Peters, J. C.; Jaramillo, T. F. Benchmarking Hydrogen Evolving Reaction and Oxygen Evolving Reaction Electrocatalysts for Solar Water Splitting Devices. *J. Am. Chem. Soc.* **2015**, *137*, 4347–4357.
- (80) Jin Suntivich, Kevin J. May, Hubert A. Gasteiger, John B. Goodenough, Y. S.-H. A Perovskite Oxide Optimized for Oxygen Evolution Catalysis from Molecular Orbital Principles. *Science* **2011**, *334*, 1383–1385.
- (81) Long, X.; Li, J.; Xiao, S.; Yan, K.; Wang, Z.; Chen, H.; Yang, S. A Strongly Coupled Graphene and FeNi Double Hydroxide Hybrid as an Excellent Electrocatalyst for the Oxygen Evolution Reaction. *Angew. Chem. Int. Ed.* **2014**, *53*, 7584–7588.
- (82) Liu, Q.; Chen, Z.; Yan, Z.; Wang, Y.; Wang, E.; Wang, S.; Wang, S.; Sun, G. Crystal-Plane-Dependent Activity of Spinel  $\text{Co}_3\text{O}_4$  Towards Water Splitting and the Oxygen Reduction Reaction. *ChemElectroChem* **2018**, *5*, 1080–1086.
- (83) Zhao, Q.; Yan, Z.; Chen, C.; Chen, J. Spinel: Controlled Preparation, Oxygen Reduction/Evolution Reaction Application, and Beyond. *Chem. Rev.* **2017**, *117*, 10121–10211.
- (84) Maiyalagan, T.; Jarvis, K. A.; Therese, S.; Ferreira, P. J.; Manthiram, A. Spinel-Type Lithium Cobalt Oxide as a Bifunctional Electrocatalyst for the Oxygen Evolution and Oxygen Reduction Reactions. *Nat. Commun.* **2014**, *5*, 3949.

## VI. NATURALLY OCCURRING MINERALS AS NOVEL OXYGEN EVOLUTION REACTION ELECTROCATALYSTS: BERZELIANITE, UMANGITE AND KRUT'AITE (Cu<sub>2</sub>Se, Cu<sub>3</sub>Se<sub>2</sub> AND CuSe<sub>2</sub>) GENERATION

*Xi Cao<sup>a</sup>, Emily Johnson<sup>b</sup> and Manashi Nath<sup>a\*</sup>*

<sup>a</sup>Department of Chemistry, Missouri University of Science & Technology, Rolla, Missouri 65409, United States.

<sup>b</sup>Department of Chemical and Biochemical Engineering, Missouri University of Science & Technology, Rolla, Missouri 65409, United States.

\*Email: [nathm@mst.edu](mailto:nathm@mst.edu)

### ABSTRACT

Designing of high-efficiency, low-cost and stable oxygen evolution reaction (OER) electrocatalysts has a great significance for fuel cells and other energy conversion devices. Herein, we have reported three naturally occurring copper selenides (Cu<sub>2</sub>Se, Cu<sub>3</sub>Se<sub>2</sub> and CuSe<sub>2</sub>) as efficient OER electrocatalysts with excellent stability in the alkaline medium. Interestingly, the OER catalytic activity of three copper selenides is as following: Cu<sub>2</sub>Se > Cu<sub>3</sub>Se<sub>2</sub> > CuSe<sub>2</sub>. The superior OER activity of Cu<sub>2</sub>Se requires an overpotential of 298 mV to reach 10 mA cm<sup>-2</sup>, which can be attributed to its high surface area, optimal ratio of Cu<sup>2+</sup>/Cu<sup>+</sup> and low charge transfer resistance at the electrode-electrolyte interface.

### 1. TEXT

With the increasing demands of renewable energy, hydrogen has been viewed as a promising replacement for fossil fuels attributed to its high energy density and low

environmental impact.<sup>1</sup> The traditional method of producing hydrogen (H<sub>2</sub>) is through the reforming of natural gas, however, it suffers the drawbacks of low purity, high cost and release of pollution gas.<sup>2</sup> Water splitting has been considered as an emerging and promising technique to generate high purity H<sub>2</sub> with the assistance of electricity.<sup>3</sup> Water splitting is composed of two half reactions, oxygen evolution reaction (OER,  $4\text{OH}^- \rightarrow \text{O}_2 + 2\text{H}_2\text{O} + 4\text{e}^-$ ) occurring at the anode and hydrogen evolution reaction (HER,  $2\text{H}_2\text{O} + 2\text{e}^- \rightarrow \text{H}_2 + 2\text{OH}^-$ ) taking place at the cathode.<sup>4</sup> Unfortunately, OER is a kinetically sluggish process due to four electrons involved and therefore makes the large-scale manufacture of H<sub>2</sub> through water splitting unreasonable.<sup>5,6</sup> This hindrance has created an urgent need for an electrocatalyst to facilitate the reaction rate of OER and thereby enhance the efficiency of water splitting process.<sup>7,8</sup> Presently, precious metal based catalysts such as RuO<sub>2</sub> and IrO<sub>2</sub> have been well-known for their high catalytic efficiency, but their rarity on Earth results in too high a cost to produce for bulk use in industry.<sup>9</sup> Recent efforts have been poured into the investigation of earth abundant transition-metal (Fe, Co, Ni and Mn) based materials, especially oxides and oxyhydroxides as electrocatalysts towards OER.<sup>10,11,12</sup> Besides that, transition metal based chalcogenides, including sulfides and selenides, have emerged as immense promise due to their improved intrinsic properties and prime electrocatalytic performance in increasing current density.<sup>13,14,15,16</sup> Among these chalcogenides, transition metal selenides, such as Ni<sub>3</sub>Se<sub>2</sub>, CoSe<sub>2</sub>, NiFeSe and NiCoSe, etc., have been widely reported as more efficient electrocatalysts in comparison to oxides and oxyhydroxides.<sup>17,18,19,20</sup> This probably results from the optimal covalency of metal-Se in selenides leading to a faster charge transfer rate at the interface of catalyst-electrolyte and facilitating the OER reaction.<sup>21,22</sup> More recently, copper based compounds (such as Cu<sub>2</sub>O,



CuCo<sub>2</sub>O<sub>4</sub>, CuCo<sub>2</sub>S<sub>4</sub> and Cu<sub>2</sub>S), where Cu is one of the earth abundant elements as well as with its high *d*-electron density, have shown excellent OER catalytic activity and have been expected to be a new series of OER electrocatalysts<sup>23,24,25,26</sup> Some compounds from copper-selenide family, such as Cu<sub>2</sub>Se and (CoNiCu)<sub>3</sub>Se<sub>2</sub>, have been reported by us and others as showing excellent OER catalytic activity, however, the study about copper selenides as the OER electrocatalysts is still under scarcity.<sup>27,28</sup> It is necessary to develop copper based selenides and test their activity towards OER. Interestingly, most of the binary copper selenides can have been found in naturally occurring earth minerals, especially in the lake area, such as krutaite (or CuSe<sub>2</sub>), berzelianite and bellidoite (or Cu<sub>2</sub>Se), and umangite (or Cu<sub>3</sub>Se<sub>2</sub>).<sup>29,30,31</sup> Given the fact that lots of impurities might form along with minerals, which greatly limits the utilization of most naturally occurring minerals as OER electrocatalysts.<sup>32,33</sup> In this work, we have the first time systematically investigated three binary copper selenide minerals (CuSe<sub>2</sub>, Cu<sub>2</sub>Se, and Cu<sub>3</sub>Se<sub>2</sub>) as OER electrocatalysts. To provide a fair comparison, all copper selenides were synthesized by a typical hydrothermal method and test their activity and stability under same condition. Detailed electrochemical measurements in the harsh alkaline medium revealed the OER activity trend is as following: Cu<sub>2</sub>Se > Cu<sub>3</sub>Se<sub>2</sub> > CuSe<sub>2</sub>, where Cu<sub>2</sub>Se needs an overpotential of 298 mV to achieve 10 mA cm<sup>-2</sup>. The optimal OER activity of Cu<sub>2</sub>Se can probably be attributed to the highest surface area along with the smallest particle size as well as the optimal intrinsic ratio of Cu<sup>2+</sup>/Cu<sup>+</sup> as active centers and relatively fastest charge transfer rate at the catalyst-electrolyte surface.

Three binary copper selenides (Cu<sub>2</sub>Se, Cu<sub>3</sub>Se<sub>2</sub> and CuSe<sub>2</sub>) were obtained by hydrothermal method with simply adjusting the precursor ratios, oven temperatures and

reaction time. All copper selenides were characterized through powder X-ray diffraction (pxrd), scanning electron microscopy (SEM) and X-ray photoelectron spectroscopy (XPS) to confirm their pure phase, structure and morphologies. All experimental and characterization details have been presented in the supporting information. The purity and crystallinity of copper selenides were confirmed using pxrd as shown in Figure 1a-c. In Figure 1a, all peaks of  $\text{Cu}_2\text{Se}$  indeed match with those of standard diffraction pattern of  $\text{Cu}_{2-x}\text{Se}$  (PDF # 00-006-0680) indicating the pure phase of  $\text{Cu}_2\text{Se}$ . Similarly, peaks of  $\text{Cu}_3\text{Se}_2$  (in Figure 1b) and  $\text{CuSe}_2$  (in Figure 1c) match with their standard diffraction pattern of  $\text{Cu}_3\text{Se}_2$  (PDF # 00-047-1745) and  $\text{CuSe}_2$  (PDF # 00-019-0400) respectively. The sharp and narrow XRD peaks shown in Figure 1a-c suggest the high purity and crystallinity of each copper selenides. From detailed structural information of copper selenides listed in Table S1,  $\text{Cu}_2\text{Se}$  belongs to the cubic crystal system, while  $\text{Cu}_3\text{Se}_2$  and  $\text{CuSe}_2$  are tetragonal crystal system. The atomic ratio of EDS in Table S2 were further confirmed the elemental composition of three copper selenides. The morphology of copper selenides was studied by SEM as shown in Figure 1d-f, where each copper selenide exhibits non-uniform granular-like nanoparticles with various particle size. As can be seen, the particle size of  $\text{Cu}_2\text{Se}$  is smaller than  $\text{Cu}_3\text{Se}_2$  and tailed by  $\text{CuSe}_2$ , indicating  $\text{Cu}_2\text{Se}$  probably has the largest surface area among three copper selenides.

The deconvoluted X-ray photoelectron spectroscopy (XPS), the graphs for which are in Figures 2a-c, was used to investigate the oxidation states and the chemical compositions of the catalysts. The bonding energies of Cu and Se were calibrated against the reference binding energy at C 1s (284.5 eV). The presence of metal ions' mixed valence was confirmed with the deconvoluted Cu 2p and Se 3d spectra. As shown in the XPS

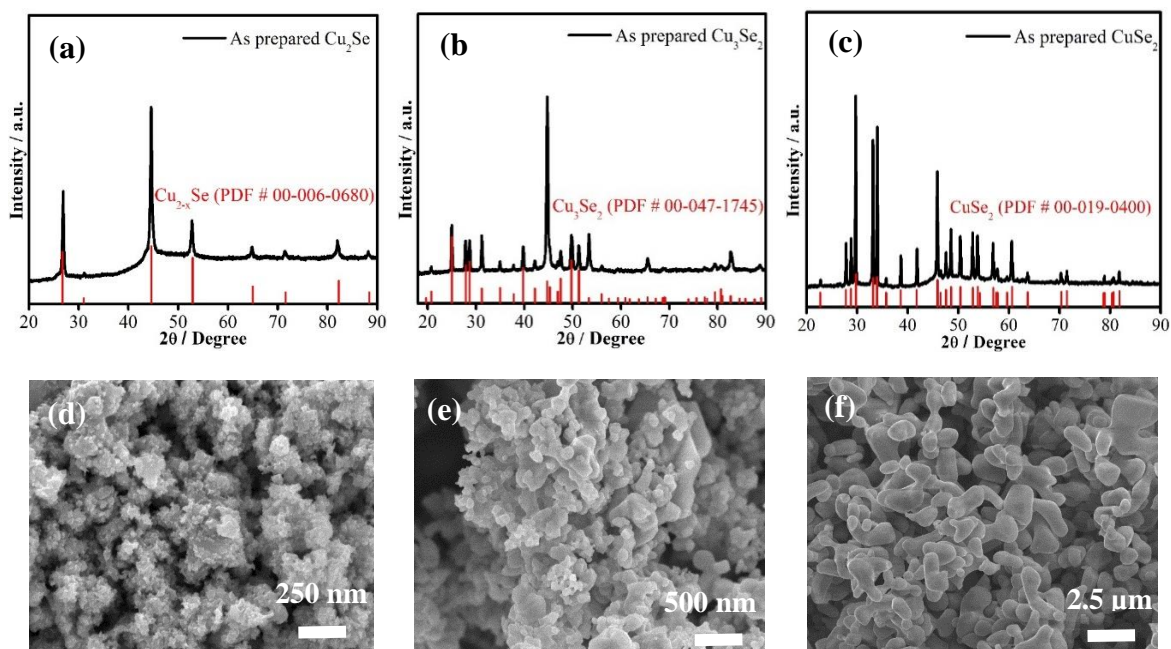


Figure 1. XRD pattern of  $\text{Cu}_2\text{Se}$  (a),  $\text{Cu}_3\text{Se}_2$  (b) and  $\text{CuSe}_2$  (c). Scanning electron microscopy (SEM) images of  $\text{Cu}_2\text{Se}$  (d),  $\text{Cu}_3\text{Se}_2$  (e) and  $\text{CuSe}_2$  (f).

spectra of  $\text{Cu}_2\text{Se}$  in Figure 2a, the peaks at 931.2 eV and 951.1 eV were attributed to  $\text{Cu}^+$   $2p_{3/2}$  and  $\text{Cu}^+$   $2p_{1/2}$  respectively, while those at 933.1 eV and 953.2 eV corresponded to  $\text{Cu}^{2+}$   $2p_{3/2}$  and  $\text{Cu}^{2+}$   $2p_{1/2}$  with its shakeup satellite peaks at 940.9 eV and 960.9 eV.<sup>25,27</sup> In the Se 3d spectra shown in Figure 2a, peaks at 54.5 eV and 55.3 eV were correspond to  $\text{Se}3d_{5/2}$  and  $\text{Se}3d_{3/2}$  respectively, while the peak at 59 eV is attributed to  $\text{SeO}_x$  which is the result of surface selenium oxidation.<sup>34,35</sup> Similarly, in the XPS spectra of  $\text{Cu}_3\text{Se}_2$  shown in Figure 2b, peaks at 931.3 eV and 951.2 eV corresponded to the  $\text{Cu}^+$   $2p_{3/2}$  and  $\text{Cu}^+$   $2p_{1/2}$  while those at 933.1 eV and 953.2 eV represented to  $\text{Cu}^{2+}$   $2p_{3/2}$  and  $\text{Cu}^{2+}$   $2p_{1/2}$  peaks with its satellite peaks at 941.5 eV and 961.7 eV. The peaks at 54.7 eV, 55.6 eV, and 59.6 eV of the Se 3d spectrum in Figure 2b were ascribed to  $\text{Se}3d_{5/2}$ ,  $\text{Se}3d_{3/2}$ , and  $\text{SeO}_x$  respectively. As shown in the  $\text{CuSe}_2$  spectra in Figure 2c, the Cu 2p XPS spectrum showed

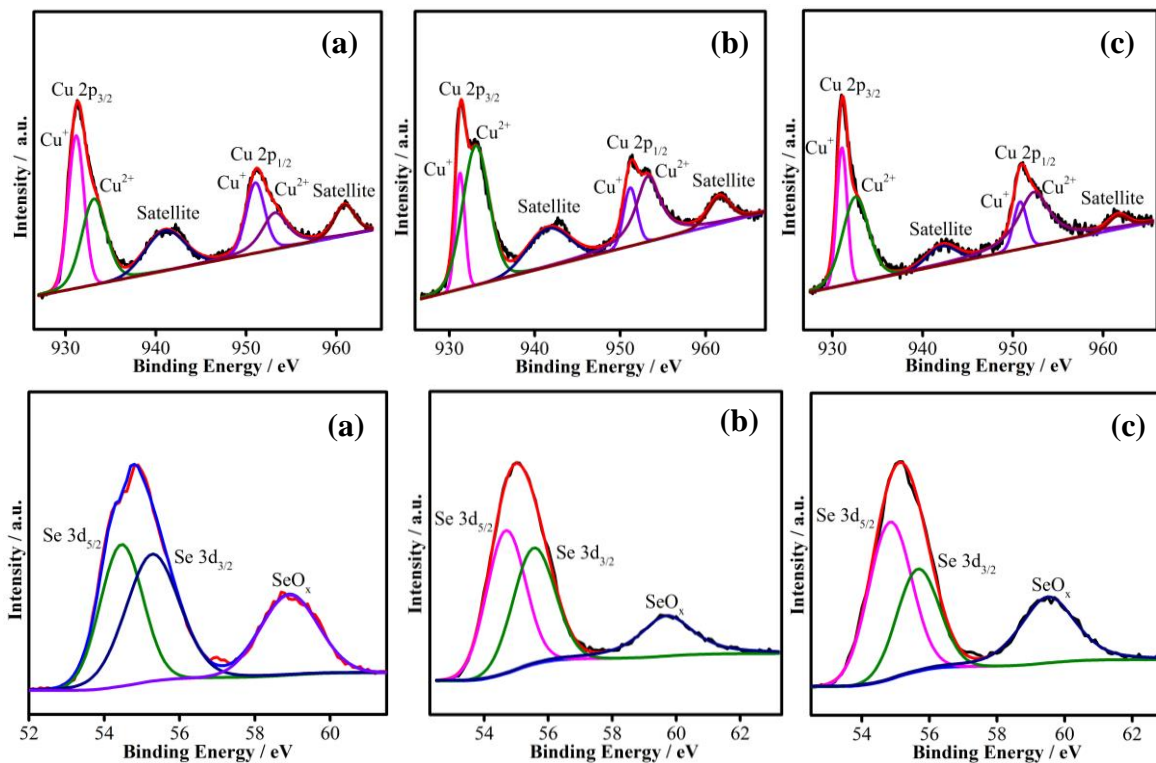


Figure 2. XPS spectra of Cu 2p and Se 3d of Cu<sub>2</sub>Se (a), Cu<sub>3</sub>Se<sub>2</sub> (b) and CuSe<sub>2</sub> (c) respectively.

peaks at 931.0 and 950.8 eV assigning to Cu<sup>+</sup> 2p<sub>3/2</sub> and Cu<sup>+</sup> 2p<sub>1/2</sub> and peaks at 932.6 and 952.3 eV assigning to Cu<sup>2+</sup> 2p<sub>3/2</sub> and Cu<sup>2+</sup> 2p<sub>1/2</sub>, respectively, while the satellite peaks can be observed at 941.9 and 961.8 eV. In the Se 3d spectrum, the peaks at 54.8 eV, 55.7 eV, and 59.5 eV were attributed to Se 3d<sub>5/2</sub>, Se 3d<sub>3/2</sub>, and SeO<sub>x</sub> respectively. The percent of Cu oxidation states were calculated from the area under these peaks. As can be seen, there are 52 % Cu<sup>+</sup> and 48 % Cu<sup>2+</sup> observed in Cu<sub>2</sub>Se; 30 % Cu<sup>+</sup> and 70 % Cu<sup>2+</sup> in Cu<sub>3</sub>Se<sub>2</sub> while 23 % Cu<sup>+</sup> and 77 % Cu<sup>2+</sup> are in CuSe<sub>2</sub>.

The electrocatalytic performances of copper selenides (Cu<sub>2</sub>Se, Cu<sub>3</sub>Se<sub>2</sub>, CuSe<sub>2</sub>) were drop-casted on carbon fiber paper (CFP) and investigated in N<sub>2</sub>-saturated 1.0 M KOH

solution at room temperature in a three-electrode system with an IviumStat potentiostat. The OER catalytic activities were studied from linear scan voltammetry (LSV) while the stability of the catalysts was measured by chronoamperometry at a constant applied potential. Substrates with copper selenides drop-casted on served as the working electrode, a glassy carbon (GC) as the counter electrode and an Ag|AgCl (KCl saturated) reference as the reference electrode. The electrochemically active surface area (ECSA) was estimated by measuring the double layer charging current in the non-Faradaic region as described in previous reports and given in the supporting information.<sup>6</sup> As can be seen in Figure 3, the cyclic voltammograms at different scan rates were obtained and the cathodic and anodic plots were inserted in each figure. The ECSA of Cu<sub>2</sub>Se, Cu<sub>3</sub>Se<sub>2</sub>, and CuSe<sub>2</sub> was calculated as 2.90 cm<sup>2</sup>, 1.64 cm<sup>2</sup>, and 0.69 cm<sup>2</sup> respectively and the roughness factor was 41.43, 23.39, and 9.86 respectively. The roughness factor of the three compounds are ranked as Cu<sub>2</sub>Se > Cu<sub>3</sub>Se<sub>2</sub> > CuSe<sub>2</sub>, which is consistent with the particle sizes and morphologies as shown in SEM.

The OER polarization curves of Cu<sub>2</sub>Se, Cu<sub>3</sub>Se<sub>2</sub> and CuSe<sub>2</sub> were measured in N<sub>2</sub>-saturated 1.0 M KOH at a scan rate of 10 mV s<sup>-1</sup> and compared with state-of-the-art catalyst RuO<sub>2</sub> and bare CFP substrate as shown in Figure 3d. As can be observed, CFP substrate showed barely OER activity with a very high overpotential. And CuSe<sub>2</sub> showed an onset potential of 1.531 V vs RHE and 345 mV to reach a current density of 10 mA cm<sup>-2</sup>, while Cu<sub>3</sub>Se<sub>2</sub> exhibited a better catalytic activity with onset potential of 1.509 V vs RHE and 326 mV at 10 mA cm<sup>-2</sup>. Obviously, Cu<sub>2</sub>Se showed the best catalytic activity among them where its onset potential was 1.485 V vs RHE and it required overpotential of 298 mV to yield a current density of 10 mA cm<sup>-2</sup>, which is much higher than the well-known OER catalyst

RuO<sub>2</sub> (370 mV at 10 mA cm<sup>-2</sup>). Figure 3e showed the Tafel slopes,  $\eta$  vs  $\log j$ , for three copper selenides and RuO<sub>2</sub>. Tafel slopes were obtained as 75.1 mV dec<sup>-1</sup>, 83.3 mV dec<sup>-1</sup>, 91.2 mV dec<sup>-1</sup> and 114.4 mV dec<sup>-1</sup> for Cu<sub>2</sub>Se, Cu<sub>3</sub>Se<sub>2</sub>, CuSe<sub>2</sub> and RuO<sub>2</sub> respectively. Based on the above observations, Cu<sub>2</sub>Se showed the best OER activity with the lowest overpotentials and Tafel slope, suggesting Cu<sub>2</sub>Se is more kinetically favorable. The superior catalytic activity of Cu<sub>2</sub>Se can be attributed to its high surface area, where more catalytic active sites exposed to the electrolyte leads to high activity. Furthermore, as can be observed in the XPS, Cu<sub>2</sub>Se contained comparable percentage of Cu<sup>+</sup> to Cu<sup>2+</sup>, which might also affect its OER activity. From previous studies, the highest oxidized state Cu<sup>2+</sup> has been widely considered as the active species, while Cu<sup>+</sup> in Cu<sub>2</sub>Se has a full-filled configuration of d<sup>10</sup> which probably leads to a weak bond of Cu<sup>+</sup> with hydroxyl species and thereby facilitate the releasing rate of O<sub>2</sub> from the catalyst surface.<sup>36,37</sup>

The durability and stability of Cu<sub>2</sub>Se, Cu<sub>3</sub>Se<sub>2</sub> and CuSe<sub>2</sub> were studied using chronoamperometric measurements as inserted in Figure 5a-c, where a constant potential requiring at 10 mA cm<sup>-2</sup> was applied to continuously generate O<sub>2</sub> in alkaline medium. As can be seen, three copper selenide catalysts were indeed stable over an 8-hour period with no anodic current density loss. To further confirm the stability, LSV curves were re-measured in N<sub>2</sub>-saturated 1.0 M KOH after 8 hours chronoamperometry and compared with that of the as-prepared samples. As observed in Figure 3g-i, the onset potential was kept same while the overpotential at 10 mA cm<sup>-2</sup> was decreased for Cu<sub>2</sub>Se, Cu<sub>3</sub>Se<sub>2</sub> and CuSe<sub>2</sub> implying the OER activity has been improved after 8 hours chronoamperometric measurement.

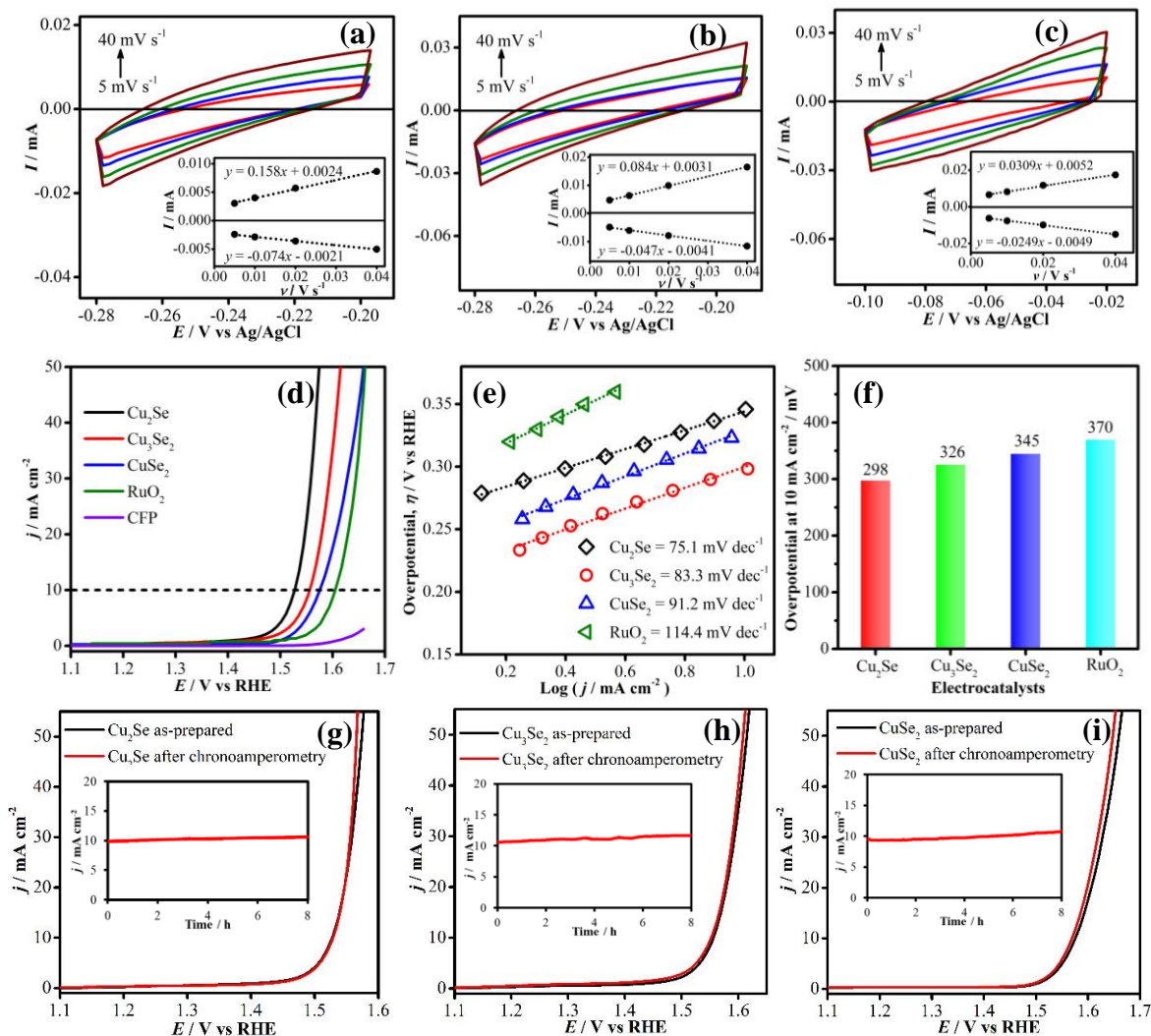


Figure 3. Cyclic voltammograms measured for Cu<sub>2</sub>Se (a), Cu<sub>3</sub>Se<sub>2</sub> (b) and CuSe<sub>2</sub> (c) catalysts in N<sub>2</sub>-saturated 1.0 M KOH solution at different scan rates from 5 to 40 mV s<sup>-1</sup>.

The inset is a plot of both anodic and cathodic currents as a function of scan rate. (d) Polarization curves of Cu<sub>2</sub>Se, Cu<sub>3</sub>Se<sub>2</sub> and CuSe<sub>2</sub> in N<sub>2</sub>-saturated 1.0 M KOH at a scan rate of 10 mV s<sup>-1</sup>. (e) Tafel plots of Cu<sub>2</sub>Se, Cu<sub>3</sub>Se<sub>2</sub> and CuSe<sub>2</sub>. (f) Bar plot comparison of overpotential at 10 mA cm<sup>-2</sup>. Comparison of LSV curves of Cu<sub>2</sub>Se (g), Cu<sub>3</sub>Se<sub>2</sub> (h) and CuSe<sub>2</sub> (i) measured in N<sub>2</sub>-saturated 1.0 M KOH before and after 8 h chronoamperometry. The inset is chronoamperometric measurement of Cu<sub>2</sub>Se (g), Cu<sub>3</sub>Se<sub>2</sub> (h) and CuSe<sub>2</sub> (i) under continuous O<sub>2</sub> evolution.

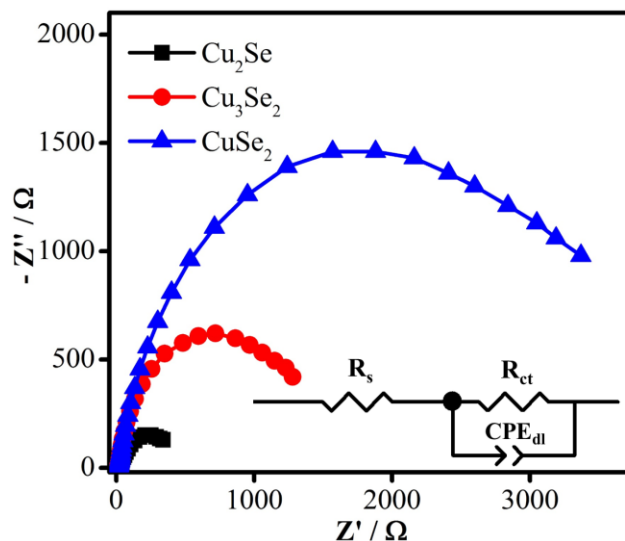


Figure 4. Nyquist plots obtained from EIS measurements of  $\text{Cu}_2\text{Se}$ ,  $\text{Cu}_3\text{Se}_2$  and  $\text{CuSe}_2$  catalysts at an applied potential of 1.49, 1.51 and 1.54 V vs RHE in  $\text{N}_2$ -saturated 1.0 M KOH solution. Symbols indicate the raw data, while solid lines represent the corresponding fit to equivalent circuit model. Inset shows the equivalent circuit of catalysts.

Electrochemical impedance spectroscopy (EIS) was also measured to investigate the kinetics of copper selenides as OER electrocatalysts. EIS spectra were collected in  $\text{N}_2$ -saturated 1.0 M KOH solution at 1.49, 1.51 and 1.54 V vs RHE where were just right after each onset potential for  $\text{Cu}_2\text{Se}$ ,  $\text{Cu}_3\text{Se}_2$  and  $\text{CuSe}_2$  respectively, and the Nyquist plots are inserted in Figure 4. The spectra were fitted to an equivalent circuit from which electrolyte resistance ( $R_s$ ), the electron charge transfer resistance ( $R_{ct}$ ), and constant phase element of double layer capacitance could be obtained, and the values are given in Table 1. In all cases, the uncompensated electrolyte resistance was obtained as ca. 5  $\Omega$ , similar to values that have been reported before.<sup>38</sup> The charge transfer resistance derived from lower frequency region was closely related to the kinetics of OER process on the catalyst surfaces. Hence, the smaller the value of  $R_{ct}$ , indicates a more efficient electron transfer at the catalyst-electrolyte interface leading to faster OER reaction rate and subsequently showing a better



catalytic activity. As can be seen in Table 1, the fitted intrinsic resistance of Cu<sub>2</sub>Se is 483.5  $\Omega$ , much smaller than those of Cu<sub>3</sub>Se<sub>2</sub> (1370.0  $\Omega$ ) and CuSe<sub>2</sub> (3699.0  $\Omega$ ) and in line with the best OER activity of Cu<sub>2</sub>Se.

Table 1. Equivalent circuit parameters obtained from fitting of EIS experimental data.

| <b>Catalysts</b>                    | <b>R<sub>s</sub>/<math>\Omega</math></b> | <b>R<sub>ct</sub>/<math>\Omega</math></b> | <b>CPE<sub>dl</sub>/F</b> |
|-------------------------------------|------------------------------------------|-------------------------------------------|---------------------------|
| <b>Cu<sub>2</sub>Se</b>             | 5.0                                      | 483.5                                     | 0.72                      |
| <b>Cu<sub>3</sub>Se<sub>2</sub></b> | 5.0                                      | 1370.0                                    | 0.86                      |
| <b>CuSe<sub>2</sub></b>             | 5.0                                      | 3699.0                                    | 0.91                      |

R<sub>s</sub> is the resistance of the electrolyte; R<sub>ct</sub> is the electron transfer resistance; CPE<sub>dl</sub> is the constant phase element of double-layer nonideal capacitance.

In summary, we have successfully synthesized three nanostructured binary copper selenides (Cu<sub>2</sub>Se, Cu<sub>3</sub>Se<sub>2</sub> and CuSe<sub>2</sub>), which can be found in naturally occurring minerals, via a typical hydrothermal method. A series of detailed electrochemical study of copper selenides were performed in alkaline solution indicating that copper selenides are indeed active towards OER with excellent stability. Among these copper selenides, Cu<sub>2</sub>Se showed the best catalytic activity which can be attributed to its highest surface area exposed to the electrolyte, as well as its optimal electronic structure leading to the smallest resistance at the electrode-electrolyte interface.

### ACKNOWLEDGEMENT

The authors would like to acknowledge financial support from National Science Foundation (DMR 1710313), American Chemical Society Petroleum Research Fund

(54793-ND10), and Energy Research and Development Center (ERDC) Missouri S&T. The authors would also like to acknowledge Materials Research Center for equipment usage.

## SUPPORTING INFORMATION

### NATURALLY OCCURRING MINERALS AS NOVEL OXYGEN EVOLUTION REACTION ELECTROCATALYSTS: BERZELIANITE, UMANGITE AND KRUT'AITE (Cu<sub>2</sub>Se, Cu<sub>3</sub>Se<sub>2</sub> AND CuSe<sub>2</sub>)

*Xi Cao<sup>a</sup>, Emily Johnson<sup>b</sup> and Manashi Nath<sup>a\*</sup>*

<sup>a</sup>Department of Chemistry, Missouri University of Science & Technology, Rolla, Missouri 65409, United States.

<sup>b</sup>Department of Chemical and Biochemical Engineering, Missouri University of Science & Technology, Rolla, Missouri 65409, United States.

\*Email: [nathm@mst.edu](mailto:nathm@mst.edu)

## 1. EXPERIMENTAL

Chemicals and Materials. Copper chloride dihydrate [CuCl<sub>2</sub>·2H<sub>2</sub>O], copper sulfate pentahydrate [CuSO<sub>4</sub>·5H<sub>2</sub>O] and potassium hydroxide [KOH] were purchased from Fisher Scientific, selenium dioxide [SeO<sub>2</sub>] and hydrazine monohydrate [N<sub>2</sub>H<sub>4</sub>·H<sub>2</sub>O] from Acros chemicals. All chemicals were used as purchased. Distilled water (18 MΩ/cm) was used to prepare all the solutions. Au-coated glass used as conductive substrates were purchased from Deposition Research Lab Incorporated (DRLI), Lebanon Missouri.

## 1.1. SYNTHESIS OF COPPER SELENIDE

**1.1.1. Synthesis of Cu<sub>2</sub>Se.** Cu<sub>2</sub>Se was synthesized by a hydrothermal method, 50 mM of CuSO<sub>4</sub>·5H<sub>2</sub>O and 25 mM of SeO<sub>2</sub> were mixed in 10 mL of deionized water, then 0.5 mL of N<sub>2</sub>H<sub>4</sub>·H<sub>2</sub>O was added carefully. The resulting solution was stirred for another 10 min and then transferred into a 23 mL Teflon-lined stainless-steel autoclave. The autoclave was tightly sealed and maintained at 145 °C for 24 h and then naturally cooled to room temperature.

**1.1.2. Synthesis of Cu<sub>3</sub>Se<sub>2</sub>.** Cu<sub>3</sub>Se<sub>2</sub> was synthesized by a hydrothermal method, 30 mM of CuCl<sub>2</sub>·2H<sub>2</sub>O and 20 mM of SeO<sub>2</sub> were mixed in 10 mL of deionized water, then 0.5 mL of N<sub>2</sub>H<sub>4</sub>·H<sub>2</sub>O was added carefully. After stirring for 10 min, the resulting solution was transferred into an autoclave. The autoclave was tightly sealed and maintained at 145 °C for 24 h and then naturally cooled to room temperature.

**1.1.3. Synthesis of CuSe<sub>2</sub>.** CuSe<sub>2</sub> was synthesized by a hydrothermal method, 30 mM of CuSO<sub>4</sub>·5H<sub>2</sub>O and 60 mM of SeO<sub>2</sub> were mixed in 10 mL of deionized water, then 0.5 mL of N<sub>2</sub>H<sub>4</sub>·H<sub>2</sub>O was added carefully. The autoclave was tightly sealed and maintained at 185 °C for 24 h and then naturally cooled to room temperature.

All final grayish products (Cu<sub>2</sub>Se, Cu<sub>3</sub>Se<sub>2</sub> and CuSe<sub>2</sub>) were centrifuged, followed by washing several times with distilled water and absolute ethanol and finally dried in the vacuum oven at room temperature overnight.

**1.1.4. Electrode Preparation.** Au coated glass was carefully cleaned by Micro-90, isopropanol and Deionized (DI) water. To prepare the catalyst ink, 2.0 mg copper selenides were dispersed into 1.0 mL 0.8 % Nafion<sup>®</sup> ethanol solution, following with 30 min ultrasonication. Au-coated glass was covered with a Taflon tape, leaving an exposed

geometric area of  $0.70 \text{ cm}^2$  on where  $20 \mu\text{L}$  of the homogeneous ink was drop casted. The electrodes with a loading of  $\sim 5.7 \text{ mg cm}^{-2}$  were dried at room temperature. After being heated at a constant temperature of  $130 \text{ }^\circ\text{C}$  for 30 min in a vacuum oven, the electrodes were ready for the electrocatalytic measurements.

**1.1.5. Characterization.** The crystalline structure of copper selenides was identified through PXRD using Philips X-Pert X-ray diffractometer (PANalytical, Almelo, The Netherlands) with a  $\text{Cu K}\alpha$  ( $1.5418 \text{ \AA}$ ) radiation. The morphology of copper selenides was observed with a scanning electron microscope (SEM, Hitachi S4700). Energy dispersive spectroscopy (EDS) was used to identify the element atomic ratio from the same microscope.

**1.1.6. Electrochemical measurements.** The electrocatalytic performances of copper selenides were investigated in  $1.0 \text{ M KOH}$  solution at room temperature in a three-electrode system with an IviumStat potentiostat. The OER and HER catalytic activities were studied from linear scan voltammetry (LSV) while the stability of the catalysts was measured by chronoamperometry at a constant applied potential. Substrates with copper selenides drop-casted on served as the working electrode, a glassy carbon (GC) as the counter electrode and an  $\text{Ag}|\text{AgCl}$  (KCl saturated) reference as the reference electrode. All measured potentials vs.  $\text{Ag}|\text{AgCl}$  (KCl saturated) were converted to the reversible hydrogen electrode (RHE) according to the Nernst equation (eq. 1).

$$E_{RHE} = E_{\text{Ag}|\text{AgCl}} + 0.059pH + E_{\text{Ag}|\text{AgCl}}^\circ \quad (1)$$

Where  $E_{RHE}$  is the calculated potential vs. RHE, and  $E_{\text{Ag}|\text{AgCl}}^\circ$  is the standard thermodynamic potential of  $\text{Ag}|\text{AgCl}$  (KCl saturated) at  $25.1 \text{ }^\circ\text{C}$  ( $0.197 \text{ V}$ ), and  $E_{\text{Ag}|\text{AgCl}}$  is the experimentally measured potential vs.  $\text{Ag}|\text{AgCl}$  (KCl saturated) reference electrode.

**1.1.7. Calculation of Tafel Slope.** The Tafel slope is an important parameter to explain the catalytic performance of  $\text{CuCo}_2\text{Se}_4$  and the equation is shown below.

$$\eta = a + \frac{2.3RT}{anF} \log(j) \quad (2)$$

Where  $\eta$  is the overpotential,  $a$  is transfer coefficient and the other symbols have their normal meaning. The Tafel slope is given by  $2.3RT/anF$ .

## 1.2. ELECTROCHEMICALLY ACTIVE SURFACE AREA (ECSA)

The electrochemically active surface area of the catalysts was measured by electrochemical double layer capacitance as described in previous reports.<sup>16</sup> It is assumed that the current response in the non-Faradaic process region is due to the double-layer charging instead of chemical reactions or charge transfer. To obtain the double layer current ( $i_{DL}$ ) in this region, cyclic voltammograms (CVs) with various scan rates were performed in an unstirred 1.0 M KOH solution. The specific electrochemical double-layer capacitance ( $C_{DL}$ ) was estimated by double-layer current  $i_{DL}$  and the scan rate ( $v$ ) of CV, which is shown in eq. 3. The cathodic and anodic charging currents were as a function of scan rates and the  $C_{DL}$  can be determined from the average of the absolute values of cathodic and anodic slopes. ECSA can be calculated by eq. 4.

$$i_{DL} = C_{DL} \times v \quad (3)$$

$$ECSA = C_{DL}/C_s \quad (4)$$

Here, double-layer capacitance ( $C_{DL}$ ) is in unit of mF. Based on other reported values, the specific capacitance ( $C_s$ ) was assumed to be  $0.040 \text{ mF cm}^{-2}$  in the alkaline

solution.<sup>16,24</sup> Roughness factor (RF) can be evaluated by ECSA divided by the geometric area  $0.07 \text{ cm}^2$ .

Table S1. The geometry structure, space group, lattice parameter of  $\text{Cu}_2\text{Se}$ ,  $\text{Cu}_3\text{Se}_2$  and  $\text{CuSe}_2$ .

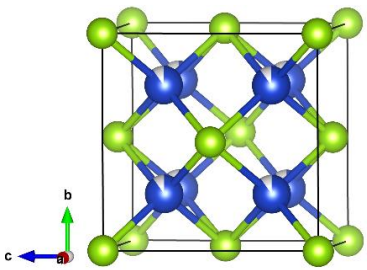
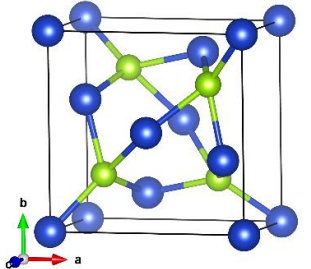
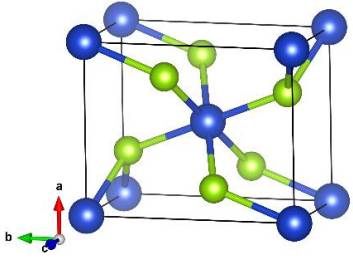
| Sample                   | Geometry structure                                                                  | Space group | Lattice parameter                                                                                                         |
|--------------------------|-------------------------------------------------------------------------------------|-------------|---------------------------------------------------------------------------------------------------------------------------|
| $\text{Cu}_2\text{Se}$   |    | Fm-3m       | $a = b = c = 5.768 \text{ \AA}$<br>$\alpha = \beta = \gamma = 90^\circ$                                                   |
| $\text{Cu}_3\text{Se}_2$ |   | P-4 21m     | $a = b = 6.402 \text{ \AA}$ ;<br>$c = 4.279 \text{ \AA}$<br>$\alpha = \beta = \gamma = 90^\circ$                          |
| $\text{CuSe}_2$          |  | Pnmm        | $a = 5.023 \text{ \AA}$ ;<br>$b = 6.196 \text{ \AA}$ ;<br>$c = 3.747 \text{ \AA}$<br>$\alpha = \beta = \gamma = 90^\circ$ |

Table S2. EDS atomic ratio of  $\text{Cu}_2\text{Se}$ ,  $\text{Cu}_3\text{Se}_2$  and  $\text{CuSe}_2$ .

| Sample                   | EDS atomic ratio / % |       |
|--------------------------|----------------------|-------|
|                          | Cu                   | Se    |
| $\text{Cu}_2\text{Se}$   | 66.78                | 33.22 |
| $\text{Cu}_3\text{Se}_2$ | 60.19                | 39.81 |
| $\text{CuSe}_2$          | 33.10                | 66.90 |

## REFERENCES

- (1) Barbir, F. PEM Electrolysis for Production of Hydrogen from Renewable Energy Sources. *Sol. Energy* **2005**, *78*, 661–669.
- (2) Dicks, A. L. Hydrogen Generation from Natural Gas for the Fuel Cell Systems of Tomorrow. *J. Power Sources* **1996**, *61*, 113–124.
- (3) Walter, M. G.; Warren, E. L.; Mckone, J. R.; Boettcher, S. W.; Mi, Q.; Santori, E. A.; Lewis, N. S. Solar Water Splitting Cells. *Chem. Rev.*, **2010**, *110*, 6446–6473.
- (4) Hong, W. T.; Risch, M.; Stoerzinger, K. A.; Grimaud, A.; Suntivich, J.; Shao-Horn, Y. Toward the Rational Design of Non-Precious Transition Metal Oxides for Oxygen Electrocatalysis. *Energy Environ. Sci.* **2015**, *8*, 1404–1427.
- (5) Man, I. C.; Su, H. Y.; Calle-Vallejo, F.; Hansen, H. A.; Martínez, J. I.; Inoglu, N. G.; Kitchin, J.; Jaramillo, T. F.; Nørskov, J. K.; Rossmeisl, J. Universality in Oxygen Evolution Electrocatalysis on Oxide Surfaces. *ChemCatChem* **2011**, *3*, 1159–1165.
- (6) Mccrory, C. C. L.; Jung, S.; Peters, J. C.; Jaramillo, T. F. Benchmarking Heterogeneous Electrocatalysts for the Oxygen Evolution Reaction. *J. Am. Chem. Soc.* **2013**, *135*, 16977–16987.
- (7) Görlin, M.; Chernev, P.; De Araújo, J. F.; Reier, T.; Dresp, S.; Paul, B.; Krähnert, R.; Dau, H.; Strasser, P. Oxygen Evolution Reaction Dynamics, Faradaic Charge Efficiency, and the Active Metal Redox States of Ni-Fe Oxide Water Splitting Electrocatalysts. *J. Am. Chem. Soc.* **2016**, *138*, 5603–5614.
- (8) Gao, M.; Sheng, W.; Zhuang, Z.; Fang, Q.; Gu, S.; Jiang, J.; Yan, Y. Efficient Water Oxidation Using Nanostructured  $\alpha$ -Nickel-Hydroxide as an Electrocatalyst. *J. Am. Chem. Soc.* **2014**, *136*, 7077–7084.
- (9) Cherevko, S.; Geiger, S.; Kasian, O.; Kulyk, N.; Grote, J. P.; Savan, A.; Shrestha, B. R.; Merzlikin, S.; Breitbach, B.; Ludwig, A.; Mayrhofer, K. J. J. Oxygen and Hydrogen Evolution Reactions on Ru, RuO<sub>2</sub>, Ir, and IrO<sub>2</sub> Thin Film Electrodes in Acidic and Alkaline Electrolytes: A Comparative Study on Activity and Stability. *Catal. Today* **2016**, *262*, 170–180.
- (10) Gong, M.; Dai, H. A Mini Review of NiFe-Based Materials as Highly Active Oxygen Evolution Reaction Electrocatalysts. *Nano Res.* **2015**, *8*, 23–39.
- (11) Liang, Y.; Wang, H.; Zhou, J.; Li, Y.; Wang, J.; Regier, T.; Dai, H. Covalent Hybrid of Spinel Manganese-Cobalt Oxide and Graphene as Advanced Oxygen Reduction Electrocatalysts. *J. Am. Chem. Soc.* **2012**, *134*, 3517–3523.

- (12) Burke, M. S.; Kast, M. G.; Trotochaud, L.; Smith, A. M.; Boettcher, S. W. Cobalt-Iron (Oxy)Hydroxide Oxygen Evolution Electrocatalysts: The Role of Structure and Composition on Activity, Stability, and Mechanism. *J. Am. Chem. Soc.* **2015**, *137*, 3638–3648.
- (13) Zhao, H.; Yang, Y.; Dai, X.; Qiao, H.; Yong, J.; Luan, X.; Yu, L.; Luan, C.; Wang, Y.; Zhang, X. NiCo-DH Nanodots Anchored on Amorphous NiCo-Sulfide Sheets as Efficient Electrocatalysts for Oxygen Evolution Reaction. *Electrochim. Acta* **2019**, *295*, 1085–1092.
- (14) Zou, Z.; Wang, X.; Huang, J.; Wu, Z.; Gao, F. An Fe-Doped Nickel Selenide Nanorod/Nanosheet Hierarchical Array for Efficient Overall Water Splitting. *J. Mater. Chem. A* **2019**, *7*, 2233–2241
- (15) Jiang, N.; Tang, Q.; Sheng, M.; You, B.; Jiang, D. E.; Sun, Y. Nickel Sulfides for Electrocatalytic Hydrogen Evolution under Alkaline Conditions: A Case Study of Crystalline NiS, NiS<sub>2</sub>, and Ni<sub>3</sub>S<sub>2</sub> Nanoparticles. *Catal. Sci. Technol.* **2016**, *6*, 1077–1084.
- (16) Liu, B.; Zhao, Y. F.; Peng, H. Q.; Zhang, Z. Y.; Sit, C. K.; Yuen, M. F.; Zhang, T. R.; Lee, C. S.; Zhang, W. J. Nickel–Cobalt Diselenide 3D Mesoporous Nanosheet Networks Supported on Ni Foam: An All-pH Highly Efficient Integrated Electrocatalyst for Hydrogen Evolution. *Adv. Mater.* **2017**, *29*, 1606521.
- (17) Swesi, A. T.; Masud, J.; Nath, M. Nickel Selenide as a High-Efficiency Catalyst for Oxygen Evolution Reaction. *Energy Environ. Sci.* **2016**, *9*, 1771–1782.
- (18) Liu, X.; Liu, Y.; Fan, L.-Z. MOF-Derived CoSe<sub>2</sub> Microspheres with Hollow Interiors as High-Performance Electrocatalysts for the Enhanced Oxygen Evolution Reaction. *J. Mater. Chem. A* **2017**, *5*, 15310–15314.
- (19) Xu, X.; Song, F.; Hu, X. A Nickel Iron Diselenide-Derived Efficient Oxygen-Evolution Catalyst. *Nat. Commun.* **2016**, *7*, 12324.
- (20) Shinde, D. V.; De Trizio, L.; Dang, Z.; Prato, M.; Gaspari, R.; Manna, L. Hollow and Porous Nickel Cobalt Perselenide Nanostructured Microparticles for Enhanced Electrocatalytic Oxygen Evolution. *Chem. Mater.* **2017**, *29*, 7032–7041.
- (21) Xu, K.; Ding, H.; Lv, H.; Tao, S.; Chen, P.; Wu, X.; Chu, W.; Wu, C.; Xie, Y. Understanding Structure-Dependent Catalytic Performance of Nickel Selenides for Electrochemical Water Oxidation. *ACS Catal.* **2017**, *7*, 310–315.
- (22) Zhang, G.; Zang, S.; Lan, Z. A.; Huang, C.; Li, G.; Wang, X. Cobalt Selenide: A Versatile Cocatalyst for Photocatalytic Water Oxidation with Visible Light. *J. Mater. Chem. A* **2015**, *3*, 17946–17950.



- (23) Li, Q.; Xu, P.; Zhang, B.; Tsai, H.; Zheng, S.; Wu, G.; Wang, H. L. Structure-Dependent Electrocatalytic Properties of Cu<sub>2</sub>O Nanocrystals for Oxygen Reduction Reaction. *J. Phys. Chem. C* **2013**, *117*, 13872–13878.
- (24) Du, X.; Zhang, X.; Xu, Z.; Yang, Z.; Gong, Y. CuCo<sub>2</sub>O<sub>4</sub> microflowers Catalyst with Oxygen Evolution Activity Comparable to That of Noble Metal. *Int. J. Hydrogen Energy* **2018**, *43*, 5012–5018.
- (25) Chauhan, M.; Reddy, K. P.; Gopinath, C. S.; Deka, S. Copper Cobalt Sulfide Nanosheets Realizing a Promising Electrocatalytic Oxygen Evolution Reaction. *ACS Catal.* **2017**, *7*, 5871–5879.
- (26) He, L.; Zhou, D.; Lin, Y.; Ge, R.; Hou, X.; Sun, X.; Zheng, C. Ultrarapid in Situ Synthesis of Cu<sub>2</sub>S Nanosheet Arrays on Copper Foam with Room-Temperature-Active Iodine Plasma for Efficient and Cost-Effective Oxygen Evolution. *ACS Catal.* **2018**, *8*, 3859–3864.
- (27) Masud, J.; Liyanage, W. P. R.; Cao, X.; Saxena, A.; Nath, M. Copper Selenides as High-Efficiency Electrocatalysts for Oxygen Evolution Reaction. *ACS Appl. Energy Mater.* **2018**, *1*, 4075–4083.
- (28) Liu, S.; Zhang, Z.; Bao, J.; Lan, Y.; Tu, W.; Han, M.; Dai, Z. Controllable Synthesis of Tetragonal and Cubic Phase Cu<sub>2</sub>Se Nanowires Assembled by Small Nanocubes and Their Electrocatalytic Performance for Oxygen Reduction Reaction. *J. Phys. Chem. C* **2013**, *117*, 15164–15173.
- (29) Milman, V. Klockmannite, CuSe: Structure, Properties and Phase Stability from Ab Initio Modeling. *Acta Crystallogr. Sect. B Struct. Sci.* **2002**, *58*, 437–447.
- (30) Heyding, R. D.; Murray, R. M. The Crystal Structures of The crystal structures of Cu<sub>1.8</sub>Se, Cu<sub>3</sub>Se<sub>2</sub>, α- and γCuSe, CuSe<sub>2</sub>, and CuSe<sub>2</sub>II. *Can. J. Chem.*, **1976**, *54*, 841–848.
- (31) Growth, H.; Single, O. F.; Berzelianite, C. C.; Kopp, O. C.; Cavin, B. Hydrothermal Growth of Single Crystal Cu<sub>2</sub>Se (Berzelianite). *J. Crystal Growth*, **1984**, *67*, 391–392.
- (32) Le Formal, F.; Guijarro, N.; Bourée, W. S.; Gopakumar, A.; Prévot, M. S.; Daubry, A.; Lombardo, L.; Sornay, C.; Voit, J.; Magrez, A.; Dyson, P. J.; Sivula, K. A Gibeon Meteorite Yields a High-Performance Water Oxidation Electrocatalyst. *Energy Environ. Sci.* **2016**, *9*, 3448–3455.
- (33) Yanina, S. V.; Rosso, K. M. Linked Reactivity at Mineral-Water Interfaces Through Bulk Crystal Conduction. *Science* **2008**, *613*, 218–222.
- (34) Xia, C.; Jiang, Q.; Zhao, C.; Hedhili, M. N.; Alshareef, H. N. Selenide-Based Electrocatalysts and Scaffolds for Water Oxidation Applications. *Adv. Mater.* **2016**, *28*, 77–85.

- (35) Choi, H. M.; Ji, I. A.; Bang, J. H. Metal Selenides as a New Class of Electrocatalysts for Quantum Dot-Sensitized Solar Cells: A Tale of  $\text{Cu}_{1.8}\text{Se}$  and  $\text{PbSe}$ . *ACS Appl. Mater. Interfaces* **2014**, *6*, 2335–2343.
- (36) Chen, Z.; Meyer, T. J. Copper(II) Catalysis of Water Oxidation. *Angew. Chem. Int. Ed.* **2013**, *52*, 700–703.
- (37) Liu, X.; Cui, S.; Sun, Z.; Ren, Y.; Zhang, X.; Du, P. Self-Supported Copper Oxide Electrocatalyst for Water Oxidation at Low Overpotential and Confirmation of Its Robustness by Cu K-Edge X-Ray Absorption Spectroscopy. *J. Phys. Chem. C* **2016**, *120*, 831–840.
- (38) Masud, J.; Swesi, A. T.; Liyanage, W. P. R.; Nath, M. Cobalt Selenide Nanostructures: An Efficient Bifunctional Catalyst with High Current Density at Low Coverage. *ACS Appl. Mater. Interfaces* **2016**, *8*, 17292–17302.

## SECTION

### 2. CONCLUSIONS

Designing high efficiency electrocatalysts for water oxidation has become an increasingly important concept in the catalysis community due to its implications in clean energy generation and storage. In this respect mixed transition metal selenides incorporating earth abundant elements such as Ni, Fe, Co and Cu have attracted attention due to their unexpectedly high electrocatalytic activity toward the oxygen evolution reaction (OER) with low overpotential in alkaline medium. However, most of the reports of mixed metal based OER electrocatalysts has been with limited compositional and/or stoichiometric variations. A systematic investigation of the trend of catalytic activity as a function of transition-metal doping is still very rare. Hence, a phase diagram exploration to systematically investigate the trend of catalytic activity as a function of bimetallic and trimetallic transition metal selenides has become necessary. Combinatorial synthesis is an extremely effective method to screen compositions in the multinary phase space and study the evolution of properties as a function of systematic change in composition.

In the first part of this dissertation, combinatorial electrodeposition method was carried out to design nonstoichiometric mixed transition metal selenides as OER electrocatalysts. Paper I describes a systematic investigation of OER electrocatalytic activity of mixed-metal selenides comprising Ni-Fe-Co through combinatorial electrodeposition exploring the trigonal phase diagram. It revealed that the gradient of catalytic performance in Ni-Fe-Co phase space increased toward increasing Fe concentration and the best performance was exhibited as  $(\text{Ni}_{0.25}\text{Fe}_{0.68}\text{Co}_{0.07})_3\text{Se}_4$ , which

showed an overpotential of 230 mV (vs RHE) at  $10 \text{ mA cm}^{-2}$ .  $(\text{Ni}_{0.25}\text{Fe}_{0.68}\text{Co}_{0.07})_3\text{Se}_4$  showed excellent stability for 8 h under continuous oxygen evolution. DFT calculations were performed to understand the enhanced catalytic activity of  $(\text{Ni}_{0.25}\text{Fe}_{0.68}\text{Co}_{0.07})_3\text{Se}_4$ , consequently, the comparison of hydroxyl adsorption energy ( $E_{\text{ads}}$ ) on the surface of mixed metal selenides and three parent compounds indicates  $(\text{Ni}_{0.25}\text{Fe}_{0.68}\text{Co}_{0.07})_3\text{Se}_4$  showed the highest  $E_{\text{ads}}$  which is more kinetically favorable. Paper II presents a systematic study of Co–Ni–Cu selenides through combinatorial electrodeposition to investigate the effect of transition metal doping and identify the optimal OER catalyst in this group. Most of the quaternary metal selenides crystallized in the  $\text{Cu}_3\text{Se}_2$  (umangite) structure type, which also shows excellent OER catalytic activity by itself, with a low overpotential of 326 mV at  $10 \text{ mA cm}^{-2}$ . In this group, it was also observed that the catalytic activity was sensitive to the concentration of Cu in the catalyst. The best performing quaternary composition was identified as  $(\text{Co}_{0.21}\text{Ni}_{0.25}\text{Cu}_{0.54})_3\text{Se}_2$ , requiring an overpotential of 272 mV to reach  $10 \text{ mA cm}^{-2}$ . Powder X-ray diffraction (pxrd) pattern confirmed that  $(\text{Co}_{0.21}\text{Ni}_{0.25}\text{Cu}_{0.54})_3\text{Se}_2$  showed the same crystal structure of  $\text{Cu}_3\text{Se}_2$  with slight decrease in lattice spacing (0.0222 Å and 0.0148 Å for (101) and (210) plane, respectively), indicating that small amount Ni and Co dopants led to only small change of the lattice parameters of  $\text{Cu}_3\text{Se}_2$ . Paper III introduces a systematic investigation of a series of mixed metal selenides comprising various amounts of Fe, Co and Cu by exploring a trigonal phase diagram through combinatorial electrodeposition. Surprisingly, Fe-Cu ternary selenides showed reduced OER activity in comparison to their pure parent compounds FeSe and  $\text{Cu}_3\text{Se}_2$ , indicating that neither Fe nor Cu doping can improve the activity of  $\text{Cu}_3\text{Se}_2$  or FeSe, respectively. On the other hand, with introduction of Co dopant into the composition, all Fe-Co-Cu

quaternary selenides showed enhanced catalytic activity with low overpotential as well as lower Tafel slopes. The catalytic activity of the quaternary selenides improved as the relative amounts of either Fe or Cu increased in the catalysts. The optimal catalyst composition in this phase space has been identified as  $(\text{Fe}_{0.48}\text{Co}_{0.38}\text{Cu}_{0.14})\text{Se}$  which required an overpotential of 256 mV to achieve  $10 \text{ mA cm}^{-2}$  and a showed Tafel slope of  $40.8 \text{ mV dec}^{-1}$ . The low value of Tafel slope indicates that the catalyst has favorable kinetics for OER in alkaline medium.

In the second part of this dissertation, several interesting selenide-based naturally-occurring minerals have been hydrothermally synthesized and studied their electrocatalytic activity towards OER process. Paper IV presents nanostructured  $\text{CuCo}_2\text{Se}_4$  as superior bifunctional electrocatalyst for OER and HER under alkaline condition. The  $\text{CuCo}_2\text{Se}_4$  electrocatalyst with a spinel structure type requires a low overpotential of 320 mV to reach a current density of  $50 \text{ mA cm}^{-2}$  for OER and 125 mV to achieve  $10 \text{ mA cm}^{-2}$  for HER, respectively. The DFT results showed that  $\text{CuCo}_2\text{Se}_4$  is in the metallic state with a high electrical conductivity which plays a crucial role in the catalytic activity. Among Co and Cu, it was observed that Co showed better OER catalytic activity. Importantly, a surface enhancement of the local magnetic moment on the Co atoms is found to be limited to the top layer in the (100) slab, whereas it affects all layers of the (111) slab, strongly favoring the  $\text{OH}^-$  adsorption on the Co atom at the (111) surface and making the (111) surface more catalytically active. Paper V describes a pure phase naturally-occurring mineral – Tyrrellite  $\text{Cu}(\text{Co}_{0.68}\text{Ni}_{0.32})_2\text{Se}_4$  as a superior OER electrocatalyst in alkaline medium with richness of trivalent  $\text{Co}^{3+}$  and  $\text{Ni}^{3+}$  species in the system. Nanostructured Tyrrellite is a highly efficient OER electrocatalyst, its onset potential is 1.42 V vs RHE and it only requires an

overpotential of 205 mV to reach a current density of 10 mA cm<sup>-2</sup>. To further understand the high OER activity of Cu(Co<sub>0.68</sub>Ni<sub>0.32</sub>)<sub>2</sub>Se<sub>4</sub>, DFT calculation shows the presence of both Ni and Co atoms in the octahedral site improved its metallic state near the Fermi Level due to the *d-d* orbital delocalization. Moreover, Co served as a more favorable active site than Ni resulting from an optimal adsorption energy and enhanced magnetic moment. The synergic effects between Ni and Co in the octahedral site plays an important role in enhancing the OER catalytic activity of Cu(Co<sub>0.68</sub>Ni<sub>0.32</sub>)<sub>2</sub>Se<sub>4</sub>. Paper VI introduces three binary copper selenide minerals (CuSe<sub>2</sub>, Cu<sub>2</sub>Se, and Cu<sub>3</sub>Se<sub>2</sub>) as OER electrocatalysts. Detailed electrochemical measurements in the harsh alkaline medium revealed the OER activity trend is as following: Cu<sub>2</sub>Se > Cu<sub>3</sub>Se<sub>2</sub> > CuSe<sub>2</sub>, where Cu<sub>2</sub>Se needs an overpotential of 298 mV to achieve 10 mA cm<sup>-2</sup>. The optimal OER activity of Cu<sub>2</sub>Se can probably be attributed to the highest surface area along with the smallest particle size as well as the optimal intrinsic ratio of Cu<sup>2+</sup>/Cu<sup>+</sup> as active centers and relatively fastest charge transfer rate at the catalyst-electrolyte surface.

## REFERENCES

- (1) Lewis, N. S.; Nocera, D. G. Powering the Planet: Chemical Challenges in Solar Energy Utilization. *Proc. Natl. Acad. Sci.* **2006**, *103*, 15729–15735.
- (2) Lewis, N. S. Toward Cost-Effective Solar Energy Use. *Science*. **2007**, *315*, 798–801.
- (3) Seh, Z. W.; Kibsgaard, J.; Dickens, C. F.; Chorkendorff, I.; Nørskov, J. K.; Jaramillo, T. F. Combining Theory and Experiment in Electrocatalysis: Insights into Materials Design. *Science*. **2017**, *355*, eaad4998.
- (4) Massetti, E.; Brown, M. A.; Lapsa, M.; Sharma, I.; Bradbury, J.; Cunliff, C.; Li, Y. Environmental Quality and the U.S. Power Sector: Air Quality, Water Quality, Land Use and Environmental Justice. *United States: N. p.*, **2017**, DOI: 10.2172/1339359.
- (5) Schneider, M.; Virzonis, D.; Gao, X.; Kodzius, R.; Damiani, S.; Schulze, F. Air Quality Effects on Human Health and Approaches for Its Assessment through Microfluidic Chips. *Genes* **2017**, *8*, 244.
- (6) Baccarelli, A.; Bollati, V. Epigenetics and Environmental Chemicals. *Curr. Opin. Pediatr.* **2009**, *21*, 243–251.
- (7) Gong, P.; Liang, S.; Carlton, E. J.; Jiang, Q.; Wu, J.; Wang, L.; Remais, J. V. Urbanisation and Health in China. *Lancet* **2012**, *379*, 843–852.
- (8) Zhang, J.; Smith, K. R. Household Air Pollution from Coal and Biomass Fuels in China: Measurements, Health Impacts, and Interventions. *Environ. Health Perspect.* **2007**, *115*, 848–855.
- (9) Turner, J. A. A Realizable Renewable Energy Future. *Science*. **1999**, *285*, 687–689.
- (10) Willie, S.; Sallie, L. B.; Arthur, B. R.; Zachary, W. R. Environmental Effects of Increased Atmospheric Carbon Dioxide. *Clim. Res.* **1999**, *13*, 149–164.
- (11) Woodroffe, C. D.; Morrissey, D. J.; Morrison, M. A.; Beard, C. M.; Craggs, R.; Lowe, M.; Alongi, D. M.; Council, A. R.; Morrissey, D. J.; Skilleter, G. A.; et al. Irreversible Climate Change Due to Carbon Dioxide Emissions. *Estuar. Coast. Shelf Sci.* **2007**, *56*, 581–592.
- (12) Products of Combustion, EGEE 102: Energy Conservation and Environmental Protection, John A. Dutton e-Education Institute.
- (13) Tuller, H. L. Solar to Fuels Conversion Technologies: A Perspective. *Mater. Renew. Sustain. Energy* **2017**, *6*:3.

- (14) Jacobson, M. Z.; Delucchi, M. A. Providing All Global Energy with Wind, Water, and Solar Power, Part I: Technologies, Energy Resources, Quantities and Areas of Infrastructure, and Materials. *Energy Policy* **2011**, *39*, 1154–1169.
- (15) Cook, T. R.; Dogutan, D. K.; Reece, S. Y.; Surendranath, Y.; Teets, T. S.; Nocera, D. G. Solar Energy Supply and Storage for the Legacy and Nonlegacy Worlds. *Chem. Rev.* **2010**, *110*, 6474–6502.
- (16) Clean Energy, *Science & Innovation*, Department of Energy.
- (17) Whittingham, M. S.; Savinell, R. F.; Zawodzinski, T. Introduction: Batteries and Fuel Cells. *Chem. Rev.* **2004**, *104*, 4243–4244.
- (18) Cameron, D. S. Catalysts for Fuel Cell Applications. *Platin. Met. Rev.* **1985**, *29*, 107–112.
- (19) Ali, D. M.; Salman, S. K. A Comprehensive Review of the Fuel Cells Technology and Hydrogen Economy. *Robert Gordon University*, **1970**, 98–102.
- (20) Cheng, F.; Chen, J. Metal-Air Batteries: From Oxygen Reduction Electrochemistry to Cathode Catalysts. *Chem. Soc. Rev.* **2012**, *41*, 2172–2192.
- (21) Li, Y.; Dai, H. Recent Advances in Zinc–air Batteries. *Chem. Soc. Rev.* **2014**, *43*, 5257–5275.
- (22) Rahman, M. A.; Wang, X.; Wen, C. High Energy Density Metal-Air Batteries: A Review. *J. Electrochem. Soc.* **2013**, *160*, A1759–A1771.
- (23) Li, Y.; Lu, J. Metal-Air Batteries: Will They Be the Future Electrochemical Energy Storage Device of Choice? *ACS Energy Lett.* **2017**, *2*, 1370–1377.
- (24) Carrette, L.; Friedrich, K. A.; Stimming, U. Fuel Cells - Fundamentals and Applications. *Fuel Cells* **2001**, *1*, 5–39.
- (25) Xuan, J.; Leung, M. K. H.; Leung, D. Y. C.; Ni, M. A Review of Biomass-Derived Fuel Processors for Fuel Cell Systems. *Renew. Sustain. Energy Rev.* **2009**, *13*, 1301–1313.
- (26) Vehicles-and-fuels, *Electricity & Fuel*, Department of Energy
- (27) Lee, S. W. Feasibility Study of a Fuel Cell Technology in Automobile Application. February, **2003**.
- (28) MacKinnon, M. A.; Samuelson, S. Assessment of Fuel Cell Technologies to Address Power Requirements at the Port of Long Beach. *Advanced Power & Energy Program*, **2016**.
- (29) Corbo, P.; Migliardini, F.; Veneri, O. Hydrogen as Future Energy Carrier, *Hydrogen Fuel Cells for Road Vehicles*, **2011**, 33–70.



- (30) Dresselhaus, M.S.; Thomas, I. Alternative Energy Technologies. *Nature* **2001**, *414*, 332–337.
- (31) Markovic, H. A. G. and N. M. References 1. **2009**, *324*, 48–49.
- (32) Crabtree, G. W.; Dresselhaus, M. S.; Buchanan, M. V. The Hydrogen Economy. *Phys. Today* **2004**, *57*, 39–44.
- (33) Rostrup-Nielsen, J. R.; Rostrup-Nielsen, T. Large-Scale Hydrogen Production. *Cattech* **2002**, *6*, 150–159.
- (34) Walter, M. G.; Warren, E. L.; Mckone, J. R.; Boettcher, S. W.; Mi, Q.; Santori, E. A.; Lewis, N. S. Solar Water Splitting Cells. *Chem. Rev.* **2010**, *110*, 6446–6473.
- (35) Turner, J. A. Sustainable Hydrogen Production. *Science*. **2004**, *305*, 972–974.
- (36) Jia, J.; Seitz, L. C.; Benck, J. D.; Huo, Y.; Chen, Y.; Ng, J. W. D.; Bilir, T.; Harris, J. S.; Jaramillo, T. F. Solar Water Splitting by Photovoltaic-Electrolysis with a Solar-to-Hydrogen Efficiency over 30%. *Nat. Commun.* **2016**, *3*, 546–550.
- (37) Licht, S.; Mukerji, S.; Soga, T.; Wang, B.; Umeno, M.; Tributsch, H. Efficient Solar Water Splitting, Exemplified by RuO<sub>2</sub>-Catalyzed AlGaAs/Si Photoelectrolysis. *J. Phys. Chem. B* **2002**, *104*, 8920–8924.
- (38) Rossmeis, J.; Qu, Z. W.; Zhu, H.; Kroes, G. J.; Nørskov, J. K. Electrolysis of Water on Oxide Surfaces. *J. Electroanal. Chem.* **2007**, *607*, 83–89.
- (39) Kudo, A.; Miseki, Y. Heterogeneous Photocatalyst Materials for Water Splitting. *Chem. Soc. Rev.* **2009**, *38*, 253–278.
- (40) Doyle, R. L.; Lyons, M. E. G. The Oxygen Evolution Reaction: Mechanistic Concepts and Catalyst Design, *Photoelectrochemical Solar Fuel Production*, **2016**, 1–104.
- (41) Salem, R. R. The Electrolysis of Water. *J. Electroanal. Chem.* **1999**, *476*, 92–93.
- (42) Kreuter, W.; Hofmann, H. Electrolysis: The Important Energy Transformer in a World of Sustainable Energy. *Int. J. Hydrogen Energy* **1998**, *23*, 661–666.
- (43) Krstajić, N. V.; Elezović, N. R.; Zabinski, P.; Lačnjevac, U. Č.; Jović, V. D.; Jović, B. M. Accelerated Service Life Test of Electrodeposited NiSn Alloys as Bifunctional Catalysts for Alkaline Water Electrolysis under Industrial Operating Conditions. *J. Electroanal. Chem.* **2017**, *819*, 16–25.
- (44) Dau, H.; Limberg, C.; Reier, T.; Risch, M.; Roggan, S.; Strasser, P. The Mechanism of Water Oxidation: From Electrolysis via Homogeneous to Biological Catalysis. *ChemCatChem* **2010**, *2*, 724–761.
- (45) Fabbri, E.; Haberer, A.; Waltar, K.; Kötz, R.; Schmidt, T. J. Developments and Perspectives of Oxide-Based Catalysts for the Oxygen Evolution Reaction. *Catal. Sci. Technol.* **2014**, *4*, 3800–3821.

- (46) Sørensen, B.; Sørensen, B. HYDROGEN GENERATION BY WATER SPLITTING. *Hydrog. Fuel Cells* **2005**, *2*, 5–111.
- (47) Jiao, Y.; Zheng, Y.; Jaroniec, M.; Qiao, S. Z. Design of Electrocatalysts for Oxygen and Hydrogen-Involving Energy Conversion Reactions. *Chem. Soc. Rev.* **2015**, *44*, 2060–2086.
- (48) Man, I. C.; Su, H. Y.; Calle-Vallejo, F.; Hansen, H. A.; Martínez, J. I.; Inoglu, N. G.; Kitchin, J.; Jaramillo, T. F.; Nørskov, J. K.; Rossmeisl, J. Universality in Oxygen Evolution Electrocatalysis on Oxide Surfaces. *ChemCatChem* **2011**, *3*, 1159–1165.
- (49) Burke, M. S.; Enman, L. J.; Batchellor, A. S.; Zou, S.; Boettcher, S. W. Oxygen Evolution Reaction Electrocatalysis on Transition Metal Oxides and (Oxy)Hydroxides: Activity Trends and Design Principles. *Chem. Mater.* **2015**, *27*, 7549–7558.
- (50) Hernández-Pagán, E. A.; Vargas-Barbosa, N. M.; Wang, T.; Zhao, Y.; Smotkin, E. S.; Mallouk, T. E. Resistance and Polarization Losses in Aqueous Buffer–membrane Electrolytes for Water-Splitting Photoelectrochemical Cells. *Energy Environ. Sci.* **2012**, *5*, 7582–7589.
- (51) Burke, M. S.; Enman, L. J.; Batchellor, A. S.; Zou, S.; Boettcher, S. W. Oxygen Evolution Reaction Electrocatalysis on Transition Metal Oxides and (Oxy)Hydroxides: Activity Trends and Design Principles. *Chem. Mater.* **2015**, *27*, 7549–7558.
- (52) Vargas-Barbosa, N. M.; Geise, G. M.; Hickner, M. A.; Mallouk, T. E. Assessing the Utility of Bipolar Membranes for Use in Photoelectrochemical Water-Splitting Cells. *ChemSusChem* **2014**, *7*, 3017–3020.
- (53) Kraysberg, A.; Ein-Eli, Y. Review of Advanced Materials for Proton Exchange Membrane Fuel Cells. *Energy and Fuels* **2014**, *28*, 7303–7330.
- (54) Ogawa, T.; Takeuchi, M.; Kajikawa, Y. Analysis of Trends and Emerging Technologies in Water Electrolysis Research Based on a Computational Method: A Comparison with Fuel Cell Research. *Sustain.* **2018**, *10*, 478.
- (55) McCrory, C. C. L.; Jung, S.; Ferrer, I. M.; Chatman, S. M.; Peters, J. C.; Jaramillo, T. F. Benchmarking Hydrogen Evolving Reaction and Oxygen Evolving Reaction Electrocatalysts for Solar Water Splitting Devices. *J. Am. Chem. Soc.* **2015**, *137*, 4347–4357.
- (56) Walter, M. G.; Warren, E. L.; Mckone, J. R.; Boettcher, S. W.; Mi, Q.; Santori, E. A.; Lewis, N. S. Solar Water Splitting Cells, *Chem. Rev.*, **2010**, *110*, 6446–6473.
- (57) Durst, J.; Siebel, A.; Simon, C.; Hasché, F.; Herranz, J.; Gasteiger, H. A. New Insights into the Electrochemical Hydrogen Oxidation and Evolution Reaction Mechanism. *Energy Environ. Sci.* **2014**, *7*, 2255–2260.

- (58) Krischer, K.; Savinova, E. R. *Special Catalytic Systems*; **2008**.
- (59) Jukic, A.; Piljac, J.; Metikoš-Hukovic, M. Electrocatalytic Behavior of the  $\text{Co}_{33}\text{Zr}_{67}$  Metallic Glass for Hydrogen Evolution. *J. Mol. Catal. A Chem.* **2001**, *166*, 293–302.
- (60) Zeng, M.; Li, Y. Recent Advances in Heterogeneous Electrocatalysts for the Hydrogen Evolution Reaction. *J. Mater. Chem. A* **2015**, *3*, 14942–14962.
- (61) Vesborg, P. C. K.; Seger, B.; Chorkendorff, I. Recent Development in Hydrogen Evolution Reaction Catalysts and Their Practical Implementation. *J. Phys. Chem. Lett.* **2015**, *6*, 951–957.
- (62) Safizadeh, F.; Ghali, E.; Houlachi, G. Electrocatalysis Developments for Hydrogen Evolution Reaction in Alkaline Solutions - A Review. *Int. J. Hydrogen Energy* **2015**, *40*, 256–274.
- (63) Trasatti, S. Work Function, Electronegativity, and Electrochemical Behaviour of Metals: III. Electrolytic hydrogen evolution in acid solutions. *J. Electroanal. Chem. Interf. Electrochem.* **1972**, *39*, 163–184.
- (64) Raj, I. A.; Vasu, K. I. Transition Metal-Based Hydrogen Electrodes in Alkaline Solution - Electrocatalysis on Nickel Based Binary Alloy Coatings. *J. Appl. Electrochem.* **1990**, *20*, 32–38.
- (65) Preparation and Characterization of Low Overvoltage Transition Metal Alloy Electrocatalysts for Hydrogen Evolution in Alkaline Solutions.
- (66) Low Voltage Electrocatalysts for Hydrogen Evolving Electrodes.
- (67) Raj, I. A. Nickel-Based, Binary-Composite Electrocatalysts for the Cathodes in the Energy-Efficient Industrial Production of Hydrogen from Alkaline-Water Electrolytic Cells. *J. Mater. Sci.* **1993**, *28*, 4375–4382.
- (68) Wendt, H.; Imarisio, G. Nine Years of Research and Development on Advanced Water Electrolysis. A Review of the Research Programme of the Commission of the European Communities. *J. Appl. Electrochem.* **1988**, *18*, 1–14.
- (69) Jayalakshmi, M.; Kim, W. Y.; Jung, K. D.; Joo, O. S. Electrochemical Characterization of Ni-Mo-Fe Composite Film in Alkali Solution. *Int. J. Electrochem. Sci.* **2008**, *3*, 908–917.
- (70) McKay, I. S.; Schwalbe, J. A.; Goodman, E. D.; Willis, J. J.; Majumdar, A.; Cargnello, M. Elucidating the Synergistic Mechanism of Nickel-Molybdenum Electrocatalysts for the Hydrogen Evolution Reaction. *MRS Commun.* **2016**, *6*, 241–246.
- (71) Suntivich, J.; Gasteiger, H. A.; Yabuuchi, N.; Nakanishi, H.; Goodenough, J. B.; Shao-Horn, Y. Design Principles for Oxygen-Reduction Activity on Perovskite Oxide Catalysts for Fuel Cells and Metal-air Batteries. *Nat. Chem.* **2011**, *3*, 546.

- (72) Zhao, Z.; Li, M.; Zhang, L.; Dai, L.; Xia, Z. Design Principles for Heteroatom-Doped Carbon Nanomaterials as Highly Efficient Catalysts for Fuel Cells and Metal-Air Batteries. *Adv. Mater.* **2015**, *27*, 6834–6840.
- (73) Nørskov, J. K.; Bligaard, T.; Hvolbæk, B.; Abild-Pedersen, F.; Chorkendorff, I.; Christensen, C. H. The Nature of the Active Site in Heterogeneous Metal Catalysis. *Chem. Soc. Rev.* **2008**, *37*, 2163–2171.
- (74) Rossmeisl, J.; Logadottir, A.; Nørskov, J. K. Electrolysis of Water on (Oxidized) Metal Surfaces. *Chem. Phys.* **2005**, *319*, 178–184.
- (75) Suen, N.-T.; Hung, S.-F.; Quan, Q.; Zhang, N.; Xu, Y.-J.; Chen, H. M. Electrocatalysis for the Oxygen Evolution Reaction: Recent Development and Future Perspectives. *Chem. Soc. Rev.* **2017**, *46*, 337–365.
- (76) Matsumoto, Y.; Sato, E. Electrocatalytic Properties of Transition Metal Oxides for Oxygen Evolution Reaction. *Mater. Chem. Phys.* **1986**, *14*, 397–426.
- (77) Koper, M. T. M. Thermodynamic Theory of Multi-Electron Transfer Reactions: Implications for Electrocatalysis. *J. Electroanal. Chem.* **2011**, *660*, 254–260.
- (78) Gong, M.; Dai, H. A Mini Review of NiFe-Based Materials as Highly Active Oxygen Evolution Reaction Electrocatalysts. *Nano Res.* **2015**, *8*, 23–39.
- (79) Idrees, F.; Zhang, X.; Tahir, M.; Wang, Z. L.; Zou, J.-J.; Pan, L.; Wang, L. Electrocatalytic Oxygen Evolution Reaction for Energy Conversion and Storage: A Comprehensive Review. *Nano Energy* **2017**, *37*, 136–157.
- (80) Chakhranont, P.; Benck, J. D.; Jaramillo, T. F.; Hellstern, T. R.; Kibsgaard, J. Catalyzing the Hydrogen Evolution Reaction (HER) with Molybdenum Sulfide Nanomaterials. *ACS Catal.* **2014**, *4*, 3957–3971.
- (81) Trotochaud, L.; Boettcher, S. W. Precise Oxygen Evolution Catalysts: Status and Opportunities. *Scr. Mater.* **2014**, *74*, 25–32.
- (82) Mccrory, C. C. L.; Jung, S.; Peters, J. C.; Jaramillo, T. F. Benchmarking Heterogeneous Electrocatalysts for the Oxygen Evolution Reaction. *J. Am. Chem. Soc.* **2013**, *135*, 16977–16987.
- (83) Weber, M. F. Efficiency of Splitting Water with Semiconducting Photoelectrodes. *J. Electrochem. Soc.* **2006**, *131*, 1258.
- (84) Shinagawa, T.; Garcia-Esparza, A. T.; Takanabe, K. Insight on Tafel Slopes from a Microkinetic Analysis of Aqueous Electrocatalysis for Energy Conversion. *Sci. Rep.* **2015**, *5*, 1–21.
- (85) Huang, Z. F.; Wang, J.; Peng, Y.; Jung, C. Y.; Fisher, A.; Wang, X. Design of Efficient Bifunctional Oxygen Reduction/Evolution Electrocatalyst: Recent Advances and Perspectives. *Adv. Energy Mater.* **2017**, *1700544*, 13801.

- (86) Jin, L.; Lv, C.; Wang, J.; Xia, H.; Zhao, Y.; Huang, Z. Co<sub>9</sub>S<sub>8</sub> Nanotubes as an Efficient Catalyst for Hydrogen Evolution Reaction in Alkaline Electrolyte. *Am. J. Anal. Chem.* **2016**, *7*, 210–218.
- (87) Trasaw, S. Electrocatalysis in the Anodic Evolution Oxygen and Chlorine. *Electrochim. Acta* **1984**, *29*, 1503–1512.
- (88) Jamesh, M. I. Recent Progress on Earth Abundant Hydrogen Evolution Reaction and Oxygen Evolution Reaction Bifunctional Electrocatalyst for Overall Water Splitting in Alkaline Media. *J. Power Sources* **2016**, *333*, 213–236.
- (89) Mohammed-Ibrahim, J.; Xiaoming, S. Recent Progress on Earth Abundant Electrocatalysts for Hydrogen Evolution Reaction (HER) in Alkaline Medium to Achieve Efficient Water Splitting – A Review. *J. Energy Chem.* **2019**, *400*, 111–160.
- (90) Mette, K.; Bergmann, A.; Tessonnier, J. P.; Hävecker, M.; Yao, L.; Ressler, T.; Schlögl, R.; Strasser, P.; Behrens, M. Nanostructured Manganese Oxide Supported on Carbon Nanotubes for Electrocatalytic Water Splitting. *ChemCatChem* **2012**, *4*, 851–862.
- (91) Kelso, M. V.; Tubbesing, J. Z.; Chen, Q.; Switzer, J. A. Epitaxial Electrodeposition of Chiral Metal Surfaces on Silicon(643). *J. Am. Chem. Soc.* **2018**, *140*, 15812–15819.
- (92) Xu, B.; Cao, X.; Wang, G.; Li, Y.; Wang, Y.; Su, J. Controlled Synthesis and Novel Luminescence Properties of String SrWO<sub>4</sub>:Eu<sup>3+</sup> Nanobeans. *Dalt. Trans.* **2014**, *43*, 11493–11501.
- (93) Reier, T.; Oezaslan, M.; Strasser, P. Electrocatalytic Oxygen Evolution Reaction (OER) on Ru, Ir, and Pt Catalysts: A Comparative Study of Nanoparticles and Bulk Materials. *ACS Catal.* **2012**, *2*, 1765–1772.
- (94) Park, S.; Shao, Y.; Liu, J.; Wang, Y. Oxygen Electrocatalysts for Water Electrolyzers and Reversible Fuel Cells: Status and Perspective. *Energy Environ. Sci.* **2012**, *5*, 9331–9344..
- (95) Cruz, J. C.; Ramos Hernández, A.; Guerra-Balcazar, M.; Chávez-Ramirez, A. U.; Ledesma-García, J.; Arriaga, L. G. Electrochemical Evaluation of a Ir-Ru Binary Oxide for Oxygen Evolution Reaction. *Int. J. Electrochem. Sci.* **2012**, *7*, 7866–7876.
- (96) Siracusano, S.; Van Dijk, N.; Payne-Johnson, E.; Baglio, V.; Aricò, A. S. Nanosized IrO<sub>x</sub> and IrRuO<sub>x</sub> Electrocatalysts for the O<sub>2</sub> Evolution Reaction in PEM Water Electrolysers. *Appl. Catal. B Environ.* **2015**, *164*, 488–495.
- (97) Lee, Y.; Suntivich, J.; May, K. J.; Perry, E. E.; Shao-Horn, Y. Synthesis and Activities of Rutile IrO<sub>2</sub> and RuO<sub>2</sub> Nanoparticles for Oxygen Evolution in Acid and Alkaline Solutions. *J. Phys. Chem. Lett.* **2012**, *3*, 399–404.

- (98) Frydendal, R.; Paoli, E. A.; Knudsen, B. P.; Wickman, B.; Malacrida, P.; Stephens, I. E. L.; Chorkendorff, I. Benchmarking the Stability of Oxygen Evolution Reaction Catalysts: The Importance of Monitoring Mass Losses. *ChemElectroChem* **2014**, *1*, 2075–2081.
- (99) Li, Y.; Hasin, P.; Wu, Y. Ni<sub>x</sub>Co<sub>3-x</sub>O<sub>4</sub> Nanowire Arrays for Electrocatalytic Oxygen Evolution. *Adv. Mater.* **2010**, *22*, 1926–1929.
- (100) Dionigi, F.; Strasser, P. NiFe-Based (Oxy)Hydroxide Catalysts for Oxygen Evolution Reaction in Non-Acidic Electrolytes. *Adv. Energy Mater.* **2016**, *6*, 1600621
- (101) Osgood, H.; Devaguptapu, S. V.; Xu, H.; Cho, J.; Wu, G. Transition Metal (Fe, Co, Ni, and Mn) Oxides for Oxygen Reduction and Evolution Bifunctional Catalysts in Alkaline Media. *Nano Today* **2016**, *11*, 601–625.
- (102) Gong, M.; Li, Y.; Wang, H.; Liang, Y.; Wu, J. Z.; Zhou, J.; Wang, J.; Regier, T.; Wei, F.; Dai, H. An Advanced Ni-Fe Layered Double Hydroxide Electrocatalyst for Water Oxidation. *J. Am. Chem. Soc.* **2013**, *135*, 8452–8455.
- (103) Kargar, A.; Yavuz, S.; Kim, T. K.; Liu, C. H.; Kuru, C.; Rustomji, C. S.; Jin, S.; Bandaru, P. R. Solution-Processed CoFe<sub>2</sub>O<sub>4</sub> Nanoparticles on 3D Carbon Fiber Papers for Durable Oxygen Evolution Reaction. *ACS Appl. Mater. Interfaces* **2015**, *7*, 17851–17856.
- (104) He, Z.; Koza, J. A.; Liu, Y. C.; Chen, Q.; Switzer, J. A. Room-Temperature Electrochemical Reduction of Epitaxial Bi<sub>2</sub>O<sub>3</sub> Films to Epitaxial Bi Films. *RSC Adv.* **2016**, *6*, 96832–96836.
- (105) Subbaraman, R.; Tripkovic, D.; Chang, K. C.; Strmcnik, D.; Paulikas, A. P.; Hirunsit, P.; Chan, M.; Greeley, J.; Stamenkovic, V.; Markovic, N. M. Trends in Activity for the Water Electrolyser Reactions on 3d M(Ni,Co,Fe,Mn) Hydr(Oxy)Oxide Catalysts. *Nat. Mater.* **2012**, *11*, 550–557.
- (106) Yang, L.; Xie, L.; Ren, X.; Wang, Z.; Liu, Z.; Du, G.; Asiri, A. M.; Yao, Y.; Sun, X. Hierarchical CuCo<sub>2</sub>S<sub>4</sub> Nanoarray for High-efficient and Durable Water Oxidation Electrocatalysis. *Chem. Commun.* **2017**, No. 04, 52–54.
- (107) Chen, Q.; Switzer, J. A. Electrodeposition of Nanometer-Thick Epitaxial Films of Silver onto Single-Crystal Silicon Wafers. *J. Mater. Chem. C* **2019**, *7* (6), 1720–1725.
- (108) Singh, A.; Spiccia, L. Water Oxidation Catalysts Based on Abundant 1<sup>st</sup> Row Transition Metals. *Coordination Chemistry Reviews.* **2013**, *257*, 2607–2622.
- (109) Galán-Mascarós, J. R. Water Oxidation at Electrodes Modified with Earth-Abundant Transition-Metal Catalysts. *ChemElectroChem* **2015**, *2*, 37–50.

- (110) Du, P.; Eisenberg, R. Catalysts Made of Earth-Abundant Elements (Co, Ni, Fe) for Water Splitting: Recent Progress and Future Challenges. *Energy Environ. Sci.* **2012**, *5*, 6012–6021.
- (111) Chen, Q.; Switzer, J. A. Photoelectrochemistry of Ultrathin, Semitransparent, and Catalytic Gold Films Electrodeposited Epitaxially onto n-Silicon (111). *ACS Appl. Mater. Interfaces* **2018**, *10*, 21365–21371.
- (112) Suen, N. T.; Hung, S. F.; Quan, Q.; Zhang, N.; Xu, Y. J.; Chen, H. M. Electrocatalysis for the Oxygen Evolution Reaction: Recent Development and Future Perspectives. *Chem. Soc. Rev.* **2017**, *46*, 337–365.
- (113) Maiyalagan, T.; Jarvis, K. A.; Therese, S.; Ferreira, P. J.; Manthiram, A. Spinel-Type Lithium Cobalt Oxide as a Bifunctional Electrocatalyst for the Oxygen Evolution and Oxygen Reduction Reactions. *Nat. Commun.* **2014**, *5*, 3949.
- (114) Jin Suntivich, Kevin J. May, Hubert A. Gasteiger, John B. Goodenough, Y. S.-H. A Perovskite Oxide Optimized for Oxygen Evolution Catalysis from Molecular Orbital Principles. *Science*. **2011**, *334*, 1383–1385.
- (115) Grimaud, A.; May, K. J.; Carlton, C. E.; Lee, Y.-L.; Risch, M.; Hong, W. T.; Zhou, J.; Shao-Horn, Y. Double Perovskites as a Family of Highly Active Catalysts for Oxygen Evolution in Alkaline Solution. *Nat. Commun.* **2013**, *4*, 2439.
- (116) Long, X.; Li, J.; Xiao, S.; Yan, K.; Wang, Z.; Chen, H.; Yang, S. A Strongly Coupled Graphene and FeNi Double Hydroxide Hybrid as an Excellent Electrocatalyst for the Oxygen Evolution Reaction. *Angew. Chem. Int. Ed.* **2014**, *53*, 7584–7588.
- (117) Petitto, S. C.; Marsh, E. M.; Carson, G. A.; Langell, M. A. Cobalt Oxide Surface Chemistry: The Interaction of CoO(100), Co<sub>3</sub>O<sub>4</sub>(110) and Co<sub>3</sub>O<sub>4</sub>(111) with Oxygen and Water. *J. Mol. Catal. A Chem.* **2008**, *281*, 49–58.
- (118) Wang, H. Y.; Hsu, Y. Y.; Chen, R.; Chan, T. S.; Chen, H. M.; Liu, B. Ni<sup>3+</sup>-Induced Formation of Active NiOOH on the Spinel Ni-Co Oxide Surface for Efficient Oxygen Evolution Reaction. *Adv. Energy Mater.* **2015**, *5*, 1500091.
- (119) Landon, J.; Demeter, E.; Inoğlu, N.; Keturakis, C.; Wachs, I. E.; Vasić, R.; Frenkel, A. I.; Kitchin, J. R. Spectroscopic Characterization of Mixed Fe-Ni Oxide Electrocatalysts for the Oxygen Evolution Reaction in Alkaline Electrolytes. *ACS Catal.* **2012**, *2*, 1793–1801.
- (120) Liu, Y.-C.; Koza, J. A.; Switzer, J. A. Conversion of Electrodeposited Co(OH)<sub>2</sub> to CoOOH and Co<sub>3</sub>O<sub>4</sub>, and Comparison of Their Catalytic Activity for the Oxygen Evolution Reaction. *Electrochim. Acta* **2014**, *140*, 359–365.
- (121) Louie, M. W.; Bell, A. T. An Investigation of Thin-Film Ni-Fe Oxide Catalysts for the Electrochemical Evolution of Oxygen. *J. Am. Chem. Soc.* **2013**, *135*, 12329.

- (122) Hsieh, M.; Koga, H.; Nogi, M.; Suganuma, K. Epitaxial Lift-off of Electrodeposited Single-Crystal Gold Foils for Flexible Electronics. *2014*, *1206*, 186–189.
- (123) Li, Y.; Cao, X.; Wang, G.; Liu, S.; Feng, L.; Xu, B.; Wang, Y.; Su, J. Synthesis and Tunable Upconversion Luminescence of NaLuF<sub>4</sub>: Yb<sup>3+</sup>/Er<sup>3+</sup> Nanocrystals by Pb<sup>2+</sup> Tridoping. *Sci. Adv. Mater.* **2014**, *6*, 1037–1042.
- (124) Trotochaud, L.; Young, S. L.; Ranney, J. K.; Boettcher, S. W. Nickel-Iron Oxyhydroxide Oxygen-Evolution Electrocatalysts: The Role of Intentional and Incidental Iron Incorporation. *J. Am. Chem. Soc.* **2014**, *136*, 6744–6753.
- (125) Klaus, S.; Cai, Y.; Louie, M. W.; Trotochaud, L.; Bell, A. T. Effects of Fe Electrolyte Impurities on Ni(OH)<sub>2</sub>/NiOOH Structure and Oxygen Evolution Activity. *J. Phys. Chem. C* **2015**, *119*, 7243–7254.
- (126) Shen, M.; Ruan, C.; Chen, Y.; Jiang, C.; Ai, K.; Lu, L. Covalent Entrapment of Cobalt-Iron Sulfides in N-Doped Mesoporous Carbon: Extraordinary Bifunctional Electrocatalysts for Oxygen Reduction and Evolution Reactions. *ACS Appl. Mater. Interfaces* **2015**, *7*, 1207–1218.
- (127) Liu, Q.; Jin, J.; Zhang, J. NiCo<sub>2</sub>S<sub>4</sub>@graphene as a Bifunctional Electrocatalyst for Oxygen Reduction and Evolution Reactions. *ACS Appl. Mater. Interfaces* **2013**, *5*, 5002–5008.
- (128) Ganesan, P.; Prabu, M.; Sanetuntikul, J.; Shanmugam, S. Cobalt Sulfide Nanoparticles Grown on Nitrogen and Sulfur Codoped Graphene Oxide: An Efficient Electrocatalyst for Oxygen Reduction and Evolution Reactions. *ACS Catal.* **2015**, *5*, 3625–3637.
- (129) Xu, X.; Song, F.; Hu, X. A Nickel Iron Diselenide-Derived Efficient Oxygen-Evolution Catalyst. *Nat. Commun.* **2016**, *7*, 12324.
- (130) Liu, B.; Zhao, Y. F.; Peng, H. Q.; Zhang, Z. Y.; Sit, C. K.; Yuen, M. F.; Zhang, T. R.; Lee, C. S.; Zhang, W. J. Nickel–Cobalt Diselenide 3D Mesoporous Nanosheet Networks Supported on Ni Foam: An All-pH Highly Efficient Integrated Electrocatalyst for Hydrogen Evolution. *Adv. Mater.* **2017**, *29*, 1606521.
- (131) Swesi, A. T.; Masud, J.; Nath, M. Nickel Selenide as a High-Efficiency Catalyst for Oxygen Evolution Reaction. *Energy Environ. Sci.* **2016**, *9*, 1771–1782.
- (132) Masud, J.; Liyanage, W. P. R.; Cao, X.; Saxena, A.; Nath, M. Copper Selenides as High-Efficiency Electrocatalysts for Oxygen Evolution Reaction. *ACS Appl. Energy Mater.* **2018**, *1*, 4075–4083
- (133) De Silva, U.; Masud, J.; Zhang, N.; Hong, Y.; Liyanage, W. P. R.; Asle Zaem, M.; Nath, M. Nickel Telluride as a Bifunctional Electrocatalyst for Efficient Water Splitting in Alkaline Medium. *J. Mater. Chem. A* **2018**, *6*, 7608–7622.



- (134) Patil, S. A.; Kim, E. K.; Shrestha, N. K.; Chang, J.; Lee, J. K.; Han, S. H. Formation of Semimetallic Cobalt Telluride Nanotube Film via Anion Exchange Tellurization Strategy in Aqueous Solution for Electrocatalytic Applications. *ACS Appl. Mater. Interfaces* **2015**, *7*, 25914–25922.
- (135) Gao, Q.; Huang, C. Q.; Ju, Y. M.; Gao, M. R.; Liu, J. W.; An, D.; Cui, C. H.; Zheng, Y. R.; Li, W. X.; Yu, S. H. Phase-Selective Syntheses of Cobalt Telluride Nanofleeces for Efficient Oxygen Evolution Catalysts. *Angew. Chem. Int. Ed.* **2017**, *56*, 7769–7773.
- (136) Zhu, W.; Yue, X.; Zhang, W.; Yu, S.; Zhang, Y.; Wang, J.; Wang, J. Nickel Sulfide Microsphere Film on Ni Foam as an Efficient Bifunctional Electrocatalyst for Overall Water Splitting. *Chem. Commun.* **2016**, *52*, 1486–1489.
- (137) Xu, K.; Ding, H.; Lv, H.; Tao, S.; Chen, P.; Wu, X.; Chu, W.; Wu, C.; Xie, Y. Understanding Structure-Dependent Catalytic Performance of Nickel Selenides for Electrochemical Water Oxidation. *ACS Catal.* **2017**, *7*, 310–315.
- (138) Zhang, G.; Zang, S.; Lan, Z. A.; Huang, C.; Li, G.; Wang, X. Cobalt Selenide: A Versatile Cocatalyst for Photocatalytic Water Oxidation with Visible Light. *J. Mater. Chem. A* **2015**, *3*, 17946–17950.
- (139) Gong, F.; Xu, X.; Li, Z.; Zhou, G.; Wang, Z. S. NiSe<sub>2</sub> as an Efficient Electrocatalyst for a Pt-Free Counter Electrode of Dye-Sensitized Solar Cells. *Chem. Commun.* **2013**, *49*, 1437–1439.
- (140) Tang, C.; Cheng, N.; Pu, Z.; Xing, W.; Sun, X. NiSe Nanowire Film Supported on Nickel Foam: An Efficient and Stable 3D Bifunctional Electrode for Full Water Splitting. *Angew. Chem. Int. Ed.* **2015**, *54*, 9351–9355.
- (141) Shi, J.; Hu, J.; Luo, Y.; Sun, X.; Asiri, A. M. Ni<sub>3</sub>Se<sub>2</sub> film as a non-precious metal bifunctional electrocatalyst for efficient water splitting. *Catal. Sci. Technol.* **2015**, *5*, 4954–4958.
- (142) Swesi, A. T.; Masud, J.; Liyanage, W. P. R.; Umapathi, S.; Bohannan, E.; Medvedeva, J.; Nath, M. Textured NiSe<sub>2</sub> Film: Bifunctional Electrocatalyst for Full Water Splitting at Remarkably Low Overpotential with High Energy Efficiency. *Sci. Rep.* **2017**, *7*, 2401.
- (143) Kong, D.; Wang, H.; Lu, Z.; Cui, Y. CoSe<sub>2</sub> Nanoparticles Grown on Carbon Fiber Paper: An Efficient and Stable Electrocatalyst for Hydrogen Evolution Reaction. *J. Am. Chem. Soc.* **2014**, *136*, 4897–4900.
- (144) Carim, A. I.; Saadi, F. H.; Soriaga, M. P.; Lewis, N. S. Electrocatalysis of the Hydrogen-Evolution Reaction by Electrodeposited Amorphous Cobalt Selenide Films. *J. Mater. Chem. A* **2014**, *2*, 13835–13839.

- (145) Yu, B.; Qi, F.; Wang, X.; Zheng, B.; Hou, W.; Hu, Y.; Lin, J.; Zhang, W.; Li, Y.; Chen, Y. Nanocrystalline  $\text{Co}_{0.85}\text{Se}$  as a Highly Efficient Non-Noble-Metal Electrocatalyst for Hydrogen Evolution Reaction. *Electrochim. Acta* **2017**, *247*, 468–474.
- (146) Dai, C.; Tian, X.; Nie, Y.; Tian, C.; Yang, C.; Zhou, Z.; Li, Y.; Gao, X. Successful Synthesis of 3D  $\text{CoSe}_2$  Hollow Microspheres with High Surface Roughness and Its Excellent Performance in Catalytic Hydrogen Evolution Reaction. *Chem. Eng. J.* **2017**, *321*, 105–112.
- (147) Yuan, M.; Wang, M.; Lu, P.; Sun, Y.; Dipazir, S.; Zhang, J.; Li, S.; Zhang, G. Tuning Carbon Nanotube-Grafted Core-Shell-Structured Cobalt Selenide@carbon Hybrids for Efficient Oxygen Evolution Reaction. *J. Colloid Interface Sci.* **2019**, *533*, 503–512.
- (148) Liao, M.; Zeng, G.; Luo, T.; Jin, Z.; Wang, Y.; Kou, X.; Xiao, D. Three-Dimensional Coral-like Cobalt Selenide as an Advanced Electrocatalyst for Highly Efficient Oxygen Evolution Reaction. *Electrochim. Acta* **2016**, *194*, 59–66.
- (149) Li, W.; Gao, X.; Xiong, D.; Wei, F.; Song, W. G.; Xu, J.; Liu, L. Hydrothermal Synthesis of Monolithic  $\text{Co}_3\text{Se}_4$  Nanowire Electrodes for Oxygen Evolution and Overall Water Splitting with High Efficiency and Extraordinary Catalytic Stability. *Adv. Energy Mater.* **2017**, *7*, 1–7.
- (150) Masud, J.; Swesi, A. T.; Liyanage, W. P. R.; Nath, M. Cobalt Selenide Nanostructures: An Efficient Bifunctional Catalyst with High Current Density at Low Coverage. *ACS Appl. Mater. Interfaces* **2016**, *8*, 17292–17302.
- (151) Lu, B.; Cao, D.; Wang, P.; Wang, G.; Gao, Y. Oxygen Evolution Reaction on Ni-Substituted  $\text{Co}_3\text{O}_4$  Nanowire Array Electrodes. *Int. J. Hydrogen Energy* **2011**, *36*, 72–78.
- (152) Kanan, M. W.; Nocera, D. G. In Situ Formation of an Oxygen-Evolving Catalyst in Neutral Water Containing Phosphate and  $\text{Co}^{2+}$ . *Science*. **2008**, *321*, 1072–1075.
- (153) Zou, X.; Su, J.; Silva, R.; Goswami, A.; Sathe, B. R.; Asefa, T. Efficient Oxygen Evolution Reaction Catalyzed by Low-Density Ni-Doped  $\text{Co}_3\text{O}_4$  Nanomaterials Derived from Metal-Embedded Graphitic  $\text{C}_3\text{N}_4$ . *Chem. Commun.* **2013**, *49*, 7522–7524.
- (154) Moureaux, F.; Stevens, P.; Chatenet, M. Effect of Lithium and Potassium Cations on the Electrocatalytic Properties of Carbon and Manganese Oxide Electrocatalysts Towards the Oxygen Reduction Reaction in Concentrated Alkaline Electrolyte. *Electrocatalysis* **2013**, *4*, 123–133.
- (155) Han, X.; He, G.; He, Y.; Zhang, J.; Zheng, X.; Li, L.; Zhong, C.; Hu, W.; Deng, Y.; Ma, T. Y. Engineering Catalytic Active Sites on Cobalt Oxide Surface for Enhanced Oxygen Electrocatalysis. *Adv. Energy Mater.* **2018**, *8*, 1702222.

- (156) Liu, Y.; Kelly, T. G.; Chen, J. G.; Mustain, W. E. Metal Carbides as Alternative Electrocatalyst Supports. *ACS Catal.* **2013**, *3*, 1184–1194.
- (157) Danilovic, N.; Subbaraman, R.; Chang, K. C.; Chang, S. H.; Kang, Y. J.; Snyder, J.; Paulikas, A. P.; Strmcnik, D.; Kim, Y. T.; Myers, D.; et al. Activity-Stability Trends for the Oxygen Evolution Reaction on Monometallic Oxides in Acidic Environments. *J. Phys. Chem. Lett.* **2014**, *5*, 2474–2478.
- (158) Zhao, D.; Pi, Y.; Shao, Q.; Feng, Y.; Zhang, Y.; Huang, X. Enhancing Oxygen Evolution Electrocatalysis via the Intimate Hydroxide-Oxide Interface. *ACS Nano* **2018**, *12*, 6245–6251.
- (159) Zhou, T.; Cao, Z.; Zhang, P.; Ma, H.; Gao, Z.; Wang, H.; Lu, Y.; He, J.; Zhao, Y. Transition Metal Ions Regulated Oxygen Evolution Reaction Performance of Ni-Based Hydroxides Hierarchical Nanoarrays. *Sci. Rep.* **2017**, *7*, 46154.
- (160) Lyons, M. E. G.; Brandon, M. P. The Oxygen Evolution Reaction on Passive Oxide Covered Transition Metal Electrodes in Aqueous Alkaline Solution. Part I - Nickel. *Int. J. Electrochem. Sci.* **2008**, *3*, 1425–1462.
- (161) Lyons, M.; Brandon, M. The Oxygen Evolution Reaction on Passive Oxide Covered Transition Metal Electrodes in Alkaline Solution. Part II - Cobalt. *Int. J. Electrochem. Sci.* **2008**, *3*, 1425–1462.
- (162) He, X.; Yin, F.; Li, G. A Co/Metal-Organic-Framework Bifunctional Electrocatalyst: The Effect of the Surface Cobalt Oxidation State on Oxygen Evolution/Reduction Reactions in an Alkaline Electrolyte. *Int. J. Hydrogen Energy* **2015**, *40*, 9713–9722.
- (163) Surendranath, Y.; Dincă, M.; Stich, T. A.; Britt, R. D.; Stoian, S. A.; McAlpin, J. G.; Nocera, D. G.; Casey, W. H. EPR Evidence for Co(IV) Species Produced During Water Oxidation at Neutral pH. *J. Am. Chem. Soc.* **2010**, *132*, 6882–6883.
- (164) Lyons, M. The Oxygen Evolution Reaction on Passive Oxide Covered Transition Metal Electrodes in Alkaline Solution. Part III-Iron. *Int. J. Electrochem. Sci.* **2008**, *3*, 1463–1503.
- (165) Burke, M. S.; Kast, M. G.; Trotochaud, L.; Smith, A. M.; Boettcher, S. W. Cobalt-Iron (Oxy)Hydroxide Oxygen Evolution Electrocatalysts: The Role of Structure and Composition on Activity, Stability, and Mechanism. *J. Am. Chem. Soc.* **2015**, *137*, 3638–3648.
- (166) Kötz, R.; Stucki, S. Stabilization of RuO<sub>2</sub> by IrO<sub>2</sub> for anodic oxygen evolution in acid media. *Electrochim. Acta* **1986**, *31*, 1311–1316.
- (167) Wang, Z.; Li, J.; Tian, X.; Wang, X.; Yu, Y.; Owusu, K. A.; He, L.; Mai, L. Porous Nickel-Iron Selenide Nanosheets as Highly Efficient Electrocatalysts for Oxygen Evolution Reaction. *ACS Appl. Mater. Interfaces* **2016**, *8*, 19386–19392.

- (168) Nai, J.; Lu, Y.; Yu, L.; Wang, X.; Lou, X. W. D. Formation of Ni–Fe Mixed Diselenide Nanocages as a Superior Oxygen Evolution Electrocatalyst. *Adv. Mater.* **2017**, *29*, 1703870.
- (169) Umapathi, S.; Masud, J.; Swesi, A. T.; Nath, M.; Umapathi, S.; Masud, J.; Swesi, A. T.; Nath, M. FeNi<sub>2</sub>Se<sub>4</sub>–Reduced Graphene Oxide Nanocomposite: Enhancing Bifunctional Electrocatalytic Activity for Oxygen Evolution and Reduction through Synergistic Effects. *Adv. Sustain. Syst.* **2017**, *1*, 1700086.
- (170) Shinde, D. V.; De Trizio, L.; Dang, Z.; Prato, M.; Gaspari, R.; Manna, L. Hollow and Porous Nickel Cobalt Perselenide Nanostructured Microparticles for Enhanced Electrocatalytic Oxygen Evolution. *Chem. Mater.* **2017**, *29*, 7032–7041.
- (171) Xu, X.; Liang, H.; Ming, F.; Qi, Z.; Xie, Y.; Wang, Z. Prussian Blue Analogues Derived Penroseite (Ni,Co)Se<sub>2</sub> Nanocages Anchored on 3D Graphene Aerogel for Efficient Water Splitting. *ACS Catal.* **2017**, *7*, 6394–6399.
- (172) Akbar, K.; Jeon, J. H.; Kim, M.; Jeong, J.; Yi, Y.; Chun, S. H. Bifunctional Electrodeposited 3D NiCoSe<sub>2</sub>/Nickel Foam Electrocatalysts for Its Applications in Enhanced Oxygen Evolution Reaction and for Hydrazine Oxidation. *ACS Sustain. Chem. Eng.* **2018**, *6*, 7735–7742.
- (173) Fang, Z.; Peng, L.; Lv, H.; Zhu, Y.; Yan, C.; Wang, S.; Kalyani, P.; Wu, X.; Yu, G. Metallic Transition Metal Selenide Holey Nanosheets for Efficient Oxygen Evolution Electrocatalysis. *ACS Nano* **2017**, *11*, 9550–9557.
- (174) Anantharaj, S.; Ede, S. R.; Sakthikumar, K.; Karthick, K.; Mishra, S.; Kundu, S. Recent Trends and Perspectives in Electrochemical Water Splitting with an Emphasis on Sulfide, Selenide, and Phosphide Catalysts of Fe, Co, and Ni: A Review. *ACS Catal.*, **2016**, *6*, 8069–8097
- (175) Cao, X.; Hong, Y.; Zhang, N.; Chen, Q.; Masud, J.; Zaeem, M. A.; Nath, M. Phase Exploration and Identification of Multinary Transition-Metal Selenides as High-Efficiency Oxygen Evolution Electrocatalysts through Combinatorial Electrodeposition. *ACS Catal.* **2018**, 8273–8289.
- (176) Qin, F.; Zhao, Z.; Alam, M. K.; Ni, Y.; Robles-Hernandez, F.; Yu, L.; Chen, S.; Ren, Z.; Wang, Z.; Bao, J. Trimetallic NiFeMo for Overall Electrochemical Water Splitting with a Low Cell Voltage. *ACS Energy Lett.* **2018**, *3*, 546–554.
- (177) Cao, X.; Johnson, E.; Nath, M. Identifying High-Efficiency Oxygen Evolution Electrocatalysts from Co–Ni–Cu Based Selenides through Combinatorial Electrodeposition. *J. Mater. Chem. A*, **2019**, *7*, 9877–9889.
- (178) Chi, J. Q.; Yan, K. L.; Xiao, Z.; Dong, B.; Shang, X.; Gao, W. K.; Li, X.; Chai, Y. M.; Liu, C. G. Trimetallic Ni–Fe–Co Selenides Nanoparticles Supported on Carbon Fiber Cloth as Efficient Electrocatalyst for Oxygen Evolution Reaction. *Int. J. Hydrogen Energy* **2017**, *42*, 20599–20607.

- (179) Maier, W. F. Combinatorial Chemistry—Challenge and Chance for the Development of New Catalysts and Materials. *Angew. Chemie Int. Ed.* **1999**, *38*, 1216–1218.
- (180) Andrus, M. B.; Turner, T. M.; Asgari, D.; Li, W. The Synthesis and Evaluation of a Solution-Phase Indexed Combinatorial Library of Non-Natural Polyenes for Multidrug Resistance Reversal. *J. Org. Chem.* **1999**, *64*, 2978–2979.
- (181) Lew, A.; Krutzik, P. O.; Hart, M. E.; Chamberlin, A. R. Increasing Rates of Reaction: Microwave-Assisted Organic Synthesis for Combinatorial Chemistry. *J. Comb. Chem.* **2001**, *4*, 95–105.
- (182) Discovery and Optimization of Heterogeneous Catalysts by Using Combinatorial Chemistry. *Angew. Chem. Int. Ed.* **1999**, *38*, 791–795.
- (183) Mao, S. S.; Burrows, P. E. Combinatorial Screening of Thin Film Materials: An Overview. *J. Materiomics* **2015**, *1*, 85–91.
- (184) Wang, J. Identification of a Blue Photoluminescent Composite Material from a Combinatorial Library. *Science* **1998**, *279*, 1712–1714.
- (185) Wessler, B.; Jéhanno, V.; Rossner, W.; Maier, W. F. Combinatorial Synthesis of Thin Film Libraries for Microwave Dielectrics. *Appl. Surf. Sci.* **2004**, *223*, 30–34.
- (186) Maxwell, I. E. Connecting with Catalysis. *Nature* **1998**, *394*, 325–326.
- (187) Schlögl, R. Combinatorial Chemistry in Heterogeneous Catalysis : A New Scientific Approach or “the King’s New Clothes”? *Angew. Chem. Int. Ed.* **1998**, *37*, 2333–2336.
- (188) Jin, K.; Suchoski, R.; Fackler, S.; Zhang, Y.; Pan, X.; Greene, R. L.; Takeuchi, I. Combinatorial Search of Superconductivity in Fe-B Composition Spreads. *APL Mater.* **2013**, *1*, 042101.
- (189) Park, W. B.; Singh, S. P.; Yoon, C.; Sohn, K.-S. Combinatorial Chemistry of Oxynitride Phosphors and Discovery of a Novel Phosphor for Use in Light Emitting Diodes,  $\text{Ca}_{1.5}\text{Ba}_{0.5}\text{Si}_5\text{N}_6\text{O}_3:\text{Eu}^{2+}$ . *J. Mater. Chem. C* **2013**, *1*, 1832–1839.
- (190) Zhang, Y.; Gong, X.; Zhang, H.; Larock, R. C.; Yeung, E. S. Combinatorial Screening of Homogeneous Catalysis and Reaction Optimization Based on Multiplexed Capillary Electrophoresis. *J. Comb. Chem.* **2000**, *2*, 450–452.
- (191) Guerin, S.; Hayden, B. E. Physical Vapor Deposition Method for the High-Throughput Synthesis of Solid-State Material Libraries. *J. Comb. Chem.* **2006**, *8*, 66–73.
- (192) Fukumoto, H.; Muramatsu, Y.; Yamamoto, T.; Yamaguchi, J.; Itaka, K.; Koinuma, H. Combinatorial Physical Vapor Deposition of  $\pi$ -Conjugated Organic Thin Film Libraries. *Macromol. Rapid Commun.* **2004**, *25*, 196–203.

- (193) Kim, D. H.; Bi, L.; Aimon, N. M.; Jiang, P.; Dionne, G. F.; Ross, C. A. Combinatorial Pulsed Laser Deposition of Fe, Cr, Mn, and Ni-Substituted SrTiO<sub>3</sub> Films on Si Substrates. *ACS Comb. Sci.* **2012**, *14*, 179–190.
- (194) Akporiaye, D. E.; Dahl, I. M.; Karlsson, A.; Wendelbo, R. Combinatorial Approach to the Hydrothermal Synthesis of Zeolites. *Angew. Chem. Int. Ed.* **1998**, *37*, 609–611.
- (195) Miller, E.; Phillippi, J.; Fisher, G.; Campbell, P.; Walker, L.; Weiss, L. Inkjet Printing of Growth Factor Concentration Gradients and Combinatorial Arrays Immobilized on Biologically-Relevant Substrates. *Comb. Chem. High Throughput Screen.* **2009**, *12*, 604–618.
- (196) Tekin, E.; de Gans, B.-J.; Schubert, U. S. Ink-Jet Printing of Polymers ? From Single Dots to Thin Film Libraries. *J. Mater. Chem.* **2004**, *14*, 2627–2632.
- (197) Grill, C. D.; Kollender, J. P.; Hassel, A. W. Combinatorial Electrodeposition of Cobalt-Copper Material Libraries. *J. Electrochem. Soc.* **2016**, *163*, D3069–D3075.
- (198) Beattie, S. D.; Dahn, J. R. Combinatorial Electrodeposition of Ternary Cu–Sn–Zn Alloys. *J. Electrochem. Soc.* **2005**, *152*, C542–C542.
- (199) Danielson, E.; Golden, J.; McFarland, E. A Combinatorial Approach to the Discovery and Optimization of Luminescent Materials. *Nature* **1997**, *389*, 2331–2333.
- (200) Smith, R. D. L.; Preot, M. S.; Fagan, R. D.; Trudel, S.; Berlinguette, C. P. Water Oxidation Catalysis: Electrocatalytic Response to Metal Stoichiometry in Amorphous Metal Oxide Films Containing Iron, Cobalt, and Nickel. *J. Am. Chem. Soc.* **2013**, *135*, 11580–11586.
- (201) Takeuchi, I.; Lauterbach, J.; Fasolka, M. J. Combinatorial Materials Synthesis. *Mater. Today* **2005**, *8*, 18–26.
- (202) Chen, G.; Delafuente, D. A.; Sarangapani, S.; Mallouk, T. E. Combinatorial Discovery of Bifunctional Oxygen Reduction - Water Oxidation Electrocatalysts for Regenerative Fuel Cells. *Catal. Today* **2001**, *67*, 341–355.
- (203) Reddington, E. Combinatorial Electrochemistry: A Highly Parallel, Optical Screening Method for Discovery of Better Electrocatalysts. *Science*. **1998**, *280*, 1735–1737.
- (204) Rowley, J. G., Do, T. D., Cleary, D. A. and Parkinson, B. A., “Combinatorial Discovery Through a Distributed Outreach Program: Investigation of the Photoelectrolysis Activity of p-type Fe, Cr, Al Oxides”, *Applied Materials and Interfaces*, **2014**, *6*, 9046–9052.
- (205) Guerin, S.; Hayden, B. E.; Lee, C. E.; Mormiche, C.; Owen, J. R.; Russell, A. E.; Theobald, B.; Thompson, D. Combinatorial Electrochemical Screening of Fuel Cell Electrocatalysts. *J. Comb. Chem.* **2004**, *6*, 149–158.

- (206) Dokoutchaev, A. G.; Abdelrazzaq, F.; Thompson, M. E.; Willson, J.; Chang, C.; Bocarsly, A. Multicomponent Electrodes for Water Oxidation: From Combinatorial to Individual Electrode Study. *Chem. Mater.* **2002**, *14*, 3343–3348.
- (207) Seley, D.; Ayers, K.; Parkinson, B. A. Combinatorial Search for Improved Metal Oxide Oxygen Evolution Electrocatalysts in Acidic Electrolytes. *ACS Comb. Sci.* **2013**, *15*, 82–89.
- (208) Haber, J. A.; Cai, Y.; Jung, S.; Xiang, C.; Mitrovic, S.; Jin, J.; Bell, A. T.; Gregoire, J. M. Discovering Ce-Rich Oxygen Evolution Catalysts, from High Throughput Screening to Water Electrolysis. *Energy Environ. Sci.* **2014**, *7*, 682–688.
- (209) Shinde, A.; Guevarra, D.; Liu, G.; Sharp, I. D.; Toma, F. M.; Gregoire, J. M.; Haber, J. A. Discovery of Fe-Ce Oxide/BiVO<sub>4</sub> Photoanodes through Combinatorial Exploration of Ni-Fe-Co-Ce Oxide Coatings. *ACS Appl. Mater. Interfaces* **2016**, *8*, 23696–23705.

## VITA

Xi Cao was born in Qiqihaer, Heilongjiang, P. R. China. She then went to Heilongjiang University in Harbin, Heilongjiang. She obtained her Bachelor of Science degree in Applied Chemistry in July 2013 from Heilongjiang University. In August 2014, she joined in the Chemistry Department in Missouri University of Science and Technology. In the spring of 2015, she started her research in Dr. Manashi Nath's group working on designing novel high efficiency mixed transition metal selenide based OER electrocatalysts as well as conducting DFT calculations for surface properties study. During her PhD, she was awarded as outstanding Teaching Assistant in Chemistry Department in 2017, 2018 and 2019. She received an outstanding graduate research award in Chemistry Department in 2019. She received her PhD in Chemistry from Missouri University of Science and Technology in July 2019.